An Experimental Study of Turbulence by Phase-Contrast Imaging in the DIII–D Tokamak

by

Stefano Coda

Laurea, Physics
Università di Pisa, 1986

SUBMITTED TO THE DEPARTMENT OF PHYSICS IN PARTIAL FULFILLMENT OF THE REQUIREMENTS FOR THE DEGREE OF

DOCTOR OF PHILOSOPHY
AT THE
MASSACHUSETTS INSTITUTE OF TECHNOLOGY

FEBRUARY 1997

Signature of Author: _____

Department of Physics
February 7, 1997

Certified by: _____

Miklos Porkolab
Professor of Physics
Thesis Supervisor

Accepted by: _____

George F. Koster
Professor of Physics
Chairman, Departmental Graduate Committee

An Experimental Study of Turbulence by Phase-Contrast Imaging in the DIII–D Tokamak

by

Stefano Coda

Submitted to the Department of Physics
on February 7, 1997 in Partial Fulfillment of the
Requirements for the Degree of Doctor of Philosophy in
Physics

ABSTRACT

A CO_2-laser imaging system employing the Zernike phase-contrast technique was designed, built, installed, and operated on the DIII–D tokamak. This system measures the line integrals of plasma density fluctuations along 16 vertical chords at the outer edge of the tokamak ($0.85 < r/a < 1.15$), with radial resolution adjustable from 0.5 to 0.04 cm, sensitivity 10^9 cm^{-3}, and bandwidth 20 MHz. The measurement is primarily sensitive to radial wave vectors, as confirmed by extensive analytical and numerical modeling, and is essentially immune to Doppler shifts from plasma rotation; thus, frequency spectra are measured in the plasma frame. Radial-wave-number spectra in the range 1–16 cm^{-1} are calculated from spatial correlation analysis. Mechanical vibrations are damped by a novel dual-axis focal-spot feedback stabilization system. The theoretical treatment of scattering and imaging techniques was extended to finite-frequency fluctuations in the Rytov approximation. An extensive comparative analysis of the properties of phase-contrast imaging (PCI) and of other imaging and scintillation techniques was also carried out.

Studies of edge turbulence were performed. The radial-wave-number spectrum peaks at finite wave numbers, both positive and negative. This first observation of radial modes is in agreement with recent predictions from theoretical and numerical work. The dependence of the correlation length and peak wave number on plasma parameters and on the frequency was studied in detail. Frequency spectra typically obey an inverse square law, consistent with a Lorentzian distribution.

At the transition from L to H mode the amplitude and correlation length of the turbulence decrease, while the decorrelation time remains approximately constant. The Biglari-Diamond-Terry shear-decorrelation criterion was verified quantitatively; theoretical scaling laws for the correlation parameters were also tested. The turbulence amplitude follows a mixing-length scaling in L mode only: the lower level seen in H mode may indicate a weaker turbulence regime. The fluctuation content of Edge Localized Modes (ELMs) was thoroughly characterized, and systematic differences between type-I and type-III ELMs were discovered.

Future applications of PCI, including crossed-beam localization and heterodyne radio-frequency-wave detection, are also discussed.

Thesis Supervisor: Miklos Porkolab
Title: Professor of Physics

Ad Andreina
ed Alessandro

E pensare che questa farsa durerà ancora miliardi di anni, dicono.

Ennio Flaiano.

Acknowledgments

Over the several years spanned by this project, I have benefited from my interactions with a great many people. I owe an enormous debt of gratitude towards all of them, which can hardly be expressed properly by a few words of acknowledgment. Perhaps the best tribute I can offer is to pass on their legacy of inspired mentoring to the students I might encounter in my career.

I am especially grateful to my thesis advisor, Professor Miklos Porkolab, for trusting me with an off-campus project and for standing by it through some very difficult years for fusion research in the U.S.. He has believed in me to the very end and has always understood my desire for completeness, in spite of the maddening delays that it caused. His love of physics had a profound effect on me and allowed me to rediscover my own passion for it in times of doubt and frustration. Others before me have commended him on his candid and direct manner; but perhaps the most remarkable thing about him is how good a scientist he is: I have been continually amazed by his quick insights into the problems that I was facing in my research. I want to thank him also for his continuous encouragement, especially along the lines of "so write it up already", which has narrowly deprived me of the dubious distinction of authoring the first thesis of the third millennium.

My lack of experience in the laboratory would have made a thesis work away from campus very difficult, had I not had help and support from physicists at General Atomics. In this, I must single out Dr. Tom Carlstrom, an expert in CO_2 lasers and optical systems, who provided technical assistance and advice from the very beginning, thereby giving me a sense of security that I sorely needed. Tom was always willing to spend time with me, to answer my questions at length, and to back up my tests in the laboratory with his considerable experience. It is an added fortune that we also shared a common interest in music, which made for some pleasant extracurricular activities.

Dr. Henri Weisen of the CRPP in Lausanne deserves my heartfelt thanks for providing me with essential information and advice in the early stages of project design and development. Henri developed the first phase-contrast imaging system on a tokamak (the TCA device), and our application of the technique to DIII-D stems directly from a seminar that he gave at MIT. I also benefited greatly from my subsequent visit to Lausanne, where I had the opportunity to study his apparatus in detail. I also wish to thank the TCA group for lending me several phase plates for my initial tests.

This thesis would not have been possible without the participation of Dick Phelps, a mechanical engineer who was assigned to the project by General Atomics. I consider this a very fortunate choice: Dick was instrumental in keeping the project on track and did all he could to ensure that it would be completed on time, including working late hours with me to install equipment. His "can-do" attitude had a strong influence on my own way of planning and thinking about projects.

I wish to thank Professor Bruno Coppi, who was initially responsible for persuading me to choose the field of plasma physics and for giving me the opportunity to go to MIT. I learned much from him in the several courses that I attended and in my conversations with him over the last few years. His encouragement of my work has been steadfast. I am also grateful to Professor John Belcher for serving on my thesis committee and for giving me useful advice in these last few months.

My work at General Atomics was supervised first by Dr. Ron Prater and later by Dr. Keith Burrell. I offer my thanks to both of them for their staunch support and for giving me a freedom of action that is nothing short of remarkable for a visiting graduate student. I have interacted with Keith also directly in my research, since he is one of the foremost experts in edge and H–mode physics. Through this interaction and simply by observing him, I have learned a gret deal about organizing my research and collaborating with other physicists, and about communicating my results to the community.

I count myself fortunate for having worked at General Atomics. The difficulties of working on a large project such as DIII–D were overshadowed by an exceptionally pleasant working environment and by the friendliness and helpfulness of the many people with whom I interacted. It is surely to their credit that a private company such as G.A. came to feel entirely like a university research facility. I would recommend this experience wholeheartedly to any student.

Although the people of G.A. to whom I feel indebted are too numerous to mention individually, I would like to name a few. Dr. Tom Simonen, director of the DIII–D project, and Drs. Dick Freeman and Ron Stambaugh, the division leaders under whom I worked, deserve thanks for approving this venture and believing in it: G.A. provided most of the financial support for this thesis work. Dr. Matt Mayberry supervised and guided my initial work and also helped design and build some of the mechanical structures. Drs. Bob Pinsker and Craig Petty also provided helpful advice and assisted me in testing some of the electronic components. A large fraction of the data that are discussed in this thesis were collected during experiments organized and directed by Drs. Tom Carlstrom, Punit Gohil, Rick Moyer, and Jon Watkins, to all of whom I am very grateful. I also wish to acknowledge valuable interactions with the physicists in the H–mode and fluctuation group, namely Drs. Rich Groebner, Edward Doyle, Curt Rettig, Terry Rhodes, and Dan Thomas, in addition to Drs. Burrell and Moyer; I am also obliged for their generously allowing me to use their data on several occasions. To all others, including the DIII–D Operations and Neutral-Beams groups that made these experiments possible, I wish to express my appreciation.

I am thankful to Drs. Roger Durst and Ray Fonck of the University of Wisconsin for sharing their ART maximum-entropy algorithm with me.

In the recent past I have had several conversations and discussions with theorists both in the U.S. and abroad, which allowed me to achieve a better understanding of their work and to gain a deeper insight in the significance of my own data. I want to thank in particular Professor Pat Diamond for his interest in my results and for his many insightful observations and recommendations; I also benefited from attending

his course on plasma turbulence. Drs. Ben Carreras, Taik Soo Hahm, Gary Staebler, and Ron Waltz deserve mention for their patience in answering my questions and for their commendable interest in experimental results. I am indebted also to Drs. Ron Cohen and Xueqiao Xu for valuable discussions and for sharing results from their computer simulations. I offer additional thanks for stimulating exchanges to Drs. Mike Beer, Bill Dorland, Xavier Garbet, Nathan Mattor, and Scott Parker, and to Professor Jim Drake.

I am beholden to the people of Colombia for growing their Excelso beans, without which this thesis would *definitely* not have been possible, and to the people at Visa for lending me the money with which to buy those beans.

Even in the life of a scientist there is room for miracles. Your crossing my path, Lisa, was a miracle. Your patience and support have been as wonderful as they have been undeserved. You selflessly gave me those moments of peace and serenity that allowed me to finally complete this endeavor, and asked for nothing in return. I can never repay you.

This work is a tribute to my long-suffering parents, both of them people of science, who gave me both the genes and the inspiration to follow this unsung muse. Their support has been unwavering, even when my pursuits took me halfway around the planet. As I write this, they have not seen me in nearly two years. To them I dedicate this thesis.

Contents

	Abstract	**3**
	Acknowledgments	**7**
	Contents	**11**
	Chapter 1. Introduction	**15**
1.1	Motivation: Physics Aspects	16
1.2	Motivation: Instrumental Aspects	26
1.3	Synopsis of Experimental Results	28
1.4	Thesis Outline	31
1.5	Units and Dimensions	33
	Chapter 2. Experimental Technique	**34**
2.1	The Physics of Light-Plasma Interaction	35
2.2	Integration of the Wave Equation	39
2.3	The Born Approximation	42
2.4	The Rytov Approximation	46
2.5	Diffraction from an Aperture	49
2.6	Scattering of a Gaussian Beam	53
2.7	Far-Field Detection	56
2.8	Near- and Intermediate-Field Detection	61
2.9	Overview of Collective Small-Angle Scattering Techniques	70
2.10	The Phase-Contrast Technique	75
2.11	Response Properties of the Phase-Contrast Technique	81
2.12	Signal-to-Noise Ratio	94
2.13	A Comparative Analysis of Internal-Reference Techniques	101
2.14	Calibration Techniques	110
	Chapter 3. Experimental Apparatus	**115**
3.1	The DIII–D Tokamak	116
3.2	Geometry of the Measurement	121
3.3	Experimental Setup	125
3.4	Optical Design	134
3.5	Feedback Vibration-Control System	140
3.6	Electronics and Data Acquisition	162
3.7	Response Properties and Sensitivity	168
3.8	Tests and Calibrations	169
3.9	Data-Analysis Techniques	179

Chapter 4. Modeling of the Measurement 182

4.1 The Integral Inversion Problem 183
4.2 The Correlation Structure of Plasma Fluctuations 185
4.3 A Model of Plasma Turbulence 189
4.4 Approximate Analytical Modeling 195
4.5 Numerical Modeling 204

Chapter 5. Fluctuation Measurements in the DIII–D Tokamak 216

5.1 Review of Turbulence Measurements in Tokamaks 218
5.2 Overview of Recent Turbulence Measurements in DIII–D 228
5.3 PCI Fluctuation Measurements in DIII–D: Generalities 229
5.4 Frequency- and Time-Domain Analysis 232
5.5 Spatial Correlations and Wave-Number Spectra 240
5.6 Fluctuation Amplitude 265
5.7 The Probability Distribution Function 270
5.8 The L– to H–Mode Transition 274
5.9 Slow L–H Transitions 288
5.10 The Evolution of Turbulence During a Plasma Discharge 292
5.11 Edge Localized Modes 297
5.12 Transient Phenomena 310
5.13 Concluding Remarks 314

Chapter 6. Discussion of Experimental Results 316

6.1 Review of Some Aspects of Tokamak Turbulence Theory 318
6.2 The Physics of Radial Modes 333
6.3 Convective Cells 340
6.4 Density-Fluctuation Well in the SOL in H Mode 343
6.5 Frequency Spectra and Time-Delayed Correlation Function 344
6.6 Spatial Correlations and Wave-Number Spectra 348
6.7 Fluctuation Amplitude and Test of the Mixing-Length Scaling 352
6.8 Self-Organized Criticality 357
6.9 Estimates of Turbulent Diffusivity 359
6.10 Tests of Theories of the L–H Transition 360
6.11 Slow L–H Transitions 365
6.12 Edge Localized Modes and Other Transient Events 366
6.13 Conclusions 368

Chapter 7. Other Applications of Phase-Contrast Imaging 370

7.1 Heterodyne Phase-Contrast Imaging 370
7.2 Localization of the Measurement by Symmetry Considerations 374

7.3 Crossed-Beam Correlation Technique 380
7.4 Suggestions for Future Upgrades on DIII–D 395

Chapter 8. Summary and Conclusions 398

8.1 Summary 398
8.2 Suggestions for Future Work 401
8.3 Conclusions 402

Appendix A. Derivation of the Scattering Equation 403

Appendix B. Evaluation of Diffraction Effects 406

Appendix C. Derivation of the Scattering Signal in the Rytov Approximation 409

Appendix D. Time-Dependent Geometrical Optics 423

Appendix E. Calculation of an Integral 431

Appendix F. Transfer Function of a Generalized Spatial Filter 432

Appendix G. Density Correlation Function in a Gaussian-Spectrum Model 441

Bibliography 4455

1 Introduction

The physics of thermonuclear plasmas remains largely an empirical and heuristic science in spite of considerable recent progress in theoretical understanding. In the quest for a scientifically successful and economically viable fusion reactor, accurate measurements of the plasma parameters in existing experiments play an essential role. Nowhere is this more evident than in the DIII–D magnetic fusion experiment at General Atomics in San Diego (California), which is one of the leading research enterprises of its kind in the world and one whose experimental results have had and continue to have a profound impact on the ongoing design of the demonstration reactor ITER (International Thermonuclear Experimental Reactor). Accordingly, DIII–D is equipped with an extensive array of state-of-the-art measuring instruments, or *diagnostics*.

This thesis describes a new phase-contrast imaging (PCI) diagnostic installed on DIII–D for measuring electron density fluctuations. This introductory chapter illustrates the motivation for this experimental effort and summarizes the work contained in the thesis. The motivation has two distinct origins. Firstly, the plasma physics topics that can be explored with this diagnostic are specifically relevant to the DIII–D research program and to fusion: this is discussed in §1.1, which also provides a brief introduction to the DIII–D device and magnetic fusion in general. Secondly, the diagnostic technique is of general interest, reaching outside the realm of plasma physics: this motivated not only the experimental development of the diagnostic but also a thorough theoretical characterization of its properties, as described in §1.2.

A synopsis of the physics results, which constitute the most important outcome of the work described in this thesis, is found in §1.3. A general summary of the thesis is contained in §1.4, where particular care is taken to identify the sections that describe original research, as opposed to those in which previously published material is reviewed. Finally, a brief comment on physical units is offered in §1.5.

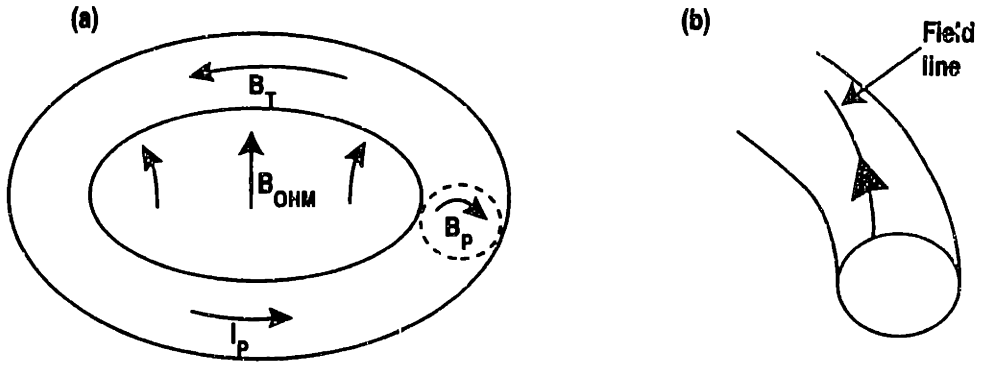

Fig. 1.1 (a) Toroidal magnetic field B_T and poloidal magnetic field B_p generated by toroidal current I_p. The current is generated inductively by a variable vertical magnetic field B_{OHM}; (b) combination of B_T and B_p results in helical field lines.

1.1 Motivation: Physics Aspects

The short-range nature of the strong nuclear force responsible for fusion reactions is the source of a fundamental difficulty in the utilization of fusion energy: the potential barrier of the weaker, but longer-range electrostatic force between two nuclei must be overcome before fusion can occur. In *thermonuclear* fusion, the necessary energy is supplied to a plasma of ions and electrons in the form of heat. As the temperature of the plasma is increased, the reaction rate, and consequently the energy release rate, increases also, up to a maximum point. The reaction rate increases also with density, as can be expected intuitively.[1]

Since the operating temperatures in thermonuclear fusion are on the order of several keV, the plasma would instantaneously lose its energy if it came in contact with material walls. Thus, non-contact containment techniques are a necessity. In *magnetic fusion*, the plasma is confined by means of magnetic forces. The most successful configuration in magnetic fusion is the tokamak,[2] a toroidal device with a toroidally circulating current and a toroidal magnetic field. The toroidal current is essentially self-confining, as it generates a poloidal magnetic field that exerts an inward force on the plasma. The larger, externally applied toroidal magnetic field (see Fig. 1.1) is necessary for stability considerations.

In a tokamak, the initial current is driven by the toroidal electric field generated inductively by a variable vertical magnetic field, as shown in Fig. 1.1; thus, in the absence of other sources of current, a tokamak discharge is always limited in time by the maximum magnetic flux achievable. The desirability of steady-state operations has therefore prompted the exploration of noninductive current-drive schemes, based on the injection of neutral beams, rf waves, or microwaves.[3] These methods are widely used also for heating the plasma, complementing the Ohmic heating effect that results from the plasma's finite resistivity.

An equal mixture of deuterium (D) and tritium (T) is generally envisioned as the optimal fuel for the first demonstration reactor, owing to the relatively large cross section of the D–T reaction. However, a majority of experiments are still conducted

with deuterium and hydrogen, owing to their greater availability and tractability in comparison with tritium. Many plasma physics issues either are independent of the atomic number or have a known dependence on it, allowing ready extrapolation between isotopes.

The edge of a magnetically confined plasma can be defined by a material limiter or by a magnetic divertor. In the latter case the magnetic field lines are designed to exhaust the diffusing plasma into a separate chamber, thus reducing the direct plasma-wall interaction and the consequent influx of impurities. Impurities of high atomic number are undesirable since bremsstrahlung radiation losses are proportional to Z^2.

The DIII–D tokamak[4] will be described in some detail in §3.1. The main focus of the DIII–D experimental program[5] is the investigation of advanced divertor configurations and advanced tokamak modes of operation by means of noninductive current drive.

(a) Plasma Turbulence

In a reactor, the fusion power must exceed the power supplied to the plasma, which, in steady-state conditions, must balance the power lost through radiation and energy transport. Consequently, one of the basic goals of tokamak research has been the containment of such losses to their minimum irreducible values. The inescapable rate of energy transport caused by Coulomb collisions is known in toroidal geometry as *neoclassical transport.*[6] A universal result of tokamak experiments is that while the rate of ion thermal transport is similar to the neoclassical prediction, electron thermal transport is substantially higher.[7,8] In addition, plasmas with auxiliary (non-Ohmic) heating exhibit even higher transport rates than their Ohmic counterparts. The poor confinement of auxiliary-heated discharges is known as the low mode (L mode) of confinement.

This *anomalous transport* has long been believed to be caused by microinstabilities.[9–11] These can be broadly defined as instabilities that cannot be predicted by a fluid, or magnetohydrodynamic (MHD), description of a plasma, but require a kinetic analysis instead. A multitude of microinstabilities can be invoked as the cause of anomalous transport. The energy for driving these unstable modes can originate either from the non-Maxwellian nature of the distribution function in velocity space or from the spatial gradients of the density or temperature of a locally Maxwellian distribution. The fluctuations in the electric and magnetic fields caused by microinstabilities lead in turn to fluctuations in the velocities and positions of the plasma particles, and thus to transport.

The connection between instabilities and transport has been a strong motivation for the development of diagnostics to measure fluctuations in tokamaks. The earliest measurements were carried out with magnetic coils located outside the tokamak, which provided information on low-frequency oscillations of the poloidal magnetic field.[12] Soft-x-ray detectors were also employed early on to investigate fluctuations in

the plasma emission, which depends on temperature, density, and effective charge.[13] Although these types of measurements have been applied more recently to the study of microturbulence, they were initially used mostly to determine the structure of global MHD instabilities, i.e., unstable modes that can be described by a fluid treatment of the plasma. External coil arrays and soft-x-ray detectors remain standard diagnostics in a majority of tokamaks today.

The first measurements of microturbulence were carried out in the mid-1970's in the ST[14] and ATC[15] tokamaks, using the technique of microwave scattering, which is sensitive to fluctuations in the electron density. Soon afterwards, a scattering diagnostic employing a CO_2 laser[16] was added in ATC. The results of these early investigations displayed many of the features that were to be later observed in many other tokamaks. The fluctuations were broadband both in frequency and in wave number; in addition, the frequency spectrum at a single wave number was also broadband.[15,16] This type of behavior is indicative of strong nonlinear coupling between individual modes, resulting in a strongly turbulent plasma.

Measurements of density fluctuations by microwave scattering continued in TFR,[17] PLT,[18] PDX,[19] and TFTR,[20] while CO_2-laser scattering at the 10.6-μm wavelength was employed in Alcator A,[21] TFR,[22] PDX,[19] Alcator C,[23] and other devices. Scattering systems using far-infrared wavelengths were developed initially at UCLA for the Microtor tokamak;[24] similar diagnostics were then installed on the WT-1 and WT-2 tokamaks[25] at Kyoto University, followed by TEXT,[26] DIII–D,[27] and ASDEX,[28] and others.

Scattering measurements provide a representation of the fluctuations in wave-number space; in most cases data at only one wave number are collected in a given plasma discharge. The main limitation of scattering is the lack of spatial resolution, especially at long wavelengths. In addition, the practical need to separate the scattered beam from the incident beam effectively sets an upper limit to the wavelengths that can be resolved; such limit, especially in the CO_2-laser case, is often smaller than the fundamental physical limit given by the width of the beam.[29]

The need to overcome the limitations of scattering has motivated the recent development of imaging techniques, which provide a direct representation of the fluctuations in real space. To this family belong the scintillation interferometer of LT-4[30] and the phase-contrast imaging system of TCA[31]. The phase-contrast imaging technique was chosen for the work described in this thesis.

Another alternative to scattering is offered by various types of material probes,[32] which present the advantage of providing a localized measurement. Magnetic probes are used to measure magnetic field fluctuations. Langmuir probes can measure fluctuations both in density and in electric field and potential; in addition, they can measure the average values of these quantities and of the electron temperature. Estimates of crosscorrelations between the fluctuating components of these different physical quantities can provide direct information on transport. The primary disadvantage of probes is that they cannot withstand the heat loads to which they would be subjected in the core of a discharge and thus are limited to the cooler edge re-

gion. Another potential problem of Langmuir probes is the perturbative nature of the measurement; indeed, an understanding of the perturbative effects of the probe is an integral part of the data interpretation technique.[32] However, tests have been performed in several experiments[33] to prove that the probe did not significantly affect the general properties of the turbulence. Given the local nature of the measurement, an array of probes is necessary to reconstruct the wave-number spectrum and to infer the correlation properies of the turbulence.

A minimal history of probes in tokamaks must mention the magnetic fluctuation measurements performed in T-4,[34] PLT,[35] and ISX-B,[36] and the Langmuir probes installed on Macrotor,[37] the Caltech Research Tokamak,[38] and TEXT.[39] The density fluctuations in the Caltech Research Tokamak were also found to be highly correlated with fluctuations in visible-light emission in the H_α line.[33]

A more recent diagnostic development has been the application of reflectometry to the study of density fluctuations. This technique is based on the reflection of a microwave beam from a location of given plasma density and magnetic field, corresponding to an index of refraction of zero. When applied to the study of fluctuations, reflectometry permits to localize the measurement to a narrow region near the reflecting layer.[40] Combined with an independent knowledge of the density profile, the measurement has the potential for affording good spatial resolution without being restricted to the edge and without perturbing the plasma, as in the case of probes. The reflectometry technique has been employed in several tokamaks, including TFR,[41] DIII–D,[42] and TFTR.[43] As in the case of probes, no information can be gained on the wave-number spectrum unless multiple reflectometers are used. The method of correlation reflectometry[44] uses two microwave sources at slightly different frequencies to infer the correlation properties of the turbulence. This technique, which has been applied to JET,[45] DIII–D,[46] and TFTR,[47] is not immune to problems and is currently an object of study and debate.[48] In the case of large fluctuation amplitudes, a reliable measurement of the correlation lengths may be possible only with the aid of an imaging configuration.[49]

The latest addition to the family of fluctuation diagnostics is beam emission spectroscopy (BES).[50] This technique measures fluctuations in the fluorescence of excited atoms in a neutral beam traversing the plasma; from this measurement the plasma density fluctuations can then be inferred. Spatial localization is ensured by geometric means, since the light is collected only from the region of intersection between the beam and the line of sight. Measurements with multiple arrays allow reconstruction of the wave-number spectrum. The BES technique has been applied successfully to core fluctuation measurements in TFTR,[51] where the existing heating neutral beams were used as the source. A similar system has recently been installed on the DIII–D tokamak.[52] Although these high-power beams present the advantage of good penetration, thus permitting access to the core, spectroscopy techniques based on them suffer from poor rejection of background light, resulting in the need for long averaging times (up to 0.5 s), which severely limit the temporal resolution of the measurement. The alternative solution of using a dedicated nonhydrogenic beam

allows the observation of fast transients in the plasma edge. Such systems have been implemented in DIII–D[53] with a lithium beam, and in Phaedrus–T[54] and TEXT–U[55] with helium beams. The possibility of achieving two-dimensional fluctuation imaging and thus a simultaneous two-dimensional wave-number spectrum is also being explored.[56,53] One important difficulty of BES is the beam-power modulation that is caused by large density fluctuations at the plasma edge; this results in an apparent fluctuation signal that is not of local origin but can be a large fraction of the total signal. Techniques have been developed to correct for this effect.[51]

One final density fluctuation diagnostic deserves a mention: the heavy-ion beam probe (HIBP), operating on the TEXT tokamak.[57] In this system, singly charged thallium or caesium ions injected into the plasma become doubly ionized through collisions with electrons. A detector array receives these secondary ions, whose trajectories can be reconstructed precisely, thereby providing a local measurement of the electron density. Beam modulation from edge fluctuations has to be taken into account as in the case of the BES diagnostic.

Temperature fluctuation measurements are considerably more difficult to perform. Some progress has been made recently in this direction by applying correlation techniques to measurements of electron cyclotron emission.[58]

In spite of the increasing sophistication of fluctuation diagnostics over the years, many issues remain unresolved. In particular, a thorough characterization of the relation between microturbulence and anomalous transport is still missing. Also, relatively little knowledge has been acquired on the physical nature of the turbulence and of the underlying microinstabilities; such information is necessary for testing several proposed theories.

Several features of microturbulence in tokamaks are nearly universal.[10,11] The fluctuation spectrum is broadband and lies mostly at frequencies below 1 MHz in the plasma frame, although in the presence of an electric field the actual measured spectrum in many cases is Doppler-shifted considerably by the $\mathbf{E} \times \mathbf{B}$ drift velocity. The wave-number spectrum is also broadband, with the fluctuation amplitude generally decreasing for increasing wave number. There is in fact considerable evidence that the bulk of the fluctuation power lies in the region of the spectrum corresponding to wavelengths much longer than the ion gyroradius. That region is also the least accessible to traditional scattering measurements; this has been a strong motivating factor in the development of alternative methods in the last decade. The spatial dependence of the relative density fluctuation amplitude ($\tilde{n}/n$) is similar in many tokamaks: the amplitude generally increases with the minor radius and is largest at the plasma edge. The edge is an important region to explore for several reasons, particularly because it plays a leading role in determining the overall plasma confinement, as will be discussed shortly.

In addition to the broadband turbulence spectra, coherent or semicoherent modes are occasionally observed. These modes are characterized by peaks in the frequency spectrum and are identified as MHD instabilities. While measurements with external magnetic coil arrays have provided extensive information on the global structure of

these modes, relatively little is known about their internal characteristics, especially their density component.

Studies of turbulence and transport have received an added boost in recent years from the growing diffusion and universality of a regime of enhanced confinement known as high-confinement mode, or H mode.[59] In this regime the confinement is approximately a factor of 2 better than in L mode. The good confinement and the good overall properties of the H mode render it a strong contender as an operational regime for a reactor. The H mode was first discovered in ASDEX, a divertor tokamak,[60] and has since been observed in all tokamaks with diverted plasmas and in several with limiter plasmas; in addition, the H mode has also been obtained in several non-tokamak devices.[61] This seemingly universal character is also reflected in the wide variety of heating sources used to obtain the H mode: these include rf and microwave heating, neutral-beam injection, and Ohmic heating.

The H mode generally begins with an abrupt transition from the L–mode regime (see Fig. 1.2). The transition is accompanied by the formation of a transport barrier at the plasma edge, with a corresponding steepening of the pressure profile in the same region; at the same time, the fluctuation amplitude in the edge region is suddenly reduced. In addition, the radial electric field develops a steep gradient, also localized in the plasma edge.[61] In fact, the H mode has also been produced by actively biasing the plasma.[62]

There is now general agreement on the basic physical mechanism responsible for the H mode, although many of the details are still unresolved. This mechanism is the stabilization of turbulence by a sheared $\mathbf{E} \times \mathbf{B}$ flow.[63] In the simplest terms, the sheared flow tears and separates the turbulent eddies in the plasma, reducing their radial correlation and extent and, thus, limiting the transport of energy across the field lines. This scenario, not being dependent on the specific nature of the turbulent modes in the plasma, has the universality required to explain the occurrence of H mode in such a disparate set of experiments and conditions.

The clear correlation between the suppression of turbulence and the formation of the transport barrier at the edge offers compelling evidence in support of the postulated causal relation between microturbulence and anomalous transport. This has stimulated new diagnostic investigations of tokamak plasma fluctuations, and particularly of their changes at the L– to H–mode transition. Further impetus was provided more recently by the discovery, first in DIII–D[64] and later in JET[65], of a regime of confinement enhanced by up to a factor of 2 over H mode. In this regime, called very-high-confinement mode or VH mode, the transport barrier extends further into the core of the discharge; a spatial extension of the shear-stabilization effect appears to offer the best explanation of the improved confinement to date.[66] The VH mode is generally terminated abruptly by the occurrence of a global MHD "event", or instability, that returns the plasma to normal H–mode confinement.

A phenomenon that is currently the object of renewed interest on the part of fluctuation diagnosticians is the edge localized mode (ELM). ELMs are semiperiodic edge instabilities that occur in the H–mode regime and that quickly destroy the trans-

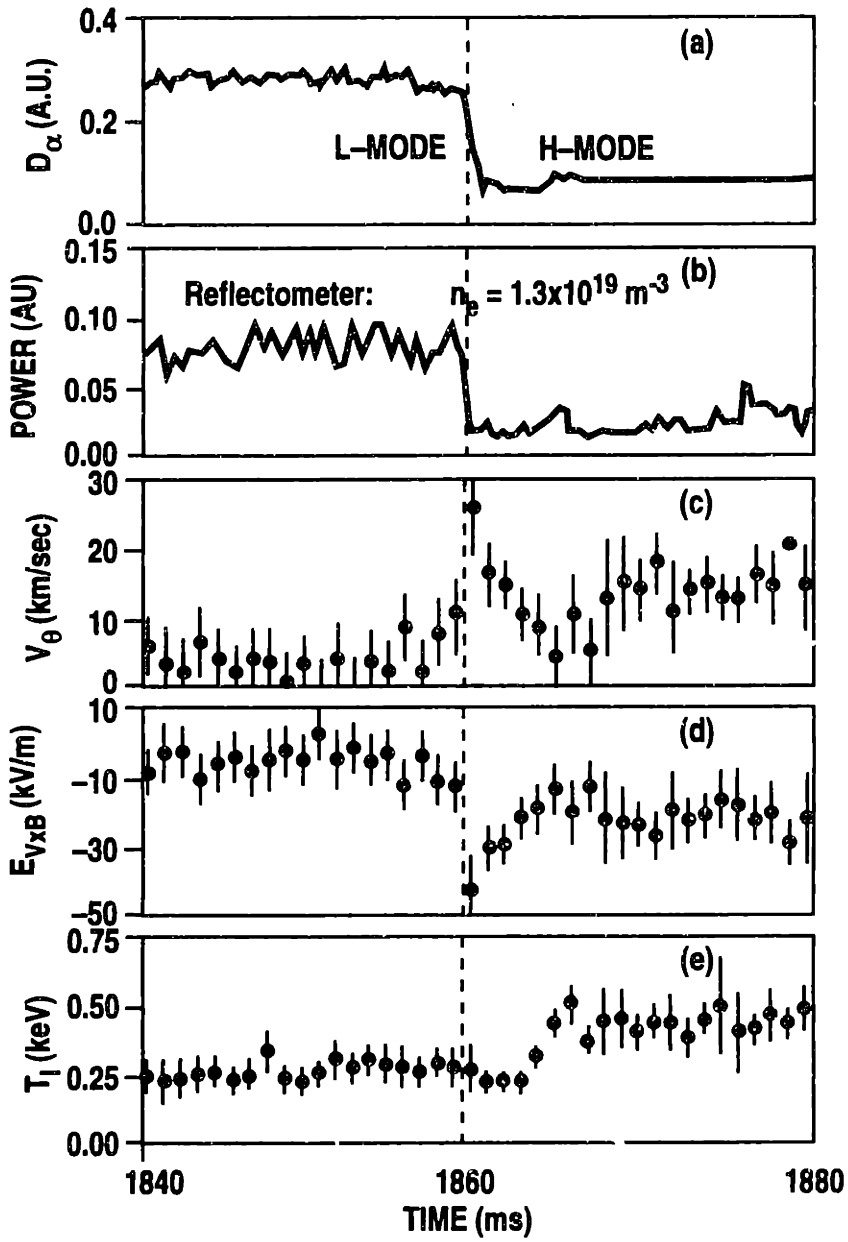

Fig. 1.2 Typical time evolution of fluctuation and rotation signals at an L–H transition: (a) the D_α emission, which is a measure of edge transport, drops at the transition; (b) integrated fluctuation power in the 75–400 kHz band, measured by a reflectometer a few cm inside the last closed flux surface; (c), (d) and (e) show the poloidal rotation velocity, the radial electric field, and the ion temperature measured by charge-exchange recombination spectroscopy ~1 cm inside the last closed flux surface [reproduced with permission from E.J. Doyle, et al., Phys. Fluids B **3**, 2300 (1991).]

port barrier, which is then rapidly restored; during this transient phase, turbulence is enhanced and confinement is degraded. An ELMing H mode generally exhibits transport rates 15%–20% higher than an ELM-free H mode; however, ELMs are beneficial for their ability to clamp the plasma density and prevent impurity buildup, which

can otherwise raise the radiated power to deleterious levels.[59] It is generally believed that a reactor, such as the proposed prototype ITER,[67] will operate in an ELMing H–mode regime. A better understanding of ELMs is a prerequisite of reactor design, particularly in consideration of the large heat loads that ELM events deposit on the divertor.

ELMs are generally interpreted as MHD instabilities, and theoretical efforts have been made to incorporate ELM dynamics in a general theory of the H mode.[68] However, considerable more work is clearly necessary in both theory and experiment, particularly in the study of the fluctuations that accompany the occurrence of an ELM. The existence of at least three distinct categories of ELMs[69] is an added complication.

The foregoing discussion clearly underscores the importance of continued turbulence measurements, particularly at the edge of the plasma. The work described in this thesis was largely motivated by the desire to achieve a better understanding of microturbulence. This project consisted of designing, building, and operating a CO_2-laser phase-contrast imaging (PCI) diagnostic to measure density fluctuations at the outer edge of the DIII–D tokamak.[70]

A uniquely diverse set of fluctuation diagnostics exists on the DIII–D device, including a far-infrared (FIR) scattering system,[27] a fast reciprocating Langmuir probe,[71] a multi-frequency reflectometry system,[42] a correlation reflectometer,[46] and a lithium-beam emission spectroscopy apparatus.[53] A deuterium BES diagnostic has recently been installed.[52] Because of the different spatial regions and parameter ranges accessed by different fluctuation diagnostics and because of their various limitations, complementarity has been a key criterion in the planning and in the design of the DIII–D diagnostic array, although some overlap was also sought for comparison and verification purposes. The PCI and reflectometer systems are mostly sensitive to fluctuations with radial wave vectors, whereas the probe and the FIR scattering diagnostic are sensitive to poloidal wave vectors. The probe scans the region outside the last closed flux surface (the "scrape-off layer", or SOL) and the region immediately inside; the PCI system has access to part of the SOL but penetrates further inside the plasma; the lithium-beam diagnostic overlaps with PCI but reaches further inside; and the reflectometer and FIR scattering systems have access to a substantial portion of the plasma core.

The principal advantages of the PCI diagnostic are an excellent spatial resolution in the radial direction (≈ 0.5 cm), a very high sensitivity ($\tilde{n}_{\min} \simeq 10^9$ cm^{-3}), and access to long wavelengths (up to 7.6 cm), in addition to a very wide frequency bandwidth (100 MHz). The main limitation is the lack of spatial resolution in the vertical direction: the measured fluctuations are line-averaged. Absolute calibration of the system is possible, permitting a determination of the absolute fluctuation amplitude, albeit line-integrated. The properties of PCI made it possible to conduct unprecedented studies of the radial dependence of microturbulence at the edge, determining its spectral characteristics both in the wave-number and in the frequency domain. The frequency measurement in particular is made possible by the absence of

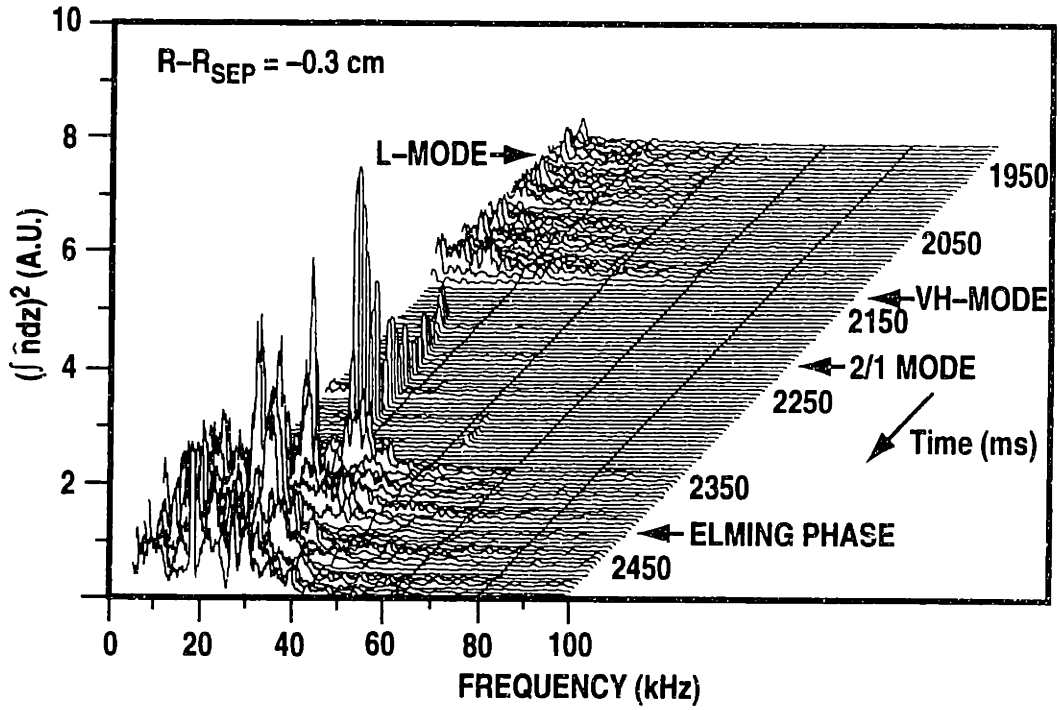

Fig. 1.3 Temporal evolution of the autopower spectrum of a PCI signal on a chord located 0.3 cm inside the separatrix (last closed flux surface). The L–mode phase, the VH–mode phase (with a coherent MHD mode at 18 kHz), and the ELMing H–mode phase are visible.

substantial Doppler shifts, which is due in turn to the perpendicularity of the radial wave vectors to the direction of the $\mathbf{E} \times \mathbf{B}$ rotation.

These studies were carried out in the context of the L– to H–mode transition and of ELMs, and comprise the bulk of the results presented in this thesis. The location of the diagnostic is ideal for investigating those phenomena, as the observable events are strongly localized in a narrow region comprising the edge of the plasma and the SOL. Whenever possible, efforts were made to carry out comparisons with data from the other diagnostics. An illustrative example of the type of data generated by the PCI diagnostic is shown in Fig. 1.3.

(b) Radio-Frequency Waves

In a tokamak discharge, the plasma is initially heated resistively by the toroidal current flowing through it. However, since the resistivity of a plasma decreases as the temperature increases, Ohmic heating becomes inefficient at the many-keV temperatures that are necessary in a reactor. Several alternative heating methods have therefore been developed over the years. Among them are techniques based on the resonant absorption by the plasma of externally launched, high-power electromagnetic waves.[2] Resonances ranging from the ion cyclotron frequency (in the radio-frequency spectrum) to the electron cyclotron frequency (in the microwave spectrum) have been utilized for heating purposes. In addition, by using waves incident unidirectionally

on the plasma, noninductive currents can be generated.[3] This line of research, which holds the best promise for steady-state operations, is also viewed as critical for the design of a successful reactor.

In the ion cyclotron range of frequencies (ICRF), three different types of waves have been employed for heating or current drive. Shear Alfvén waves propagate only at frequencies below the ion cyclotron frequency, and their phase-velocity component in the direction parallel to the magnetic field is typically equal to the local Alfvén velocity. These waves have been employed for heating in several tokamaks, the largest being the TCA device in Lausanne, Switzerland.[72] A second type of wave, the fast magnetosonic or compressional Alfvén wave, propagates primarily in the radial direction across the magnetic field and can be absorbed near the ion cyclotron harmonic resonances or by electrons whose parallel velocity equals the wave's parallel phase velocity.[73] Fast waves are widely used for plasma heating[74], and the first fast-wave current-drive experiment is being currently carried out in DIII–D with good initial success.[75] The third and final member of the ICRF family of modes is a hot-plasma wave known as ion Bernstein wave (IBW). Plasma heating schemes using IBWs have been implemented in several tokamaks.[76]

While the effect of rf waves on plasmas, whether in the form of energy or current, can be routinely monitored through established diagnostic techniques, relatively few direct measurements of the wave characteristics have been carried out. The dynamics of rf wave propagation in plasmas are rather complicated and are usually estimated numerically by computer, with necessary simplifications. When only macroscopic measurements are performed, it is difficult to understand the detailed physical mechanisms responsible for the discrepancies between prediction and experiment. A thorough characterization of the spatial structure of the waves would thus be an invaluable aid to experimenters.

Some of the techniques reviewed in part (a) of this section have been sporadically applied to the study of externally launched ICRF waves. CO_2-laser scattering was employed in Alcator C to study the propagation and absorption of IBWs.[77] Phase-contrast imaging (PCI) was applied to the study of shear Alfvén waves in TCA.[78] Recently, initial results on fast waves have been obtained with a reflectometer system in DIII–D.[79] Of these diagnostics, all of which are sensitive to the density component of the wave, only an imaging technique such as PCI is capable of providing a direct spatial measurement of the phase and amplitude of the wave over an extended range and, in principle, for arbitrary wavelengths (limited in practice by the width of the beam). When the direction of propagation of the laser beam is perpendicular to the main direction of propagation of the rf wave, the line-averaging effect is a lesser limitation than in the case of turbulence. The integration length can be estimated with good accuracy from analytical and numerical computations. The TCA results have shown[78] that a very detailed reconstruction of the wave can be obtained.

These considerations provided added motivation to the development of the PCI diagnostic for DIII–D concomitantly with the start of the fast-wave current-drive program. Fast-wave measurements are one of the main goals of a possible future

upgrade of the PCI system; this system would utilize the existing apparatus except for a reorientation of the beam, which would traverse the plasma in the core region rather than at the edge. The present configuration does not allow the detection of fast waves, as their wave number at the edge of the plasma is lower than the minimum wave number detectable by PCI. This was confirmed by direct measurements.

When ICRF waves are launched into a plasma, secondary oscillations may arise in the rf range, either from mode conversion between the different waves described earlier or from nonlinear wave-wave coupling. The process of nonlinear mode generation known as parametric decay instability (PDI)[80] has been observed in DIII–D during both fast-wave and IBW launching.[81] The potential of the PCI system for measuring the internal structure of these decay modes has motivated some additional exploratory work during the course of this project, including the development of a large computer code to calculate and plot the PDI dispersion relation under a variety of conditions.

1.2 Motivation: Instrumental Aspects

Fluctuation imaging is a relative newcomer to experimental plasma physics but is rapidly gaining acceptance and constantly finding new applications. Just as flow visualization is revolutionizing the field of experimental fluid dynamics, so are imaging techniques responding to the need for increased sophistication in the study of thermonuclear plasmas. Applications are not limited to the light-transmission diagnostics discussed in this thesis: the benefits of combining the techniques of beam-emission spectroscopy[56,53] and reflectometry[49] with imaging configurations have also recently been recognized.

The conditions encountered in modern-day tokamaks are especially conducive to the utilization of imaging diagnostics. The gradient scale lengths of the macroscopic plasma parameters in a tokamak, particularly at the edge, are often of the same order as the fluctuation wavelengths, effectively blurring the distinction between average and fluctuating quantities. A similar situation is encountered to some extent in the time domain, with very fast large-scale transients, such as the L–H transition and ELMs, occurring in time scales comparable to the period of the fluctuations. A direct spatial mapping with good temporal resolution is clearly the most natural representation of such a plasma.

The choice of an imaging configuration for this project was motivated also by the desire to access the long-wavelength region of the spectrum of both turbulence and rf waves. Using the same laser source, the traditional scattering method is limited in practice to shorter wavelengths than its imaging counterpart.[23] The excellent sensitivity attainable by the use of liquid-nitrogen-cooled detectors provided additional incentive.

In a reactor such as ITER,[67] laser imaging at optical or infrared wavelengths may prove especially advantageous, since it is not limited by cutoff or absorption, as are methods employing microwaves or neutral beams. The most sensitive components, such as the laser source and the detectors, can be placed at a safe distance from the reactor. The proof of principle provided by our project is particularly significant

for such a future application, in view of its greatest foreseeable problem: that of mechanical vibrations. Vibrations of the optics can be very disruptive for an imaging technique such as phase contrast. The ITER device can be expected to provide a rather hostile environment in this respect; however, our configuration in DIII–D was also very unfavorable, owing to the late addition of the diagnostic to the machine and to the severe space limitations that dictated an overlong optical design with support structures particularly prone to vibrations. These conditions should adequately simulate the vibration scenario of a larger device such as ITER, if a careful optical design is included in the early planning stages. The vibration problem in DIII–D was eliminated by active feedback control of the laser beam orientation. This constituted a significant portion of the development of this project and required innovative solutions employing state-of-the-art equipment.[70,82]

The principal limitation of transmission techniques is the inherent lack of spatial resolution along the direction of propagation of the probing electromagnetic beam. This problem can be partially or totally circumvented by orienting the beam to be tangential to the magnetic field lines, or by utilizing crossed-beam correlation techniques.[83] In the case of the DIII–D PCI system, the edge location and the relative shortness of the integration path limit the impact of the longitudinal averaging effect: a simple qualitative analysis can be used to impose significant constraints on the measured spectra.[84] The importance attached to this issue, however, was deemed sufficient to motivate an extensive quantitative analysis, involving analytical and numerical modeling.[82] The results of this study confirmed the qualitative analysis and complemented it quantitatively under a variety of realistic plasma conditions.

The theoretical foundation of all transmission techniques lies in the physics of light-plasma interaction. Historically, different theoretical approaches and approximation schemes have been applied to different types of transmission techniques. However, the underlying principles are the same. One assumption that all these methods have in common is that the frequency of the plasma fluctuations can be neglected in the analysis. During the course of this project, it was realized that this assumption had to be relaxed somewhat for rf applications, when the propagation time of the laser beam through the plasma becomes comparable to the period of the fluctuations. The inclusion of a finite fluctuation frequency was found to engender some new consequences, which may be important in certain experimental applications. This analysis generated additional interest in achieving a better understanding of these physical processes and in providing a unifying view of the various analytical schemes found in the literature. Accordingly, their equivalence was clarified, and the finite-frequency analysis was extended well beyond the needs of the DIII D PCI diagnostic, embracing both near-field and far-field techniques, including conventional scattering. This theory occupies a significant fraction of this thesis.

Additional work was devoted to a specific characterization of the response properties of transmission imaging techniques. Since these techniques, particularly phase contrast, are relatively novel in a plasma-physics setting, a thorough comparative study of their properties had not previously been performed. This study, carried out

for the specific case of a Gaussian beam, produced some new results that should prove useful to existing and planned experiments. The analysis was further expanded for the phase-contrast case, particularly in the DIII–D geometry, for which diffraction effects were also carefully evaluated.

1.3 Synopsis of Experimental Results

Owing to geometrical constraints, the DIII–D PCI system is primarily sensitive to radial wave vectors, with poloidal wave number close to zero. The wave-number spectra measured by PCI invariably peak at finite values of the radial wave number k_r, both positive and negative. This phenomenology is in agreement with predictions generated by recent theoretical and numerical work, and represents the first documented observation of finite-k_r radial modes. These modes are believed to be generated nonlinearly by stronger, poloidally propagating instabilities (such as ion-temperature-gradient modes), which are capable of causing radial transport through turbulent $\mathbf{E} \times \mathbf{B}$ drifts; this transport in turn is strongly regulated by the radial modes through a second nonlinear mechanism. Radial modes have been thoroughly documented with PCI, whereas only a limited set of cases was explored by the numerical work; it is thus expected that this experimental work will motivate further numerical analysis for a more complete comparison.

Structures consistent with convective cells have been measured by PCI in high-current L–mode plasmas. These structures straddle the plasma boundary and are capable of causing rapid outward transport; they are observed to disappear or move away from the boundary at the onset of the H mode, in agreement with theoretical predictions.

In some cases, the spatial correlation pattern in the SOL in H mode is found to be consistent with strongly reduced turbulent electric fields, even though the density fluctuation level is high; the correspondingly lower $\mathbf{E} \times \mathbf{B}$ drift may then explain the reduced transport that characterizes the H mode.

Since PCI is sensitive to radial wave vectors and plasma drifts are perpendicular to the radial direction, no significant Doppler shifts are expected: that is, the frequency spectrum is measured essentially in the frame of reference of the plasma. This important and novel feature is confirmed by experimental results, as the turbulent spectra are found to be monotonically decreasing with frequency, and components with frequency larger than 200 kHz give a negligible contribution to the autopower spectrum. The spectra in Ohmic and L–mode plasmas are also found to obey an approximate inverse power law, with an exponent in the range 1–3 and most commonly near 2; this power law is consistent with a Lorentzian spectrum, which would arise from an exponentially decaying mode, provided the decay rate lies below the instrumental cutoff point of 8 kHz.

In H mode, the spectrum becomes broader and more irregular, with several individual peaks indicating the existence of stabler (long-lived) modes. The time-delayed correlation function becomes correspondingly broader at large delays and narrower at small delays as the plasma goes from L to H mode. The overall result is

generally a small increase in the decorrelation time. As a function of the radial wave number, the decorrelation time is found to be monotonically decreasing; its indefinite increase as the wave number tends to zero ("infrared divergence") is in contrast with the peaking of the spectrum $s(k_r)$ at finite wave number.

The wave-number spectrum also decreases for high k_r: most of the turbulent energy is concentrated at values of a fraction of an inverse ion gyroradius. The radial correlation length typically lies between 10 and 40 gyroradii, and is reduced suddenly in the transition from L to H mode. As a function of plasma parameters, the correlation length depends more strongly on global parameters than on local ones; in particular, it increases with input power and plasma density and decreases with plasma current. The correlation length is also decidedly shorter when the ∇B points away from the dominant X-point, in indirect agreement with some theoretical predictions.

The radial spectra are often balanced, but in many cases also display predominant inward or outward propagation. The variation of the propagation coefficient with plasma parameters has been studied in detail and is offered for future theoretical work, as no predictions exist at present. The characteristic spectral lengths (average wavelength and correlation length) have also been examined as functions of frequency: both generally increase with frequency; in particular, the dispersion relation (average wave number vs. frequency) is offset-linear, with group velocities of the order of 1.5–4 km/s in Ohmic and L-mode plasmas, and up to 20 km/s in H mode. These velocities are subsonic and are probably determined by toroidal or nonlinear coupling of drift waves.

Although the PCI system is absolutely calibrated, the calibration factors are subject to considerable uncertainties, of the order of 30–40%. Nevertheless, some studies of the spatial and parametric variation of the turbulence amplitude have been carried out. The relative fluctuation amplitude $\tilde{n}/n$ is a decreasing function of input power, density, temperature, and density-gradient scale length. The spatial distribution of the line-integrated fluctuations displays a peak just inside the plasma boundary and is fairly flat in the region from 6 cm inside to 1 cm outside the boundary; further out in the SOL, the fluctuation level drops rapidly. These measurements are consistent with a peaking of the local turbulence level just inside the boundary, although the measurement itself is nonlocal.

A test of the mixing-length criterion in a number of discharges has shown that the amplitude follows an approximate mixing-length scaling in Ohmic and L-mode plasmas, whereas it is significantly below the mixing-length level in H mode, just after the L–H transition. This may indicate that the H mode is characterized by a weaker type of turbulence. However, the H-mode amplitude obeys the mixing-length scaling when the latter is obtained by using the L-mode density profile; thus, it is possible that the initial H-mode phase is also a strong-turbulence regime in which the turbulence has not had enough time to recover under the effect of the increased gradients.

Some tests of the theory of self-organized criticality (SOC) have been performed.

Although some possible similarities were found, namely, discontinuities in the slope of the frequency spectrum and double-peaked time-delayed correlation functions, many details differ, and the results must be regarded as preliminary and inconclusive. The probability distribution function (PDF) of the turbulence was also studied and was found to be Gaussian in all regimes over time intervals of 40 ms or less; however, over longer intervals the PDF is increasingly non-Gaussian, with an asymptotic kurtosis of 5.3–5.6. This is consistent with long-time-scale intermittency — a critical prediction of SOC — but it is not a definite proof of it.

The random walk diffusivity (the square of the correlation length divided by the decorrelation time)in L mode is found to be of the order of the ion diffusivity at the edge; both increase with input power.

The L–H transition has been investigated in detail. PCI has provided the first time-resolved measurements of the changes in the correlation quantities: as mentioned before, the correlation length decreases at the transition, whereas the decorrelation time remains approximately constant. The amplitude of the fluctuations also decreases, as shown previously by several other diagnostics. The random-walk diffusivity is found to decrease by a factor of 2.5 to 10 at the L–H transition; the experimental diffusivity is also reduced.

The leading theoretical explanation of the transition attributes the reduction in turbulence and transport to a decorrelation effect engendered by a sudden increase in the $\mathbf{E} \times \mathbf{B}$ flow shear. This theory also provides a quantitative criterion for the shear-decorrelation effect, which can be tested by PCI with the assistance of other diagnostics. The criterion has been shown to be valid. In addition, two different theories have supplied quantitative expressions for the changes in the correlation length and in the decorrelation time at the transition. Tests of these theories, performed for the first time with PCI, have yielded mixed results: each of the two theories is successful in predicting only one of the two quantities.

A special class of "slow" L–H transitions, obtained by keeping the input power only slightly above the transition threshold, has displayed a novel phenomenology in the transition phase: after a rapid suppression, the turbulence amplitude increases again in the region just outside the plasma boundary, reaching levels larger than those of L mode; this renewed activity then subsides again slowly as the L–H transition is completed. We hypothesize that this SOL turbulence is related to the appearance of a parallel-ion-velocity-gradient instability or possibly of a Kelvin-Helmholtz instability.

Edge Localized Modes (ELMs) are also phenomena of considerable interest, in particular for future reactor operation. ELMs are always accompanied by bursts of turbulent activity. A first systematic study of ELMs with PCI has been performed in this thesis. Since ELMs are short-lived events, averages have been taken over multiple ELMs in order to determine the statistical properties of turbulence during ELMs. The turbulent spectra and dispersion relations are generally similar to those of L mode, but the absolute amplitude of the turbulence is considerably larger in the case of ELMs. Two major systematic differences between type-I and type-III ELMs have been identified: firstly, the peak in the fluctuation amplitude occurs at the time

of maximum diffusivity for a type-I ELM, whereas it occurs 0.4–0.6 ms earlier for a type-III ELM; this could be related to ideal and resistive MHD times, respectively. Secondly, type-III ELMs are accompanied also by a coherent, outward-propagating mode at approximately 100 kHz, which may be related to a resistive MHD instability.

Coherent and semicoherent modes, presumably of the MHD type, are often observed by PCI, primarily during H mode. These fluctuations are generally well correlated with signals from soft-x-ray diodes and external magnetic coils. A detailed study of these phenomena has not yet been performed with PCI.

1.4 Thesis Outline

The remainder of this thesis is configured as follows.

Chapter 2 is devoted to the theoretical foundation of the diagnostic technique. The fundamentals of the physics of light-plasma interaction are reviewed and the equations for wave propagation are derived. The mathematical techniques and the approximation schemes used in solving the wave equation are also reviewed and discussed. To emphasize the equivalence of the different techniques, the scattering equation is derived in the framework of a plasma dielectric model; this novel approach, whose mathematical details can be found in Appendix A, is shown to yield the same result as the customary derivation from the radiation equations.

The problem of diffraction from an aperture is investigated analytically and numerically; in particular, the effects of diffraction in the specific geometry of our measurement are studied in Appendix B. A general theory of scattering and imaging measurements, valid for a Gaussian beam in an arbitrary detection geometry, is then presented; the relevant calculations are contained in Appendix C. This theory includes for the first time the effects of a finite fluctuation frequency. In the zero-frequency limit, previous results are recovered; a detailed discussion of various known results is thus carried out in a common perspective.

The limiting case of this theory that is relevant to our measurements is equivalent to the geometrical-optics limit. A detailed proof of this equivalence necessitates also a novel approach to geometrical optics that incorporates finite-frequency effects. The proof is given in Appendix D, with an expansion of the geometrical-optics equations to include the time dependence of the eikonal and amplitude functions.

The response properties of phase-contrast imaging are derived for the first time, for a truncated Gaussian beam and for both the one-dimensional and the two-dimensional case. This is followed by a discussion of the signal-to-noise ratio that can be obtained with photon detectors. Then, a comparative analysis of various imaging techniques is carried out for the case of a Gaussian beam; the mathematical details are in Appendix F. As previous comparisons either were not quantitative or used an idealized plane-wave model, some of the results obtained here have significant consequences for existing systems, as discussed in the text. The chapter is concluded by a description of the calibration methods available for phase contrast.

The phase-contrast imaging apparatus designed and installed on DIII–D is the subject of Chapter 3. A brief introduction to the DIII–D tokamak is followed by a

description of the specific geometry of the PCI measurement. The appropriate limit of the theory developed in Chapter 2 is identified by verifying that all the necessary approximations are satisfied. The various components of the hardware are described next, along with the main design criteria. Details are provided on the optimization of the optical design (with related software development), on the elimination of initial electronic noise problems, and on the testing procedures used. Special emphasis is placed on the novel solutions adopted in the development of the feedback vibration-control system.

Testing and calibration results are discussed, with a comparison between the experimental determination of the response characteristics and the corresponding theoretical predictions. Finally, the data-analysis techniques employed in the course of this work are presented. Some software was developed specifically for this application, especially to calculate time-domain correlation functions, as it was not readily available otherwise.

Chapter 4 presents the modeling of the measurement that was carried out to aid in the interpretation of the results. A basic model for plasma fluctuations is introduced; from it, the pointwise correlation function is derived analytically. This is then used with some approximations to infer the qualitative properties of the measured PCI correlation function. The development of a computer code to effect a more rigorous and quantitative analysis is described next; this is followed by a discussion of the results in a number of realistic DIII–D conditions. This chapter is concluded by some comments on the applicability of inversion techniques to derive local quantities from PCI measurements.

The physics results obtained with the PCI diagnostic are presented in Chapter 5. Most of the chapter is devoted to measurements of microturbulence. The character of edge turbulence in L mode is discussed at length, with details on the spatial distribution, on the frequency dependence, and on the wave-number spectrum derived through correlation analysis. Differences between the region inside the last closed flux surface and the scrape-off layer are examined, and the dependence of turbulence on the macroscopic plasma parameters is discussed. The results are also compared with data from different diagnostics in DIII–D and with the existing body of knowledge on tokamak turbulence. A similar analysis for H–mode conditions follows, with emphasis on the changes occurring at the L–H transition. A particularly important case is that of low-power H modes, which display a peculiar phenomenology in the early phase immediately following the transition.

Results on ELMs are then presented, with an illustration of the systematic differences discovered between different sub-types, particularly giant and type-III ELMs. The analysis, again, is organized as a systematic exploration of turbulence in real space, in frequency space, and in wave-number space.

While the results summarized thus far were obtained in the course of systematic studies, much phenomenological information was also gathered during various experiments not specifically devised for turbulence studies. Nevertheless these results are of some consequence and are therefore briefly discussed in the remainder

of Chapter 5. Some of these data have been analyzed only in an incomplete fashion and some simply point the way to future lines of investigation. Results on VH–mode and ohmic turbulence, and on coherent or semicoherent MHD activity are included in this group. Finally, some comments are offered on the difficulties associated with rf measurements in the present geometry and on the expected null results obtained during fast-wave launching.

Chapter 6 is devoted to the interpretation of the results and to comparisons with existing theories of plasma turbulence, of the L–H transition, and of ELMs. The main conclusions of this research were summarized in §1.3.

Chapter 7 briefly examines possible applications and configurations of the PCI technique that were not employed in our project. These ideas have been considered by other authors but are analyzed here in greater detail. First, the properties of a heterodyne version of PCI are presented, and advantages and disadvantages are discussed. Methods for improving the spatial localization are considered next: these include the crossed-beam correlation technique and, for the specific case of turbulence in a tokamak, toroidal launching. Data-analysis methods to study the nonlinear interaction of turbulent modes are briefly mentioned, especially in connection with the crossed-beam technique. The chapter is concluded by a description of a possible future upgrade of the DIII–D PCI system.

Finally, general conclusions are offered in Chapter 8, with some additional suggestions for future work and future applications.

1.5 Units and Dimensions

Equations in this thesis are written in the Gaussian cgs system of units. A few formulas are given in practical units; this is always stated explicitly. In the text, practical tokamak units are often used, including amperes for electrical current, volts for potential, tesla for magnetic induction, and eV for temperature.

2 Experimental Technique

The interaction of an externally launched electromagnetic wave with a plasma, giving rise to such diverse and complementary phenomena as reflection, refraction, scattering, and diffraction, provides the experimenter with a wealth of powerful diagnostic tools.[32] The nonperturbative nature of this class of techniques in all practical situations, combined with its sound underlying theoretical foundation, is the principal reason for the attractiveness of this family of diagnostics in the study of laboratory plasmas. The wide availability of coherent sources in a broad region of the electromagnetic spectrum has greatly contributed to the current widespread usage of these techniques. In particular, Thomson scattering diagnostics have been employed since the dawn of the magnetic fusion program and had a pivotal role in the 1960's[85] in proving the superiority of the tokamak concept and in providing the basis for the tokamak's subsequent predominance in worldwide magnetic fusion research.

The following are some of the most common techniques employed today: incoherent Thomson scattering at visible and near-infrared wavelengths, to determine the local electron density and temperature;[86,87] far-infrared[88] and microwave[89] transmission interferometry, to measure the line-integrated electron density; coherent scattering and imaging at infrared[29] and microwave[15] wavelengths, to investigate fluctuations in density; and microwave reflectometry, to study density profiles[90] and fluctuations.[40]

The technique that is the subject of the present work belongs to the class of density fluctuation imaging diagnostics. In this chapter the theoretical foundation of the method is established in the context of a broad comparative analysis of various techniques in this class. The starting point is a review of the physics of light-plasma interaction in the limit of interest for the present study. The equations for wave propagation are introduced in §2.1. Several mathematical approaches to their solution are reviewed in §§2.2–2.4, with emphasis on their equivalence and on their respective limits of applicability. Part of the mathematical derivation can be found in Appendix A. The effect of diffraction from a circular aperture is studied both analytically and numerically in §2.5 and Appendix B.

General solutions to the wave equation, applicable to a variety of experimental conditions, are obtained both in the Rytov approximation and in the geometrical-optics approximation for the specific case of a Gaussian beam. The problem is introduced in §2.6. The case of far-field detection is considered in §2.7 and that of near- and intermediate-field detection is presented in §2.8. These results unify the work of previous authors and extend it by relaxing certain key assumptions: in particular, the temporal dependence of the density fluctuations is included explicitly and is shown to generate new consequences in some situations of experimental interest. The mathematical derivations related to these sections are carried out in detail in Appendixes C and D. It should be noted that this treatment, although specifically presented for the case of a plasma, applies to any dielectric medium with low susceptibility.

A historical and technical overview of a number of closely related small-angle scattering techniques, which follows naturally from the foregoing analysis, is presented in §2.9. The phase-contrast method is described in some detail in §2.10. In §2.11 the response characteristics of the phase-contrast technique are derived explicitly for the first time for cases ranging from a simple plane wave to a truncated Gaussian beam. Considerations of signal-to-noise ratio are reserved for §2.12. The formalism developed in the previous sections is then applied in §2.13 to a broad class of techniques, including scintillation, dark ground, Mach-Zehnder interferometry, and a family of spatial filtering configurations that incorporates the phase-contrast and schlieren methods as special cases. Novel analytical results are obtained for the responsitivies and signal-to-noise ratios of these techniques in the case of a Gaussian beam; some of the mathematical derivations are contained in Appendix F. This comparative study comprises as limiting cases some of the results reported in the literature. Finally, §2.14 is devoted to the calibration methods available for the phase-contrast imaging diagnostic.

A majority of the original work in this chapter is contained in §§2.5, 2.6, 2.7, 2.11, and 2.13, and in the related appendixes.

2.1 The Physics of Light-Plasma Interaction

In this section we briefly review the theory of the interaction between visible or infrared electromagnetic waves and a magnetized fusion-grade plasma. The analysis is greatly simplified by two crucial assumptions: both the electron plasma frequency and the electron cyclotron frequency are taken to be much smaller than the angular frequency ω_0 of the electromagnetic waves under consideration, i.e.,

$$\omega_0 \gg \omega_{pe} \tag{2.1}$$

and

$$\omega_0 \gg \omega_{ce}, \tag{2.2}$$

where $\omega_{pe} \equiv (4\pi n_e e^2/m_e)^{1/2}$ and $\omega_{ce} \equiv eB/(m_e c)$, n_e being the electron plasma density, B the magnetic field, e the electronic charge, and m_e the mass of the electron. Equations (2.1) and (2.2) are generally well satisfied, as exemplified by the following representative set of parameters: $n_e = 10^{14}$ cm^{-3} and $B = 10$ T yield $\omega_{pe} = 5.6 \times 10^{11}$ rad/s and $\omega_{ce} = 1.8 \times 10^{12}$ rad/s, whereas the frequency of a far-infrared light wave of 100-μm wavelength is $\omega_0 = 1.9 \times 10^{13}$ rad/s. Under the conditions of the experiments described in the present work, the margins are in fact much larger.

The significance of Eq. (2.2) is that the magnetic field is negligible; thus, the plasma is effectively isotropic. If we make the further assumption, subject to eventual verification, that $v_{te} \ll v_\phi$, where v_{te} is the electron thermal velocity and v_ϕ is the phase velocity of the wave, thermal effects can be ignored and the plasma can be treated as a cold medium.[91] The word "fluid" has been deliberately avoided thus far, because the discrete nature of the charged particles that are the constituents of a plasma plays an important role, which we shall now discuss.

We are considering a macroscopically neutral plasma composed of electrons and ions. The motion of the ions caused by the wave's electric field is ignored in view of their large inertia ($m_i/m_e \geq 1836.2$). Thus, we need only to determine the motion of the electrons and the fields generated by them, viz., the *scattered* fields. Clearly, some knowledge of the relative positions of the electrons is necessary to make such a determination. If the plasma could be treated as an ideal gas, a completely random distribution could be assumed; this in turn would cause the phases of the scattered fields to be randomly distributed as well. In that case the fields from the individual electrons would add up incoherently, that is, the *intensities*, rather than the amplitudes, would be additive. The behavior of a plasma, however, departs from that of an ideal gas owing to the Coulomb forces between the charges, which generate some degree of correlation or collective behavior. To lowest order, this degree of correlation is expressed quantitatively by the two-particle, electron-electron correlation function, which for a plasma in thermodynamic equilibrium is[91]

$$P_{12}(\mathbf{x_1}, \mathbf{x_2}) = -\frac{g}{8\pi} \frac{\exp(-|\mathbf{x_1} - \mathbf{x_2}|/\lambda_D)}{|\mathbf{x_1} - \mathbf{x_2}|/\lambda_D}. \tag{2.3}$$

This expression introduces two important parameters. The *Debye length* λ_D is defined as $\lambda_D \equiv (\kappa T/8\pi n_e e^2)^{1/2}$, where κ is Boltzmann's constant and T is the plasma temperature; the *plasma parameter* g is defined as $g \equiv 1/(n_e \lambda_D^3)$. It is clear from Eq. (2.3) that the plasma parameter is a measure of the overall level of correlation in the plasma. If $g \gtrsim 1$, collective effects cannot be neglected, and in fact correlation functions of higher degree may also come into play. The condition $g \ll 1$, which is generally termed *plasma approximation*, ensures that a first-order expansion based on Eq. (2.3) is adequate. This condition is generally well satisfied in thermonuclear plasmas, as shown by the following example, in which the parameters are deliberately chosen to be unrealistically unfavorable: since $g \propto n_e^{1/2} T^{-3/2}$, we take a temperature of 10 eV (appropriate for the edge region explored in this study) and a density of 10^{14} cm^{-3}, to be found at the center of the discharge, obtaining $g = 7.7 \times 10^{-4}$. The plasma approximation will be assumed implicitly henceforth.

The Debye length takes the role of an effective correlation distance. This can be explained physically as follows: each particle repels like charges and attracts unlike charges, causing the formation of an equilibrium "cloud" whose total charge is equal and opposite to the charge of the test particle under consideration. The characteristic dimension of the cloud is λ_D. The Coulomb force between two electrons separated by distances larger than λ_D is effectively shielded by their respective clouds, and the electrons do not interact. It should be noted that Eq. (2.3) breaks down when P_{12} is of order unity or greater, i.e., for distances smaller than $g\lambda_D$. However, since $g\lambda_D/(n_e^{-1/3}) = g^{2/3} \ll 1$, it follows that the distance for which Eq. (2.3) is not applicable is much smaller than the average distance between electrons.

To explore the relevance of plasma correlations to the problem of wave-plasma

interaction, it is useful to calculate the spatial Fourier transform of P_{12}:

$$\hat{P}_{12}(\mathbf{k}) = -\frac{1}{2n_e}\frac{1}{1+1/\alpha^2}, \tag{2.4}$$

where $\alpha \equiv 1/(k\lambda_D)$. Thus, correlations in wave-number space are significant for $\alpha \gg 1$ (wavelengths much longer than λ_D) and vanish in the short-wavelength limit, i.e., when $\alpha \ll 1$. To corroborate the significance of the parameter α, one can calculate the fluctuations in the equilibrium density induced by two-particle correlations: the Fourier spectrum of the fluctuations is found[86] to be proportional to α^2. To interpret this result physically, consider the following. The two-particle correlation function [Eq. (2.3)] is small in absolute value owing to the smallness of g; hence the positions of any two electrons, even if they are close, are essentially uncorrelated. In the short-wavelength regime, the phase undergoes large changes over a Debye volume, causing these small correlation effects to average out. Conversely, when the wavelength becomes of order λ_D, a large number of particles contribute in phase: although the correlation strength is of order $1/(n_e\lambda_D^3)$, there are $\approx n_e\lambda_D^3$ electrons contributing, and the total effect is of order unity. Increasing the wavelength beyond a few Debye lengths does not alter this picture, since the particles located outside the Debye sphere do not contribute at all.

The short-wavelength limit, $\alpha \ll 1$, coincides with the ideal-gas approximation and produces *incoherent scattering*, which is used for diagnostic purposes to measure density and temperature. The long-wavelength limit, $\alpha \gg 1$, gives rise to *coherent*, or *collective, scattering*. In the latter limit the amplitudes of the fields generated by the electrons add up coherently. The experiments described in the present work were carried out in the coherent regime: typical values were $\lambda_D \simeq 10$–60 μm and $\lambda \simeq 0.5$–7.6 cm, resulting in $\alpha \geq 13$. Hereafter this limit will be assumed implicitly throughout.

We can now examine the effect of an externally launched electromagnetic wave on the plasma. The plasma current due to the wave's electric field is carried almost entirely by the electrons because of their small inertia:

$$\mathbf{J} = -en_e\mathbf{v}_e, \tag{2.5}$$

where $\mathbf{v_e}$ is the electron fluid velocity and e is the positive electronic charge. In a perturbative approach, we ignore the effect of the wave's magnetic field in calculating the electron velocity, since the Lorentz force $(e/c)(\mathbf{v}_e \times \mathbf{B})$ is of second order. The equation of motion of a single cold electron in the presence of a monochromatic wave $\mathbf{E}(\mathbf{x})e^{-i\omega_0 t}$ is

$$\mathbf{v}_e = -i\frac{e}{m_e\omega_0}\left(\mathbf{E} + \frac{\mathbf{v}_e}{c} \times \mathbf{B}_0\right). \tag{2.6}$$

If we ignore for the moment the static magnetic field $\mathbf{B}_0$, we can solve Eq. (2.6) and obtain the relation

$$\mathbf{v}_e = -i\frac{e}{m_e\omega_0}\mathbf{E}. \tag{2.7}$$

Using this expression in the right-hand side of Eq. (2.6), and recalling Eq. (2.2), we immediately conclude that the magnetic-field term that we have ignored is indeed negligible. Inserting Eq. (2.7) into Eq. (2.5) yields

$$\mathbf{J} = i\frac{\omega_{pe}^2}{4\pi\omega_0}\mathbf{E}, \tag{2.8}$$

which defines an effective conductivity

$$\sigma \equiv i\frac{\omega_{pe}^2}{4\pi\omega_0}. \tag{2.9}$$

A general comment on the temporal dependence of σ is in order at this point. Here, σ could be time-dependent through the electron density n_e. Nevertheless, the characteristic frequency ω of the density is generally much smaller than ω_0; accordingly, *multiplicative* quantities of order ω/ω_0 are ignored. The temporal dependence of n_e can be potentially significant, however, when it appears in exponents and phases; if an exponent or phase is of order unity, it must be retained even if exponents or phases of order ω_0/ω are concurrently present.

The effect of the plasma on the electromagnetic wave can now be examined from two equivalent perspectives: the wave can be thought of as propagating in vacuum in the presence of a charge distribution ρ and of a current distribution $\mathbf{J}$; alternatively, the plasma can be seen as a dielectric, characterized by a dielectric function ϵ, in which no charges are present. The two pictures are easily unified by the Maxwell-Ampère equation,

$$\nabla \times \mathbf{H} = \frac{4\pi}{c}\mathbf{J} - i\frac{\omega_0}{c}\mathbf{E} = \frac{1}{c}\left(-i\omega_0\epsilon + \frac{\partial\epsilon}{\partial t}\right)\mathbf{E}. \tag{2.10}$$

The linear superposition of the fields generated by the individual particles is ensured by the conditions for coherent scattering. If we ignore the $\partial\epsilon/\partial t$ term, this expression, by virtue of Eq. (2.8), implies

$$\epsilon = 1 + i\frac{4\pi\sigma}{\omega_0} = 1 - \frac{\omega_{pe}^2}{\omega_0^2}. \tag{2.11}$$

Clearly, since $\partial\epsilon/\partial t$ is of order $\omega\omega_{pe}^2/\omega_0^2$, and since $\omega/\omega_0 \ll 1$ and $\omega_{pe}/\omega_0 \ll 1$ [Eq. (2.1)], it was legitimate to neglect the $\partial\epsilon/\partial t$ term in Eq. (2.10). We note in passing that, having neglected the Lorentz force from the wave's magnetic field, we find no magnetization effects; hence, the permeability μ is unity.

The plasma-wave interaction can now be described simply by the wave equation in a dielectric, which, neglecting terms of order ω/ω_0, is[92]

$$\left(\nabla^2 - \frac{\epsilon}{c^2}\frac{\partial^2}{\partial t^2}\right)\mathbf{E} + \nabla(\mathbf{E}\cdot\nabla\ln\epsilon) = 0, \tag{2.12}$$

with ϵ given by Eq. (2.11). The last term in the left-hand side of Eq. (2.12) can be written in a different fashion by making use of Coulomb's law

$$\nabla \cdot (\epsilon \mathbf{E}) = 0, \tag{2.13}$$

which yields

$$\nabla(\mathbf{E}\cdot\nabla \ln \epsilon) = -\nabla(\nabla \cdot \mathbf{E}) = -4\pi\nabla\rho, \tag{2.14}$$

where ρ is the polarization charge density. The polarization term is often neglected in small-angle scattering calculations; although such an approximation, as we shall see, is appropriate in the context of far-forward scattering, it is important to retain it in a more general treatment.

Note that Eq. (2.1), combined with Eq. (2.11), ensures that $\epsilon \approx 1$. Thus, in the simple case of a homogeneous plasma, the polarization term in Eq. (2.12) vanishes, and we are left with the equation of a plane electromagnetic wave with phase velocity $|v_\phi| \approx c$. This proves that the cold-plasma approximation is adequate if the plasma is nonrelativistic. This condition is well satisfied in present thermonuclear experiments. As an example, an electron temperature $T_e = 5$ keV corresponds to a thermal velocity $v_{te} \simeq 0.10 \times c$.

2.2 Integration of the Wave Equation

In the previous section we derived a differential equation for the wave field in the plasma. To obtain an analytical expression for $\mathbf{E}$, whether by solving Eq. (2.12) or by starting from first principles, it is necessary to adopt certain approximations. Several such approximation schemes are reviewed in this section and in the ones that follow. These various methods differ somewhat in the physical scenarios to which they are applicable; it will be shown, however, that in reality these schemes portray different aspects of the same problem. The aim of §§2.2–2.8 is to provide a unifying view of the problem and to set the stage for a comparative analysis of a broad class of scattering and imaging diagnostics.

The wave equation (2.12) can be rewritten as a classical inhomogeneous vectorial wave equation, which, if terms of order ω/ω_0 are neglected, takes the form

$$\left(\nabla^2 - \frac{1}{c^2}\frac{\partial^2}{\partial t^2}\right)\mathbf{E}(\mathbf{x},t) = -4\pi\mathbf{f}(\mathbf{x},t), \tag{2.15}$$

where

$$\mathbf{f}(\mathbf{x},t) = \frac{\omega_0^2}{c^2}\frac{\epsilon-1}{4\pi}\mathbf{E} + \frac{1}{4\pi}\nabla(\mathbf{E}\cdot\nabla\ln\epsilon), \tag{2.16}$$

or, by virtue of Eq. (2.11),

$$\mathbf{f}(\mathbf{x},t) = -r_e n_e \mathbf{E} + \frac{1}{4\pi}\nabla(\mathbf{E}\cdot\nabla\ln\epsilon), \tag{2.17}$$

where $r_e \equiv e^2/(m_e c^2)$ is the classical radius of the electron. Note that the three scalar equations (2.15) are vectorially coupled through the last term in Eq. (2.17).

Each component of Eq. (2.15) can formally be solved by means of Green function techniques. However, the resulting integral expressions will still contain the unknown functions E_i. In effect, we are simply transforming differential equations into integral equations; but, as we shall see, the integral formulation is naturally conducive to a perturbative approach. The time-dependent, retarded Green function is[93]

$$G(\mathbf{x},t;\mathbf{x}',t') = G(R,\tau) = \frac{1}{R}\,\delta\left(\tau - \frac{R}{c}\right), \tag{2.18}$$

where $R = |\mathbf{x}-\mathbf{x}'|$ and $\tau = t-t'$. We consider here the case of an externally launched monochromatic wave whose field $\mathbf{E}_0$ satisfies the homogeneous equation at the time $t \to -\infty$. The appropriate solution is then

$$\mathbf{E}(\mathbf{x},t) = \mathbf{E}_0(\mathbf{x})e^{-i\omega_0 t} + \iint G(\mathbf{x},t;\mathbf{x}',t')\mathbf{f}(\mathbf{x}',t')d^3x'dt'. \tag{2.19}$$

Using Eq. (2.18), this becomes

$$\mathbf{E}(\mathbf{x},t) = \mathbf{E}_0(\mathbf{x})e^{-i\omega_0 t} + \int \frac{[\mathbf{f}(\mathbf{x}',t')]_{\text{ret}}}{R} d^3x', \tag{2.20}$$

where $[\ ]_{\text{ret}}$ indicates that the expression is to be evaluated at the retarded time $t' = t - R/c$. We can now substitute the explicit expression for $\mathbf{f}$ from Eq. (2.17) in Eq. (2.20), obtaining finally

$$\mathbf{E}(\mathbf{x},t) = \mathbf{E}_0(\mathbf{x})e^{-i\omega_0 t} + \int \frac{1}{R}\left[-r_e n_e' \mathbf{E}' + \frac{1}{4\pi}\nabla'(\mathbf{E}'\cdot\nabla'\ln\epsilon')\right]_{\text{ret}} d^3x', \tag{2.21}$$

where the prime indicates quantities to be evaluated at $(\mathbf{x}',t')$.

We now make the very weak assumption $k_0 R \gg 1$ (where $k_0 = \omega_0/c$), which is satisfied, even for far-infrared waves, whenever R is larger than a few cm. By virtue of this approximation and of the relation $|1-\epsilon| \ll 1$, Eq. (2.21) can be recast in the following form:

$$\mathbf{E}(\mathbf{x},t) = \mathbf{E}_0(\mathbf{x})e^{-i\omega_0 t} + r_e \int \left[n_e' \frac{\hat{\mathbf{n}}\times(\hat{\mathbf{n}}\times\mathbf{E}')}{R}\right]_{\text{ret}} d^3x', \tag{2.22}$$

$\hat{\mathbf{n}}$ being a unit vector in the direction of $\mathbf{x}-\mathbf{x}'$. The derivation of Eq. (2.22) is carried out in detail in Appendix A.

Equation (2.22) has a very immediate physical interpretation. The electrons in the plasma are accelerated by the electric field:

$$\dot{\mathbf{v}}_e = -\frac{e}{m_e}\mathbf{E}. \tag{2.23}$$

Accelerated electrons generate a radiation field, which in the nonrelativistic limit is given by[93]

$$\mathbf{E}_{\rm rad} = \frac{-e}{c^2}\left[\frac{\hat{\mathbf{n}}\times(\hat{\mathbf{n}}\times\dot{\mathbf{v}}_e)}{R}\right]_{\rm ret} = r_e\left[\frac{\hat{\mathbf{n}}\times(\hat{\mathbf{n}}\times\mathbf{E})}{R}\right]_{\rm ret}. \tag{2.24}$$

The sum of the radiation fields produced by the individual electrons, in the coherent-scattering limit, can be replaced by the integral $\int n_e d^3x'$. Thus, Eq. (2.22) states simply that the total scattered field is the sum of the field of the incident wave and of the radiation field generated by the plasma electrons. Here we are ignoring the velocity fields because of their $1/R^2$ dependence; this is the same key assumption used in Appendix A to derive Eq. (2.22). In fact, the radiation argument is universally used to obtain Eq. (2.22) in the context of scattering.[86,29] Our aim here has been to show that the wave-equation approach is entirely equivalent to the radiation approach, provided that the polarization term is retained.

We now turn our attention to the conditions under which it is permissible to ignore the polarization term. We shall later see that the condition $|1-\epsilon| \ll 1$ ensures that the scattered field is small in comparison with the field of the incident wave. For the moment we can therefore replace the field $\mathbf{E}$ in the polarization term [Eq. (2.14)] with the incident field, which is taken to be a plane wave, $\mathbf{E}_0 e^{i\mathbf{k}_0\cdot\mathbf{x}}$. For the sake of definiteness we also take a harmonic density perturbation of the form $\tilde{n}_e = \hat{n}_e e^{i\mathbf{k}\cdot\mathbf{x}}$. Then, using Eq. (2.11), we can write

$$\begin{aligned}\nabla(\mathbf{E}\cdot\nabla\ln\epsilon) &\simeq -i\frac{\omega_{pe}^2}{\omega_0^2}\nabla\left(\mathbf{k}\cdot\mathbf{E}_0 e^{i(\mathbf{k}_0+\mathbf{k})\cdot\mathbf{x}}\right)\\ &= \frac{\omega_{pe}^2}{\omega_0^2}(\mathbf{E}_0\cdot\mathbf{k})(\mathbf{k}_0+\mathbf{k})e^{i(\mathbf{k}_0+\mathbf{k})\cdot\mathbf{x}}.\end{aligned} \tag{2.25}$$

The conditions under which this term can be neglected can be easily assessed by imposing that the polarization term be negligible in the right-hand side of Eq. (2.17). That requirement is

$$\frac{\omega_{pe}^2}{c^2}\frac{k}{k_0}\left(1+\frac{k}{k_0}\right)|\mathbf{E}_0| \ll 4\pi r_e \hat{n}_e |\mathbf{E}_0|, \tag{2.26}$$

which implies

$$\frac{k}{k_0} \ll 1. \tag{2.27}$$

This equation states that the wavelength of the diffracting perturbation must be much longer than that of the incident wave. We shall show shortly that, in the case of the monochromatic density perturbation considered here, the scattered power is peaked about the scattering angles ϕ_B given by the Bragg relation

$$\phi_B = \pm\frac{k}{k_0}. \tag{2.28}$$

Thus, Eq. (2.27) expresses the condition for small-angle scattering. This condition will be assumed in the remainder of this work, and the polarization term in Eqs. (2.17) and (2.21) will accordingly be neglected. In addition, it is clear from the form of Eq. (2.17) that the small-angle scattering condition allows us also to ignore the coupling between the vectorial components of $\mathbf{E}$, so that the equations become effectively scalar. Under these conditions, Eq. (2.21) reduces to

$$\mathbf{E}(\mathbf{x},t) = \mathbf{E}_0(\mathbf{x})e^{-i\omega_0 t} + \int \frac{1}{R}\left[-r_e n_e' \mathbf{E}'\right]_{\text{ret}} d^3x'. \tag{2.29}$$

In order to obtain an explicit solution to Eq. (2.29), some approximations are necessary. Perturbation techniques, of either an additive (*Born approximation*) or a multiplicative (*Rytov approximation*) nature, are commonly employed to that end. In general, the key assumption is $|1-\epsilon| \ll 1$, although the detailed requirements vary depending on the particular technique under exam. The analysis that occupies the next six sections concerns the specific case of a plasma, but is equally applicable to a generic dielectric medium for which the condition $|1-\epsilon| \ll 1$ holds. The transition to the general case can be made at each step by using Eq. (2.11).

2.3 The Born Approximation

In the Born approximation the wave field is written as a series

$$\mathbf{E} = \mathbf{E}_0 + \mathbf{E}_1 + \mathbf{E}_2 + \ldots \tag{2.30}$$

and only terms up to first order are retained. The condition for the exclusion of the polarization term, expressed by Eq. (2.27), implies that that term is of second order in the Born sense. The function $\mathbf{f}$, defined by Eq. (2.16), does not contribute any zeroth-order terms to the wave equation (2.15); thus, the zeroth-order solution is simply the incident wave $\mathbf{E}_0(\mathbf{x})e^{-i\omega_0 t}$. The first-order solution $\mathbf{E}_1$ is obtained by replacing $\mathbf{E}'$ with $\mathbf{E}_0'$ inside the integral in Eq. (2.29). Hence,

$$\mathbf{E}_1(\mathbf{x},t) = -r_e e^{-i\omega_0 t} \int \frac{e^{i\omega_0 R/c}}{R}\left[n_e'\right]_{\text{ret}} \mathbf{E}_0'\, d^3x'. \tag{2.31}$$

For this approximation to be consistent, the second-order terms in Eq. (2.16) must be small. Since the ordering parameter is $|1-\epsilon|$, we must require that $|\mathbf{E}_1|/|\mathbf{E}_0| \sim O(|1-\epsilon|)$ inside the plasma. To interpret this requirement, we can examine the simple case in which ϵ is constant across a plasma column: the wave is then dispersionless and simply propagates with a phase velocity $c/\sqrt{\epsilon}$, whereas the *unperturbed* wave would propagate with velocity c. If the wave is propagating along the z direction (see Fig. 2.1), one can then write

$$\mathbf{E}_1(z,t) = \mathbf{E}_0(z,t)\left[e^{ik_0(\sqrt{\epsilon}-1)z} - 1\right]. \tag{2.32}$$

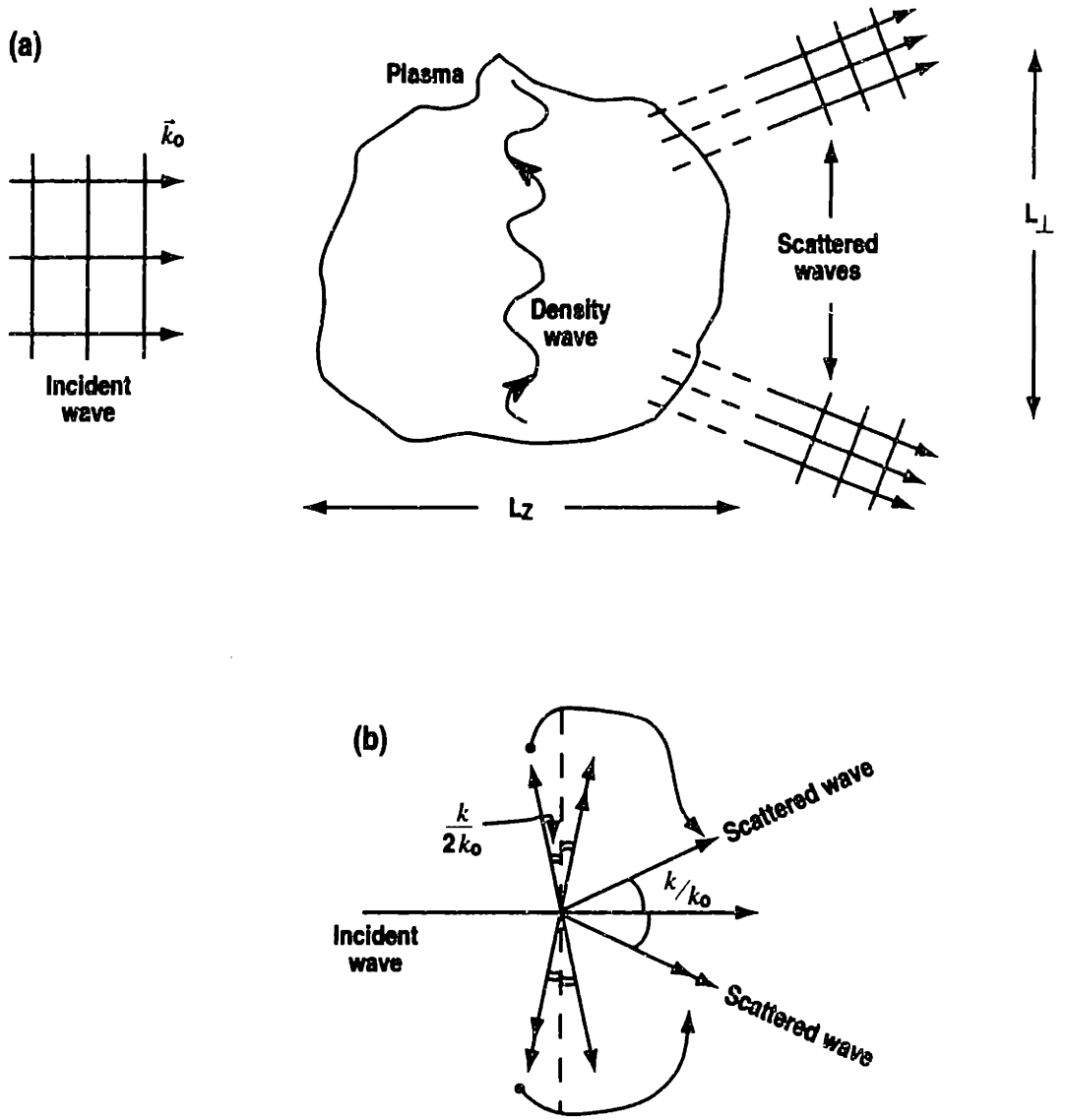

Fig. 2.1 (a) Interaction of an electromagnetic wave with a plasma; (b) selection rules for scattering vectors and scattered waves.

For $|\mathbf{E}_1|/|\mathbf{E}_0|$ to be of the same order as $|1-\epsilon|$, we must impose $\frac{1}{2}|1-\epsilon|k_0 L_z \sim O(|1-\epsilon|)$, or

$$\lambda_0 r_e L_z n_e \ll 1. \tag{2.33}$$

Here, $\lambda_0 = 2\pi/k_0$, and L_z is the length of the plasma column. Thus, the Born approximation in the present context translates into three separate conditions: $\omega_{pe}^2/\omega_0^2 \ll 1$, $\lambda_0 r_e L_z n_e \ll 1$, and $k/k_0 \ll 1$.

We can now apply the Born approximation to the scattering equation (2.29). We adopt the following additional approximation: *in the phase of the field*, $k_0 R \simeq k_0(R_0 - \hat{\mathbf{n}} \cdot \mathbf{x}')$, where $\hat{\mathbf{n}} = \mathbf{R}_0/R_0$, and $\mathbf{R}_0$ is a vector joining an average location in the plasma to the observation point. This is a first-order Taylor expansion of the

phase, which requires that the second-order term be much smaller than 1 radian, i.e.,

$$R_0 \gg \frac{k_0 L_\perp^2}{8}, \tag{2.34}$$

where $L_\perp$ indicates a characteristic dimension of the interaction region in the plane perpendicular to the direction of propagation of the incident wave [see Fig. 2.1(a)]. Here we have used the fact, which will be verified at the end of the derivation, that the direction of $\hat{\mathbf{n}}$ deviates little from that of the unperturbed wave vector $\mathbf{k}_0$. The dimension $L_\perp$ is defined by the intersection of the cross section of the plasma and the region of space occupied by the incident wave. Under these conditions we can also replace $1/R$ with $1/R_0$.

We now adopt a simplified scenario in order to illustrate the physical mechanism behind the Bragg condition, Eq. (2.28). In this scenario we take the incident wave to be a plane wave and we isolate a sinusoidal component of the electron density, $n_e(\mathbf{x},t) = \hat{n}_k \cos(\mathbf{k}\cdot\mathbf{x} - \omega t)$. The perturbed field takes the form

$$\mathbf{E}_1(\mathbf{x},t) \simeq -\frac{r_e}{R_0}\hat{n}_k \mathbf{E}_0 \frac{1}{2}\sum_{\pm} e^{-i(ck_0 \pm \omega)(t - R_0/c)} \int e^{i[\mathbf{k}_0 \pm \mathbf{k} - (k_0 \pm \omega/c)\hat{\mathbf{n}}]\cdot\mathbf{x}'} d^3x'. \tag{2.35}$$

Upon integration, we are left with the sum of two delta functions, which yield the following selection rules:

$$\hat{\mathbf{n}}_\pm = \frac{\mathbf{k}_0 \pm \mathbf{k}}{k_0 \pm \omega/c}. \tag{2.36}$$

Imposing the condition $\hat{\mathbf{n}}\cdot\hat{\mathbf{n}} = 1$, we then find the relations $k^2 \pm 2kk_0\cos\theta = \pm 2k_0\omega/c + \omega^2/c^2$, where θ is the angle between $\mathbf{k}_0$ and $\mathbf{k}$; since most plasma perturbations are characterized by phase velocities much smaller than the speed of light, the last term can be ignored and we find

$$\cos\theta_\pm \simeq \frac{\omega}{ck} \mp \frac{k}{2k_0}, \tag{2.37}$$

from which we conclude that $|\cos\theta_\pm| \ll 1$, i.e., that the density wave must propagate nearly at right angles with the probing electromagnetic wave (see Fig. 2.1). Making use of Eqs. (2.36) and (2.37), we can now calculate the scattering angles $\Phi_{B\pm}$:

$$\cos\Phi_{B\pm} = \hat{\mathbf{n}}_\pm \cdot \frac{\mathbf{k}_0}{k_0} = 1 - \frac{k^2}{2k_0^2(1 \pm \omega/\omega_0)}. \tag{2.38}$$

Neglecting ω/ω_0, one can write

$$\Phi_B = 2\arcsin\left(\frac{k}{2k_0}\right). \tag{2.39}$$

For small-angle scattering ($k \ll k_0$) this equation is equivalent to the Bragg condition [Eq. (2.28)].

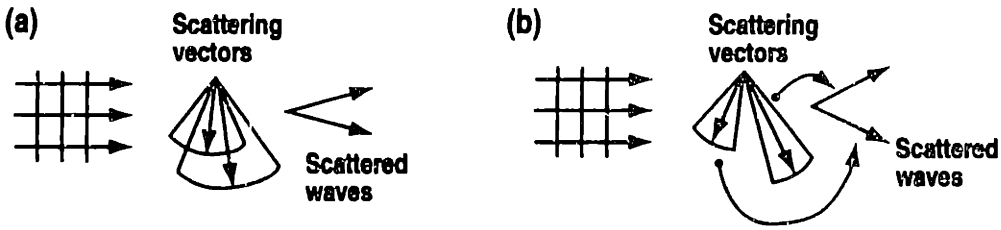

Fig. 2.2 Indetermination cones of scattering vectors: (a) overlapping (Raman-Nath regime), (b) not overlapping (Bragg regime).

The meaning of this condition is clarified by the transition from Eq. (2.31) to Eq. (2.35). Each electron radiates in all directions; if we concentrate on the wave radiated by an electron in one particular direction and follow it as it propagates through the plasma, we will see it change as other electrons contribute to it. Each contribution, however, has a different phase, equal to the sum (or difference) of the phase of the density wave and of the phase of the accelerating electric field at the delayed time the radiated wave reaches that particular point. The resulting radiated field, therefore, is generally zero, except in the two directions that allow all electrons to contribute in phase, i.e., the Bragg directions.

Two important observations must be made at this point. The first is that the selection rules that we have derived impose constraints both on the scattering directions *and* on the direction of propagation of the scattering perturbation. No scattering occurs at angles other than the Bragg angles, and no scattering occurs if the density wave is not nearly perpendicular to the electromagnetic wave. The second observation is that the two Bragg angles $\pm k/k_0$ correspond to two different density waves, propagating in the different, albeit very close, directions specified by Eq. (2.37) and shown in Fig. 2.1(b). Thus, under the conditions of our derivation, a single sinusoidal density perturbation generates at most *one* scattered wave. These conditions are, however, simplified and idealized. In reality the integration volume in Eq. (2.35) is not infinite; as a result, the delta functions are replaced by functions of finite width, $\delta k_z \approx \pi/L_z$, and the selection rules for the density waves are relaxed to a finite angular spread, $\delta\theta \approx \delta k_z/k$. If there is substantial overlap between the θ_+ and θ_- cones, as shown in Fig. 2.2(a), both scattered waves exist simultaneously. This condition can be written as $|\cos\theta_+ - \cos\theta_-| \lesssim \delta k_z/k$, i.e.,

$$L_z \lesssim \frac{\pi k_0}{k^2}. \tag{2.40}$$

The regime in which this condition is satisfied is known as the *Raman-Nath regime*. The opposite limit, in which only one scattering angle is allowed, is called the *Bragg regime* [Fig. 2.2(b)].

These regimes were given their names in the context of diffraction from ultrasonic waves in fluids, a branch of optics with a long history both in experiment and in theory. It must be stressed that the distinction between scattering and diffraction is entirely of a historical nature. Both terms describe departures from geometrical

optics caused by the finite wavelengths of the waves. Diffraction, however, is generally associated with the interaction of waves with obstacles or apertures whose dimensions are large compared with a wavelength. In particular, a spatially periodic arrangement of obstacles or apertures is called a diffraction grating. It was recognized as early as in 1921[94] that a fluid traversed by a compression wave would behave as a diffraction grating, giving rise to the same Bragg condition [Eq. (2.28)] that we have derived through a scattering treatment. In the diffraction picture, additional scattering angles at integral multiples (known as *diffraction orders*) of the Bragg angle appear naturally. These higher diffraction orders correspond to higher orders of expansion in the Born approximation, which include the effects of multiple scattering. Raman and Nath were the first to obtain approximate expressions for the intensities of the different scattering orders,[95] adopting the approximation expressed by Eq. (2.40). Their result for the amplitude of the l-th order, adapted for the case of a plasma[96] traversed by a sinusoidal density wave $n_e = \hat{n}_k \cos(\mathbf{k}\cdot\mathbf{x} - \omega t)$, is

$$|E_l| \simeq |E_0||J_l(\lambda_0 r_e L_z \hat{n}_k)|. \tag{2.41}$$

This expression shows that the intensities of the positive and negative orders are identical in the Raman-Nath regime. Also, the argument of the Bessel function is the expansion parameter of the Born approximation, as indicated by Eq. (2.33). Thus, for small arguments Eq. (2.41) can be approximated by[97]

$$|E_l| \simeq |E_0|\frac{1}{|l|!}\left(\frac{1}{2}\lambda_0 r_e L_z \hat{n}_k\right)^{|l|}. \tag{2.42}$$

Each diffraction order is thus associated with the corresponding order of expansion in the Born approximation.

As a corollary, it is easy to see now that the physical meaning of the Born approximation is to ignore multiple scattering, which arises from radiation emitted by electrons accelerated by the *scattered* field itself.

2.4 The Rytov Approximation

We now turn our attention to a different type of approximation, which is due to Rytov[98]. The wave's field is written in exponential form $\mathbf{E} = \mathbf{e}_0 e^{\psi}$, where $\mathbf{e}_0$ is a unit polarization vector. The complex phase ψ is expanded in a Taylor series

$$\psi = \psi_0 + \psi_1 + \psi_2 + \ldots, \tag{2.43}$$

in which terms up to first order are retained. If the polarization term is neglected, the wave equation (2.15), combined with Eq. (2.16), can be written

$$\nabla^2\psi + \nabla\psi \cdot \nabla\psi - \frac{\ddot{\psi}}{c^2} - \frac{\dot{\psi}^2}{c^2} = (1-\epsilon)k_0^2. \tag{2.44}$$

The unperturbed solution ψ_0 satisfies the equation

$$\nabla^2\psi_0 + \nabla\psi_0 \cdot \nabla\psi_0 - \frac{\ddot{\psi}_0}{c^2} - \frac{\dot{\psi}_0^2}{c^2} = 0. \tag{2.45}$$

Although this is a nonlinear equation, a comparison with Eq. (2.15) shows that e^{ψ_0} must be identical with the zeroth-order (viz., free-space) Born solution.

The first-order equation can be written

$$\nabla^2\psi_1 + 2\nabla\psi_0 \cdot \nabla\psi_1 - \frac{\ddot{\psi}_1}{c^2} - 2\frac{\dot{\psi}_0\dot{\psi}_1}{c^2} = (1-\epsilon)k_0^2, \tag{2.46}$$

where we have ignored the second-order terms $\nabla\psi_1 \cdot \nabla\psi_1$ and $\dot{\psi}_1^2/c^2$. Multiplying Eq. (2.45) by ψ_1 and adding the result to Eq. (2.46), we obtain

$$e^{-\psi_0}\left[\nabla^2\left(\psi_1 e^{\psi_0}\right) - \frac{1}{c^2}\frac{\partial^2}{\partial t^2}\left(\psi_1 e^{\psi_0}\right)\right] = (1-\epsilon)k_0^2, \tag{2.47}$$

which has the formal structure of a wave equation and can be solved with the Green function techniques introduced in the solution of Eq. (2.15). The analogy, it must be stressed, is merely of a formal nature. In particular, the appropriate homogeneous solution for $t \to -\infty$ in this case is zero, since ψ_1 is a perturbation caused by the plasma-wave interaction. Hence, by analogy with Eq. (2.20), we find the solution

$$\psi_1(\mathbf{x},t) = -e^{-\psi_0(\mathbf{x},t)}\, r_e \int \frac{1}{R}\left[n_e' e^{\psi_0'}\right]_{\text{ret}} d^3x', \tag{2.48}$$

where again the prime indicates quantities to be evaluated at (x',t'). A comparison with Eq. (2.31) yields the following remarkable corollary:

$$\psi_1(\mathbf{x},t) = E_1(\mathbf{x},t)/E_0(\mathbf{x},t), \tag{2.49}$$

where E_0 and E_1 are the complex scalar Born fields. Hence, the first-order complex Rytov phase is equal to the ratio of the first- and zeroth-order Born fields. This nontrivial result does not imply that the two approximations are equivalent. In fact, in the Born approximation we write the field as $\mathbf{E}_{\text{Born}} = \mathbf{e}_0(E_0 + E_1)$, whereas in the Rytov approximation, expanding the exponential and making use of Eq. (2.49), we can write $\mathbf{E}_{\text{Rytov}} = \mathbf{e}_0[E_0 + E_1 + E_1^2/(2E_0) + \ldots]$. The additional terms not included in the Born scheme can be interpreted as contributions from multiple-scattering events: in this sense the Rytov approximation is superior to the Born approximation.

The clearest advantage of the Rytov approximation can be gleaned by determining the conditions for its validity. The requirement is that the second-order terms in Eq. (2.44) be negligible with respect to the first-order terms. Repeating the arguments that followed Eq. (2.31), we assume ϵ for the moment to be constant and uniform and write $\psi_1(z) = ik_0(\sqrt{\epsilon} - 1)z$. The second-order term here is $\nabla\psi_1 \cdot \nabla\psi_1$, and the appropriate inequality is

$$|\nabla\psi_1 \cdot \nabla\psi_1| \ll |1 - \epsilon| k_0^2, \tag{2.50}$$

which translates into

$$|1 - \epsilon| \ll 4. \tag{2.51}$$

So the condition $|\epsilon - 1| \ll 1$ is sufficient for the Rytov approximation, without additional constraints on the length of the plasma column as in the Born case [Eq. (2.33)].

From these arguments the Rytov approximation would appear to be preferable to the Born scheme. At this point, however, a caveat is in order. The Born fields E_1, E_2, etc., all obey a wave equation of the form of Eq. (2.15) and therefore automatically follow the laws of free-space propagation once the wave exits the plasma ($\epsilon \to 1$); this is a consequence of the linearity of the expansion in the field variables. The same cannot be said about the Rytov fields, even to first order, since the approximation entails the elimination of a term of the type $\nabla\psi_1 \cdot \nabla\psi_1$, which appears in the *left side* of Eq. (2.44). In particular, if ψ_1 is calculated by means of Eq. (2.48) at some point beyond the plasma, it will contain information on the density fluctuations in the plasma and thus, in general, its gradient will be finite. In this case the inequality of Eq. (2.50) clearly breaks down, since its right-hand side is zero. Hence, if Eq. (2.48) is used to calculate the Rytov field well beyond the end of the plasma column, significant errors may arise. To prevent these errors, a better procedure is to break the problem in two parts: first, Eq. (2.48) is used to derive ψ_1 in the near field, i.e., in a plane perpendicular to $\mathbf{k}_0$ situated at the end of the plasma column; then, the homogeneous (free-space) wave equation is used to propagate the full Rytov field $\exp(\psi_0 + \psi_1)$ from the plasma to the detection plane. This procedure is inconsistent, since the Rytov field, strictly speaking, does not satisfy the wave equation. Nevertheless, it is in general a good approximation as it avoids compounding the error through propagation in free space.

This difficulty notwithstanding, the Rytov method remains advantageous as it encompasses both the Born approximation and geometrical optics as special cases

and is the natural framework for measurement techniques, such as dark ground and shadowgraphy[99], that are sensitive to the second-order term in the Taylor expansion of e^{ψ_1}. We shall therefore use it in §§2.6–2.8 to derive general expressions that are relevant to the measurement of density fluctuations in plasmas. Ultimately it will generally be assumed that $|\psi_1| \ll 1$, and a first-order Taylor expansion of the exponential $e^{\psi_1} \simeq 1 + \psi_1$ will bring us back to the Born approximation. However, this is a special case of a result that applies to arbitrarily long plasma columns.

It should be remarked in closing that much theoretical and experimental work has been devoted to the subject of the relative merits of the Born and Rytov schemes, mostly in the context of scattering from ultrasonic waves in the atmosphere.[100–102]

2.5 Diffraction from an Aperture

Before we can explore the consequences of Eq. (2.48) in detail, we must obtain an expression for the unperturbed wave field $\mathbf{E}_0 e^{\psi_0}$. The unperturbed wave obeys the laws of free-space propagation, embodied in the homogeneous wave equation, viz., Eq. (2.15) with $\mathbf{f} = 0$. For a monochromatic wave $\mathbf{E}_0 e^{-i\omega_0 t}$, this reduces to the Helmholtz equation

$$\left(\nabla^2 + k_0^2\right) \mathbf{E}_0(\mathbf{x}) = 0, \tag{2.52}$$

where $k_0 \equiv \omega_0/c$.

In the analysis carried out thus far, we have approached the problem of wave propagation either by solving the differential wave equation directly or by means of a Green function technique, in which the solution was expressed in the form of a *volume* integral. The present problem is best approached by a third route, involving *surface* integrals. It can be shown[93] that if the Helmholtz equation (2.52) is satisfied in a region of space, knowledge of either the fields or their derivatives on a surface enclosing that region is sufficient to determine the fields everywhere in the region. This statement can be extended to the circumstance in which the surface is an infinite plane screen and the region under consideration is all the space on one side of it. We shall prove it for the case in which the known boundary quantity is the field.

In examining such a situation, we now take the screen S to be the plane $z = 0$. If the incident wave is propagating in the positive z direction, as shown in Fig. 2.1(a), we can decompose the field into its two-dimensional Fourier components with respect to the perpendicular-plane coordinates $\mathbf{x}_\perp = (x, y)$:

$$\mathbf{E}_0(\mathbf{x}_\perp, z) = \frac{1}{(2\pi)^2} \int \mathbf{A}_0(\mathbf{k}_\perp; z) e^{i\mathbf{k}_\perp \cdot \mathbf{x}_\perp} d^2 k_\perp. \tag{2.53}$$

Equation (2.52) then becomes a simple differential equation in the variable z, admitting the elementary solution[103]

$$\mathbf{A}_0(\mathbf{k}_\perp; z) = \mathbf{A}_0(\mathbf{k}_\perp; 0) e^{iz\sqrt{k_0^2 - k_\perp^2}}. \tag{2.54}$$

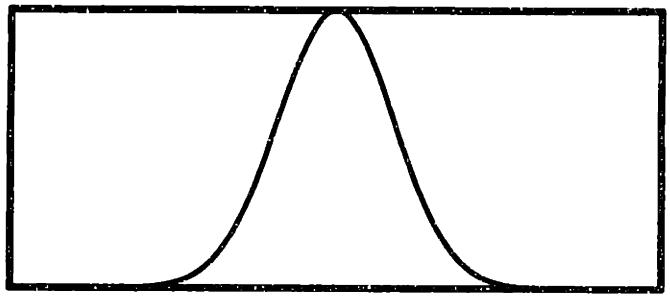

Fig. 2.3 Gaussian function.

This expression conveys the intuitive notion that each Fourier component is simply a plane wave, whose absolute wave number must therefore be equal to ω_0/c. Substituting for $\mathbf{A}_0$ from Eq. (2.54) in Eq. (2.53), we are able to conclude our proof by deriving the field distribution in any plane z from the knowledge of its distribution in the screen plane $z = 0$:

$$\mathbf{E}_0(\mathbf{x}_\perp, z) = \frac{1}{(2\pi)^2} \int d^2k_\perp e^{i\mathbf{k}_\perp \cdot \mathbf{x}_\perp} e^{iz\sqrt{k_0^2 - k_\perp^2}} \int \mathbf{E}_0(\mathbf{x}'_\perp, 0) e^{-i\mathbf{k}_\perp \cdot \mathbf{x}'_\perp} d^2x'_\perp. \quad (2.55)$$

If the incident wave is a plane wave, $\mathbf{E}_0$ does not depend on $\mathbf{x}_\perp$ and Eq. (2.55) yields the trivial result

$$\mathbf{E}_0(z) = e^{ik_0 z}\, \mathbf{E}_0(0). \quad (2.56)$$

With more complicated distributions, the integral over the wave numbers is customarily simplified by adopting the *Fresnel approximation* (also known as *parabolic*, or *paraxial, approximation*) for the exponential propagator:

$$\exp\left(iz\sqrt{k_0^2 - k_\perp^2}\right) \simeq \exp\left(ik_0 z - i\frac{k_\perp^2}{2k_0} z\right). \quad (2.57)$$

This approximation is justified if the lowest-order phase term that is not included is negligible, that is, if $zk_\perp^4/(8k_0^3) \ll 1$. In the paraxial approximation, Eq. (2.54) becomes

$$\mathbf{A}_0(\mathbf{k}_\perp; z) = \mathbf{A}_0(\mathbf{k}_\perp; 0) \exp\left(ik_0 z - i\frac{k_\perp^2}{2k_0} z\right). \quad (2.58)$$

In Eq. (2.55), the integral over the wave numbers can now be computed, and we obtain the result

$$\mathbf{E}_0(\mathbf{x}_\perp, z) = \frac{1}{2\pi} \frac{k_0}{iz} e^{ik_0 z} \int \mathbf{E}_0(\mathbf{x}'_\perp, 0) \exp\left(i\frac{k_0}{2z}|\mathbf{x}_\perp - \mathbf{x}'_\perp|^2\right) d^2x'_\perp. \quad (2.59)$$

In experiments involving laser beams, the Gaussian field distribution (see Fig. 2.3) is a particularly common one. By taking the beam to have a planar wave front in the plane $z = 0$ (called the *beam waist*), and defining w_0 as the e^{-1} radius of the amplitude profile, one can write[104]

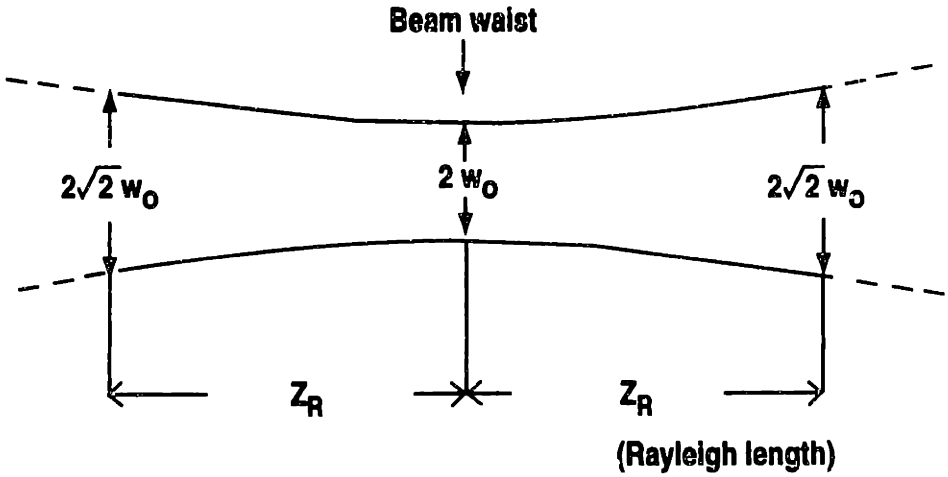

Fig. 2.4 Gaussian laser beam.

$$\mathbf{E}_0(\mathbf{x}_\perp, 0) = \left(\frac{8\pi}{c}P\right)^{1/2}\left(\frac{2}{\pi}\right)^{1/2}\frac{1}{w_0}\exp\left(-\frac{x_\perp^2}{w_0^2}\right)\mathbf{e}_0, \tag{2.60}$$

where P is the total beam power. The Fourier transform of this field is also Gaussian,

$$\mathbf{A}_0(\mathbf{k}_\perp; 0) = 4\pi\left(\frac{P}{c}\right)^{1/2} w_0\ \exp\left(-\frac{w_0^2 k_\perp^2}{4}\right)\mathbf{e}_0, \tag{2.61}$$

so that the condition for the paraxial approximation $zk_\perp^4/(8k_0^3) \ll 1$ can be rewritten as

$$\frac{2z}{k_0^3 w_0^4} \ll 1. \tag{2.62}$$

Applying the propagation formula, Eq. (2.59), to Eq. (2.60), we find, for a Gaussian beam,

$$\begin{aligned}\mathbf{E}_0(\mathbf{x}_\perp, z) = &\left(\frac{8\pi}{c}P\right)^{1/2}\left(\frac{2}{\pi}\right)^{1/2}\frac{1}{w_0(1+z^2/z_R^2)^{1/2}} \\ &\times \exp\left[-\frac{x_\perp^2}{w_0^2(1+iz/z_R)}\right]\exp\left[ik_0 z - i\arctan\left(\frac{z}{z_R}\right)\right]\mathbf{e}_0,\end{aligned} \tag{2.63}$$

where $z_R \equiv k_0 w_0^2/2$ is the *Rayleigh range*: this is the distance the beam travels from the waist before its diameter increases by $\sqrt{2}$ and is thus a measure of the beam collimation (see Fig. 2.4).

The Gaussian distribution will be used for all our subsequent calculations, with the additional assumption

$$k_0 w_0 \gg 1. \tag{2.64}$$

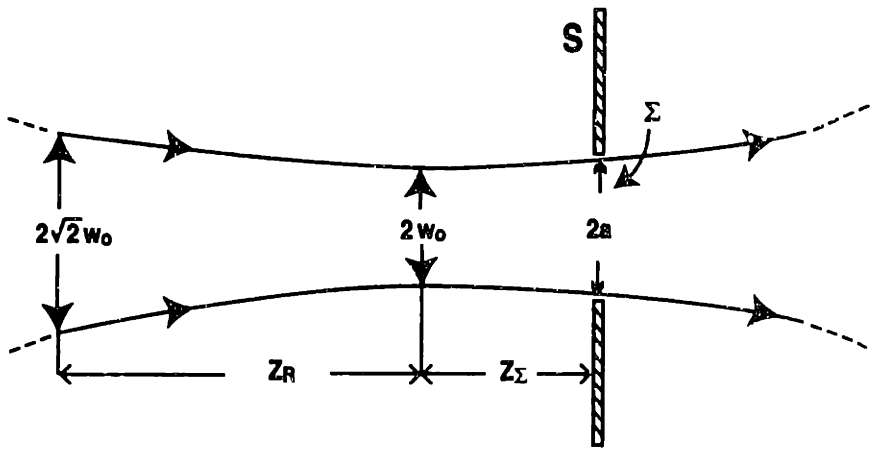

Fig. 2.5 Gaussian beam diffracted by a circular aperture of radius a.

In real experimental situations, however, one rarely deals with ideal Gaussian beams. The laser beam generally must pass through one or more apertures, which cause diffraction effects unless they are much larger than the beam diameter. In many cases, the aperture width defines how large a region of plasma can be accessed and studied. Selecting a beam diameter substantially smaller than the aperture width is therefore disadvantageous, as it further reduces access. The opposite limit, on the other hand, may produce unacceptable diffraction. The usual compromise is to choose a beam diameter comparable to the aperture width (see Fig. 2.5).

In approaching the diffraction problem, we observe that Eq. (2.59) is still valid. However, the field in the $z = 0$ plane is itself affected by the presence of the aperture and cannot generally be known exactly. Thus, if Eq. (2.59) is to be useful, approximate expressions must be obtained for the field on the screen. The theory of diffraction is based on the simple assumption that the field is zero everywhere on the screen except in the aperture, where it takes the value it would have in the absence of the screen. The validity of this ansatz rests on the requirement that the aperture be much larger than a wavelength. Equation (2.59) then takes the form

$$\mathbf{E}_0(\mathbf{x}_\perp, z) = \frac{1}{2\pi}\frac{k_0}{iz}e^{ik_0 z}\int_\Sigma \mathbf{E}_0(\mathbf{x}'_\perp, 0)\exp\left(\frac{ik_0}{2z}|\mathbf{x}_\perp - \mathbf{x}'_\perp|^2\right)d^2x'_\perp, \tag{2.65}$$

where the integral is calculated over the aperture surface Σ (see Fig. 2.5).

From a practical standpoint, the task of calculating the Rytov phase [Eq. (2.48)] with the Fresnel diffracted field given by Eq. (2.65) as the unperturbed field presents a formidable challenge. Fortunately, in many experimentally relevant situations one can use the undiffracted gaussian field [Eq. (2.63)] with little error. Let us examine the case of a circular aperture of radius a. Noting that no depolarization effects are observed in the framework of our approximation and thus that the diffraction equations derived above are effectively scalar, we introduce the *diffraction ratio*

$$\mathcal{D}(x_\perp, z; a, z_\Sigma) \equiv \frac{|E_0(\mathbf{x}_\perp, z; a, z_\Sigma)|}{|E_0(\mathbf{x}_\perp, z; \infty)|}, \tag{2.66}$$

where the origin of the z axis has now been taken to be at the beam waist, and z_Σ is the position of the diffracting screen (see Fig. 2.5); the notation $E_0(\mathbf{x}_\perp, z; a, z_\Sigma)$ denotes the diffracted field, whereas $E_0(\mathbf{x}_\perp, z; \infty)$ is the field diffracted by an aperture of infinite radius, i.e. the undiffracted field (which is of course independent of z_Σ). The quantity $\mathcal{D}$ is expressed as a function of $x_\perp = |\mathbf{x}_\perp|$ as required by the cylindrical symmetry of the problem.

An integral expression for the diffraction ratio is derived in Appendix B and has been computed numerically for different values of the parameters. The discussion in the appendix shows that if $a/w_\Sigma \geq 1$ and $z/z_R \leq 0.007$, $\mathcal{D}$ deviates by less than 10% from 1 over 95% of the aperture radius [here, $w_\Sigma = w_0(1 + z_\Sigma^2/z_R^2)^{1/2}$ is the half-width measured in the aperture plane]. No dependence on the value of z_Σ/z_R can be detected over the range from 0 to 0.5, which is quite large for most experimental situations.

In addition, as discussed in the appendix, in many experimental configurations, including the one used in the present work, spatial averaging due to the finite area of the detector elements effectively suppresses the residual effects of diffraction.

On the basis of these findings, we shall derive all subsequent expressions using the undiffracted gaussian profile [Eq. (2.63)].

2.6 Scattering of a Gaussian Beam

We now proceed to utilize Eq. (2.48) to derive useful relations between the scattered fields and the quantity n_e that is the ultimate object of the measurements. The mathematical details of several of the calculations in this section and the following two have been left for Appendix C.

The first step is to recast Eq. (2.48) in a form that explicitly displays the frequency and wave-number spectrum of the electron density. We work again in the framework of the paraxial approximation. The result is [Eq. (C.11)]

$$\begin{aligned}\psi_1(\mathbf{x}, t) = -\frac{i}{(2\pi)^2}\frac{r_e}{k_0}\int d\omega e^{-i\omega t}\int dz' \exp\left[i\frac{\omega}{c}\frac{2\omega_0+\omega}{\omega_0+\omega}(z-z')\right] \\ \times \int d^2k_\perp \exp\left(i\mathbf{k}_\perp\cdot\mathbf{x}_\perp - i\frac{ck_\perp^2}{\omega_0+\omega}\frac{z-z'}{2}\right) \\ \times \hat{n}_e(\mathbf{k}_\perp, \omega; z')\frac{E_0(\mathbf{x}_{u\perp}, z_u)}{E_0(\mathbf{x})},\end{aligned} \tag{2.67}$$

where $\hat{n}_e(\mathbf{k}_\perp, \omega; z)$ is the Fourier transform of n_e with respect to $\mathbf{x}_\perp$ and t. Here, we have introduced the *unperturbed coordinates* $z_u = (\omega_0 z + \omega z')/(\omega_0 + \omega)$ and $\mathbf{x}_{u\perp} = \mathbf{x}_\perp - \mathbf{k}_\perp(z_u - z')/k_0$. These are the coordinates of the unperturbed ray emanating from the point in the plasma that is the source of the scattered ray observed at $(\mathbf{x}_\perp, z)$ (see Fig. 2.6). In the limit $\omega \to 0$, z_u becomes equal to z and $\mathbf{x}_{u\perp} \to \mathbf{x}_\perp - (z - z')\mathbf{k}_\perp/k_0$, and Eq. (2.67) reduces to the result derived by Howard and Sharp[105].

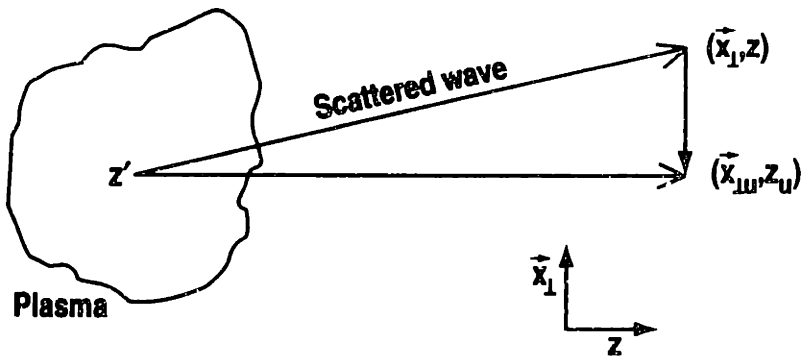

Fig. 2.6 Unperturbed coordinates.

Physically, Eq. (2.67) can be interpreted as follows: the contribution of each scattered wave to the overall Born scattered field $E_0\psi_1$ is simply equal to the corresponding spectral component of the index of refraction, multiplied by the Fresnel propagator $\exp[i(k_0 - k_\perp^2/2k_0)(z-z')]$ and by the unperturbed field calculated at the unperturbed coordinates.

We now specialize our remarks to the case of a Gaussian beam. The Rytov phase for this case is given by Eq. (C.14):

$$\begin{aligned}\psi_1(\mathbf{x},t) = -\frac{i}{(2\pi)^2}\frac{r_e}{k_0}\int e^{-i\omega t}d\omega \int dz' \frac{\gamma}{\gamma_u}\exp\left[i\frac{\omega}{c}(z-z')\right] \\ \times \exp\left[-\left(\frac{1}{\gamma_u}-\frac{1}{\gamma}\right)\frac{x_\perp^2}{w_0^2}\right]\int d^2k_\perp \exp\left(i\frac{\gamma'}{\gamma_u}\mathbf{k}_\perp\cdot\mathbf{x}_\perp\right) \\ \times \exp\left[-i\frac{\gamma'}{\gamma_u}\frac{k_\perp^2}{2k_0}(z_u-z')\right]\hat{n}_e(\mathbf{k}_\perp,\omega;z'),\end{aligned} \tag{2.68}$$

where we have used the normalized coordinates $\zeta = z/z_R$, $\zeta' = z'/z_R$, and $\zeta_u = z_u/z_R$, and we have introduced the collimation parameters[105] $\gamma = 1 + i\zeta$, $\gamma' = 1 + i\zeta'$, and $\gamma_u = 1 + i\zeta_u$. The origin of the z axis is taken to be at the beam waist.

This expression can be seen as a compendium of the information about the plasma density that can be extracted from a transmitted Gaussian beam under the small-angle-scattering and Rytov approximations. In practice, different parts of this information are available experimentally, depending on the detection technique and on the detector location. In addition, it should be remembered that Eq. (2.68) is valid beyond the near field only in the Born approximation.

In experimental situations, detection is effected with square-law detectors, viz., devices that respond to the power flux. Common detection schemes involve either using a local oscillator derived from the unperturbed beam with a controllable phase shift, or detecting the transmitted beam without any local oscillator. The first case is usually referred to as *heterodyne detection*, while the second one is called *homodyne detection*. In the absence of a local oscillator, the detected signal is proportional to $U_{\text{hom}} = (\mathbf{E}_0 \cdot \mathbf{E}_0^*)\exp(\psi_1 + \psi_1^*)$: the measurement is sensitive to amplitude variations but does not detect phase changes; therefore only the real part of the Rytov phase

comes into play. With heterodyne detection, the signal is proportional to[105]

$$U_{\rm het} = (\mathbf{E}_0 \cdot \mathbf{E}_0^*) \left[\rho^2 + e^{2\xi_1} + 2\rho e^{\xi_1} \cos(\varphi_1 + \Omega_{\rm LO} t - \varphi_{\rm LO})\right], \tag{2.69}$$

where ρ is the ratio of the amplitudes of the local-oscillator (LO) beam and of the probing beam, and ξ_1 and φ_1 are the real and imaginary parts, respectively, of the Rytov phase ψ_1. The LO phase shift has been assumed to have a linear dependence on time, $-\Omega_{\rm LO} t + \varphi_{\rm LO}$, which is obtained by shifting the frequency of the LO beam with an acousto-optical modulator or a similar device. A frequency shift is useful in practice to distinguish the interference term from the dc LO power and from the homodyne term through spectral-analysis techniques. It should be remarked that in the literature the term *heterodyne* is often restricted to the case $\Omega_{\rm LO} \neq 0$.

In many cases the intensity fluctuations ξ_1 can be assumed to be small, i.e., $\exp(\xi_1) \simeq 1 + \xi_1$. Under this assumption, we can write

$$U_{p,\rm het} = 2\,(\mathbf{E}_0 \cdot \mathbf{E}_0^*) \left[\xi_1 + \rho(1 + \xi_1) \cos(\varphi_1 + \Omega_{\rm LO} t - \varphi_{\rm LO})\right], \tag{2.70}$$

where the suffix p indicates that only the terms affected by the plasma, i.e., the perturbed terms, have been kept. A further level of approximation can be attained if the phase φ_1 is also small. This is the Born approximation. However, in the Rytov scheme very useful results can be obtained by relaxing this condition and applying it only to a fluctuating component $\tilde{\varphi}_1$ that is the object of the measurement. There must be an experimental method for separating this component from the remaining part of the phase, $\langle\varphi_1\rangle = \varphi_1 - \tilde{\varphi}_1$: this method could rely, for instance, on a different frequency spectrum or a different spatial dependence perpendicularly to the beam. (In some cases, $\varphi_{\rm LO}$ is adjusted in real time to compensate for changes in $\langle\varphi_1\rangle$). If this is possible, we can impose the condition $|\tilde{\varphi}_1| \ll 1$ while $\langle\varphi_1\rangle$ can be large. It should be noted that for measurements performed in the far field the considerations at the end of §2.4 apply: that is, the average phase $\langle\varphi_1\rangle$ cannot be calculated with the Rytov method by means of Eq. (2.48); rather Eq. (2.48) must be used in the near field and then the full field $\mathbf{E}_0 \exp(\psi_1)$ must be propagated in free space to the far field.

We can now rewrite Eq. (2.70), to first order,

$$\begin{aligned} U_{p,\rm het} = 2\,(\mathbf{E}_0 \cdot \mathbf{E}_0^*) \big\{ & \xi_1 [1 + \rho \cos(\langle\varphi_1\rangle + \Omega_{\rm LO} t - \varphi_{\rm LO})] \\ & - \rho \tilde{\varphi}_1 \sin(\langle\varphi_1\rangle + \Omega_{\rm LO} t - \varphi_{\rm LO}) \big\}. \end{aligned} \tag{2.71}$$

When these approximations are applicable, the complex quantity $u(\mathbf{x}_\perp, t) \equiv (\mathbf{E}_0 \cdot \mathbf{E}_0^*)\,\tilde{\psi}_1$ contains all the relevant information regarding the detected signal. In the next two sections this quantity will be called the *signal* for simplicity, although it is understood that the actual detector signal is not equal to it, rather a function of it. Also, the real part of u will be referred to as the *homodyne signal*; by analogy, the fluctuating imaginary part will be loosely called the *heterodyne signal*, although

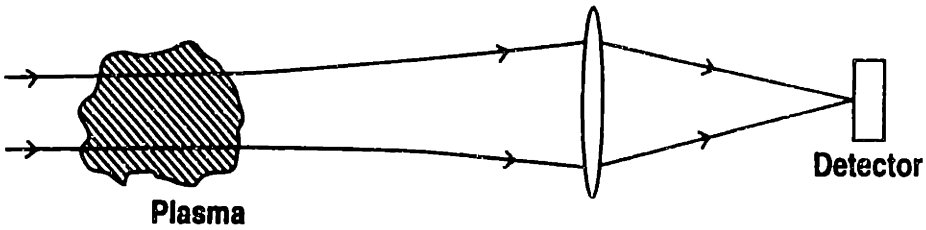

Fig. 2.7 Far-field detection in the focal plane of a lens.

in general both the real and the imaginary component contribute in the heterodyne case, as indicated by Eq. (2.71).

In the next two sections we shall explore several detection schemes that have been used in laboratory experiments, with the aim of providing a unifying view and a comparative analysis of their relative merits.

2.7 Far-Field Detection

In this section we explore a class of measurement techniques characterized by *extreme far-field detection.* This is accomplished experimentally by either satisfying the condition expressed by Eq. (2.34), with $L_\perp$ now replaced by $2w_0$, or by placing the detector in the front focal plane of a focusing optic[106] (see Fig. 2.7). We shall explore this second scenario in detail and then briefly examine the first one by analogy. For simplicity we revert to the Born scheme by assuming $|\psi_1| \ll 1$.

In Appendix C the unperturbed field $\mathbf{E}_{0f}$ and the Rytov phase ψ_{1f} (the subscript f denotes focal-plane quantities) are calculated under very general conditions. The general expression for the phase [Eq. (C.21)] is too complicated for our present purposes. In practice, one simple observation and some relatively weak assumptions can be used to greatly simplify the results. The observation is that the Born field at the focal plane, $\mathbf{E}_{0f}\psi_{1f}$, is found to have a Gaussian dependence $\propto \exp\left[-(k_0^2 w_0^2/4F^2)\right.$ $\left.|\mathbf{x}_\perp - F\mathbf{k}_\perp/k_0|^2\right]$, which essentially defines the region of observation as $|\mathbf{x}_\perp - F\mathbf{k}_\perp/k_0|$ $\lesssim 2F/(k_0 w_0)$. The assumptions are as follows. We introduce a fictitious ordering parameter $\tau \ll 1$, which for the purposes of this discussion can be identified with $(\omega/\omega_0)^{1/2}$, and we ignore all exponents or phases of order τ^l, with $l > 0$. We then assume that $k_\perp^2 w_0^2 \sim O(\tau^l)$, with $l \geq -1$, for the entire spectrum under exam. Since in practice ω/ω_0 is usually a very small quantity, this is clearly a rather conservative upper limit on $k_\perp$, but it permits us to ignore terms of order $k_\perp^2 w_0^2(\omega/\omega_0)$. Similarly, we also require that the quantities z'/z_R and $(z'/z_R)k_\perp^2 w_0^2$ be of order larger than or equal to -1, for all values of z'. These three conditions are independent and must all be satisfied. Physically, they imply a weak lower limit on the wavelengths under study and a modest degree of beam collimation. Finally, the conditions for the validity of the Fresnel approximation [Eqs. (2.62) and (C.6)] can be stated as $2|z_l|/(k_0^3 w_0^4) \sim O(\tau^l)$, $2|z'|/(k_0^3 w_0^4) \sim O(\tau^l)$, and $|z_l - z'|k_\perp^4/8k_0^3 \sim O(\tau^l)$, with $l \geq 1$ (z_l is the distance from the beam waist to the focusing optic).

Since $\tilde{n}_e$ is a real quantity, the spectrum $\hat{n}_e$ must be Hermitian, that is, $\hat{n}_e(\mathbf{k}_\perp, \omega; z) = \hat{n}_e^*(-\mathbf{k}_\perp, -\omega; z)$. The real and imaginary parts of u_f, respectively

u_{fr} and u_{fi}, are then given by Eq. (C.29):

$$u_{f\,\substack{r\\i}}(\mathbf{x}_\perp,t) = -\frac{E_{f,00}^2}{(2\pi)^2}\frac{r_e}{k_0}\int_0^\infty d\omega \int d^2k_\perp \exp\left(-\frac{k_\perp^2 w_0^2}{8}\right)$$
$$\times \int dz' |\hat{n}_e(\mathbf{k}_\perp,\omega;z')| \left\{ \exp\left[-\frac{k_0^2 w_0^2}{2F^2}\left(\mathbf{x}_\perp - \frac{F}{2k_0}\mathbf{k}_\perp\right)^2\right]\right.$$
$$\times \begin{matrix}\sin\\ \cos\end{matrix}\left[\omega t' - z'\left(\frac{\mathbf{k}_\perp\cdot\mathbf{x}_\perp}{F} - \frac{k_\perp^2}{2k_0} - \frac{\omega}{c}\right) - \beta\right]$$
$$\mp \exp\left[-\frac{k_0^2 w_0^2}{2F^2}\left(\mathbf{x}_\perp + \frac{F}{2k_0}\mathbf{k}_\perp\right)^2\right]$$
$$\left.\times \begin{matrix}\sin\\ \cos\end{matrix}\left[\omega t' - z'\left(\frac{\mathbf{k}_\perp\cdot\mathbf{x}_\perp}{F} + \frac{k_\perp^2}{2k_0} - \frac{\omega}{c}\right) - \beta\right]\right\}, \qquad (2.72)$$

where we have defined the retarded time $t' = t - (z_l + F)/c + (z_l - F)x_\perp^2/(2cF^2)$. Also, F is the focal length, $\beta = -(i/2)\ln(\hat{n}_e/\hat{n}_e^*)$ is the phase of the spectrum, and $E_{f,00} = 2(P/c)^{1/2}k_0 w_0/F$ is the amplitude of the unperturbed Gaussian field at $\mathbf{x}_\perp = 0$.

If the spectrum is monochromatic and the fluctuations are localized, i.e., $|\hat{n}_e(\mathbf{k}_\perp,\omega;z)| \propto \delta(z'-z_p)\sum_\pm \delta(\mathbf{k}_\perp \mp \mathbf{K})\delta(\omega \mp \Omega)$ and $\Omega L_z/c \to 0$, Eq. (2.72) reduces to the result derived by Evans et al.[106]

Let us now explore the physical significance of Eq. (2.72) for the homodyne signal $u_{fr} = \left(\mathbf{E}_{0f}\cdot\mathbf{E}_{0f}^*\right)\xi_1$. The exponential in the first line reflects the profile of the unperturbed Gaussian field and weights the signal for $k_\perp \lesssim 2\sqrt{2}/w_0$; thus, only wavelengths longer than the beam diameter produce a significant signal. The term in curly braces is the difference of two functions, which peak at the positions $\mathbf{x}_\perp = \mp F\mathbf{k}_\perp/(2k_0)$, respectively, and oscillate with frequency ω. The first function transforms into the second one upon translation by $\Delta\mathbf{x}_\perp = -F\mathbf{k}_\perp/k_0$. Owing to the antisymmetric nature of this term, the functions' width must be smaller than their separation for the signal to be significant, as shown in Fig. 2.8. That requirement is $k_\perp \gtrsim 1/(2\sqrt{2}w_0)$, i.e., the wavelength must not exceed a value of ~ 10 times the beam diameter. For the case $z' = 0$ (plasma located at the beam waist) this term can be shown[106] to peak in the vicinity of $k_\perp \sim 1/w_0$, as these qualitative arguments would suggest.

Under these conditions, if the spectrum is monochromatic $[|\hat{n}_e(\mathbf{k}_\perp,\omega;z)| = (1/2)\tilde{n}_0(z)\sum_\pm \delta(\mathbf{k}_\perp \mp \mathbf{K})\delta(\omega \mp \Omega)]$, the two peaks can be studied separately. Carrying out the line integration along the plasma column, one obtains two signals that oscillate at the frequency Ω; their amplitudes are simply the longitudinal Fourier components of $\tilde{n}_0$ at the wave numbers

$$k_z = \frac{\mathbf{K}\cdot\mathbf{x}_\perp}{F} \pm \frac{K^2}{2k_0} - \frac{\Omega}{c}. \qquad (2.73)$$

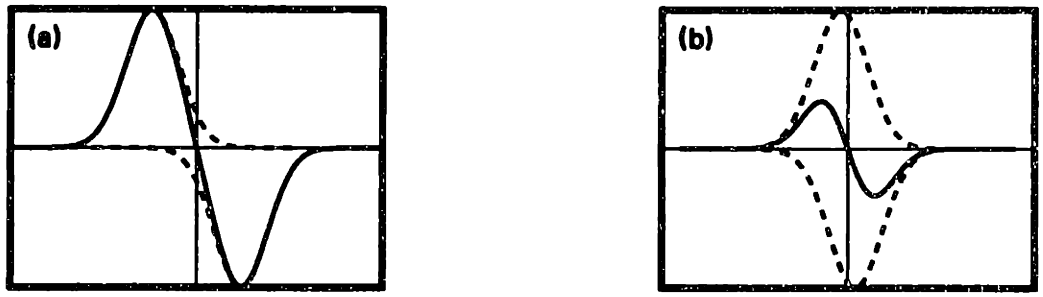

Fig. 2.8 Sum (solid line) of the antisymmetric components (dashed lines) of the envelope of the homodyne far-field signal [Eq. (2.72)]: (a) separation larger than the width, (b) separation smaller than the width.

Through arguments similar to those following Eq. (2.37), these selection rules are relaxed in practice to a finite range $\delta k_z \approx \pi/L_z$ around those values. There is therefore a one-to-one correspondence, on each Gaussian curve, between the focal-plane coordinate and the k_z value: both peaks correspond to the same value $k_{z0} = -\Omega/c$, and the e^{-2} half-width is $\bar{\kappa}_z = 2K/(k_0 w_0)$. Theoretically one could then measure the k_z spectrum, to within a δk_z uncertainty, by scanning the focal plane, and then reconstruct the $\tilde{n}_0(z')$ distribution. For this procedure to be meaningful, two conditions must be satisfied. The first one is that the value $k_{z0} = -\Omega/c$ must lie within the longitudinal-wave-number spectrum of the plasma; this is generally true for low-frequency turbulence, whose Ω/c values are in the 10^{-4} cm^{-1} region, but may be marginal for perpendicularly launched rf waves. The second condition is $\bar{\kappa}_z \gg \delta k_z$, i.e., $2KL_z/(\pi k_0 w_0) \gg 1$; since $1/w_0$ is of order K, an equivalent requirement is $L_z \gg \pi k_0/(2K^2)$. Recalling Eq. (2.40) and the discussion following it, we identify this condition as the defining inequality of the Bragg regime (within a factor of two).

We have thus reached the conclusion that the longitudinal distribution can be measured by homodyne, extreme-far-field detection in the Bragg regime only. It must be stressed that this conclusion is valid in the single-wave case: if the density fluctuations in the plasma have a finite $k_\perp$ spectrum, the Gaussian functions are broadened and it is not possible in general to determine the $k_\perp$ spectrum and the longitudinal distribution indipendently. On the other hand, in the Raman-Nath regime ($\bar{\kappa}_z \lesssim \delta k_z$) very little information can be extracted at all. Although it is theoretically possible to gain some information on the $k_\perp$ spectrum, the resolution is limited by the Gaussian widths to $\delta k_\perp \simeq 2\sqrt{2}/w_0$; the Gaussian weighting function $\exp(-k_\perp^2 w_0^2/8)$ then causes the signal to vanish in the region of interest.

In a heterodyne scheme, similar considerations apply to the imaginary signal u_{fi}, with one fundamental difference: the two Gaussians now add in phase, and the signal is large for arbitrarily small K values.

One can eliminate the homodyne part by choosing $\Omega_{\rm LO} = 0$, $\rho \gg 1$, and $\langle\varphi_1\rangle - \varphi_{\rm LO} = \pi/2$: Eq. (2.71) then shows that the signal is proportional to u_{fi}. Alternatively, the contribution from u_{fr} can be eliminated by integrating the signal over a wide-area detector: the translational symmetry of the two antisymmetric

components ensures that the integral is exactly zero. To calculate the integral of the imaginary part, we shall assume that the dependence of the retarded time on $x_\perp$ can be neglected; this requires the following ordering postulates: $(z_l - F)/z_R \sim O(\tau^{-1})$ and $w_0^2 k_\perp^2 (z_l - F)/z_R \sim O(\tau^{-1})$ (it is understood here that the specified order indicates only a lower limit); that is, a modest amount of collimation must exist at the front focal plane of the lens. In this case $t' = t - (z_l + F)/c$. Assuming also $\Omega L_z/c \ll 1$ and integrating Eq. (2.72) over the focal plane, we obtain

$$\int u_{fi}(\mathbf{x}_\perp, t) d^2x_\perp = -\frac{1}{\pi} E_{f,00}^2 \frac{r_e F^2}{k_0^3 w_0^2} \int_0^\infty d\omega \int d^2k_\perp \int dz' \cos(\omega t'' - \beta) \times |\hat{n}_e(\mathbf{k}_\perp, \omega; z')| \exp\left[-\frac{k_\perp^2 w_0^2}{8}\left(1 + \frac{z'^2}{z_R^2}\right)\right], \tag{2.74}$$

where we have defined a new retarded time $t'' = t - (z_l + F - z')/c$ relative to the propagation from z' to $z_l + F$. If it is assumed that the variables can be separated in the function $\hat{n}_e$, i.e., $\hat{n}_e = \tilde{n}_0(z) G(\mathbf{k}_\perp, \omega)$, and if the plasma column is all contained within a Rayleigh length of the beam waist, Eq. (2.74) becomes

$$\int u_{fi}(\mathbf{x}_\perp, t) d^2x_\perp = -\frac{1}{\pi} E_{f,00}^2 \frac{r_e F^2}{k_0^3 w_0^2} \int_0^\infty d\omega \int d^2k_\perp |G(\mathbf{k}_\perp, \omega)| \times e^{-k_\perp^2 w_0^2/8} \cos(\omega t - \beta) \int \tilde{n}_0(z') dz', \tag{2.75}$$

i.e., the signal is proportional to the line integral of the density and the measurement acts as a low-pass filter[105,107] for $k_\perp \lesssim 2/w_0$.

In the short-wavelength limit, $k_\perp \gtrsim 1/(2\sqrt{2}w_0)$, homodyne and heterodyne detection are essentially equivalent, if one localizes the measurement to only one of the two Gaussians. The difficulty in using either measurement to gain information on the $k_\perp$ spectrum, as mentioned before, lies in the Gaussian weighting function $\exp(-k_\perp^2 w_0^2/8)$. This limitation can be overcome by adopting a modified heterodyne configuration in which the local-oscillator beam is reoriented so that it reaches the focusing optic at a small angle θ. Let us define a vector $\mathbf{K}_{\rm LO}$ lying in the plane of the original and deflected LO beams, perpendicular to z, and whose magnitude is $K_{\rm LO} = \theta k_0$: it can be easily shown that to first order in θ the field pattern in the focal plane is simply shifted by $\Delta\mathbf{x}_\perp = F\mathbf{K}_{\rm LO}/k_0$. The equivalent of Eq. (2.71) for this situation is

$$U_{p,\rm het}(\mathbf{x}_\perp) = 2\rho \,\mathrm{Re}\Big[\big(\mathbf{E}_{0f}(\mathbf{x}_\perp) \cdot \mathbf{E}_{0f}^*(\mathbf{x}_\perp - F\mathbf{K}_{\rm LO}/k_0)\big) \times \psi_1(\mathbf{x}_\perp) e^{i(\langle\varphi_1(\mathbf{x}_\perp)\rangle + \Omega_{\rm LO} t - \varphi_{\rm LO})}\Big], \tag{2.76}$$

where we have assumed $\rho \gg 1$. This heterodyne signal is calculated in Appendix C, with the result [Eq. (C.32)]

$$U_{p,\rm het}(\mathbf{x}_\perp, t) = \frac{2}{(2\pi)^2} \rho E_{f,00}^2 \frac{r_e}{k_0} \int_0^\infty d\omega \int d^2k_\perp$$

$$\times \left\{ |\hat{n}_e(\mathbf{k}_\perp, k_{z+}, \omega)| \exp\left[-\frac{k_0^2 w_0^2}{2F^2} \left(\mathbf{x}_\perp - \frac{F}{k_0} \frac{\mathbf{K}_{\mathrm{LO}} + \mathbf{k}_\perp}{2} \right)^2 \right] \right.$$
$$\times \exp\left[-\frac{w_0^2}{8} (\mathbf{K}_{\mathrm{LO}} - \mathbf{k}_\perp)^2 \right] \sin\left[(\Omega_{\mathrm{LO}} - \omega)t + \theta_{H+} \right]$$
$$- |\hat{n}_e(\mathbf{k}_\perp, k_{z-}, \omega)| \exp\left[-\frac{k_0^2 w_0^2}{2F^2} \left(\mathbf{x}_\perp - \frac{F}{k_0} \frac{\mathbf{K}_{\mathrm{LO}} - \mathbf{k}_\perp}{2} \right)^2 \right]$$
$$\left. \times \exp\left[-\frac{w_0^2}{8} (\mathbf{K}_{\mathrm{LO}} + \mathbf{k}_\perp)^2 \right] \sin\left[(\Omega_{\mathrm{LO}} + \omega)t + \theta_{H-} \right] \right\}, \qquad (2.77)$$

where $\hat{n}_e(\mathbf{k}_\perp, k_z, \omega)$ is the complete temporal and spatial Fourier transform of $\tilde{n}_e$, with phase $\Gamma(\mathbf{k}, \omega) = -(i/2)\ln(\hat{n}_e/\hat{n}_e^*)$, and $k_{z\pm} = \omega/c - \mathbf{k}_\perp \cdot (\mathbf{x}_\perp/F \mp \mathbf{k}_\perp/2k_0)$. Also, the phases $\theta_{H\pm}(\mathbf{x}_\perp)$ are given by Eq. (C.33) but their explicit functional form is unimportant for our purposes. This expression shows that the signal is strongly weighted for wave numbers in the vicinity of $-\mathbf{K}_{\mathrm{LO}}$ and $\mathbf{K}_{\mathrm{LO}}$; it acts in fact as a spatial bandpass filter around those values, with a half-width of $\bar{K} = 2\sqrt{2}/w_0$. For both signs of $\mathbf{k}_\perp$, the spatial peak occurs at $\mathbf{x}_\perp = F\mathbf{K}_{\mathrm{LO}}/k_0$. If $\Omega_{\mathrm{LO}} \neq 0$, and in particular if Ω_{LO} is larger than the largest characteristic frequency of the density fluctuations, one can also distinguish between the two directions of propagation through frequency discrimination. By repeating this measurement and reorienting the LO beam each time, the complete $\mathbf{k}_\perp$ spectrum can be measured in principle with a resolution of $\delta k_\perp \simeq 2\sqrt{2}/w_0$.

If the Rytov field is expanded to second order in the phase, Eq. (2.69) can be written, in the homodyne case, $U_{\mathrm{hom}} = (\mathbf{E}_0 \cdot \mathbf{E}_0^*)[1 + 2\xi_1 + 2\xi_1^2]$. This expansion is only valid, however, in the near field, for the reasons put forward in the discussion following Eq. (2.51). In the far field one can expand the field as follows: $\mathbf{E}_{\mathrm{far}} = \mathbf{E}_{0,\mathrm{far}} + \mathbf{E}'_{\mathrm{far}} + \mathbf{E}''_{\mathrm{far}} = \mathbf{E}_0 + \mathbf{E}_0\psi_1 + \mathbf{E}''_{\mathrm{far}}$, where the second-order quantity $\mathbf{E}''_{\mathrm{far}}$ can be obtained by applying Eqs. (2.59) and (C.16) to propagate the field $\mathbf{E}_0\psi_1^2/2$ from the near field, through the lens, to the focal plane. The second-order homodyne signal can then be expressed as $U''_{\mathrm{hom}} = (\mathbf{E}_0 \cdot \mathbf{E}_0^*)|\psi_1|^2 + \mathrm{Re}(\mathbf{E}''_{\mathrm{far}} \cdot \mathbf{E}''_{\mathrm{far}})$.

Evans et al.[106] derived an exact expression for the Rytov field, $\exp(\psi_0 + \psi_1)$, in the extreme far field in the Raman-Nath regime, assuming a sinusoidal (monochromatic) density dependence and, implicitly, $\omega L_z/c \ll 1$. The second-order homodyne signal is comprised of a time-independent term and of a term oscillating with frequency 2Ω. The time-independent term consists of two symmetrical Gaussian functions centered at $\mathbf{x}_\perp = \pm F\mathbf{k}_\perp/k_0$ with half-width $\sqrt{2}\,F/(k_0 w_0)$. The time-dependent term is identified with the shadowgraph effect,[99,108] which is based on the focusing properties of a medium whose refractive index has a nonzero second derivative in the direction perpendicular to the direction of propagation of the wave.

All the foregoing considerations apply equally well to extreme-far-field detection without the use of a lens. The extreme far field in this case is defined by the Fraunhofer condition $R_0 \gg k_0 w_0^2/2$, where R_0 is the distance from the plasma to

the detection plane. This condition can be recast as $z \gg z_R$. Once the correspondence $\mathbf{x}_\perp \rightarrow F\mathbf{R}_{0\perp}/R_0$, based on Fourier optics[103], is made between the focal-plane coordinates and the far-field coordinates, Eq. (2.72) becomes equivalent to the result derived by Slusher and Surko[29] for homodyne detection in the context of Thomson scattering (again in the limit $\omega L_z/c \ll 1$). The time-averaged scattered power, expressed as the square of the modulus of the Born field $\mathbf{E}_0\psi_1$, coincides with the second-order time-independent term in the focal-plane analysis. Finally, the "modified" heterodyne configuration described earlier is the standard one in Thomson scattering experiments,[29] in which the LO beam is oriented to be colinear with the scattered component $\mathbf{k}_0 + \mathbf{k}_\perp$ under exam. The exponentials involving $\mathbf{x}_\perp$ in Eq. (2.77) now impose the condition $\mathbf{R}_{0\perp}/R_0 \simeq \mathbf{K}_{\mathrm{LO}}/k_0$, i.e., the direction of the LO beam must coincide with the spatial vector joining the interaction region to the detector. The interaction region is thus *defined* as the intersection of the Gaussian cross sections of the beam that traverses the plasma and of the LO beam (although the latter may not in fact propagate through the plasma, its geometrical extension from the detector, ignoring all beam-combining optics, does). This region has the shape of an elongated romboid of approximate length $L_z \simeq 4k_0 w_0/K_{\mathrm{LO}}$ (see Fig. 2.9). This spatial-selection capability can be obtained also with the focal-plane configuration, of course, provided that the collecting optic has an aperture not larger than the width of the LO beam and is centered on it. It should be noted that the requirement $k_\perp > \delta k_\perp = 2\sqrt{2}/w_0$ implies that $(k_\perp^2/\pi k_0)L_z > 8\sqrt{2}/\pi$; thus, this type of measurement is always restricted to the Bragg regime. This means that for a given perpendicular wave number the two scattering directions correspond to opposite *longitudinal* wave numbers [see Fig. 2.1(b)], that is (assuming $\omega L_z/c \ll 1$), $k_{z\pm} = \pm k_\perp^2/2k_0$. Also, for each scattering direction the direction of propagation of the density waves can be determined only if $\Omega_{\mathrm{LO}} \neq 0$.

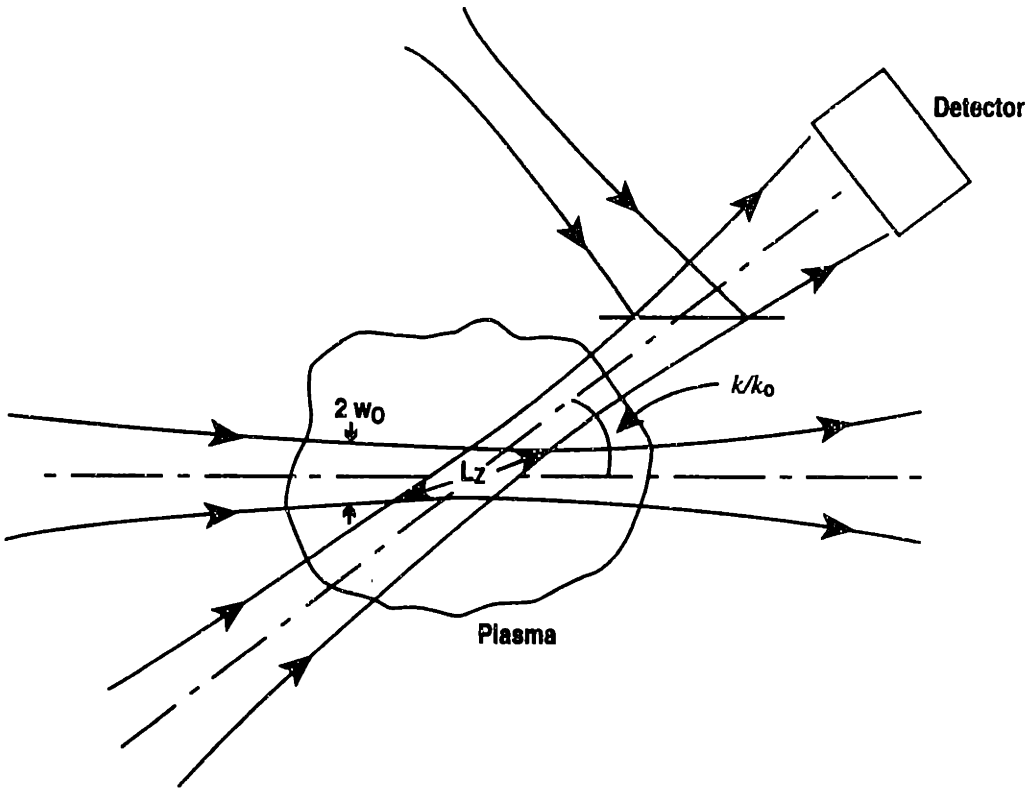

Fig. 2.9 Geometry of Bragg scattering measurement.

2.8 Near- and Intermediate-Field Detection

We shall now examine the near- and intermediate-field detection scenarios. The starting point is, again, the Rytov phase, expressed by Eq. (2.68), combined with the unperturbed Gaussian field, expressed by Eq. (2.63). In the intermediate-field case, i.e., when the beam propagates some distance away from the plasma column, the Born approximation is also implicitly assumed. We introduce again a fictitious ordering parameter $\tau \ll 1$ and we make the following assumptions. The beam is assumed to be collimated between the interaction and the detection region: thus $|\zeta - \zeta'|$ is taken to be of order τ; the *absolute* values of ζ and ζ' are arbitrary at this point. The frequency ratio ω/ω_0 is assumed to be of first order or smaller. Also, a weak upper limit is imposed on the value of $k_\perp$ by requiring that $k_\perp w_0(1+\zeta^2)^{1/2} \sim O(\tau^{-1})$ (the order indicated represents only a lower limit): thus $k_\perp$ could still be much larger than $1/w_0(1+\zeta^2)^{1/2}$ (the inverse width of the beam in the detection plane), but terms of order $(\zeta - \zeta')^2 k_\perp w_0(1+\zeta^2)^{1/2}$ must be small. We also note that in the Born field $\mathbf{E}_0 e^{\psi_1}$ the sum of the real parts of the exponentials gives, to leading order, a Gaussian dependence $\propto \exp\{-[1/w_0^2(1+\zeta^2)][\mathbf{x}_\perp \pm w_0^2(\zeta' - \zeta)\mathbf{k}_\perp/2]^2\}$, which imposes a limit $|\mathbf{x}_\perp| \lesssim w_0(1+\zeta^2)^{1/2} + k_\perp w_0^2|\zeta' - \zeta|/2$. We can therefore state that $x_\perp^2/w_0^2(1+\zeta^2) \sim O(\tau^0)$. Finally, the Fresnel conditions [Eqs. (2.62) and (C.6)] imply the following additional requirements: $|\zeta|/(k_0 w_0)^2 \sim O(\tau^2)$, $|\zeta'|/(k_0 w_0)^2 \sim O(\tau^2)$, and $|z - z'|k_\perp^4/(8k_0^3) \sim O(\tau^2)$.

In this approximation, the Rytov phase is calculated in Appendix C to first order

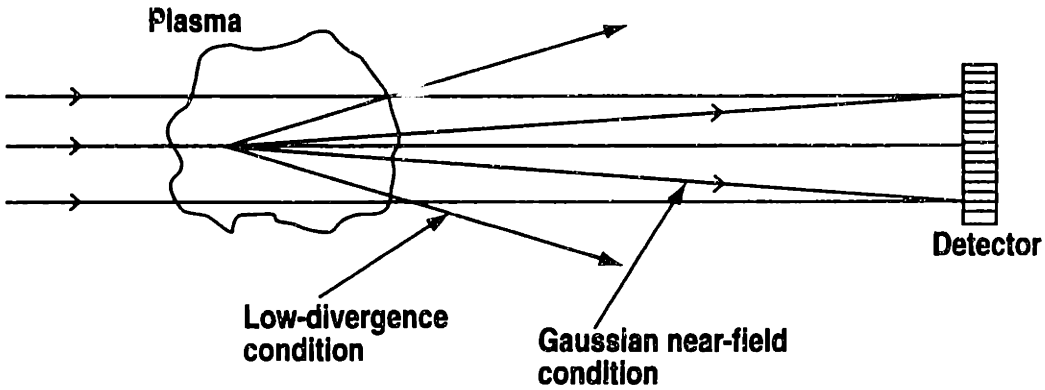

Fig. 2.10 Illustration of low-divergence condition (scattered waves stay within the Gaussian cross section in the plasma) and more stringent Gaussian near-field condition (scattered waves stay within the Gaussian cross section at the detector).

in τ. The resulting expression, Eq. (C.36), is quite formidable and of limited interest. Considerable simplification is attained at the next level of approximation, in which we retain only terms of zeroth-order and larger, and we introduce the additional *low-divergence* approximation $L_z \ll k_0 w_0 / k_\perp$, specifically $L_z k_\perp / (k_0 w_0) \sim O(\tau)$. This inequality requires that the scattered beamlets, after propagating through the entire length of the plasma column, not stray outside the width of the Gaussian beam (measured at the waist), as shown in Fig. 2.10. The temporal and spatial Fourier transform of the signal, defined as

$$\hat{u}(\mathbf{K}, \Omega; z) = \iint (\mathbf{E}_0 \cdot \mathbf{E}_0^*)\, \psi_1(\mathbf{x}_\perp, z, t) e^{-i(\mathbf{K}\cdot\mathbf{x}_\perp - \Omega t)} d^2x_\perp dt, \tag{2.78}$$

is calculated in Appendix C with the following result [Eq. (C.46)]:

$$\begin{aligned}
\hat{u}_{\substack{H \\ a}}(\mathbf{K}, \Omega; z) = {} & \frac{E_{00}^2 w_0^2}{4} \frac{r_e}{k_0} e^{-i\pi/4} \int d^2k_\perp \exp\left[-\frac{(\zeta - \zeta_p)^2}{1+\zeta^2} \frac{w_0^2 k_\perp^2}{8} \right] \\
& \times \exp\left[-\frac{w_0^2(1+\zeta^2)}{8} \left| \mathbf{K} - \mathbf{k}_\perp \left(1 - \frac{\zeta(\zeta - \zeta_p)}{1+\zeta^2} \right) \right|^2 \right] \\
& \times \exp\left[i \frac{\Omega}{\omega_0} (\zeta - \zeta_p) \frac{w_0^2 k_\perp^2}{4} \right] \int dz'\, \hat{n}_e(\mathbf{k}_\perp, \Omega; z') e^{i\Omega(z-z')/c \pm i\pi/4} \\
& \times \begin{matrix} \sin \\ \cos \end{matrix} \left[(\zeta' - \zeta_p) \frac{w_0^2 k_\perp^2}{4} - (\zeta - \zeta_p) \frac{w_0^2}{4} (\mathbf{k}_\perp \cdot \mathbf{K}) \right],
\end{aligned} \tag{2.79}$$

where $\hat{u}_H$ and $\hat{u}_a$ denote the Hermitian and anti-Hermitian components, respectively, of $\hat{u}$; here, $E_{00} = 4(P/cw_0^2)^{1/2}$, z_p is an average plasma coordinate (measured from the beam waist), and $\zeta_p = z_p / z_R$. Although this expression is still quite complicated, two important features emerge in a rather simple way. Firstly, the first exponential is

consistent with our assumption that the quantity $w_0 k_\perp (1+\zeta^2)^{1/2}(\zeta - \zeta_p)$ is of order unity or smaller. This term acts as a low-pass spatial filter: a larger distance between the plasma and the detector results in a smaller passband. The second observation is that the Fourier component of the signal at a given $\mathbf{K}$ is affected by the density spectrum only in the vicinity of that wave number, with a spread approximately equal to $\pm 2\sqrt{2}/w_0(1+\zeta^2)^{1/2}$, defined by the second exponential in Eq. (2.79). This can be understood intuitively as the result of the uncertainty principle, which states that the wave number in the plasma can be known only to within the inverse dimensions of the probing beam.

The dependence of the measured signal, whether homodyne (Hermitian) or heterodyne (anti-Hermitian), on the longitudinal distribution $\tilde{n}_0(z')$ remains quite convoluted at this level of approximation. That dependence is simplified considerably by assuming that both the plasma and the detector lie in the *Gaussian near field*,[105] defined by the inequality $|\zeta - \zeta'| w_0 k_\perp \ll 1$. The scattered beamlets now must remain within the Gaussian cross section (measured at the waist) *when they reach the detector plane* (see Fig. 2.10). In terms of expansion orders, we assume $|\zeta - \zeta'| w_0 k_\perp \sim O(\tau)$. Using also the fact that $|\mathbf{K} - \mathbf{k}_\perp| \lesssim 2\sqrt{2}/w_0(1+\zeta^2)^{1/2}$, we can rewrite Eq. (2.79) as

$$\hat{u}_{\substack{H \\ a}}(\mathbf{K}, \Omega; z) = \frac{E_{00}^2 w_0^2}{4} \frac{r_e}{k_0} e^{-i\pi/4} \int d^2 k_\perp \exp\left[-\frac{w_0^2(1+\zeta^2)|\mathbf{K} - \mathbf{k}_\perp|^2}{8}\right] \int dz' \times \hat{n}_e(\mathbf{k}_\perp, \Omega; z') e^{i\Omega(z-z')/c \pm i\pi/4} \times \begin{matrix} \sin \\ \cos \end{matrix} \left[\frac{k_\perp^2}{2k_0}(z' - z)\right]. \tag{2.80}$$

The significance of the Gaussian-near-field approximation can best be understood by writing the frequency spectrum of the Rytov phase, which in this approximation is given by [Eq. (C.48)]

$$\hat{\psi}_{\substack{H \\ a}}(\mathbf{x}; \Omega) = -\frac{1}{2\pi} \frac{r_e}{k_0} \int d^2 k_\perp e^{i\mathbf{k}_\perp \cdot \mathbf{x}_\perp} \int dz' e^{i\Omega(z-z')/c} \times \hat{n}_e(\mathbf{k}_\perp, \omega; z') \times \begin{matrix} \sin \\ i\cos \end{matrix} \left[\frac{k_\perp^2}{2k_0}(z - z')\right], \tag{2.81}$$

where, again, the subscripts H and a denote respectively the Hermitian and anti-Hermitian components. As noted in Appendix C, the Rytov phase in this approximation is the same as that obtained when the incident field is a plane wave. It is important to note that under these conditions it is impossible to determine the three-dimensional distribution (or, equivalently, the wave-number spectrum) of the density fluctuations, since Eq. (2.81) associates to each value of $\mathbf{k}_\perp$ a single value of k_z. This is, of course, the selection rule expressed by the Bragg condition [Eq. (2.37)].

For illustration purposes, let us now assume that the spectral variables can be separated from z in $\hat{n}_e$, i.e., $\hat{n}_e = \tilde{n}_0(z) G(\mathbf{k}_\perp, \omega)$, and let us take a sample Gaussian density function $\tilde{n}_0(z) = \tilde{n}_{00} \exp[-(z - z_p)^2/2L_z^2]$ (the plasma "extremes", $z = z_p \pm$

$L_z/2$, are the half-standard-deviation points); by direct substitution in Eq. (2.81) we find

$$\hat{\psi}_{\substack{H\\a}}(\mathbf{x};\Omega) = \frac{1}{\sqrt{2\pi}}\frac{r_e}{k_0}L_z\tilde{n}_{00}e^{iD_d}\int d^2k_\perp G(\mathbf{k}_\perp,\Omega)e^{i\mathbf{k}_\perp\cdot\mathbf{x}_\perp}e^{-(Q^2+D^2)/2} \times\left(\mp\sin Q_d\times\begin{matrix}\cosh(QD)\\ \sinh(QD)\end{matrix} - i\cos Q_d\times\begin{matrix}\sinh(QD)\\ \cosh(QD)\end{matrix}\right), \tag{2.82}$$

where $Q = L_z k_\perp^2/(2k_0)$ is the *Klein-Cook parameter*;[96] we have also introduced the *transit phase* $D = L_z\Omega/c$, and, by analogy, the parameters $Q_d = (z - z_p)\times k_\perp^2/2k_0$ and $D_d = (z - z_p)\Omega/c$.

If we assume for the moment $D \ll 1$, the factor $\exp(-Q^2/2)$ indicates that the signal is nonvanishing only in the Raman-Nath regime, $Q \lesssim 1$. This is simply a consequence of the Gaussian spatial distribution we have chosen, which corresponds to a Gaussian k_z spectrum $\propto \exp(-k_z^2L_z^2/2)$: in the Bragg regime ($Q \gg 1$) the conditions for wave-number matching require a k_z value that lies in the tail of this spectrum. If we allow a finite D, we see that the condition becomes $D \sim \pm Q$, which is the condition for scattering from near-perpendicular waves, as stated by Eq. (2.37).

In the Raman-Nath regime we can rewrite Eq. (2.81) as

$$\hat{\psi}_{\substack{H\\a}}(\mathbf{x};\Omega) = -\frac{1}{2\pi}\frac{r_e}{k_0}\int d^2k_\perp e^{i\mathbf{k}_\perp\cdot\mathbf{x}_\perp}e^{iD_d}\times\begin{matrix}\sinh Q_d\\ \cosh Q_d\end{matrix} \times\int\hat{n}_e(\mathbf{k}_\perp,\Omega;z')\exp\left[-i\frac{\Omega}{c}(z'-z_p)\right]dz'. \tag{2.83}$$

Thus, in the Raman-Nath regime, the signal is proportional to the line integral of the density, multiplied by $\exp[-i\Omega(z' - z_p)/c]$. The appearance of this term is due to the fact that the probing incident wave travels along the plasma column at the finite velocity c; during the time it takes to go from point z_1' to point z_2', the phase of the density wave changes by $\Omega(z_1' - z_2')/c$. If $D \gtrsim 1$, this dephasing effect can cause the line integral to vanish: this is the meaning of the $\exp(-D^2/2)$ term in the case of the gaussian distribution. When, on the other hand, the longitudinal wave number $k_z = \Omega/c$ lies within the spectral bandwidth of the fluctuations, the line integration selectively chooses that component. This is yet another example of the Bragg selection rule.

Within the Raman-Nath approximation, the distance that the wave is allowed to propagate before being detected essentially determines the wave-number transfer function of the system, through the parameter Q_d. The homodyne signal, proportional to the Hermitian component of $\hat{\psi}_1$, peaks at all wave numbers that satisfy the relation $Q_d = \pi(m + 1)/2$ and is equal to zero for $Q_d = m\pi$, where m is any integer. This translates into the condition $k_\perp = [(m + 1)\pi k_0/(z - z_p)]^{1/2}$ for the peaks and $k_\perp = [2m\pi k_0/(z - z_p)]^{1/2}$ for the zeros. The opposite is true for the heterodyne (anti-Hermitian) signal.

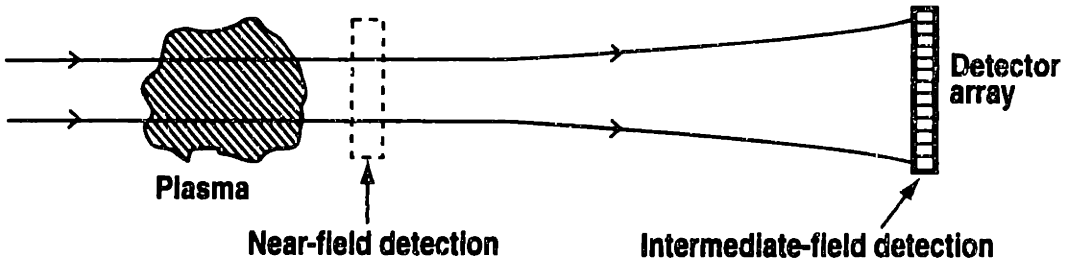

Fig. 2.11 Near- and intermediate-field detection.

The advantage of intermediate-field detection (Fig. 2.11) is that the homodyne signal — that is, the amplitude variation — is nonzero and thus a measurement can be made without employing a local oscillator. The occurrence of an amplitude variation can be understood by realizing that the two scattered waves that correspond to the two signs of $\mathbf{k}_\perp$ propagate in the two different directions given by Eq. (2.36); the interference of the two waves at the detection plane produces an amplitude modulation (see Fig. 2.12). This phenomenon is generally called *scintillation.* The inherent disadvantage of the technique is the oscillatory character of its wave-number transfer function: the zeros represent loss of information. In particular, since the first zero is at $k_\perp = 0$, there is a low-$k_\perp$ cutoff (defined as the point with 50% of peak response) at $k_{\perp,\min} = [\pi k_0/3(z - z_p)]^{1/2}$. The collimation condition, on which these results are predicated, imposes $k_{\perp,\min} \gg 2/w_0$. Hence, only wavelengths considerably shorter than the beam diameter are accessible with this technique.

When a local oscillator is used (*scintillation interferometry*), the heterodyne transfer function is also oscillatory but peaks at $k_\perp = 0$. Thus, ignoring the higher-$k_\perp$ oscillations, this system can be viewed as a low-pass filter, with the 50% cutoff point at $k_{\perp,\max} = [2\pi k_0/3(z - z_p)]^{1/2}$.

In the near-field limit ($Q_d \to 0$), the homodyne signal vanishes and the heterodyne signal becomes independent of $k_\perp$. Calculating the inverse Fourier transform of Eq. (2.83) we find

$$\psi_1(\mathbf{x}_\perp, z, t) = -i\lambda_0 r_e \int \tilde{n}_e[\mathbf{x}_\perp, z', t - (z - z')/c]\, dz'. \tag{2.84}$$

Assuming also $D \ll 1$, we can write

$$\psi_1(\mathbf{x}_\perp, z, t) = -i\lambda_0 r_e \int \tilde{n}_e[\mathbf{x}_\perp, z', t - (z - z_p)/c]\, dz'. \tag{2.85}$$

This remarkably simple expression states that the effect of the plasma is to impress on the incident wave a phase shift proportional to the line integral of the density. It should be remembered that in the near-field limit it is legitimate to abandon the Born approximation; thus, Eqs. (2.85) and (2.87) are valid in the Rytov sense, and ψ_1 is not constrained to be small in absolute terms. In particular, assuming a monochromatic density perturbation $\tilde{n}_e = \hat{n}_k \cos(\mathbf{k}_\perp \cdot \mathbf{x}_\perp - \omega t)$, the near-field Rytov

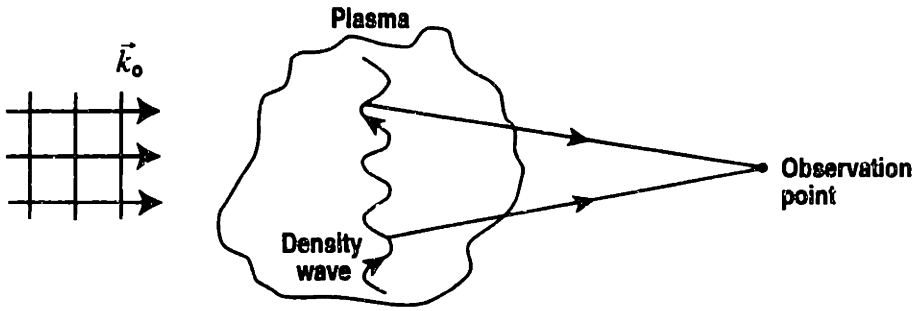

Fig. 2.12 The scintillation effect: the interference of the positive and negative orders causes an amplitude modulation.

field can be written

$$\begin{aligned}\exp(\psi_0+\psi_1) &= E_0 \exp\left[\lambda_0 r_e L_z \hat{n}_k \cos(\mathbf{k}_\perp \cdot \mathbf{x}_\perp - \omega t)\right] \\ &= \sum_{l=-\infty}^{+\infty} i^l J_l(\lambda_0 r_e L_z \hat{n}_k) \exp(i\mathbf{k}_\perp \cdot \mathbf{x}_\perp), \end{aligned} \tag{2.86}$$

which coincides with the Raman-Nath result[95,96] expressed by Eq. (2.41).

By defining the index of refraction $\mathcal{N} = \sqrt{\epsilon} \simeq 1 - 2\pi r_e n_e / k_0^2$, Eq. (2.85) can be recast as

$$\psi_1(\mathbf{x}_\perp, z, t) = ik_0 \int \tilde{\mathcal{N}}[\mathbf{x}_\perp, z', t - (z - z_p)/c]dz'. \tag{2.87}$$

This form of the Rytov phase suggests a natural correspondence with geometrical optics. In geometrical optics one expresses the wave's electric field in the form

$$\mathbf{E}(\mathbf{x}, t) = \mathbf{e}(\mathbf{x}, t) e^{-i\omega_0 t} e^{ik_0 \mathcal{S}(\mathbf{x},t)}, \tag{2.88}$$

where $\mathcal{S}(\mathbf{x}, t)$ is a real function, called the *eikonal* or optical-path function. Substituting for $\mathbf{E}$ from Eq. (2.88) in the wave equation (2.12), one obtains terms proportional to k_0^2, k_0^1, and k_0^0. The geometrical-optics approximation is the limit $\lambda_0 \to 0$, in which only the k_0^2 terms are kept. When this approximation is combined with a first-order expansion in $|1-\epsilon|$, or, equivalently, $\tilde{\mathcal{N}}$, Eq. (2.85) is obtained. This derivation, which extends the standard treatment of geometrical optics to include the time dependence of $\mathcal{S}$ and $\mathbf{e}$, is carried out in detail in Appendix D.

The result expressed by Eq. (2.85) can thus be reached by two rather disparate routes, leading to the important conclusion that the region of validity of geometrical optics coincides with the Raman-Nath regime combined with near-field detection. The appeal of such a simple relation makes near-field heterodyne detection one of the most desirable techniques available in the Raman-Nath regime. Near-field conditions are generally ensured in practice by the use of imaging optics with sufficient aperture to collect all the scattered radiation. The choice of the LO source can vary substantially; a comparison of several suitable techniques is the subject of the next section.

One important comment needs to be made about the $Q \lesssim 1$ and $D \lesssim 1$ conditions upon which all our subsequent considerations will be based. A common phenomenon encountered in plasma-density fluctuation studies is random turbulence. In that case the correlation function of the fluctuations is often more meaningful than the instantaneous measurement itself.

We assume here for simplicity that the correlation properties of the plasma are translationally invariant in the perpendicular direction, but we allow for slow variations in the z direction; we also postulate a Gaussian correlation function in the variable z. We can then use a quasi-homogeneous approximation[109] for z and a random-phase approximation for the perpendicular plane, expressed by the ansatz

$$\langle \hat{n}_e(\mathbf{k}_{\perp 1}, \Omega_1; z_1) \hat{n}_e^*(\mathbf{k}_{\perp 2}, \Omega_2; z_2) \rangle = |G(\mathbf{k}_{\perp 1}, \Omega_1)|^2 \left\langle \tilde{n}_e^2 \left(\frac{z_1 + z_2}{2} \right) \right\rangle e^{-(z_1 - z_2)^2/\mathcal{L}_z^2} \times \delta(\mathbf{k}_{\perp 1} - \mathbf{k}_{\perp 2}) \delta(\Omega_1 - \Omega_2), \tag{2.89}$$

where $\mathcal{L}_z$ is an effective longitudinal correlation length, and the angular brackets $<>$ denote the operation of ensemble averaging. Here we have implicitly assumed that the characteristic gradient length $|d\left(\ln \left\langle \tilde{n}_e^2(z) \right\rangle\right)/dz|^{-1}$ is much longer than $\mathcal{L}_z$ (these concepts will be discussed in depth in Chapter 4). Also, the quasi-homogeneous approximation hinges on the separability of the correlation function from the average-intensity function: if the correlation length, e.g., is itself a function of z, the approximation breaks down.

We can now calculate the crosscorrelation function of the Rytov phase. Let us suppose that we have carried out a measurement of the real (homodyne) or of the imaginary (heterodyne) component of the signal, or of both. We shall examine the correlation functions $\langle \xi_1(\mathbf{x}_\perp, t) \xi_1(\mathbf{x}'_\perp, t') \rangle$ and $\langle \tilde{\varphi}_1(\mathbf{x}_\perp, t) \tilde{\varphi}_1(\mathbf{x}'_\perp, t') \rangle$. The calculation is carried out in Appendix C and yields the result [Eq. (C.50)]

$$\left\langle \begin{matrix} \xi_1 \\ \tilde{\varphi}_1 \end{matrix} (\mathbf{x}_\perp, z, t) \begin{matrix} \xi_1 \\ \tilde{\varphi}_1 \end{matrix} (\mathbf{x}'_\perp, z, t') \right\rangle = \frac{r_e^2}{2(2\pi)^4 k_0^2} \int d\omega e^{-i\omega(t-t')} \int d^2k_\perp \, |G(\mathbf{k}_\perp, \omega)|^2 \times e^{i\mathbf{k}_\perp \cdot (\mathbf{x}_\perp - \mathbf{x}'_\perp)} \int dz' \sqrt{\pi} \mathcal{L}_z \left\langle \tilde{n}_e^2(z') \right\rangle e^{-D_c^2/4} \times \left\{ e^{-Q_c^2/4} \cosh\left(\frac{Q_c D_c}{2} \right) \mp \cos\left[\frac{k_\perp^2}{k_0} (z - z') \right] \right\}, \tag{2.90}$$

where $Q_c = k_\perp^2 \mathcal{L}_z/(2k_0)$ and $D_c = \omega \mathcal{L}_z/c$.

Several important features of this expression must be noted. The parameter D_c takes the same role here as D does in the instantaneous signal. Since generally $\mathcal{L}_z \ll L_z$, the condition $D_c \ll 1$ is much more easily satisfied than $D \ll 1$. Also, the first term in the curly braces is independent of the detector position. This term represents the sum of the autocorrelations of the two k_z components ($k_{z\pm} = \omega/c \mp k_\perp^2/2k_0$). Since the dependence of $\hat{\psi}_1$ on the detector position is due to the dephasing between

these two components, "selecting" only one of the two effectively eliminates that dependence, and the effect of propagation in free space only manifests itself in the crosscorrelation term (the second term in the curly braces). Note that the effective Klein-Cook parameter for the first term is now Q_c. Again, this term is often negligible.

Let us now study the autocorrelation function, which is obtained from Eq. (2.90) for $\mathbf{x}_\perp = \mathbf{x}'_\perp$ and $t = t'$. Assuming $D_c \ll 1$ and $Q_c \ll 1$, and noting the Fourier relation $\iint |G|^2 d^2k_\perp d\omega = (2\pi)^6$ [which can be proven by calculating the autocorrelation function of $\tilde{n}_e$ and making use of Eq. (2.89)], we can write

$$\left\langle \begin{matrix} \xi_1^2 \\ \tilde{\varphi}_1^2 \end{matrix} \right\rangle = \frac{1}{2}(\lambda_0 r_e)^2 \int \langle \tilde{n}_e^2(z') \rangle \sqrt{\pi}\mathcal{L}_z dz' \mp \frac{1}{2}\frac{(\lambda_0 r_e)^2}{(2\pi)^6} \int \langle \tilde{n}_e^2(z') \rangle \sqrt{\pi}\mathcal{L}_z dz' \times \int d^2k_\perp \int d\omega |G(\mathbf{k}_\perp, \omega)|^2 \cos\left[\frac{k_\perp^2}{k_0}(z - z')\right]. \tag{2.91}$$

In the Raman-Nath, near-field regime the second term is identical with the first one, canceling it in the homodyne case and doubling it in the heterodyne case, as could be expected from Eq. (2.85). The new features of Eq. (2.91) can best be understood by resorting again to a sample Gaussian distribution $\langle \tilde{n}_e^2(z) \rangle = \tilde{n}_{00}^2 \exp[-(z - z_p)^2/L_z^2]$. Using this expression in Eq. (2.91) and taking the square root we obtain

$$\left\langle \begin{matrix} \xi_1^2 \\ \tilde{\varphi}_1^2 \end{matrix} \right\rangle^{1/2} = \frac{1}{\sqrt{2}} \lambda_0 r_e \tilde{n}_{00} (\pi \mathcal{L}_z L_z)^{1/2} \times \left[1 \mp \int \frac{|G(\mathbf{k}_\perp, \Omega)|^2}{(2\pi)^6} e^{-Q^2} \cos(2Q_d)\, d^2k_\perp\right]^{1/2}. \tag{2.92}$$

The remarkable result is that in going from the Raman-Nath regime ($Q \ll 1$) to the Bragg regime ($Q \gg 1$) the average near-field heterodyne signal is simply reduced by a factor of two. In addition, in the Bragg regime the remaining signal is the same for heterodyne and homodyne detection and is independent of the detector position (provided the collimation conditions are satisfied). In intermediate cases ($Q \sim 1$) the near-field heterodyne signal exhibits a $k_\perp$-dependent response, which varies only by a factor of two.

We can also obtain the autopower spectral functions in perpendicular-wavenumber and frequency space by calculating the three-dimensional Fourier transform of Eq. (2.90) with respect to $(\mathbf{x}_\perp - \mathbf{x}'_\perp)$ and $(t - t')$. Assuming again $D_c \ll 1$ and $Q_c \ll 1$, we find

$$\left\langle \hat{\psi}_{1\,\underset{a}{H}} \hat{\psi}^*_{1\,\underset{a}{H}} \right\rangle (\mathbf{k}_\perp, \omega; z) = \frac{(\lambda_0 r_e)^2}{2} |G(\mathbf{k}_\perp, \omega)|^2 \int dz' \mathcal{L}_z \sqrt{\pi} \langle \tilde{n}_e^2(z') \rangle \times \left\{1 \mp \cos\left[\frac{k_\perp^2}{k_0}(z - z')\right]\right\}. \tag{2.93}$$

The form of this equation suggests that the form factor can be eliminated if separate measurements of the Hermitian and anti-Hermitian signals are available from a heterodyne experiment. Specifically, one can then calculate the quantity

$$\frac{\left\langle \hat{\psi}_{1H}\hat{\psi}^*_{1H}\right\rangle - \left\langle \hat{\psi}_{1a}\hat{\psi}^*_{1a}\right\rangle}{\left\langle \hat{\psi}_{1H}\hat{\psi}^*_{1H}\right\rangle + \left\langle \hat{\psi}_{1a}\hat{\psi}^*_{1a}\right\rangle} = -\frac{\int \left\langle \tilde{n}_e^2(z')\right\rangle \cos\left[\frac{k_\perp^2}{k_0}(z-z')\right] dz'}{\int \left\langle \tilde{n}_e^2(z')\right\rangle dz'} \tag{2.94}$$

at different values of $\mathbf{k}_\perp$ and thus reconstruct the normalized Fourier transform of the function $\left\langle \tilde{n}_e^2(z)\right\rangle$. This procedure, which was proposed in slightly different form by Nazikian,[110] is feasible if the plasma turbulence spectrum extends well into the Bragg region, i.e., if $k_{z,\max} = k_{\perp,\max}^2/k_0 \gg 2\pi/L_z$. Also, it should be recalled that this result is contingent on the validity of the quasi-homogeneous approximation.

2.9 Overview of Collective Small-Angle Scattering Techniques

Collective scattering from plasma density fluctuations occurs when the wave number k of the fluctuations obeys the relation $k\lambda_D \ll 1$. Small-angle scattering occurs when $k \ll k_0$, where k_0 is the wave number of the probing electromagnetic wave. These two conditions are frequently satisfied in laboratory plasmas when the diagnostic beam belongs to the infrared or microwave regions of the spectrum.

Collective, or coherent, far-field scattering techniques were applied early on to the study of ionospheric plasmas.[111] In these pioneering experiments the backscattering of radio waves was used to measure the fluctuations caused in an otherwise uniform plasma by the discreteness of the constituent particles. Early theoretical investigations of this effect[112] proved that the detected signals depended strongly on the ion temperature and could thus be used to measure that quantity.

In denser laboratory plasmas shorter wavelengths must be used, both for considerations of practical access and to ensure that the wave frequency remains larger than the plasma frequency. The condition for collective scattering, then, often implies small scattering angles. However, the need to separate the incident beam from the scattered radiation imposes a practical lower limit on the scattering angle. As a result, visible radiation is generally useful in the context of ion-temperature measurements only in rather dense plasmas ($n_e \gtrsim 10^{16}$ cm^{-3}). On the other hand, in the history of these techniques,[87] the ready availability of coherent microwave and infrared sources gave an early boost to collective-scattering diagnostics in a variety of laboratory plasma experiments,[113] ranging from arc plasmas[114] to high-density plasma-focus devices.[115]

In the mid-1960's, while these ion-temperature diagnostic techniques were being explored, scattering methods began to be applied also to the detection of ion acoustic and plasma electron waves,[116] electron Bernstein waves,[117] plasma-density inhomogeneities,[118] and broadband microturbulence.[119] By the time the tokamak configuration conquered a leading position in worldwide fusion research, collective

scattering had become an established experimental technique. The earliest applications to tokamaks, employing microwave sources, were developed for the ST device to measure ion acoustic turbulence,[14] and for the ATC[15] and TFR[17] tokamaks for the study of drift-wave instabilities. Infrared scattering experiments using CO_2 lasers soon followed on ATC,[16] Alcator A,[21] TFR,[22] TOSCA,[120] Alcator C,[23] and other devices. The intermediate range, i.e., the far-infrared region of the spectrum, was chosen for turbulence studies on Microtor,[24] TEXT,[26] DIII–D,[27] and ASDEX,[28] among others.

The use of near- and intermediate-field techniques in the study of plasma density fluctuations has been decidedly more sparse. Heterodyne far-forward detection methods employing classical interferometric configurations have been applied for the most part to the measurement of the macroscopic plasma density.[88,89] Spatial resolution, when required, was often obtained by using multiple beams,[121] in which case the distance between the plasma and the detectors was not critical; alternatively, imaging techniques were used to establish near-field conditions and attain some degree of spatial resolution within the cross section of a single beam.[122,123] The latter approach was adopted for investigating fluctuations on the LT-4 tokamak[30], where a CO_2 laser was employed in a Mach-Zehnder interferometer configuration. The authors called their technique *scintillation interferometry* (this terminology has been used in the literature to describe a broader class of configurations, not necessarily limited to near-field detection). The multiple-beam approach is embodied instead in the *scanning interferometer* proposed by Howard.[124]

The difficulties encountered by heterodyne configurations in the presence of mechanical vibrations have led researchers to resort to homodyne techniques, as in the intermediate-field *scintillation* method.[125,126] Alternatively and in very few instances, internal-reference heterodyne systems, based on spatial-filtering methods, have been employed. To this category belong the schlieren techniques that were employed in early studies of high-density plasmas,[127] and the phase-contrast method,[128,31] which will be discussed in detail in the following section.

Within the confines of collective small-angle scattering, techniques differ only in the way that they process the information contained in the radiation transmitted by the plasma. Far-field detection, whether in the Fraunhofer limit or in the focal plane of a collecting optic, lends itself naturally to a representation in wave-number space. In particular, the generalized heterodyne technique discussed in §2.7 selects for each direction of the local-oscillator beam a specific wave number $\mathbf{k}_\perp$, with a resolution $\pm|\delta k_\perp| \simeq \pm 2\sqrt{2}/w_0$, where w_0 is the half-width of the Gaussian probing beam (defined, as in §2.5, as the $1/e$ point of the *amplitude*). It is important to note that a constraint is placed also on the longitudinal wave number: its value is $k_\perp^2/2k_0$ and is different from zero within the intrinsic uncertainty of the measurement, which is $\pm|\delta k_\parallel| \simeq \pm\pi k_\perp/(8k_0w_0)$. This last statement reaffirms that this particular scattering technique is restricted to the Bragg regime. The spatial resolution of the measurement is defined by the dimensions of the interaction volume, which is an approximate romboid of maximum width $\sim 2w_0$ and length $L_z \simeq 4k_0w_0/k_\perp$ (see Fig.

2.9).

This technique is rather attractive at relatively short wavelengths, $\lambda \ll 2w_0$, where the relative resolution $\delta k_\perp / k_\perp$ is good and the length of the interaction region can be much smaller than the length of the plasma column, providing some degree of localization. However, as the wavelengths become of the same order as the beam width, both the wave-number resolution and the spatial resolution become poor. These limitations, on the other hand, are inherent in the physics of the interaction process and are not specific of this measurement technique. If one measures directly the spatial distribution of the plasma fluctuations and then derives the wave-number spectrum through a spatial Fourier transform, the uncertainty principle will still impose $|\delta k_\parallel| \simeq \pi k_\perp / (8 k_0 w_0)$.

This is a manifestation of a broader reciprocity principle, which states that the information obtained in real space is entirely equivalent to that obtained in the reciprocal wave-number space, *provided that all the information is collected simultaneously.* Thus, if one could measure the amplitude *and phase* of all the spectral components at once, the information would be equivalent to a direct spatial mapping of the fluctuation distribution. However, the need for a different direction of the LO beam for each spectral component implies that scattering experiments in practice select only one wave number at a time. Even if the scattering vector can be changed during a series of repeatable experiments, the phase information is certainly lost.

These specific aspects of the generalized heterodyne Fraunhofer detection technique engender three significant difficulties. At long wavelengths ($\lambda \gtrsim 1$ cm) the very concept of wave number may be of dubious value: often, especially near the edge of a tokamak plasma, the gradient scale lengths of the macroscopic plasma parameters are on the order of a few centimeters, and the distinction between fluctuations and average parameters is blurred; in such inhomogeneous conditions, a direct spatial mapping is clearly a more natural representation of the structure of the fluctuations. It should also be noted that in Fraunhofer scattering the long path lengths that are necessary to separate the incident beam from the scattered radiation often lead to severe vibration problems at the longer wavelengths;[29] as a result, the upper limit on the wavelengths that can be resolved is generally smaller than the fundamental physical limit given by the width of the beam.

In addition, the interaction volume changes shape and position when the scattering angle is changed. Again, this adds a degree of complication to the interpretation of the measurements when the plasma is not homogeneous.

Finally, as was observed earlier, the measurement selects a specific longitudinal wave number, which is different for each scattering angle. Measurements that are carried out in the Raman-Nath regime, such as the near-field measurements that will be discussed later, also select a particular parallel wave number, but one that is always equal to zero within the limits of the uncertainty principle. This situation is especially advantageous in view of the generally anisotropic character of tokamak turbulence.

In the homodyne case, far-field detection has more severe limitations, as we ob-

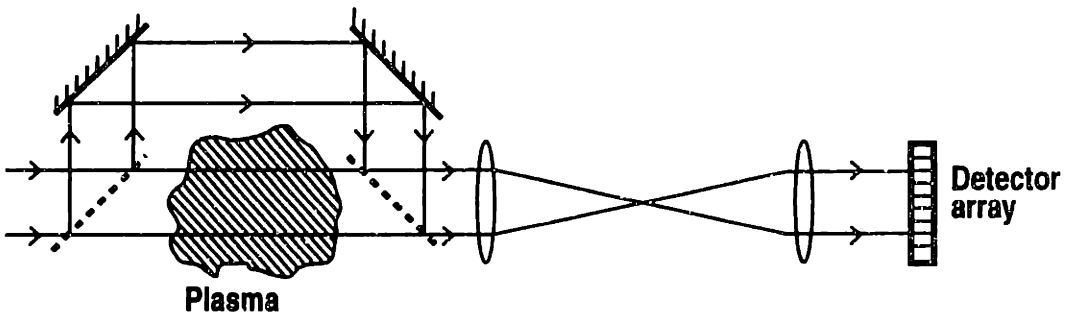

Fig. 2.13 Near-field Mach-Zehnder interferometer.

served in §2.7. The wave-number resolution is essentially the same as in the heterodyne case. However, there is now also a strong weighting factor $\exp(-k_\perp^2 w_0^2/8)$ that imposes an upper limit on the wave number. In addition, there is also a lower limit, approximately equal to the wave-number resolution. Evans et al.[120] proposed this technique mainly as a tool to determine the longitudinal distribution of the plasma fluctuations. However, such a determination is limited to a resolution $|\delta L_z| \simeq 2k_0/k_\perp^2$. It is difficult to satisfy the Bragg condition $L_z \gg |\delta L_z|$ concurrently with the requirement of a small scattering angle, which is necessary to ensure the validity of the equations and is also dictated by the practical need to collect all the scattered radiation. More importantly, this specific technique is only applicable to the case of a single perpendicular wave number, i.e., of a very narrow fluctuation spectrum. This assumption is in sharp contrast with the broadband nature of the turbulent spectra seen in a wide variety of laboratory plasma experiments.

In the realm of near-field techniques, the heterodyne imaging configuration (Fig. 2.13) represents the ultimate ideal. In the Raman-Nath regime, which is the one most frequently encountered in tokamak experiments, the near-field phase fluctuation is given by Eq. (2.84). At each point in the detection plane the measured phase is proportional to the longitudinal line integral of the density perturbation at the corresponding transversal coordinate in the plasma. Employing a detector array, one can perform a measurement with nearly arbitrary spatial resolution in the transversal plane. The main limitation is a lack of longitudinal resolution, which is inherent in the Raman-Nath regime regardless of the detection method. The wave-number spectrum can be reconstructed from the measured spatial distribution by means of Fourier transform techniques. Of course, the indetermination principle still generates an uncertainty $|\delta k_\perp| \simeq 2\sqrt{2}/w_0$.

Since this type of measurement is sensitive to absolute changes in the index of refraction of the plasma, extracting the fluctuating component from the measured phase can be a difficult and noise-prone process. For this reason, the scintillation interferometer of Nazikian and Sharp[30] included a feedback mechanism that adjusted the LO path length on a slow time scale to hold the phase difference between the plasma and the reference arms at $\pi/2$, where the sensitivity to refractive-index fluctuations is maximum [the derivative of the signal is proportional to the sine of the phase, as can be gleaned from Eq. (2.71)]. In the general form of the signal expressed

by Eq. (2.71), this corresponds to $\Omega_{LO} = 0$ and $\langle\varphi_1\rangle - \varphi_{LO} = \pi/2$. Under these conditions, the response to a small perturbation ($\tilde{\varphi}_1 \ll 1$ rad) is approximately linear. This experimental approach relies on the large difference in amplitude between the lowest-frequency ($\lesssim$ 1 kHz) components of the density (the "bulk" density) and the fluctuation spectrum, which can extend to tens or hundreds of kHz.

The main disadvantage of a heterodyne system relying on an external reference signal is its sensitivity to mechanical vibrations. Relative movements of the optics along the LO and plasma paths result in phase shifts that are erroneously interpreted as density fluctuations. This will generally define the ultimate sensitivity of the measurement, i.e., the smallest phase change that can be detected. Nazikian and Sharp[30] were able to attain an excellent sensitivity by painstakingly reducing the amplitude of the vibrations through careful isolation of the components. On large tokamaks, however, the vibrations induced by the large currents flowing in the coils and in the plasma would likely impose significantly higher limits on the measurable phase.

A heterodyne system without imaging optics, in which detection is effected in the intermediate field,[129] is decidedly inferior to its near-field counterpart, as the former shares the latter's vibrational problems but does not exhibit the same linear response.[130] The response is now $k_\perp$-dependent, and in particular, if the distance d between the plasma and the detector plane is not too large, there is an upper cutoff at $k_\perp \approx (2\pi k_0/3d)^{1/2}$, as was discussed in §2.8.

The difficulties associated with mechanical vibrations in a heterodyne system have provided impetus to the development of homodyne detection systems. In the Raman-Nath regime, the frequency spectrum of the Rytov phase ($\hat{\psi}_1$) is given by Eq. (2.83). With homodyne detection, one measures the Hermitian component of $\hat{\psi}_1$ (which corresponds to the real part of the phase). Since the homodyne signal is proportional to $\sin Q_d = \sin(k_\perp^2 d/2k_0)$, where d is the distance between the plasma and the detection plane, the measurement must be performed at some distance from the plasma (or from its image plane, if focusing optics are used). As was pointed out in §2.8, the usefulness of this *scintillation* technique is hampered by its oscillatory transfer function in $k_\perp$ space. This has two major consequences. Firstly, the accessible spectral range in $k_\perp$ space is reduced; in particular, there is a low cutoff value. Since the distance d must be well within the Rayleigh range for Eq. (2.83) to be valid, that cutoff value must be much larger than $2/w_0$. This can be a very significant limitation in practice. Secondly, since different $k_\perp$ components contribute to the signal with different weights, the resulting spatial distribution will be a complicated function of the spatial distribution of the density in the plasma. This result should be contrasted with the direct one-to-one mapping provided by a heterodyne imaging interferometer.

A compromise between homodyne and heterodyne detection is provided by a class of techniques that can be called *internal-reference interferometry*.[131] These techniques rely on optical filtering to extract a component of the transmitted beam, which is then used as a local oscillator to measure the phase of the remaining components. Thus, the vibrational problems associated with an external reference arm are circumvented;

yet, the measurement is sensitive to the phase, so that detection can be effected in the image plane and the problems of intermediate-field techniques are avoided. The sacrifice to be made for this is that some of the information is, by necessity, lost. The amount and the character of the lost information are different for different filtering techniques.

These techniques have been in existence for the better part of this century but have only recently been applied to the study of plasma density fluctuations. The phase-contrast method will be described in detail in the next two sections. The dark-ground and schlieren methods and several types of filtering techniques will be described in §2.13, in the context of a general comparative analysis.

2.10 The Phase-Contrast Technique

(a) A Brief History

Some of the greatest and most exciting advances in the field of optics in our century have occurred in the area of spatial-filtering processes. The earliest appearance of these processes dates from the 19th century, when the *central dark ground* technique and the *schlieren* (German for "streak") technique were introduced (the latter by August Töpler in 1864[132]) as procedures for examining defects in lenses.

The most significant advancement was the application of spatial filtering to imaging systems. In particular, much of the progress in this area was generated by one of the two main lines of research whose aim was the improvement of optical microscopes. While one line pursued improvements in the instrument itself, a second line sought to diversify its capabilities by taking into account the properties of the specimens.[133] The conventional microscope is an extension of the human eye, in the sense that it forms an image in terms of brightness and color, which the eye is able to detect. Thus many specimens, such as bacteria and algae, that do not appreciably absorb or reflect light are not visible in this fashion. These specimens do, however, have a refractive index that generally differs from that of their surroundings, and they accordingly alter the path length of the light as it traverses them, producing a phase change. These transparent objects are called *phase objects* to differentiate them from the visible *amplitude objects*. The eventual development of the phase-contrast method stemmed largely from attempts to render phase objects "visible".

The earliest recorded efforts in this field were the classical experiments of Ernst Abbe, who, sometime before 1892, introduced glass wedges into the rear focal plane of the microscope objective, thereby changing the phase relationships between the diffraction lines generated by a grating, which he used as a specimen.[134] This line of investigation was continued by Conrady[135] and Rheinberg[136] in the early twentieth century. It was not until some twenty-seven years later, however, that the Dutch physicist Fritz Zernike, of the University of Groningen, invented the method of *phase contrast* and showed[137,138] that it held substantial advantages over the schlieren and dark-ground techniques. Although the earliest applications were again in the investigation of defects in optical components,[139] patent rights granted to the Carl Zeiss

optical firm show that Zernike recognized the full potential of a phase-contrast microscope as early as in 1932, two years before his first published work on the subject.[133] Results from the first experiments with the phase-contrast method in microscopy, carried out at the Zeiss firm, were finally published in 1941,[140] followed a year later by the first photomicrographs with an absorbing material in the phase-contrast filter, taken by Zernike himself.[141]

The importance and usefulness of the phase-contrast microscope can hardly be exaggerated. A few years after the first prototype had been made by Zeiss, the new instrument had found extensive applications in the fields of biology and medicine, soon becoming an indispensable aid in the study of bacteria, fungi, algae, and animal cells and tissues. In 1953 Fritz Zernike was awarded the physics Nobel prize for his invention.

Applications outside the field of microscopy have been less frequent. Phase-contrast techniques have been used to image aerodynamic flows. The first known application to the study of plasmas was the work of Presby and Finkelstein of Yeshiva University,[128] who called their technique "plasma phasography". These authors employed a pulsed ruby laser to image gas jets and high-density ($n_e \sim 10^{17}$ cm^{-3}) plasma shock waves in air and argon. They also carried out a direct comparison with the schlieren method, showing that the phase-contrast technique produced superior results. As Weisen pointed out,[142] these authors failed to study the transfer properties of their system and their results remained qualitative.

Henri Weisen, of the Ecole Polytechnique Fédérale of Lausanne, Switzerland, was the first to employ phase-contrast imaging to study fluctuations in a thermonuclear plasma.[31,131,142] He employed a 23-cm-wide CO_2 laser beam to image turbulence[143] and driven Alfvén waves in the TCA tokamak. The latter measurement was used to determine the safety-factor profile,[78] by virtue of its known effect on the position of the Alfvén-wave resonance.

Following the development of our apparatus on the DIII–D tokamak,[70,82] phase-contrast imaging systems have recently been developed or planned for other fusion experiments, including the Heliotron-E device at Kyoto University in Japan,[144,145] the TEXT–U tokamak of the University of Texas at Austin,[146] and the CDX–U tokamak at Princeton University.[147]

(b) Physical Principles

For an elementary description of the principles of phase contrast, our starting assumption, upon which all our subsequent analysis will be based, is that the effect of the plasma on the incident electromagnetic wave can be described entirely by Eq. (2.84). This equation states that the amplitude of the wave is unchanged upon propagation through the plasma, while its phase is shifted by an amount proportional to the line integral of the density at each point within the cross section of the beam. In addition, we assume that the phase shift caused by the fluctuating component of the density is much smaller than 1 radian.

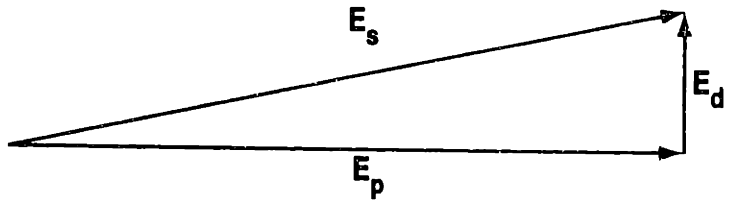

Fig. 2.14 Complex-plane phasors of undiffracted, diffracted, and total fields.

Since the perturbation induced by the plasma fluctuations is small, the value of any component of the transmitted wave does not differ much from the value it would take if the plasma fluctuations were absent. We can formally write

$$\mathbf{E}_s(\mathbf{x}_\perp, t) = \mathbf{E}_p(\mathbf{x}_\perp, t) + \mathbf{E}_d(\mathbf{x}_\perp, t), \tag{2.95}$$

where $\mathbf{E}_s$ denotes the total ("scattered") field, $\mathbf{E}_p$ is the field in the absence of fluctuations, and $\mathbf{E}_d$ is defined by Eq. (2.95) and will be called *diffracted field.* In accordance with the discussion following Eq. (2.70), the field $\mathbf{E}_p$ is not in general the unperturbed field (in the Born sense) $\mathbf{E}_0$; rather it is the total field generated by the interaction of the incident field with the plasma, *minus the fluctuating component*, but including, in general, the potentially large phase shifts caused by the bulk plasma density. The subscript p has been used to emphasize that this component, which will be called "undiffracted", is indeed affected by the plasma.

The difference between "bulk density" and "fluctuating density" is to some extent arbitrary and has not been defined in any rigorous way thus far. A precise definition is not necessary in general, but it is important to be able to distinguish between the two experimentally. Typically, changes involving the plasma on a large scale are slower than small-scale fluctuations. Therefore, if highpass filtering with a ~ 1 kHz cutoff is applied to the data, the result generally contains information only on the fluctuating components of the density. The exception to this statement is the case in which the phase shift from the bulk density is large (of the order of 1 radian or larger) *and* undergoes significant spatial variations across the width of the beam. As will become clear at the end of this section, such conditions cause severe difficulties to a phase-contrast fluctuation measurement.

The fact that the wave experiences no amplitude change implies that

$$\mathbf{E}_s \cdot \mathbf{E}_s^* = \mathbf{E}_p \cdot \mathbf{E}_p^*, \tag{2.96}$$

and the fact that the only change that the wave does experience, i.e., its phase shift, is small, implies in turn

$$\mathbf{E}_d \cdot \mathbf{E}_d^* \ll \mathbf{E}_p \cdot \mathbf{E}_p^*. \tag{2.97}$$

It is easy to conclude from these two equations alone that the diffracted field is $\sim 90°$ out of phase with respect to the undiffracted field. This is illustrated geometrically by Fig. 2.14, which shows the phasors of the fields in the complex plane (not to be confused with vectors in real space). The difference between two phasors with identical magnitude and nearly identical direction is a phasor that is approximately perpendicular to both.

From a mathematical point of view, the same conclusion can be reached from the expression

$$\mathbf{E}_s(\mathbf{x},t) = \mathbf{E}_p(\mathbf{x},t)e^{i\tilde{\varphi}(\mathbf{x}_\perp,t)} \simeq \mathbf{E}_p(1+i\tilde{\varphi}), \tag{2.98}$$

where $\tilde{\varphi}$ is the fluctuating imaginary part of the Rytov phase; this expression, combined with Eq. (2.95), yields in turn

$$\mathbf{E}_d \simeq i\tilde{\varphi}\mathbf{E}_p, \tag{2.99}$$

where the i factor provides precisely the 90° phase shift discussed above.

If the diffracted and undiffracted components of the scattered wave could somehow be separated, and a ±90° phase shift could be applied to the undiffracted component alone, the resulting field could be written

$$\mathbf{E}'_s = \mathbf{E}_p(\pm i + i\tilde{\varphi}). \tag{2.100}$$

Now to first order in $\tilde{\varphi}$ the intensity can be written

$$|E'_s|^2 = |E_p|^2\,(1 \pm 2\tilde{\varphi}). \tag{2.101}$$

This operation therefore results in an intensity with a fluctuating component that is *directly proportional* to the phase of the original beam. Thus on the image plane a detector, or a human eye in the case of the microscope, would register a signal proportional to the line integral of the density. Note that this would be true even if the phase shift were not exactly 90°, although the proportionality factor is maximum in that case.

The process just described presents remarkable similarities with the heterodyne detection techniques described in §§2.6–2.8. Indeed, one can look upon this process as a heterodyne method for the detection of the diffracted radiation, where the role of the local oscillator is played by the undiffracted radiation. This is an example of an internal-reference interferometer. The lack of an external reference renders the overall phase shift from the bulk plasma density, regardless of its magnitude, essentially irrelevant to the measurement, since it is carried by both the diffracted and the undiffracted radiation, and therefore it does not affect the interference term.

It should be noted that this procedure produces an intensity variation regardless of the magnitude of $\tilde{\varphi}$. In general, the dependence is nonlinear, and the calculation cannot be carried out analytically as it involves the Fourier transform of the exponential of a function.

It remains to be seen how the separation of the undiffracted from the diffracted component can be achieved. Let us assume for simplicity that the incident wave is a plane wave: $\mathbf{E}_p = \mathbf{E}_{p0}e^{i\mathbf{k}_0\cdot\mathbf{x}}$. The undiffracted component travels in the same direction as the incident wave; in diffraction terms, this is the zeroth-order component. The diffracted components, on the other hand, propagate at the Bragg angle $k_\perp/k_0$ with respect to the incident wave. This can be seen directly from Eq. (2.99): if the

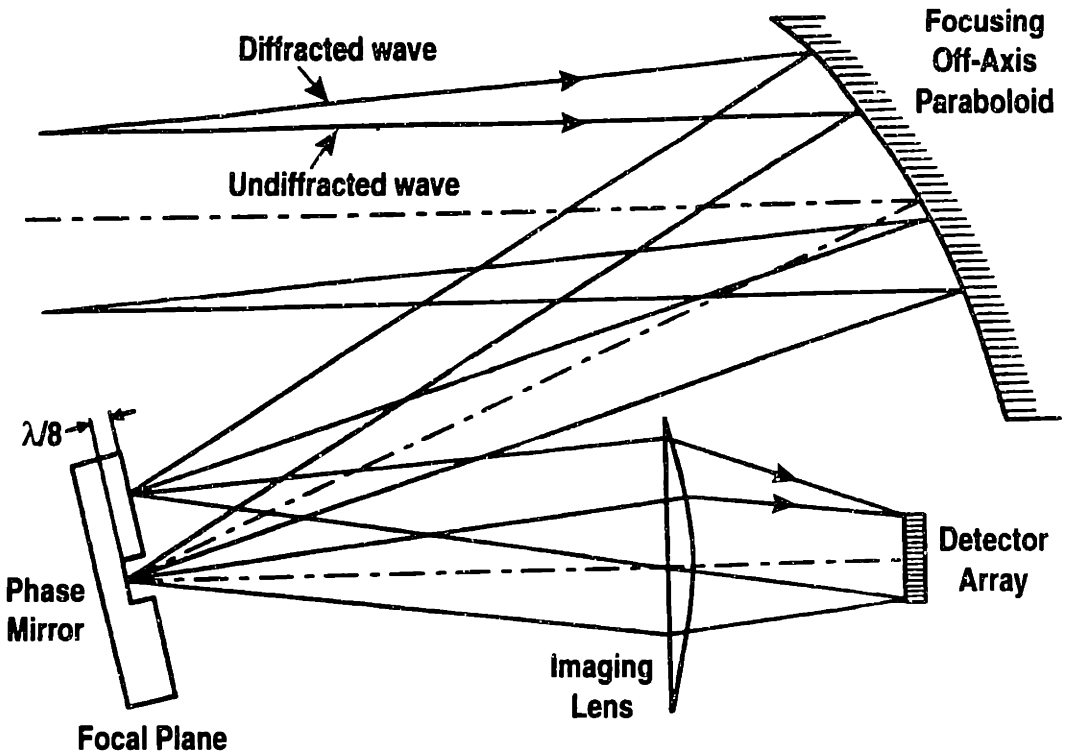

Fig. 2.15 Principles of phase contrast. Before imaging, the diffracted component is shifted in phase by 90° with respect to the undiffracted component.

perturbed phase is taken to have the form $\tilde{\varphi}(\mathbf{x}_\perp, t) = \tilde{\varphi}_0 \cos(\mathbf{K}\cdot\mathbf{x}_\perp - \Omega t)$, Eq. (2.99) can be rewritten

$$\mathbf{E}_d \simeq i\tilde{\varphi}_0 \mathbf{E}_{p0} \frac{1}{2}\left(e^{i(\mathbf{k}_0+\mathbf{K})\cdot\mathbf{x}-i(\omega_0+\Omega)t} + e^{i(\mathbf{k}_0-\mathbf{K})\cdot\mathbf{x}-i(\omega_0-\Omega)t}\right), \tag{2.102}$$

which is the sum of two waves propagating at the two angles specified by the Bragg condition [Eq. (2.28)].

The different directions of propagation of the undiffracted and diffracted components permit them to be easily separated in the focal plane of a collecting optic (see Fig. 2.15). According to the laws of geometrical optics, a ray impinging on a lens of focal length F at a small angle θ to the optical axis reaches the focal plane at a distance $y = F\theta$ from the optical axis. This implies that the undiffracted rays are focused at the center of the focal plane, while the diffracted rays intercept the same plane at varying distances from the center, depending on the wave number of the perturbation that generated them.

Having thus separated the two components, the necessary phase shift can be introduced by means of a thin refractive strip [for a one-dimensional (1D) bundle] or dot [in the two-dimensional (2D) case] located at the center of the focal plane and designed to increase the path length by a quarter of a wavelength. This region is called the *conjugate area*, whereas the remainder of the focal plane is known as the *complementary area.*

In the case of the phase-contrast microscope, the incident bundle is generally obtained in practice by passing light generated by a broad source through an annular diaphragm and a substage condenser; the resulting bundle therefore lies on the surface of a cone, viz., the zeroth-order diffraction component is inclined by a given angle with respect to the optical axis. The conjugate area then takes the form of an annulus. In macroscopic experiments involving plasmas, a reflective, rather than refractive, *phase plate* is normally used for reasons of practicality and expense. In this case a mirror is placed in the focal plane, with a thin groove (1D) or circular depression (2D) of depth $\lambda_0/8$ in the center (Fig. 2.15). The undiffracted component undergoes a $\pi/2$ phase shift upon reflection.

Upon re-examining Eq. (2.101), it can be noted that the component of interest in the signal is overshadowed by the much larger unperturbed component. The two can generally be distinguished on the basis of their different frequency spectra. However, the finite dynamic range of all instruments renders a strong and unneeded dc signal a hindrance to the achievement of high sensitivity. This difficulty can be overcome by requiring that the conjugate area of the phase plate transmit (if refractive), or reflect (if reflective), only a fraction $\rho < 1$ of the incident power. In this case Eq. (2.100) clearly must be modified as follows:

$$\mathbf{E}_s' = \mathbf{E}_p(\pm i\sqrt{\rho} + i\tilde{\varphi}). \tag{2.103}$$

Similarly, Eq. (2.101) is replaced by

$$|E_s'|^2 = |E_p|^2\,(\rho \pm 2\sqrt{\rho}\;\tilde{\varphi}). \tag{2.104}$$

Thus the dc signal level is reduced by a factor ρ and the strength of the ac signal relative to the dc signal (the "contrast") is improved by a factor $1/\sqrt{\rho}$. This reduction is generally achieved by using absorbent materials in a refractive conjugate area, and antireflective coatings or materials in a reflective one.

The need for attenuation of the undiffracted wave is particularly pressing in the case of the microscope, owing to the relatively limited dynamic range of the eye, and when the light is detected by a photographic film. Working with film, Presby and Finkelstein[128] reported being forced to achieve attenuation factors as small as 0.04%.

Thus far nothing has been said about the width of the phase-plate groove (or radius of the depression). The undiffracted wave in the plane-wave approximation is focused on the center of the plate, but in the real case of a beam of finite width diffraction effects will broaden the focal spot to a finite size. The groove must be large enough to accommodate a significant fraction of the focal spot in order to retain most of the local-oscillator strength. However, the passband in wave-number space shrinks as the groove becomes wider. The search for an optimal groove width must be undertaken in the framework of a diffraction analysis. This will be the object of the next section.

It is clear at this point that if the "undiffracted" field $\mathbf{E}_p$ contains large-amplitude, short-wavelength components generated by scattering from the bulk

plasma density, the spatial dependence of the measured signal will be determined both by $\mathbf{E}_p$ and by $\tilde{\varphi}$, in a nonlinear fashion in general, and discriminating between the two will be difficult. One can look upon this also as a diffraction problem: when large phase variations exist, a finite fraction of the power will be diffracted out of the phase plate groove, and additional, unwanted interference signals will result. Under such conditions, the groove width should be broadened to accommodate the entire focal spot, including those components. Thus, linearity will be preserved at the expense of a smaller passband.

2.11 Response Properties of the Phase-Contrast Technique

For a complete description of a spatial-filtering process the geometrical-optics approximation is not sufficient. Instead one must adopt the formalism of diffraction theory, which was introduced in §2.5. In general, a phase-contrast imaging system will include an aperture stop, a phase object, a focusing optic, a phase plate, imaging optics, and a detector located in the image plane. Our objective is to derive the field distribution in the image plane. We assume that the field distribution behind the aperture stop is known and, in addition, that no appreciable diffraction occurs between the aperture and the phase object. This assumption was justified in §2.5 and was used throughout §§2.5–2.8. Also, all optics and apertures beside the stop will be taken to be much wider than the cross section of the beam and will be considered infinitely wide. Finally, the phase shift $\tilde{\varphi}$ impressed on the incident wave by the plasma is assumed to be much smaller than 1 radian.

We shall use a scalar notation, as no depolarization effects are included in the analysis. A general approach to this type of problem involves successive applications of the diffraction integral [Eq. (2.55)]. In addition, the effect of each focusing optic (which we assume to be a lens for simplicity, although the same considerations would apply to a concave mirror) is described by the phase shift given by Eq. (C.16). However, the peculiar characteristics of the system under exam can greatly simplify the problem. In particular, we can make use of the Fourier-transforming properties of lenses. If we denote the frequency spectrum of the field directly in front of the lens as $E_l(\mathbf{x}_\perp;\omega_s)$, the field in the focal plane will be given by[103] [Eq. (C.17)]

$$E_f(\mathbf{x}_\perp;\omega_s) = \frac{-i\omega_s}{2\pi F c}\exp\left[i\frac{\omega_s}{c}\left(F+\frac{x_\perp^2}{2F}\right)\right] A_l\left(\frac{\omega_s}{c}\frac{\mathbf{x}_\perp}{F},\omega_s\right), \tag{2.105}$$

where F is the focal length and A_l is the 2D spatial Fourier transform of E_l. Hence, the field distribution in the focal plane is proportional to the Fourier transform of the field in front of the lens. The proportionality factor contains a phase, which is a function of $\mathbf{x}_\perp$ or, equivalently, of $\mathbf{k}_\perp$, through the relation

$$\mathbf{k}_\perp = \frac{\omega_s}{Fc}\mathbf{x}_\perp. \tag{2.106}$$

This result suggests that the problem we are considering is best tackled in wavenumber space. To this end, we need two more ingredients.

Firstly, the wave-number-space equivalent of the diffraction integral is given by Eq. (2.54), which we rewrite as

$$A(\mathbf{k}_\perp, \omega_s; z) = A(\mathbf{k}_\perp, \omega_s; z') \exp\left[i\left(\frac{\omega_s^2}{c^2} - k_\perp^2\right)^{1/2}(z - z')\right]. \tag{2.107}$$

The effect of propagation is thus simply a $k_\perp$-dependent multiplicative factor.

Secondly, imaging by a single lens is described in the paraxial approximation by the following equation:[103]

$$E(M\mathbf{x}_\perp, z_{\text{im}}; \omega_s) = \frac{1}{M} \exp\left[i\frac{\omega_s}{c}\left(z_{\text{im}} - z_{\text{obj}} + \frac{M^2 x_\perp^2}{2z_{\text{im}}} - \frac{x_\perp^2}{2z_{\text{obj}}}\right)\right] E(\mathbf{x}_\perp, z_{\text{obj}}; \omega_s), \tag{2.108}$$

where M is the magnification of the system, and the subscripts *im* and *obj* denote respectively the image and object coordinates, with the lens at $z = 0$. This equation can be derived by means of successive applications of the diffraction integral [Eq. (2.59)], with the inclusion of the phase shift given by Eq. (C.16). The phase term in Eq. (2.108) represents the accumulated phase shift along the path of the principal ray in the paraxial approximation. This path is represented by the line connecting the point $(\mathbf{x}_\perp, z_{\text{obj}})$ with its corresponding point at the image, $(M\mathbf{x}_\perp, z_{\text{im}})$, and intersecting the lens on the optical axis (see Fig. 2.16). When an image is formed by a series of several optical components, the total path length will be the sum of the individual ones joining each intermediate image with the following one. It can be shown by direct calculation that the general expression

$$E(M\mathbf{x}_\perp, z_{\text{im}}; \omega_s) = \frac{1}{M} \exp\left[i\frac{\omega_s}{c}\left(z_{\text{im}} - z_{\text{obj}} + \frac{(M-1)^2 x_\perp^2}{2(z_{\text{im}} - z_{\text{obj}})}\right)\right] E(\mathbf{x}_\perp, z_{\text{obj}}; \omega_s) \tag{2.109}$$

applies, where M now refers to the global magnification of the system, and $z_{\text{im}} - z_{\text{obj}}$ is the total distance between object and image along the optical axis. Equation (2.109) permits to derive the field distribution at the detector if the field at the object is known: a detailed knowledge of the imaging system is thus unnecessary. The frequency Fourier transform of Eq. (2.109) is

$$E(M\mathbf{x}_\perp, z_{\text{im}}, t) = \frac{1}{M} E(\mathbf{x}_\perp, z_{\text{obj}}, t - t_d), \tag{2.110}$$

where

$$t_d = \frac{1}{c}\left(z_{\text{im}} - z_{\text{obj}} + \frac{(M-1)^2 x_\perp^2}{2(z_{\text{im}} - z_{\text{obj}})}\right). \tag{2.111}$$

The problem can now be reduced to the following sequence of steps. The $\mathbf{k}_\perp$ distribution behind the aperture stop is obtained by taking the Fourier transform

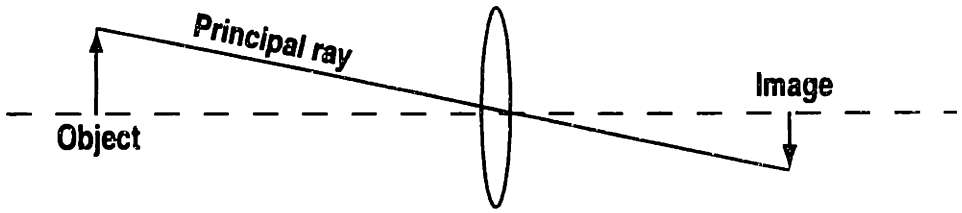

Fig. 2.16 One-lens imaging geometry. The diagonal line is the principal ray.

A_s of the complete *scattered field*, which as usual is taken to be $E_s = E_p(1 + i\tilde{\varphi})$ in the aperture and zero elsewhere. The propagation from the aperture to the focusing lens is decribed by Eq. (2.107); the passage through the lens is described by Eq. (2.105), from which the spatial distribution in the focal plane can be calculated. This distribution must then be multiplied by an appropriate transfer function that describes the effect of the phase plate. The next step is a virtual propagation of the resulting field through the lens back to the object plane. It is immediately clear from the structure of Eqs. (2.105) and (2.107) that the phase factors introduced by the forward propagation and by the passage through the lens are exactly canceled by the second passage and by the backward propagation. Finally, the imaging process, i.e., the propagation from the object to the detector, is described by Eqs. (2.109) and (2.110).

Therefore the whole problem reduces to a simple multiplication of the original spectrum by the transfer function of the phase plate, followed by an inverse Fourier transform and application of Eq. (2.110) to obtain the field distribution in the detection plane. The entire operation can thus be carried out in real space, replacing the multiplication by the transfer function with a convolution integral.

The aperture will be taken to be a circle of radius a. Assuming that the incident wave is monochromatic, and that any large phase shifts from the bulk plasma density are spatially uniform, we can write $E_s(\mathbf{x}, t) = E_{p0}(\mathbf{x}_\perp) \times \exp\left[ik_0 z - i\omega_0 t + i\left\langle\tilde{\varphi}(t)\right\rangle\right]$ $[1 + i\tilde{\varphi}(\mathbf{x}, t)]$; we take E_{p0} to be a real quantity. (The case of a diverging or converging wave, with E_{p0} complex, can be treated by attributing the divergence or convergence to a fictitious lens and moving the focal and image planes accordingly). Denoting the transfer function by $\hat{T}(\mathbf{k}_\perp)$, and its inverse Fourier transform by $T(\mathbf{x}_\perp)$, we can write the field distribution at the detection plane as follows:

$$E_{\rm im}(M\mathbf{x}_\perp, t) = \frac{1}{M} e^{i[k_0 z_{\rm obj} - \omega_0(t - t_d) + \langle\tilde{\varphi}(t - t_d)\rangle]} \left\{T \circ [P_a E_{p0}(1 + \tilde{\varphi})]\right\}(\mathbf{x}_\perp, t - t_d), \tag{2.112}$$

where t_d is given by Eq. (2.111). The convolution operation is defined by the relation $(f \circ g)(\mathbf{x}_\perp) \equiv \int f(\mathbf{x}'_\perp) g(\mathbf{x}_\perp - \mathbf{x}'_\perp) d^2x'_\perp$, and $P_a(|\mathbf{x}_\perp|)$ is the pupil function of the aperture, defined as

$$P_a(y) = \begin{cases} 1 & \text{if } |y| \le a \\ 0 & \text{otherwise.} \end{cases} \tag{2.113}$$

The detector signal is proportional to the power flux in the detection plane, averaged over a time interval large with respect to $1/\omega_0$ but small with respect to

$1/\omega$ (taking ω to be at the high end of the fluctuation spectrum, and larger than the bandwidth of E_{p0}). The flux can then be written

$$\mathcal{E}(M\mathbf{x}_\perp, t) = \frac{c}{8\pi}\left[E_{\rm im}(M\mathbf{x}_\perp, t)E^*_{\rm im}(M\mathbf{x}_\perp, t)\right]. \tag{2.114}$$

The dependence of t_d on $\mathbf{x}_\perp$ is in general an undesirable effect. Fortunately, that dependence can almost invariably be neglected. The condition for this to be true is

$$\frac{\omega}{c}\frac{(M-1)^2 w_0^2}{2(z_{\rm im} - z_{\rm obj})} \ll 1, \tag{2.115}$$

where ω is a characteristic frequency of the fluctuation spectrum and w_0 is the half-width of the interaction region. This condition will be assumed henceforth and the time delay will be assumed to be a constant.

We can now substitute Eq. (2.112) in Eq. (2.114), obtaining

$$\mathcal{E}(M\mathbf{x}_\perp, t) = \frac{c}{8\pi M^2}\left|T \circ \left[P_a E_{p0}(1 + i\tilde{\varphi})\right]\right|^2(\mathbf{x}_\perp, t - t_d), \tag{2.116}$$

Expanding Eq. (2.116) to first order in $\tilde{\varphi}$, we can write $\mathcal{E} = \mathcal{E}_{\rm dc} + \tilde{\mathcal{E}}$, where

$$\mathcal{E}_{\rm dc}(M\mathbf{x}_\perp, t) = \frac{c}{8\pi M^2}\left|T \circ (P_a E_{p0})\right|^2(\mathbf{x}_\perp, t - t_d) \tag{2.117}$$

and

$$\tilde{\mathcal{E}}(M\mathbf{x}_\perp, t) = \frac{c}{4\pi M^2}\,{\rm Im}\left\{\left[T \circ (P_a E_{p0})\right]\left[T \circ (P_a E_{p0}\tilde{\varphi})\right]^*\right\}(\mathbf{x}_\perp, t - t_d). \tag{2.118}$$

We consider the one-dimensional (1D) case first. We take the coordinate of interest to be x, so that the transfer function is independent of y. The phase plate contains a central strip of width $2v$ and power transmissivity (or reflectivity, for a reflective plate) ρ that advances or retards the phase by $\pi/2$, while the surrounding area has no effect on the fields [see Fig. 2.17(a)]. Taking the case of phase advancement for definiteness, the amplitude transfer function is

$$T(x_F) = 1 - P_v(x) + i\sqrt{\rho}\,P_v(x), \tag{2.119}$$

with the pupil function P_v defined as in Eq. (2.113). Using the correspondence between focal-plane coordinates and wave numbers expressed by Eq. (2.106), and approximating ω_s with ω_0, we can write the transfer function directly in the reciprocal space

$$\hat{T}^{(1)}(\mathbf{k}_\perp) = 1 + P_{k_c}(k_x)(i\sqrt{\rho} - 1), \tag{2.120}$$

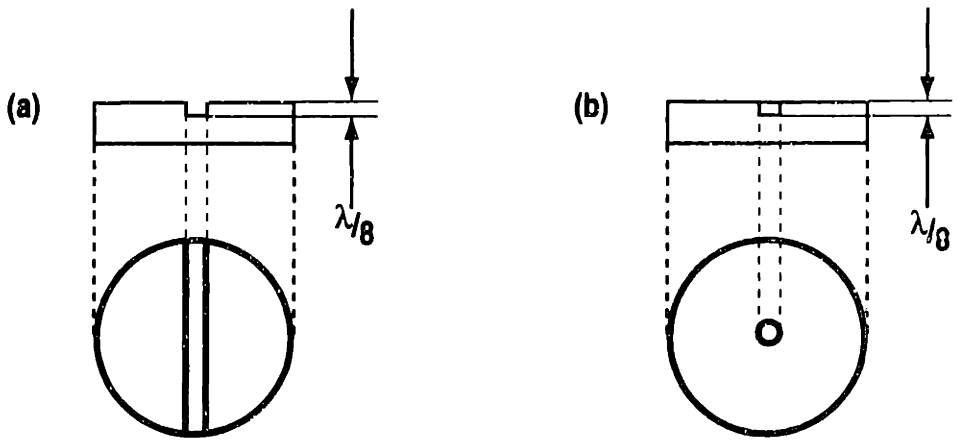

Fig. 2.17 Reflective phase plate, (a) one-dimensional and (b) two-dimensional.

where $k_c = k_0 v/F$. The equivalent transfer function for the two-dimensional (2D) case, with the strip replaced by a circular depression of radius v [see Fig. 2.17(b)], is simply

$$\hat{T}^{(2)}(\mathbf{k}_\perp) = 1 + P_{k_c}(|\mathbf{k}_\perp|)(i\sqrt{\rho} - 1). \tag{2.121}$$

The inverse Fourier transform of the transfer function can be written

$$T(\mathbf{x}_\perp) = \delta(\mathbf{x}_\perp) + (i\sqrt{\rho} - 1)\hat{P}_{k_c}(\mathbf{x}_\perp), \tag{2.122}$$

where $\hat{P}_{k_c}$ is a real function given by

$$\hat{P}^{(1)}_{k_c}(\mathbf{x}_\perp) = \frac{1}{\pi x}\sin(k_c x)\delta(y) \tag{2.123}$$

for the 1D case, and by

$$\hat{P}^{(2)}_{k_c}(\mathbf{x}_\perp) = \frac{1}{2\pi}\frac{k_c}{|\mathbf{x}_\perp|}J_1(k_c|\mathbf{x}_\perp|) \tag{2.124}$$

for the 2D case.

The expressions for the dc signal $\mathcal{E}_{\rm dc}$ and for the fluctuating signal $\tilde{\mathcal{E}}$ can be written in more explicit form by substituting Eq. (2.122) in Eqs. (2.117) and (2.118). We obtain, respectively,

$$\mathcal{E}_{\rm dc}(M\mathbf{x}_\perp, t) = \frac{c}{8\pi M^2}\left\{\left[P_a E_{p0} - \hat{P}_{k_c} \circ (P_a E_{p0})\right]^2 + \rho\left[\hat{P}_{k_c} \circ (P_a E_{p0})\right]^2\right\}, \tag{2.125}$$

and

$$\begin{aligned}\tilde{\mathcal{E}}(M\mathbf{x}_\perp, t) &= \frac{c}{4\pi M^2}\,\mathrm{Im}\Big\{\left[P_a E_{p0} + (i\sqrt{\rho} - 1)\hat{P}_{k_c} \circ (P_a E_{p0})\right] \\ &\quad \times \left[P_a E_{p0}\tilde{\varphi} + (-i\sqrt{\rho} - 1)\hat{P}_{k_c} \circ (P_a E_{p0}\tilde{\varphi})\right]\Big\} \\ &= \frac{c}{4\pi M^2}\sqrt{\rho}P_a E_{p0}\Big\{\tilde{\varphi}\left[\hat{P}_{k_c} \circ (P_a E_{p0})\right] - \left[\hat{P}_{k_c} \circ (P_a E_{p0}\tilde{\varphi})\right]\Big\},\end{aligned} \tag{2.126}$$

where it is now implicit that the right-hand sides are object, rather than image, quantities and must thus be calculated at $\mathbf{x}_\perp$ and at $t - t_d$.

(a) Plane Wave and Infinite Aperture

We begin with a highly idealized situation and then gradually add increasing levels of complication, to better illustrate the intuitive aspects of the phase-contrast technique.

As a first approximation, let us assume that the incident wave is a plane wave, i.e., that $E_{p0}(\mathbf{x}_\perp) = E_{p0}$ is a constant; and that the aperture is infinite, i.e., that P_a can be replaced by 1. In Eq. (2.125) the first term in square brackets is equal to zero, and we find

$$\mathcal{E}_{\rm dc}(M\mathbf{x}_\perp, t) = \rho \frac{cE_{p0}^2}{8\pi M^2}. \tag{2.127}$$

Similarly, Eq. (2.126) becomes

$$\tilde{\mathcal{E}}(M\mathbf{x}_\perp, t) = \sqrt{\rho}\frac{cE_{p0}^2}{4\pi M^2}\left(\tilde{\varphi} - \hat{P}_{k_c} \circ \tilde{\varphi}\right). \tag{2.128}$$

The spatial Fourier transform of this equation takes a particularly simple form:

$$\hat{\mathcal{E}}(\mathbf{k}_\perp/M; t) = \mathcal{T}(\mathbf{k}_\perp)\hat{\varphi}(\mathbf{k}_\perp; t - t_d), \tag{2.129}$$

where we have defined a *transfer function* given by

$$\mathcal{T}(\mathbf{k}_\perp) = \begin{cases} \sqrt{\rho}\, cE_{p0}^2/(4\pi) & \text{if } |k_x| \geq k_c \\ 0 & \text{otherwise} \end{cases} \tag{2.130}$$

in the 1D case, and by

$$\mathcal{T}(\mathbf{k}_\perp) = \begin{cases} \sqrt{\rho}\, cE_{p0}^2/(4\pi) & \text{if } |\mathbf{k}_\perp| \geq k_c \\ 0 & \text{otherwise} \end{cases} \tag{2.131}$$

in the 2D case.

Hence, in this approximation, the phase-contrast technique acts as a highpass spatial filter for k_x or $k_\perp$ (see Fig. 2.18). The cutoff value k_c can be arbitrarily small. If it is chosen small enough to include the whole fluctuation spectrum in the passband, we recover the simple result of §2.10 [Eq. (2.104)]. Since in this limit the transfer function is independent of $\mathbf{k}_\perp$, we can say that this is an *image-preserving* process: not only is the phase information converted into a measurable amplitude variation, but this conversion is also local, i.e., the amplitude at each point in the

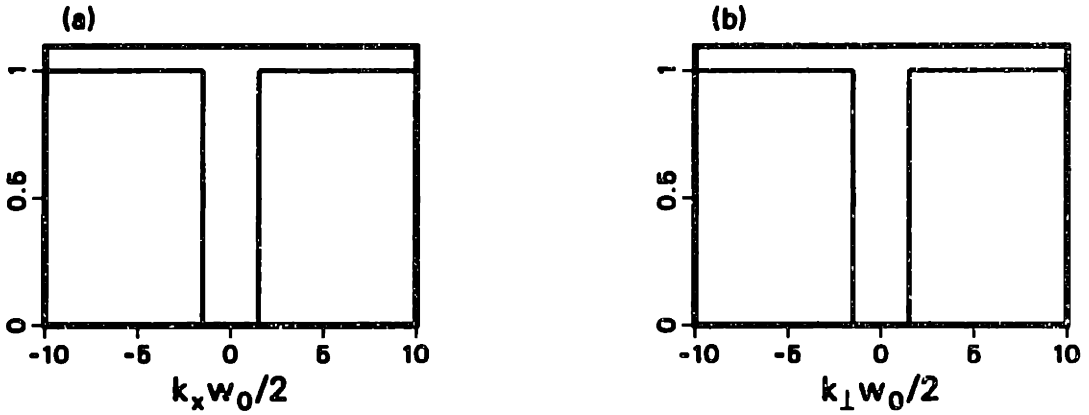

Fig. 2.18 Response function of phase contrast in the plane-wave approximation ($k_c w_0/2 = 1.5$): (a) 1D, (b) 2D.

detection plane is proportional to the phase *at the corresponding point* in the object plane.

As we move to more realistic situations, one of our principal aims will be to preserve this imaging property to a good approximation, i.e., to retain a nearly flat transfer function.

(b) Gaussian Beam and Infinite Aperture

The simplified example of the infinite plane wave will provide guidance in more complicated situations. At the next level of approximation we can replace the plane wave with a Gaussian distribution, but we still assume an infinite aperture. The Gaussian beam is supposed collimated, so that its distribution at the aperture can be approximated by the distribution at the waist, given by Eq. (2.60):

$$E_{p0}(\mathbf{x}_\perp) = \left(\frac{8\pi}{c}P\right)^{1/2}\left(\frac{2}{\pi}\right)^{1/2}\frac{1}{w_0}\exp\left(-\frac{x_\perp^2}{w_0^2}\right). \tag{2.132}$$

(If the beam is not collimated, i.e., if the distance from the waist to the object plane is of the order of a Rayleigh length, all the considerations to follow are still valid, provided that the phase plate is located at the beam waist created by the lens, rather than in the focal plane; Eq. (2.132) retains its validity, but w_0 must then be replaced by the half-width in the object plane, i.e., $w_0(1+\zeta_p^2)^{1/2}$; finally, the image geometry must also include a fictitious lens that accounts for the beam's divergence.) Here we shall only study the fluctuating component of the signal, deferring an analysis of the dc component to the next section.

The signal $\tilde{\mathcal{E}}$ is no longer obtained from $\tilde{\varphi}$ through a simple convolution. The implication of this is that a transfer function in $\mathbf{k}_\perp$ space cannot be defined. Physically, this is a consequence of the loss of the translational symmetry of the system in going from an infinite plane wave to a Gaussian beam, which is by necessity localized in a

specific region of space. Thus even if $\tilde{\varphi}$ is a pure spatial sine function, the measured signal will not be sinusoidal, i.e., its spectrum will exhibit some degree of broadening around the $\mathbf{k}_\perp$ value of $\tilde{\varphi}$. It is still meaningful, however, to ask what the signal level is for different sinusoidal inputs. An inspection of Eq. (2.126) shows that the signal $\tilde{\mathcal{E}}$ is the difference of two terms, one proportional to $\tilde{\varphi}$ and the other obtained from a convolution involving $\tilde{\varphi}$. The plane-wave case [Eq. (2.128)] suggests that the first term will dominate at wave numbers $k_\perp \geq k_c$, whereas the two terms will be comparable at low $k_\perp$. If we focus on the high-$k_\perp$ case and on the first term only, we still cannot define a transfer function because the proportionality factor is a function of $\mathbf{x}_\perp$. However, by considering the weighted signal

$$\tilde{\mathcal{E}}'(M\mathbf{x}_\perp) = \frac{\tilde{\mathcal{E}}(M\mathbf{x}_\perp)P_a(|\mathbf{x}_\perp|)}{W(\mathbf{x}_\perp)}, \tag{2.133}$$

where we define the weighting function W as

$$W(\mathbf{x}_\perp) = \frac{E_{p0}(\mathbf{x}_\perp)\left[\hat{P}_{k_c} \circ (P_a E_{p0})\right](\mathbf{x}_\perp)}{E_{p0}(0)\left[\hat{P}_{k_c} \circ (P_a E_{p0})\right](0)}, \tag{2.134}$$

we obtain a quantity that at high $k_\perp$ is approximately proportional to $\tilde{\varphi}$ (with, now, a constant coefficient of proportionality).

We can now define an approximate transfer function[131] by simply studying the weighted signal $\tilde{\mathcal{E}}'$ at the center of the beam, where the dc signal is maximum. We take the input to be

$$\tilde{\varphi}(\mathbf{x}_\perp, t) = \hat{\varphi}_{\mathbf{K}}(t)\cos(\mathbf{K}\cdot\mathbf{x}_\perp + \vartheta_0), \tag{2.135}$$

and by analogy with Eq. (2.129) we can write

$$\tilde{\mathcal{E}}'(0,t) = \tilde{\mathcal{E}}(0,t) = \mathcal{T}(\mathbf{K})\hat{\varphi}_{\mathbf{K}}(t - t_d)\cos\vartheta_0. \tag{2.136}$$

This expression is always formally permissible, but $\mathcal{T}$ depends on ϑ_0 in general. A sufficient condition for $\mathcal{T}$ to be independent of ϑ_0 is that the beam, the aperture, and the filter be spatially symmetric. This will be shown rigorously in the general analysis of §2.13.

After the transfer function has been calculated, it can be used in the *approximate* expression

$$\tilde{\mathcal{E}}'(M\mathbf{x}_\perp, t) \simeq \mathcal{T}(\mathbf{K})P_a(|\mathbf{x}_\perp|)\hat{\varphi}_{\mathbf{K}}(t - t_d)\cos(\mathbf{K}\cdot\mathbf{x}_\perp + \vartheta_0), \tag{2.137}$$

and thus

$$\tilde{\mathcal{E}}(M\mathbf{x}_\perp, t) \simeq W(\mathbf{x}_\perp)\mathcal{T}(\mathbf{K})P_a(|\mathbf{x}_\perp|)\hat{\varphi}_{\mathbf{K}}(t - t_d)\cos(\mathbf{K}\cdot\mathbf{x}_\perp + \vartheta_0). \tag{2.138}$$

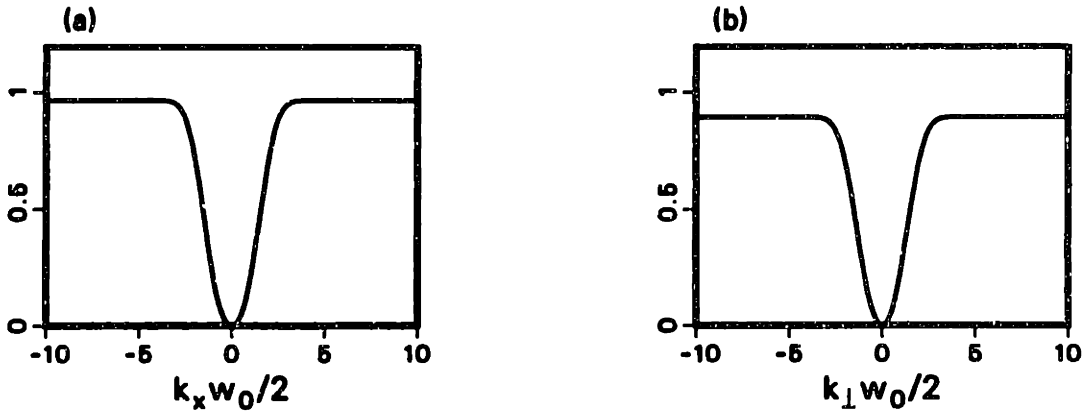

Fig. 2.19 Phase-contrast response function with Gaussian beam and infinite aperture ($k_c w_0/2 = 1.5$): (a) 1D, (b) 2D.

We now replace the pupil function P_a with 1 in Eq. (2.126). Comparing Eq. (2.136) with Eq. (2.126) we find

$$\mathcal{T}(\mathbf{K}) = \frac{c}{4\pi M^2}\sqrt{\rho}\frac{E_{p0}(0)}{(2\pi)^2}\left(\left[P_{k_c} \circ \hat{E}_{p0}\right] - \frac{\left\{P_{k_c} \circ \left[\hat{E}_{p0} \circ (\delta_+ e^{i\vartheta_0} + \delta_- e^{-i\vartheta_0})\right]\right\}}{2\cos\vartheta_0}\right)_{\mathbf{k}_\perp=0}, \tag{2.139}$$

where $\delta_\pm(\mathbf{k}_\perp) = \delta(\mathbf{k}_\perp \mp \mathbf{K})$, P_{k_c} is understood to have the argument k_x in the 1D case and $|\mathbf{k}_\perp|$ in the 2D case, and use has been made of the relation $[f \circ g^*]_{\mathbf{x}_\perp=0} = (1/2\pi)^2[\hat{f} \circ \hat{g}^*]_{\mathbf{k}_\perp=0}$. Calculating the Fourier transform of Eq. (2.132) yields

$$\hat{E}_{p0}(\mathbf{k}_\perp) = 4\pi\left(\frac{P}{c}\right)^{1/2} w_0 \exp\left(-\frac{w_0^2 k_\perp^2}{4}\right), \tag{2.140}$$

and substituting Eq. (2.140) in Eq. (2.139) we find

$$\mathcal{T}^{(1)}(\mathbf{K}) = 2\sqrt{\rho}\,u_0(0)\left[\operatorname{erf} Q - \frac{1}{2}\operatorname{erf}(Q + K'_x) - \frac{1}{2}\operatorname{erf}(Q - K'_x)\right] \tag{2.141}$$

for the 1D case, where we have introduced the dimensionless quantities $Q = k_c w_0/2$ and $\mathbf{K}' = w_0\mathbf{K}/2$, and the dc power flux at the center of the image in the absence of a phase plate, $u_0(0) = 2P/(\pi M^2 w_0^2)$. Here, $\operatorname{erf}(y) = (2/\sqrt{\pi})\int_0^y e^{-\xi^2} d\xi$ is the error function. Similarly, the result for the 2D case is

$$\mathcal{T}^{(2)}(\mathbf{K}) = 2\sqrt{\rho}\,u_0(0)\left[1 - e^{-Q^2} - 2e^{-K'^2}\int_0^Q e^{-\xi^2} I_0(2K'\xi)\,\xi d\xi\right], \tag{2.142}$$

where I_0 is the modified Bessel function. These transfer functions are plotted in Fig. 2.19.

As these expressions show, the transfer function is zero for $\mathbf{K} = 0$ and the phase-contrast technique acts as a highpass filter as in the plane-wave case. This is a general property of internal-reference interferometry: the lack of an external phase reference makes it impossible to measure the *absolute* phase shift (the $\mathbf{K} = 0$ component). Also, the transfer function has the symmetry property $\mathcal{T}(\mathbf{K}) = \mathcal{T}(-\mathbf{K})$: this is a general property of optical processing that does not depend on the symmetry of either the filter or the optical aperture. Rather, the symmetry stems from the impossibility of defining a direction of propagation in the spatial domain, or, mathematically, from the fact that the input function [Eq. (2.135)] is real. This will be proven in §2.13.

Finally, note that the asymptotic value of $\mathcal{T}$ for $K \to \pm\infty$ is reduced by a factor (erf Q) in the 1D case, and by a factor $(1 - e^{-Q^2})$ in the 2D case, from the plane-wave value.

If we now study in particular the 1D case described by Eq. (2.141), we see that the experimental choice of the k_c parameter must strike a compromise between the two conflicting requirements of ensuring a smooth transfer function over a wide range of wave numbers and of obtaining a strong overall signal. The first requirement is met by lowering Q, i.e., by reducing the cutoff wave number; however, an arbitrary reduction eventually eliminates a large fraction of the LO power, conflicting with the second requirement. There is of course no rigorous quantitative criterion for deciding the "best" Q: this experimental choice must rely to some degree on qualitative judgment. Our next level of approximation will constitute a better framework for these considerations.

(c) Gaussian Beam and Finite Aperture

We now carry our approximation hierarchy one step further by taking into account the diffraction from the aperture stop. The Gaussian field distribution is replaced now by a truncated Gaussian. Substituting Eqs. (2.132), (2.135), (2.123), and (2.124) in Eq. (2.126), which now includes the pupil function P_a, and comparing with Eq. (2.136), we find

$$\mathcal{T}^{(1)}(\mathbf{K}) = 2\sqrt{\rho}u_0(0)\int_{-a}^{+a}\frac{\sin(k_c x)}{\pi x}e^{-x^2/w_0^2}[1-\cos(K_x x)]dx \tag{2.143}$$

for the 1D case, and

$$\mathcal{T}^{(2)}(\mathbf{K}) = 2\sqrt{\rho}u_0(0)\int_{0}^{a}k_c e^{-r^2/w_0^2}J_1(k_c r)[1-J_0(Kr)]dr \tag{2.144}$$

for the 2D case. The symmetry property $\mathcal{T}(\mathbf{K}) = \mathcal{T}(-\mathbf{K})$ is still satisfied. It is interesting to note that the asymptotic values for $K \to \infty$ are

$$\mathcal{T}^{(1)}(\infty) = 2\sqrt{\rho}u_0(0)\int_{-a}^{+a}\frac{\sin(k_c x)}{\pi x}e^{-x^2/w_0^2}dx \tag{2.145}$$

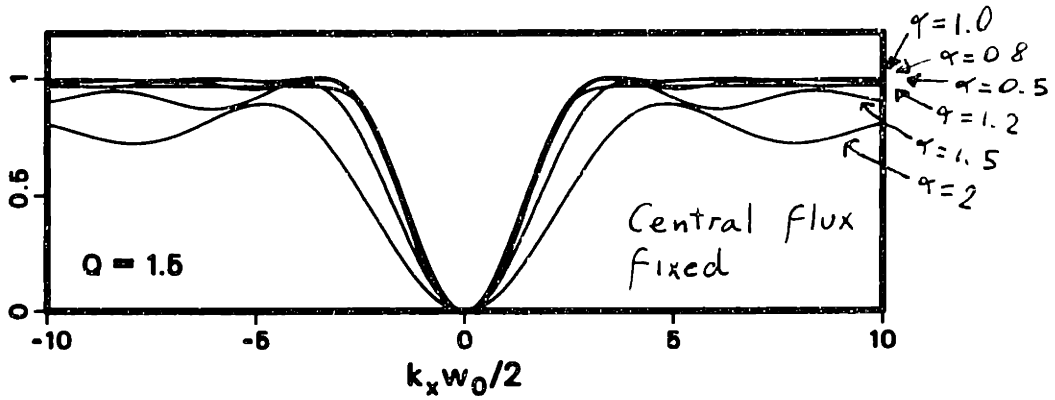

Fig. 2.20 Phase-contrast response function for varying α.

and

$$\mathcal{T}^{(2)}(\infty) = 2\sqrt{\rho}u_0(0)\int_0^a k_c e^{-r^2/w_0^2} J_1(k_c r)dr, \tag{2.146}$$

which, depending on the value of of a, can be smaller or larger than the corresponding values in the limit $a \to \infty$.

We shall study in detail only the 1D case. In experimental practice, the aperture radius a is usually fixed but one can choose both w_0 and k_c. The transfer function should then be studied by varying the two dimensionless parameters $Q = k_c w_0/2$ and $\alpha = w_0/a$. In particular, increasing α causes the beam profile to depart from a truncated Gaussian and approach a truncated plane wave. The focal-plane distribution of a truncated plane wave is the well-known Airy pattern,[132] which is characterized by high-**K** oscillations. Figure 2.20 shows a set of transfer functions for constant Q ($Q = 1.5$) and different values of α: there is an evident loss of smoothness in **K** space with increasing α. Also, the overall responsivity decreases with increasing α: this effect is due to the decrease in k_c, necessary to keep Q constant while w_0 is increasing, and the consequent loss of LO power.

Figure 2.20 is somehat deceptive, as it is based upon the assumption that the power flux at the center, $u_0(0)$, is kept fixed. To do so while α increases requires an increase in the overall power. The usable power, however, is finite and will have a specific upper limit for each given laser system. If the power is fixed, $u_0(0)$ acquires a $1/\alpha^2$ dependence, and the reduction in responsivity for increasing α is much more prononunced (see Fig. 2.21). In practice, the transition from the scenario of Fig. 2.20 to that of Fig. 2.21 occurs when α reaches a critical value for which all the available power can be used without saturating the detectors.

Both Figs. 2.20 and 2.21 appear to suggest that α should be as small as possible. In reality, as the width of the beam becomes much smaller than the aperture diameter, spatial uniformity is lost. This effect lies outside the present approximation scheme, which considers only the response at the center. However, it is clearly an important consideration; in fact, the existence of a certain degree of spatial uniformity is an essential condition for the validity of this approximation. In general, a value of $\alpha \simeq 1$ is a good compromise: the energy density at the edge of the aperture is e^{-2} times that

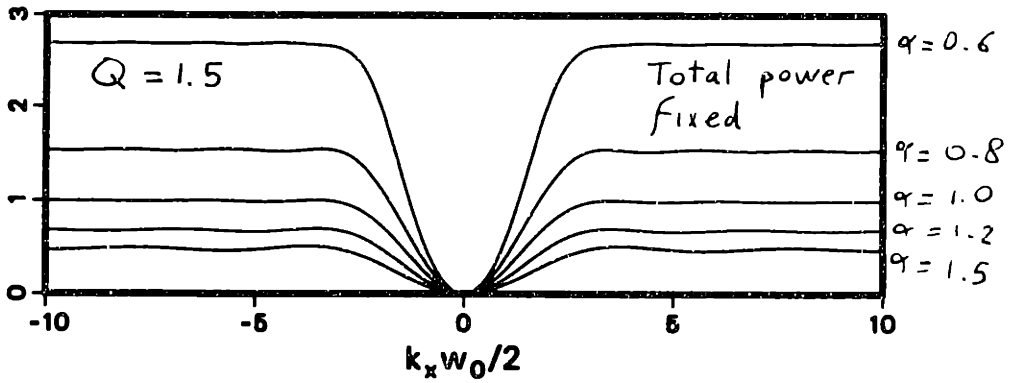

Fig. 2.21 Phase-contrast response function for varying α (total power fixed).

at the center, and Fig. 2.20 shows that the diffraction effects (high-**K** oscillations) are quite small.

From a visual analysis of $\mathcal{T}^{(1)}$ for various values of Q, for $\alpha = 1$ (Fig. 2.22), we conclude that values in the range $1.4 \lesssim Q \lesssim 1.8$ all produce an acceptable compromise between the requirements of smoothness (good relative responsivity at low K) and of a good overall signal level. Taking the value $Q = 1.5$ for reference, we find that at $K = k_c$ the transfer function is equal to 0.51, and that in the region $K > 2\pi/w_0$ the transfer function varies by less than 1%.

If the wave-number spectrum of the phase $\tilde{\varphi}$ occupies mostly the region above k_c, the transfer function can be approximated by a constant and we can write

$$\tilde{\mathcal{E}}(Mx, 0, t) \simeq W(x, 0) P_a(x) \mathcal{T}(\infty) \tilde{\varphi}(x, 0, t - t_d), \tag{2.147}$$

thus recovering the direct proportionality between signal and input phase that was obtained by the simplified treatment of §2.10 [Eq. (2.104)].

(d) Response Properties: an Exact Treatment

To conclude the analysis of the response properties of phase contrast, it is necessary to explore the behavior of the signal at locations other than the center of the image and to tackle the issue of spatial variation. As was mentioned before, a true transfer function does not in fact exist, and an input sinusoidal function will be somewhat distorted in the measured signal, as its spectrum is broadened. Substituting Eqs. (2.132), (2.123), (2.124), (2.126), and (2.134) in Eq. (2.133), we can write in the 1D case

$$\tilde{\mathcal{E}}'(Mx, 0, t) = 2 P_a(x) \sqrt{\rho}\, u_0(0)\, C^{(1)}(0) \left[\tilde{\varphi}(x, 0, t - t_d) - \int_{-a}^{+a} \tilde{\varphi}(x', 0, t - t_d)\, K^{(1)}(x, x') dx' \right], \tag{2.148}$$

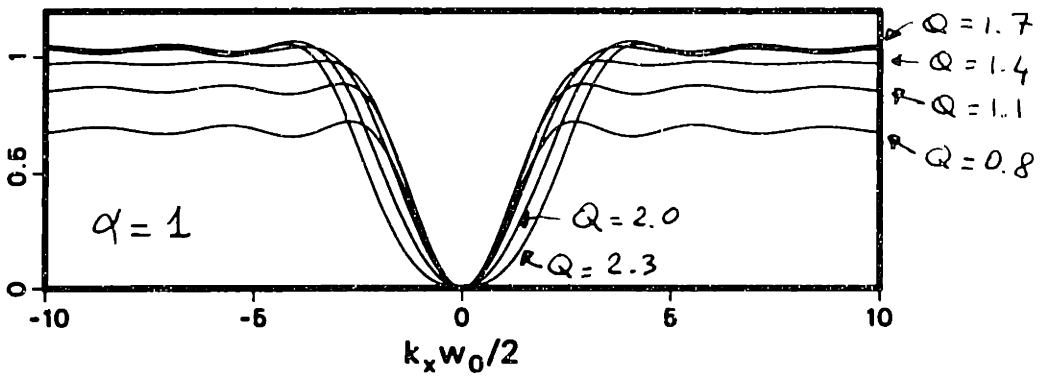

Fig. 2.22 Phase-contrast response function for varying Q.

where we have assumed for simplicity that the measurement is performed only at $y = 0$, and where

$$\mathcal{C}^{(1)}(x) = \int_{-a}^{+a} \frac{\sin[k_c(x - x')]}{\pi(x - x')} e^{-x'^2/w_0^2} dx'. \tag{2.149}$$

Equation (2.148) has the form of a Fredholm integral equation with kernel

$$\mathcal{K}^{(1)}(x, x') = \frac{\sin[k_c(x - x')]}{\pi(x - x')} \frac{e^{-x'^2/w_0^2}}{\mathcal{C}^{(1)}(x)}. \tag{2.150}$$

The lack of translational symmetry and, as a consequence, the absence of a true transfer function are highlighted by the fact that the kernel is *not* simply a function of $(x - x')$.

The corresponding expression in the 2D case is

$$\tilde{\mathcal{E}}'(M\mathbf{x}_\perp, t) = 2P_a(|\mathbf{x}_\perp|)\sqrt{\rho}\, u_0(0)\, \mathcal{C}^{(2)}(0) \Big[\tilde{\varphi}(\mathbf{x}_\perp, t - t_d) - \int \tilde{\varphi}(\mathbf{x}'_\perp, t - t_d)\, \mathcal{K}^{(2)}(\mathbf{x}_\perp, \mathbf{x}'_\perp) d^2x'_\perp \Big], \tag{2.151}$$

where

$$\mathcal{C}^{(2)}(x_\perp) = \frac{k_c^2}{2\pi} \int_0^a x'_\perp dx'_\perp e^{-x'^2_\perp/w_0^2} \int_0^{2\pi} \frac{J_1\left(k_c\sqrt{x_\perp^2 + x'^2_\perp - 2x_\perp x'_\perp \cos\phi}\right)}{k_c\sqrt{x_\perp^2 + x'^2_\perp - 2x_\perp x'_\perp \cos\phi}} d\phi. \tag{2.152}$$

The integral over ϕ is calculated in Appendix E, and using Eq. (E.8) we can write

$$\mathcal{C}^{(2)}(x_\perp) = k_c^2 \int_0^a \frac{x'_\perp e^{-x'^2_\perp/w_0^2}}{x_\perp^2 - x'^2_\perp} \left[x_\perp J_1(x_\perp) J_0(x'_\perp) - x'_\perp J_1(x'_\perp) J_0(x_\perp)\right] dx'_\perp. \tag{2.153}$$

The kernel is

$$\mathcal{K}^{(2)}(\mathbf{x}_\perp, \mathbf{x}'_\perp) = \frac{k_c^2}{2\pi} \frac{J_1(k_c|\mathbf{x}_\perp - \mathbf{x}'_\perp|)}{k_c|\mathbf{x}_\perp - \mathbf{x}'_\perp|} \frac{P_a(|\mathbf{x}'_\perp|)e^{-x'^2_\perp/w_0^2}}{\mathcal{C}^{(2)}(|\mathbf{x}_\perp|)}. \tag{2.154}$$

General analytical solutions exist for Fredholm equations.[148] The inversion is performed by calculating an integral over the aperture area. The integrand is the product of the measured signal and of a resolvent function, expressed in the form of an infinite sum. If the sum converges fairly quickly, it is possible in principle to calculate the phase $\tilde{\varphi}$ numerically from the signal measured at several points in the detection plane. In practice, this procedure would not represent a substantial improvement over the simpler methods based on the approximate transfer function unless many measurements were available, e.g., from a large detector array. Also, the inversion is likely to be noisy and slowly converging for the low-$k_\perp$ components, since the responsivity is low at low $k_\perp$. Therefore it would be necessary to accompany the inversion with a form of numerical highpass filtering.

For our present purposes, the usefulness of these complete equations lies in determining the goodness of the transfer-function approximation and the amount of spectral broadening in the case of a sinusoidal input. We limit our analysis to the 1D case with the set of parameters $\alpha = 1$, $Q = 1.5$ (see Fig. 2.23). It is easy to see that in the case of a sinusoidal input with $K > k_c$ [Fig. 2.23(a)] the exact expression [Eq. (2.148)] is closely approximated by Eq. (2.137), with the transfer function given by Eq. (2.143); and both are faithful reproductions of the input. The approximation becomes poor for $K < k_c$ [Fig. 2.23(b)]. Similarly, since the broadening in wavenumber space is of order π/w_0, the relative broadening $\delta K/K$ decreases rapidly for increasing K, as shown in Fig. 2.24.

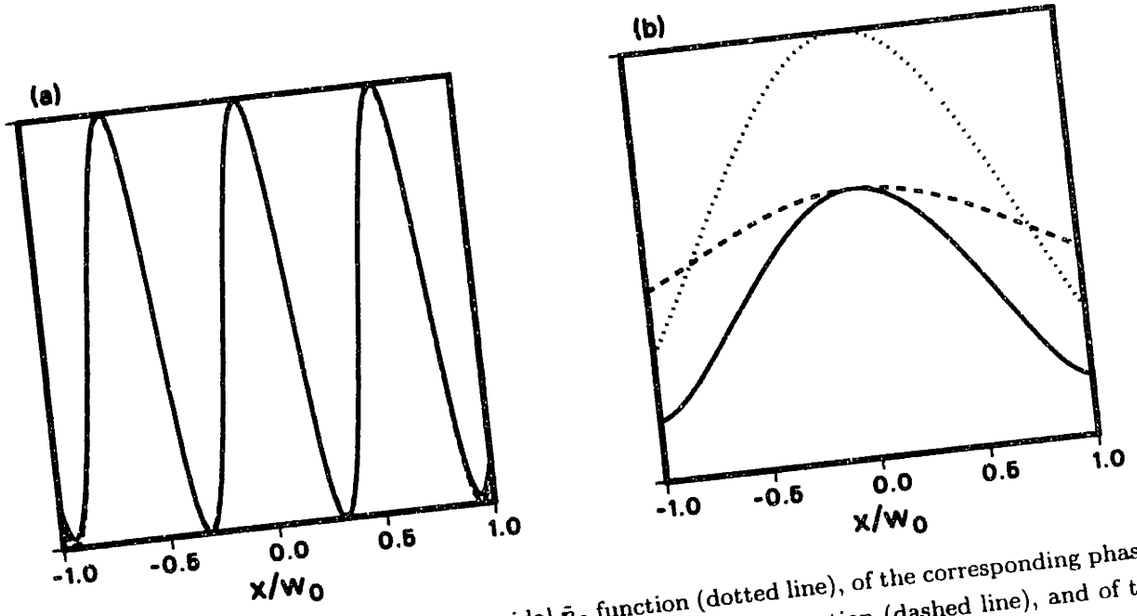

Fig. 2.23 Comparison of a sample sinusoidal $\tilde{n}_e$ function (dotted line), of the corresponding phase-contrast signal calculated by means of the approximate response function (dashed line), and of the exact phase-contrast signal calculated with a convolution integral (solid line), for (a) $kw_0/2 = 5$, (b) $kw_0/2 = 1$. Here, Q=1.5 and α=1.

2.12 Signal-to-Noise Ratio

In the case of experiments performed with CO_2 lasers, which emit in the intermediate-infrared spectrum, detection is generally performed with a photon detector of the photoconductive or photovoltaic type. The typical detector-preamplifier circuit is shown in Fig. 2.25.

In a photoconductive detector, incident photons produce free charge carriers, which change the electrical conductivity of the crystal.[149] This change in turn can be measured by an associated electronic circuit. The detector can be operated in current mode (i.e., at nearly constant voltage) by choosing a load resistance much smaller than the detector resistance, or in voltage mode (at constant current): the latter is the more common arrangement for photoconductors in the $\sim$ 10 μm wavelength range, owing to their low impedance (typically in the 50–200 Ω range). Our considerations in this section apply to n–type materials, where electrons are the majority carriers. These include in particular the HgCdTe and HgMnTe alloys when operated at liquid-nitrogen temperature (77 K).[150] The characteristic response time in a photoconductor is the average free charge-carrier lifetime τ_c.

In the photovoltaic process, infrared photons are absorbed near a p–n junction, forming electron-hole pairs that shift the Fermi levels and generate an externally detectable voltage. Photovoltaic detectors too can be operated in voltage or current mode, depending on the load impedance. The mechanisms affecting the response time are more complex than in a photoconductor. Fundamental limits are set by the transit time through the depletion layer, by the characteristic diffusion time, and by the RC

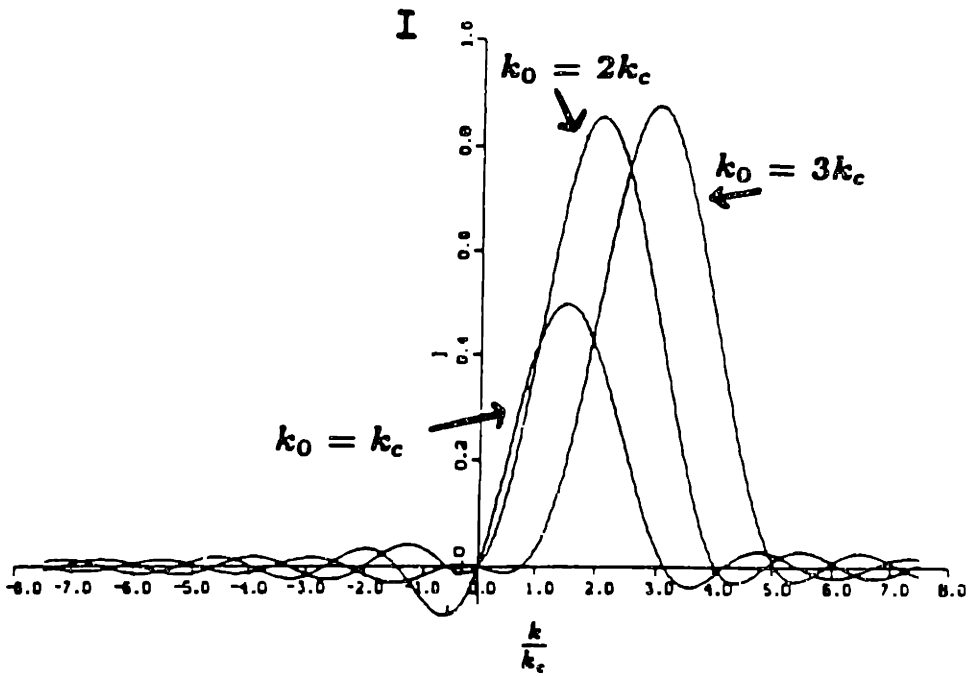

Fig. 2.24 Spectrum of the phase-contrast signal generated by a sinusoidal input, for three different wave numbers. The broadening is caused by diffraction effects.

constant of the crystal-preamplifier system; the last limit is usually the most stringent, but can generally be tailored for very high-frequency applications. Responses in excess of 1 GHz have been achieved, whereas photoconductors are usually limited to a few MHz. Common techniques used to lower the RC constant include choosing a low input impedance for the preamplifier and applying a reverse bias to increase the width (and thus reduce the capacitance) of the depletion layer. These procedures increase the bandwidth but generally reduce the signal-to-noise ratio and the quantum efficiency.

We assume here that in all cases the bandwidth of the input power flux is well within the response bandwidth of the detector. We also assume that we are operating in the small-signal regime. This applies to the vast majority of heterodyne configurations in which the dc power flux is much larger than the ac component to be measured. We define the voltage responsivity $\Re$ as follows:

$$v_s = \Re A_d \tilde{\mathcal{E}}, \tag{2.155}$$

where v_s is the signal voltage, A_d is the detector area, and $\tilde{\mathcal{E}}$ is the flux to be measured. The responsivity, which has dimensions of voltage/power, is given by[151]

$$\Re = V_B \frac{\eta}{\hbar\omega_0} \frac{R_d}{R_L + R_d} \frac{\tau_c}{N} \tag{2.156}$$

for an n–type photoconductive detector, and by

$$\Re = -\frac{e\eta}{\hbar\omega_0} \frac{R_d R_L}{R_d + R_L} \tag{2.157}$$

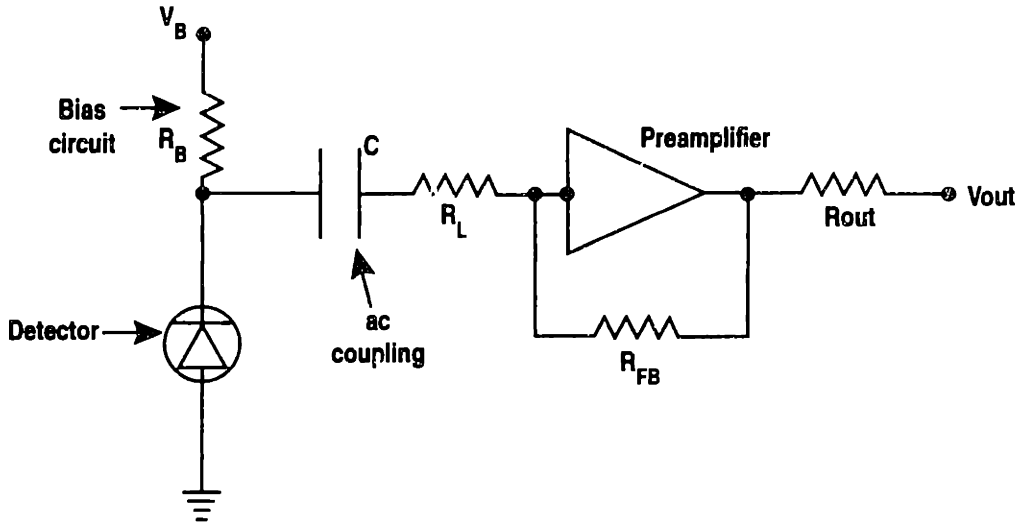

Fig. 2.25 Detector–preamplifier circuit.

for a photovoltaic detector. Here, e is the (positive) elementary charge, η is the quantum efficiency, $\hbar\omega_0$ is the photon energy, R_d is the dynamic resistance of the detector, R_L is the load resistance, V_B is the bias voltage, and N is the total number of free charges in the unilluminated crystal.

We now specialize our remarks to the phase-contrast case with a one-dimensional phase plate and assume that the measurement is being carried out with a linear detector array located at $y = 0$. If we consider only the signal components at $k_x > k_c$, the ac flux is given approximately by Eq. (2.147); substituting for the ac flux in Eq. (2.155) we obtain for the signal voltage

$$v_s(x) = \Re A_d \mathcal{T}(\infty) W(x) P_a(x) \tilde{\varphi}(x), \tag{2.158}$$

where we have removed the time dependence for simplicity.

Several forms of noise are present in photon detectors. They are usually classified according to their origin; thus, one distinguishes between intrinsic noise generated in a dark crystal lattice, photon noise due to background blackbody radiation, and photon noise due to the dc component in a heterodyne system. To these must be added any external noise from the associated electronics, which is generally dominated by preamplifier noise.

Various forms of intrinsic noise exist. The so-called "$1/f$", or modulation noise, is observed on contacts and crystal surfaces and is generally negligible at frequencies above 100 Hz in a well-built detector.[152] The dominant forms of noise in a photoconductor are thermal Johnson noise and thermal generation and recombination (G-R) noise. The latter is usually negligible in a photovoltaic detector, whereas it is generally the dominant one in photoconductive elements.

Fluctuations in the background blackbody radiation cause additional noise, which can be greatly reduced, however, by limiting the field of view of the detector and, in a cooled system, by placing a cold, narrow bandpass filter on the viewing

in a photoconductor this expression must be multiplied by a factor of 2 owing to recombination effects.[153] Substituting Eq. (2.157) in Eq. (2.162), and introducing the dc output voltage $v_{\rm dc} = \Re A_d \mathcal{E}_{\rm dc}$, we obtain for a photovoltaic element

$$v_{n,\rm LO}^2 = 2ev_{\rm dc}(\Delta f)R_d R_L/(R_d + R_L). \tag{2.163}$$

We can now use Eqs. (2.158), (2.159), and (2.162) to write the signal-to-noise ratio:

$$\frac{S}{N} \equiv \frac{v_s^2}{v_n^2} = \frac{A_d}{\Delta f}[\mathcal{T}(\infty)W(x)\tilde{\varphi}(x)]^2 \left[1/D^{*2} + 2F_d\mathcal{E}_{\rm dc}(x)\hbar\omega_0/\eta\right]^{-1}, \tag{2.164}$$

where F_d is a correction factor ($F_d = 1$ for a photovoltaic element, $F_d = 2$ for a photoconductor).

The dc power flux can be calculated from Eq. (2.125), using Eqs. (2.132) and (2.123); a numerical calculation for the case $a = w_0$ and $k_c = 3/w_0$ (see §2.11) shows that $\mathcal{E}_{\rm dc}(x)$ can be approximated by $\rho u_0(x) = \rho u_0(0)\exp(-2x^2/w_0^2)$ with an accuracy of 5% throughout the width of the beam, provided $\rho \geq 0.03$. Similarly, $W(x)$ [Eq. (2.134)] is approximated by $\exp(-2x^2/w_0^2) = u_0(x)/u_0(0)$ with a discrepancy of less than 5%. Finally, Eqs. (2.145) and (2.149) allow us to write $\mathcal{T}(\infty) = 2\sqrt{\rho}\,u_0(0)\,\mathcal{C}^{(1)}(0)$. Therefore we can write Eq. (2.164) as

$$\frac{S}{N} = \frac{4A_d}{\Delta f}\left[\mathcal{C}^{(1)}(0)u_0(x)\tilde{\varphi}(x)\right]^2 \left[1/(\rho D^{*2}) + 2F_d u_0(x)\hbar\omega_0/\eta\right]^{-1}. \tag{2.165}$$

To calculate the minimum detectable phase shift, we set $S/N = 1$ and find

$$\tilde{\varphi}_{\rm min}(x) = \frac{1}{\mathcal{C}^{(1)}(0)}\left(F_d + \frac{P_{\rm cr}}{\rho P_d(x)}\right)^{1/2}\left(\frac{W_0\Delta f}{P_d(x)}\right)^{1/2}, \tag{2.166}$$

where $P_d = A_d u_0(x,0)$ is the total power incident on the detector element when $\rho = 1$, $P_{\rm cr}$ is a critical power given by

$$P_{\rm cr} = \frac{\eta A_d}{2\hbar\omega_0 D^{*2}}, \tag{2.167}$$

and

$$W_0 = \frac{\hbar\omega_0}{2\eta} \tag{2.168}$$

is a parameter with the dimensions of an energy.

When the wave number approaches the critical value k_c, these expressions are no longer valid; the signal-to-noise ratio becomes poorer and $\tilde{\varphi}_{\rm min}$ increases. As a first approximation, one can simply multiply Eq. (2.166) by $\mathcal{T}(\infty)/\mathcal{T}(k)$.

We can now recognize two opposite limits. If $\rho P_d > P_{\rm cr}/F_d$, shot noise dominates. The signal-to-noise ratio is independent of ρ and the minimum detectable phase decreases with increasing power as $1/\sqrt{P_d}$. Therefore the power should be as large as possible, i.e., the detector should be operated only slightly below its saturation point, $P_{\rm sat}$. Under these conditions, when the performance of the detector is limited by saturation, one can write $P_d = P_{\rm sat}/\rho$, and the minimum detectable phase becomes in fact proportional to $\sqrt{\rho}$. Thus, in practice, it is beneficial to reduce the ρ factor to increase the usable power. When the ρ factor reaches the critical value that renders $P_{\rm sat}/\rho$ equal to the maximum power available from the system, a further reduction in ρ does not result in any further changes in $\tilde{\varphi}_{\rm min}$. In general it is clearly desirable to use a detector with a high saturation limit; since this is specified as a flux, a large-area detector is better than a small-area one.

In the opposite limit, when $\rho P_d < P_{\rm cr}/F_d$, the intrinsic detector and preamplifier noise dominates and $\tilde{\varphi}_{\rm min} \propto 1/(P_d\sqrt{\rho})$. In the saturation-limited regime, this dependence becomes in fact $\tilde{\varphi}_{\rm min} \propto \sqrt{\rho}$, as in the previous case. In this situation, however, when the critical ρ is reached, a further reduction of its value is actually deleterious because of the $1/\sqrt{\rho}$ dependence. Thus, the optimal value of ρ is the one that produces marginal saturation when all the available power is used without attenuation.

Since the two limits just discussed also depend on the power, a general analysis must use the full expression given by Eq. (2.166). We shall study here the relevant set of parameters for the experimental setup described in Chapter 3. With a photovoltaic detector used in current mode, $F_d = 1$ and the detectivity is given by Eq. (2.161). Substituting Eq. (2.161) in Eq. (2.167), the critical power can be written as

$$P_{\rm cr} = \frac{2\kappa(T_d + FT_{\rm pa})\hbar\omega_0}{\eta e^2 R_L} \tag{2.169}$$

and is thus an intrinsic parameter independent of the detector area.

We shall now study Eq. (2.166) at the 10.6 μm wavelength, with the parameters $R_L = 50\ \Omega$, $T_d = 77$ K, $T_{\rm pa} = 300$ K, $NF = 2.8$ dB, and $\eta = 0.02$. A bandwidth $\Delta f = 1$ MHz is assumed. Also, with the parameters $w_0 = a$ and $k_c = 3/w_0$, Eq. (2.149) gives $\mathcal{C}^{(1)}(0) = 0.95$. Equation (2.161) gives $D^* = 2.6 \times 10^8$ Hz cm$^{1/2}$/W. The minimum detectable phase shift, given by Eq. (2.166), is plotted as a function of P_d in Fig. 2.26. Each curve in the figure corresponds to a different ρ value. We examine here four values: $\rho = 1$, for a reflectively coated phase-plate groove, and $\rho =$ 0.36, 0.17, 0.027, corresponding to the reflectivities of three materials commonly used in this region of the spectrum, respectively germanium (Ge), zinc selenide (ZnSe), and barium fluoride (BaF_2). Each of the curves is drawn up to the saturation limit $\rho P_d = P_{\rm sat}$ or to the maximum available power $P_{\rm max}$, whichever is smaller. Here, we assume a saturation flux of 1 W/cm^2 and an area $A_d = 1.6 \times 10^{-3}$ cm^2, hence $P_{\rm sat} =$ 1.6 mW. Also, the available power for the central element in the array is 8.4 mW. For these parameters, Fig. 2.26 shows that the optimum substrate for the phase-plate groove is ZnSe. The power must be attenuated by $\sim 11\%$ (from 8.4 mW to 7.5 mW),

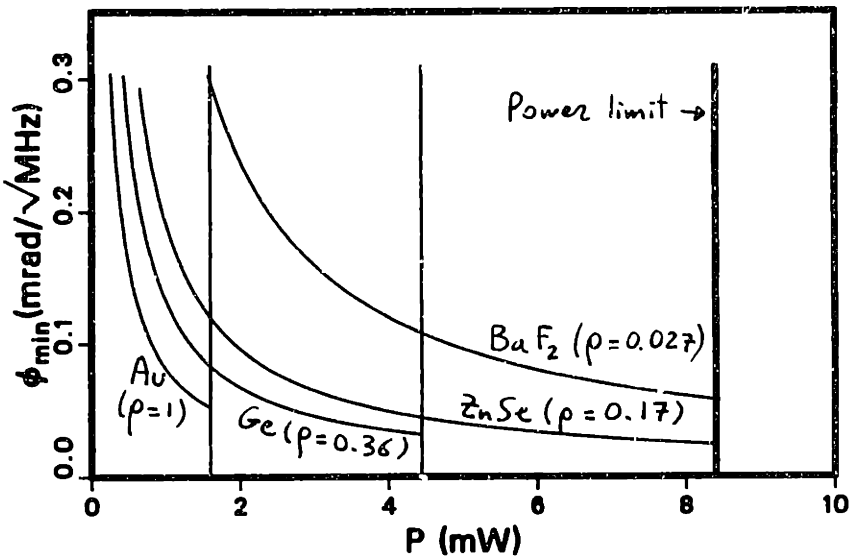

Fig. 2.26 Minimum detectable phase shift vs. power incident on a detector element.

and the minimum measurable phase shift is $\tilde{\varphi}_{\min} = 5 \times 10^{-5}$ rad. The noise level is $v_n = 1.4\ \mu$V rms.

2.13 A Comparative Analysis of Internal-Reference Techniques

The formalism developed in §2.11 can easily be applied to techniques other than phase contrast. In this section we shall study the response properties of alternative techniques and compare them with those of phase contrast. Firstly, we shall explore some imaging configurations that differ from phase contrast only in the nature of the spatial filter that is used in the focal plane. The analysis will be limited to one-dimensional configurations and to the case of a collimated Gaussian beam, ignoring the effects of aperture diffraction (i.e., in the limit $a \to \infty$). The direction of interest is x and detection is assumed to occur at $y = 0$. To better illustrate the properties of the different techniques, we take a rather general type of filter, characterized by a central strip of transmissivity ρ, a negative k_x side of transmissivity ρ_-, and a positive k_x side of transmissivity ρ_+. In addition, the negative and positive sides introduce phase shifts α and β, respectively (see Fig. 2.27). The transfer function can now be written as follows:

$$\hat{T}(\mathbf{k}_\perp) = \sqrt{\rho_-}\, e^{i\alpha} H(-k_x - k_c) + \sqrt{\rho_+}\, e^{i\beta} H(k_x - k_c) + \sqrt{\rho} P_{k_c}(k_x), \qquad (2.170)$$

where $H(x)$ is the Heaviside function [$H(x) = 1$ for $x > 0$, $H(x) = 0$ for $x < 0$], and $P_{k_c}(k_x)$ is the pupil function defined by Eq. (2.113). A number of well-known techniques, including schlieren and phase contrast, belong to this general class. A degenerate case is the dark ground method, for which $\rho_+ = \rho_- = 1$, $\alpha = \beta = 0$, and $\rho = 0$; i.e., the zeroth order is removed entirely, while the positive and negative orders

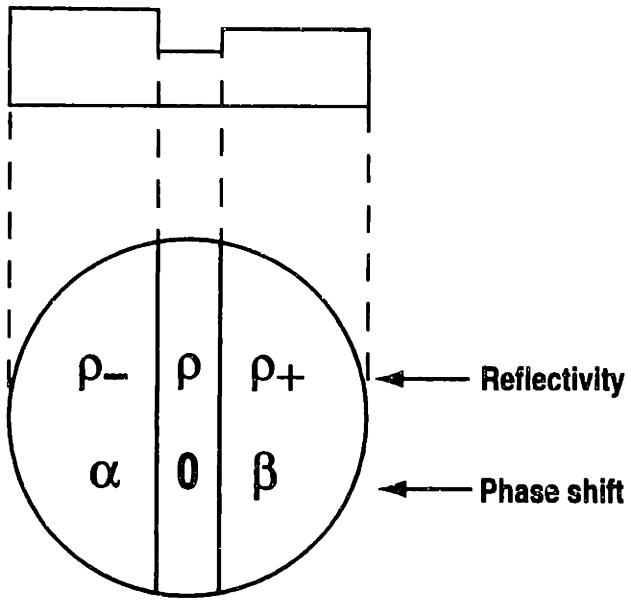

Fig. 2.27 General reflective spatial filter.

are transmitted unaltered. This technique must be examined separately since, as we shall soon see, it is radically different from the others.

In addition, we include in this analysis a nonimaging technique that was discussed in §2.9, called *scintillation*. This is an intermediate-field measurement performed without any filtering, which relies instead on amplitude variations generated by the free propagation of the beam after its interaction with the plasma (see Fig. 2.11). The Rytov phase is given by the Hermitian component of Eq. (2.83); by direct comparison with the near-field anti-Hermitian phase given by Eq. (2.84), and referring to Eq. (2.71), we can formally describe the scintillation technique as equivalent to a measurement of the phase characterized by the transfer function

$$\mathcal{T}(\mathbf{k}_\perp) = 2u_0(0)\sin\left[\frac{k_\perp^2}{2k_0}(z - z_p)\right]. \tag{2.171}$$

One common feature of all internal-reference interferometers is that the transfer function is zero at $\mathbf{k}_\perp = 0$. This can be understood intuitively by noting that the absence of an external phase reference precludes the determination of the *absolute* phase shift; that is, only differences in the path lengths between different chords within the beam can be measured. The $\mathbf{k}_\perp = 0$ component represents precisely the absolute phase shift.

Weisen[131] put these observations on a more quantitative footing by employing general physical arguments based solely on the conservation of energy. He defined a "maximum homodyning efficiency", which for a sinusoidal input can be seen as an upper bound on the transfer function. For a Gaussian beam, the maximum homodyning efficiency in the one-dimensional case is $[1 - \exp(-k_x^2 w_0^2/4)]$.

At the conclusion of this section, all the above techniques will be compared with a heterodyne, Mach-Zehnder interferometer (Fig. 2.12); it was shown in §2.9 that

this configuration, if the path difference is adjusted to keep the nonfluctuating phase shift at $\pi/2$, yields a "perfect" transfer function, i.e., one that is independent of $\mathbf{k}_\perp$.

(a) Central Dark Ground

Seeing dark ground as a limiting case of phase contrast with $\rho = 0$, we find that the approximate transfer function given by Eq. (2.143) is identically zero. That equation was derived from a first-order expansion in $\tilde{\varphi}$. We conclude that the lowest-order signal in the dark-ground case is proportional to $\tilde{\varphi}^2$. This is, of course, a consequence of the elimination of the local oscillator (LO). From Eq. (2.116), setting $P_a = 1$, we can derive the second-order power flux as

$$\tilde{\mathcal{E}} = \frac{c}{8\pi M^2}\left|T \circ (E_{p0}\tilde{\varphi})\right|^2, \tag{2.172}$$

where T is the inverse Fourier transform of the transfer function

$$\hat{T}(\mathbf{k}_\perp) = 1 - P_{k_c}(k_x). \tag{2.173}$$

As before, we assume a sinusoidal input $\tilde{\varphi} = \hat{\varphi}_{\mathbf{K}} \cos(\mathbf{K} \cdot \mathbf{x}_\perp + \vartheta_0)$. With the field given by Eq. (2.132) and the transfer function given by Eq. (2.173), we can calculate

$$\tilde{\mathcal{E}}(Mx) = u_0(x)\hat{\varphi}_{\mathbf{K}}^2 \Bigg[\cos(\mathbf{K} \cdot \mathbf{x}_\perp + \vartheta_0) - \frac{1}{2}\mathrm{erf}(Q + K_x')\cos\vartheta_0 - \frac{1}{2}\mathrm{erf}(Q - K_x')\cos\vartheta_0\Bigg]^2, \tag{2.174}$$

where $Q = k_c w_0/2$, $\mathbf{K}' = w_0\mathbf{K}/2$, and $u_0(x) = 2P/(\pi M^2 w_0^2)\exp(-2x^2/w_0^2)$. In the limit $K_x \gg k_c$, this equation reduces to $\tilde{\mathcal{E}}(Mx) \simeq u_0(x)\tilde{\varphi}^2(x)$, which describes an imaging system with direct proportionality between the measured signal and the *square* of the phase.

The main difficulty associated with this technique is the smallness of the second-order signal. In the absence of the LO component, detector noise will be dominated by intrinsic noise; using Eqs. (2.159), (2.155), and (2.174) in the high-$k_\perp$ limit, we can write the signal-to-noise ratio as

$$\frac{S}{N} = \frac{D^{*2}P_d^2}{A_d \Delta f}\tilde{\varphi}^4, \tag{2.175}$$

where $P_d = A_d u_0$. Using the set of parameters introduced at the end of §2.12, i.e., P_d = 10 mW, $A_d = 1.6 \times 10^{-3}$ cm^2, $\Delta f = 1$ MHz, and $D^* = 2.6 \times 10^8$ cm$^{1/2}$Hz$^{1/2}$/W, we find a minimum detectable phase shift of 3.9×10^{-3} rad, which, as expected, is much poorer than in the phase-contrast case. It should be mentioned in passing that the D^* we are using here is rather poor; this is due to the low quantum efficiency (2%) of

our high-frequency detector. With low-frequency detectors the performance can be at least an order of magnitude better for both the phase-contrast and dark-ground methods, while their relative merits remain the same.

(b) General Spatial Filtering

We move now to the general type of phase plate shown in Fig. 2.27 and described by Eq. (2.170). By analogy with the analysis carried out in §2.11, assuming again a sinusoidal input $\tilde{\varphi} = \hat{\varphi}_K \cos(Kx + \vartheta_0)$, we write the first-order power flux in the general form

$$\tilde{\mathcal{E}}(Mx, t) = \mathcal{T}_x(K)\hat{\varphi}_K(t - t_d)\cos\Big(Kx + \vartheta_0 + \theta_x(K)\Big). \tag{2.176}$$

The functions $\mathcal{T}_x(K)$ and $\theta_x(K)$ are uniquely determined and are independent of ϑ_0 for any real and linear functional relation between $\tilde{\varphi}$ and $\tilde{\mathcal{E}}$. To see this, let us write $\tilde{\mathcal{E}} = \mathcal{F}(\tilde{\varphi})$, where $\mathcal{F}$ is a functional: then

$$\mathcal{T}_x(K) = \big(\mathcal{F}^2\big(\cos(Kx)\big) + \mathcal{F}^2\big(\sin(Kx)\big)\big)^{1/2}, \tag{2.177}$$

and

$$\theta_x(K) = \arctan\left(\frac{\mathcal{F}\big(\sin(Kx)\big)}{\mathcal{F}\big(\cos(Kx)\big)}\right) - Kx. \tag{2.178}$$

Note that the linearity of $\mathcal{F}$ ensures that $\mathcal{T}_x(K)$ is symmetric and $\theta_x(K)$ antisymmetric upon reversal of either K or x: this is a very general property, as it does not depend on the symmetries of the functional and it applies also to the case of a diverging or converging beam (E_{p0} complex).

If the phase shift θ_x, in the limit $K \gg k_c$ and $K \gg 1/w_0$, becomes independent of x, we can then write the *approximate* expression

$$\tilde{\mathcal{E}}(Mx, t) \simeq \mathcal{T}(K)W(x)\hat{\varphi}_K(t - t_d)\cos\Big(Kx + \vartheta_0 + \theta(K)\Big), \tag{2.179}$$

which will be valid for large K. Here, $W(x) = \mathcal{T}_x(\infty)/\mathcal{T}_{x=0}(\infty)$, $\mathcal{T}(K) = \mathcal{T}_{x=0}(K)$, and $\theta(K) = \theta_{x=0}(K)$. This equation shows that a monochromatic input will generate an approximately monochromatic output, multiplied by a weighting function. If the weighting function is known, the detected signal can be inverted to calculate the phase $\hat{\varphi}_K$. However, if the phase shift θ is different from 0 or π and the spectrum is not monochromatic, the technique does not generate an *image* of $\tilde{\varphi}$; different sinusoidal components will add out of phase and the signal distribution in general will bear no resemblance to the distribution of $\tilde{\varphi}$. A deconvolution operation is necessary in order to invert the signal.

Note that if the functional $\mathcal{F}$ is spatially symmetric, i.e. if $\mathcal{F}\,(\tilde{\varphi}(-x)) = \mathcal{F}\,(\tilde{\varphi}(x))$ for any $\tilde{\varphi}(x)$, it follows that $\mathcal{F}\,(\sin(Kx)) = 0$ and, by virtue of Eq. (2.178), $\theta_{x=0}(K) =$

0. Therefore, the spatial symmetry of the beam, of the aperture, and of the filter is a sufficient condition for the central phase shift θ to be zero.

If the phase shift θ_x is *not* independent of x in the limit $K \to \infty$, Eq. (2.179) is not applicable at all, and distortion will occur even when the input signal is monochromatic.

I. Imaging Conditions

To avoid clutter, the derivation of the functions $\mathcal{T}_x$, W, and θ_x is carried out in Appendix F. The condition for phase imaging, i.e. $\theta_x(\infty) = 0$ or π, implies [Eqs. (F.23) and (F.24)] $\rho_+ = \rho_-$ and $\alpha = \beta$. This is a generalized form of phase contrast with arbitrary phase shift and reflectivity. The transfer function at high K is [Eq. (F.25)]

$$\mathcal{T}_x(\infty) = -2u_0(x)\sqrt{\rho\rho_-}\,\mathrm{Re}\big(\mathcal{W}_0(x)\big)\sin\beta, \tag{2.180}$$

where

$$\mathcal{W}_0(x) = \mathrm{erf}(Q - ix/w_0). \tag{2.181}$$

This transfer function is maximized, for a given ρ, when $\rho_+ = \rho_- = 1$ and $\alpha = \beta = \pm\pi/2$. This is phase contrast proper: we thus reach the important conclusion that phase contrast is the only technique that both provides phase imaging and maximizes the signal. Note that this conclusion holds for arbitrary values of $Q = k_c w_0/2$. However, we know from §§2.11 and 2.12 that to obtain an optimal transfer function the quantity $k_c w_0/2$ must be in the vicinity of 1.5. The weighting and transfer functions for phase contrast are calculated in Appendix F and coincide with the expressions derived in the previous sections, as expected. In addition, the phase $\theta(K) = \theta_{x=0}(K)$ is found to be zero for all values of K.

If the condition $k_c w_0/2 \simeq 1.5$ is assumed, the expressions for $\mathcal{T}_x$ and θ_x can be simplified considerably by noting that the function $\mathcal{W}_0$ is nearly equal to 1 (within $\sim$ 6%) throughout the region $|x/w_0| < 1$. The transfer function and the phase shift are then given to a good approximation by Eqs. (F.29) and (F.30), respectively

$$\mathcal{T}_x(\infty) = u_0(x)\sqrt{\rho}\left[\rho_- + \rho_+ - 2\sqrt{\rho_-\rho_+}\cos(\alpha+\beta)\right]^{1/2} \tag{2.182}$$

and

$$\theta_x(\infty) = \arctan\left(\frac{\sqrt{\rho_-}\cos\alpha - \sqrt{\rho_+}\cos\beta}{\sqrt{\rho_-}\sin\alpha + \sqrt{\rho_+}\sin\beta}\right). \tag{2.183}$$

In addition, the dc power flux is simply [Eq. (F.31)]

$$\mathcal{E}_{\mathrm{dc}}(x) = \rho u_0(x), \tag{2.184}$$

i.e., approximately all the power flux, attenuated by the transmissivity ρ, is used in the LO component. Thus, the signal-to-noise considerations of §2.12 apply. For a given ρ, the signal [Eq. (2.182)] and the signal-to-noise ratio are maximized when

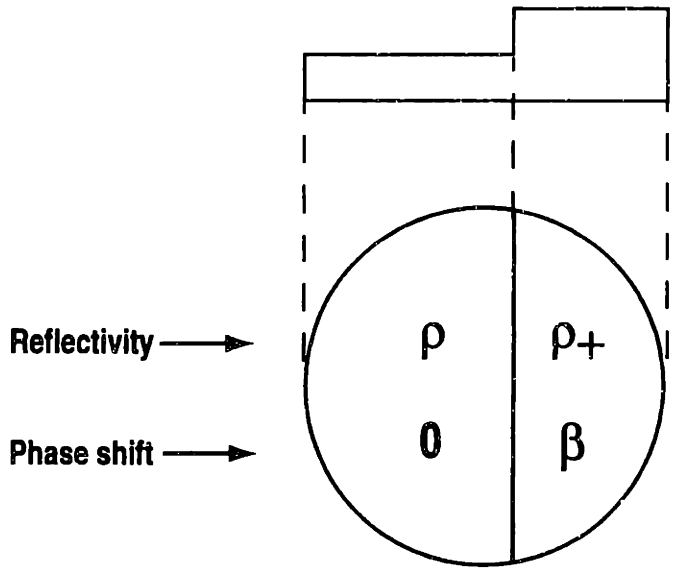

Fig. 2.28 Two-zone spatial filter.

$\rho_- = \rho_+ = 1$ and $\alpha = \pm\pi - \beta$. Whenever these conditions are satisfied, the signal-to-noise ratio is the same as in the phase-contrast case. The condition for phase imaging ($\theta = 0$ or π), by virtue of Eq. (2.183), can be written $\sqrt{\rho_-}\cos\alpha = \sqrt{\rho_+}\cos\beta$. Again, the phase-contrast configuration ($\rho_- = \rho_+ = 1$ and $\alpha = \beta = \pm\pi/2$) is the only one to provide phase imaging *and* to maximize the signal-to-noise ratio.

One special subclass of the configurations discussed here is obtained when the spatial filter is divided into only two separate zones instead of the three described by Eq. (2.170). This has practical advantages: a single filter of this type can be used in different applications by simply shifting it in space, whereas, e.g., a phase-contrast filter must be built to specifications and generally has little or no flexibility. In addition, optical alignment is usually less critical with a two-zone filter. This class of filters can be defined by the conditions $\rho_- = \rho$ and $\alpha = 0$. Thus the negative-k side and the zeroth-order zone become indistinguishable (see Fig. 2.28). The phase-imaging condition is now

$$\cos\beta = \sqrt{\rho/\rho_+}. \tag{2.185}$$

This condition can be satisfied only when $\rho \leq \rho_+$. From Eq. (2.182) we find $\mathcal{T}_x(\infty) = u_0(x)\sqrt{\rho}\sqrt{\rho_+ - \rho}$, which, for a given ρ, is maximized by $\rho_+ = 1$. The signal-to-noise ratio is a factor of $(1-\rho)/4$ lower than in the phase-contrast case. If a low value of ρ is chosen to improve contrast, the phase-imaging condition [Eq. (2.185)], which can be obtained through a simplified plane-wave analysis, is insufficient. It is pointed out in Appendix F that in the case of a finite beam one must also ensure that the LO power ($\sim \rho u_0$) is larger than the dc power lost in the positive-k zone of the spatial filter ($\sim u_0|1 - \operatorname{erf} Q|^2/4$). The approximation we have previously made, $\operatorname{erf} Q \simeq 1$, must thus be quantified by requiring $|1 - \operatorname{erf} Q| \ll 2\sqrt{\rho}$. Depending on the value of ρ, this condition may require a value of Q somewhat larger than 1.5.

The transfer function $\mathcal{T}(K)$ and the phase angle $\theta(K)$, given respectively by Eq. (F.33) and Eq. (F.34), are plotted in Fig. 2.29(b); for comparison, Fig. 2.29(a) shows the corresponding functions for the phase-contrast case.

II. Schlieren Techniques

We shall now proceed to examine some limiting cases of this general type of filter, which correspond to various techniques described in the literature. "Knife-edge" schlieren techniques are among the oldest in the history of optical filtering and are widely employed even today. A knife-edge filter, as the name suggests, is characterized by a step transfer function with values 0 and 1. Thus, again, there are only two separate zones instead of three.

The standard schlieren configuration transmits all positive orders and blocks all negative orders (or vice versa). This is obtained by setting $\rho_- = 0$, $\rho_+ = 1$, $\beta = 0$, and $k_c = 0$. The high-K transfer function and phase shift are given by Eqs. (F.37) and (F.38), respectively

$$\mathcal{T}_x(\infty) = -\frac{1}{2}u_0(x)\left[1 - \mathcal{W}_0^2(x)\right]^{1/2} \tag{2.186}$$

and

$$\theta_x(\infty) = \arctan\left(\frac{1}{i\mathcal{W}_0(x)}\right). \tag{2.187}$$

It is shown in Appendix F that this phase shift decreases monotonically from 90° at $x = 0$ to 31° at $x = w_0$. Hence, the constancy requirement is clearly not satisfied. In addition, the signal-to-noise ratio is degraded with respect to phase contrast by a factor of 1/4 to 1/16, depending on the operational regime of the detector.

Some of the more undesirable properties of the basic schlieren configuration can be avoided with a minor modification that involves a simple spatial shift. We now keep the positive orders *and* the zeroth order, eliminating the negative orders ($\rho_- = 0$, $\rho = \rho_+ = 1$, and $\beta = 0$). The result is [Eqs. (F.42) and (F.43)]

$$\mathcal{T}_x(\infty) = \frac{1}{2}u_0(x)\left|1 + \mathcal{W}_0(x)\right|, \tag{2.188}$$

and

$$\theta_x(\infty) = -\arctan\left(\frac{1 + \mathrm{Re}(\mathcal{W}_0)}{\mathrm{Im}(\mathcal{W}_0)}\right). \tag{2.189}$$

When $Q \simeq 1.5$, one finds $\mathcal{T}_x(\infty) \simeq u_0(x)$ and $\theta_x(\infty) \simeq \pi/2$. The phase is approximately constant but nonzero. The signal is one-half that of the phase contrast case, resulting in a reduction by a factor of four in the signal-to-noise ratio. The transfer function and the phase angle, given by Eqs. (F.46) and (F.47) respectively, are plotted in Fig. 2.29(c).

III. Compensation of Plasma Transfer Function

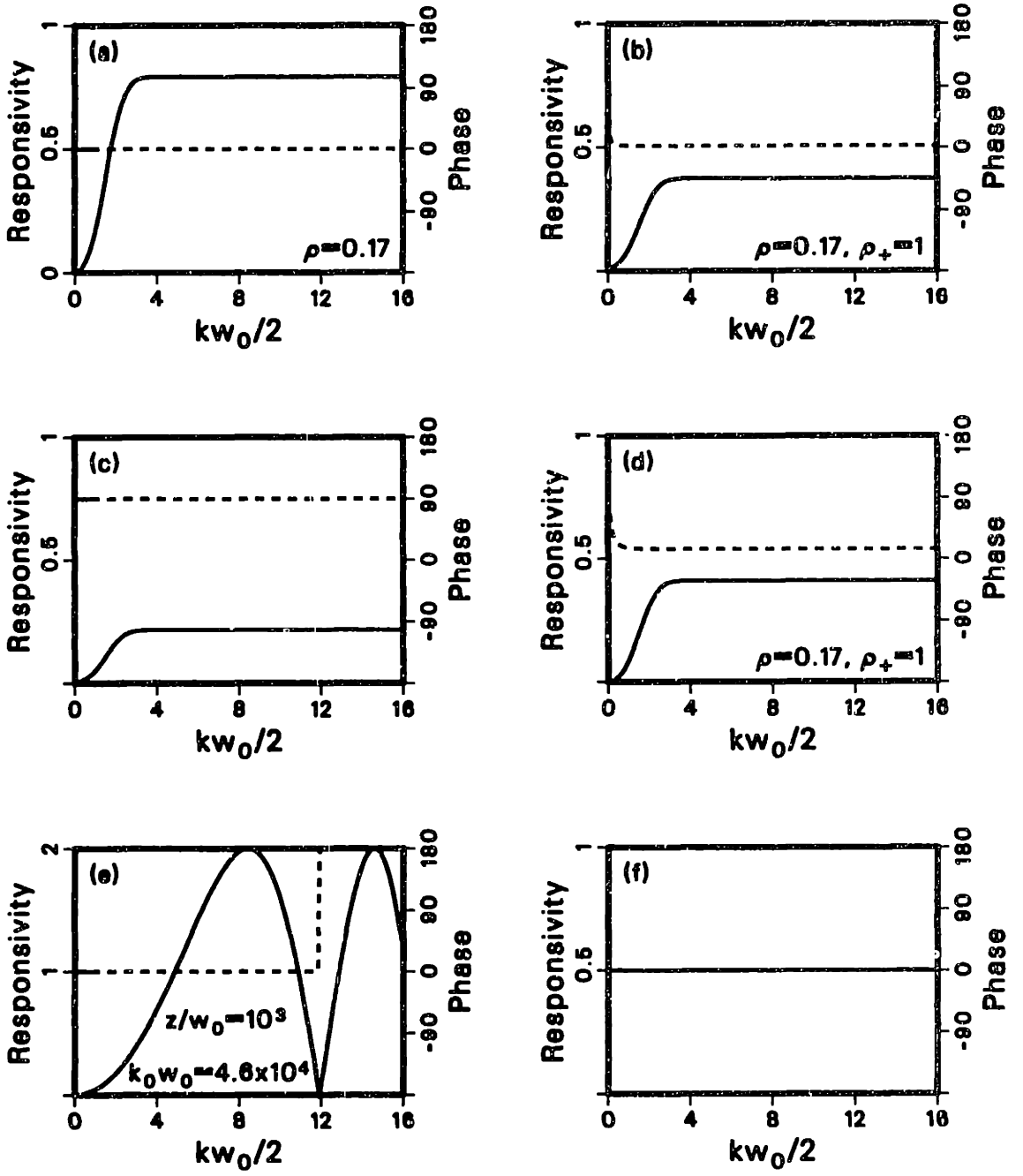

Fig. 2.29 Response functions and phase angles of (a) phase contrast, (b) imaging two-zone filter, (c) schlieren, (d) two-zone filter with toroidal launching in a tokamak, (e) scintillation, and (f) Mach-Zehnder interferometry, for infinite aperture and [for (a)-(d)] Q=1.5.

Finally, we examine a type of filter proposed by Lo et al.,[147] for a special situation arising from toroidal launching in a tokamak with azimuthally symmetric turbulence.

Under these conditions, the plasma itself imposes upon the phase of the laser a transfer function characterized by a $-\pi/4$ phase shift for negative K, and by a $+\pi/4$ shift for positive K. The spatial filter is a modified version of a schlieren filter, with the negative and zeroth orders unshifted in phase, and the positive orders shifted by γ. The problem can be studied by combining the transfer functions of the plasma and of the filter in a function of the type described by Eq. (F.2), with parameters $\alpha = -\pi/4$ and $\beta = \gamma + \pi/4$. The condition $Q \simeq 1.5$ is assumed. (We are not considering here the $1/\sqrt{|K|}$ dependence of the plasma transfer function, which the authors of Ref. 147 propose to compensate with a filter of continuously variable reflectivity $\propto \sqrt{|K|}$.)

In Appendix F it is shown that the conditions for phase imaging and for maximizing the signal-to-noise ratio are $\rho_+ = \rho_- = 1$ and $\gamma = -\pi/2$. This is not surprising, as this configuration renders the plasma-filter system equivalent to a generalized phase-contrast system; since the phase shift is 45° instead of 90°, the signal-to-noise ratio is degraded by a factor of two.

For reasons of practicality, a simplified, two-zone version of this filter was proposed,[147] with $\rho_- = \rho \ll \rho_+ = 1$ and $\gamma = \pi/4$. This set of parameters leads to a phase shift $\theta = 0$ in a simplified plane-wave analysis. However, it is pointed out in appendix F that the additional phase-imaging condition $|1 - \operatorname{erf} Q| \ll 2\sqrt{\rho}$ arises in the case of a finite beam. Depending on the value of ρ, this condition may require a value of Q somewhat larger than 1.5. When this condition is satisfied, the signal-to-noise ratio is 1/4 that of phase contrast. The transfer function and the phase angle are given by Eq. (F.52) and Eq. (F.53), respectively, and are shown in the comparison plot of Fig. 2.29(d).

(c) Scintillation

The scintillation technique is described entirely by the transfer function given by Eq. (2.171) and plotted in Fig. 2.29(e). Although there is no phase shift, the oscillatory nature of the transfer function in general precludes the formation of an accurate image. The zeros of the function represent loss of information. If lowpass filtering is applied to eliminate the high-K oscillations, the scintillation transfer function acts as a highpass filter, analogously to phase contrast. However, the phase-contrast transfer function is much closer to an ideal filter, with a wider flat region and a faster rolloff. In addition, it was shown in §2.8 that the applicability of this analysis requires that the beam be collimated; if we define the critical wave number k_c as the 50% response point of the scintillation curve, the collimation condition is $Q = k_c w_0/2 \gg 1$. This should be compared with an ideal value of $Q \sim 1.5$ for phase contrast.

The signal-to-noise ratio at the peak of the transfer curve is equal to that of phase contrast with $\rho = 1$. In a saturation-limited regime, a higher performance can thus be achieved with phase contrast by reducing ρ.

(d) Mach-Zehnder Interferometer

Finally, we turn to the Mach-Zehnder interferometer. Since the transfer function [see Fig. 2.29(f)] is independent of K, only the signal-to-noise ratio remains to be determined. For a fair comparison, the function $u_0(x)$ must now represent *all* the power flux available from the laser. The optimal signal-to-noise ratio is obtained when the plasma and reference beams are equal. Since one half of the power is lost at the beam combiner (see Fig. 2.12), each beam will carry one fourth of the original power when it reaches the detector. For the interference signal we can write to first order in $\tilde{\varphi}$

$$\tilde{\mathcal{E}} = \frac{u_0(x)}{2}\tilde{\varphi}\sin\varphi_0, \tag{2.190}$$

where $\varphi_0 = \langle\varphi_1\rangle - \varphi_{\mathrm{LO}}$ is the total phase difference between the beams, defined in accordance with Eq. (2.71). The dc flux is

$$\mathcal{E}_{\mathrm{dc}} = \frac{u_0(x)}{2}(1+\cos\varphi_0). \tag{2.191}$$

In the regime in which intrinsic noise dominates, the signal must be maximized; thus, the interferometer will ideally be operated at $\varphi_0 = \pi/2$. If the detector is saturated, the phase φ_0 should be moved *toward* π (to reduce the dc signal and thus the shot noise) until the signal is just below saturation. The signal-to-noise ratio is 1/16 that of the phase-contrast case if the saturation level is larger than $u_0(x)$. If the saturation level is lower than $u_0(x)$, that ratio will be larger but always less than 1/4.

In the regime in which shot noise dominates, the signal-to-noise ratio is proportional to $\tilde{\mathcal{E}}^2/\mathcal{E}_{\mathrm{dc}} \propto \sin^2\varphi_0/(1+\cos\varphi_0)$. This function increases monotonically from 1 at $\varphi_0 = \pi/2$ to a maximum of 2 at $\varphi_0 = \pi$. The maximum is a limiting case in which both the signal and the noise are zero. In practice, if shot noise dominates at $\varphi_0 = \pi/2$, there exists an angle between $\pi/2$ and π that maximizes the signal-to-noise ratio; in these conditions the intrinsic noise and the shot noise are approximately equal. In all these cases it can be easily proven that the signal-to-noise ratio is between 1/8 and 1/4 that of phase contrast.

To conclude this section, it is instructive to illustrate the benefits provided by a phase-imaging system with a simple example. In Fig. 2.30 an arbitrary sample function, representing the $\tilde{n}_e$ distribution in the plasma, is compared with the calculated signals generated by the phase-contrast, scintillation, and schlieren techniques, appropriately normalized. Clearly the phase-contrast case is the only one in which the spatial distribution of the signal follows that of $\tilde{n}_e$. In the other two cases there is no such resemblance, and a deconvolution operation is necessary to reconstruct the $\tilde{n}_e$ profile from the measured signal; if only a limited number of spatial measurements can be effected, the operation of deconvolution can be a source of large uncertainties. These problems are avoided with a phase-imaging technique such as phase contrast.

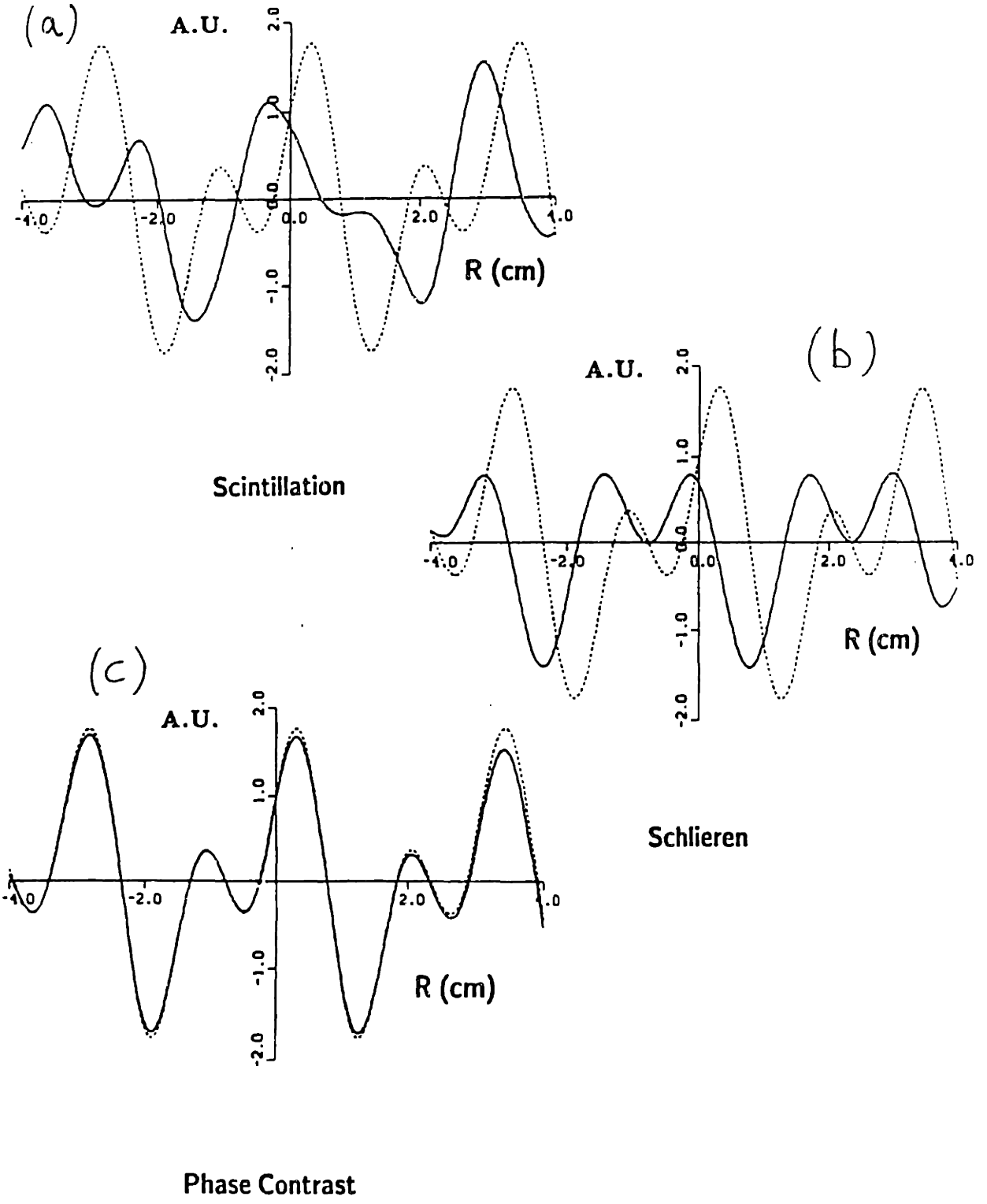

Fig. 2.30 Sample $\tilde{n}_e$ function (dashed lines) compared with the detector signals calculated for (a) scintillation, (b) schlieren, (c) phase contrast.

2.14 Calibration Techniques

The simplest and most straightforward way to calibrate an infrared phase-contrast

imaging apparatus is to apply it to the detection of acoustic and ultrasonic waves in air, as their wavelength range coincides with the range of interest for most plasma experiments. For instance, a 34 kHz ultrasonic wave has a wavelength of 1 cm, and a 3.4 kHz sound wave has a wavelength of 10 cm.

The appropriate expression for the perturbed phase in the case of propagation through air is given in the geometrical-optics approximation by the imaginary part of Eq. (2.87):

$$\tilde{\varphi}(\mathbf{x}_\perp) = k_0 \int \tilde{\mathcal{N}}(\mathbf{x}_\perp, z) dz, \tag{2.192}$$

where $\tilde{\mathcal{N}}$ is the perturbed index of refraction in response to the sound waves, and we have removed the dependence on time owing to the low frequency of these oscillations.

The dependence of the index of refraction on the perturbed air density $\tilde{\rho}$ is given to a good approximation by the Gladstone-Dale law[154]

$$\tilde{\mathcal{N}} = k_{\mathrm{GD}}\, \tilde{\rho}, \tag{2.193}$$

where the Gladston-Dale constant k_{GD} is a function of the optical wavelength but is approximately constant in the near- to intermediate-infrared region, taking the value[149] $k_{\mathrm{GD}} = 0.22$ cm^3/g. It should be noted that when the molecular mass of air is factored into Eq. (2.193), the dependence of the phase on the particle density given by Eq. (2.192) is approximately a factor 2.1×10^{-4} smaller than in the case of the plasma, as can be gleaned by re-examining Eq. (2.85). This dissimilarity is a consequence of the low polarizability of a neutral gas in comparison with a plasma, which is composed of charged particles.

The perturbed density is related to the perturbed pressure $\tilde{P}$ by the expression $\tilde{\rho} = \tilde{P}/c_s^2$, where c_s is the speed of sound. At 20°C, the speed of sound is $c_s = 3.44 \times 10^4$ cm/s; using the CO_2 laser wavelength of 10.6 μm in Eq. (2.192), one can thus write the numerical relation

$$\tilde{\varphi}(\mathbf{x}_\perp) = 1.1 \times 10^{-11} \int \tilde{P}(\mathbf{x}_\perp, z) dz, \tag{2.194}$$

where $\tilde{\varphi}$ is in radians, $\tilde{P}$ is in μPa, and z is in cm. This relation forms the basis of an acoustic calibration. The sound level can be measured with a calibrated sound-level meter and converted to pressure units (20 μPa rms represents the audible threshold, generally referred to as the 0 dB point). If the sound wave is a plane wave, and if the integration length is known, the phase can be calculated from Eq. (2.194) and compared with the detected phase-contrast signal to determine the calibration factor. As an example, a phase shift of 1 mrad rms, with an integration length of 20 cm, corresponds to a sound level of 107 dB.

The transfer function can also be determined for a range of wave numbers by varying the sound frequency. Thus it is possible to experimentally verify the validity of the functions derived theoretically in §2.11. In addition, it should be noted that a

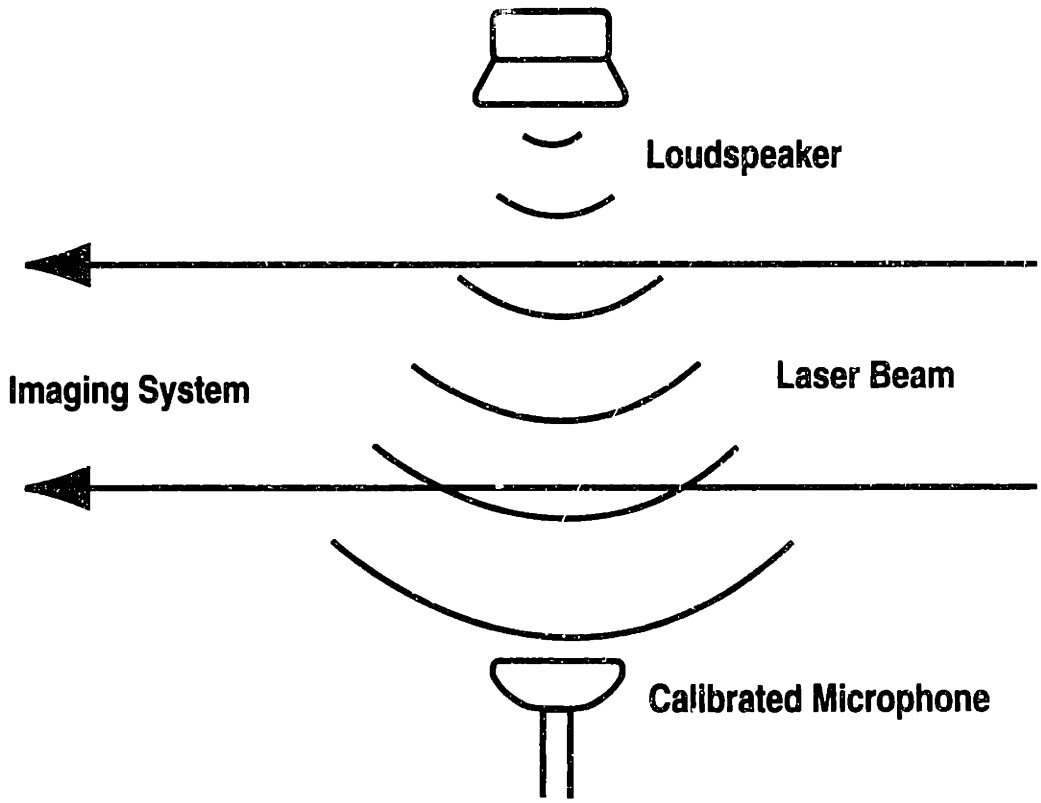

Fig. 2.31 Acoustic calibration setup.

calibration can be performed even if the region occupied by the acoustic field does not coincide with the object plane of the imaging apparatus. For a monochromatic wave, Eq. (2.83) shows that the effect of a spatial shift d from the object plane is a simple multiplication of the perturbed phase [Eq. (2.192)] by a factor $\cos(k_\perp^2 d/2k_0)$. If d is known, the calibration results can be corrected for the cosine factor (although this correction becomes noisy when the cosine is close to zero). This is very convenient, e.g., in a tokamak experiment, where the object plane is typically in the vacuum chamber. Conversely, this effect can be used to verify that the imaging configuration is correct and that the object plane is in fact at the desired location. In practice, such a test in general requires the ability to sweep a broad range of sonic and ultrasonic frequencies.

A common calibration setup involves a loudspeaker emitting a sound wave that is approximately spherical (Fig. 2.31). One must then study the effect of the line integration [Eq. (2.194)] through the field of the sound wave. A spherical wave is described by the equation

$$\tilde{P}(r) = r_0 \tilde{P}_0 \frac{\cos(kr - \omega t)}{r}, \tag{2.195}$$

where $r_0\tilde{P}_0$ is a constant factor, and r is the distance from the source. Taking the source to be at the origin of the coordinate system, we can write $r = (x_\perp^2 + z^2)^{1/2}$.

Rewriting Eq. (2.194) as $\tilde{\varphi} = C_0 \int \tilde{P} dz$, where C_0 is a constant factor, we obtain

$$\tilde{\varphi}(\mathbf{x}_\perp) = C_0 r_0 \tilde{P}_0 \int_{-\infty}^{+\infty} \frac{\cos\left[k\sqrt{x_\perp^2 + z^2} - \omega t\right]}{\sqrt{x_\perp^2 + z^2}} dz. \tag{2.196}$$

This integral can be calculated,[155] with the result

$$\tilde{\varphi}(\mathbf{x}_\perp) = \pi C_0 r_0 \tilde{P}_0 \left[J_0(k|\mathbf{x}_\perp|)\sin(\omega t) - Y_0(k|\mathbf{x}_\perp|)\cos(\omega t)\right], \tag{2.197}$$

where J_0 and Y_0 are the Bessel functions of the first and second kind, respectively. If $k|\mathbf{x}_\perp| \gg 1$, one can write to a good approximation

$$\tilde{\varphi}(\mathbf{x}_\perp) = \left(\frac{2\pi}{k|\mathbf{x}_\perp|}\right)^{1/2} C_0 r_0 \tilde{P}_0 \cos(k|\mathbf{x}_\perp| - \omega t + \pi/4). \tag{2.198}$$

The $1/\sqrt{k}$ dependence and the $\pi/4$ phase shift are strictly a consequence of the spherical nature of the wave and would disappear in a plane-wave case.

Since the field pattern in practice fills only a fraction of the total solid angle, it is important to determine the conditions under which Eq. (2.198) is approximately valid when the integration length is finite. This can be accomplished by recalculating the integral in Eq. (2.196) with a Taylor expansion for small z, and also by numerical integration; both procedures yield the condition $z_{\max} \gg \sqrt{\pi|\mathbf{x}_\perp|/k}$. In the opposite case, $z_{\max} \ll \sqrt{\pi|\mathbf{x}_\perp|/k}$, a plane-wave approximation is appropriate.

With more complicated field patterns, numerical methods can be used to calculate the phase from Eq. (2.194) and provide a more accurate calibration (see §3.8).

An alternative method of determining the transfer function in wave-number space consists of imposing a known phase distribution and measuring the resulting spatial distribution. The transfer function can be determined by Fourier transforming the result. The most useful sample functions and the most viable experimentally are step functions and delta functions.[31] However, the accuracy with which these functions can be obtained experimentally is far inferior to that of an acoustic wave.

3 Experimental Apparatus

The measurements described in this thesis were carried out with a CO_2-laser phase-contrast imaging (PCI) diagnostic. This system measures the vertical line integrals of the density fluctuations at 16 radial locations within a 7.6-cm-wide region at the outer edge of the DIII–D tokamak.[70] The principal characteristics of the PCI diagnostic are a flat response to wave numbers in the range 1–16 cm^{-1}, a radial resolution of ~ 0.5 cm, a density sensitivity of the order of 10^9 cm^{-3}, and a detection bandwidth of $\sim$ 20 MHz (the data-acquisition bandwidth is 1 MHz).

The development of the PCI system was motivated principally by an interest in microturbulence and in its relation with anomalous transport. The region explored by this diagnostic comprises the range $r/a = 0.9$–1.15, where r/a is the normalized minor radius (although only a fraction of that range is accessible in a given plasma discharge). This is the region in which the most dramatic changes in transport and in the character of microturbulence occur at the L– to H–mode transition.[61] This is also the region where the ELMs (or edge localized modes) are found.[69] The PCI diagnostic bridges the spatial gap between the reciprocating Langmuir probe[71] and the reflectometer[42]; in addition, both the reflectometer and the PCI system are mostly sensitive to radial wave vectors, whereas the probe responds to poloidal wave vectors, providing additional complementarity. Some spatial overlap exists also between the PCI system and the lithium-beam emission spectroscopy diagnostic.[53]

Phase-contrast imaging is a novel technique in thermonuclear plasma measurements. The pioneering work of Weisen[31] demonstrated unequivocally the benefits of this method, in both low-frequency and radio-frequency applications, as well as its advantages over conventional scattering techniques in the characterization of long-wavelength fluctuations. From a theoretical perspective, the analysis presented in Chapter 2 clearly confirms those advantages, particularly in the high-gradient region explored by the DIII–D PCI diagnostic.

The development of PCI on a large tokamak such as DIII–D presented considerable technical challenges for which little guidance could be gained from previous applications. The main difficulty was that of mechanical vibrations, exacerbated by the tortuous optical path forced by the existing equipment that surrounds the DIII–D vessel. Indeed, the design and successful completion of a high-gain feedback vibration-control system was the crucial element in the development of the diagnostic.

This chapter describes the experimental apparatus in detail. The DIII–D tokamak and its main diagnostic systems are delineated in §3.1. In §3.2 the geometry of the measurement is introduced, with a verification of the validity of the approximations on which the theory of Chapter 2 is predicated. The experimental setup, with details on the individual hardware components, is the subject of §3.3. Section 3.4 contains a discussion of the optical design, including the main design criteria, the alignment techniques used, and an illustration of the resulting performance.

The feedback vibration-control system is presented in §3.5. Data on the measured vibrations are shown in order to introduce and justify the design parameters; a

discussion of the choice of components is then followed by a theoretical analysis of the design procedure and by a description of the optimization techniques adopted. Finally, the performance of the system is demonstrated by means of data from vibration measurements.

Section 3.6 is devoted to the electronic data-acquisition system, which can be structured in two different configurations, respectively for low-frequency and radio-frequency applications. The considerations on responsivity presented in Chapter 2 are reexamined in §3.7 for the specific case of the DIII–D system, with additional observations arising from the geometry and from the details of the optical layout. Results from acoustic-wave calibrations are offered in §3.8, including comparisons between the theoretical and measured transfer functions (in wave-number space) and signal-to-noise ratios, and a general assessment of the performance of the diagnostic.

Finally, §3.9 contains a description of the data-analysis techniques employed in the course of this work, including details on error analysis and on specially developed software for the estimation of correlation functions.

3.1 The DIII–D Tokamak

The DIII–D tokamak fusion research program is carried out by General Atomics under contract to the U.S. Department of Energy. The DIII–D program represents the culmination of over thirty years of successful nuclear-fusion research at General Atomics. Collaborations with other U.S. and international fusion programs are an essential feature of the program. In addition, General Atomics has made the DIII–D facility available as training ground for graduate students from numerous universities: the present work is one example of such a collaboration.

The mission of the DIII–D program is to provide data needed for next-generation fusion devices, such as ITER.[67] In particular, the program is organized into two main lines of research: the development of advanced tokamak concepts and the development of an advanced divertor.[5]

The advanced tokamak program addresses the achievement of high confinement, high beta (the ratio of the plasma pressure to the magnetic energy density, an important parameter for considerations of reactor economics), and high noninductive current fraction. The first two goals are being pursued through continued studies of enhanced confinement regimes (H– and VH–mode) and of the effects of plasma shaping on both beta and confinement.[156] Noninductive current-drive experiments[75] are being carried out both as a path to steady-state operations and as a means to modify the current profile in order to obtain improved plasma performance.[157]

The advanced divertor program aims to improve the efficiency of ash exhaust and to reduce the heat load on the divertor. Demonstration of helium ash removal is a prerequisite of reactor development: without an efficient extraction method, the accumulation of helium in the core of the plasma would progressively reduce the D–T reaction rate and hinder the reactor's performance. The recent installation of a cryopump in the divertor region has allowed a convincing demonstration of helium removal; in addition, the cryopump has been proven to be beneficial as a tool for

TABLE 3.1. Peak DIII–D parameters

Major radius	1.67 m
Minor radius	0.67 m
Toroidal field	2.2 T
Plasma current	3.0 MA
Vertical elongation ratio	2.5
Line-averaged electron density	1.4×10^{14} cm^{-3}
Central electron temperature	7 keV
Central ion temperature	21 keV
Volume-averaged beta	12%
Neutral-beam power	22 MW
Radio-frequency power	6 MW

plasma density control, which is necessary for efficient current drive.[5] In the area of divertor heat reduction, studies are continuing with the present, flexible divertor configuration; at the end of 1996, a new radiative divertor will be installed on DIII–D: in the new configuration, radiation will be used to dissipate the heat flux before it reaches the material wall.[156]

The DIII–D tokamak (see Fig. 3.1) has a major radius of 1.67 m and a minor radius of 0.67 m, with a D-shaped cross section; the maximum magnetic field is 2.2 T and the maximum plasma current is 3 MA. The main parameters of the device are listed in Table 3.1. The principal subsystems of the tokamak can be seen in Fig. 3.2. The large, toroidal magnetic field is generated by 24 coils that encircle the plasma cross section; the ohmic magnetic field, whose temporal variation drives the main plasma current, is generated by a solenoid located in the center column of the device; and the vertical field that is necessary for plasma positioning and shaping is generated by 18 distributed horizontal coils that surround the vacuum vessel.[4] Two additional coils are used to apply fine corrections to the overall field, allowing a better control of certain plasma instabilities.

The vacuum vessel, made of Inconel 625, has recently been completely covered with graphite tiles on the plasma-facing surface[156] (see Fig. 3.3). This has greatly reduced the influx of metallic impurities, while also providing better protection to the wall. The outer surface of the plasma cross section can be defined either with material limiters or with a magnetic divertor; the present divertor affords considerable flexibility in the choice of a plasma shape. In addition to the ohmic heating derived from the current flowing in the plasma, auxiliary heating can be applied in the form of energetic neutral beams (22 MW), 110-GHz electron-cyclotron waves (1–8 MW), and 30–120-MHz ICRF (fast) waves (6 MW). All three methods have been used also to drive noninductive plasma currents.[158]

One of the key factors in the success of the DIII–D program has been the evolution of the plasma control system, recently upgraded with the use of digital techniques.[159] This system is now capable of controlling the neutral beam power, the

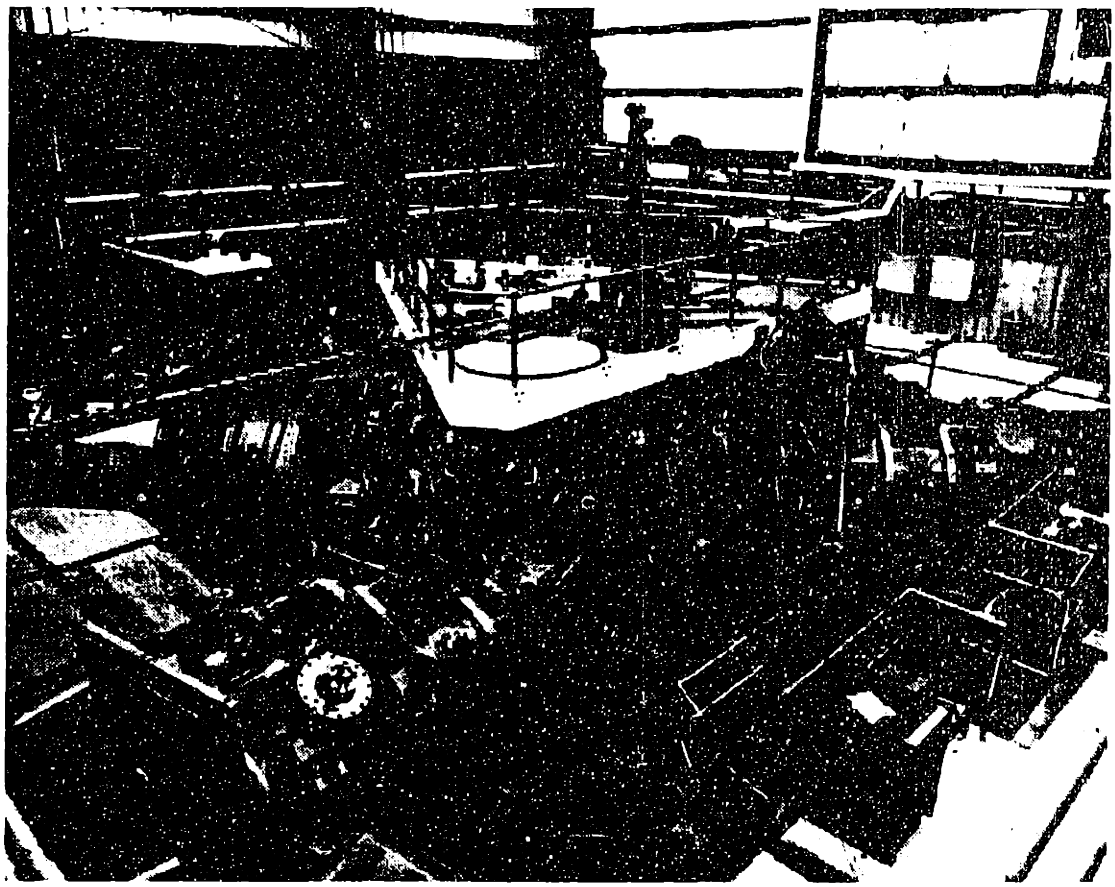

Fig. 3.1 Outside view of the DIII–D tokamak with the neutral-beam injectors, after assembly.

ICRF antenna loading, the pumping speed of the cryopump (and thus the plasma density), and a number of other plasma parameters.

DIII–D is also equipped with an extensive set of diagnostics. The development of state-of-the-art systems to measure the profiles of the electron density and of the electron and ion temperatures has been the centerpiece of the DIII–D diagnostic program for most of its lifetime. The multipulse Thomson scattering system can measure n_e and T_e profiles with a spatial resolution of 1 cm and a dynamic range (in temperature) of 10 eV to 20 keV; four CO_2-laser interferometers measure the line integrals of n_e over one horizontal chord and three vertical ones; the electron cyclotron emission (ECE) radiometer provides 10-point radial profiles of T_e with a time resolution of 0.1 ms; the 32-chord charge exchange recombination (CER) diagnostic is used to derive profiles of T_i and of the plasma rotation velocity with a spatial resolution as fine as 3 mm in the T_i data at the edge. These systems, combined with a visible bremsstrahlung imaging array that provides the effective charge profile, form a core of kinetic diagnostics that allow a detailed physics analysis of a wide variety of plasma discharges.

The magnetic diagnostics, which comprise a large array of external loops and internal probes, are essential for the operation of the tokamak as they are used for feedback control of discharge current, shape, and position; in addition, magnetic

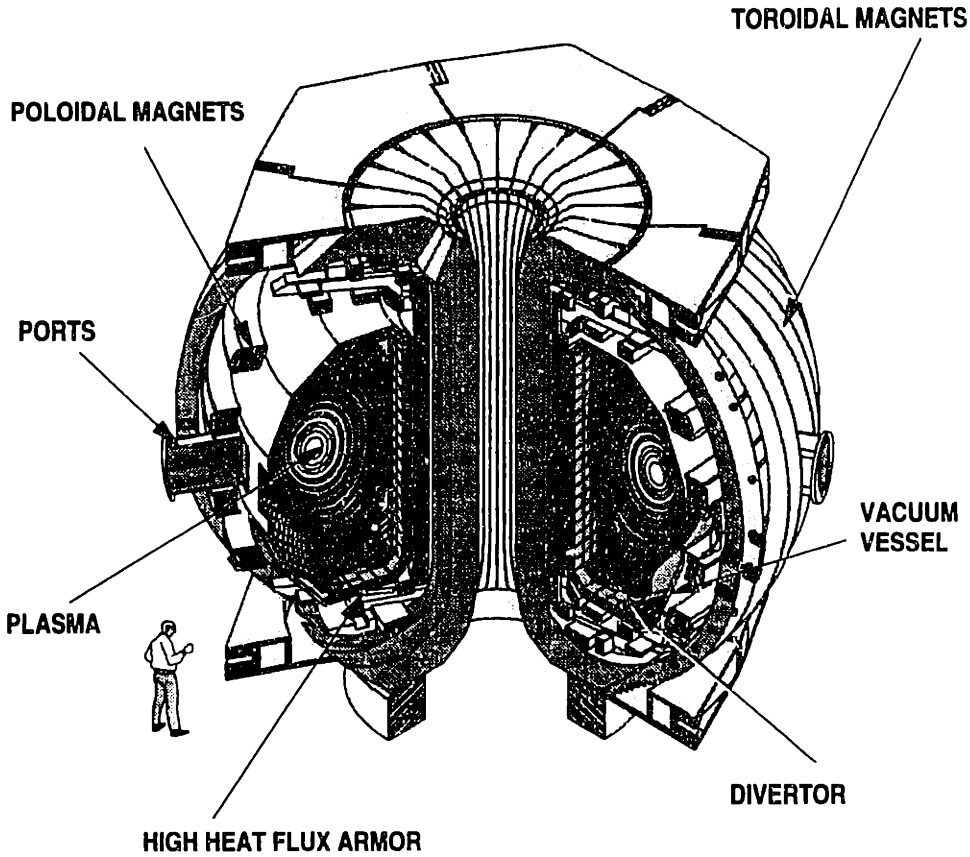

Fig. 3.2 Schematic diagram of the DIII–D tokamak.

data are used for reconstructing the plasma equilibrium geometry between discharges. Visible and infrared TV systems provide information on the heat loads on the material structures of the vessel. An array of 16 photodiodes is employed to measure the H_α radiation, which is related to the amount of recycling and to the level of transport.

In recent years, the main emphasis of the DIII–D diagnostic program has shifted toward the development of systems to measure the plasma current and the divertor parameters. To the first group belong the eight-channel motional Stark effect (MSE) current-profile diagnostic and an ECE Michelson spectrometer designed to study the high-energy tail of the electron distribution function. Examples of divertor diagnostics include a dedicated Thomson scattering system and a visible spectrometer.

We conclude this incomplete survey with a brief description of the DIII–D fluctuation diagnostics. The FIR scattering system[27] measures density fluctuations with wave numbers in the range 3–24 cm^{-1} and wave vectors oriented in the poloidal direction, with access to most of the plasma cross section. The microwave reflectometer[42] provides multiple localized measurements of density fluctuations with radially oriented wave vectors, integrating over the range 0–31 cm^{-1}. In addition, a two-frequency correlation reflectometer[46] is used to study the radial correlation length of the fluctuations. These diagnostics are all operated by the University of California, Los Angeles.

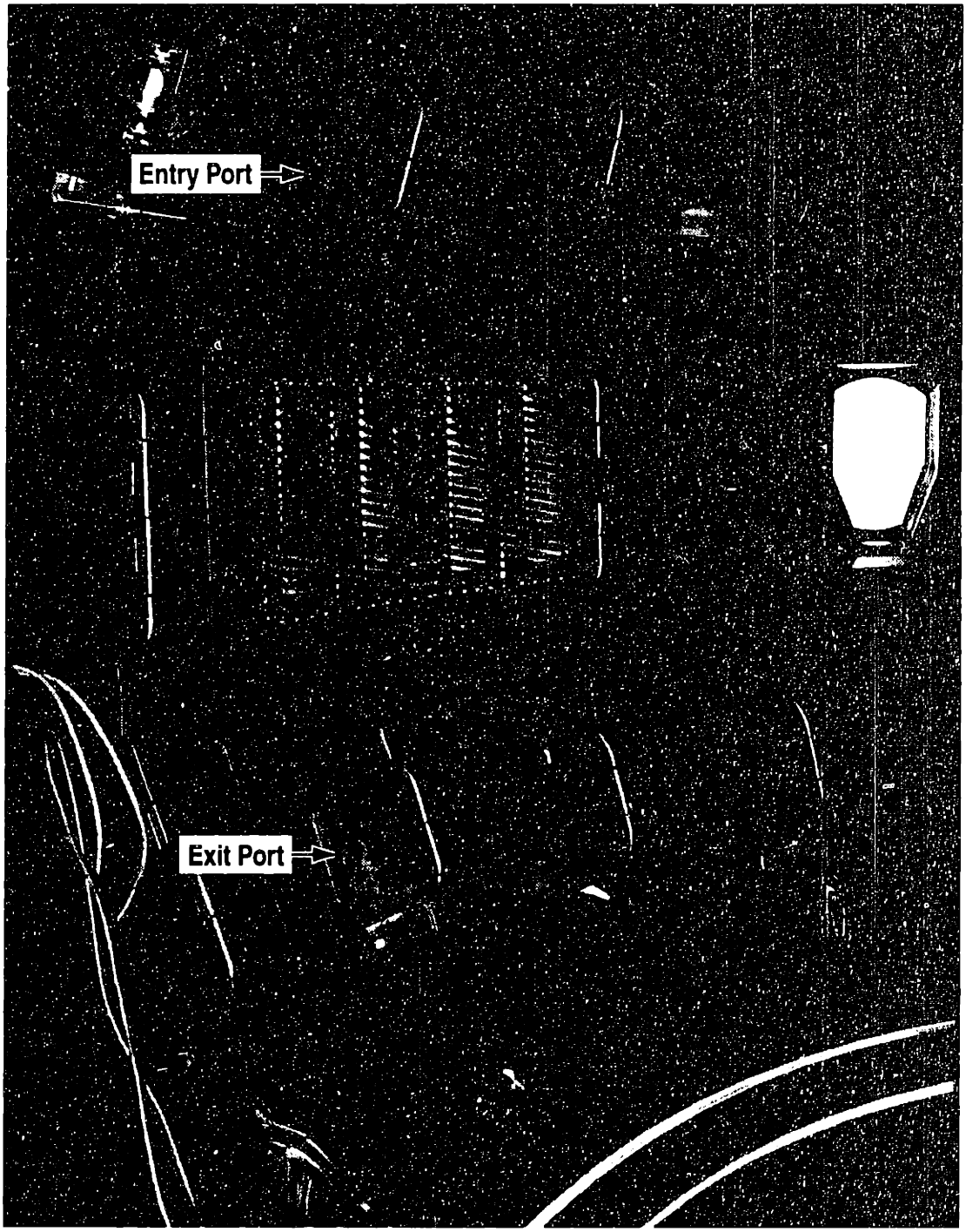

Fig. 3.3 Inside view of the DIII-D tokamak, showing the all-graphite wall, the ICRF antenna, and the two PCI ports.

A fast reciprocating Langmuir probe,[71] operated jointly by Sandia National Laboratory and the University of California, San Diego, provides measurements of density and electric-potential fluctuations, in addition to the density and temperature profiles, in the scrape-off layer and just inside the last closed plasma surface, with excellent

spatial resolution; a two-point correlation technique is employed to reconstruct the poloidal wave-number spectrum in the range 0.3–12 cm^{-1}. Spatially resolved density fluctuation profiles are obtained in the plasma edge region with a lithium-beam emission spectroscopy system;[53] wave numbers are in the range 0.4–5 cm^{-1} without restrictions on the orientation of the wave vectors. A core deuterium-beam emission spectroscopy diagnostic, resulting from a collaboration between General Atomics and the University of Wisconsin, has recently become operational.[52]

Magnetic fluctuation measurements are carried out with a large array of magnetic coils located inside the vacuum vessel and thus immune to the high-frequency shielding effect of the vessel. An extensive array of soft-x-ray diodes is employed to detect fluctuations in the plasma emission, which depends on temperature, density, and effective charge.

The list of fluctuation diagnostics is completed by the MIT PCI system, which will be described at length in the remainder of this chapter.

3.2 Geometry of the Measurement

The PCI diagnostic employs a CO_2-laser beam with a wavelength of 10.6 μm. The cross section of the beam in the plasma is circular with a radius of 3.8 cm, defined by the entrance window. The power distribution within the cross section is Gaussian, with a half-width (i.e., radius of the e^{-2} point) of 3.8 cm also. As will be discussed in §3.3, the parameter ζ_p (the distance between the beam waist and the plasma, divided by the Rayleigh length) is set to zero with an experimental accuracy of ± 0.5. The half-width at the waist, w_0, can therefore differ somewhat from the half-width in the plasma, $w_p = 3.8$ cm. As pointed out in the paragraph following Eq. (2.132), the only practical consequence is that the phase plate must be positioned at the beam waist (created by the focusing optic) rather than in the focal plane, provided that there is no appreciable *change* in collimation between the plasma and the focusing optic.

The beam propagates vertically downwards at the outer edge of the DIII–D vessel (see Figs. 3.3 and 3.4), occupying the region from $R = 227.3$ cm to $R = 234.9$ cm (where R is the major radius). The surface of the graphite tiles on the outer wall is located at $R = 237.5$ cm. In a given discharge, the region probed by the beam may lie partly inside the last closed flux surface or entirely outside it (in the scrape-off layer), depending on the plasma geometry (see Fig. 3.5). Combining those different cases, the range from 0.9 to 1.15 in normalized minor radius (r/a) can be explored. The total distance covered by the beam inside the vessel wall, from port to port, is 137 cm. As the windows are recessed into the ports, the total distance between the entrance window — i.e., the aperture stop — and the lower port is 219 cm.

We now proceed to verify the validity of various approximations used in the derivation of the scattering equations in Chapter 2; we shall thus identify the appropriate limit of the measurement in our specific geometry. In §2.5 it was concluded that the effects of diffraction from the aperture stop could be ignored in the interaction region under the conditions $|\zeta_p| < 0.5$, $a/w_p \geq 1$, and $z/z_R \leq 0.007$. In our

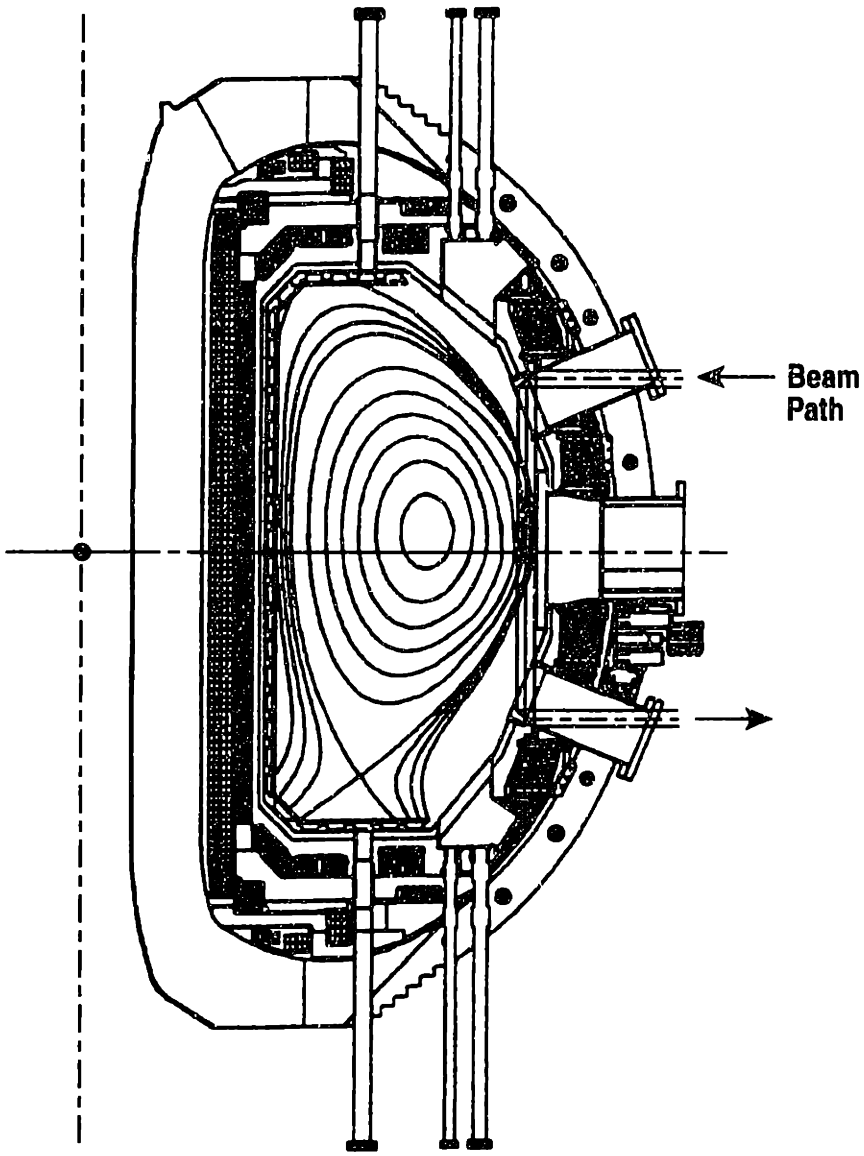

Fig. 3.4 Cross section of the DIII–D vessel showing the PCI beam path and the magnetic flux surfaces.

geometry, $|\zeta_p| \leq 0.5$, $a = w_p = 3.8$ cm, $z \leq 219$ cm, and 344 m $\leq z_R \leq$ 430 m; therefore, all three conditions are satisfied.

Since the detector bandwidth is $\sim$ 20 MHz, we can write $\omega/\omega_0 < 3.3 \times 10^{-6}$; thus, the low-frequency condition is well satisfied. In wave-number space, spatial antialiasing lowpass filtering was applied, limiting the spectrum in all cases to $k \leq 40$ cm^{-1}; therefore, $k/k_0 \leq 6.8 \times 10^{-3}$, and the low-angle scattering condition is also satisfied.

Detection is performed in the near field by means of an imaging configuration: the detector plane is the image of the DIII–D midplane. Hence, we must now inspect the approximations used in §2.8 for the case of near-field detection. The condition

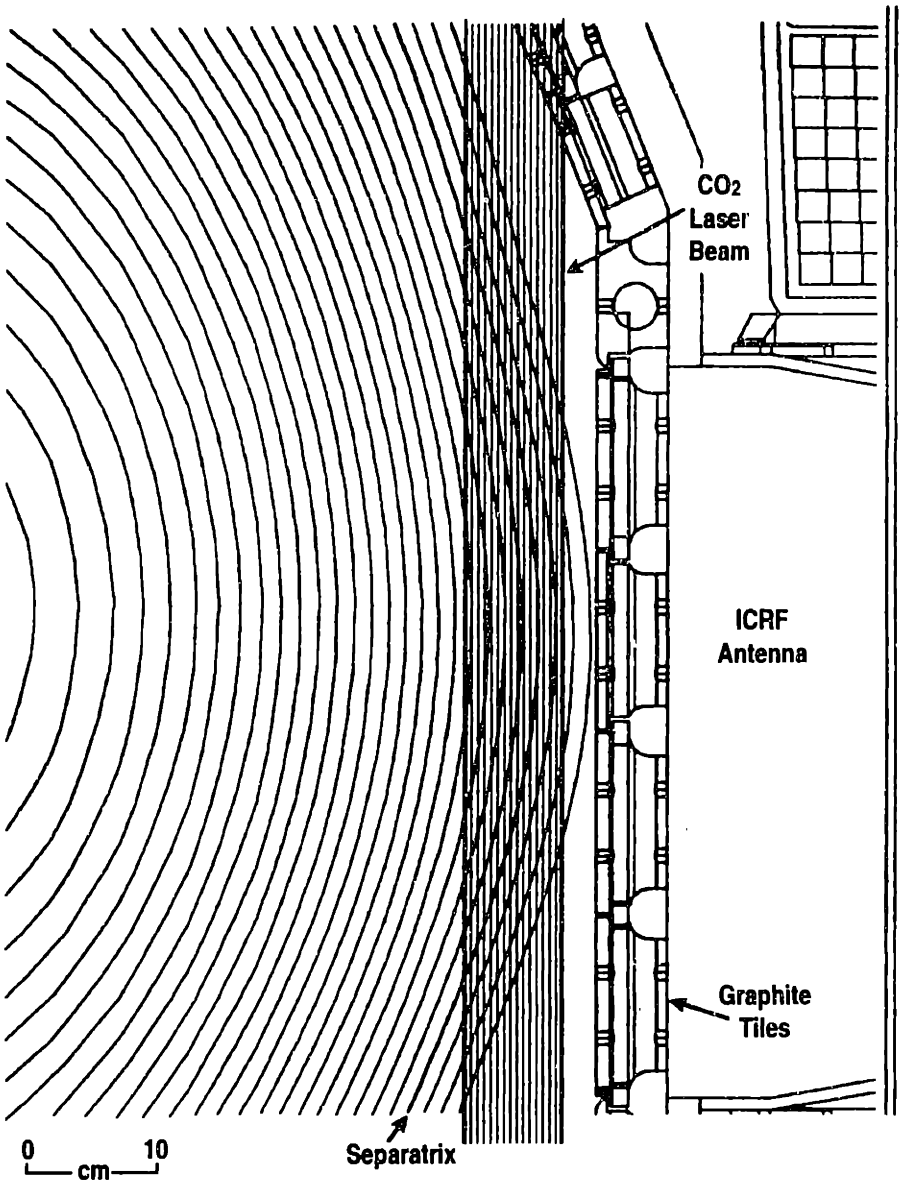

Fig. 3.5 Geometry of the PCI measurement.

the detector plane is the image of the DIII–D midplane. Hence, we must now inspect the approximations used in §2.8 for the case of near-field detection. The condition $k_0 w_0 \gg 1$ is well satisfied, as $k_0 w_0 \geq 2.0 \times 10^4$. The Fresnel conditions [Eqs. (2.62) and (C.6)] translate into $|z-z'|k^4/(8k_0^3) \ll 1$, $|\zeta|/(k_0 w_0)^2 \ll 1$, and $|\zeta'|/(k_0 w_0)^2 \ll 1$: to verify these three relations, we insert the numerical values for our system and find respectively $|z-z'|k^4/(8k_0^3) < 1.1\times10^{-4}$, $|\zeta|/(k_0 w_0)^2 < 1.3\times10^{-9}$, and $|\zeta'|/(k_0 w_0)^2 < 1.3 \times 10^{-9}$. The collimation condition is also satisfied, as $|\zeta - \zeta'| \leq 4 \times 10^{-3} \ll 1$. It must also be noted that the distance between the plasma and the front focal plane of the focusing optic is approximately 4 meters, i.e., much less than a Rayleigh length.

Under near-field detection conditions, the low-divergence condition [Eq. C.42] is essentially equivalent to the Gaussian-near-field condition: both are expressed by the

relation $L_z k/(k_0 w_0) \ll 1$. With $L_z = 137$ cm, we find for our system $L_z k/(k_0 w_0) \leq 0.27$. Although this number is not much smaller than one, the approximations made in Appendix C are still quite good. We note here that in most of our experiments the cutoff value of the spatial lowpass filter was not larger than 10 cm^{-1}, resulting in the relation $L_z k/(k_0 w_0) \leq 0.07$. Thus, in these cases the Gaussian-near-field condition was well satisfied. As will be discussed in Chapter 5, only in one experiment, characterized by very fine spatial resolution, was the wave-number cutoff value raised to ~ 40 cm^{-1}.

Under the usual conditions ($k \leq 10$ cm^{-1}) the relation $L_z k^2/(\pi k_0) \leq 1$ is satisfied, and the measurement is carried out in the Raman-Nath regime [cf. Eq. (2.40)]. The case $k > 12$ cm^{-1} corresponds to the Bragg regime; thus, the high-resolution experiment mentioned above must be analyzed in a different fashion from all our other experiments. However, since only the correlation properties of the measurements were analyzed in that study, the considerations at the end of §2.8 apply: in particular, since the vertical correlation length $\mathcal{L}_z$ is typically of the order of 4 cm or smaller, the effective Klein-Cook parameter, $Q_c = k^2 \mathcal{L}_z/(2k_0)$, is smaller than one even at $k = 40$ cm^{-1}. Therefore, as indicated by Eq. (2.90), each spectral component $S(k_R)$ of the crosscorrelation function in this regime is the sum of the $k_z = 0$ spectral component and of one-half each of the $k_z = \pm k_R^2/(2k_0)$ components. If the latter components become negligible well into the Bragg regime, the autocorrelation function is simply reduced by a factor of two with respect to its value in the Raman-Nath regime, as indicated by Eq. (2.92).

Let us now examine the transit phase $D = L_z \omega/c$. For $L_z = 137$ cm, D is equal to one at a frequency of 35 MHz. Hence, the transit phase is irrelevant to low-frequency turbulence measurements: in particular, all the data presented in this thesis are characterized by frequencies below 1 MHz. In the proposed DIII–D core configuration described in Chapter 7, when used to detect externally launched rf waves, the transit phase would be a potentially significant parameter. The appropriate integration length L_z for that case is the vertical width of the rf wave front, which can be estimated by computer codes.

The condition for the validity of the Born approximation, i.e. for the Rytov phase to be much smaller than one, is given by Eq. (2.33), which in the present case limits the line integrated density to

$$N < 3.3 \times 10^{15}\,\text{cm}^{-2}. \tag{3.1}$$

This relation is invariably well satisfied for the fluctuating component of the density, characterized by frequencies above 1 kHz. According to the discussion in §2.10, the bulk density may safely violate this condition, provided that its gradient length is larger than the beam width; in practice, in most cases the Born condition is satisfied by the bulk density also, since the average is taken over the entire distance traversed by the beam, including the low-density scrape-off layer. To verify that the condition is satisfied, let us now inspect a worst-case scenario.

The maximum density achieved in DIII–D in the region of the PCI beam is approximately 5×10^{13} cm^{-3}. In the case in which the plasma boundary crosses the midplane in the middle of the beam, the maximum length of the innermost chord inside the plasma is 40 cm. The maximum line-integrated density is therefore $N_{\max} \simeq 2 \times 10^{15}$ cm^{-2}. Let us now take the extreme case of a step function for the line-integrated density $N(R)$: we can then write

$$N(R) = \frac{N_{\max}}{2} + \frac{N_{\max}}{2} \operatorname{sgn}(R_{\text{boun}} - R),$$

where $\operatorname{sgn}(x)$ is the sign function and R_{boun} is the boundary radius. The first term on the right-hand side of this equation is a constant ($k = 0$) component and can thus be ignored. We are then left with the second component, which gives an effective line-integrated density of $N_{\max}/2 \simeq 1 \times 10^{15}$ cm^{-2}, safely below the limit set by Eq. (3.1). In the vast majority of cases, of course, conditions are more favorable: the density is typically lower and its variation is more gradual.

Our final verification concerns Eq. (2.115), which permitted to ignore the spatial dependence of the delay time in the image plane. We shall take the most unfavorable conditions, with a 100-MHz frequency and a magnification $M = -2$ (used in the high-resolution experiment); the distance between object and image is ~ 10 meters. With these values, we find $(\omega/2c)(M-1)^2 w_0^2/(z_{\text{im}} - z_{\text{obj}}) \simeq 1.4 \times 10^{-3} \ll 1$. Thus, the condition is well satisfied.

3.3 Experimental Setup

The light source and the beam-generating optical components, as well as the imaging optics, the detector, and the primary electronics, are installed on an aluminum breadboard optical table (see Fig. 3.6). The table measures 122 by 183 cm and is mounted vertically to limit space demands and to minimize the distance from the tokamak (see Fig. 3.7).

The light source is a dc-excited carbon dioxide laser, manufactured by MPB Technologies (Dorval, Canada). The laser consists of a two-meter-long, sealed-off glass tube, with two CdTe Brewster windows, housed in a two-mirror cavity; each mirror can be adjusted externally on both axes by means of micrometers to obtain a pure $\text{TEM}_{0,0}$ (Gaussian) mode. The cavity is ordinarily installed on four invar rods; in our case, these were replaced with carbon fiber rods, owing to concern over the performance of the laser in the high ambient magnetic fields that exist in the proximity of the tokamak.

The temperature of the laser is stabilized with an external closed-loop cooler. The laser has no grating; rather, line stability is achieved by means of a dither stabilization feedback system. The output coupler, made of coated germanium, is mounted on a piezoelectric translator that is made to oscillate at a frequency of 490 Hz, with an excursion of a few nanometers. The power oscillations are monitored and the equilibrium position is adjusted for maximum power. The resulting long-term

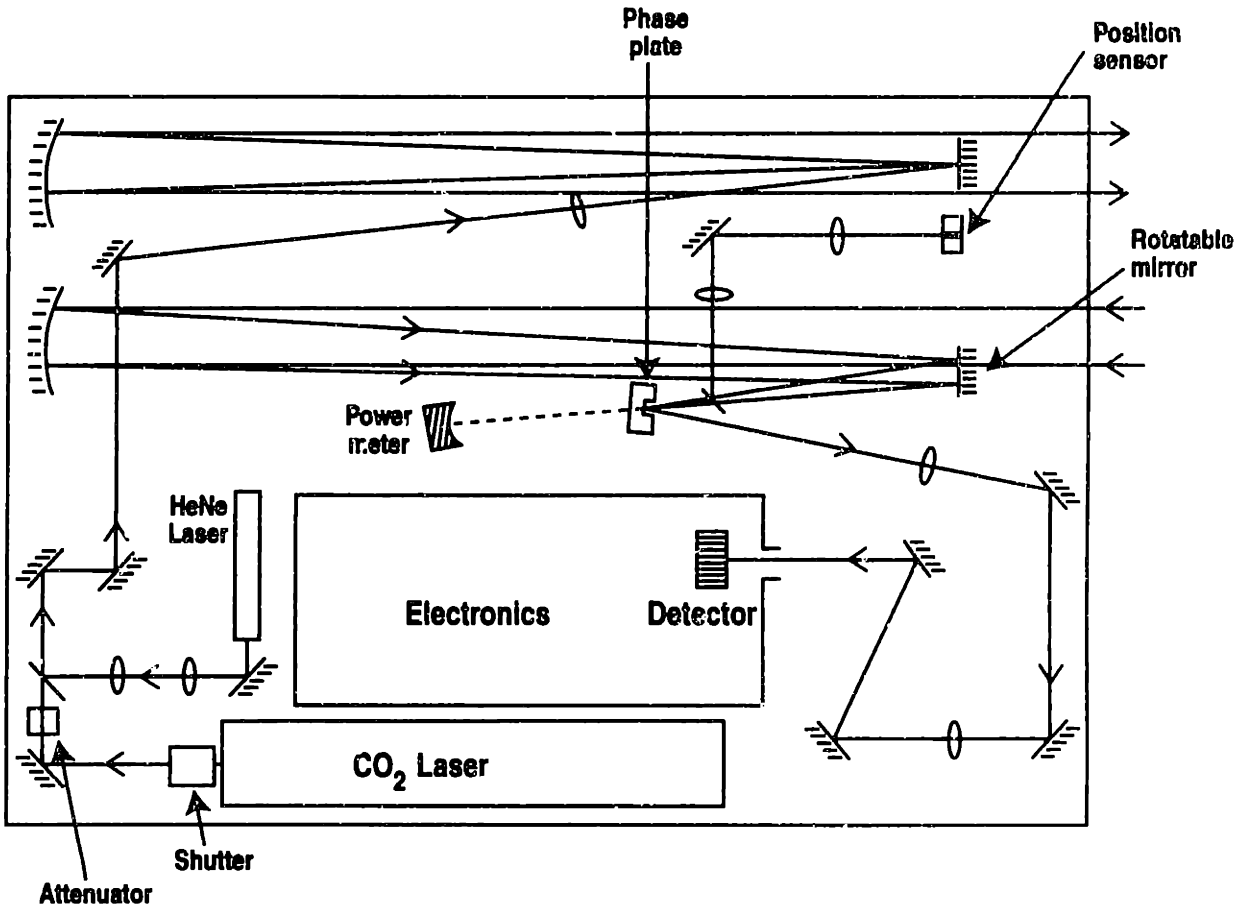

Fig. 3.6 Schematics of optical-table layout.

power stability is better than 0.5%. Nominal power at delivery was 20 W (22 W measured); a slow decrease over time was observed, down to the present value of 14 W. The lasing line is the $P(20)$ line of the $00°1 \rightarrow 10°0$ transition, with a wavelength of 10.59 μm. The nominal beam width at the output coupler is 3.7 mm, and the full-angle divergence is 3.6 mrad; the light is linearly polarized.

The choice of a CO_2 laser and of the 10.6 μm wavelength was dictated by several considerations. All the approximations examined in §3.2 (small-angle scattering, Gaussian near field, Raman-Nath, and Born) are more easily satisfied by shorter wavelengths, e.g. in the visible spectrum. In addition, diffraction and refraction effects are reduced at short wavelengths. However, longer wavelengths (e.g., in the far-infrared spectrum) also have advantages, such as higher tolerances on optical quality and aberrations and reduced sensitivity to damage and contaminants on optical surfaces; in addition, a longer wavelength implies a larger focal spot and thus a wider phase-plate groove, simplifying both fabrication and alignment and reducing the power density on the phase plate. The sensitivity to density fluctuations is also proportional to the wavelength. The 10.6 μm wavelength was found to provide an ideal compromise between all these conflicting requirements.

The laser power can be attenuated if necessary by up to a factor of 30 by means

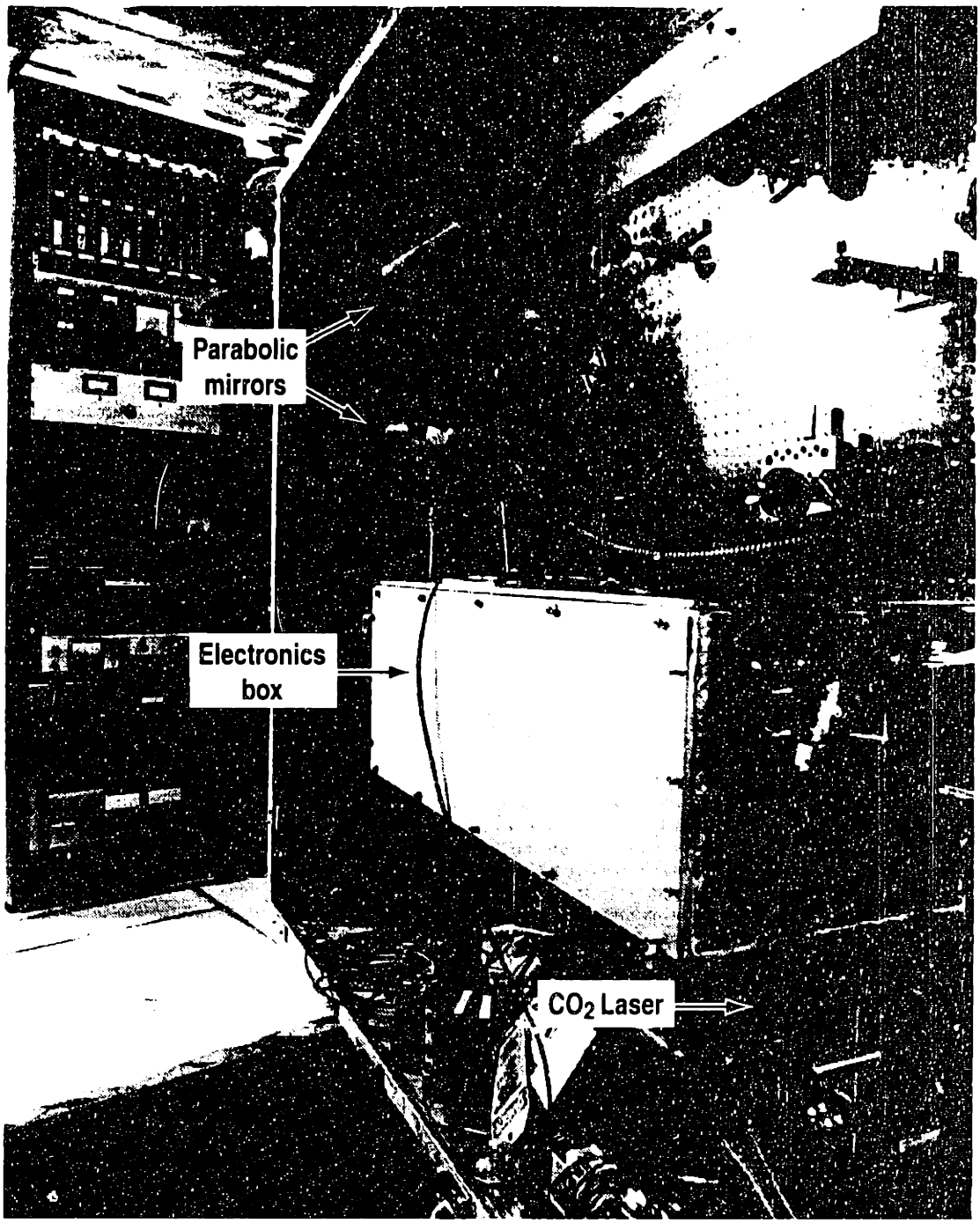

Fig. 3.7 Optical table: the parabolic mirrors, the rf-shielded electronics box, and the CO_2 laser are visible from top to bottom.

of a continuously variable attenuator located in front of the cavity opening. Also, a mechanical shutter is present for personnel safety; the shutter is interlocked with the doors of the DIII–D hall and prevents beam propagation when closed. A secondary interlock shuts off the high voltage to the laser head if the shutter fails to close.

The CO_2-laser beam is combined with a visible HeNe-laser beam by a ZnSe

beam combiner. All transmissive components in the optical system were chosen to be transparent to visible light to facilitate alignment. The HeNe laser operates at a wavelength of 632.8 nm and has a power of 15 mW; two lenses are used to match the beam's width and divergence to those of the CO_2-laser beam.

The CO_2-laser beam is allowed to propagate and expand freely through several reflections on the optical table, in order to reach the required width: this free optical path was originally 315 cm long, but was shortened over time to compensate for the slowly increasing divergence of the laser beam; the length of the path is currently 224 cm. The beam is then expanded to its final width of 7.6 cm by means of a telescope arrangement, composed of a plano-convex ZnSe lens of focal length 25.4 cm and of an off-axis parabolic mirror of focal length 203 cm. The distance between the lens and the paraboloid is ideally set at a value designed to place the expanded beam waist in the DIII–D vessel; with an estimated uncertainty of ± 5 mm in the position of the lens, the uncertainty on ζ_p (distance between the beam waist and the plasma, divided by the Rayleigh length) is approximately ± 0.5.

The parabolic mirror has a diameter of 22.9 cm, with the center located 12.7 cm from the optical axis; this mirror, as well as an identical one used for focusing the beam on the phase plate, was obtained by cutting and coating a 50.8-cm-diameter parabolic Pyrex blank. The aluminum reflective coating is protected with an overcoat of silicon monoxide. This type of coating is used in all the mirrors in the apparatus; also, all the mirrors located outside the DIII–D vacuum vessel have Pyrex substrates.

After leaving the optical table, the expanded beam is steered to the tokamak by a series of three 23-cm-diameter mirrors and is directed into the DIII–D port by a final 10.2-cm-diameter mirror. The larger mirrors were designed to accommodate a 12.7-cm-diameter beam to be used in the future at a different location in the vessel. The optical path between the parabolic mirror and the entrance port measures approximately 5.5 meters; owing to space constraints, the path could not be made to be planar (see Fig. 3.8). The mirrors are housed in precision gimbal mounts equipped with micrometer adjustments that afford an angular resolution of 0.04 arcseconds. The mounts are installed in turn on gimbaled support mechanisms, which permit coarse initial adjustment and are normally fixed in position.[160] The first two mirrors in the system are anchored to support beams attached to the concrete floor; the following two are mounted directly on the port flange of the DIII–D vessel.

It is particularly important to ensure that the first two mirrors along the optical path are free from vibrations, as they are farthest from the vessel and can cause substantial displacement of the beam before it reaches the tokamak. While the feedback vibration control system can compensate for angular shifts experienced by the beam after traversing DIII–D, *prior* displacements would clearly result in a degradation of the absolute spatial resolution, or worse, in a loss of power from beam clipping. Precisely such a problem was encountered after the reciprocating probe[71] was installed: owing to mechanical coupling between the mirror supports and the probe, the PCI beam experienced large oscillations whenever the probe was fired. This problem was corrected by redesigning the mirror supports and separating them from the probe

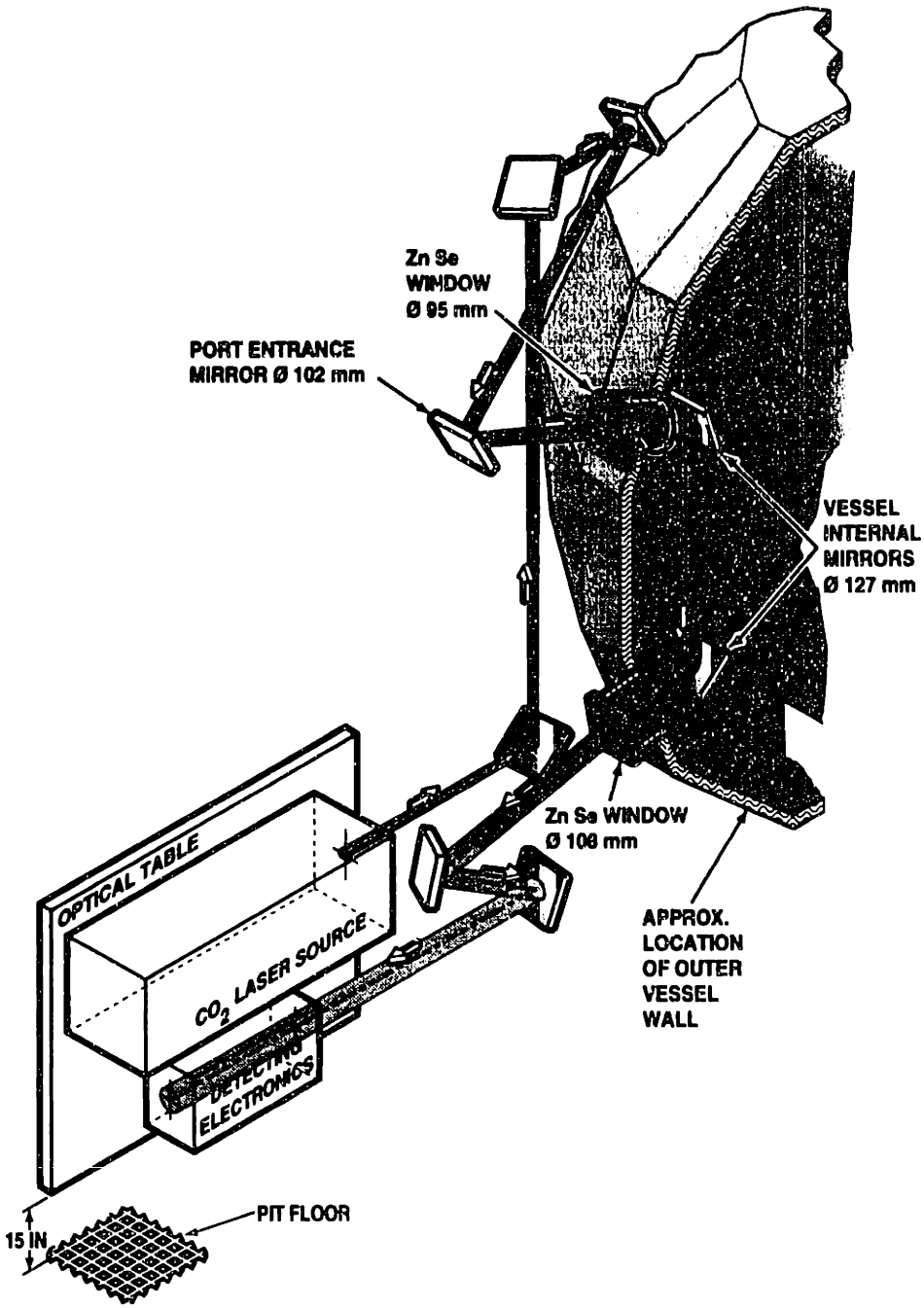

Fig. 3.8 Schematics of optical path.

supports.

The vacuum windows installed on the vessel were supplied by II-VI Inc. (Saxonburg, PA). The windows are made of zinc selenide with an antireflective coating on each surface. The entrance (upper) window has a diameter of 9.5 cm, with a clear aperture of 7.6 cm: this is the aperture stop of the system. The exit (lower) window has a diameter of 10.8 cm, with a clear aperture of 8.9 cm; the larger diameter is designed to accommodate the scattered radiation: indeed, in the absence of an

antialiasing spatial filter, this window would be the effective aperture stop for the scattered radiation from the edge of the beam. The windows are mounted with their normal approximately 1° off the optical axis of the beam, to prevent any residual reflections into the laser cavity. Each window flange houses a series of O-rings that provide the primary high-vacuum seal. The window flange is bolted to a vacuum flange welded to a short section of pipe, which is in turn welded to the main port flange bolted to the vessel. The pipe supports the window assembly as well as an internal tube that holds the in-vessel mirror mount.[160]

The laser beam travels through the port in a nearly horizontal direction (see Fig. 3.4). A mirror, 12.7 cm in diameter, directs the beam vertically through the vacuum vessel immediately in front of one of the ICRF antennas, and a second, identical mirror then steers the beam horizontally through the exit port. The mirrors are made of fused quartz, coated with protected aluminum, and are mounted in a ring attached to the main support assembly. A defect in the design of the mounts initially caused some asymmetric deformation of the mirror surfaces that resulted in a slight astigmatism; this was soon corrected through a design modification. Adjustment of the mirror mounts in the toroidal direction is performed upon installation, after which the mounts are welded in position. Adjustments of each mount in the poloidal direction can be effected from outside the vessel by means of a linear mechanical vacuum feedthrough equipped with a micrometer actuator, which is connected to one of two pivot rods attached to the mirror mount; precision-ground graphite bearings are located between the rods and the support plate. This adjustment capability is essential, as space constraints limited the clear apertures of the mirrors and, consequently, left little freedom in their orientation.

The mirrors and the windows are protected by two inconel shield plates. The original plates were thoroughly redesigned[161] when the inside wall was covered entirely with graphite tiles. The shields themselves were covered with a layer of carbon-carbon composite material (K-Karb). Built into the plate is a shutter that is flush with the plate when closed and can be opened outward to allow passage of the laser light. The shutter is opened and closed by a second linear feedthrough, actuated pneumatically and controlled by computer. The in-vessel mirrors have suffered some minor damage on occasion and have been replaced a few times; no damage has been observed on the windows, which are better protected by their distance from the plasma. Periodic cleaning is necessary to remove accumulated deposits, but the performance of the optical system has never been significantly affected.

After exiting the vacuum vessel, the laser beam returns to the optical table via two additional 23-cm-diameter mirrors, supported by the building floor. The distance between the exit window and the focusing paraboloid is approximately 4 meters. The entire beam path outside the vessel is enclosed by round thin-walled aluminum tubes, and the mirrors are housed in aluminum boxes; the optical table is also totally enclosed by removable panels. These enclosures are designed to protect the optics and to minimize airborne sound waves and turbulence that might interfere with the measurements. The option of lining the enclosures with sound-absorbing

material was left as a possible future improvement in case the initial solution proved unsatisfactory; however, baseline measurements indicated that ambient acoustic noise was undetectable. Electrically conductive loops were carefully avoided in all the support structures and enclosures by installing G-10 fiberglass spacers and inserts at various connections and joints.

The second off-axis parabolic mirror focuses the beam onto the phase plate (see Fig. 3.6) by way of two rotatable mirrors that are part of the feedback stabilization system (described in §3.5). Before reaching the phase plate, the beam passes through a ZnSe beamsplitter: 25% of the power is reflected and imaged onto the position sensor, and the remaining 75% is transmitted to the phase plate.

Four phase plates, on loan from the TCA laboratory in Lausanne, Switzerland, were employed in the initial shakedown tests. Subsequently, three plates were fabricated to our specifications by Infrared Optical Products, Inc. (S. Farmingdale, NY). The plates are one-dimensional filters (i.e., the conjugate area is a central recessed strip) and have three different substrates with different reflectivities: BaF_2, ZnSe, and Ge (see §2.12). The complementary area is coated with protected aluminum; antireflective coatings cover the back surfaces of the ZnSe and Ge plates (the reflectivity of BaF_2 is too low to present a concern). The manufacturer was not able to control the width of the groove within the specified tolerance. After a few iterations, the following widths were obtained, as measured: 635 μm (BaF_2), 700 μm (ZnSe), and 560 μm (Ge). With a focal length of 203 cm, these widths correspond to Q values of 1.76, 1.94, and 1.55, respectively: based on the discussion in §2.11 (part *c*), these values were considered to be acceptable; however, the ZnSe plate has a cutoff wave number that is slightly higher than the ideal value. The majority of the work presented in Chapter 5 was carried out with the 560-μm Germanium phase plate; some work was done with the ZnSe plate, and one ELM study was performed using a TCA reflective plate with a width of 450 μm.

The normal orientation of the groove corresponds to the toroidal direction in the tokamak, so that the measurement is sensitive to wave vectors oriented along the major radius. The angle of incidence of the beam on the phase plate is $\sim 9°$; if the depth of the groove is exactly one eighth of a wavelength, the phase shift caused by it upon reflection will not be exactly 90°, rather 91.1°: this corresponds to a loss in signal amplitude of $[1 - \cos(1.1°)] \simeq 2 \times 10^{-4}$, a clearly negligible factor.

The phase plate is housed in a rotatable ring within a kinematic mirror mount with dual-axis adjustability, mounted in turn on a dual-axis, micrometer-driven, precision translation stage (see Fig. 3.9). This allows the accurate positioning of the phase plate in the focal plane, with the groove intersecting the focal axis. This task is aided considerably by a power meter located behind the phase plate: by virtue of the finite transmissivity of the substrates, the phase plate can be positioned correctly by maximizing the transmitted power.

The correct orientation of the phase plate is established by placing a narrow rectangular opaque object horizontally against the entrance window on the tokamak, and rotating the phase plate until the shadow of the object in the HeNe-laser beam

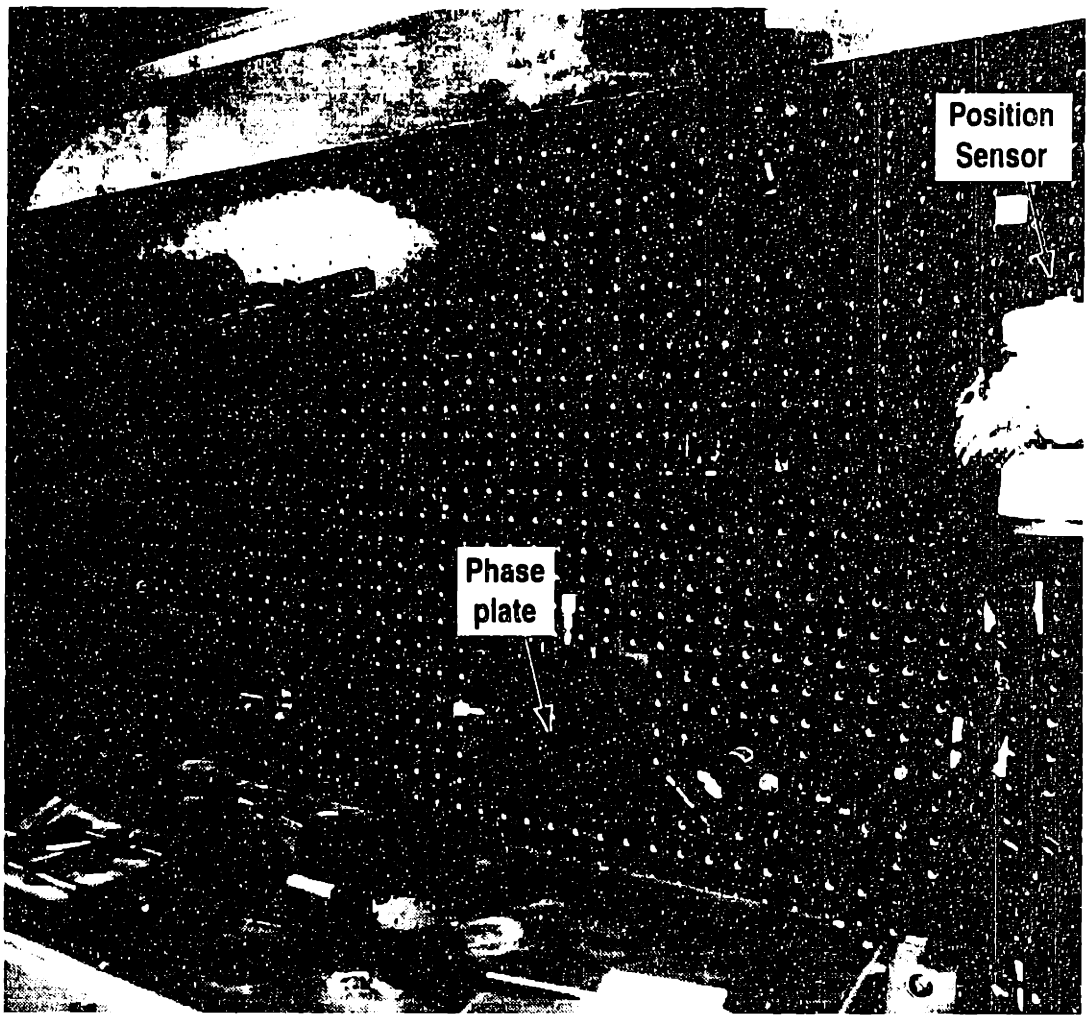

Fig. 3.9 Frontal view of the optical table. The phase plate is visible in the center. To the right of the frame is the feedback vibration-control system.

overlies the groove. The power that reaches the phase plate is approximately 20% of the laser power, i.e., currently, $\sim$ 2.7 W. Thus, the peak energy flux at the center is $\sim$ 5.3 kW/cm^2. All three substrates were tested with incident fluxes approximately twice as large, and no heating was observed over a period of several hours. The installed phase plate is cleaned daily during operations to minimize the likelihood of dust being burned by the beam and damaging the optical surface. No such damage has ever been noticed. Precautions have been taken to protect all objects located near the focal plane, even at some transversal distance from the phase plate, since the rotatable mirrors can displace the beam by a considerable distance: this usually happens after a plasma disruption, when the feedback stabilization system becomes unable to track the beam position.

The beam reflected from the phase plate is passed through two or three ZnSe lenses, depending on the magnification required (see §3.4): the most common config-

uration involves two lenses of focal length 25.4 cm. The lenses, combined with the parabolic mirror, create an image of the DIII-D midplane on the plane of the detector array. The beam is folded by several mirrors that are designed to orient the image plane so that the direction of the linear array corresponds to the radial direction at the object (this procedure is necessitated by the nonplanar nature of the optical path). The orientation procedure is similar to the one used for the phase plate, but the opaque object is now placed vertically; two mirrors are then adjusted iteratively to rotate the beam while keeping the total path constant: the procedure is complete when the shadow of the object in the HeNe-laser beam overlies the detector array.

A second focus is created between the phase plate and the detector: an antialiasing spatial filter, consisting of an iris of variable aperture, is used at that location. This constitutes also the aperture stop for the scattered radiation.

The detector, custom built by Semiconductor Diagnostics, Inc. (Woburn, MA), is a 16-element HgMnTe photovoltaic linear array, operated at the temperature of liquid nitrogen (77 K) and housed in a Dewar, equipped with a ZnSe window with a field of view of 60°. The detector elements are circular with a diameter of 450 μm and a center-to-center separation of 700 μm. The saturation level is approximately 3 W/cm^2, with "soft" saturation beginning around 1 W/cm^2. Back-bias is applied to the detectors to reduce their response time (see §2.12); the bias is of the order of a few mV, but slightly different voltages are applied to different elements in an attempt to obtain matching responsivities. The 3-dB frequency was rated at 100 MHz. While we initially lacked the equipment to test the frequency response, a recent measurement that was carried out with an interferometer setup and an acousto-optical modulator has led us to estimate the 3 dB point at only 20 MHz. Unfortunately, an even larger discrepancy was found in the detector responsivity, which was approximately an order of magnitude lower than rated. With wide variations between elements (up to a factor of five), we measured an average responsivity of $\sim$ 0.15 A/W, corresponding to a quantum efficiency of $\sim$ 2%.

The detector and related electronics, as well as the position-sensor amplifiers, are located in an aluminum box for rf shielding; the box is attached to the optical table (see Fig. 3.7). Two removable covers are attached to the box with bolts, and rf leakage is prevented by fingerstock seals. The box is equipped with two ventilation openings, and air is circulated into the box by an external fan. The laser beam enters the box via an additional opening.

The detector Dewar is equipped with SMA connectors; the signals are carried by short (46-cm-long) coaxial cables to the input SMA connectors of 16 preamplifiers. The preamplifiers, Perry Amplifier (Brookline, MA) model 490, are characterized by low noise (noise figure = 2.8 dB) and wide bandwidth (100 MHz), as rated and confirmed by direct testing. Input and output impedances are 50 Ω, and the gain is 26 dB.

To prevent unwanted noise, the $\pm$12 Vdc voltage required by the preamplifiers and by the detector bias circuits is provided by batteries, also located inside the shield box. An automatic relay circuit interrupts the battery current after each plasma

discharge and restarts it two minutes before the following one. This permits to use only a fraction of the capacity of the battery during a day and prolongs its lifetime. The battery is recharged overnight by an in-built circuit powered by an external ±14 Vdc power supply. The same supply powers all the other electronics (described in §3.6) in the box during operations; a separate power supply is used for the position-sensor amplifiers and sensor bias voltage. Both supplies are ungrounded and draw ac house current through isolation transformers. All the power and ground leads are fed into the box through lowpass EMI filters. The shield box is insulated from the optical table by means of G-10 fiberglass spacers and washers; the ground reference for all the electronic components is taken at a single point on the box, connected by a braided conductor to a main building ground. Ground loops between the box and the optical-table enclosure are avoided by using insulated feedthroughs for the cables exiting the enclosure; differential amplifiers are used at the receiving end, located approximately 60 meters away.

A relative calibration of the PCI diagnostic is generally performed before each plasma discharge. A tweeter is permanently installed in the enclosure of one of the 23-cm-diameter mirrors, located approximately 280 cm from the plasma midplane in the direction of beam propagation. The tweeter, which is driven by an audio amplifier, can launch acoustic waves in a direction equivalent to the radial direction in the tokamak. The amplifier-loudspeaker system operates in the range 2–20 kHz and can generate sound levels of up to 100 dB. The amplifier is driven by a sinewave generator; normally, this is automatically triggered 50 ms before plasma breakdown and gated for a duration of 10 ms. Since standing waves are quickly established in the mirror box, only about the first millisecond is useful for calibration purposes. This procedure permits to account for variations in detector responsivity and other slow changes in conditions. Thorough absolute calibrations are performed during in-vessel maintenance periods ("vents").

3.4 Optical Design

Two main criteria were adopted in the design of the optical system: diffraction-limited performance, and flexibility in the choice of magnification and image orientation.

To satisfy the first criterion, aberrations, as well as wave-front distortions caused by defects in the optical components, had to be minimized. Let us examine the latter effect first. To avoid image degradation from irregularities in the optical surfaces, a "scratch-and-dig" surface quality[162] of 40-20 was specified for most optics: although this parameter is in general of limited importance, this is a safe specification that ensures that the light absorbed or scattered by local defects will be a negligible percentage of the total radiation.

A more relevant parameter is the surface accuracy, which accounts for errors in the radius of curvature and irregularities in the curvature. The accuracy was specified by using the Rayleigh quarter-wave criterion, which permits a maximum deviation of one quarter of a wavelength between the distorted wave front and the ideal spherical wave centered on a selected image point. To account for irregularities in the deformation, the maximum deviation, or optical path difference (OPD), is generally estimated to be between 3.5 and 5 times the rms value. Thus, an rms OPD between one fourteenth and one twentieth of a wavelength is usually required.[162] The OPD produced by a series of optical surfaces is given by the formula

$$\mathrm{OPD}_{\mathrm{rms}} = \left[\sum e^2 A^2 (N - N')^2 (\cos i)^2\right]^{1/2}, \tag{3.2}$$

where e is the individual surface rms error, A is the ratio between the illuminated area and the surface area of the optic, $(N - N')$ is the change in refractive index across the surface (= 2 for a mirror), and i is the angle of incidence of the beam; the sum is taken over all surfaces in the imaging system, i.e., in our case, over all surfaces located between the plasma and the detector.

In our analysis, the illuminated area was taken to be the entire cross section of the Gaussian beam. This is a very conservative approach, as in reality the relevant area is that filled by the scattered bundle emanating from a single point in the plasma; since antialiasing filtering, with a passband $k \leq 10\ \mathrm{cm}^{-1}$, was applied in the majority of our experiments, it follows that the scattered bundle had a full spread of ~ 3.4 mrad, occupying only a small fraction of each optical surface (e.g., a 2.1-cm-diameter circle on the focusing paraboloid). Even in the case of the high-resolution experiment, with $k_{\mathrm{max}} \simeq 40\ \mathrm{cm}^{-1}$, most of the optics are considerably larger than the area intercepted by the bundle (the paraboloid is an effective aperture stop for this case). In addition, it should be remarked that errors in the radius of curvature are corrected in practice by shifting the focal and image planes, further reducing the OPD.

The error budget was distributed unevenly among the optics because of cost considerations. The vacuum windows, being the most expensive item, were specified with the highest tolerance, a maximum peak-to-peak deviation of one fringe per inch (one fringe is one half of a visible wavelength of 650 nm); as a result, the exit window

accounts for a peak-to-peak OPD of 2.6 μm. The contribution of the 23-cm-diameter mirrors is much smaller, in spite of a relatively high tolerance of one half of a fringe per inch, owing to their oversized diameter. All the other optical components have specifications of one fringe or better over the whole surface, and their contributions to the OPD are completely negligible compared to that of the window. Applying Eq. (3.2) to the complete imaging system, using a factor 3.5 between rms and peak-to-peak values, the result is $\mathrm{OPD_{rms}} \simeq \lambda_0/14$ (where $\lambda_0 = 10.6$ μm), as required by the Rayleigh quarter-wave criterion.

The Rayleigh quarter-wave criterion was adopted also in the analysis of third-order aberrations. The aberration OPD was calculated as the sum of the contributions from all the reflective and refractive surfaces in the imaging system, using standard formulas.[149,162] In addition, the various types of transverse aberrations at the image (spherical aberration, coma, astigmatism, Petzval curvature, and distortion) were also separately calculated and compared with the spatial resolution of the measurement. In all the configurations employed, as will be discussed shortly, the peak-to-peak aberration OPD was within a quarter of a wavelength, and the transverse aberrations were much smaller than the size of the detector elements.

The imaging system was designed in stages. The focal length of the paraboloid was maximized compatibly with practical constraints imposed by the dimensions of the optical table. A large f-number is advantageous as it results in smaller aberrations, it reduces the power density on the phase plate, and it allows to increase the groove size, facilitating fabrication and alignment. In addition, the longitudinal tolerance on the position of the phase plate is an increasing function of the focal length. With our value of $F = 203$ cm, the Rayleigh length in the vicinity of the focal plane is ~ 1 cm; with the method of maximizing the power transmitted by the phase plate, described in §3.3, a resolution of a few mm is achieved.

Zinc selenide was chosen as the lens material because of its transparency to visible light, as opposed to germanium. Both two- and three-lens systems were considered. For a given magnification, the distance between object and image being essentially fixed by geometric constraints, a two-lens system has no positional degrees of freedom, whereas a three-lens system has one degree of freedom. A Fortran program was written to calculate the positions of the lenses (with a free parameter in the three-lens case), the aberrations, and the sensitivity of the magnification and of the image position to small positional errors. Several sets of focal lengths were explored.

The majority of the experiments called for a magnification $|M| = 0.15$, to image the Gaussian width of the beam in the plasma onto the length of the detector array. The spatial resolution is equal to the spacing between detector elements divided by $|M|$, i.e., 4.7 mm. Antialiasing lowpass filtering is applied, limiting the bandwidth to the Nyquist spatial frequency $k = 6.7$ cm^{-1}. A simple two-lens system, shown in Fig. 3.10(a), was employed in nearly all the studies discussed in this thesis. Both lenses have a focal length of 25.4 cm; the peak-to-peak aberration OPD is $7 \times 10^{-3} \times \lambda_0$, with the dominant transverse image aberration being a distortion of 2.7 μm: therefore, aberrations are completely negligible. In this configuration, the second

lens is essentially a relay lens; thus, a small shift of this lens produces a change in magnification without altering the image position (to first order): a shift of 1 cm corresponds to a 16% variation in magnification. The position of the image can be fine-tuned with the first lens, using the second one to readjust the magnification. Also, a real focus is formed approximately 2 cm after the relay lens, allowing the convenient placement of an antialiasing iris.

This two-lens setup is robust and easy to align. However, it does not allow large changes in magnification. The two-lens configuration shown in Fig. 3.10(b), with the second lens now having a focal length of 6.35 cm, was used in a high-magnification ($|M| = 1.2$) experiment. In this case only a small fraction of the beam width is imaged onto the detector length, but the spatial resolution is now 0.6 mm. The cross section of the beam can be scanned by adjusting the mirror in front of the detector; however, measurements are confined to the central 4.6-cm-diameter circle to prevent eccessive aberrations. The bandwidth is limited to 40 cm^{-1} by an iris located, again, in a focal plane between the second lens and the detector. With these parameters, the peak-to-peak aberration OPD is $\lambda_0/4$ and the image distortion is 0.2 mm; thus, the Rayleigh criterion is satisfied and transverse aberrations are a factor of 3.5 lower than the detector spacing. The cylindrical mirror ($F = 7.6$ cm) shown in the figure was employed to condense the radiation in the direction corresponding to the toroidal direction in the plasma, to increase the power density and raise the signal-to-noise ratio to an acceptable level (still a factor of approximately 100 lower than in the standard case).

The desire to attain better flexibility in varying the magnification motivated the design of the three-lens systems seen in Figs. 3.10(c) and (d). The focal length of the first two lenses is 25.4 cm and that of the third one is 6.35 cm. The magnification can easily be increased by shifting the last lens away from the detector, without moving the other optics. This convenience is offset by relatively severe aberrations, particularly spherical aberration and distortion; these can be contained by limiting, respectively, the spatial bandwidth and the field of view. The case shown in Fig. 3.10(c) yields a magnification of 0.54 and an attendant spatial resolution of 1.3 mm; with a bandwidth equal to the Nyquist limit, 24 cm^{-1}, the spherical aberration is 0.2 mm; to contain the OPD within the Rayleigh limit, the field of view was then restricted to a 4.6-cm diameter. The case of Fig. 3.10(d) is characterized by $|M| = 0.24$ and a spatial resolution of 2.9 mm; with a Nyquist limit of 11 cm^{-1}, the field of view could be expanded to a 5.5-cm diameter, yielding a distortion of 0.15 mm and a peak-to-peak OPD equal to $\lambda_0/4$.

It should be noted that when the role of the aperture stop is played by an antialiasing iris, set at the Nyquist limit, the transverse spatial resolution at the image, given by the Sparrow criterion,[162] is exactly equal to the detector separation.

The longitudinal resolution at the object, or depth of field, can be evaluated by imposing the near-field condition $Q_d = (k_{max}^2/2k_0) \times |\delta z| < 1$ (see §2.8), where k_{max} is the largest wave number admitted by the system. The resulting limit,

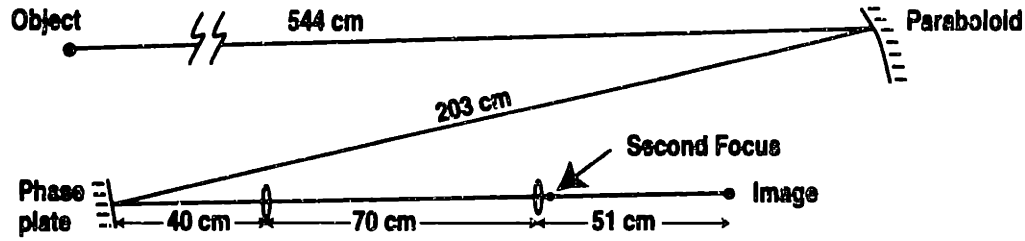

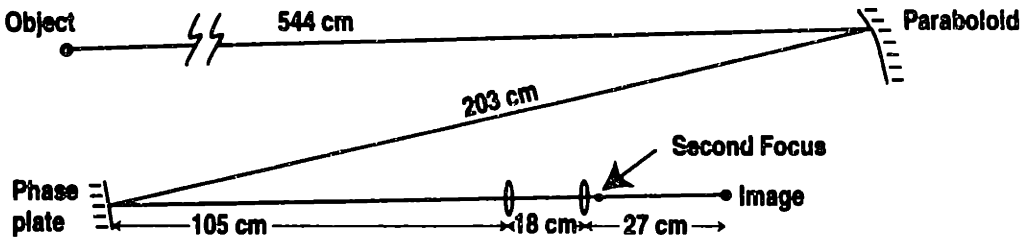

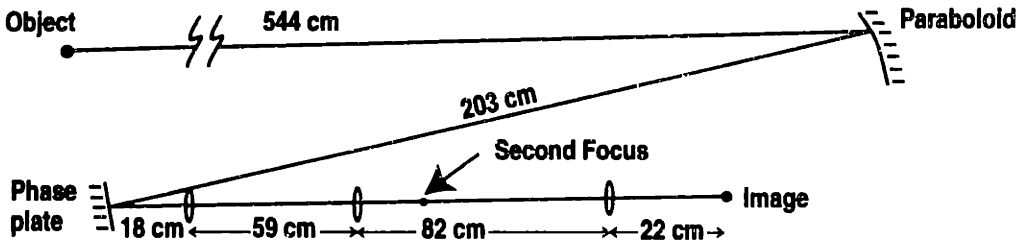

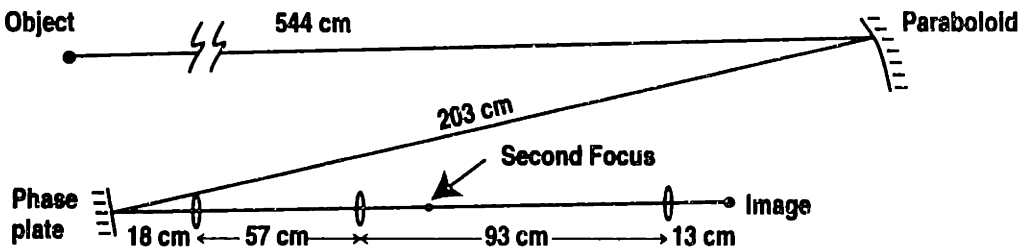

Fig. 3.10 Imaging geometries.

$$|\delta z| < \frac{\lambda_{\min}^2}{\pi \lambda_0}, \tag{3.3}$$

is equivalent, within a factor $\pi/2$, to the Rayleigh quarter-wave criterion applied to the wavefront aberration caused by defocusing.[149] In the most common case, $k_{\max} = 6.7$ cm^{-1}, and $\delta z = \pm 264$ cm; this distance exceeds the length of the plasma column, a consequence of operating in the Raman-Nath regime. In the Bragg regime ($k > 12$ cm^{-1}), the nominal depth of field becomes shorter than the plasma column, and near-field conditions simply cannot be established. In that case the k-dependent longitudinal modulation expressed by Eq. (2.81) must be taken into consideration.

The tolerance on the longitudinal position of the detector is equal to the depth of field times the longitudinal magnification (the square of the transversal magnification). Therefore,

$$\delta z_{\text{image}} \simeq \pm M^2 \lambda_{\min}^2 / (\pi \lambda_0). \tag{3.4}$$

If the bandwidth is set at the Nyquist limit, one can write $\delta z_{\text{image}} \simeq \pm(4/\pi) \times (s^2/\lambda_0)$, where s is the detector spacing; thus, $\delta z_{\text{image}} \simeq \pm 6$ cm.

As was mentioned in §2.14, acoustic waves are a useful tool for verifying the correct location of the detector. A displacement d from the object plane causes the signal from a monochromatic acoustic wave to be reduced by a factor $\cos(k^2 d/2k_0)$ (naturally, the antialiasing filter is removed when an acoustic test is performed). When $d = 264$ cm (the longitudinal tolerance derived above), the first zero of the cosine factor occurs at $k = 8.4$ cm^{-1}, corresponding to a frequency of 46 kHz. Operating between 5 and 20 kHz, where the cosine factor remains very close to 1, a more sensitive procedure is to observe the *scintillation* signal; this is given by the Hermitian component of Eq. (2.80), i.e., by simply replacing the cosine with a sine. With $d = 264$ cm and a frequency of 20 kHz, one finds $\sin(k^2 d/2k_0) \simeq 0.3$; therefore, the imaging is considered correct if the scintillation signal at 20 kHz is less than 0.3 times the phase-contrast signal: usually, for better precision, the position of the image is varied slowly until a point of minimum scintillation signal is found. The change from the phase-contrast to the scintillation configuration is effected very simply by translating the phase plate until all the unscattered and scattered radiation impinges on the complementary area, which then acts simply as a reflector.

Acoustic waves are also used in the important task of centering the antialiasing iris correctly. By launching a wave at a fixed frequency, and then slowly closing the aperture of the iris, the signal should disappear suddenly at a given point; if the disappearance is gradual, the iris is off-center. This test is repeated by launching the wave in the perpendicular direction, and the iris is adjusted over a few iterations.

3.5 Feedback Vibration-Control System

An internal-reference interferometer, such as a phase-contrast imaging apparatus, is insensitive to vibration-induced variations in the path length. This permits in general the achievement of a better sensitivity than that obtained with an external-reference system. However, the phase-contrast technique is vulnerable to vibrations in a different way: if the beam focus is displaced from the phase-plate groove, the contrast is lost and the signal disappears. Thus, angular displacements of the beam are deleterious, while to first order translational shifts are not. The design and successful implementation of a feedback vibration-control system to keep the beam correctly focused was the single most challenging task in the development of this diagnostic.

(a) Design Criteria

The design criteria were based on direct measurements of the vibrations during various plasma discharges, using a HeNe-laser position sensor located in the focal plane. It was found that the dominant component in the vibration spectrum, on both the vertical and the horizontal axis, was an oscillation at $\sim$ 20 Hz, the resonant frequency of the vessel; superimposed on this is a slow irregular drift observed throughout the duration of the discharge (see Fig. 3.11).

The amplitude of the vibrations depends on the magnitude of the currents circulating in the magnetic-field coils, with the ohmic-field coils playing the dominant role; with a plasma current of 2 MA, the 20-Hz vibration in the focal plane is typically of the order of ± 1 mm, while the slower drift ranges from 1 to 2 mm. Higher-frequency resonances are also observed with diminishing amplitudes, as shown in Fig. 3.12. A plasma disruption can cause displacements of up to 5 mm in a very short time scale. For comparison, we recall that the width of the phase-plate groove is in the range 0.56–0.70 mm and that the diameter of the Gaussian focal spot is 0.36 mm.

To evaluate the effect on the measurement of a vibrational shift in the focal plane, it is useful to recall Eq. (2.120), which gives the transfer function of the phase-contrast filter. Expressing the shift in wave-number space as k_s, the modified transfer function is obtained by replacing the function $P_{k_c}(k_x)$ by $P_{k_c}(k_x - k_s)$ [these functions are defined by Eq. (2.113)]. The modified phase-contrast transfer function is now accompanied by a nonzero phase shift in general, and must be defined through the general expression given in Eq. (2.176). By using Eq. (2.118) for the case of an infinite aperture, the transfer function can be written explicitly as a sum of error functions, which reduces to Eq. (2.141) for $k_s = 0$. For simplicity, we express here

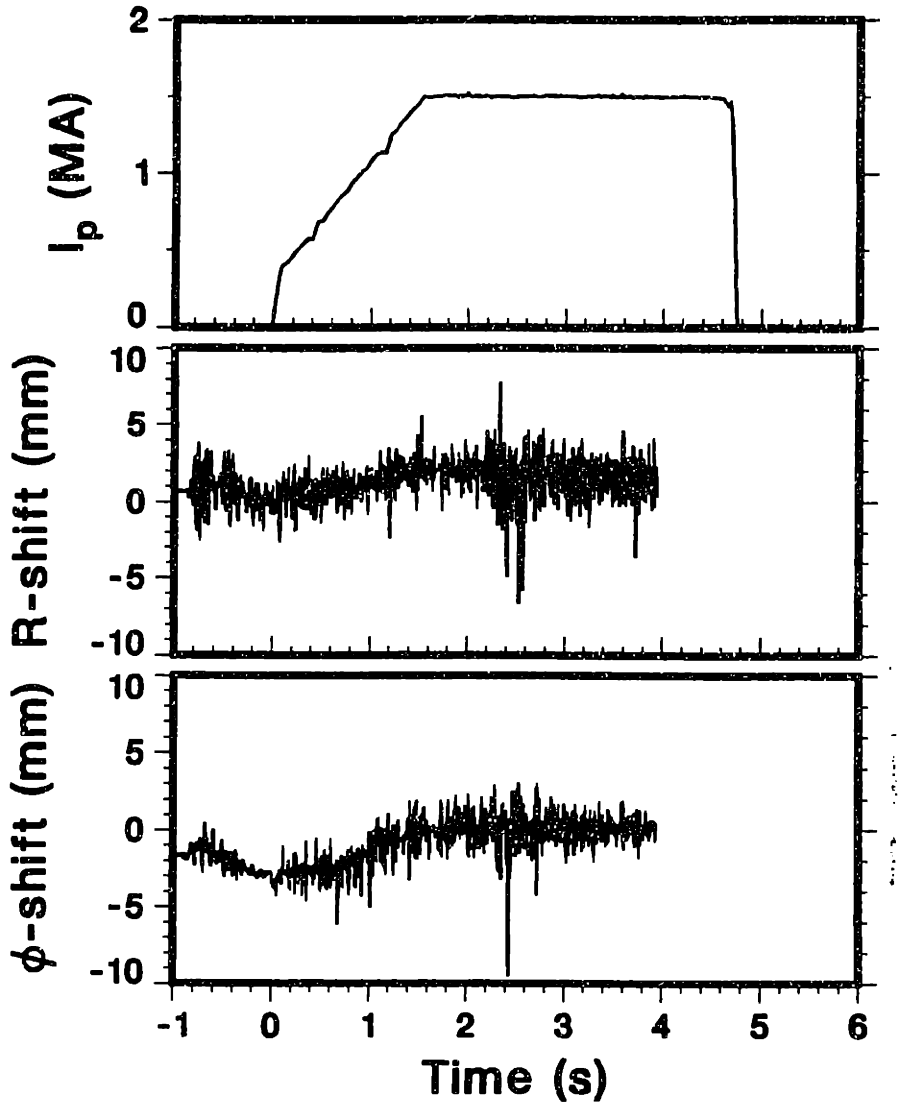

Fig. 3.11 Focal-plane vibrations along the radial (R) and toroidal (ϕ) directions during a plasma discharge.

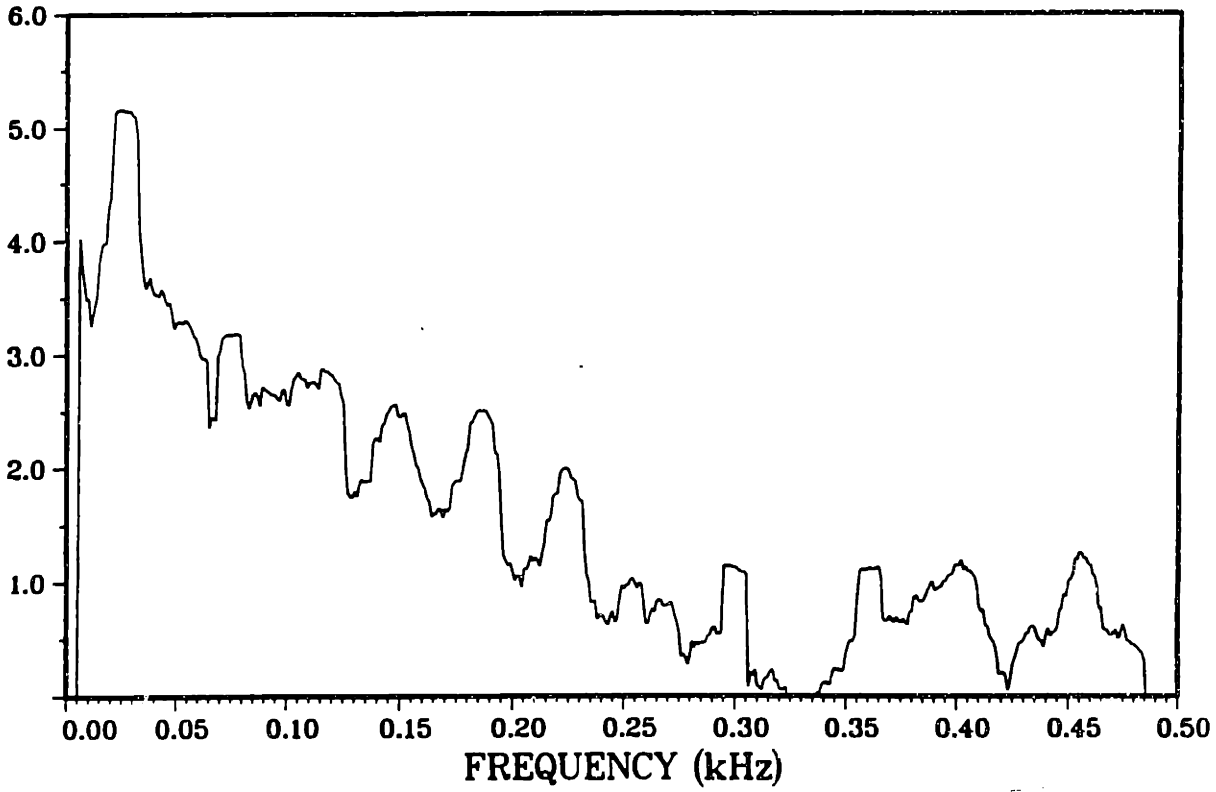

Fig. 3.12 Frequency autospectrum in logarithmic scale of the focal-plane vibrational shift.

the transfer function and the phase in the following form:

$$\begin{aligned}\mathcal{T}(K)\cos\theta(K) = \sqrt{\rho}\,u_0(0)\Big\{&\operatorname{erf}(Q+k_s') + \operatorname{erf}(Q-k_s') \\ &- \frac{1}{2}\big[\operatorname{erf}(Q+K_x'+K_s') + \operatorname{erf}(Q+K_x'-K_s') \\ &\quad + \operatorname{erf}(Q-K_x'+K_s') + \operatorname{erf}(Q-K_x'-K_s')\big]\Big\}, \\ \mathcal{T}(K)\sin\theta(K) = \frac{1}{2}\sqrt{\rho}\,u_0(0)\big[&\operatorname{erf}(Q+K_x'+K_s') - \operatorname{erf}(Q+K_x'-K_s') \\ &- \operatorname{erf}(Q-K_x'+K_s') + \operatorname{erf}(Q-K_x'-K_s')\big],\end{aligned} \tag{3.5}$$

where $Q = k_c w_0/2$, $K_x' = K_x w_0/2$, and $k_s' = k_s w_0/2$.

The percentage variation in the value of the transfer function can be taken as a measure of the error introduced by the shift. By imposing that the error be less than 1% for $k > \pi/w_0$, one can find the condition $|k_s| < 0.13 \times k_c$. With this condition, we also find that the percentage of dc power lost from the phase-plate groove is less than 1×10^{-3}.

The condition $|k_s| < 0.13 \times k_c$ corresponds to a maximum acceptable shift of

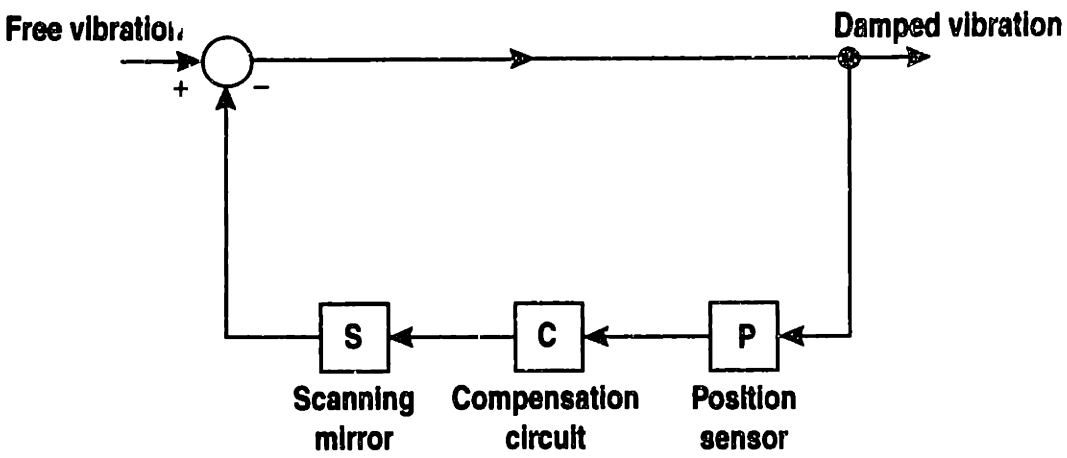

Fig. 3.13 Feedback vibration-control system.

± 35 μm. Thus, on the basis of the measurements performed, it was decided that the minimum requirements for the feedback system would be a damping factor of 1/30 (in amplitude) at 20 Hz and a factor of 1/60 below 5 Hz. The design goals for the suppression factor were set conservatively at 40 dB (1/100 in amplitude) at 20 Hz and 50 dB at 5 Hz. No attempt was made to control the vibrations during a disruption event. The need for a high degree of precision was the main motivating factor behind the choice of a feedback configuration, with the position sensor at the focus, over a simple open-loop compensation configuration, with the position sensor located before the correcting mirror.

The design requirements discussed above apply to the direction perpendicular to the orientation of the groove, i.e., the direction corresponding to the major radius in the plasma. For better control, a second, independent feedback system was also built for the toroidal direction; the damping factors for this system, however, were set a factor of 3 lower than those for the perpendicular system.

The single-loop negative-feedback control system is shown in block-diagram form in Fig. 3.13. Two similar configurations are used for the two degrees of freedom represented by the two perpendicular axes. The position of the beam focus on the phase plate is measured by a dual-axis position sensor located in an image plane of the phase plate. This image is created by a set of optics that utilize a small percentage of the radiation, extracted from the main beam by means of a beamsplitter. The position signals are processed by two electronic frequency-compensation circuits, whose outputs are used to drive two rotatable mirrors located at a distance of 50 cm from the phase plate. The two mirrors control the orientation of the beam in the two perpendicular directions, and attempt to keep the position signals at zero (see Fig. 3.14). The only optical element between the mirrors and the phase plate is the beamsplitter.

In the absence of feedforward control elements, and under the assumption that no vibrational errors are introduced between the rotatable mirrors and the phase plate, the forward path is characterized simply by a unity transfer function. The

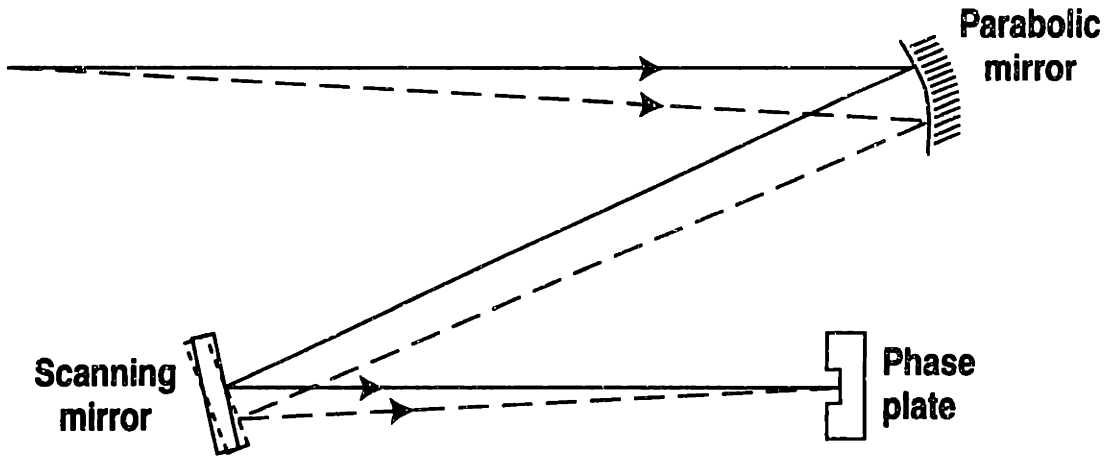

Fig. 3.14 Illustration of the correction mechanism in the feedback system.

feedback elements comprise the position sensing circuit (including the delivery optics, the sensor, and the position-computing circuitry), the frequency compensation circuit, and the rotatable mirrors.

(b) Position-Sensing Circuit

The feasibility of the concept was proven initially by using a visible-light sensor that monitored the position of the colinear HeNe-laser beam. The availability of lateral-effect detectors, providing continuous, approximately linear position measurements over a wide area, lent considerable attractiveness to the visible-light scheme. Minor difficulties included the need to block ambient light from reaching the detection region, and the modest transmissivity of the vessel optics, which initially imposed unacceptable limits on the signal-to-noise ratio and on the related sensitivity. When a 15-mW HeNe laser replaced the original 5-mW model, the sensitivity became satisfactory; however, it was discovered that the laser power was not sufficiently stable for this application: the power flicker introduced a disturbance in the system, resulting in an additional vibration of the focal spot on the phase plate. It was decided then that the system should be based directly on the CO_2-laser beam.

The first quadrant detectors for the 10.6-μm wavelength were being developed commercially at the time our system was being designed. Our sensor was built by Belov Technology (New Brunswick, NJ); it is composed of four square (2-mm side) HgCdTe photoconductive elements in a quadrant configuration (with a spacing of $\sim$ 50 μm), as shown in Fig. 3.15, housed in a Dewar for operation at liquid-nitrogen temperature (77 K). The detectors have a responsivity of $\sim$ 600 V/W (with a bias current of 20–40 mA) and a detectivity $D^* \simeq 2 \times 10^{10}$ Hz cm$^{1/2}$/W. The resistance of the unilluminated element is $\sim$ 50 Ω.

Each position signal is proportional to the difference between the signals from two opposing elements, divided by their sum. These operations are performed by two signal-conditioning amplifiers, United Detector Technology (Hawthorne, CA) model

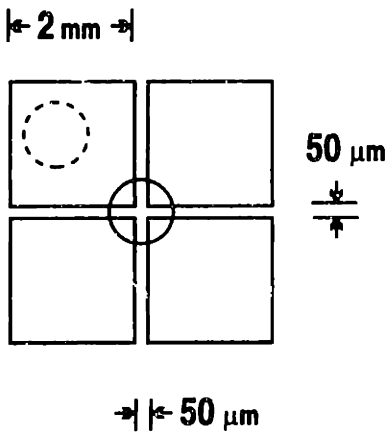

Fig. 3.15 Quadrant position sensor. The solid circle represents a centered focal spot. The dashed circle represents a spot displaced onto one element only: the sensitivity is zero in this case.

301DIV: each module provides an analog output proportional to the position (±10 V at full range) and also one proportional to the sum of the signals, for monitoring purposes. This model is designed for use with visible photodiodes that operate in current mode (see §2.12): thus, the input stage is a transimpedance amplifier. Since the Belov sensors operate in voltage mode, the input stage had to be modified with the addition of an appropriate front-end impedance; we also added the necessary biasing circuit.

Figure 3.16 shows the schematics of the modified circuitry. The common ground of the four sensors is left floating. The four 100-Ω potentiometers are adjusted to equalize the four signals when the detector is unilluminated; the 50-Ω potentiometers are then used to bring the signals close to zero (but not *exactly* zero, to prevent the position signal from becoming too large), to achieve maximum sensitivity. This procedure is repeated every few months to counteract the slow drifts that occur in the system. The bias current provided by the circuit is ∼ 30 mA. Six different values can be chosen, by means of a switch, for the gain of the input amplification stage; this gain is not critical, as the position signal does not depend on it: however, the best performance (largest signal-to-noise ratio) is obtained at a highest gain that does not cause saturation.

To further reduce the noise, especially at 60 Hz, the internal transformers of the units are bypassed and the ±15 Vdc voltage is provided by an external power supply, which is carefully filtered and isolated. To avoid rf interference from ICRF sources, and the attendant amplifier rectification (which was seen early on to constitute a severe problem), the 301DIV modules are located in the shield box that contains all the electronics. The power cables are filtered and the sensor cables are shielded. The position and sum signals are carried by coaxial cables to the control-room area, approximately 60 meters away.

One disadvantage of quadrant detectors over lateral-effect photodiodes is that the "position" signal does not depend linearly on the actual position of the beam spot on the sensor. The response clearly drops to zero when the spot is located on one

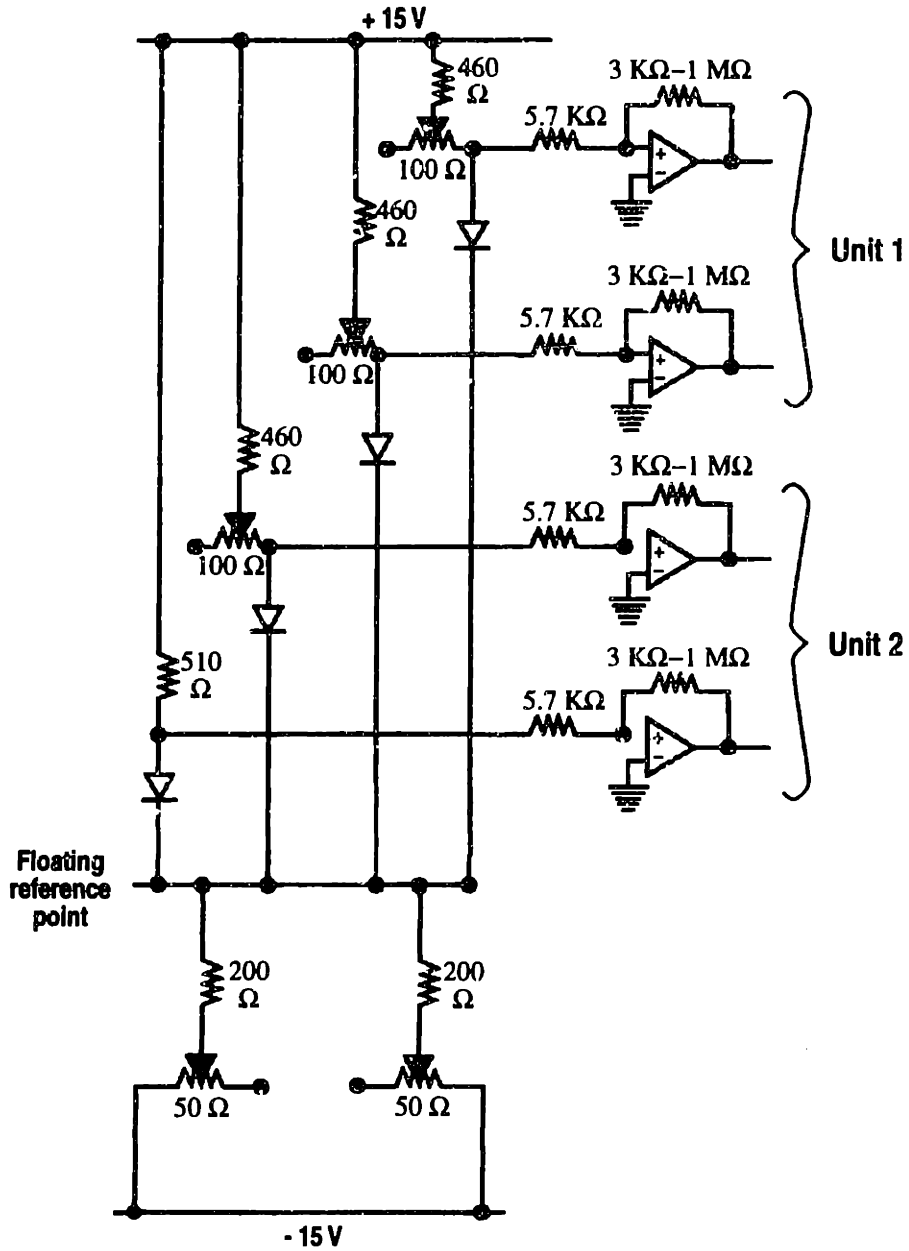

Fig. 3.16 Schematics of the sensor circuitry and input stage of the position-compensation circuit.

element only (see Fig. 3.15). More generally, the sensitivity decreases monotonically as the beam spot moves away from a centered position. Central to the modeling and design of our feedback system was the assumption that the displacement is sufficiently small for the sensitivity to be treated as a constant. The sensitivity at the center can be calculated for a Gaussian spot; in our case, with a focal half-width of 180 μm, the sensitivity (assuming a full-range swing of ± 10 V) is 125 V/mm.

The optics delivering the beam to the position sensor (see Fig. 3.17) serve three purposes: creating an image of the phase plate on the sensor, providing the desired magnification, and attenuating the power to avoid damaging the sensor. In

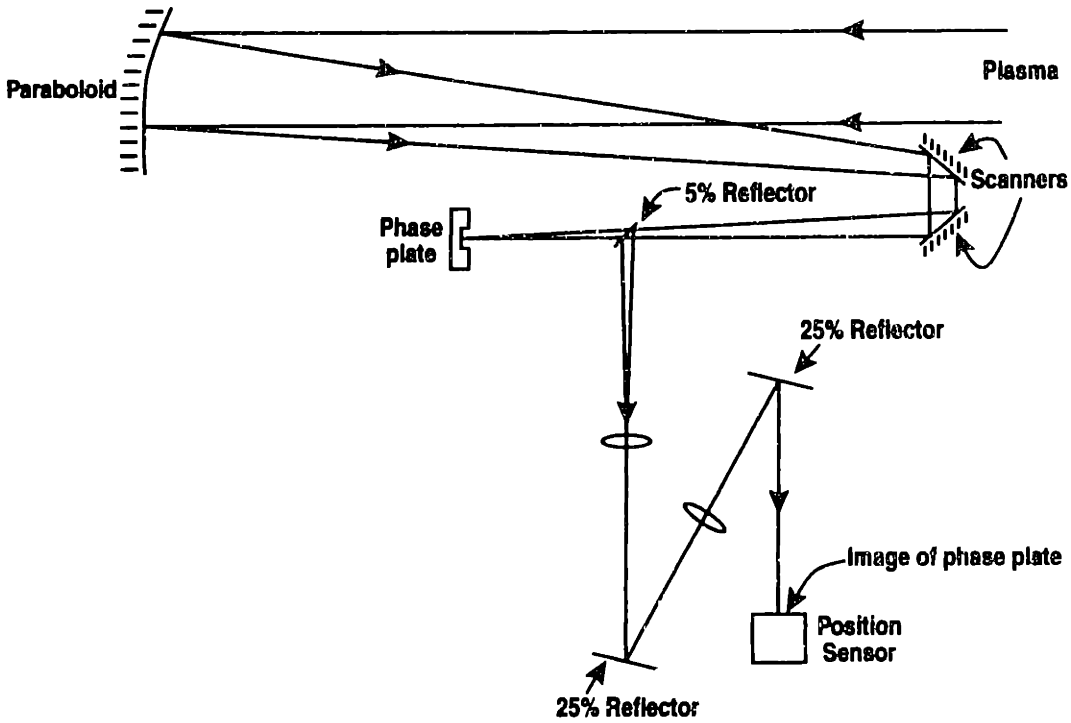

Fig. 3.17 Schematics of feedback-system optics.

the constant-sensitivity approximation, the magnification does not affect the position sensitivity: although the sensitivity is inversely proportional to the spot size, the shifts are also magnified by the same factor. However, it is important to tailor the magnification to obtain a spot size substantially larger than the element separation (50 μm), while keeping the vibration amplitude sufficiently small to allow operating essentially in the linear regime. Also, it should be noted that by increasing the spot size, the flux saturation level is reached at a larger overall power, resulting in a better signal-to-noise ratio. In our system we opted for a magnification of 2.5: hence, the Gaussian width at the sensor is 0.9 mm.

The saturation level of the sensor elements is of the order of 10 mW/cm^2. An extended region of "soft" saturation exists above this power level, with the responsivity progressively decreasing, but with the signal still slowly increasing. Flux levels of the order of 3 W/cm^2 can be handled safely. Operating well into the saturation regime is advantageous, since the responsivity is not a factor in the position calculation, while the signal-to-noise ratio is larger at higher signal levels.

The beamsplitter has a front-surface reflectivity of 25%, while the back surface is antireflectively coated. Two additional partial reflectors along the path further reduce the power by a factor of 80, down to a final level of 10 mW (and a maximum flux on the sensor of 3.1 W/cm^2). A beamsplitter with a much lower reflectivity would prevent this loss of essentially one quarter of the available power: however, direct testing showed that in that case the residual reflectivity from the back surface of the beamsplitter generates a ghost image that significantly disturbs the performance of the feedback system. In addition, the discussion of §2.12 proved that at the present

power levels the sensitivity of the diagnostic depends only weakly on power (cf. Fig. 2.26).

The position of the sensor is fine-tuned with the feedback system in operation. A deliberate angular displacement is introduced in the beam by tilting one of the mirrors in the optical path, typically the parabolic mirror. If the sensor is in the correct location, the beam focus should not move from the phase-plate groove; if the spot moves, the position of the sensor is corrected slightly and the process is iterated until the desired configuration is obtained. This testing procedure is quite accurate, as very small shifts on the phase plate can be detected by monitoring the power transmitted by it.

(c) Scanning Mirrors

Several solutions were considered for the rotatable mirrors. The two key requirements, range and speed, are difficult to satisfy simultaneously. Motors lack speed and piezoelectric devices do not have sufficient range. The choice fell on scanning mirrors mounted on galvanometers, manufactured by General Scanning Inc. (Watertown, MA). With these devices, the deflection of the mirror is proportional to the applied current, supplied by an amplifier. The amplifier has external offset and gain controls; the gain can be varied by a factor of six. The resonant frequency of the scanner decreases and the range increases with increasing size; since the available range was generally adequate for our purposes, increasing the resonant frequency was the first priority. The required mirror size depends on the distance of the mirrors from the focal plane: as will be discussed at the end of this section, the perturbation introduced by the feedback system is mimimized by maximizing this distance. This conflicts with the frequency requirement. The compromise choice was a distance of 50 cm; the scanners selected have resonant frequencies in the range 90–100 Hz.

The analysis of a linear and stationary control system is best carried out through the Laplace transformation.[163] In the Laplace-variable space, the closed-loop transfer function can be written

$$T(s) = \frac{G(s)}{1 + G(s)H(s)}, \tag{3.6}$$

where $G(s)$ is the forward transfer function and $H(s)$ is the feedback transfer function. In our case, $G = 1$ and, referring to Fig. 3.13, we can write

$$T(s) = \frac{1}{1 + P(s)C(s)S(s)}, \tag{3.7}$$

where P, C, and S are the transfer functions of the position-sensing circuit, of the frequency-compensation circuit, and of the scanning mirror, respectively.

A prerequisite to the design of the compensation circuit is a knowledge of $P(s)$ and $S(s)$. Although we are chiefly concerned with the low-frequency range, the magnitude of the required damping factor is such that the high-frequency (up to 2–3

kHz) characteristics must also be considered in a stability and response analysis. The bandwidth of the position-sensing circuit is defined by the 301DIV amplifiers and is $\sim$ 10 kHz; thus, $P(s)$ can be approximated by a constant.

The frequency response function of the mirrors, $S(i\omega)$, was determined experimentally by applying a sinusoidal input to the scanner driver and measuring the amplitude and phase of the corresponding deflection (by means of a position sensor). The transfer function $S(s)$ is the analytic continuation of $S(i\omega)$. [We are using here, as is customary in control theory, the "engineering" convention for the sign of ω: a harmonic term is represented by the exponential $\exp(+i\omega t)$.] The response functions for the two mirrors are plotted in Fig. 3.18 in the form of Bode diagrams (log-magnitude and phase). The behavior of these curves suggests that the scanners may be modeled approximately as forced oscillators. The transfer function of an oscillator can be written

$$S(s) = \frac{\omega_n^2}{s^2 + 2\zeta\omega_n s + \omega_n^2} S(0), \tag{3.8}$$

where ω_n is the natural, or resonant, angular frequency and ζ is the damping ratio. The parameters are derived from experimental measurements by means of least-squares fits: the values obtained for $\nu_n = \omega_n/(2\pi)$ for the two mirrors were 99 Hz and 87 Hz, and the damping ratios were 0.07 and 0.13, respectively. The time constant ($1/e$ time in response to a step input) is equal to $1/(\zeta\omega_n)$, i.e., 23 ms and 14 ms, respectively, for the two mirrors.

This initial model was then improved by including a time delay, and an additional pole to account for a faster descent at high frequency: the result is

$$S(s) = \frac{\omega_n^2}{s^2 + 2\zeta\omega_n s + \omega_n^2} \frac{e^{-s\tau}}{1 + s/\omega_d} S(0)\sigma(s), \tag{3.9}$$

where $\omega_d/(2\pi) \simeq 270$ Hz and $\tau \simeq 65$ μs for both mirrors. The function $\sigma(s)$ is not modeled explicitly: it accounts for high-frequency irregularities, such as the secondary resonance at $\sim$ 2.9 kHz (see Fig. 3.18), and it is equal to unity at low frequency.

(d) Design of the Compensation Circuit

Ideally, the optimal transfer function of the compensation circuit, $C(s)$, can be obtained by dividing the desired open-loop function by P and S. In practice, there are usually several constraints that force departures from the "ideal" transfer function. The principal challenge lies in obtaining the desired overall gain at low frequency (20 Hz) without rendering the system unstable at high frequency. The system is stable if and only if all the poles of the closed-loop function $T(s)$ have negative real parts. The poles of T are the zeros of the function $1 + PCS$.

Our compensation circuit was built from a combination of integration, derivative, phase-lead, and phase-lag networks, whose poles and zeros are real and negative. The

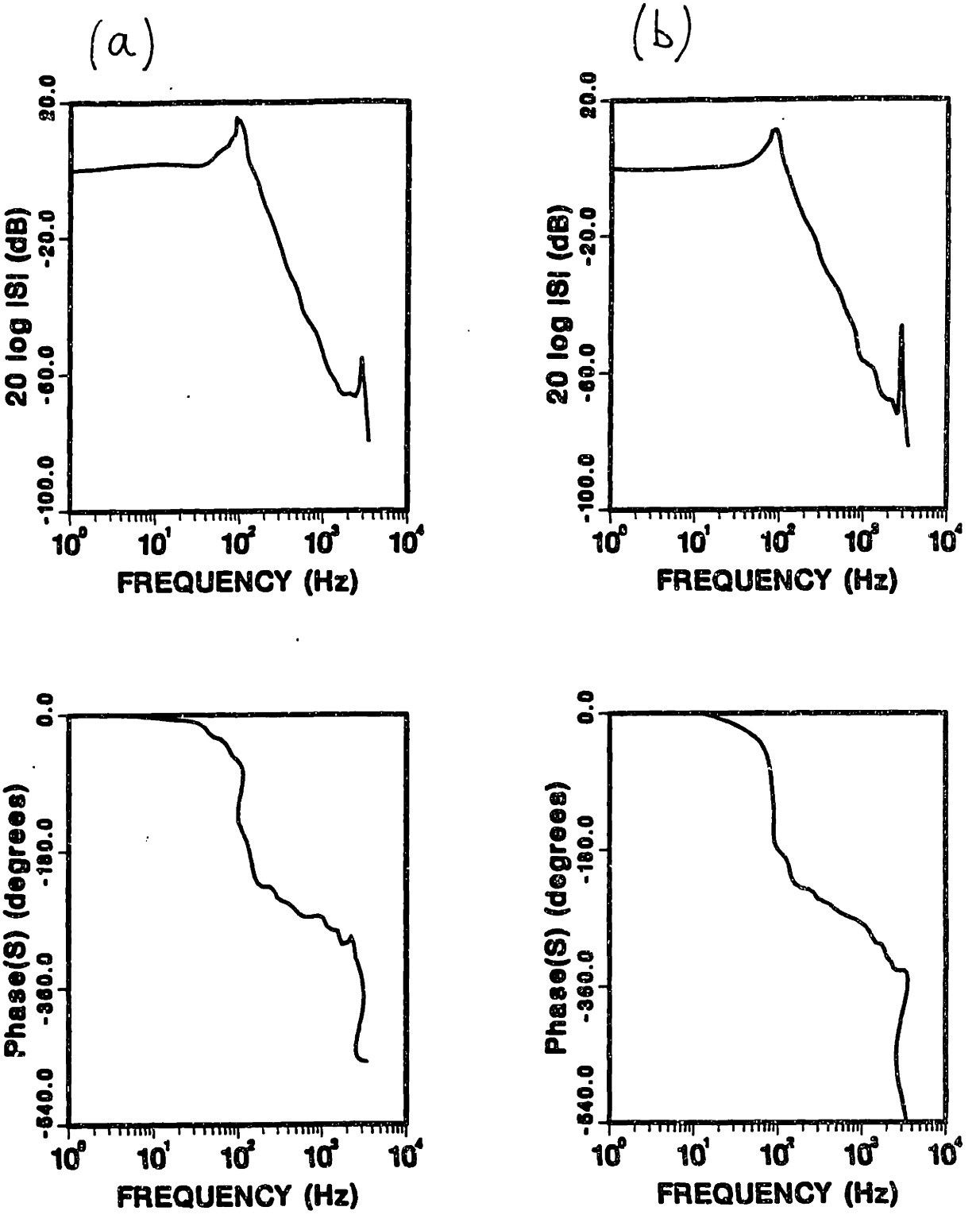

Fig. 3.18 Bode diagrams for the two scanning mirrors used in the feedback system.

poles of $S(s)$ [cf. Eq. (3.9)] are $s = -\zeta\omega_n \pm i\omega_n(1-\zeta^2)^{1/2}$ and $s = -\omega_d$; their real parts are also negative (an obvious consequence of the stability of the scanners!). It follows that all the poles of $1 + PCS$ lie in the left-hand s-plane. Also, since all polynomial coefficients in the open-loop function PCS are real, a contour that is up-down symmetric in the s-plane maps onto a similarly symmetric contour in the PCS-plane.

In the light of these observations, it is convenient to employ the *Nyquist stability criterion*[163]. First, we draw the Nyquist contour in the s-plane, shown in Fig. 3.19(a): the integration limits on the imaginary axis are $\pm\infty$, so the contour encloses the entire right-hand s-plane. We then map this contour onto the PCS-plane, as shown in Fig. 3.19(b) (for two different cases). The Nyquist criterion, for an open-loop function free of poles with positive real parts, states that the feedback system is stable if and only if the PCS-plane contour does not encircle the $(-1, 0)$ point. Under the assumption that the open-loop function PCS is zero for $|s| \to \infty$, and by virtue of the up-down symmetry of the plot, the Nyquist criterion can be restated in the following way: at any point in which the phase of PCS is 180°, the modulus $|PCS|$ must be smaller than one. Figure 3.19(b) shows an example of a stable system and one of an unstable system. This criterion has a simple intuitive meaning: when the phase is 180°, the feedback becomes positive instead of negative, and the error signal is reinforced rather than damped: if the modulus of the open-loop transfer function is larger than one, the error is amplified indefinitely and the system becomes unstable.

The alternative formulation of the Nyquist criterion can be utilized in a natural fashion to define the *relative* stability of the system. Two measures of relative stability are the *gain margin*, i.e. the value of $1/|PCS|$ at the frequency at which the phase angle reaches 180°, and the *phase margin*, i.e. the smallest phase lag that has to be added before the system becomes unstable. In general, increasing the margins serves to shorten the damping time in response to a step-function input. In the frequency domain, the margin region is one where, if the margin is too small, the closed-loop transfer function may have a modulus larger than one, that is, it may amplify rather than dampen vibrations. Thus, it is important to evaluate not only the open-loop transfer function, to ensure that the system is stable, but also the closed-loop transfer function, to ensure that the phase and gain margins are sufficiently large to avoid undesired amplification.

The model for the transfer function of the scanner, expressed by Eq. (3.9), was used as a guide in the development of the compensation circuit. A function of the type $s^2 + 2\zeta\omega_n s + \omega_n^2$ would compensate the oscillator component perfectly. However, this function is difficult to obtain in practice, owing to saturation problems and high-frequency instabilities. We opted therefore for a function of the type $(1+s\tau_a)(1+s\tau_b)$, corresponding to a double-derivative network; an additional derivative, $(1 + s\tau_c)$, was added to compensate the $(1 + s/\omega_d)^{-1}$ term in $S(s)$ and prevent an excessively rapid descent at high frequency. A lag network, $(1 + s\tau_d)/(1 + s\tau_e)$, with $\tau_d < \tau_e$, was added to enhance the response around 20 Hz. We then added a second lag network, $(1 + s\tau_f)/(1 + s\tau_g)$, to provide better control over the high-frequency response; and

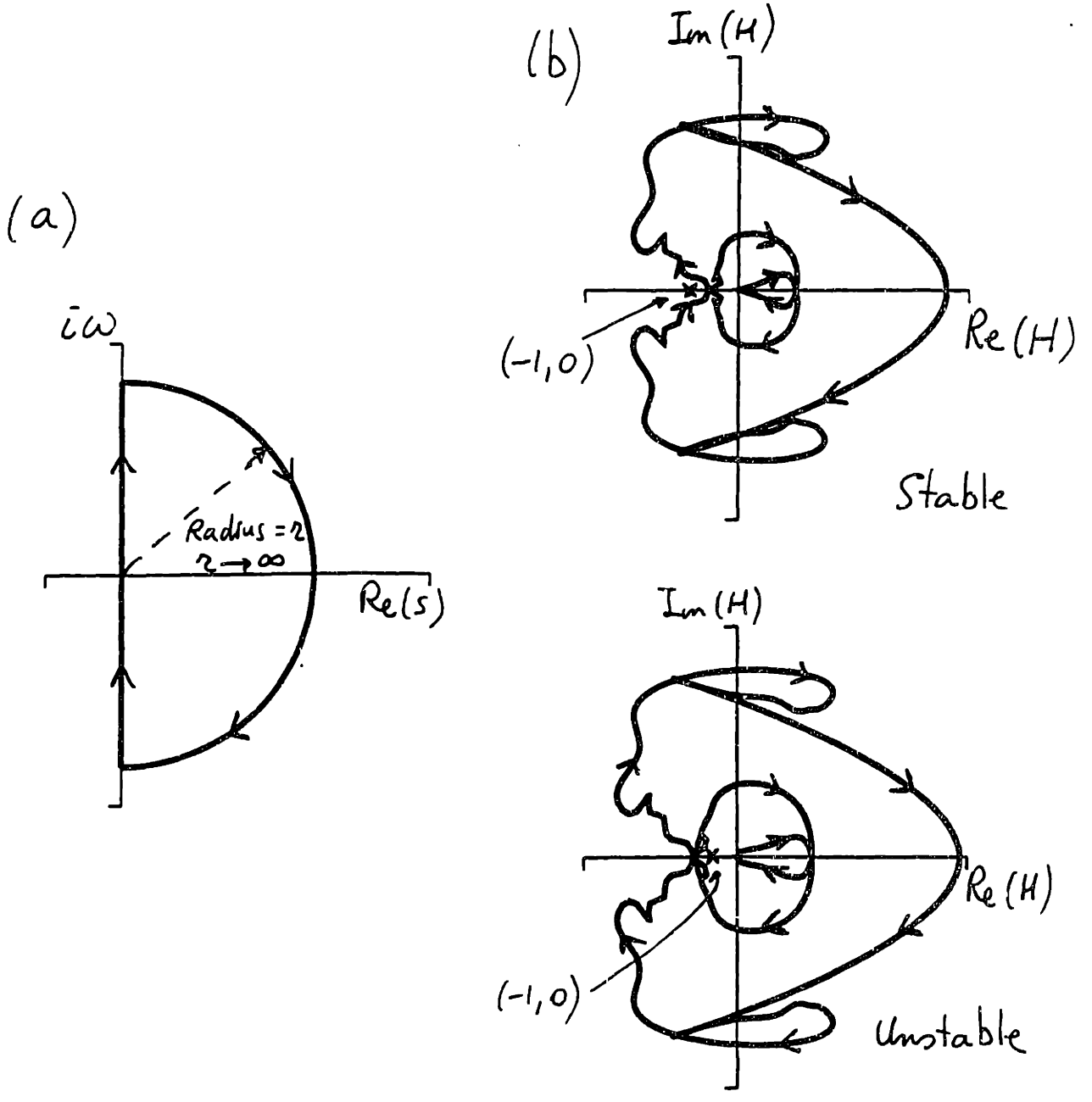

Fig. 3.19 (a) Nyquist contour; (b) mapping for $H(s) = PCS(s)$, for a stable case (top) and an unstable case (bottom).

finally we included an integrator (with a low-frequency limiter) $(1+s\tau_h)^{-1}$ to enhance the low frequencies. The resulting function has five zeros and three poles, thus it diverges quadratically at high frequency; therefore, it was necessary to add also a four-pole rolloff function to prevent resonances at very high frequency. The complete transfer function is then

$$C(s) = \frac{(1+s\tau_a)(1+s\tau_b)(1+s\tau_c)}{(1+s\tau_{\rm ro1})(1+s\tau_{\rm ro2})(1+s\tau_{\rm ro3})(1+s\tau_{\rm ro4})} \frac{1+s\tau_d}{1+s\tau_e} \frac{1+s\tau_f}{1+s\tau_g} \frac{1}{1+s\tau_h} C(0), \tag{3.10}$$

where the $\tau_{\rm ro}$'s are the rolloff times.

The logical steps described above allowed us to obtain tentative values for all the τ parameters, resulting in a function that approached the design requirements. At this point a Fortran program was developed to scan the 12-dimensional parameter space in a region around the initial values, in order to optimize the global transfer function. The optimization criterion consisted of maximizing the ratio of the gains ($|PCS|$) calculated at 20 Hz and at the 180° point, without exceeding a given phase margin. The set of τ parameters defines the *relative* open-loop function; the global gain can then be varied as an independent parameter to control the gain margin. This numerical analysis did not employ the approximate function $S(i\omega)$ derived from the model; rather it used the actual measured values at a discrete set of frequency points, including the second resonance at $\sim$ 2.9 kHz. This program was rather CPU-intensive and was run on the NERSC Cray-2 supercomputer at Lawrence Livermore National Laboratory. The results for different values of the phase margin were evaluated by calculating the closed-loop transfer function and also by experimental testing.

For the sake of brevity we shall discuss only the principal (radial) feedback system. The results for the second circuit are qualitatively similar, with some changes due to the slightly different response of the mirror. In Fig. 3.20 are shown the calculated open-loop [Fig. 3.20(a)] and closed-loop [Fig. 3.20(b)] transfer functions for three values of the phase margin (20°, 30°, and 40°) and for a gain margin of 1.4. All three systems satisfy the design requirements, both theoretically and experimentally. The Nyquist diagrams of Fig. 3.19(b) correspond to the 20°-margin system, and to gain margins of 1.4 (stable curve) and 0.7 (unstable curve). It should be noted that at the second resonance (2.9 kHz) the gain is above unity, but the overall phase at that frequency is near zero and the system remains stable.

The choice of the phase and gain margins depends on the details of the closed-loop transfer function in the high-frequency range (> 100 Hz). The phase margin is reached in the vicinity of 200 Hz; since vibrations in that frequency range are not negligible, a damping ratio of approximately 0.2 is desirable. It is also important to avoid large amplification factors at all frequencies. Systems characterized by the three phase margins documented in Fig. 3.20 were employed and tested extensively, and our preference went to the most aggressive configuration, that is, the 20° system. The τ parameters for this system are as follows: $\tau_a = \tau_b = \tau_c = \tau_d = 1.8$ ms; $\tau_e = \tau_h = 32$ ms; $\tau_f = 78$ μs; $\tau_g = 320$ μs; $\tau_{\rm ro1} = 15$ μs; $\tau_{\rm ro2} = 13$ μs; $\tau_{\rm ro3} = 36$ μs; and $\tau_{\rm ro4} = 3.7$ μs.

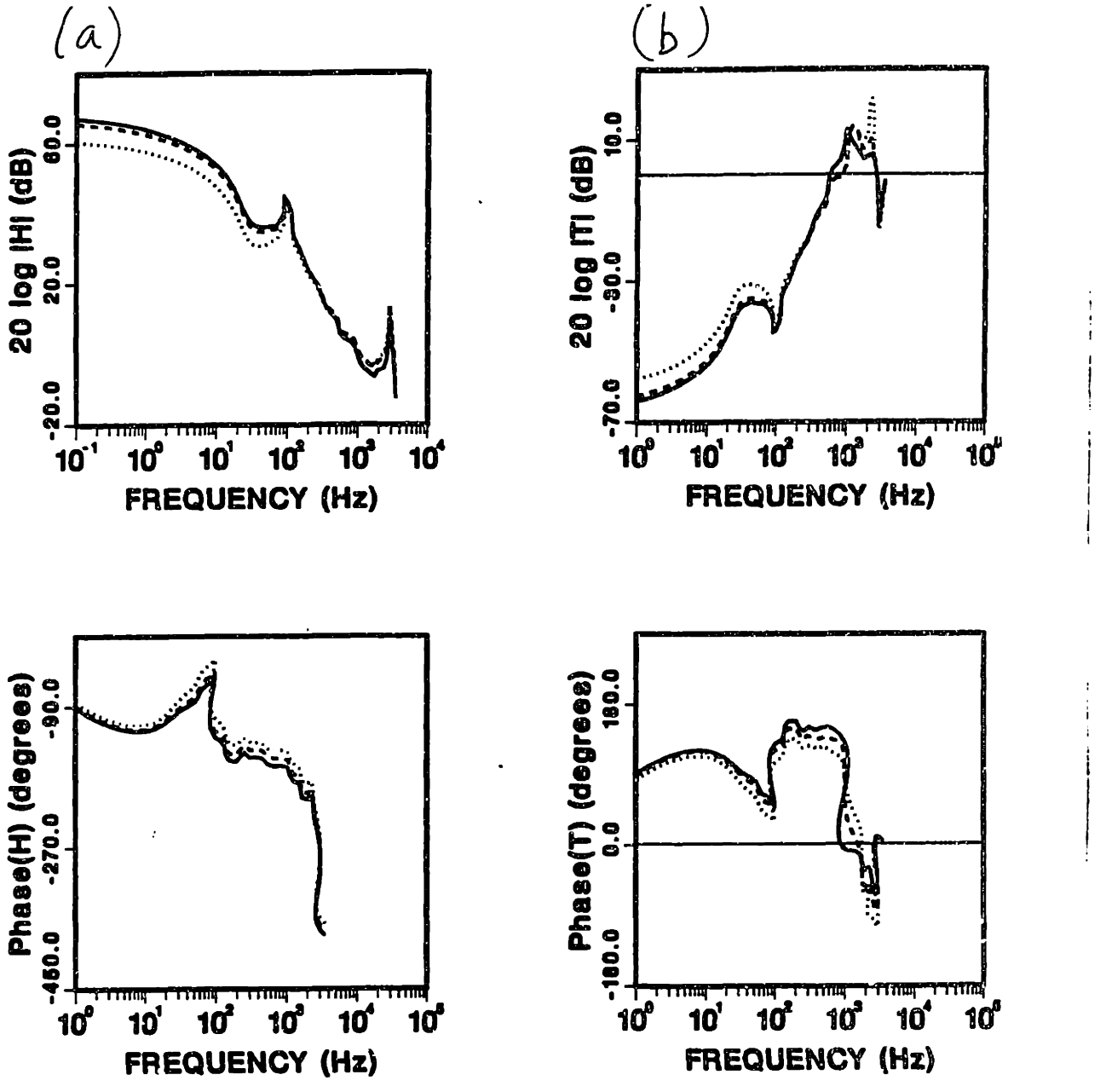

Fig. 3.20 (a) Open-loop and (b) closed-loop transfer functions, in the form of Bode diagrams, for phase margins of 20° (solid lines), 30° (dashed lines), and 40° (dotted lines). The gain margin is 1.4.

Once the system is in place, the gain margin remains a free parameter, as it can be varied by an overall gain control. We used a modified Nichols chart[164] to aid in the choice of the optimal gain. A Nichols chart is normally defined for a unity feedback transfer function; in our modified version, we defined it for a unity forward transfer function, which corresponds to our case. [Our chart can be obtained from the standard one by a simple 180° rotation about the $(-180°, 0\ \text{dB})$ point.] The coordinate system of the chart is defined by the phase (abscissa) and by the logarithm of the modulus (ordinate) of the open-loop transfer function $H = PCS$; the chart itself is simply a set of phase and log-magnitude contours of the closed-loop transfer function $1/(1 + PCS)$.

Figure 3.21 shows a Nichols chart with a set of curves, each of which represents the $PCS(i\omega)$ locus that corresponds to a particular dc gain value, for the 20° system. The dashed line corresponds to a gain that causes unacceptable amplification of secondary vibrational frequencies; the solid lines are considered acceptable. A dc gain of 2560 (68 dB), corresponding to a gain margin of 1.4, was chosen as the optimal operation point. The very high value of the dc gain implies that steady-state shifts are corrected with a high degree of accuracy.

A compensation circuit with the desired transfer function can be obtained in simple and inexpensive fashion utilizing two operational amplifiers and a combination of resistors and capacitors, as shown in Fig. 3.22. The values of the resistances and capacitances are calculated from the desired τ values by solving the set of equations shown in the figure. A simple Fortran program was written to carry out this calculation routinely.

The circuitry for the compensation circuits relative to the two directions of vibration was assembled in a box with input and output BNC connectors; a reset button was included on each channel to set the output voltage transiently to zero, for alignment purposes. The resistors and capacitors are not hard-wired, rather they are housed in IC sockets for easy interchangeability. The box is located in a room, called the "annex", adjacent to the DIII–D control room. The position signals are carried from the tokamak hall to the annex by twisted-shielded cable pairs, and are then conditioned by differential-input CAMAC amplifiers (Aeon 3204 modules) to avoid any ground loops. The amplifiers can also provide additional gain control as needed, although they are normally set at unity gain. The outputs from the amplifiers are fed into the compensation circuits; the same signals are monitored on an oscilloscope during operations and are also digitized and recorded. The output signals from the compensation circuits are used to drive the scanner controllers, also located in the annex; these units provide a separate output, proportional to the current driven in the galvanometers, for monitoring purposes: these signals are also digitized during plasma discharges. Finally, the output currents are carried to the scanners in the machine hall by twisted-shielded cable pairs.

(e) Sensitivity and Resolution

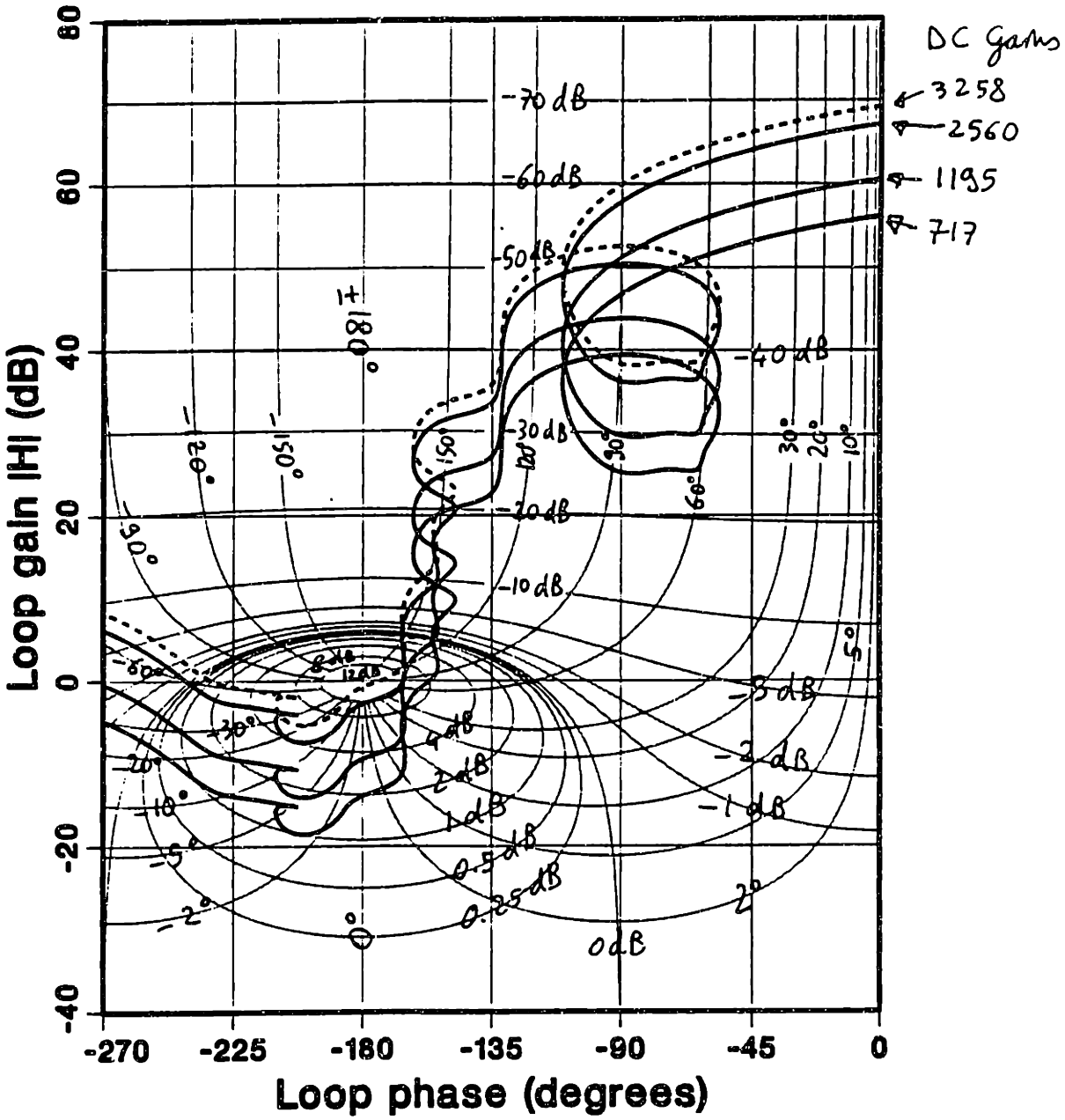

Fig. 3.21 Modified Nichols chart of constant-magnitude and constant-phase contours of the closed-loop transfer function.

The overall gain of each individual component of the feedback circuit can be adjusted, so the required global dc gain can be distributed in different ways among

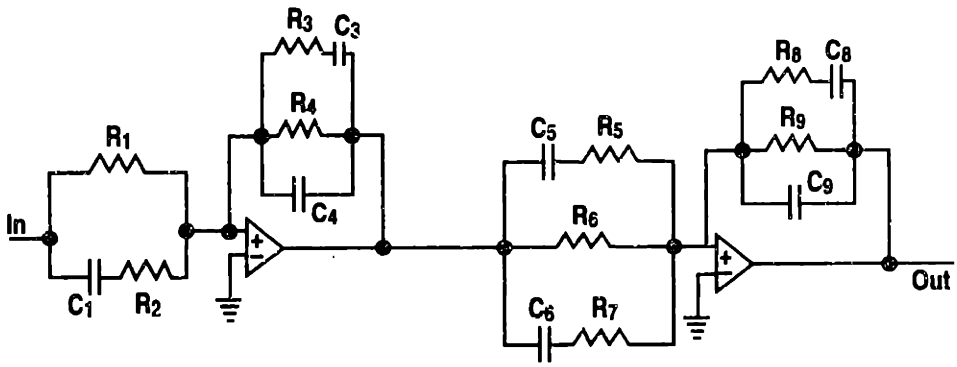

$R_1C_1 = \tau_b$
$R_2C_1 = \tau_{ro1}$
$R_3C_3 = \tau_c$
$R_4C_3 = \tau_e - \tau_c$
$R_3C_4 = \tau_{ro2}$

$\frac{R_4}{R_1} \times \frac{R_9}{R_6}$ = dc gain

$R_5C_5 = \tau_g$
$R_6C_6 = \tau_f \tau_a / \tau_g$
$R_6C_5 = \tau_f + \tau_a - \tau_g - \frac{\tau_f \tau_a}{\tau_g}$
$R_7C_6 = \tau_{ro3}$
$R_8C_8 = \tau_d$
$R_9C_8 = \tau_h - \tau_d$
$R_8C_9 = \tau_{ro4}$

Fig. 3.22 Schematics of the compensation circuit and defining equations.

the components. This decision is chiefly dependent on sensitivity considerations. The ultimate limit to the precision of the error correction attained by the feedback network is determined by the signal-to-noise ratio. The average squared error on the position can be formally written as follows:

$$(\delta x)^2 = \int \frac{|PCS|^2\varepsilon_p^2 + |CS|^2\varepsilon_c^2 + |S|^2\varepsilon_d^2 + \varepsilon_m^2}{|1 + PCS|^2} \frac{d\omega}{2\pi}, \tag{3.11}$$

where ε_p^2 is the squared intrinsic positional uncertainty per unit frequency of the position-sensing circuit, ε_c^2 is the noise associated with the compensation circuit (at input), ε_d^2 is the input noise from the scanner electronics, and ε_m^2 is a disturbance in the mirror position.

For a given value of PCS, the effect of ε_p and ε_m on the spot position is fixed; the effects of ε_c and ε_d, however, can be minimized by minimizing $|CS|$ and $|S|$, respectively. Hence, the best performance is obtained by maximizing $|P|$. The value of $|P|$ can be varied via a range control on the 301DIV unit: the maximum value corresponds to an output swing of ± 10 V, as mentioned earlier. The individual gain values of the various components are as follows: the position-sensing circuit, as seen earlier, has a gain of 125 V/mm; the input and output stages (op-amps) of the compensation circuit provide dc gains of 0.16 and 4.14, respectively; and the driver-scanner system has a dc responsivity in the range 18–72 mm/V.

The gain control on the scanner driver is very useful for locating the optimal operation point. By increasing the gain, one can reach an unstable point, characterized by the sudden onset of a steady sinusoidal oscillation at the 180° frequency ($\sim$

1.3 kHz). From this point the gain must then be reduced by an amount equal to the desired gain margin.

It must be remarked that the gain of the position-sensing circuit is such that its output signal reaches saturation (±10V) when the displacement of the spot is only 0.2 mm on the phase plate, and 0.5 mm on the sensor. Therefore, accurate positioning is necessary before the feedback loop can be closed. The offset controls on the scanner drivers are quite useful in this respect. In addition, when the loop is closed, the offset control can be used for very fine adjustments, since its range is now reduced by a factor equal to the dc gain (= 2560).

The various sources of noise and disturbances included in Eq. (3.11) have been evaluated both theoretically and experimentally. The total positional uncertainty in the position-sensing circuit, $\varepsilon_p\sqrt{\Delta f}$, is estimated conservatively at ~ 1 μm rms. Electronic noise is negligible in comparison with thermal and magnetic drifts; thermal drifts were monitored over a period of several hours, and magnetic-field effects were evaluated by using a horseshoe magnet and applying a magnetic field larger than the ambient field during a discharge. Since the dominant components of ε_p are at low frequency (0–10 Hz), where $|PCS| \gg 1$, Eq. (3.11) tells us that the contribution of this uncertainty to the total error is $\delta x_p \simeq 1$ μm rms.

The electronic noise in the compensation circuit is broadband, and $\varepsilon_c\sqrt{\Delta f} <$ 1 mV rms; the contribution to the positional error is $\delta x_c < \varepsilon_c\sqrt{\Delta f}/|P| < 8\times10^{-3}$ μm rms, a negligible amount. Similarly, the noise in the scanner driver is broadband and was experimentally determined to be less than 1 mV rms. We can then write $\delta x_d < \varepsilon_d\sqrt{\Delta f}/(|P||C|_{\min})$, where $|C|_{\min} \simeq 0.01$ (at ~ 100 Hz); hence, $\delta x_d < 0.8$ μm rms.

The only other potentially important disturbance is the effect of the ambient magnetic fields on the scanner galvanometers. This is a low-frequency effect: thus, its effect on the positional error in Eq. (3.11) is $\delta x_m \simeq \varepsilon_m\sqrt{\Delta f}/|PCS|$, i.e., it is suppressed by a factor of 2560 (at dc). Rather than measuring ε_m, it proved simpler to measure δx_m with the feedback loop closed, by using a horseshoe magnet. With an estimated field of 400 Gauss, we found $\delta x_m \leq 10$ μm (measured by shifting the micrometer-driven base of the phase plate to the point where the transmitted power is maximum). With an average field during a plasma discharge of ~ 200 Gauss, we can estimate an average error of ±5 μm. Since our primary design requirement was to contain the shift within ±35 μm, an error of this magnitude is considered acceptable.

(f) Performance of the System

The design criteria outlined at the beginning of this section were met successfully by the feedback system described above. Figure 3.23 shows the rms vibration traces, along with the plasma current, for two similar plasma discharges, with no compensation and with feedback applied; the design target level is also shown in the figure: the performance achieved is well within this limit. magnified, Fig. 3.23(c)]. A similar comparison is shown for the frequency spectra of the vibrations in Fig. 3.24.

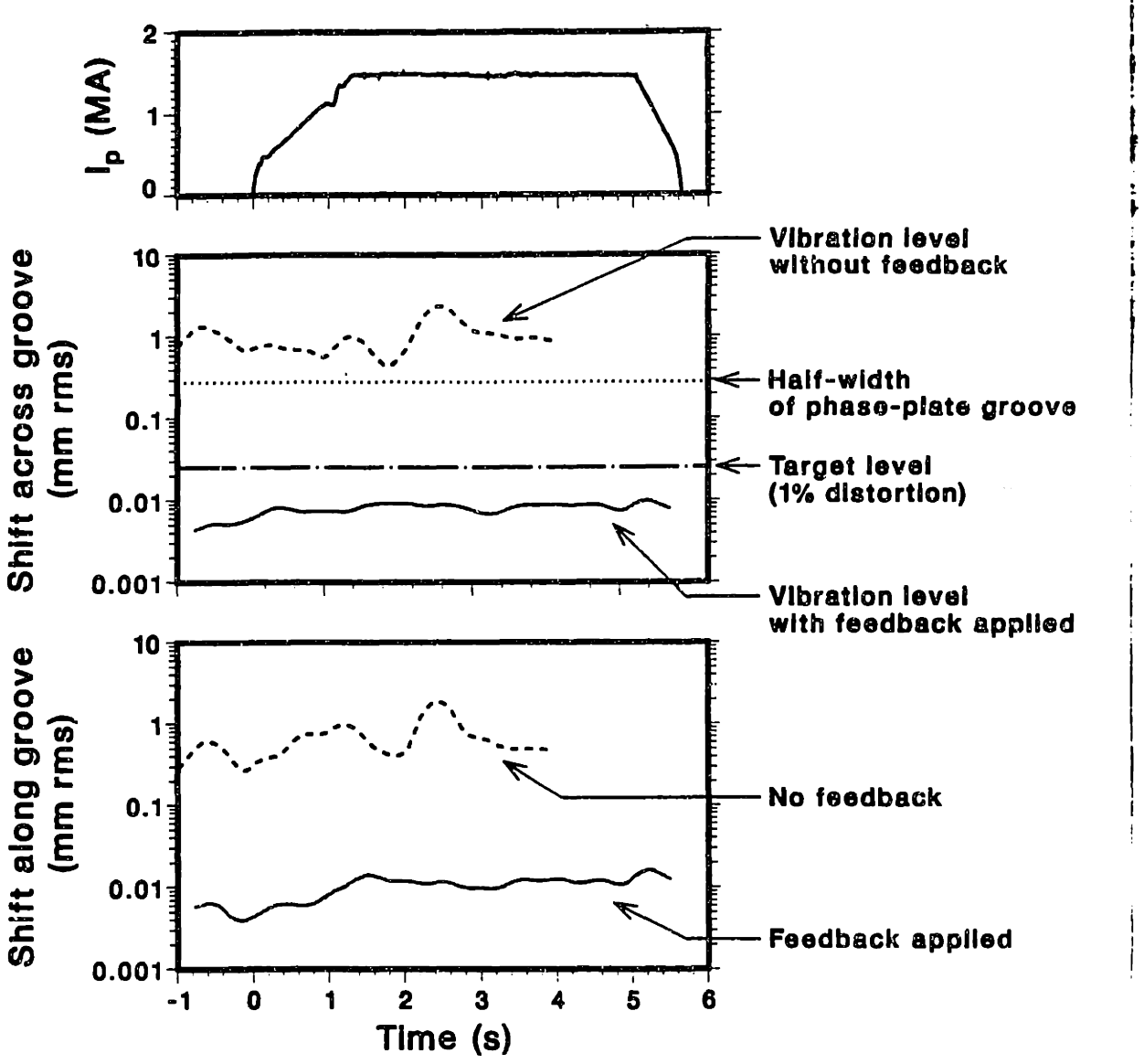

Fig. 3.23 Comparison of rms vibration levels with and without feedback.

Disruption events generally cause the beam spot to move outside the range of the position sensor; after a discharge terminated by such an event, the feedback system must be reset manually, by depressing the reset buttons on the compensation-circuit box.

It must be remarked in closing that lateral translations of the beam, unlike angular displacements, are not corrected by this feedback system. Therefore, any such translations caused by vibrations of the optics result in an error in the image position. In addition, the correction applied by the feedback system at the focus is

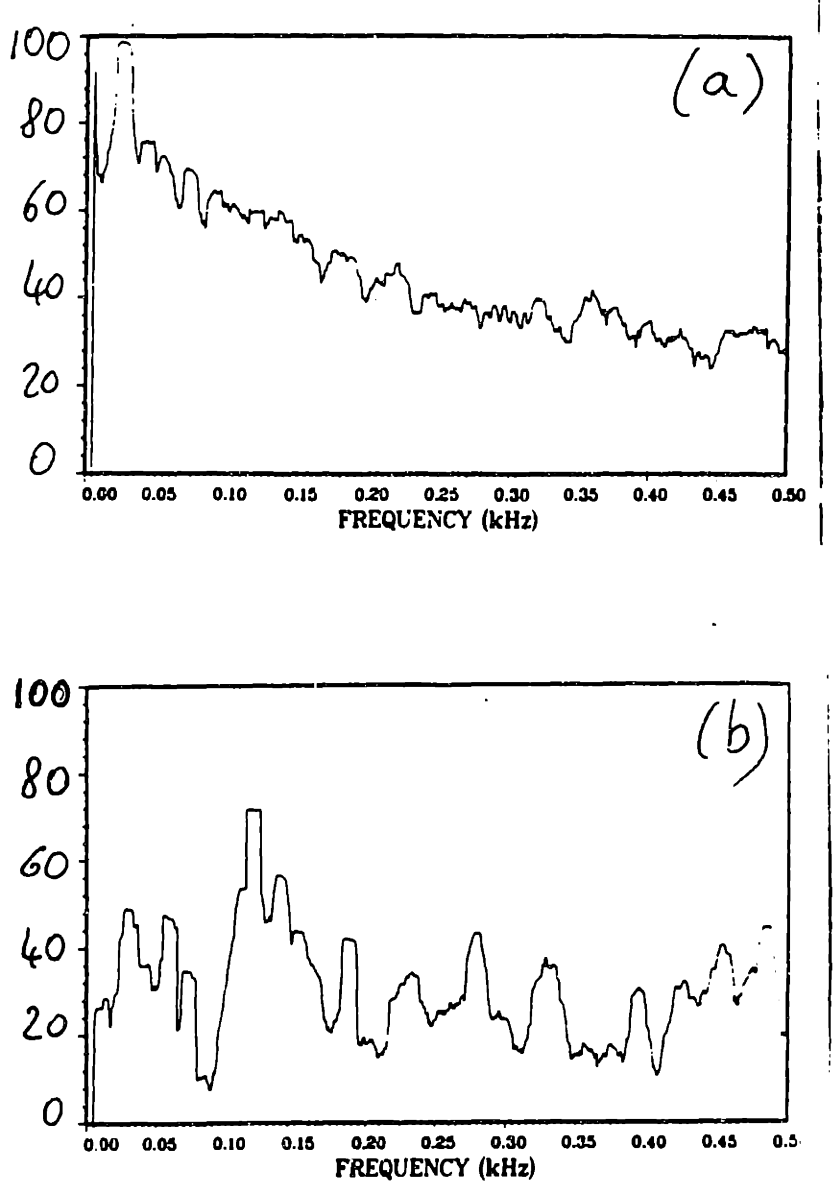

Fig. 3.24 Vibration autospectrum (a) without feedback and (b) with feedback applied.

also a source of displacement at the image, as shown schematically in Fig. 3.25. To evaluate the magnitude of these effects, let us assume that the error is due to a single mirror, located a distance D from the focusing paraboloid and tilted by a small angle θ from its set position. Then, in the absence of a feedback system, the apparent position of the object (the plasma) is shifted by a distance

$$\Delta_p = 2\theta(L - D), \tag{3.12}$$

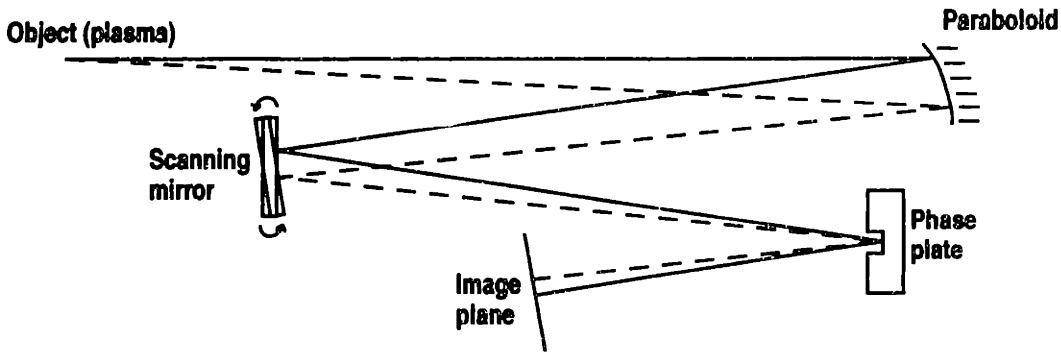

Fig. 3.25 Illustration of image-plane shift caused by focal-plane compensation.

where $L \simeq 5.5$ m is the distance between the plasma and the parabolic mirror. With the feedback loop in operation, the shift becomes

$$\Delta_p = -2\theta \left[D + F \left(\frac{F}{d} - 1 \right) \right], \tag{3.13}$$

where F is the focal length of the paraboloid and d is the distance between the focal plane and the rotatable mirrors. Clearly the error is reduced as d is increased, as can be intuitively understood by inspecting Fig. 3.25. As was discussed at the beginning of this section, the magnitude of d is limited in practice by considerations of mirror size; in our case, $F/d \simeq 4$, and $F(F/d-1) \simeq 6$ m. A comparison between Eqs. (3.12) and (3.13), with the values given, yields the conclusion that the error is worsened by the feedback system.

The total error can be estimated as follows: we assume that all the vibrations are caused by the four mirrors mounted on the DIII–D vessel, and we further assume that they vibrate with equal average amplitude. We then write the mean square value of the *uncorrected* focal displacement as

$$\left\langle (\delta x)^2 \right\rangle = 4F^2 \left\langle (2\theta)^2 \right\rangle. \tag{3.14}$$

Using the experimentally measured value of ~ 0.7 mm for $(\delta x)_{\rm rms}$, Eq. (3.14) gives $\theta_{\rm rms} \simeq 0.08$ mrad. By virtue of Eq. (3.13) we can also write

$$\left\langle \Delta_p^2 \right\rangle = 4 \left\langle \theta^2 \right\rangle \sum_{i=1}^{4} \left[D_i + F \left(\frac{F}{d} - 1 \right) \right]^2. \tag{3.15}$$

Using the distances D_i measured in our system, we finally obtain $\Delta_{p,\rm rms} \simeq 4$ mm. This value is used as the experimental uncertainty on the absolute spatial location. The relative spatial resolution, i.e. the distance between chords, is of course known with greater accuracy (typically 3–8%), both from the geometry of the detector and of the optical system, and from independent measurements with acoustic waves.

The absolute spatial uncertainty could be improved by adding a second dual-axis feedback system at the image. This was considered as a possible future upgrade.

This system could be designed in a much simpler fashion than in the case of the focal system, owing to more relaxed requirements: a damping factor of ~ 0.2 at 20 Hz would be sufficient to ensure a spatial resolution of ~ 1 mm.

Most of the vibrations at the image are not detected as signal because their frequency is below the 2-kHz highpass cutoff point of the electronics. However, there are residual vibrations in the 2–4 kHz range, with a typical amplitude of ± 15 μm, corresponding to a power modulation of $\pm 0.5\%$. This generates a signal equivalent to the PCI signal from an apparent laser phase shift of ± 1 mrad, a value considerably larger than the sensitivity of the diagnostic. No vibrations are generally observed above 5 kHz; the low-frequency limit of our measurements is usually set conservatively at 8 kHz. Owing to the smallness of the power modulation, no modulational effects are observed in the spectrum above 8 kHz.

3.6 Electronics and Data Acquisition

Each of the 16 data-acquisition channels that process the 16 detector signals can be configured in one of two basic forms: one for low-frequency (< 1 MHz) measurements and the other for rf measurements.

The original low-frequency setup was a straightforward homodyne configuration. After the preamplification stage, the signals were passed through 14-MHz lowpass filters and 33-dB-gain amplifiers, and then sent directly to the annex by means of 60-meter-long coaxial cables. In the annex the signals were then further conditioned and digitized by CAMAC equipment. The cables were all grounded on the rf-shield box on the optical table and were not grounded in the annex.

The performance of this system was unsatisfactory because of excessive noise. A noise level of ~ 10 mV rms at the CAMAC input stage, well above the intrinsic system noise, was observed regularly on all channels. The frequency content of the noise was broadband, peaking at approximately 250 kHz with a width of 300 kHz; this circumstance made it difficult to eliminate the noise through filtering. In addition, voltage spikes were occasionally observed. All our efforts to eliminate this noise were unsuccessful: these included modifying the grounding scheme (grounding the cables in the annex or floating the reference), routing the cables differently, and using double-shielded cables. It was ascertained that this broadband noise was caused by electromagnetic pickup occurring in the long cable run between the machine hall and the annex.

The homodyne configuration was then abandoned in favor of an amplitude-modulation (AM), suppressed-carrier technique using radio frequencies. In this new scheme, the signal traveling from the machine hall to the annex is at the rf carrier frequency; low-frequency electromagnetic noise can then be eliminated by appropriate filtering at the receiving end. A superheterodyne receiver with an intermediate frequency (IF) of zero effects the demodulation before the final digitization stage.

With this new configuration, the 250 kHz noise became undetectable, implying a suppression factor of more than 20 dB. The occasional voltage spikes also disappeared. The sensitivity of this heterodyne system is limited only by the detector-preamplifier

noise. Although much early work was carried out with the homodyne system, the majority of the physics results described in this thesis were obtained with the new configuration.

The low-frequency AM configuration is shown schematically in Fig. 3.26(a). The output signals from the preamplifiers are passed through lowpass filters with a 3-dB frequency of 14 MHz. A 33-dB amplification and line-driving stage follows. These amplifiers were assembled in the laboratory and are designed to drive a current of 400 mA; the nominal bandwidth is 1 MHz: the measured gain at 1 MHz is 88% of the dc gain. The output signals from the amplifiers were sent directly to the annex in the old homodyne setup; in the AM configuration, each of these signals is sent instead to the rf port of a double-balanced mixer, Mini-Circuits (Brooklyn, NY) model ZLW-6, with a bandwidth .003–100 MHz. A reference 7-dBm rf signal is applied at the LO port. The modulated IF signal is further amplified by an rf amplifier (Mini-Circuits model ZFL-500: 20-dB gain, 0.05–500-MHz bandwidth) and then sent to the annex via a 60-meter-long coaxial cable.

All of these components are housed in the rf-shield box on the optical table (see Fig. 3.27), and powered by an external isolated power supply through filtered power leads; as described in §3.3, the ground reference is taken from a single point on the box, connected to a building ground. All components are connected by coaxial cables. All input and output impedances are matched at 50 Ω.

Since only eight digitizers are available, eight data-acquisition channels exist in the annex. An isolated patch panel permits to connect eight of the sixteen signal cables to the eight acquisition channels in any desired permutation. Changes can be effected between plasma discharges. The receiving point of each channel is an isolated rf transformer, designed to break the ground loop. The output of the transformer is grounded in the annex, as are all subsequent electronics, all located in a single equipment rack. The signal from the transformer is conditioned first by a lowpass filter (3-dB point: 35 or 67 MHz, depending on the LO frequency) for harmonic rejection, and then by a highpass filter (3-dB point: 25 MHz) for initial noise damping; the highpass filter is removed whenever the LO frequency is lower than 30 MHz: in any case the low-frequency noise is eliminated completely at the mixing stage.

The filtered signal is sent to the rf port of a Mini-Circuit ZLW-3H double-balanced mixer (0.05–200-MHz bandwidth); at the LO port is applied a 17-dBm signal obtained from the same reference that produced the initial modulation: thus, the IF output is proportional to the original audio signal. With this configuration, both sidebands are used and the total loss from the double mixing process is only 6 dB. The image signal at twice the LO frequency is eliminated by an additional 14-MHz lowpass filter.

The last segment of the superheterodyne data-acquisition setup is composed of the entire annex section of the old homodyne system. Eight antialiasing filters are used with 3-dB passband frequency 1 MHz; these units are 11-pole elliptical lowpass filters, with 60 dB minimum attenuation at 1.1 MHz, manufactured by TTE, Inc. (Los Angeles, CA). The final amplification stage consists of four two-channel LeCroy 8100

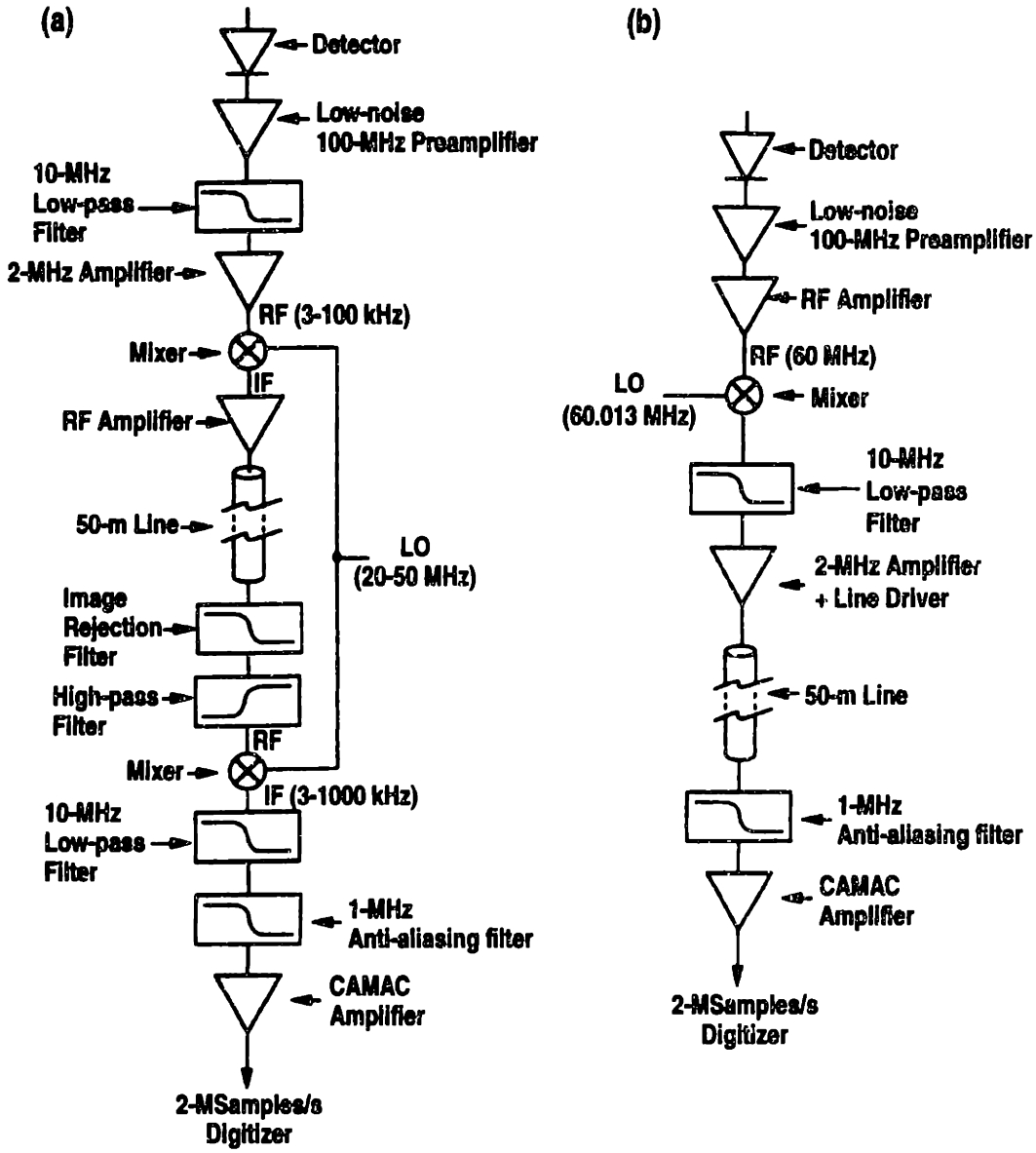

Fig. 3.26 (a) Low-frequency data-acquisition configuration; (b) rf data-acquisition configuration.

CAMAC amplifiers; the bandwidth is 1 MHz and the gain can be varied by computer between 0.2 and 100. The CAMAC digitizers are eight DSP Traq P 2824 ADC modules, with 12-bit resolution and a maximum sampling rate of 2 Megasamples/s. All impedances, including the input impedance of the digitizer, are matched at 50 Ω.

Two DSP 5003A memory modules provide a data capacity of 128 kilosamples per tokamak discharge (64 ms at the maximum sampling rate). The digitizers are controlled by two DSP 4012A controllers, and the system is completed by a 2-MHz clock. All the equipment is housed in a DSP Optima-860 CAMAC crate. The data are collected after each DIII–D discharge by the DIII–D MODCOMP computers via a CAMAC highway; later the data are sent to a VAX 6410 and stored in a permanent data file.

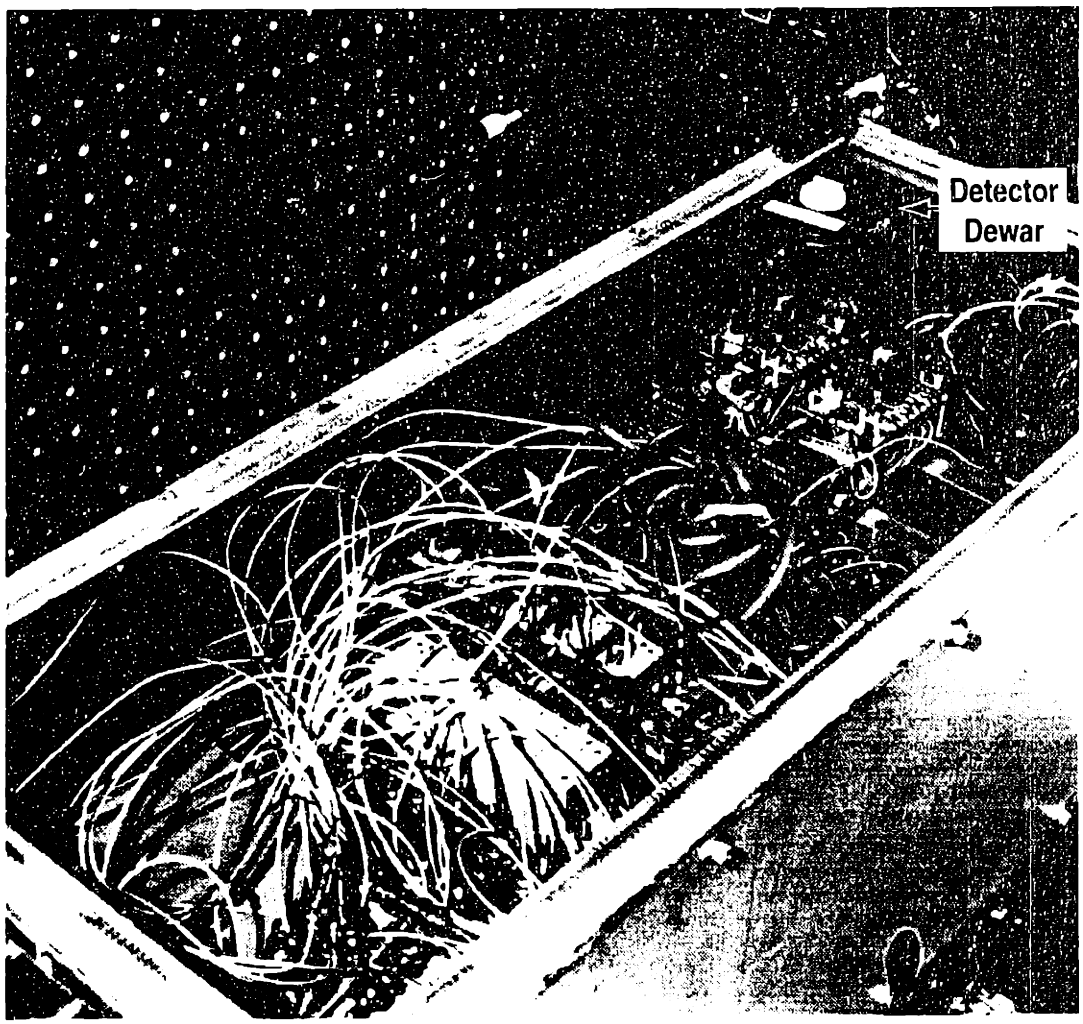

Fig. 3.27 Rf-shielded box with view of electronics inside.

Two additional four-channel Aeon 3204 amplifiers are used to condition the position signals in the feedback vibration-control system (see §3.5), and for various testing purposes. The position and scanner signals are digitized by a separate 500-kHz, 8-bit digitizer (LeCroy 2264H).

The configuration used for rf measurements is heterodyne; the rf signals are mixed with the LO reference and downshifted to the audio range: the resulting signals are then sent to the annex and digitized. Therefore, this setup is susceptible to the broadband noise that was described earlier. However, an opportune choice of the LO frequency and appropriate filtering can eliminate the problem. For coherent detection of an ICRF wave,[75] the LO frequency is chosen to be slightly different from the launching frequency, so that the IF is in the 0 15 kHz range: this allows phase and quadrature detection through Fourier analysis of the data. For exploration of broadband phenomena (e.g., parametric-decay waves[80]), the LO frequency is set at the edge of the region of interest, but no sideband selection is effected.

The set of components used in the rf configuration [shown schematically in Fig.

3.26(b)] is a subset of those used in the low-frequency setup: any number of channels can be switched from one configuration to the other overnight. The signals from the preamplifiers are sent to the rf amplifiers (as an option, they may be conditioned by 25-MHz highpass filters first), and then to the mixers. The IF signals from the mixers are amplified by the 1-MHz amplifiers and sent to the annex, where they are processed directly by the LeCroy amplifiers (through differential inputs) and then digitized.

The LO reference signal is generated by a Hewlett-Packard 8656A synthesizer, operating in the range 0.1–990 MHz with a resolution of 10 Hz. The synthesizer is located in the annex. The signal is amplified once by a 16-dB amplifier and then divided by a 2-way power splitter: one half of the signal is used in the machine hall and the other half is used in the annex. The first branch consists of a double-shielded, 60-meter-long coaxial cable, an isolation transformer (to break the ground loop), and a 16-way splitter; the second branch consists of a further amplification stage and a 16-way splitter (only eight channels of which are used). The resulting levels are 7 dBm and 17 dBm, respectively.

In the zero-IF superheterodyne configuration, the LO frequency cannot be chosen arbitrarily. The phase of the LO component of the signal reaching the final mixer and the phase of the reference signal applied at the LO port of the same mixer must be equal or differ by 180° for the two sidebands to add in phase. If the difference is ±90°, total cancellation occurs. Quantitatively, the IF signal is proportional to $\cos(2L\omega_{\mathrm{LO}}/v)$, where $L \simeq 60$ m is the length of the cable run from the machine hall to the annex, and $v \simeq (2/3)c$ is the velocity of energy propagation along a coaxial cable. The frequencies that maximize the signal are then given by the formula $f_m \simeq mc/(6L)$, where m is any integer. In practice, it is easy to locate the maxima by varying the synthesizer frequency and observing the variation of the output signal on an oscilloscope (with a reference signal in input).

It should be noted that small differences in cable length between channels result in differences in responsivity that increase with the harmonic number m. The largest discrepancy has been determined to be $\sim$ 40 cm, corresponding to a responsivity variation of 13% at 40 MHz. Differences in responsivity between detector elements are far larger; however, since the effects due to cable-length differences are dependent on the LO frequency, it is important to carry out a relative calibration before each plasma discharge.

The fundamental interval $c/(6L)$ was experimentally determined to be 0.78 MHz; so there is considerable freedom in the choice of the LO frequency: this is useful to avoid regions where noise and interference may exist. The range 20–40 MHz has been used in most of our experiments. When some channels are configured for rf detection and the others for low-frequency detection, the LO frequency must be suitable for both; since the maximum data-acquisition bandwidth (1 MHz) is larger than the separation between the LO maxima, it is always possible to find an appropriate frequency.

Synchronous and asynchronous triggers are provided by the DIII–D timing sys-

tem. The Traq P digitizers can be pretriggered or post-triggered, and can be programmed to collect data on multiple and separate intervals.

The digitization rate can be varied between intervals. In low-frequency measurements, the maximum Nyquist frequency of 1 MHz is obtained at the 2 Megasamples/s rate. It is often found, however, that most of the activity of interest in the plasma occurs at considerably lower frequencies; thus, sampling rates of 500 or 200 ksamples/s are often used, trading bandwidth for acquisition time. The 500-ksamples/s rate is particularly convenient, as each LeCroy CAMAC amplifier contains a 200-kHz antialiasing filter that can be activated by software. For coherent-wave detection in the rf case, with the IF in the 0–15 kHz range, 15-kHz antialiasing filters are available to eliminate the 100–400 kHz cable noise.

The various components in the data-acquisition system were chosen carefully to ensure that harmonic generation and electronic noise would not degrade the performance of the diagnostic. The ultimate sensitivity is indeed limited by the detector-preamplifier noise, as confirmed by experimental tests (see §3.8). The dynamic range achievable is given by the resolution of the digitizers: a 12-bit resolution corresponds to a dynamic range of 66 dB. The leading mixer harmonic intermodulation signals, excluding those that are suppressed by the various filtering stages, are the following: the third-order rf, first-order LO term from the first mixer, which generates a third harmonic of the original signal; the second-order rf, second-order LO term from the second mixer, producing a second harmonic; and the LO-IF coupling in the first mixer, generating a dc signal at the end. The last term is relatively large (≤ 9 mV at the CAMAC input), but it is unimportant since it is a simple dc offset and is small compared to the instrumental range. The first term was measured to be -59 dB and the second one -60 dB below the signal; therefore, with a broadband spectrum the signal-to-noise ratio is effectively limited to ~ 56 dB. In practice this is not a limitation, as the noise level at the detector output is -105 dBm (on a 1-MHz bandwidth), while the signal typically does not exceed -59 dBm (corresponding to a laser phase shift of ~ 6 mrad rms). Thus the experimental signal-to-noise ratio is ≤ 46 dB.

Harmonic generation can potentially be a problem in the presence of coherent, narrowband signals; similarly, the two-tone third-order intermodulation distortion, rated at ~ -48 dB, could come into play in the presence of pairs of coherent signals, generating signals at their sum and difference frequencies. The frequency autopower spectra are always inspected during the data-analysis phase to identify cases in which the sensitivity at certain frequencies may be limited by these effects.

The amplitude distortion introduced by mixers and amplifiers, at a signal level of -59 dBm, is rated at less than 3×10^{-4}. The desire to minimize the distortion, as well as the two-tone intermodulation, was the main reason behind the choice of a 17-dBm-level mixer for the downshifting stage, where the signal is relatively high.

When the time delay introduced by an electronic component varies as a function of frequency, phase distortions arise. In our system, the distortion, primarily due to the antialiasing filters, is less than 20 ns in the 0–500 kHz range, and less than 130 ns in the 0–800 kHz range. Relative delays between data channels are caused chiefly by

the antialiasing filters and by the digitizers; a maximum delay of 50 ns is estimated. At 100 kHz, this assigns a cross-phase uncertainty of $\sim 2°$.

3.7 Response Properties and Sensitivity

The transfer function of the phase-contrast-imaging diagnostic in wave-number space was derived in §2.11. The transfer function for our system is represented by the curve marked $\alpha = 1$ in Fig. 2.21. We remark again here that the transfer function is essentially flat (to within 1%) for $k \gtrsim 2\pi/w_0$ and has a low-wave-number cutoff (1/2 of the maximum responsivity) at $k = \pi/w_0$.

The treatment of §2.11 did not take into account the specific detection geometry. With a finite-area detector, components of sufficiently short wavelength will clearly be averaged out. To analyze this effect, we adopt the following simple model: we assume that the output signal from a detector element centered at the coordinate x is proportional to the surface average of the fluctuating incident flux over a circle of radius r ($r = 225$ μm in our case); we also assume that the system is one-dimensional, i.e., that the incident flux is constant in the y direction; and, finally, we neglect any variation of the dc power over the element surface. The transfer function of this averaging process can easily be calculated and can be written, in object coordinates,

$$\mathcal{T}_{\rm av}(k) = \frac{1}{\pi r'^2} \int_{-r'}^{+r'} 2\sqrt{r'^2 - x'^2}\, e^{-ikx'}\, dx' = \frac{2J_1(kr')}{kr'}, \tag{3.16}$$

where $r' = r/|M|$ is the radius of the averaging surface in the plasma. In our most common configuration (see §3.4), $|M| = 0.15$ and $r' = 1.5$ mm. The complete transfer function is then the product of $\mathcal{T}$, given by Eq. (2.143) with $a = w_0$ and $k_c = 3/w_0$, and $\mathcal{T}_{\rm av}$, and is plotted in Fig. 3.28. The vertical lines in the figure correspond to the Nyquist spatial frequency; the components of the spectrum above that frequency are stopped by a lowpass antialiasing filter. When the magnification is changed, the horizontal scale varies identically for both the Nyquist frequency and the function $\mathcal{T}_{\rm av}$.

The frequency response of the PCI diagnostic, without antialiasing filters, is flat in the region 5 kHz–1 MHz; the 3-dB points, determined by the detector and preamplifiers, are 1 kHz and 20 MHz; the estimated compression at 100 MHz is $\sim$ 16 dB. Residual mechanical vibrations impose a low-frequency limit of 8 kHz. In the case of low-frequency (turbulence) measurements, the antialiasing filters have a 3-dB passband of 1 MHz and a 60-dB stopband of 1.1 MHz. Lower-frequency filters (200-kHz passband) are used with lower sampling rates.

The overall gain from the detector output to the digitizer, with the CAMAC amplifiers set at unity gain, is 63 dB in the low-frequency electronics configuration, and 71 dB in the rf configuration. The theoretical detector-preamplifier rms noise level, confirmed by experimental data, is ~ 1.4 $\mu V/\sqrt{\rm MHz}$, corresponding to a minimum measurable laser phase shift of $\sim 5 \times 10^{-5}$ rad (see §2.12). In the low-frequency setup, this translates into a noise level of ~ 2 mV rms at the digitizer input. The typical

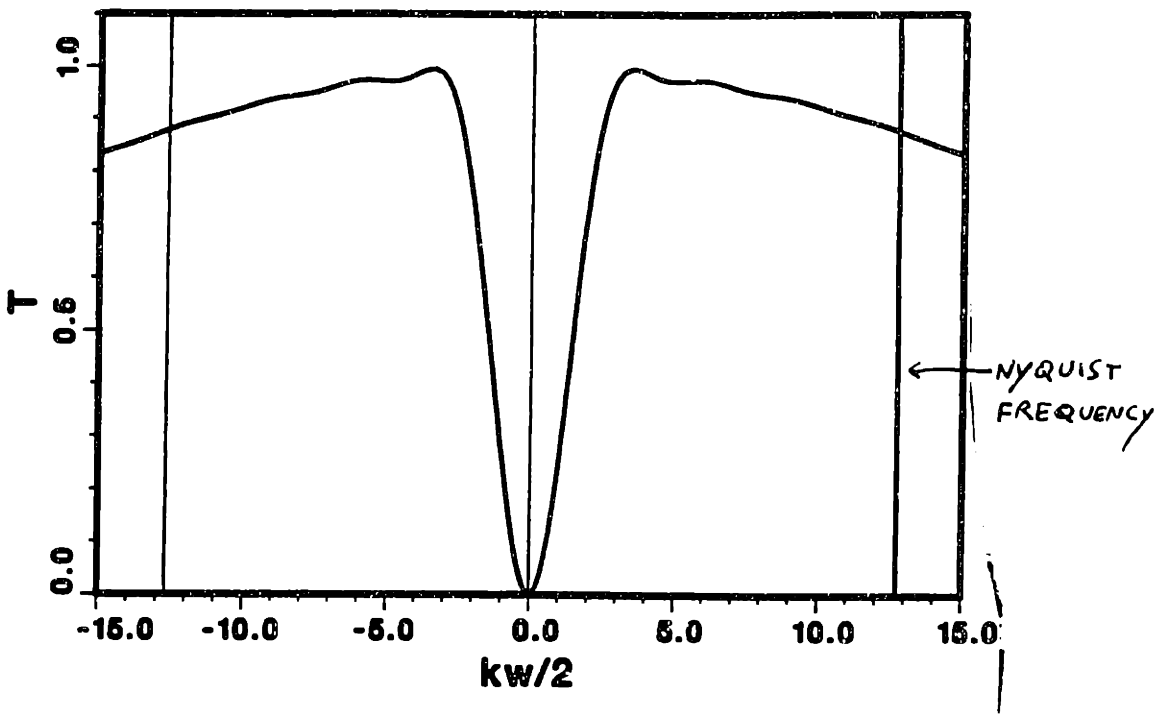

Fig. 3.28 Phase-contrast transfer function, including finite-sampling-area effect.

signal level does not exceed ±0.36 mV at the detector, i.e. ±0.5 V at the digitizer; therefore CAMAC gains of 10 or 20 are typically applied, bringing the noise level comfortably above the resolution of the digitizer, equal to 2.44 mV (the standard deviation of the quantization error is equal to $1/\sqrt{12}$ times this resolution[165]).

In studies of ICRF-wave propagation, the intrinsic noise is rather small owing to the narrow bandwidth of the launched waves. The limiting factor is generally the residual rf pickup. Optically heterodyne schemes using mechanical choppers have been employed to improve the sensitivity.

The principal parameters of the DIII–D phase-contrast-imaging diagnostic are summarized in Table 3.2.

TABLE 3.2. PCI parameters

Sensitivity ($\int n_e dl$)	1.7×10^{11} cm$^{-2}/\sqrt{\text{MHz}}$
Radial wave-number range	0.8–40.0 cm^{-1}
Vertical wave-number range (instantaneous measurement)	-0.02–0.02 cm^{-1}
Vertical wave-number range (correlation measurement)	$\sim$ -0.6–0.6 cm^{-1}
Low-frequency cutoff	8 kHz
Frequency bandwidth (3 dB)	15 MHz
Frequency bandwidth (20 dB)	100 MHz
Data-acquisition bandwidth	1 MHz
Radial resolution	4.7 mm (typical)
Absolute radial uncertainty	$\pm$ 4 mm
Vertical resolution	None
Signal-to-noise ratio (20 kHz)	$\leq$60 dB
Signal-to-noise ratio (100 kHz)	$\leq$40 dB
Signal-to-noise ratio (overall)	$\leq$46 dB

3.8 Tests and Calibrations

The PCI system has been extensively tested to ensure a performance in agreement with theoretical expectations. In particular, the electronics were tested during plasma discharges by collecting data in the absence of a detector signal. One particular cause of concern was the sensitivity of the rf mixers to the ambient magnetic field; testing was done before work began on the full 16-channel superheterodyne data-acquisition system, and no measurable effect was observed. Noise measurements have led to constant improvements of the performance of the diagnostics; the sensitivity, initially limited by electronic-pickup problems (see §3.6), eventually reached its ultimate limit, determined by the intrinsic noise of the detector-preamplifier circuit.

Tests were also performed to determine whether infrared emission from the plasma could cause a degradation in sensitivity. The detector is sensitive to wavelengths in the range 8–12 μm. The test is carried out by opening the vibration-control feedback loop, with the system properly aligned, and then turning off the CO_2 laser. The signals are then digitized over an interval longer than the main vibration period (50 ms). The result of this test was negative: the emission signal was unobservable.

The diagnostic is able to detect acoustic waves in air. The possibility of interference from sounds or air turbulence was investigated by collecting data during power-supply test shots. This test also produced negative results.

As was discussed in §2.14, acoustic waves are used to calibrate the diagnostic. Absolute calibrations are carried out during vents, by installing a loudspeaker and a calibrated microphone (Brüel & Kjær model 4136) on the tokamak midplane on opposite sides of the laser beam (in the radial direction). A short ($\sim$ 10 ms) wave train is launched from the loudspeaker. The time interval that is considered useful for the calibration is approximately 2 ms: this was chosen to be shorter than the travel times of the wave to the opposite wall and to the nearest mirror in the system, to

prevent spurious signals from echoes or mirror vibrations.

The wave pattern of the loudspeaker is measured separately by scanning the wave field with the microphone. The angular dependence is modeled with Gaussian functions, and the analytical model is then used in a Fortran computer code to generate the expected signal as a function of chord position. This is an improvement over the spherical-wave approximation that yields the analytical formula expressed by Eq. (2.197).

The reference wave number for calibration is chosen to be in the region in which the transfer function is flat, i.e., $k \geq 2\pi/w_0$. The radial positions of the chords are determined by iteratively comparing the phases of the signals with the phases predicted by the code; this in turn permits to obtain the value of the optical magnification. It should be noted that slight variations in the detector-to-detector spacing were uncovered with this technique, and that the measured numbers are always used in all spatial plots. The absolute responsivities of the 16 data channels are then derived by dividing the amplitudes of the signals by the amplitudes provided by the code. The code can also optimize the results by employing a number of free parameters; in particular, it allows for a longitudinal displacement of the detector from the image of the vessel midplane.

Shown in Fig. 3.29 are the time traces of the detector signals, along with the 11-kHz reference oscillator voltage applied to the loudspeaker. The loudspeaker employed in this test was a piezoelectric tweeter, Realistic model 40-1379. The Gaussian half-width of its angular pattern in the direction of propagation of the beam was 28°. The time delay and phase difference between the channels are qualitatively consistent with a chord separation of 4.7 mm, as expected.

The quantitative analysis described above was applied to this data set, yielding the spatial distribution of the chords shown in Fig. 3.30 and the responsivity profile shown in Fig. 3.31(a) (the voltage is as digitized, with the CAMAC amplifiers set at unity gain). The instrumental responsivity is given by the absolute responsivity divided by the weighting function $W(x)$ [Eq. (2.134)], in accordance with Eq. (2.138). The instrumental responsivity, calculated by approximating the weighting function with the Gaussian function $\exp(-2x^2/w_0^2)$, is shown in Fig. 3.31(b). The irregularity of the profile is primarily due to differences in responsivity between detector elements; the detector responsivities reported on the right-hand side of Fig. 3.31(b) are only indicative, as they were calculated by assuming that the gains of the electronics are equal to their rated values (and using the measured value of the power flux on the detector). A separate determination is unnecessary for our purposes.

By varying the frequency of the acoustic waves, the wave-number transfer function can be measured. Ideally, the result should be independent of the position within the cross section of the beam; thus, the observed spatial variation is taken as a measure of the experimental uncertainty on the transfer function. (We recall that the transfer-function approximation is rigorously valid only in the center of the beam.) The result is shown in Fig. 3.32, along with the theoretical function that was presented in Fig. 3.28. The experimental function in Fig. 3.32(a) is determined

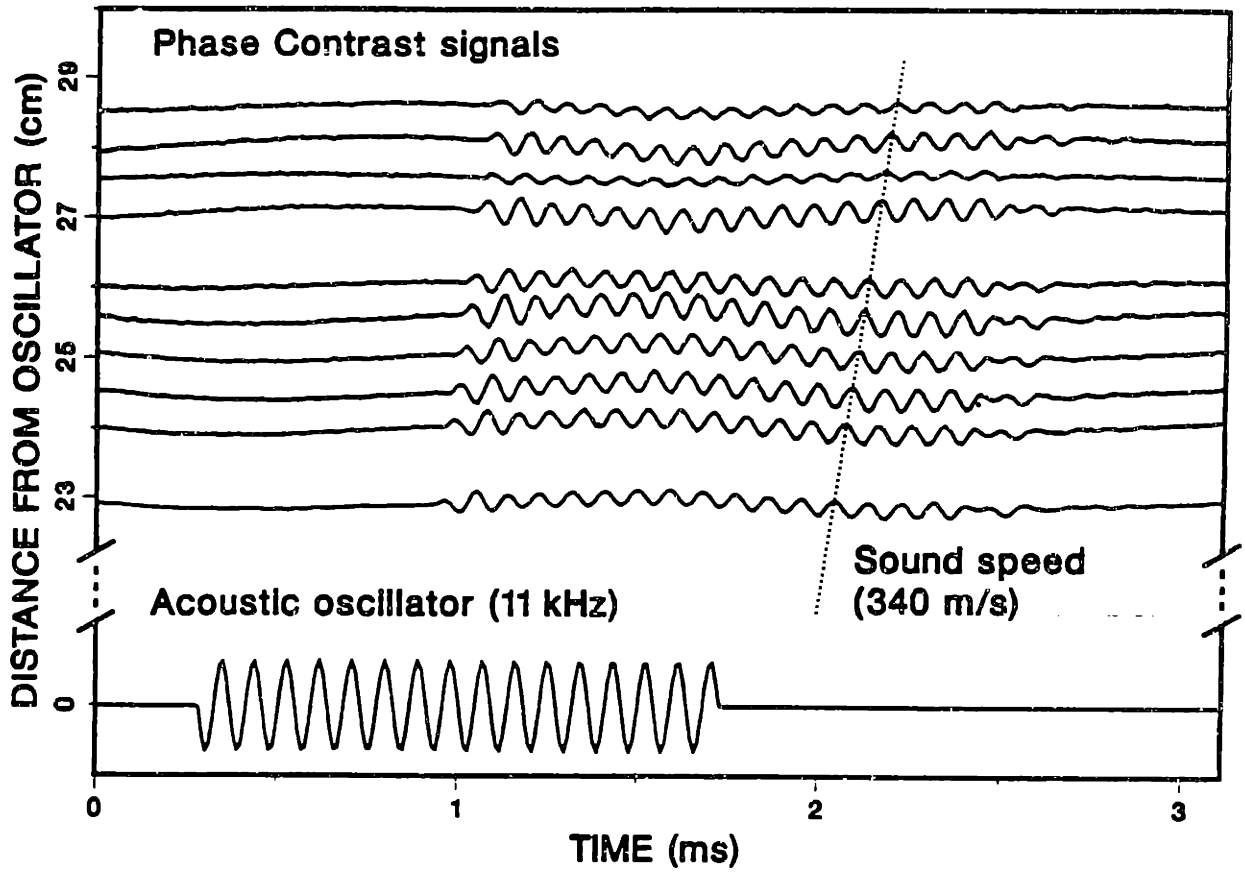

Fig. 3.29 Acoustic-wave calibration of the PCI system.

by averaging the transfer function over the eight chords closest to the center of the beam; the error bars correspond to the standard deviations. In Fig. 3.32(b) is the corresponding result using all 16 chords.

As was mentioned in §3.3, a relative calibration is carried out routinely before each plasma discharge. This is performed by launching a single-frequency acoustic wave at a location outside the DIII–D vessel; the effect of the spatial shift is merely a small reduction in amplitude, identical on all chords. The sound level is not measured separately in this case. The wave pattern is factored into the modeling code as in the in-vessel case.

These calibrations are very valuable for several reasons: the overall responsivity changes slightly when the LO frequency of the superheterodyne data-acquisition system is varied, or when the links between detector channels and digitizer channels are permuted; more importantly, substantial variations are observed in the responsivities of the individual detector elements over relatively short periods of time (of the order of weeks). In addition, this procedure permits a recalculation of the optical magnification on every run day; by comparing the starting time of the acoustic wave on the PCI signal with a reference time, it is also possible to calculate the absolute

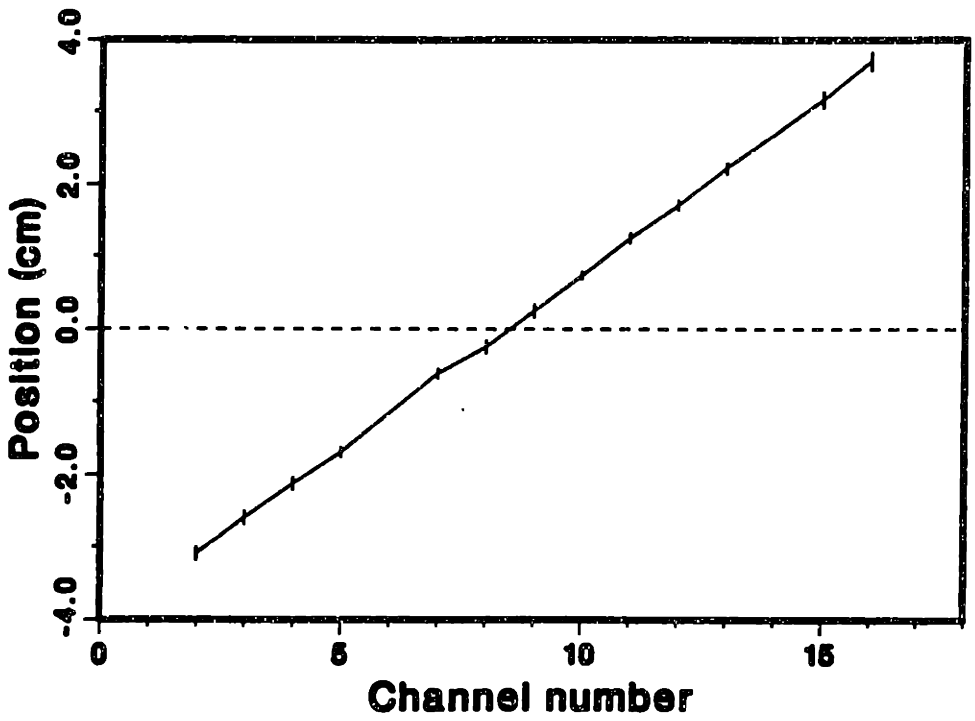

Fig. 3.30 Position of the chords as a function of the channel number, as measured through acoustic calibration (chords 1, 6, and 14 are missing because of burnt-out detector elements).

position of the beam with an accuracy of a few mm. This is especially valuable in high-resolution (high-magnification) experiments, when only a portion of the beam is sampled by the detector array. The absolute uncertainty on the position is dominated by the vibrational error, which, as discussed in §3.5(f), is of the order of 0.4 cm. The uncertainty on the magnification varies between 3% and 8%, depending on the signal-to-noise ratio.

While an accurate knowledge of the relative normalization factors is generally very useful, a knowledge of the absolute responsivity is of limited importance in many cases. However, when that information is desired and significant changes in the relative calibration factors are observed (as is often the case), an indirect measurement of the absolute responsivity is obtained by estimating the sound level from the amplitude of the signal applied to the tweeter and from the known efficiency of the tweeter. Uncertainties in the measurement of the signal amplitude limit the accuracy of the relative calibration to approximately 10–15%. The absolute calibration is also strongly affected by uncertainties in the knowledge of the wave pattern, resulting in an accuracy of 30–40%.

As was mentioned at the end of §3.3, pre-shot calibrations are carried out with a short wave train to avoid echoes. Only 10 to 20 wave cycles can typically be used before the onset of standing waves renders the calibration meaningless. Hence, the spectrum is broadened to 5–10% of the acoustic frequency; this makes a calibration

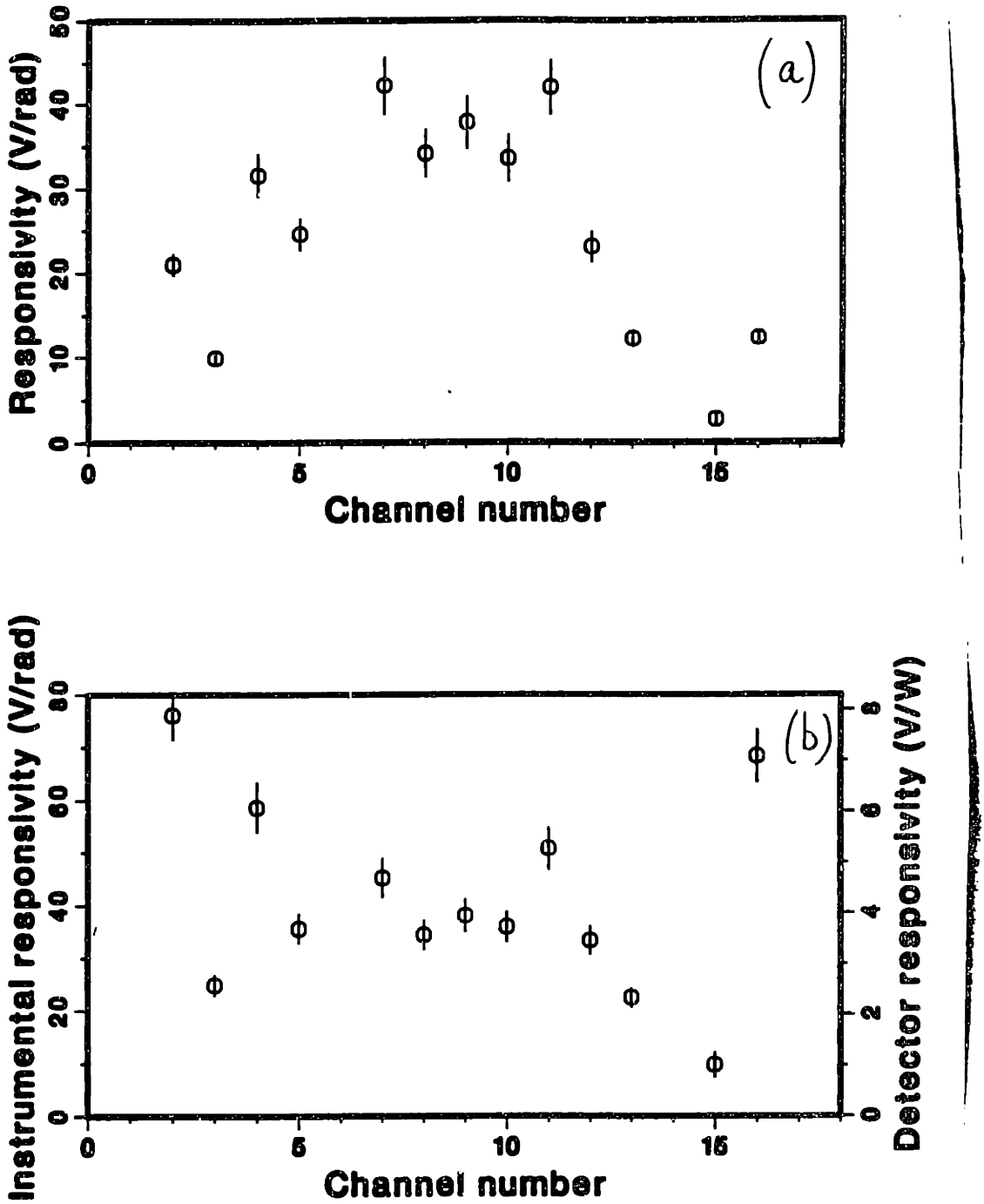

Fig. 3.31 Measured responsivity: (a) absolute and (b) instrumental.

during a plasma shot difficult because of the strong turbulent background. It may be possible to add this capability in the future by employing high-frequency ultrasonic waves: this would provide a valuable test of the theoretical prediction (discussed in §3.2) that the bulk plasma density does not distort the PCI transfer function

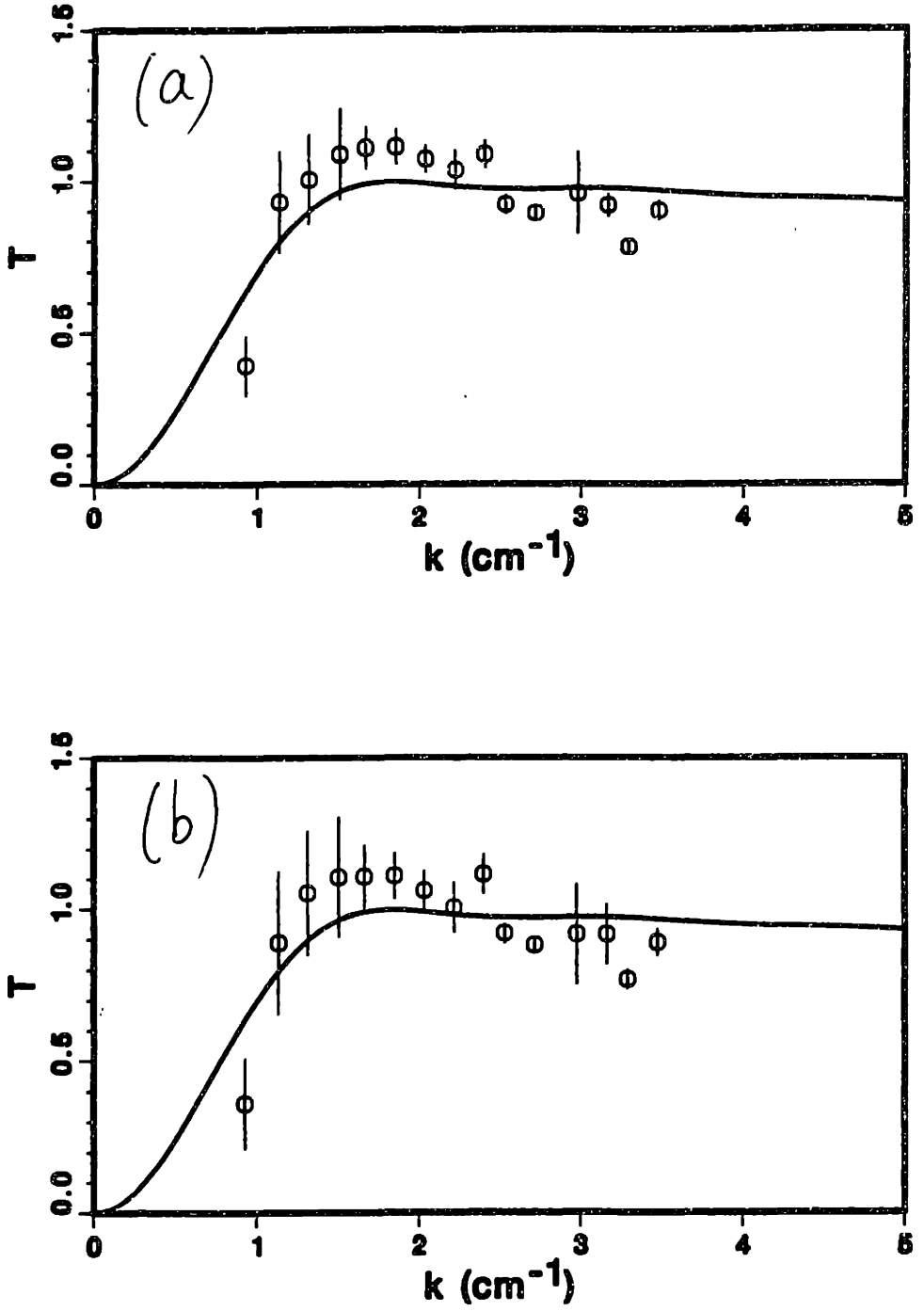

Fig. 3.32 Theoretical transfer function (solid line) vs. transfer function determined through acoustic calibration, averaged over (a) 8 and (b) 16 channels.

appreciably.

3.9 Data-Analysis Techniques

This section provides a brief overview of the basic techniques of error analysis and data reduction that are used routinely to extract the relevant physical information from the raw diagnostic data. More details will be offered in Chapter 5 to better elucidate the significance of specific results.

During a given run day, at least one shot is recorded with the laser shutter closed, for noise verification purposes. In addition, a baseline is obtained by digitizing the signals with the laser on well before the beginning of a shot, to obtain a record of the laser photon noise.

In each plasma discharge, the amplitude of mechanical vibrations is checked by inspecting the signals from the position sensors in the feedback system and the low-frequency (< 5 kHz) PCI signals. These vibrations occur at the detector, whereas residual vibrations at the focal planes are negligible [see §3.5 (f)]. The complete time traces of the eight digitized PCI signals are also examined visually to ensure that the data are not compromised by saturation, noise spikes, or other unusual disturbances.

The acoustic signals recorded 50 ms before the beginning of the shot are used to establish the relative calibration factors. When an absolute calibration is desired, the results from the latest in-vessel acoustic test are used, with adjustments derived from the average change in the relative calibration factors. If that change is large, the absolute responsivities are recalculated by inferring the sound level from the signal applied to the loudspeaker (see §3.8). This, in fact, has been the standard procedure.

The basic analysis of fluctuation data begins with a numerical computation of the following functions: rms values; autospectral and cross-spectral density functions in the frequency domain; autocorrelation and crosscorrelation functions in the time domain. The assumptions of stationarity and ergodicity are used to replace ensemble averaging with time averaging.[165] These assumptions are valid only in an approximate sense, as the character of turbulence does in fact change over time. Care is always taken to effect the averaging over intervals in which no drastic variations in the physical conditions are observed (one such example is the L– to H–mode transition). On a time scale longer than the typical averaging time, the assumption of stationarity must be abandoned,[166] and in fact it is of interest to study the temporal variation of the average functions, as well as their spatial dependence.

An rms calculation (after removal of the mean value) is accompanied by an intrinsic relative bias error equal to the reciprocal of the signal-to-noise ratio. Since the noise is generally white and is known with good accuracy, this bias is removed in the calculation. The statistical random error can be calculated if the data are assumed to follow a normal distribution; we shall define the error as the standard deviation of the probability distribution of the quantity under exam: this corresponds to a 68% confidence level (two standard deviations correspond to a 95% confidence level). The relative random error on the rms value is given by $1/\sqrt{2m}$, where m is the number of samples over which the average is calculated.[165] When the digital sampling rate $1/\Delta t$ is larger than $2\Delta f$, where Δf is the bandwidth of the fluctuations, the number

of samples is given by $m = 2T\Delta f$, where T is the averaging interval. When, instead, $1/\Delta t < 2\Delta f$, we can write $m = T/\Delta t$.

In an analysis of the spatial dependence of the rms function, one must also consider the uncertainty on the calibration factor. As mentioned in the previous section, the typical uncertainty on the relative calibration factors (including the standard deviation of the experimental transfer function) is ~10–15%, whereas the uncertainty on the absolute calibration (systematic calibration error) is ~30–40%.

The computation of the spectral functions in frequency space is carried out through a standard procedure, employing a digital fast Fourier transform (FFT) algorithm,[167] followed by averaging over frequencies to obtain an unbiased and consistent estimate. Here, m is given by $2T \times \delta f$, where T is the temporal length of the sample, and δf is the averaging frequency interval. Data are preconditioned by linear-trend removal. Error analysis can be performed quantitatively if Gaussian statistics are assumed. The bias error on the autospectral function is equal to the autopower of the noise, which is approximately constant in the case of white detector noise, and is thus subtracted in the calculation; the relative statistical error is $\sqrt{2/m}$. In the case of the cross-spectral function, the bias error on the modulus is generally negligible and the relative random error is $\sqrt{2}/(|\gamma|\sqrt{m})$, where $|\gamma|$ is the square root of the coherence function (the coherence function is defined here, as in most textbooks, as the *square* modulus of the normalized cross-spectral function).

The coherence and cross-phase functions are also routinely calculated. The standard deviation of the phase estimate is equal to $[(|\gamma|^{-2} - 1)/m]^{1/2}$. The coherence function carries a negative relative bias given by twice the reciprocal of the signal-to-noise ratio: this is removed by subtracting the noise from the autopower value before normalization. In addition, an approximate bias error of $2(1 - |\gamma|^2)^2/m$ is generated by the sampling procedure. The random error is approximately equal to $2|\gamma|(1 - |\gamma|^2)/\sqrt{m}$; however, more complex expressions are employed to increase the accuracy of the estimate for low values of $|\gamma|^2$ (Ref. 165).

The spectral quantities just described can also be studied as they vary in time over time scales longer than the integration interval (i.e. the inverse of the smallest characteristic frequency under exam). This analysis affords a very direct visualization of the evolution of turbulence during a plasma discharge, and on phase transitions such as the L–H transition.[168]

The computations described thus far are carried out by software available on the VAX computers at General Atomics, adapted for the needs of our data (particularly to allow the inclusion of calibration factors and noise subtraction). By contrast, the software for the evaluation of time-delay correlation functions was specially written during this thesis work. The program TEMPUS calculates the crosscorrelation function, the correlation coefficient, and the envelope of the correlation coefficient between two sets of data. (The envelope is defined as $\{\rho^2 + [\mathcal{H}(\rho)]^2\}^{1/2}$, where ρ is the correlation coefficient and $\mathcal{H}(\rho)$ is its Hilbert transform.[165])

The correlation functions are computed by means of the standard double-FFT method.[165] The program offers optional detrending and filtering (lowpass, highpass,

bandpass, or band-elimination); linear detrending was used routinely in our analysis.

The error analysis in the time domain, in the case of Gaussian probability distributions, presents many similarities with the frequency-domain case. The estimate of the autocorrelation function is biased by the noise autocorrelation function only at zero delay. The correlation coefficient is then negatively biased by the normalization factors, the relative bias being equal to the reciprocal of the signal-to-noise ratio. As in the case of frequency-domain analysis, the bias is subtracted by software. The relative random error on the estimator of the correlation function is equal to $(1+\rho^{-2})^{1/2}/\sqrt{m}$, where $\rho(\tau)$ is the correlation coefficient. The standard deviation of the coefficient estimate is approximated by $(1-\rho^2)/\sqrt{m}$.

In all the cases described, digital highpass filtering is applied at a cutoff frequency of 8 kHz to eliminate vibrational effects. Different passbands have also been employed in various cases to investigate specific physics issues.

After the basic analysis is completed, various techniques of higher-level data reduction may be employed, depending on the physical problem under investigation. In all cases, the unique characteristics of the diagnostics have mandated the development of dedicated Fortran programs to perform the analysis.

It has been found that in many regimes the autospectral functions can be fitted reasonably well with an inverse power law. Therefore, this fitting procedure is applied systematically to all autospectral power estimations. In the time domain, autocorrelation functions often approach an exponentially decaying form, and a corresponding one-parameter fit is applied to these functions to estimate the local turbulence decorrelation time. By contrast, little success has been achieved in fitting the crosscorrelation functions with simple functional forms.

The equal-time coefficient and its Hilbert transform form a complex function of the radial separation that carries information on the radial correlation structure. This spatial function is generated routinely for a set of discrete time intervals in stationary regimes of the discharge; this procedure is repeated several times using all spatial channels as references in turn, to investigate the spatial *variation* of the correlation function. A general plot using all possible crosscorrelations is also generated, although this is useful in general only in the high-resolution cases. In general, it has been found that this function conforms rather well to the following form:

$$C(\Delta R;\Delta t=0)=\exp\left[-\frac{(\Delta R)^2}{\mathcal{L}_R^2}\right]\left(\frac{1+P_R}{2}e^{ik_{0,R}\Delta R}+\frac{1-P_R}{2}e^{-ik_{0,R}\Delta R}\right); \quad (3.17)$$

accordingly, regression analysis[169,170] is applied to the experimental function to obtain a three-parameter fit to this form: $k_{0,R}$ is then interpreted as an average wave number, $\mathcal{L}_R$ as a correlation length, and P_R as a propagation coefficient (1 for purely outward, -1 for purely inward propagation). These quantities can then be plotted as functions of time, along with their confidence intervals — or "error bars", obtained by standard propagation through the fit of the statistical uncertainty on $C(\Delta R;\Delta t=0)$ — with as fine a temporal resolution as allowed by the required statistics. These

quantities, particularly the correlation length, are of great interest in the study of turbulence, as they play an important role in various nonlinear theories (see Chapter 6).

The spatial Fourier transform of $C(\Delta R; \Delta t = 0)$ is the normalized radial wave-number spectrum of the fluctuations, $s(k_R)$. Since only a few spatial points are available, several different techniques of varying complexities for sparse Fourier transforms have been incorporated in the software. These include the following: simple Fourier series calculation (integration of the histogram, i.e. by trapezoidal rule); linear interpolation followed by Fourier integration; integration by a third-order finite-difference Gill-Miller method;[171] a maximum-likelihood method that integrates a cubic-spline interpolator; and a maximum-entropy Algebraic Reconstruction Technique (ART) algorithm.[172–174] Extensive testing has shown that these techniques yield acceptably similar results; the maximum-entropy technique is utilized preferentially.

After the Fourier transform has been computed, the spectrum is divided by the PCI transfer function. The low-k cutoff point is taken to be the $1/e$ folding point of the transfer function (approximately $0.8 \times k_c$, see Fig. 3.28).

In the case of our diagnostic, the spectrum that can be measured is, strictly speaking, limited to horizontal wave vectors, with the vertical component equal to zero. This is a consequence of the vertical line integration. In tokamak physics, it is more desirable in general to study the spatial distribution of the local spectra, both in the radial and in the poloidal direction. The geometric constraints of the PCI apparatus permit to extract some of this information, under appropriate conditions, from our nonlocal measurement. This is the subject of the next chapter.

Once the average wave number $k_{0,R}$ has been obtained, one can compute the spatial Fourier transform of the crosscorrelation function $C(\Delta R; \Delta t)$ at that particular wave number: the result can be described as an intrinsic (fixed-k) autocorrelation function, and its exponential decay gives a measure of the intrinsic decorrelation time of the turbulence.

A similar spatial analysis is routinely carried out also in frequency space, by substituting the complex coherence function (the normalized cross-spectral function, also sometimes called *coherency*[165]) for the spatial correlation function. This function is seen to follow approximately the same functional form, given by Eq. (3.17), and the corresponding fitting procedure is accordingly applied to the coherence also. As a result, average wave numbers and correlation lengths can be generated as functions of frequency: thus, an approximate dispersion relation $k_{0,R}(\omega)$ is found.

The obvious next step is the complete spectrum $S(k_R, \omega)$, which is also computed and plotted as a matter of course. In many cases, a more useful quantity is the *conditional spectrum* $s(k_R|\omega)$, defined as the spatial Fourier transform of the complex coherence function.[175,142] In the case of spatially uniform turbulence, the relation $s(k_R|\omega) = S(k_R, \omega)/S(\omega)$ applies: thus, the conditional spectrum provides information on the form of the wave-number spectrum as a function of frequency, factoring out the absolute dependence on frequency.

The probability distribution function (PDF) of the fluctuations and its moments

were also studied (see §5.7). A program was written for this task. The program allows the user to select the bin width and the maximum number of standard deviations employed in the calculation of the moments, and permits the introduction of lowpass and highpass filters. The relative statistical error on the PDF is given as $\sqrt{m/(W \times \mathrm{PDF})}$,[165] where W is the bin width. After the average is removed and the PDF is normalized to its standard deviation, the moments of third to sixth order are calculated: the skewness S [relative error $\epsilon = \sqrt{(15 - S^2)/m}$], the coefficient of kurtosis $K' = K - 3$ [$\epsilon = \sqrt{(105 - K'^2)/m}$], the superskewness ($\epsilon \simeq \sqrt{945/m}$), and the coefficient of super kurtosis $KK' = KK - 15$ ($\epsilon \simeq \sqrt{10395/m}$).

Two additional analysis techniques developed for this study deserve a brief mention. The investigation of the spectral characteristics of transient events such as ELMs[59,69] is often hampered by their short duration, which conflicts with the need of an adequate statistical sample. Under the assumption that the statistics of separate events are similar, averaging can be performed over a discrete set of events, rejecting the time intervals in between. This technique has been applied to ELM studies, as will be discussed in Chapter 5.

The problem of nonlocality, which will be addressed at length in the next chapter, can be tackled by exploiting the edge location of our diagnostic and the multichordal nature of the measurement. If the turbulence amplitude is assumed to be constant on a magnetic flux surface, and to vary slowly across surfaces, one can attempt to subtract the power signal on the outermost chord, multiplied by an appropriate factor, from the signal on the adjacent chord, thus removing from the latter the contributions from the outermost layer. The multiplication factor must be equal to the ratio of the lengths of the segments of the two chords delimited by the same flux surfaces (power, rather than amplitude, adds linearly in the case of broadband turbulence). This procedure can then be repeated for all chords, and a more localized measurement can in principle be obtained. The software developed for this task computes the multiplication factors for actual magnetic geometries generated by the equilibrium program EFIT.[176] Unfortunately, this technique has been generally unsuccessful, indicating — not too surprisingly — that the assumptions are not valid.

A more defensible alternative is to simply divide the power by the length of the chord, without performing any subtraction. By further dividing by an estimate of the vertical correlation length, an estimate of the absolute density fluctuation power can be obtained. The choice of the integration length is the principal difficulty in this procedure: in the SOL one can use either an estimate of the SOL width or the entire length of the beam path within the vessel; inside the LCFS, one can use the length of the chord up to the LCFS, or add to it the width of the SOL: this is an especially important question for chords close to the LCFS. These issues will be discussed in more detailed in §5.6.

The various functional fits described in this section utilize minimum-χ^2 algorithms. Analytical formulas are used in the simplest cases; more generally, numerical algorithms are employed. These allow for error bars both on the independent variable (spatial uncertainty) and on the dependent variable (statistical uncertainty), and

also for constraints on the fitting parameters. They are part of the subroutine library NAG. It should be noted here that these fits often result in large χ^2 values. This, of course, is to be expected in general, as the functional forms are chosen on the basis of physical intuition and mathematical simplicity, but do not conform to any rigorous theoretical models. To state it simply, there is no *a priori* reason to expect the experimental functions to obey these laws. The fitting parameters should then be described simply as our best experimental estimations of the correlation length, decorrelation time, etc., all quantities that are integral parts of most theories of turbulence.

4 Modeling of the Measurement

The steady increase in the complexity of magnetically-confined plasma-fusion experiments over the last three decades has been accompanied by a corresponding increase in the sophistication of diagnostic technology. The desire to improve the spatial resolution of measurements, in particular, has been the motivating force behind some of the most advanced techniques employed in the present generation of tokamak devices.

In the realm of fluctuation diagnostics, localization has been attained by geometric means (as with beam emission spectroscopy[50]), by frequency discrimination (as with reflectometry[40]), and by local detection (as with material probes[71]). Transmission and emission techniques, by contrast, provide measurements that are generally averaged along the line of sight. Crossed-beam correlation techniques have been employed to enhance the resolution of CO_2-laser scattering measurements.[177] When multiple lines of sight at different angles are available, local information can sometimes be inferred by using inversion methods,[178] as in the case of x-ray tomography;[179] similarly, the symmetry properties of the medium may permit to eliminate one or more variables from the problem and to devise an appropriate inversion algorithm. An integral inversion technique can also be employed to derive the density profile of a plasma slab from a measurement of its frequency-dependent impedance.[180]

The lack of longitudinal resolution constitutes the principal limitation of transmission techniques. In the case of the DIII–D phase-contrast imaging (PCI) apparatus, the problem is alleviated in part by the geometrical constraints of the measurement. Since the beam propagates along the edge of the plasma cross section (see Fig. 3.5), the integration volume spans a relatively small fraction of the minor radius. In addition, the line integration effectively selects wave vectors that are perpendicular to the direction of propagation; since, as shown in Fig. 3.5, that direction is nearly tangent to the poloidal magnetic-field lines, it can be concluded that the measured wave vectors are nearly perpendicular to the poloidal field. This selection rule aids considerably in the interpretation of the PCI measurements, as turbulence is generally characterized theoretically by its spectral distributions in the poloidal and radial directions (parallel and perpendicular to the poloidal field, respectively). Also, since the wave vectors are nearly perpendicular to the $\mathbf{E} \times \mathbf{B}$ drift velocity, the measurement is essentially immune to Doppler shifts; thus, the frequency spectrum of the turbulence can be observed directly in the plasma frame of reference.

These qualitative observations were corroborated by an extensive quantitative analysis. This analysis is based on a functional model of the turbulence spectrum, from which the two-point correlation function of the turbulence can be derived. The pointwise correlation function is then integrated numerically along the two respective vertical chords; both the magnetic geometry and the $\mathbf{E} \times \mathbf{B}$ velocity profile are derived from experimental measurements in an actual DIII–D discharge. The final result of the numerical integration is the correlation function of the corresponding PCI signals. By repeating this calculation for a variety of turbulence spectra and plasma

geometries, the constraints on the inverse problem — that is, inferring the spectra from the measurements — can be verified.

The remainder of this chapter is organized as follows. The inversion problem for the two-point correlation function is stated in §4.1; solutions based on various symmetry assumptions are also presented, along with a discussion of the applicability of these assumptions. A brief analysis of the significance of the correlation function in various physical scenarios is carried out in §4.2; in particular, some considerations are offered on the relation between the correlation functions in the plasma frame and in the laboratory frame in the presence of an $\mathbf{E} \times \mathbf{B}$ drift. In §4.3 our general model for the turbulence spectra is introduced; the general two-point correlation function is calculated analytically in Appendix G, while a simplified and approximate expression is discussed in §4.3 for illustration purposes. The physical meaning of the model is then explored in §4.4 by applying successive approximations to the general problem and drawing some qualitative conclusions; part of the mathematical derivation is also in Appendix G. The computer program developed for the quantitative analysis is described in §4.5; this section is completed by a discussion of the results, and by a comparison with the qualitative analysis of the previous section.

4.1 The Integral Inversion Problem

We shall consider a two-dimensional problem with spatial variables R and z; with reference to the DIII–D PCI geometry, R is identified with the major radius of the tokamak, and z is the vertical distance from the midplane. We can treat the problem as two-dimensional because of the symmetric distribution of turbulence along the magnetic-field lines, which has been proven by experimental observations.[181,182] In view of the small value of the ratio of the poloidal and toroidal fields, the helicity of the magnetic-field lines (see Fig. 1.1) may be ignored, and we can identify the direction of symmetry with the azimuthal direction for the purposes of this discussion. Also, in this section we shall only consider quantities defined in the laboratory frame.

The two-point, time-delayed correlation function of the density fluctuations is defined as

$$C_{12}(R, z, t; R', z', t') \equiv \left\langle \tilde{n}(R, z, t)\, \tilde{n}(R', z', t') \right\rangle, \tag{4.1}$$

where the angular brackets <> denote the operation of ensemble averaging.

Similarly, the correlation function of the line integrals of the density fluctuations (i.e., of the quantities measured by the PCI apparatus) is defined as

$$\Gamma_{12}(R, t; R', t') \equiv \left\langle \int \tilde{n}(R, z, t) dz \int \tilde{n}(R', z', t') dz' \right\rangle. \tag{4.2}$$

The inversion problem consists of inferring the function C_{12} from the measured function Γ_{12}. Since C_{12} is a function of four spatial variables, while Γ_{12} is a function of two spatial variables (see Fig. 4.1), the inversion cannot be performed unless two variables are eliminated from the problem through symmetry assumptions.

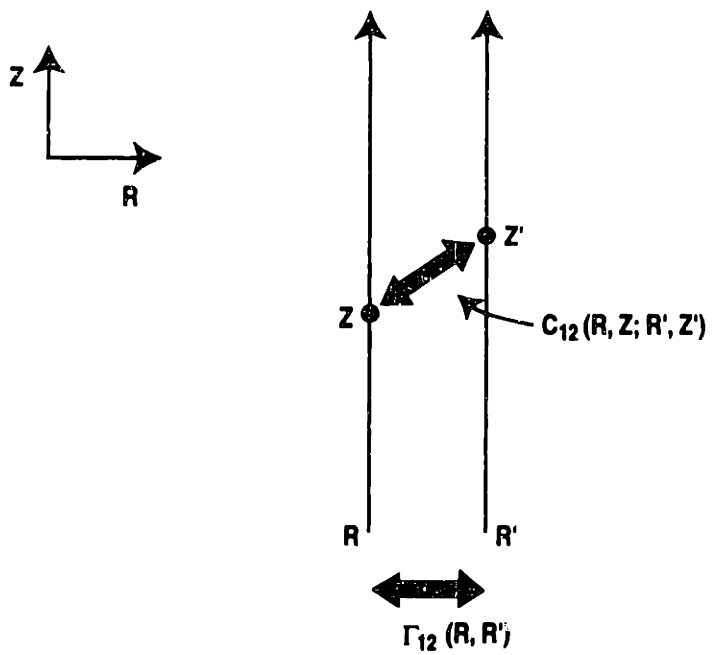

Fig. 4.1 Illustration of local correlation function C_{12} (a function of 4 variables) and line-integrated correlation function Γ_{12} (a function of two variables).

We can substitute Eq. (4.1) in Eq. (4.2) and write

$$\Gamma_{12}(R_{\rm av}, t_{\rm av}; r, \tau) = \iint C_{12}(R_{\rm av}, z_{\rm av}, t_{\rm av}; r, \zeta, \tau)\, dz_{\rm av}\, d\zeta, \tag{4.3}$$

where $R_{\rm av} = (R + R')/2$, $z_{\rm av} = (z + z')/2$, $t_{\rm av} = (t + t')/2$, $r = R - R'$, $\zeta = z - z'$, and $\tau = t - t'$.

We can obtain a useful relationship for the autocorrelation functions by defining the vertical correlation length

$$\mathcal{L}_z(R_{\rm av}, z_{\rm av}, t_{\rm av}) \equiv \frac{1}{\sqrt{\pi}} \frac{\int C_{12}(R_{\rm av}, z_{\rm av}, t_{\rm av}; 0, \zeta, 0)\, d\zeta}{C_{12}(R_{\rm av}, z_{\rm av}, t_{\rm av}; 0, 0, 0)}. \tag{4.4}$$

The factor $(\pi)^{-1/2}$ has been introduced for consistency with the Gaussian correlation function that will be used in our model, and with the definition of $\mathcal{L}$ that has been used in recent literature,[51] i.e., as the $1/e$ point of the correlation function.

If the turbulence is now assumed to be homogeneous, we can rewrite Eq. (4.3) as[143]

$$\Gamma_{12}(t_{\rm av}; r, \tau) = L_z \int C_{12}(t_{\rm av}; r, \zeta, \tau)\, d\zeta, \tag{4.5}$$

where L_z is the length of the plasma chord. We have thus removed one variable, $z_{\rm av}$, from the problem, and rendered the independent variable $R_{\rm av}$ redundant: that is, it would be sufficient to calculate the correlations with respect to a fixed chord, rather

than between all pairs of chords available. Substituting Eq. (4.4) in Eq. (4.5) for $r = 0$ and $\tau = 0$, we obtain the equal-time autocorrelation function

$$\Gamma_{12}(t_{\rm av}; 0, 0) = \left\langle \tilde{n}^2(t_{\rm av}) \right\rangle \sqrt{\pi} \mathcal{L}_z(t_{\rm av}) L_z. \tag{4.6}$$

Hence, we find for the rms value of the turbulence an effective integration length equal to $(\sqrt{\pi}\mathcal{L}_z L_z)^{1/2}$.

If we now make the further assumption that the turbulence is isotropic, we eliminate another variable and we can finally write Eq. (4.5) as

$$\Gamma_{12}(t_{\rm av}; r, \tau) = L_z \int_{r^2}^{\infty} C_{12}(t_{\rm av}; \sigma, \tau) \frac{d\sigma}{\sqrt{\sigma - r^2}}, \tag{4.7}$$

where $\sigma \equiv r^2 + \zeta^2$, and it has been assumed that the correlation function vanishes at distances of the order of the dimensions of the plasma column. Equation (4.7) is a Volterra integral equation of the first kind, and, in particular, it can be reduced to an Abel equation for the unknown function $\sigma^{-3/2} C_{12}$ by using the variable $1/\sigma$. Thus, Abel's inversion[178] can be applied to the solution of this problem under the conditions stated.[183]

If the turbulence is isotropic but not homogeneous, Abel's inversion yields $\int C_{12}(R_{\rm av}, z_{\rm av}, t_{\rm av}; \sigma, \tau)\, dz_{\rm av}$, the line integral of the pointwise correlation function at each radial point. If homogeneity over a magnetic flux surface can be assumed, in addition to isotropy, we again eliminate two variables and can solve the inverse problem.[184] In the special case of a plasma with a circular cross section, the pointwise correlation function C_{12} can then be retrieved through two applications of Abel's inversion with respect to the variables $1/r^2$ and $1/R^2$, respectively. More complicated geometries require a numerical solution of the integral equation in the mean spatial variables.

Unfortunately, all the assumptions considered thus far fail in tokamaks in general, and particularly in the highly inhomogeneous plasmas that exist at the edge of DIII-D, where our goal is to study the small-scale structure of the spectra. Recent results from beam-emission spectroscopy measurements in TFTR[51] have shown a marked anisotropy in the turbulence spectra between the poloidal and the radial direction. Even the assumption of homogeneity over a flux surface is negated by the up-down asymmetries observed in the TEXT tokamak.[185] The contributions from the scrape-off layer are a source of additional difficulties.

Nevertheless, the peculiar geometry of the PCI apparatus aids in the interpretation of the results. As can be seen in Fig. 3.5, the direction of propagation of the laser beam is nearly tangent to the field lines, i.e., it is everywhere close to the poloidal direction. The effect of the line integration is to eliminate contributions from fluctuations that have a finite spatial frequency along the beam, i.e., wave vectors with a nonzero vertical component. Thus, the measurement is only sensitive to horizontal wave vectors. As Fig. 4.2 shows, in our geometry a horizontal wave vector is primarily radial, with only a small poloidal component at locations far from the midplane. The principal aim of the remainder of this chapter will be to support this simple, but important observation with a more quantitative foundation.

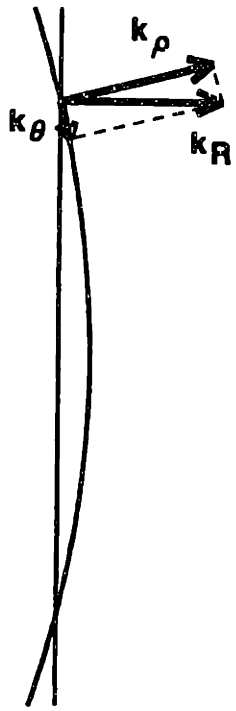

Fig. 4.2 Decomposition of a horizontal vector into its radial and poloidal components.

4.2 The Correlation Structure of Plasma Fluctuations

A great many types of fluctuations can coexist in a plasma. The individual nature of the different excitation modes, combined with the nonlinear coupling among them, can lead to a variety of spectra in both wave-number and frequency space.

Coherent modes are either generated by external means (as in the case of radio-frequency waves) or result from large-scale MHD instabilities. In general, these types of modes are easily identified experimentally by their narrowband spectral functions and by their high degree of spatial coherence. In addition, MHD modes in practice are characterized by the periodic nature of the spatial distribution of their magnetic component, which can be measured by external magnetic coils.

When the spectra are broadband in both frequency and wave-number space, but the wave-number spectrum *at a given frequency* (and vice versa) is peaked, one speaks of a semicoherent mode. In this case the plasma supports a continuous set of oscillations, characterized by a well-defined dispersion relation. The width of the frequency spectrum is then related to that of the wave-number spectrum by the approximate relation

$$\Delta\omega \sim \mathbf{v}_g \cdot \Delta\mathbf{k}, \tag{4.8}$$

where $\mathbf{v}_g$ is the group velocity of the perturbation. Experimentally, a semicoherent mode is identified by good spatial correlation at fixed frequency.

In practice, each individual excitation mode has a finite frequency bandwidth, determined both by its linear damping rate and by its nonlinear interaction with other modes.[186] The nonlinear interaction between the natural modes can lead to a turbulent state, which can be loosely defined as a condition in which a large number of degrees of freedom are excited.[187] One further distinguishes between strong turbulence, when the growth rate γ is comparable to or larger than the frequency of the mode, and weak turbulence, when $\gamma \ll \omega(\mathbf{k})$. Experimentally, the signature trait of turbulence is the broadening of the wave-number spectrum for each given frequency, and vice versa.

The standard statistical treatment of a turbulent state relies on the postulate of random phase, which can be stated as follows:

$$\langle \hat{n}^*(\mathbf{k}', \omega')\, \hat{n}(\mathbf{k}, \omega) \rangle = \langle \tilde{n}^2 \rangle\, I(\mathbf{k}, \omega) \delta(\mathbf{k} - \mathbf{k}') \delta(\omega - \omega'), \tag{4.9}$$

where $\hat{n}(\mathbf{k}, \omega)$ is the spectrum of the density fluctuations. In the general 3-dimensional case, the two-point, time-delayed correlation function can then be expressed by means of the spectral function $I(\mathbf{k}, \omega)$ as follows:

$$\langle \tilde{n}(\mathbf{x}, t)\, \tilde{n}(\mathbf{x}', t') \rangle = \frac{\langle \tilde{n}^2 \rangle}{(2\pi)^4} \iint I(\mathbf{k}, \omega)\, e^{i\mathbf{k}\cdot(\mathbf{x}-\mathbf{x}') - i\omega(t-t')}\, d^3k\, d\omega. \tag{4.10}$$

By virtue of Eq. (4.9), the spectral function is real and positive defined; in addition, since it is the Fourier transform of a real function, I must be Hermitian, that is, symmetric upon joint reversal of $\mathbf{k}$ and ω.

In the presence of an electric field in a magnetized plasma, the frequency of fluctuations in the laboratory frame is Doppler-shifted according to the following expression:

$$\omega_{\text{lab}} = \omega + \mathbf{k} \cdot \mathbf{v}_E, \tag{4.11}$$

where

$$\mathbf{v}_E = c \frac{\mathbf{E} \times \mathbf{B}}{B^2}. \tag{4.12}$$

This Doppler shift, which has been verified experimentally[188] by scattering measurements, is a universal effect independent of the particular excitation mode, since all particles drift at the $\mathbf{E} \times \mathbf{B}$ velocity.[189] A uniform and constant drift has no effect on the physics of the modes, as required by Galilean relativity. However, a spatially varying Doppler shift can significantly alter the correlation structure of the fluctuations: an $\mathbf{E} \times \mathbf{B}$ drift with a nonzero gradient will have the general effect of broadening the spectral functions.

Sheared electric fields exist in the edge of DIII–D in H mode, and to a lesser extent in L mode.[61] The effect of the $\mathbf{E} \times \mathbf{B}$ shear on the structure of the turbulence is small when the *variation* of the Doppler shift over a correlation length is small compared with the unshifted frequency of the mode. This intuitive assertion can be justified qualitatively as follows. Let us rewrite the correlation function [Eq. (4.10)]

in the laboratory frame in the presence of a sheared electric field. By making the tentative assumption that Eq. (4.9) still holds for the unshifted plasma modes, we can write

$$\langle \tilde{n}(\mathbf{x},t)\,\tilde{n}(\mathbf{x}',t')\rangle = \frac{\langle \tilde{n}^2\rangle}{(2\pi)^4}\int d^3k \int d\omega\, I(\mathbf{k},\omega)\exp\Big\{ i\mathbf{k}\cdot(\mathbf{x}-\mathbf{x}') - i\omega(t-t') - i\mathbf{k}\cdot\big[t\mathbf{v}_E(\mathbf{x}) - t'\mathbf{v}_E(\mathbf{x}')\big]\Big\}, \tag{4.13}$$

where we have assumed for simplicity that the electric field is constant in time. Equation (4.13) can be recast as

$$\langle \tilde{n}(\mathbf{x},t)\,\tilde{n}(\mathbf{x}',t')\rangle = \frac{\langle \tilde{n}^2\rangle}{(2\pi)^4}\int d^3k \int d\omega\, I(\mathbf{k},\omega)\exp\Big\{ i\mathbf{k}\cdot(\mathbf{x}-\mathbf{x}') - i(\omega+\mathbf{k}\cdot\mathbf{v}_{E,\mathrm{av}})(t-t') - it_{\mathrm{av}}\mathbf{k}\cdot\big[\mathbf{v}_E(\mathbf{x}) - \mathbf{v}_E(\mathbf{x}')\big]\Big\}, \tag{4.14}$$

where $\mathbf{v}_{E,\mathrm{av}} = [\mathbf{v}_E(\mathbf{x}) + \mathbf{v}_E(\mathbf{x}')]/2$ and $t_{\mathrm{av}} = (t+t')/2$. The last phase term breaks the temporal invariance of the system: as time (t_{av}) goes by, this phase increases indefinitely and fluctuations become increasingly decorrelated at any finite distance. This is equivalent to an unbounded broadening of the spectra. In quasi-steady-state conditions, this result is clearly paradoxical; therefore, we must conclude that our ansatz was incorrect: that is, the sheared flow must alter the spatial statistics of the turbulence, generating a new steady-state spectral function $I(\mathbf{k},\omega)$ that permits application of Eq. (4.10) in the laboratory frame.

It is important to note that this effect is not related to any specific measurement technique; rather, the fundamental structure of the turbulence is itself altered by the sheared drift velocity. Indeed, the mechanism believed to be responsible for H mode[63] is the reduction of transport due to decorrelation of the turbulence, caused in turn by a sheared $\mathbf{E}\times\mathbf{B}$ drift.

Equation (4.14), though invalid in steady-state conditions, must be applicable for a vanishingly small velocity shear. It is reasonable then to use Eq. (4.14) to determine the approximate conditions under which the shear can be ignored. We shall focus on a single frequency component ω (in the plasma frame), and postulate a finite wave packet peaked about a mean wave vector $\mathbf{k}(\omega)$. In the integral over $\mathbf{k}$, the time-dependent phase term can be neglected if

$$\big|t_{\mathrm{av}}\mathbf{k}\cdot\big[\mathbf{v}_E(\mathbf{x}) - \mathbf{v}_E(\mathbf{x}')\big]\big| \ll 1. \tag{4.15}$$

The system must be time-invariant on a time scale of the order of the reciprocal of the angular frequency of oscillation; thus, we can take $t_{\mathrm{av}} \simeq 1/\omega$. Also, the maximum significant displacement in a given direction $\hat{\imath}$ can be taken to be equal to

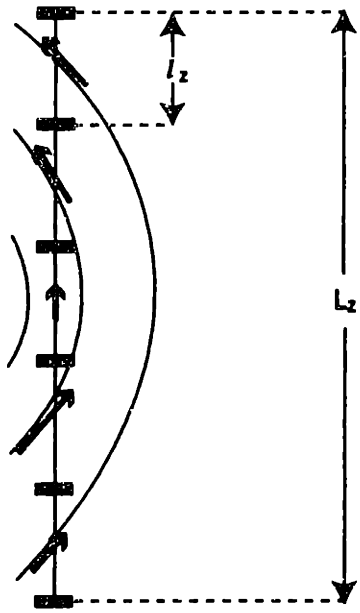

Fig. 4.3 Subdivision of integration length into segment of length l_z.

the correlation length $\mathcal{L}_i$, measured at zero $\mathbf{E} \times \mathbf{B}$ velocity and at fixed frequency. Thus, Eq. (4.15) yields, as a sufficient condition, the following approximate relations:

$$\varsigma_i \ll 1, \tag{4.16}$$

where we have introduced the *shear decorrelation parameters*

$$\varsigma_i = \frac{\mathcal{L}_i}{\omega} \left| \frac{\partial \mathbf{v}_E}{\partial x_i} \cdot \mathbf{k}(\omega) \right|. \tag{4.17}$$

The parameter ς_i is equal to the *variation* of the Doppler shift over a correlation length (in the $\hat{x}_i$ direction), divided by the unshifted frequency.

When Eq. (4.16) is satisfied, the considerations presented in §4.1 for line-integrated measurements can be applied, with the appropriate modifications. In particular, the equivalent expression to Eq. (4.3) is

$$\begin{aligned}&\Gamma_{12}(R_{\mathrm{av}}, t_{\mathrm{av}}; \tau, \tau) \\ &\quad = \iint C_{12}\left[R_{\mathrm{av}}, z_{\mathrm{av}}, t_{\mathrm{av}}; \tau - \tau v_{E,R}(R_{\mathrm{av}}, z_{\mathrm{av}}), \zeta - \tau v_{E,z}(R_{\mathrm{av}}, z_{\mathrm{av}}), \tau\right] dz_{\mathrm{av}}\, d\zeta. \end{aligned} \tag{4.18}$$

When considering the Fourier spectrum of Γ_{12}, the line integration can be seen as a sum over $L_z/\mathcal{L}_z$ segments of length $\mathcal{L}_z$, each of which contributes at the Doppler-shifted frequency that corresponds to the local drift velocity (see Fig. 4.3). When the $\mathbf{E} \times \mathbf{B}$ velocity is known with some accuracy, this circumstance can be used to improve the spatial resolution of a measurement through frequency discrimination; this method has been applied to FIR scattering measurements in DIII-D.[190]

When the shear decorrelation parameters are large and Eq. (4.16) is not satisfied, Eq. (4.18) is inapplicable, and indeed the concept of an "intrinsic" spectrum loses its meaning: the only meaningful information to be extracted from a fluctuation measurement is then the spectrum in the laboratory frame.

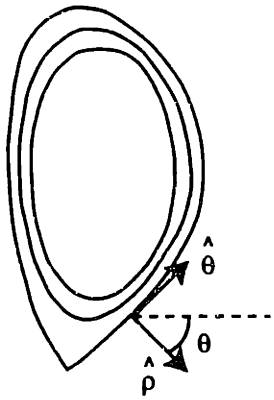

Fig. 4.4 Flux coordinate system.

4.3 A Model of Plasma Turbulence

The statistics of plasma turbulence are defined by the postulate of random phase [Eq. (4.9)] and by the spectral function $I(\mathbf{k},\omega)$. In view of the azimuthal symmetry of the system, we restrict the problem to the two-dimensional poloidal plane. We also adopt the flux coordinate system defined by the local unit vectors $\hat{\rho}$ and $\hat{\theta}$, which are in each point normal and tangent, respectively, to the local magnetic flux surface; this is defined in turn as a surface over which the *stream function*[191] $\psi = RA_\phi$ is constant (here, A_ϕ is the toroidal component of the vector potential). This coordinate system is the natural one in which to define the fluctuation spectra (see Fig. 4.4).

The conversion between the $(\hat{R},\hat{z})$ system and the $(\hat{\rho},\hat{\theta})$ system, for an arbitrary vector $\mathbf{w}$, can be readily performed by means of the simple expression

$$\begin{cases} w_\rho = w_R\cos\vartheta + w_z\sin\vartheta \\ w_\theta = -w_R\sin\vartheta + w_z\cos\vartheta, \end{cases} \tag{4.19}$$

where ϑ is the angle between $\hat{\rho}$ and the horizontal plane.

We wish to treat the large-scale and fine-scale structures of the turbulence separately. To that end, we adopt a quasi-homogeneous approximation[109] and modify Eq. (4.10) as follows:

$$\begin{aligned} \langle\tilde{n}(\mathbf{x},t)\,\tilde{n}(\mathbf{x}',t')\rangle = \frac{1}{(2\pi)^3}\langle\tilde{n}^2(\mathbf{x}_{\mathrm{av}},t_{\mathrm{av}})\rangle\int dk_R\int dk_z\int d\omega\, I(\mathbf{k},\omega) \\ \times\exp\left[i\mathbf{k}\cdot(\mathbf{x}-\mathbf{x}')-i\omega(t-t')\right], \end{aligned} \tag{4.20}$$

where $\mathbf{x}_{\mathrm{av}} = (\mathbf{x}+\mathbf{x}')/2$. The validity of this approximation rests on the assumptions

$$\begin{cases} \left|\nabla\ln\left(\langle\tilde{n}^2\rangle\right)\right|^{-1} \gg \mathcal{L} \\ \left|\partial\ln\left(\langle\tilde{n}^2\rangle\right)/\partial t\right|^{-1} \gg \tau_d, \end{cases} \tag{4.21}$$

where τ_d is the decorrelation time of the fluctuations.

In the presence of an $\mathbf{E} \times \mathbf{B}$ drift, Eq. (4.20) becomes

$$\langle \tilde{n}(\mathbf{x},t)\,\tilde{n}(\mathbf{x}',t')\rangle = \frac{1}{(2\pi)^3}\langle \tilde{n}^2(\mathbf{x}_{\mathrm{av}},t_{\mathrm{av}})\rangle \int dk_R \int dk_z \int d\omega\, I(\mathbf{k},\omega) \times \exp\left[i\mathbf{k}\cdot(\mathbf{x}-\mathbf{x}') - i(\omega + \mathbf{k}\cdot\mathbf{v}_{E,\mathrm{av}})(t-t')\right], \tag{4.22}$$

where the time-dependent term of Eq. (4.14) has been neglected under the assumption $\varsigma_i \ll 1$ [cf. Eq. (4.17)].

For the moment we do not specify the function $\langle \tilde{n}^2 \rangle$. For the spectral function, we adopt the following model:

$$I(\mathbf{k},\omega) = \frac{\pi}{2}\mathcal{L}_\rho \mathcal{L}_\theta \sum_{\pm} \exp\left[-\frac{\mathcal{L}_\rho^2(\pm k_\rho - k_{0,\rho})^2}{4}\right] \exp\left[-\frac{\mathcal{L}_\theta^2(\pm k_\theta - k_{0,\theta})^2}{4}\right] \times \hat{F}[\pm\omega - \omega(\mathbf{k})]. \tag{4.23}$$

The sum over the signs is necessary to ensure that I is Hermitian. It is important to note that this definition treats space and time asymmetrically. The wave-number spectrum is assigned first, along with a dispersion relation $\omega(\mathbf{k})$; then the function $\hat{F}$, as yet unspecified, takes into account the turbulent broadening of the frequency spectrum for each given $\mathbf{k}$. Hence, the *total* width of the frequency spectrum is determined both by $\hat{F}$ and by the Gaussian functions. In the language of fluid dynamics (drawing a parallel between the motion of a fluid and that of our wave packet), it could be said that this definition reflects a Eulerian approach for the wave-number spectrum and a Lagrangian approach for the frequency spectrum. The two approaches could be reversed; however, our choice is consistent with the definitions of correlation lengths and decorrelation time found in the majority of the literature.

It should also be noted that all the parameters in Eq. (4.23), such as the correlation lengths and the mean wave vector $\mathbf{k}_0$, could be dependent on $\mathbf{x}_{\mathrm{av}}$ and t_{av}.

Our next step consists of prescribing a dispersion relation; this task is simplified by adopting a group-velocity approximation, i.e., an expansion about the peak wave vector $\mathbf{k}_0$; hence,

$$\omega(\mathbf{k}) = \omega_0 + \mathbf{v}_g \cdot (\mathbf{k} - \mathbf{k}_0), \tag{4.24}$$

where $\omega_0 = \omega(\mathbf{k}_0)$ and $\mathbf{v}_g$ is the group velocity.

Finally, we shall explore the two following functional forms for the turbulent frequency form factor:

$$\hat{F}_1(\omega') = \sqrt{\pi}\,\tau_d \exp\left[-\frac{\omega'^2\tau_d^2}{4}\right], \tag{4.25}$$

and

$$\hat{F}_2(\omega') = \frac{2\tau_d}{1+\omega'^2\tau_d^2}, \tag{4.26}$$

where $\omega' = \pm\omega - \omega(\mathbf{k})$. The function $\hat{F}_1$ presents some advantages for a preliminary qualitative analysis, as will be seen in the next section, since it has the same functional

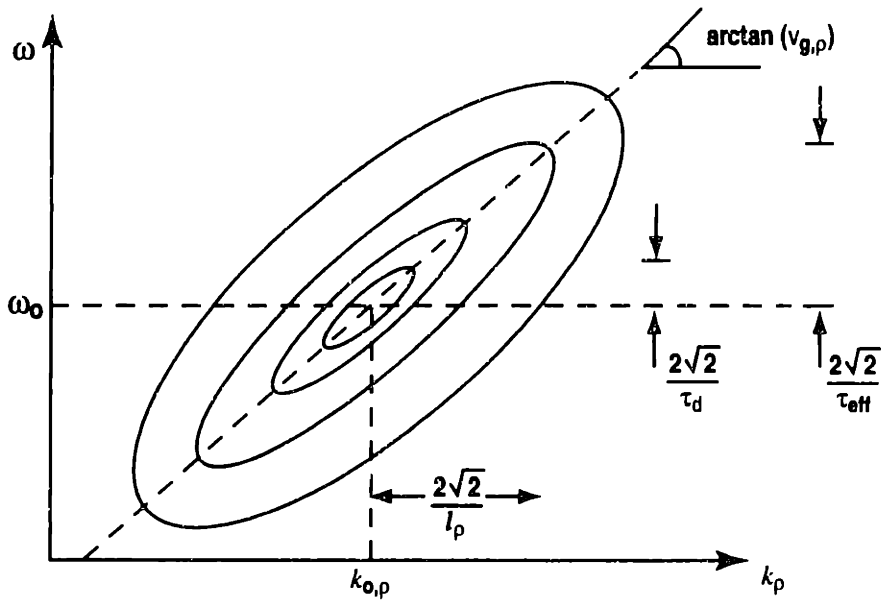

Fig. 4.5 Contour plot of $I(k_\rho, \omega)$.

form (Gaussian) as the wave-number spectral functions. However, the form factor given by Eq. (4.26) is more realistic physically, as it expresses the broadening due to a damping rate $\gamma = 1/\tau_d$.

In Fig. 4.5 the spectral function I is plotted in contour form in the (k_ρ, ω) plane (neglecting the variable k_θ for simplicity). The Gaussian form factor $\hat{F}_1$ has been used here.

We are now in possession of all the necessary ingredients to calculate the pointwise correlation function by means of Eq. (4.22). The calculation is straightforward but rather tedious: after the simple integral over ω is calculated, the remaining integrands can be rearranged so that the integrals over k_R and k_z both take the form of inverse Fourier transforms of Gaussian functions. The general result is derived in Appendix G, and the correlation function is given by Eq. (G.7).

That rather formidable expression can be simplified considerably by making the assumption that the poloidal angles ϑ and ϑ' between the $\hat{\rho}$ vectors and the horizontal are approximately equal; this approximation, which is applicable if the correlation lengths are sufficiently short, viz., if

$$\left| \frac{\mathcal{L}_i}{\vartheta} \frac{\partial \vartheta}{\partial x_i} \right| \ll 1, \tag{4.27}$$

can aid greatly in understanding the physical underpinnings of the model.

Under this approximation, the correlation function is given by [Eq. (G.16)]

$$C_{12}(\mathbf{x}, t; \mathbf{x}', t') = \left\langle \tilde{n}^2(\mathbf{x}_{\rm av}, t_{\rm av}) \right\rangle F(t - t') \exp\left[- \left(\frac{u_\rho^2}{\mathcal{L}_\rho^2} + \frac{u_\theta^2}{\mathcal{L}_\theta^2} \right) \right] \times \cos\Big[\mathbf{k}_0 \cdot (\mathbf{x} - \mathbf{x}') - (\omega_0 + \mathbf{k}_0 \cdot \mathbf{v}_{E,\rm av})\,(t - t') \Big], \tag{4.28}$$

where

$$\mathbf{u} = \mathbf{x} - \mathbf{x}' - (t - t')\mathbf{v}_T, \tag{4.29}$$

$$\mathbf{v}_T = \mathbf{v}_g + \mathbf{v}_{E,\mathrm{av}}, \tag{4.30}$$

and $F(t - t')$ is the inverse Fourier transform of $\hat{F}(\omega')$, which can take the following forms [Eqs. (G.1) and (G.2)]:

$$F_1(\tau) = \exp\left(-\frac{\tau^2}{\tau_d^2}\right), \tag{4.31}$$

and

$$F_2(\tau) = \exp\left(-\frac{|\tau|}{\tau_d}\right). \tag{4.32}$$

In particular, the equal-time correlation coefficient is equal to

$$c_{12}(\mathbf{x}, t; \mathbf{x}', t) = \exp\left[-\left(\frac{u_\rho^2}{\mathcal{L}_\rho^2} + \frac{u_\theta^2}{\mathcal{L}_\theta^2}\right)\right] \cos\left[\mathbf{k}_0 \cdot (\mathbf{x} - \mathbf{x}')\right]. \tag{4.33}$$

By taking the two-dimensional Fourier transform of this expression with respect to $(\mathbf{x} - \mathbf{x}')$, we retrieve the normalized wave-number spectral function (i.e., the form factor in the quasi-homogeneous approximation):

$$\hat{\mathcal{G}}(k_\rho, k_\theta) = \frac{\pi}{2}\mathcal{L}_\rho\mathcal{L}_\theta \sum_{\pm} \exp\left[-\frac{\mathcal{L}_\rho^2(k_\rho \mp k_{0,\rho})^2}{4}\right] \exp\left[-\frac{\mathcal{L}_\theta^2(k_\theta \mp k_{0,\theta})^2}{4}\right]. \tag{4.34}$$

These results show that the spatial structure of the turbulence is completely described by the average wave vector $\mathbf{k}_0$ and by the correlation lengths in the $\hat{\rho}$ and $\hat{\theta}$ directions.

To study the temporal correlation structure, we write the autocorrelation coefficient by setting $\mathbf{x} = \mathbf{x}'$ in Eq. (4.28) and dividing by $\langle \tilde{n}^2 \rangle$:

$$c_{12}(\mathbf{x}, t; \mathbf{x}, t') = F(t - t') \exp\left[-(t - t')^2\left(\frac{v_{T,\rho}^2}{\mathcal{L}_\rho^2} + \frac{v_{T,\theta}^2}{\mathcal{L}_\theta^2}\right)\right] \times \cos\left[(\omega_0 + \mathbf{k}_0 \cdot \mathbf{v}_{E,\mathrm{av}})(t - t')\right]. \tag{4.35}$$

If we now choose the Gaussian form factor F_1, given by Eq. (4.31), we obtain

$$c_{12}(\mathbf{x}, t; \mathbf{x}, t') = \exp\left(-\frac{(t - t')^2}{\tau_{\mathrm{eff}}^2}\right) \cos\left[(\omega_0 + \mathbf{k}_0 \cdot \mathbf{v}_{E,\mathrm{av}})(t - t')\right], \tag{4.36}$$

where

$$\tau_{\mathrm{eff}} = \left(\frac{1}{\tau_d^2} + \frac{v_{T,\rho}^2}{\mathcal{L}_\rho^2} + \frac{v_{T,\theta}^2}{\mathcal{L}_\theta^2}\right)^{-1/2}. \tag{4.37}$$

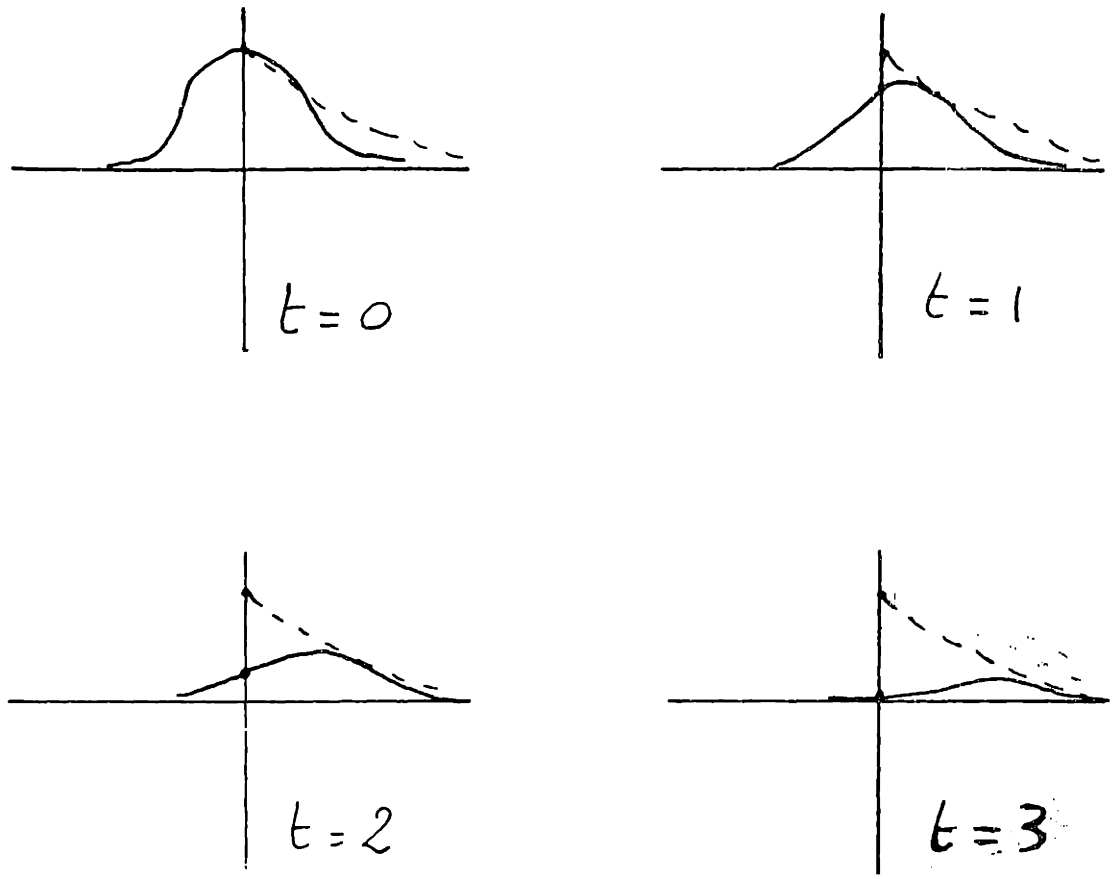

Fig. 4.6 Illustration of the reduction of the local decorrelation time in the presence of flows.

Thus, we find that both the wave-packet dispersion (nonzero $\mathbf{v}_g$) and the $\mathbf{E} \times \mathbf{B}$ drift reduce the local decorrelation time of the fluctuations. In the present analysis, we have moved from a Lagrangian to a Eulerian approach, and we are now focusing on a fixed spatial point: clearly, the faster both the wave packet and the plasma particles flow past this point, the faster does turbulence become locally uncorrelated (see Fig. 4.6).

This result is consistent with our previous observation that the *total* frequency bandwidth is determined both by the intrinsic turbulent broadening and by the widths of the wave-number spectra, as can also be seen in Fig. 4.5. To show this, we Fourier-transform Eq. (4.36) with respect to $(t - t')$ and obtain the normalized frequency spectral function

$$\hat{\mathcal{F}}(\omega) = \sqrt{\pi}\, \tau_{\text{eff}} \sum_{\pm} \exp\left(-\frac{\tau_{\text{eff}}^2 \left(\pm\omega - \omega_0 - \mathbf{k}_0 \cdot \mathbf{v}_{E,\text{av}} \right)^2}{4} \right). \tag{4.38}$$

To measure the intrinsic decorrelation time, one must revert to the Lagrangian approach by following the spatial peak of the envelope of the correlation function as a function of $(t - t')$. The envelope is given by Eq. (4.28) with the cosine term removed.

1997

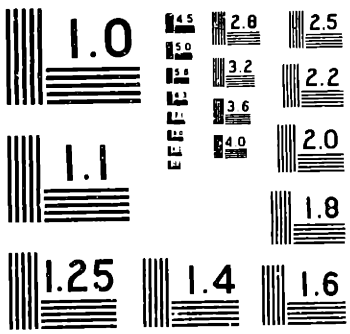

24:1

We find that the peak occurs at $\mathbf{u} = 0$, i.e., at $\mathbf{x} - \mathbf{x}' = (t - t')\mathbf{v}_T$. The dependence of the peak value on time is then clearly given by $F(t - t')$ directly, as shown in Fig. 4.6.

Let us now follow the inverse path, that is, let us find the peak of the correlation envelope as a function of $(\mathbf{x} - \mathbf{x}')$. We take $\mathcal{L}_\rho = \mathcal{L}_\theta \equiv \mathcal{L}$ for simplicity and adopt again the Gaussian form for $F(t - t')$ [Eq. (4.31)]. By inspection of Eq. (4.28) one finds that the time delay for which the envelope is maximum is

$$\tau_p = \frac{\tau_{\text{eff}}^2}{\mathcal{L}^2}\, \mathbf{v}_T \cdot (\mathbf{x} - \mathbf{x}'). \tag{4.39}$$

Assuming now that $\tau_{\text{eff}} \ll \tau_d$, we can write $\tau_p \simeq \mathbf{v}_T \cdot (\mathbf{x} - \mathbf{x}')/v_T^2$, and the peak value of the envelope of the coefficient can be written

$$A_{\max}(c_{12}) \simeq \exp\left(-\frac{[\mathbf{v}_T \times (\mathbf{x} - \mathbf{x}')]^2}{\mathcal{L}^2 v_T^2} - \frac{\tau_p^2}{\tau_d^2} \right). \tag{4.40}$$

Hence, one can reconstruct the intrinsic temporal correlation function $F(t - t')$ by varying the spatial separation and following the peak correlation value, *only if* the separation is in the same direction as the total velocity (group velocity plus $\mathbf{E} \times \mathbf{B}$ drift). This is conceptually equivalent to the Lagrangian approach.

By taking the three-dimensional Fourier transform over time and space of the correlation coefficient, we retrieve the spectral function $I(\mathbf{k}, \omega)$ [Eq. (4.23)], as expected. By inserting in Eq. (4.23) the Gaussian form of the form factor $\hat{F}$, given by Eq. (4.25), we car also determine the correlation lengths *for fixed* ω. We obtain

$$\begin{cases} \mathcal{L}'_\rho(\omega) = \left(\mathcal{L}_\rho^2 + \tau_d^2 v_{T,\rho}^2\right)^{1/2} \\ \mathcal{L}'_\theta(\omega) = \left(\mathcal{L}_\theta^2 + \tau_d^2 v_{T,\theta}^2\right)^{1/2}. \end{cases} \tag{4.41}$$

This result is easy to interpret: the motion of the wave packet and of the particles increases the correlation length by an amount equal to the distance covered over a decorrelation time.

Since in the analysis of the shear decorrelation effect, carried out in §4.2, the relevant correlation lengths were defined at fixed frequency and at zero $\mathbf{E} \times \mathbf{B}$ velocity, we can conclude now that the shear decorrelation parameters should be expressed as

$$\begin{cases} \varsigma_\rho = \frac{1}{\omega}\left(\mathcal{L}_\rho^2 + \tau_d^2 v_{g,\rho}^2\right)^{1/2} \left|(\hat{\rho} \cdot \nabla)\mathbf{v}_E \cdot \mathbf{k}(\omega)\right| \\ \varsigma_\theta = \frac{1}{\omega}\left(\mathcal{L}_\theta^2 + \tau_d^2 v_{g,\theta}^2\right)^{1/2} \left|(\hat{\theta} \cdot \nabla)\mathbf{v}_E \cdot \mathbf{k}(\omega)\right|. \end{cases} \tag{4.42}$$

These equations replace Eq. (4.17).

4.4 Approximate Analytical Modeling

In the last section, and in Appendix G, we were able to derive from our spectral-function model an analytical expression for the pointwise correlation function of the density fluctuations. The general expression is given by Eq. (G.7). To complete the model, we must now calculate Γ_{12}, the correlation function of the line integrals of the density fluctuations, expressed by Eq. (4.3). In the general case, this calculation must be carried out numerically, as will be discussed in the next section. In the present section, we shall first endeavor to elucidate the physical consequences of the model by adopting certain approximations that will permit to perform the line integrations analytically.

The approximations that we shall introduce are based on the specific geometry of the DIII–D PCI measurement. In particular, we shall assume that the change in ϑ over a vertical correlation length is small, that is,

$$\left| \frac{\mathcal{L}_z}{\vartheta} \frac{\partial \vartheta}{\partial z} \right| \ll 1, \tag{4.43}$$

where

$$\mathcal{L}_z = \left(\frac{\sin^2 \vartheta}{\mathcal{L}_\rho^2} + \frac{\cos^2 \vartheta}{\mathcal{L}_\theta^2} \right)^{-1/2}. \tag{4.44}$$

(This definition of the vertical correlation length will be justified in our subsequent analysis.) This *low-curvature* condition is generally satisfied in our geometry. In addition, it will be implicitly assumed that Eq. (4.16) is satisfied, viz., that the shear decorrelation parameters [defined by Eq. (4.42)] are small.

The angle $\vartheta(R, z)$ is a function of the variables $R = R_{\rm av} + r/2$ and $z = z_{\rm av} + \zeta/2$; our first approximation is based on the assumption that the dependence on ζ can be neglected. Thus, we shall use a functional form $\vartheta(R_{\rm av}, z_{\rm av}; r)$, and we can also write $\vartheta' = \vartheta(R_{\rm av}, z_{\rm av}; -r)$. The validity of this approximation clearly rests on the low-curvature condition. With reference to Eq. (G.7), the only remaining dependence of C_{12} on ζ is through the variable u_z [defined by Eq. (G.11)]. We are now able to carry out the integration over ζ in Eq. (4.3) analytically. This is done in Appendix G; the result is Eq. (G.18), in which the integral correlation function Γ_{12} is now expressed as an integral over $z_{\rm av}$.

This result is still too involved for our present purposes. At the next level of approximation, we impose a stronger condition on the curvature, adding to Eq. (4.43) the following requirement:

$$\left| \frac{\mathcal{L}_R}{\vartheta} \frac{\partial \vartheta}{\partial R} \right| \ll 1, \tag{4.45}$$

where

$$\mathcal{L}_R = \left(\mathcal{L}_\rho^2 \cos^2 \vartheta + \mathcal{L}_\theta^2 \sin^2 \vartheta \right)^{1/2}. \tag{4.46}$$

(Note the useful relation $\mathcal{L}_R\mathcal{L}_z = \mathcal{L}_\rho\mathcal{L}_\theta$.) We can then assume that $\vartheta \simeq \vartheta'$ within a correlation length. With this condition, the integral correlation function becomes [Eq. (G.26)]

$$\Gamma_{12}(R_{\rm av}, t_{\rm av}; r, \tau) = \int dz_{\rm av} \sqrt{\pi} \mathcal{L}_z \left\langle \tilde{n}^2(R_{\rm av}, z_{\rm av}, t_{\rm av}) \right\rangle F(\tau) \exp\left(-\frac{\mathcal{L}_z^2 k_{0,z}^2}{4} \right)$$
$$\times \exp\left(-\frac{(r - \tau v_{T,R})^2}{\mathcal{L}_R^2} \right) \cos\left(r k'_{0,R} - \tau \Omega_{\rm eff} \right), \tag{4.47}$$

where

$$k'_{0,R} = k_{0,R} + k_{0,z} \frac{(\mathcal{L}_\rho^2 - \mathcal{L}_\theta^2) \sin(2\vartheta)}{2\mathcal{L}_R^2}$$
$$= \frac{k_{0,\rho} \mathcal{L}_\rho^2 \cos\vartheta - k_{0,\theta} \mathcal{L}_\theta^2 \sin\vartheta}{\mathcal{L}_R^2}, \tag{4.48}$$

$$k_{0,z} = k_{0,\theta} \cos\vartheta + k_{0,\rho} \sin\vartheta, \tag{4.49}$$

and

$$\Omega_{\rm eff} = \omega_0 - \mathbf{k}_0 \cdot \mathbf{v}_g + k'_{0,R} v_{T,R}$$
$$= \omega(k'_{0,R}, 0) + k'_{0,R} v_{E,{\rm av},R}. \tag{4.50}$$

(Note that when $\mathcal{L}_\rho = \mathcal{L}_\theta$, one finds $k'_{0,R} = k_{0,R}$.)

Although nothing has yet been said about the large-scale $\langle \tilde{n}^2 \rangle$ distribution, Eq. (4.47) contains important physical information in an immediately accessible form. The definition of the vertical correlation length, given by Eq. (4.44), is now readily justified: its appearance as a multiplicative factor (times a coefficient $\sqrt{\pi}$) is consistent with the form of Eq. (4.6), which was based on the definition of the correlation length given by Eq. (4.4). More importantly, the $\exp(-\mathcal{L}_z^2 k_{0,z}^2/4)$ factor indicates that the line-integrated measurement is sensitive only to wave vectors whose vertical component is equal to zero, with a tolerance of the order of the reciprocal of $\mathcal{L}_z$. This is intuitively obvious, as any oscillatory component along the direction of propagation averages to zero upon integration.

Similarly, the second exponential factor in Eq. (4.47) justifies the choice of $\mathcal{L}_R$ [cf. Eq. (4.46)] as the horizontal correlation length. For $\tau = 0$, the envelope of the correlation function between chords falls off as a Gaussian function of the distance r between the chords; in the case of a finite delay, this correlation structure travels at the total horizontal velocity $v_{T,R}$.

The correlation function oscillates with a spatial frequency equal to the horizontal component of the peak wave vector $\mathbf{k}_0$, when the correlation structure is isotropic ($\mathcal{L}_\rho = \mathcal{L}_\theta$); in the presence of anisotropy, the spatial frequency is shifted according to Eq. (4.48).

Finally, the peak frequency of the signal, given by Eq. (4.50), is equal to the frequency given by the dispersion relation [Eq. (4.24)] for $k_R = k'_{0,R}$ and $k_z = 0$, Doppler-shifted by the $\mathbf{E} \times \mathbf{B}$ drift.

To further elucidate the spatial structure of the measured correlation function Γ_{12}, we can calculate from Eq. (4.47) the equal-time correlation function

$$\Gamma_{12}(R_{\rm av}, t_{\rm av}; r, 0) = \int dz_{\rm av} \sqrt{\pi} \mathcal{L}_z \langle \tilde{n}^2 \rangle \exp\left(-\frac{\mathcal{L}_z^2 k_{0,z}^2}{4}\right) \exp\left(-\frac{r^2}{\mathcal{L}_R^2}\right) \cos(r k'_{0,R}), \tag{4.51}$$

and by Fourier-transforming it with respect to r we find the wave-number spectrum

$$\hat{G}_\Gamma(R_{\rm av}, t_{\rm av}; k_R) = \int dz_{\rm av} \frac{\pi}{2} \mathcal{L}_z \mathcal{L}_R \langle \tilde{n}^2 \rangle \exp\left(-\frac{\mathcal{L}_z^2 k_{0,z}^2}{4}\right) \times \sum_{\pm} \exp\left(-\frac{\mathcal{L}_R^2 (k_R \mp k'_{0,R})^2}{4}\right). \tag{4.52}$$

As expected, the spectral function is peaked about the values $\pm k'_{0,R}$.

Similarly, we can study the temporal correlation structure by choosing the Gaussian form F_1 [cf. Eq. (4.31)] for the form factor in Eq. (4.47), and by calculating the autocorrelation function

$$\Gamma_{12}(R_{\rm av}, t_{\rm av}; 0, \tau) = \int dz_{\rm av} \sqrt{\pi} \mathcal{L}_z \langle \tilde{n}^2 \rangle \exp\left(-\frac{\mathcal{L}_z^2 k_{0,z}^2}{4}\right) \times \exp\left(-\frac{\tau^2}{\tau_{R,\rm eff}^2}\right) \cos(\tau \Omega_{\rm eff}), \tag{4.53}$$

where

$$\tau_{R,\rm eff} = \left(\frac{1}{\tau_d^2} + \frac{v_{T,R}^2}{\mathcal{L}_R^2}\right)^{-1/2}. \tag{4.54}$$

This result is reminiscent of Eqs. (4.36) and (4.37) for the pointwise correlation function. However, only the horizontal velocity now contributes, since the line integration has selected the $k_z = 0$ component of the spectrum.

The Fourier transform of Eq. (4.53) is

$$\hat{F}_\Gamma(R_{\rm av}, t_{\rm av}; \omega) = \int dz_{\rm av} \frac{\pi}{2} \mathcal{L}_z \tau_{R,\rm eff} \langle \tilde{n}^2 \rangle \exp\left(-\frac{\mathcal{L}_z^2 k_{0,z}^2}{4}\right) \times \sum_{\pm} \exp\left(-\frac{\tau_{R,\rm eff}^2 (\omega \mp \Omega_{\rm eff})^2}{4}\right). \tag{4.55}$$

To recover the intrinsic decorrelation time from the measurement, we can follow the line of reasoning developed for the pointwise correlation case in §4.3: the value of r that maximizes the envelope of the correlation function for a given τ is $r = \tau v_{T,R}$, and its peak value is proportional to $\exp(-\tau^2/\tau_d^2)$ (see Fig. 4.6). Similarly, for a given r the envelope peaks at

$$\tau_{R,p} = \frac{\tau_{R,\mathrm{eff}}^2}{\mathcal{L}_R^2} r\, v_{T,R}, \tag{4.56}$$

and if $\tau_{R,\mathrm{eff}} \ll \tau_d$, the peak value of the envelcpe is proportional to the factor $\exp(-\tau_{R,p}^2/\tau_d^2)$.

Finally, the complete spectral function $\mathcal{S}(k_R, \omega)$ is obtained by calculating the two-dimensional Fourier transform of Γ_{12}. The result is

$$\mathcal{S}(R_{\mathrm{av}}, t_{\mathrm{av}}; k_R, \omega) = \int dz_{\mathrm{av}} \frac{\pi^{3/2}}{2} \mathcal{L}_z \mathcal{L}_R\, \tau_{R,\mathrm{eff}} \left\langle \tilde{n}^2 \right\rangle \exp\left(-\frac{\mathcal{L}_z^2 k_{0,z}^2}{4}\right) \times \sum_{\pm} \exp\left(-\frac{\mathcal{L}_R^2 (k_R \mp k'_{0,R})^2}{4}\right) \exp\left(-\frac{\tau_d^2 [\omega \mp \Omega_0(k_R)]^2}{4}\right), \tag{4.57}$$

where

$$\Omega_0(k_R) = \omega(k_R, 0) + k_R v_{E,\mathrm{av},R}. \tag{4.58}$$

Thus, for a given ω the correlation length is

$$\mathcal{L}'_R(\omega) = \left(\mathcal{L}_R^2 + \tau_d^2 v_{T,R}^2\right)^{1/2}. \tag{4.59}$$

In the specific case of the DIII–D PCI measurement, the edge location allows us to write $|\vartheta| \ll 1$ (cf. Figs. 3.4 and 4.4). The immediate consequences are that $\mathcal{L}_R \simeq \mathcal{L}_\rho$ and $\mathcal{L}_z \simeq \mathcal{L}_\theta$. Also, the selection rule $k_{0,z} \simeq 0$ now translates into $k_{0,\theta} \simeq 0$. Thus, we retrieve the condition discussed qualitatively at the end of §4.1, and illustrated by Fig. 4.2.

Carrying the expansion to second order in ϑ, and barring any large correlation anisotropy, we can write

$$\mathcal{L}_{\substack{R \\ z}} \simeq \mathcal{L}_{\substack{\rho \\ \theta}} \left[1 \mp \frac{\vartheta^2}{2}\left(1 - \frac{\mathcal{L}_\theta^2}{\mathcal{L}_\rho^2}\right)\right]. \tag{4.60}$$

To proceed any further, we must make some assumptions on the spatial distribution of the fluctuations and of the angle ϑ. If both the distribution of the turbulence and the flux-surface geometry are up-down-symmetric with respect to the midplane,

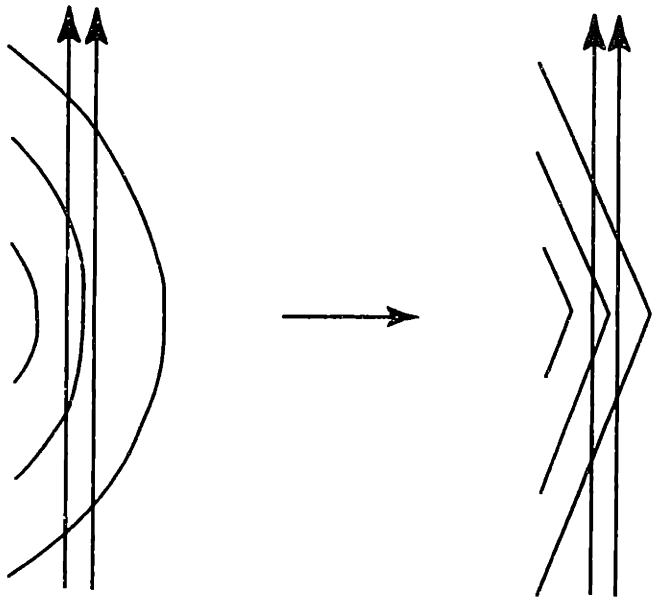

Fig. 4.7 "V" model of flux surfaces.

the angle ϑ is an odd function of $z_{\rm av}$, and the correlation function [Eq. (4.47)] can be written

$$\Gamma_{12}(R_{\rm av}, t_{\rm av}; r, \tau) = \int_0^{L_z/2} dz_{\rm av} \sqrt{\pi} \mathcal{L}_z \left\langle \tilde{n}^2 \right\rangle \exp\left(-\frac{\tau^2}{\tau_d^2}\right) \sum_{\pm} \exp\left(-\frac{\mathcal{L}_z^2 k_{0,z,\pm}^2}{4}\right) \times \exp\left(-\frac{(r - \tau v_{T,R,\pm})^2}{\mathcal{L}_R^2}\right) \cos\left(r k'_{0,R,\pm} - \tau \Omega_{\rm eff,\pm}\right), \qquad (4.61)$$

where the + and − indices refer to positive and negative ϑ, respectively. Here, we have adopted the explicit Gaussian form [Eq. (4.31)] for the form factor $F(\tau)$.

An instructive, albeit rather crude, approximation can now be made by adopting a "V" model for the poloidal flux lines. In this model, the arc of flux surface intercepted by the laser beam at the edge is approximated by an up-down-symmetric V-shaped curve with its vertex on the midplane (see Fig. 4.7). The angle ϑ has constant absolute value along a surface, and changes sign across the midplane. The value of $|\vartheta|$, naturally, will generally be different for each surface; however, to simplify the problem further, and in consideration of the edge location of the PCI apparatus, we assume that $|\vartheta|$ can be taken to be constant along the length of a vertical chord.

We can now calculate the temporal Fourier transform of Γ_{12} from Eq. (4.61), and normalize it by dividing it by the corresponding function for $r = 0$. The result is the complex coherence function,[165] whose modulus is equal to the square root of the coherence proper, and whose phase is equal to the spectral cross-phase. To simplify the calculation, we make the additional assumptions $|\Omega_{\rm eff,\pm}| \gg 1/\tau_{R,\rm eff,\pm}$ and $|\Omega_{\rm eff,+} - \Omega_{\rm eff,-}| \gg 1/\tau_{R,\rm eff,\pm}$: this ensures that the four Gaussian frequency peaks are well separated and can be treated independently. If we carry out a measurement in the vicinity of one of the two (positive) frequency peaks, we will measure the following

complex coherence function:

$$\gamma_{\pm}(r;\omega) \simeq \exp\left(-\frac{r^2}{\mathcal{L}_R^2 + \tau_d^2 v_{T,R,\pm}^2}\right) \times \exp\left[ir\left(k'_{0,R,\pm} + \frac{(\omega - \Omega_{R,\mathrm{eff},\pm})\tau_d^2\, v_{T,R,\pm}}{\mathcal{L}_R^2 + \tau_d^2\, v_{T,R,\pm}^2}\right)\right]. \tag{4.62}$$

Let us now assume $|\vartheta| \ll 1$. Equation (4.50) gives, to leading order, $\Omega_{\mathrm{eff},+} \simeq \Omega_{\mathrm{eff},-} \simeq \omega_0 - k_{0,\theta}\, v_{g,\theta}$; also, from Eq. (4.54) we can derive $\tau_{R,\mathrm{eff},+} \simeq \tau_{R,\mathrm{eff},-} \simeq (1/\tau_d^2 + v_{T,\rho}^2/\mathcal{L}_\rho^2)^{-1/2}$.

Recent experimental measurements[51] have suggested that the radial wave-number spectrum is characterized by a standing-wave structure, that is, $k_{0,\rho} = 0$ and $v_{g,\rho} = 0$. We shall now briefly examine this case. Under the conditions of our measurement, the electric and magnetic fields are predominantly radial and toroidal, respectively; therefore, the dominant component of the $\mathbf{E} \times \mathbf{B}$ velocity in the poloidal plane is in the $\hat{\theta}$ direction, and we can set $v_{E,\rho} \simeq 0$.

Taking $\mathcal{L}_\rho/\mathcal{L}_\theta$ to be of order unity, we find from Eq. (4.48) $k'_{0,R,\pm} \simeq \mp\vartheta k_{0,\theta}\mathcal{L}_\theta^2/\mathcal{L}_\rho^2$. Also, $v_{T,R,\pm} \simeq \mp\vartheta\, v_{T,\theta}$, and $k_{0,z} \simeq k_{0,\theta}$. Equation (4.61) can now be recast in the following approximate form:

$$\Gamma_{12}(r,\tau) \simeq \sqrt{\pi}\mathcal{L}_z L_z \langle\tilde{n}^2\rangle \exp\left(-\frac{\mathcal{L}_\theta^2 k_{0,\theta}^2}{4}\right) \exp\left(-\frac{\tau^2}{\tau_d^2} - \frac{r^2}{\mathcal{L}_\rho^2}\right) \times \cosh\left(2\vartheta\frac{v_{T,\theta}}{\mathcal{L}_\rho^2} r\,\tau\right) \cos\left(\vartheta\frac{\mathcal{L}_\theta^2}{\mathcal{L}_\rho^2} r k_{0,\theta}\right) \cos(\tau\Omega_{\mathrm{eff}}). \tag{4.63}$$

The envelope of this expression is even in τ, with a single peak at $\tau = 0$ if $|r| \lesssim \mathcal{L}_\rho^2/(\vartheta\,\tau_d\, v_{T,\theta}\sqrt{2})$, or two symmetrical peaks (and a local minimum at $\tau = 0$) otherwise (see Fig. 4.8). The envelope is also even in r, with the condition for a single peak now being $|\tau| \lesssim \mathcal{L}_\rho/(\vartheta\, v_{T,\theta}\sqrt{2})$.

Assuming, again, $\Omega_{\mathrm{eff}} \gg 1/\tau_d$, the complex coherence function is approximately equal to

$$\gamma(r;\omega) \simeq \exp\left(-\frac{r^2}{\mathcal{L}_\rho^2}\right) \cos\left(\vartheta\frac{\mathcal{L}_\theta^2}{\mathcal{L}_\rho^2} r k_{0,\theta}\right) \cos\left[\vartheta\frac{\tau_d^2\, v_{T,\theta}}{\mathcal{L}_\rho^2}\, r\,(\omega - \Omega_{\mathrm{eff}})\right]. \tag{4.64}$$

Thus, the coherence function is real, as implied by the time-reversal symmetry of Eq. (4.63). In an experimental measurement, the spectral cross-phase would jump between 0 or π, while the coherence itself would have an oscillatory character (see Fig. 4.9).

The spatial Fourier transform of the complex coherence function is the conditional spectrum,[175] whose value at the peak frequency is

$$s(k_R|\Omega_{\mathrm{eff}}) \simeq \sqrt{\pi}\mathcal{L}_\rho \frac{1}{2}\sum_{\pm} \exp\left[-\frac{\mathcal{L}_\rho^2}{4}\left(k_R \mp \vartheta\frac{\mathcal{L}_\theta^2}{\mathcal{L}_\rho^2} k_{0,\theta}\right)\right]. \tag{4.65}$$

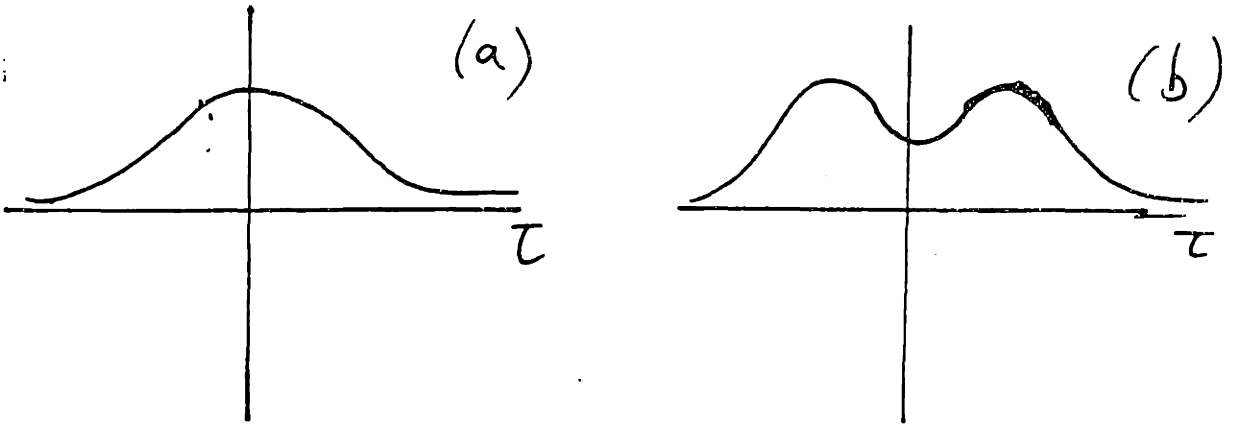

Fig. 4.8 Envelope of the correlation coefficient for (a) $|r| \leq \mathcal{L}_\rho^2/(\vartheta\tau_d v_{T,\theta}\sqrt{2})$, (b) $|r| > \mathcal{L}_\rho^2/(\vartheta\tau_d v_{T,\theta}\sqrt{2})$.

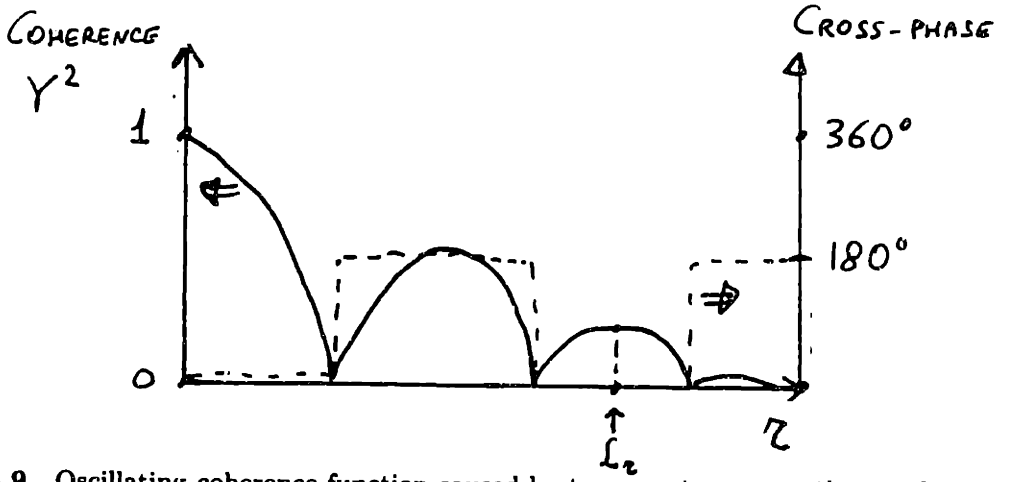

Fig. 4.9 Oscillating coherence function caused by two counterpropagating modes.

Hence, we reach the important conclusion that a traveling poloidal wave packet ($k_{0,\theta} \neq 0$, $v_{g,\theta} \neq 0$) causes the line-integrated signals to exhibit a standing-wave spatial correlation structure. This can be understood physically as follows. A vertically line-integrated measurement is sensitive only to the horizontal component of the wave vector of the fluctuations. In the presence of a poloidally propagating wave packet, the horizontal projection of the wave vector has opposite signs above and below the midplane (see Fig. 4.10). The measurement, therefore, "sees" two uncorrelated, counter-propagating waves, which give rise to the standing-wave correlation pattern shown in Fig. 4.9.

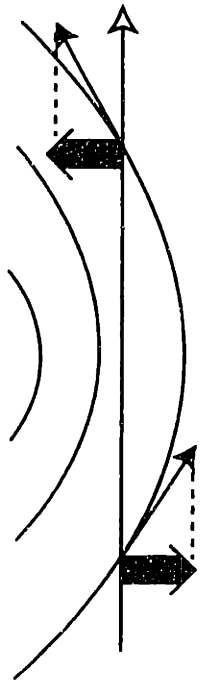

Fig. 4.10 Counter-propagating horizontal projections of a poloidally propagating wave.

This result is dependent on the postulated up-down symmetry of both the turbulence and the flux surfaces. In real experimental situations, the geometry of the flux surfaces is often slightly asymmetric (as in the single-null diverted configuration shown in Fig. 4.11); in addition, the turbulence itself may be asymmetrically distributed, as past experiments have shown.[185] In that case, the positive and negative projections of the wave vectors may not be equal, and the measured pattern may appear to be propagating inward or outward. However, since the measured wave vectors are the horizontal projections of nearly vertical wave vectors, the apparent wavelength will generally be much longer than the actual wavelength of the turbulence. If, as an extreme example, the turbulence is localized entirely on one side of the midplane (see Fig. 4.11), the measured horizontal wave number will be $k'_{0,R} \simeq \bar{\vartheta}\, k_{0,\theta}\, \mathcal{L}_\theta^2/\mathcal{L}_\rho^2$, where $\bar{\vartheta}$ is an average poloidal angle in the turbulent region. The additional constraint $|k_{0,\theta}| \leq 2/\mathcal{L}_\theta$, which arises from the first exponential term in Eq. (4.63), further limits the region of wave-number space that can be accessed by the measurement.

As a final exercise, with specific relevance to the results discussed in the next two chapters, let us posit a turbulent spectrum equal to the sum of two counterpropagating radial modes of identical amplitude; i.e., the two spectra are characterized by $\pm k_{0,\rho} \neq 0$, $\pm v_{g,\rho} \neq 0$, and $k_{0,\theta} = 0$; we further assume that $|k_{0,\rho}\mathcal{L}_\rho| \gg 1$, so that we can neglect crosscorrelations between the two modes, and $|v_{T,\theta}\vartheta| \ll |v_{g,\rho}|$. Equation (4.61) can now be written as

$$\Gamma_{12}(r,\tau) \simeq \sqrt{\pi}\mathcal{L}_z L_z \left\langle \tilde{n}^2 \right\rangle \exp\left[-\tau^2\left(\frac{1}{\tau_d^2} + \frac{v_{g,\rho}^2}{\mathcal{L}_\rho^2} - \frac{r^2}{\mathcal{L}_\rho^2}\right)\right]$$

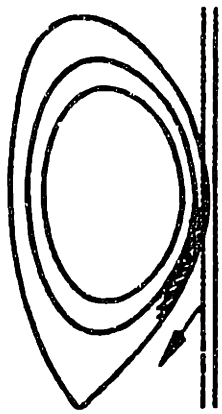

Fig. 4.11 Lower-single-null diverted configuration. The shaded area indicates the turbuelent region in the model.

$$\times \left[\cosh\left(2\frac{v_{g,\rho}}{\mathcal{L}_\rho^2} r\,\tau\right) \cos\left(r k_{0,\rho}\right) \cos(\tau\omega_0) \right.$$
$$\left. + \sinh\left(2\frac{v_{g,\rho}}{\mathcal{L}_\rho^2} r\,\tau\right) \sin\left(r k_{0,\rho}\right) \sin(\tau\omega_0) \right]. \qquad (4.66)$$

The envelope of this expression is even in τ, with either a single peak at $\tau = 0$ or two symmetrical peaks (and a local minimum at $\tau = 0$). In particular, for $|rk_{0,\rho}| \ll 1|$, the condition for the existence of two peaks is approximately $|r| \gtrsim \mathcal{L}_\rho^2/(\tau_{R,\text{eff}} v_{g,\rho}\sqrt{2})$. This insight will help us understand the measured correlation functions in Chapter 6.

In conclusion, this analysis has confirmed that the DIII-D PCI apparatus is mostly sensitive to the radial wave-number spectrum. A poloidally propagating wave packet, under normal conditions, will cause only a slight departure (of the order of the rms poloidal angle $\bar{\vartheta}$) of the measured signal from that generated by the radial spectrum alone. In particular, a measured traveling-wave pattern will generally imply the existence in the plasma of a radially traveling wave train.

4.5 Numerical Modeling

The correlation function of the line integrals of the density fluctuations, defined by Eq. (4.3), can be calculated from the analytical expression for the pointwise correlation function [Eq. (G.7)] by carrying out the double linear integration numerically. A Fortran computer program, called PREDICT_PCI, was written for this purpose. This program "predicts" the integral correlation function that would be obtained experimentally from the plasma turbulence spectrum defined in Eq. (4.23). Within the confines of this model, the numerical calculation provides an exact result, without resorting to any of the approximations adopted in the previous section. In particular, both the poloidal angle ϑ and its relative variation over a correlation length can take arbitrary values.

However, the low-shear condition, expressed by Eq. (4.16), must still be satisfied, since, as was discussed in §4.2, the model — and indeed the entire concept of an "intrinsic" plasma turbulence spectrum — loses its meaning when the shear decorrelation parameters, defined by Eq. (4.42), are larger than one.

The case of inhomogeneous turbulence can be treated by introducing a spatial distribution $\langle \tilde{n}^2(R_{\rm av}, z_{\rm av})\rangle$. This spatial distribution is specified as a function of the normalized flux (zero on the magnetic axis, one on the last closed flux surface) and of the poloidal angle; the functional dependence on both variables is Gaussian, with means and widths specified by the user.

The program PREDICT_PCI is run on the General Atomics VAX computers. The integration is carried out in the flux-surface geometry determined experimentally for actual DIII–D plasma discharges. The reconstruction of the flux-surface geometry is performed by the equilibrium program EFIT,[176] using magnetic measurements and kinetic profile measurements. Alternatively, the program also allows the user to define the stream function[191] $\psi(R, z)$ analytically.

The $\mathbf{E} \times \mathbf{B}$ velocity can also be functionally defined by the user, or it can be obtained from experimental measurements. The electric field is measured indirectly through the radial force-balance equation for a given ion species[189]

$$E_\rho = \frac{1}{Z_i e n_i}\frac{dP_i}{d\rho} - v_{\theta,i}B_\phi + v_{\phi,i}B_\theta, \tag{4.67}$$

where Z_i is the atomic number of the species, e is the (positive) electronic charge, P_i is the ion pressure, $v_{\theta,i}$ and $v_{\phi,i}$ are, respectively, the poloidal and toroidal ion velocities, and B_θ and B_ϕ are, respectively, the poloidal and toroidal magnetic fields. Both the plasma velocities and the ion pressure profile are measured in the DIII–D tokamak by charge-exchange recombination spectroscopy.[192] An example of the electric field profiles obtained by this method in the edge region is shown in Fig. 4.12.

The electric-field profile is generally measured in the midplane. Extrapolation to different elevations is permitted by the constancy of the electric-field *potential* over a flux surface [a property that can be proven from Eq. (4.67)]. The electric field at an

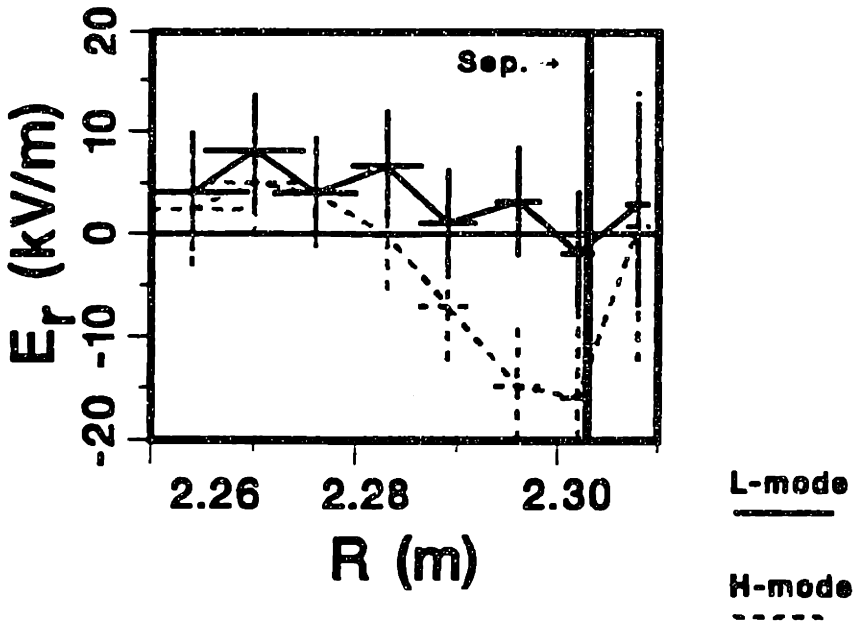

Fig. 4.12 Electric-field profile on the DIII–D midplane, measured by charge-exchange recombination spectroscopy in L and H mode.

arbitrary point (R, z) is therefore given by

$$E_\rho(R,z) = \frac{|\nabla\psi(R,z)|}{|\nabla\psi(R',0)|} E_\rho(R',0), \tag{4.68}$$

where $\psi = RA_\phi$ is the stream function, and R' is the major radius that satisfies the identity $\psi(R',0) = \psi(R,z)$.

The program PREDICT_PCI is organized as follows. The parameters $k_{0,\rho}$, $k_{0,\theta}$, $\mathcal{L}_\rho$, $\mathcal{L}_\theta$, ω_0, $v_{g,\rho}$, $v_{g\theta}$, and τ_d are provided in input. The user chooses one of the two frequency form factors ($\hat{F}$) given by Eqs. (4.25) and (4.26). Also, the spatial distribution $\langle\tilde{n}^2\rangle$ is specified by assigning the means and standard deviations of the Gaussian functions, both in the normalized flux and in the poloidal angle.

The code reads the electric-field data (typically an 8-point array) and interpolates them with a smoothing cubic spline. The flux data [typically a 65×65 (R, z) matrix] are also interpolated with a bicubic spline; the flux data are used both to derive the function $\vartheta(R, z)$ and to map the electric-field potential along the flux surfaces. (The spline subroutines employed are part of the IMSL library.) The plasma is assumed to occupy only the region inside the last closed flux surface, and no attempt is made at modeling the scrape-off layer.

For maximum efficiency, different integration algorithms are used for the outer integral (in ζ) and the inner integral (in z_{av}). A non-adaptive Patterson quadrature method[194] was chosen for the inner integral, in view of its regularity. An adaptive Patterson algorithm is used for the outer integral in the autocorrelation case ($r = 0$),

whereas in the more irregular crosscorrelation case, optimal performance is achieved with an adaptive Piessens-de Doncker quadrature method especially suited for an oscillating integrand.[195] These quadrature algorithms are part of the subroutine library NAG, with an adaptive interval-subdivision algorithm added in the program to increase efficiency. All calculations are carried out in double precision (64 bits).

The program can be run in three different modes. In mode 1, only the spatial correlation function is studied, and no use is made of the group velocity and of the $\mathbf{E} \times \mathbf{B}$ velocity. The user has the option of requesting the correlation coefficient at $\tau = 0$, or the complex coherence at a fixed (unspecified) frequency: in the second case, only one of the + and − signs in Eq. (4.23) is selected, and the spectral function is not forced to be Hermitian. In both cases, one chord is fixed and the position of the second chord scans a set of discrete values of the major radius; the wave-number spectrum is also calculated, using an FFT algorithm, and plotted.

In mode 2, the program explores the temporal correlation structure: the autocorrelation coefficient and its envelope are calculated for a number of discrete time delays, and the frequency spectrum is also computed (through an FFT routine).

Finally, in mode 3 a two-dimensional scan of both major radius and time delay is effected, and several functions are calculated: the correlation coefficient and its envelope, the coherence and cross-phase (as functions of R and ω), and the absolute and conditional spectra (as functions of k_R and ω). This mode is, naturally, more CPU-intensive and has been used only in a few cases. (The first two modes typically require a few hours of CPU time).

Although the plots generated by the program are of normalized quantities (that is, the correlation *coefficient* and its transforms), the absolute value of the autocorrelation function is also given in output (for a unity mean square density $\langle \tilde{n}^2 \rangle$ at the peak of the spatial distribution). This is important, as the exponential term $\exp(-\mathcal{L}_z^2 k_{0,z}^2/4)$ [see Eq. (4.47)] does not affect the correlation coefficient but can have a strong damping effect on the overall signal.

In modes 2 and 3, the radial and poloidal shear decorrelation parameters are also calculated at the frequency ω_0 and at several points along each vertical chord, and provided in output.

The PREDICT_PCI code was run for a large number of cases. Many of the parameter sets chosen were devised for the express purpose of testing the analysis presented in the previous section. All the qualitative results that were discussed in §4.4 were confirmed by the numerical analysis.

Results from various PREDICT_PCI runs are shown in Figs. 4.13–4.17. In all cases shown, the Gaussian form factor $\hat{F}_1$ was used (the alternative form $\hat{F}_2$ produces qualitatively similar results). In all cases except the last one, the local wave-number spectrum was chosen to approximately reproduce the spectrum derived recently from beam-emission spectroscopy measurements in TFTR.[51] The values of the main parameters are $k_{0,\rho} = 0$, $k_{0,\theta} = -1$ cm^{-1}, $\mathcal{L}_\rho = 2$ cm, and $\mathcal{L}_\theta = 3$ cm. The frequency spectrum is defined by the parameters $\omega_0/(2\pi) = 20$ kHz, $v_{g,\rho} = 0$, $v_{g,\theta} = -2$ km/s, and $\tau_d = 45$ μs. It should be noted that the damping factor due to the nonzero

peak poloidal wave number, $\exp(-\mathcal{L}_\theta^2 k_{0,\theta}^2/4)$, is ~ 0.78; thus, the signal is only mildly attenuated.

In Fig. 4.13 a spatially homogeneous case is compared with a case in which turbulence is localized below the midplane. The program was run in mode 1 (spatial) at fixed frequency, i.e., with a non-Hermitian spectral function. The analysis of §4.4 [see Eq. (4.65)] predicts a measured spectral function $S(k_R|\omega)$ equal to the sum of two Gaussian functions with two symmetrical peaks at $k_R \simeq \pm\bar{\vartheta}\, k_{0,\theta}\, \mathcal{L}_\theta^2/\mathcal{L}_\rho^2$. The resulting function, as can be seen in Fig. 4.13(a), has a single peak at $k_R \simeq 0$; the apparent broadening is due to the separation of the two peaks. The slight negative skewness is an effect of the flux-surface geometry, which is, as shown in the insets, that of a lower-single-null diverted plasma: thus, $|\vartheta|$ is a little larger below the midplane than above it, and the negative wave numbers are slightly enhanced. The main message of this plot is that the measured spectral function is rather similar to the local radial-wave-number function, while it is affected little by the poloidal-wave-number function.

A larger asymmetry is obtained, as expected, with a localized spatial distribution [Fig. 4.13(b)]. Now only the negative peak of the two described by Eq. (4.65) remains. In this inhomogeneous case, a propagating poloidal wave train results in a propagating pattern in the integrated signals. However, as was discussed at the end of §4.4, the measured wave number is $k_R \simeq \pm\bar{\vartheta}\, k_{0,\theta}\, \mathcal{L}_\theta^2/\mathcal{L}_\rho^2$, hence, generally, $|k_R| < |k_{0,\theta}|$. In the present case, $\mathcal{L}_\theta^2/\mathcal{L}_\rho^2 = 2.25$ and $\bar{\theta} \simeq 0.2$ rad; thus,as Fig. 4.13(b) shows, $k_R \simeq 0.45 \times k_{0,\theta}$.

Figure 4.14 illustrates the effect of Doppler shifts on the measured frequency spectrum. The program was run in mode 2, for homogeneous turbulence. For reference, Fig. 4.14(a) shows the frequency spectrum in the absence of an $\mathbf{E} \times \mathbf{B}$ drift. The two cases shown in Fig. 4.14(b) are characterized by $\mathbf{E} \times \mathbf{B}$ drifts calculated from, respectively, the L–mode and H–mode electric-field profiles shown in Fig. 4.12. The unshifted peak frequency in the first plot is equal to [cf. Eq. (4.50)] $\Omega_{\text{eff}}/(2\pi) \simeq \omega(k_R, 0)/(2\pi) \simeq (\omega_0 - v_{g,\theta} k_{0,\theta})/(2\pi) \simeq 40$ kHz. The half-width of the spectrum is $\sqrt{2}/(\pi\tau_{R_{\text{eff}}})$; from Eq. (4.54), $\tau_{R,\text{eff}} \simeq 33$–$40$ μs, resulting in a half-width of 11–14 kHz, as confirmed by Fig. 4.14(a).

In L mode, the radial shear decorrelation parameter has a maximum value of ~ 0.5 in our geometry. Thus, we can consider an analysis based on the concept of a Doppler shift at least marginally applicable in this case. Comparing Figs. 4.14(a) and (b), both the Doppler shift and the Doppler broadening of the spectrum appear quite modest in L mode. This is yet another consequence of the sensitivity of the system to radial wave vectors, since the drift velocity lies in the poloidal direction: the Doppler shift is $\Delta\omega \simeq \vartheta^2 k_{0,\theta}\, v_E\, \mathcal{L}_\theta^2/\mathcal{L}_\rho^2$.

In H mode the broadening is more pronounced, although the peak is still nearly unshifted. The measured frequency spectral function remains reasonably close to the plasma-frame spectral function. However, the significance of these concepts now comes into question, as the radial shear decorrelation parameter is of the order of 2.

Figure 4.15 depicts the envelope of the correlation coefficient in contour form (mode 3) as a function of r and τ, for the unshifted case (no $\mathbf{E} \times \mathbf{B}$ drift). The parity

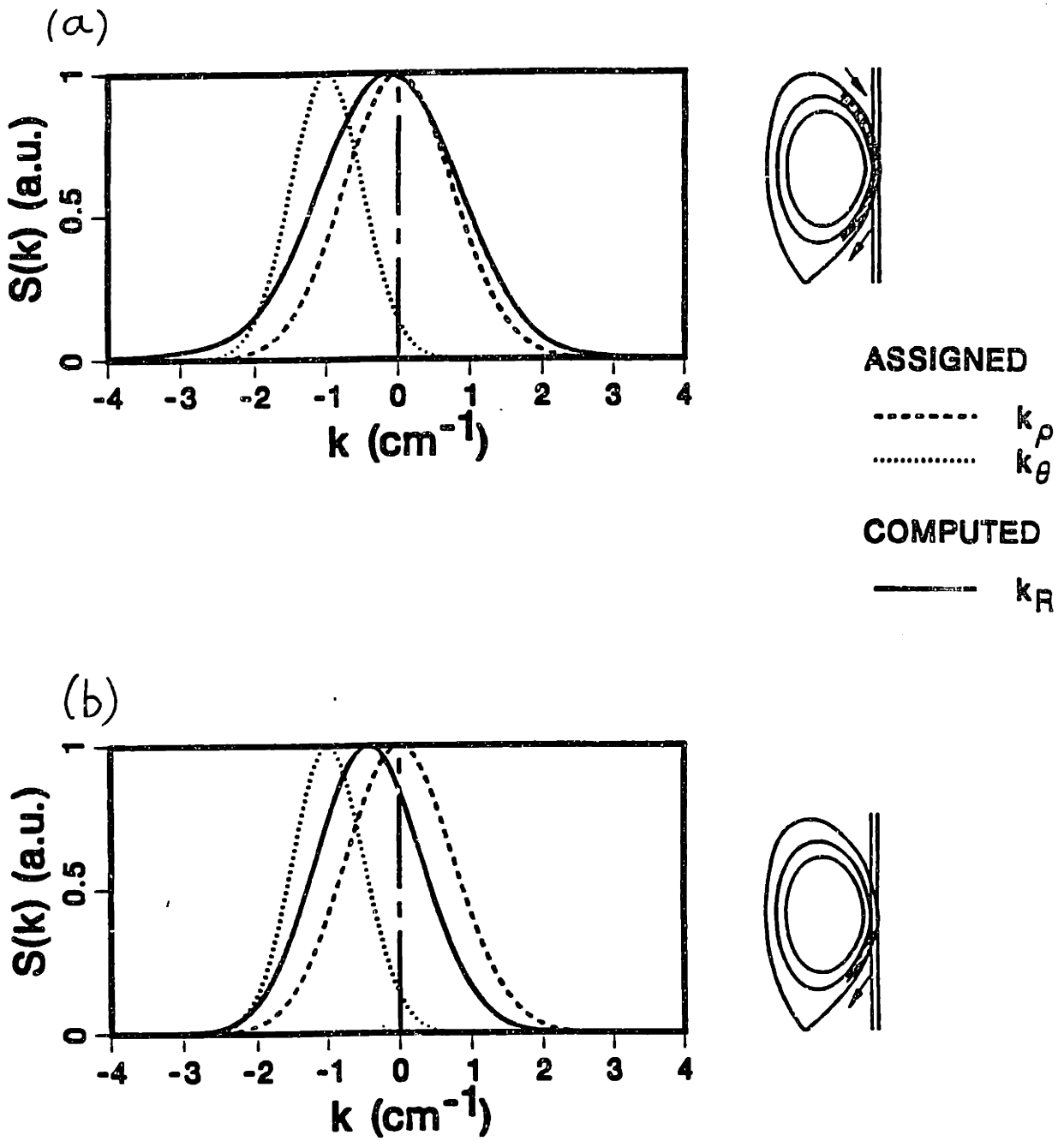

Fig. 4.13 Comparison of line-integrated k_R spectra in (a) homogeneous and (b) inhomogeneous turbulence; the source k_ρ and k_θ spectra are also plotted for reference.

in both r and τ is broken by a slight irregularity involving two secondary peaks, a consequence of the modest up-down asymmetry of the magnetic-field lines.

Shown in Fig. 4.16 is a comparison of the results of a mode-1 run for two different flux-surface geometries, i.e., those of a single-null and of a double-null diverted plasma [depicted in Fig. 4.16(b)], in the case of homogeneous turbulence. Figure 4.16(a) compares the two wave-number spectra; in going from a single-null to a double-null geometry, the symmetry increases as expected, but the change is quite modest.

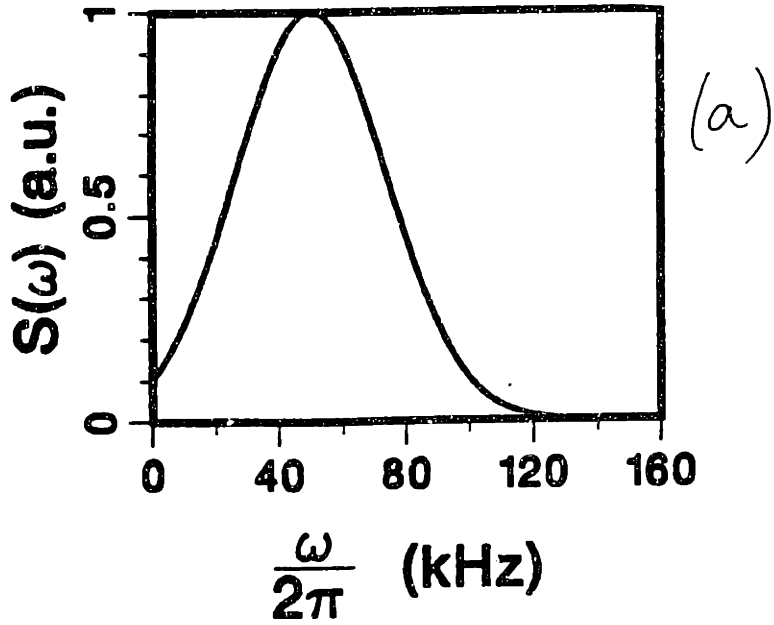

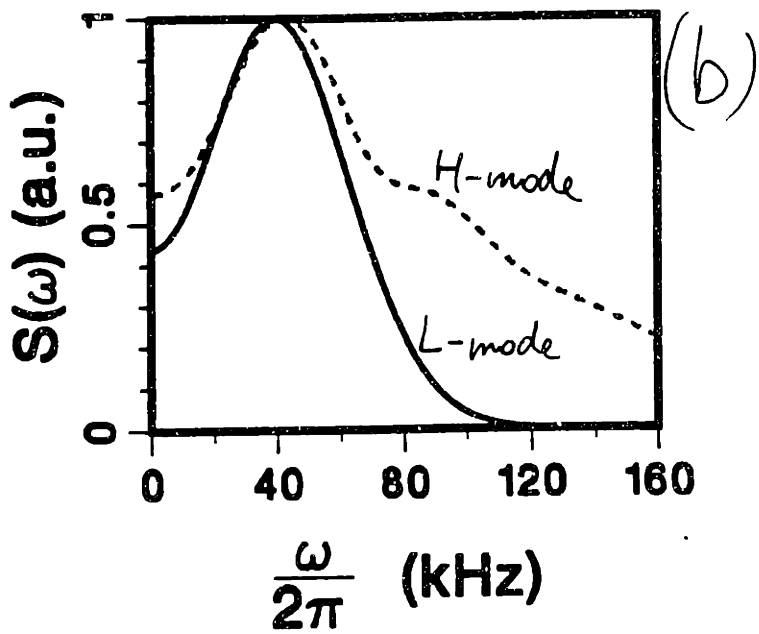

Fig. 4.14 Comparison of line-integrated frequency spectra with (a) no $\mathbf{E} \times \mathbf{B}$ drift and (b) $\mathbf{E} \times \mathbf{B}$ drift in both L and H mode.

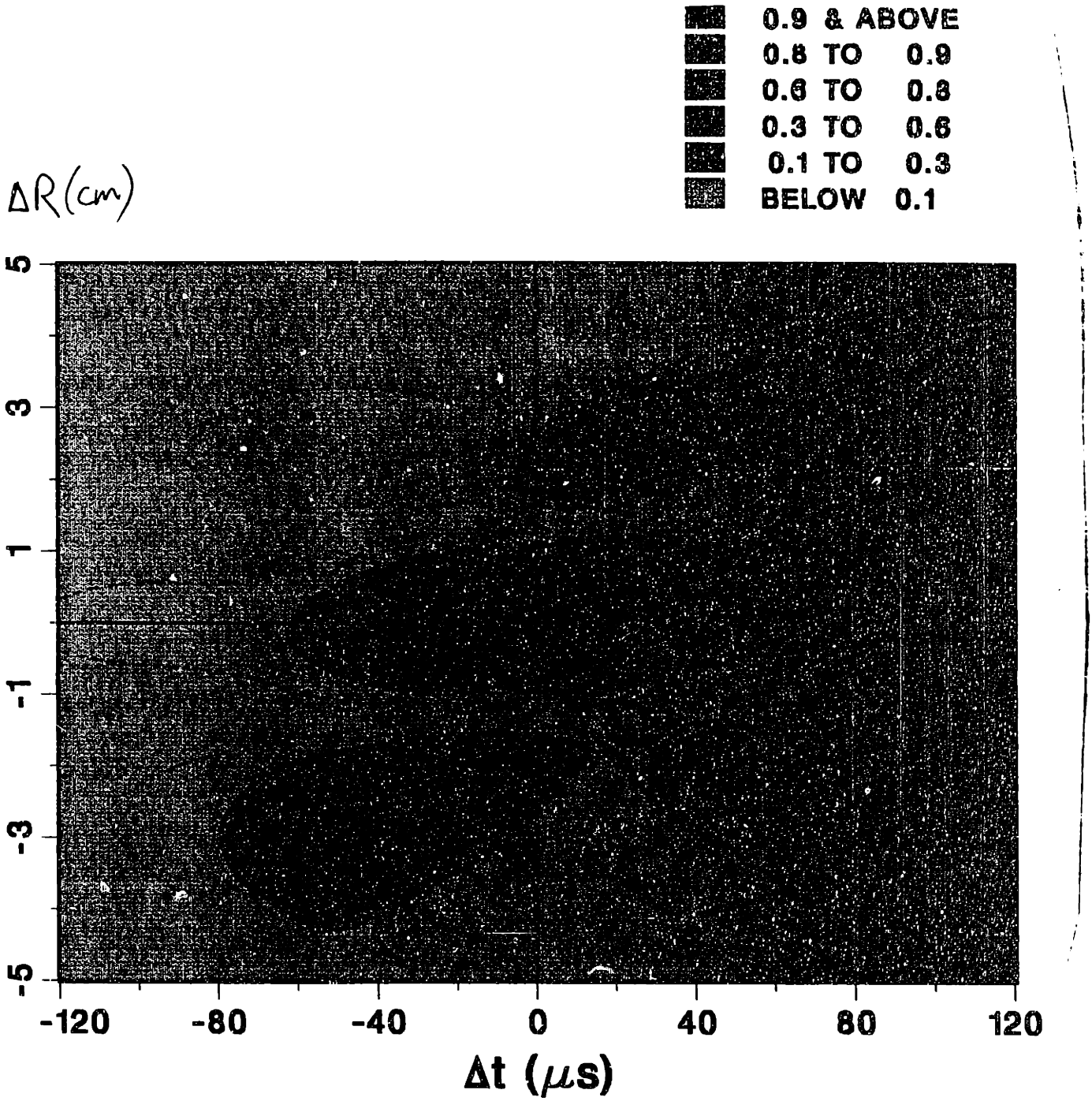

Fig. 4.15 Envelope of the correlation coefficient in contour form.

The last figure in this group, Fig. 4.17, explores two different parameter sets that produce similar results, to illustrate the intrinsic ambiguity of the inversion problem,

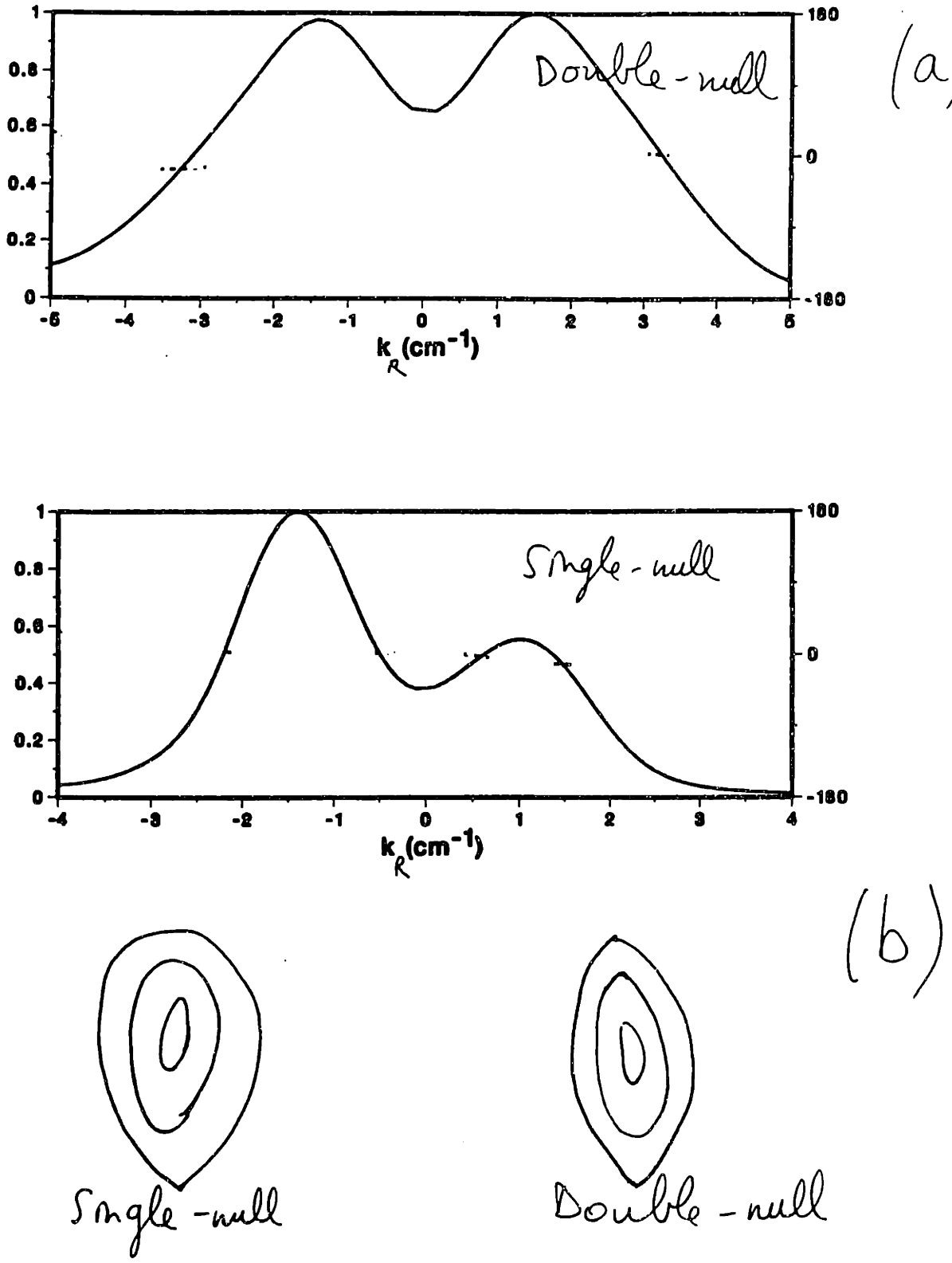

Fig. 4.16 (a) Comparison of line-integrated wave-number spectra for single-null and double-null geometries; (b) schematic flux-surface geometries for the two cases.

and the role of physical intuition and prior knowledge in selecting the most probable spectral function. In both examples, the line-integrated wave-number spectrum peaks at a negative value $k_{0,R} \simeq -2$ cm^{-1}. The functional widths are also similar. The case of Fig. 4.17(a) is based on a homogeneous spatial distribution; therefore, a negative $k_{0,\rho}$ is necessary to obtain a negative $k_{0,R}$. In the second example [Fig. 4.17(b)], $k_{0,\rho}$ is set to zero, and turbulence is localized below the midplane; one must then simultaneously satisfy the three conditions $\mathcal{L}_\rho[1 - \bar{\vartheta}^2(1 - \mathcal{L}_\theta^2/\mathcal{L}_\rho^2)/2] \simeq \mathcal{L}_R$, $\bar{\vartheta}\, k_{0,\theta}\, \mathcal{L}_\theta^2/\mathcal{L}_\rho^2 \simeq k_{0,R}$, and $|k_{0,\rho}|\mathcal{L}_\theta \lesssim 2$. The combinations of parameters that satisfy these three conditions are all rather different from those of the examples analyzed thus far; for instance, if the condition $\mathcal{L}_\rho = \mathcal{L}_\theta$ is imposed, one finds $k_{0,\theta} \simeq -10$ cm^{-1}, and $\mathcal{L} \lesssim 0.2$ cm. In the alternative solution shown in Fig. 4.17(b), the conditions are met by imposing a large $\mathcal{L}_\theta/\mathcal{L}_\rho$ ratio.

In this example, both solutions shown in the figure are somewhat in contrast with the types of spectra that have appeared most often in the literature, such as those of Figs. 4.13–4.16. However, the contrast is certainly greater in the case of Fig. 4.17(b), which would also directly contradict prior knowledge acquired with other diagnostics in DIII–D. The only unusual feature in the spectrum of Fig. 4.17(a) is the appearance of a net radial propagation, which, however, does not directly contradict previous measurements. Therefore one is bound to accept this solution as the more probable one. This example is directly relevant to our measurements, and will be discussed again in Chapter 6.

The PREDICT_PCI code has proven to be a valuable tool in the data-analysis process. The pointwise correlation function cannot be extracted in a unique way from line-integrated measurements; however, some information on the local spectra can be generated by using prior knowledge on symmetry properties and spatial distributions, and by drawing guidance from the semianalytical results of §4.4. When a spectrum and a distribution are tentatively postulated, they can be used in PREDICT_PCI, and the results of the code can then be compared with the experimental measurements. This procedure is generally iterated a few times to improve the matching. These applications of the code will be discussed in the next two chapters in connection with individual results.

The sensitivity of the PCI measurement to predominantly radial wave vectors can also be visualized in a more direct way by performing the numerical line integration on individual spectral components, and interpreting the result as a responsivity in wave-number space. This calculation is carried out with randomized phases, by separately integrating a cosine and a sine function and then taking the square root of the sum of the squares. Each horizontal (k_R) component is multiplied by the complete PCI transfer function at each step of the integration. This procedure is of lesser significance than the more realistic calculations performed by PREDICT_PCI, but the results have an appealing immediacy.

The responsivity is plotted in contour form in Fig. 4.18. At each k_ρ, the k_θ spectrum comprises all values that satisfy the relation $k_z = k_\theta \cos\vartheta + k_\rho \sin\vartheta = 0$ for all ϑ values along the PCI chord; the peak of the k_θ spectrum occurs at an approximate

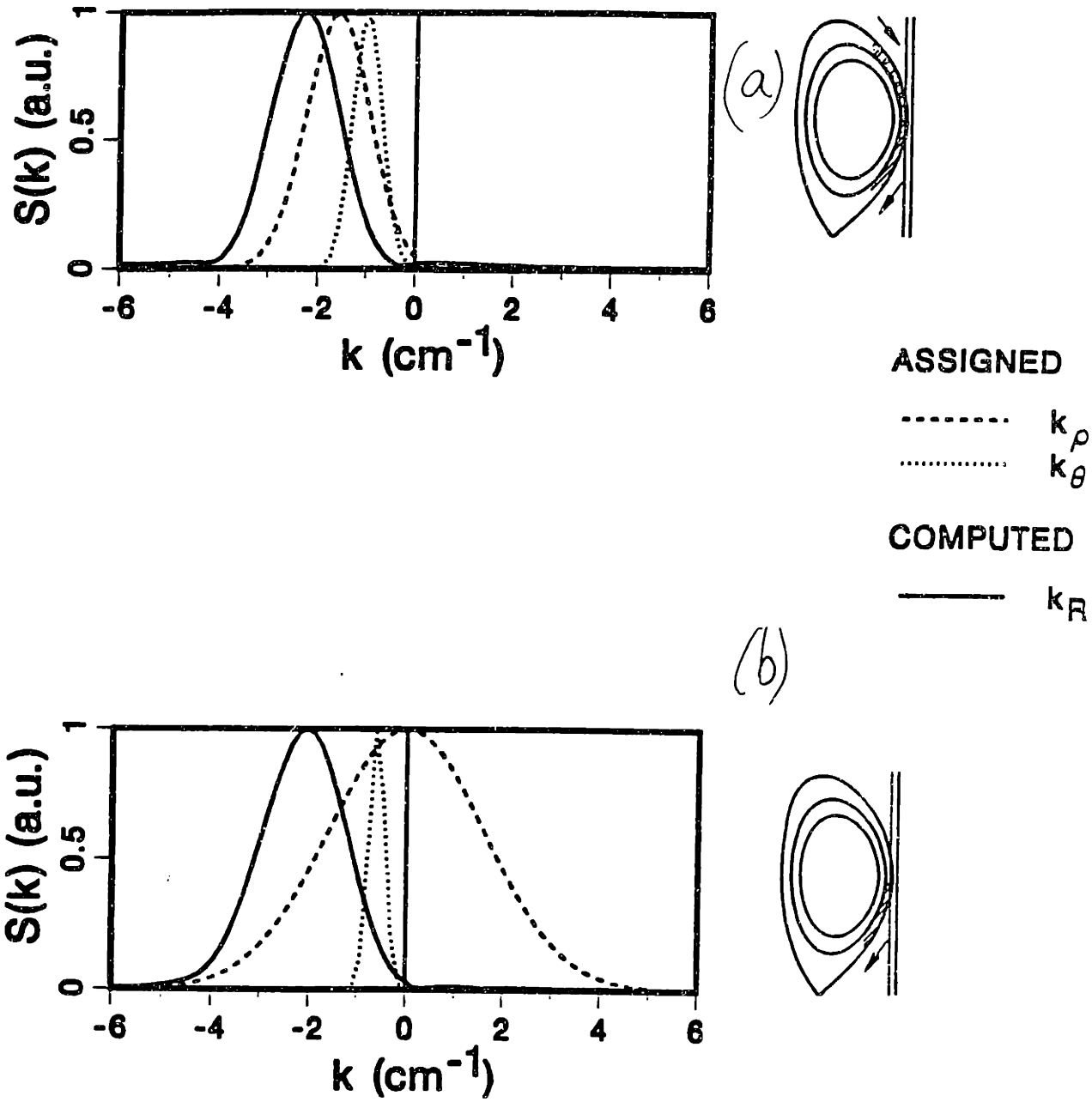

Fig. 4.17 Two different pointwise correlation spectra, with different spatial distributions, producing similar line-integrated k_R spectra.

rms value of ϑ. Since the k_θ range increases for increasing k_ρ, the responsivity must decrease; this must not be interpreted as a decrease in the responsivity of the system to k_ρ, as the integral over k_θ remains approximately constant [this is essentially the PCI transfer function, Eq. (2.143), multiplied by the finite-area smoothing function, Eq. (3.16)]. In all cases, it is immediately clear once again that $|k_\rho| \gg |k_\theta|$: this is

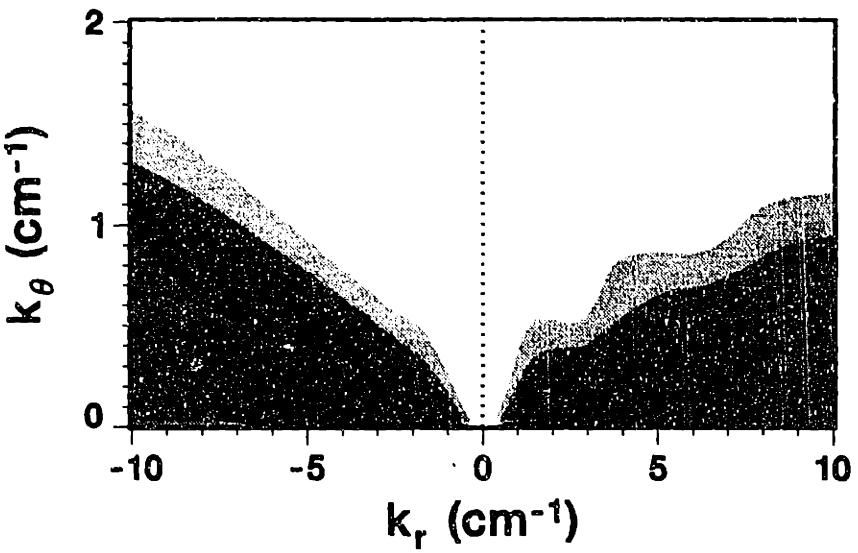

Fig. 4.18 Responsivity of the PCI system to individual (k_ρ, k_θ) modes.

the main conclusion of this chapter.

5 Fluctuation Measurements in the DIII–D Tokamak

Anomalous transport remains the single most significant obstacle to performance improvement in tokamaks. Plasma microturbulence has long been postulated to be the chief cause of the enhancement of radial transport over the level predicted from collisional calculations.[196] The experimentally observed correlation between variations in the amplitude of the turbulence and modifications in the confinement properties of the plasma has gone a long way towards confirming that postulate.[59] However, relatively little is known yet about the detailed properties of turbulence and about the fundamental nature of the underlying instabilities.

This state of affairs motivates a continued experimental effort with traditional fluctuation diagnostics, as well as the development of new and more diversified diagnostic techniques.[197] At the same time, steady progress is being made on the theoretical front, in spite of the extraordinary complexity of the subject, which is rarely amenable to extensive analytical treatment.[196] The remarkable recent advances in high-performance computing, which continue at a propitiously rapid pace, have permitted large-scale numerical simulations at an unprecedented level of detail, elevating them to the rank of a fundamental tool that can be applied directly to the interpretation of experimental results.[198]

A similar course of events has characterized the study of fluid dynamics, which has benefited greatly from developments in flow visualization[199,200] as well as in computing power. In fact, although turbulence in plasmas is considerably more complex than in fluids, the recent history of fluid dynamics is in many ways a useful blueprint for the present and future direction of plasma fluctuation studies. A clear example of this is the recent recognition of the advantages of imaging methods, which are being proposed for and applied to a variety of plasma settings and diagnostic configurations, one instance being the work described in this thesis.

The DIII–D device is arguably the best-diagnosed major tokamak in existence. The array of diagnostics employed in the study of plasma fluctuations is particularly extensive, as it embraces nearly all the techniques that have been developed in the history of this field, the major exception being the heavy-ion beam probe. Accordingly, the investigation of turbulence is one of the focal points of DIII–D activities. The experimental verification of the theory of turbulence suppression by an electric-field shear,[63] which was advanced to explain the H mode,[60] is one of the eminent success stories of the DIII–D team.[201] Clearly, then, DIII–D provides the ideal environment for the development of novel diagnostics, such as phase-contrast imaging (PCI).

The PCI technique, which was described at length in Chapters 2 and 3, provides several unique capabilities. In particular, when applied to studies of the statistical properties of turbulence, PCI allows simultaneous multi-point correlation measurements with substantially better temporal resolution than was previously possible. Its sensitivity to density fluctuations and its dynamic range also set it apart from other measurement techniques. While PCI also has important limitations — the most sig-

nificant one being its lack of line-of-sight resolution — it is important to consider these unique characteristics in the proper context.

It has long been known that low-frequency fluctuations in plasmas display a distinctly turbulent behavior.[10,196] This is reflected both in broadband wave-number spectra and in broadband frequency spectra at each given wave number. In addition, a certain amount of randomness in the temporal evolution of fluctuations and a marked variability from one discharge to the next are often observed. As PCI has moved to progressively finer temporal and spatial (in one direction) scales, this behavior has been constantly confirmed. The statistical averages undergo significant temporal and spatial variations, indicating that a certain amount of randomness survives even at the statistical level; this implies that the assumption of ergodicity, and even the less restrictive one of stationarity, upon which all statistical estimates are based, is partly violated, at least in the time-scale range necessary to achieve good statistics. Substantial differences in correlation lengths calculated over different time scales have also been seen in numerical simulations of turbulence.[202] In addition, some evidence of intermittency in tokamak turbulence has been reported in the literature.[203,204]

A comparison with ordinary fluids may help put this point in perspective. Turbulence in fluids generally exhibits approximate spatial and temporal self-similarity over a large scale range, known as the inertial range, which was formalized in the classic work of Kolmogorov.[205] However, intermittency — hence, a departure from self-similarity — has been observed, not only in the dissipation (i.e., small-scale) range,[206] but also in the higher-order moments in the inertial range, in partial violation of Kolmogorov's theory.[207] The far greater complexity of plasma dynamics, particularly in a strongly driven system such as a tokamak, may well act to reduce the spatiotemporal invariance further. (PCI data exhibit a burstier behavior during discharge phases with strong auxiliary heating than during those with Ohmic heating alone.) Indeed, the existence of an inertial range in plasma turbulence has not been verified experimentally.

In spite of these considerations, several universal features have emerged from PCI measurements in DIII–D. Many other features that will be described, however, appear to have a more irregular character. In these cases, especially when comparing with theoretical models, the results are by necessity only of a semiquantitative nature. Care will be taken to characterize the results accordingly in the text.

In view of the complexity and variety of the experimental results, and indeed because of the inherent difficulty of the subject, it was desirable to provide a complete description of the phenomenology before discussing the interpretation of the results and comparisons with theory. Although somewhat artificial, this strict partition of the material should prevent any confusion between facts and speculation. Therefore, the present chapter is devoted to the experimental results, whereas Chapter 6 will address their interpretation.

The remainder of this chapter is organized as follows. Section 5.1 contains a brief review of turbulence measurements in tokamaks; this is by no means intended as a comprehensive review, and is by necessity rather selective: its main goal is to

summarize the current knowledge in those areas that were investigated directly in the course of this thesis work. In §5.2 an overview of recent measurements in DIII–D is presented.

Preliminary considerations on PCI data in general and on the main analysis procedures are given in §5.3. The phenomenology studied with PCI is subdivided into three main lines. The first one pertains to the characteristics of turbulence in approximately stationary states, in different confinement and heating regimes (Ohmic, L–mode, H–mode): §5.4 describes the frequency spectra and time-domain correlations, §5.5 the spatial correlation structures and wave-number spectra, §5.6 the amplitude of the fluctuations, and §5.7 the probability distribution function. The second topic concerns the dynamics and evolution in time of the turbulence: the main results on the L–H transition are presented in §5.8, while §5.9 contains a description of a particular class of "slow" transitions; additional observations on dynamic changes within each confinement regime are offered in §5.10. The third and last line of research was the investigation of transient phenomena, particularly edge localized modes (ELMs), which are discussed in §5.11; a few considerations on MHD phenomena and other transients follow in §5.12. Concluding remarks are given in §5.13.

This schematic subdivision into topics and sections was chosen for optimal clarity in the exposition of the material; however, these topics are inevitably interwoven: thus, individual sections are not generally self-contained.

5.1 Review of Turbulence Measurements in Tokamaks

(a) Turbulence Measurements

Fluctuation measurements have been performed with a variety of techniques in many tokamaks.[10,208,197,196,209] Historically, more extensive measurements have been carried out in the plasma edge than in the core, owing both to easier access and to greater theoretical interest, especially since the discovery of the H mode.[60] The subsequent discovery of the VH mode[64] and, more recently, the achievement of improved core confinement in negative-magnetic-shear configurations[210,211] has placed renewed emphasis on core fluctuation studies. In some cases, the turbulence-induced fluxes have been directly calculated or estimated, and levels roughly consistent with the measured anomalous transport have been obtained. Most of the following discussion will pertain and refer implicitly to fluctuations of the density ($\tilde{n}$) and of the electrostatic potential ($\tilde{\phi}$). Measurements of the fluctuating magnetic field ($\tilde{\mathbf{B}}$) and temperature ($\tilde{T}$) in the plasma are considerably more difficult, and the database is correspondingly smaller; these results will be addressed explicitly.

The frequency spectra are almost universally seen to be broadband, with bandwidths up to 1–2 MHz;[10] in many cases, the bandwidth is mostly determined by Doppler shifts and broadening from plasma rotation.[212–214] The bandwidth measured at each wave number with scattering techniques is also broad, with $\Delta\omega \sim \bar{\omega}$, a signature of strong turbulence.[10,23] Average frequencies are roughly of the order of

$\bar{\omega} \sim \omega_{ci} * \rho_i / L_n$, where ω_{ci} is the ion cyclotron frequency, ρ_i is the ion Larmor radius, and $L_n = |\nabla(\ln n_e)|^{-1}$ is the density-gradient scale length.[208] This value is consistent with drift-wave turbulence with wavelengths of the order of an ion gyroradius. (More will be said about drift waves in Chapter 6.) In TFTR, reflectometry studies have revealed a broadening of the spectra when heating by neutral beam injection (NBI) is applied; intrinsic decorrelation times in the range 30–45 μs have been reported for beam-emission spectroscopy (BES) measurements. More exotic structures have been seen in the edge and scrape-off layer (SOL) of the Caltech Research Tokamak[38] and of ASDEX:[215] these can be characterized as short-lived ($\sim$10 μs) long-wavelength individual filaments that evolve in an irregular fashion.

In addition to the broadband turbulence, coherent or semicoherent features have been observed[10] in the edge region of several tokamaks, including PDX,[19] PBX–M,[216] ASDEX,[217] and DIII–D.[218] In TEXT–U, semicoherent activity localized around rational magnetic surfaces (corresponding to rational values of the safety factor q) has been reported.[219] These features are generally easy to distinguish from the ambient turbulence and are attributed to macroscopic or microscopic MHD instabilities. The $\tilde{\mathbf{E}} \times \mathbf{B}$ drift velocity of these modes is generally found to be 90° out of phase with respect to the fluctuating density, thus causing no net electrostatic transport.[220,61]

With few exceptions, most measurements have concentrated on poloidal wave vectors and poloidally propagating modes. This was motivated by the theoretical prediction that a variety of pressure-gradient-driven electrostatic modes of the drift-wave type, which propagate in the electron or ion diamagnetic direction, would be unstable in tokamaks. These modes were therefore expected to be one of the fundamental causes of anomalous transport.[10,221] It should be noted that measurements are carried out in the laboratory frame of reference and cannot distinguish in general between intrinsic group velocity and plasma rotation. The latter tends to dominate in NBI-heated discharges.

In Ohmic plasmas in Alcator C the group velocity was found[23] to be predominantly in the electron direction at low density, and in the ion direction at high density ($n_e > 2 \times 10^{14}$ cm-3). A similar behavior was observed in TEXT.[185] Both in TEXT[222,223] and in the Caltech Research Tokamak[38] an ion mode was detected also at lower densities in the edge region (normalized minor radius $r/a > 0.85$), whereas propagation was predominantly in the electron direction in the core. More recently, BES data from TFTR[224] have pointed to a net separation between a core region with only an ion mode, and an edge region with both an electron and an ion mode (uncorrelated with its core counterpart and with smaller average wave number); in addition, the edge ion feature continues into the SOL, whereas the electron component peaks inside the last closed flux surface (LCFS). Estimates of the plasma-frame velocities of the ion and electron modes in TEXT[225] and TFTR[226] indicate that the former is approximately of the order of the (ion) diamagnetic velocity, whereas the latter is anomalously large.

In early measurements,[10,17,177,24] the radial and poloidal wave-number spectra were generally found to be similar (i.e. the spectrum was isotropic in the poloidal

plane); the spectrum was largest at low wave numbers [$k\rho_s < 0.15$, where ρ_s is the ion Larmor radius determined from the ion sound speed $c_s = (T_e/m_i)^{1/2}$]. Some asymmetry was seen in the Macrotor[37] and Pretext[227] devices, with the poloidal correlation length exceeding the radial correlation length by a factor 1.5–4. Nonzero spectral peaks were observed in ATC[16] and PDX[228]; inward radial propagation at the edge was reported for the latter device. The component of the wave vector parallel to the magnetic field has been measured in a few cases and has been found to be much smaller than the perpendicular component.[10,25,229] Within the resolution of these measurements, however, it is generally difficult to determine whether the structure of the modes is *flutelike* ($k_\parallel \simeq 0$) or *ballooning* (predominantly concentrated on the outboard side of the torus).

More recent measurements, utilizing increasingly sophisticated techniques, have consistently displayed marked radial-poloidal asymmetries. In TEXT[39,185] and TFTR[230,51] the poloidal spectrum peaked at a finite value, which was a varying[197] fraction of ρ_s^{-1}; the radial spectrum peaked at $k_r \simeq 0$. The poloidal correlation length exceeded its radial counterpart by a factor 1–5 in TEXT–U[231] and TFTR[51]. At large wave numbers, approximate spectral power laws have been found to apply: $S(k) \propto k^{-4}$ (TEXT),[185] and $S(k) \propto k^{-3}$ (TFTR).[213] Parametric studies of the k spectra in TEXT revealed no strong dependence of the average $\bar{k}$ on the plasma current, and a dependence $\bar{k} \propto B^{0.6}$ on the toroidal magnetic field.[185]

Spatial variations of the radial correlation lengths have been investigated in TFTR. Values of 2–3 cm at the edge and of 1–2 cm in the core were derived from BES data;[230] large-scale semi-coherent oscillations were seen in NBI-heated discharges by correlation reflectometry in the core.[43] Correlation reflectometry has also been employed in JET[232], which reported core radial correlation lengths in the range 2–20 mm, and in DIII–D,[46,233] where values in the range 1–5 mm were found: in both cases, the low end of the range corresponds to Ohmic and H–mode plasmas, and the high end to L–mode plasmas. It should be noted that the interpretation of results from this technique is surrounded by some controversy.[46–49]

The relative amplitude of the density fluctuations ($\tilde{n}/n$) is difficult to measure with good precision, especially in the plasma core. Probes, BES, and HIBP can be calibrated fairly accurately, whereas scattering and reflectometry systems can provide only very approximate values. Early estimates of the relative fluctuation amplitude were found to scale inversely with the density, with a power-law exponent between -1 and -1/2.[10]

Several tests of the mixing-length scaling have also been carried out. The mixing-length concept, which has its roots in the theory of fluid turbulence,[234] is often adopted as an *ansatz* in strong-turbulence models in plasmas.[187] In the simplest terms, it is assumed that the fluctuation amplitude saturates at a level such that the gradient that generated the instability is flattened over the extent of a radial correlation length (or eddy size in fluid dynamics). Thus, the mixing-length criterion can be written approximately as $\tilde{\xi}/\xi \simeq \mathcal{L}_r/L_\xi$, where L_ξ is the gradient scale length of the field ξ (e.g. density, temperature, etc.), and $\mathcal{L}_r$ is the radial correlation length.

In experimental tests, the value $1/\bar{k}$ is often used instead of $\mathcal{L}_r$.

It is generally found that the mixing-length scaling is verified to within one-half an order of magnitude,[208] with the notable exception of TFR, which reported amplitudes one order of magnitude too small,[10] and of TFTR, where the amplitude is larger than mixing-length at the edge[196] and smaller in the core.[224] In TEXT, qualitative agreement with the scaling was found in the edge,[185] less in the core.[235]

One important issue concerning the amplitudes is the adiabatic-electron assumption. This assumption, implying the Boltzmann relationship $\tilde{n}/n \simeq e\tilde{\phi}/T_e$ (where e is the electronic charge and T_e is the electron temperature), is used in many theoretical models[197] and implies that the electrons travel the distance of a wavelength in a time that is short compared to the fluctuation period. The theoretical significance and implications of this assumption will be touched on in Chapter 6. Results suggest that the adiabatic-electron assumption is approximately valid in the core but not at the edge.[197] In particular, in TEXT the ordering $\tilde{T}/T < \tilde{n}/n < e\tilde{\phi}/T_e$ was found to hold.[196,236]

The TEXT team also reported finding little or no dependence of the broadband components of $\tilde{n}/n$ on the plasma current, and an inverse dependence on the magnetic field, in Ohmically heated plasmas[185] An increase of the amplitude with applied NBI power has been seen both by scattering and BES in the core of TFTR, but little change occurred at the edge;[213] in this tokamak, $\tilde{n}/n$ was also found to vary approximately inversely with the global energy confinement time.[224]

The relative amplitude $\tilde{n}/n$ increases almost invariably towards the edge and peaks just inside or on the LCFS.[10] This was seen in high-density discharges in Alcator A and Alcator C, which reported fluctuation levels up to 100% at the limiter;[23] similar behavior was observed in PDX,[228] in TEXT (edge $\tilde{n}/n \sim$ 10–20%,[185] with some cases of 50% levels in the SOL[185]), in TFTR (0.1–1% in the core, 5–10% at the edge),[213] and in DIII–D.[188] Some exceptions should be noted: turbulence in the low-density regimes of the Alcator machines displayed a peak at $r/a \sim 0.7$;[23] the fluctuation amplitude in H–mode discharges in DIII–D has a maximum at $0.7 < r/a < 0.9$.[188]

Strong asymmetries between the inboard and outboard edges, with the latter exhibiting considerably higher levels of turbulence, have been observed in several tokamaks [e.g. Alcator C,[237] ASDEX (SOL fluctuations),[215] DIII–D[238]]. This behavior is indicative of a ballooning character of the modes. In addition, up-down asymmetries were observed in TEXT; in that case, the direction of the asymmetry could be reversed by changing the direction of the toroidal field with respect to the current.

Measurements of magnetic turbulence (as distinct from MHD activity) have also been carried out in several machines. The fluctuating magnetic field is generally found to be isotropic in the poloidal plane, while the toroidal component is substantially smaller.[10] Typical levels[10] are of the order of $\tilde{B}/B \simeq 10^{-5} - 10^{-4}$; a level $< 10^{-5}$ was reported for the edge of Text,[196] while larger amplitudes ($\sim 10^{-4}$) were measured (by probes) in the low-temperature core of Tokapole II.[239]

Recently, it has become clear that the more traditional analysis techniques, based

on time averaging and Fourier analysis, may no longer be equal to the level of sophistication attained by the experimental techniques. The wavelet-transform technique[240] has been developed to address the problem of partial nonstationarity of the data, and has recently been applied to the study of plasma microturbulence. The issue of intermittency has also been addressed by studying directly the probability distribution function (PDF) of the turbulence, which has been found to be non-Gaussian (suggesting intermittency) under certain experimental conditions,[203,204,241] and Gaussian in other cases.[231,241,211]

Also, the nonlinear interactions between plasma modes have been studied with higher-order correlation techniques; bicoherence analysis on TEXT–U, for instance, has revealed a coherent nonlinear interaction between a long-wavelength MHD mode and the broadband turbulence.[219] More recently, wavelet bicoherence methods have been used to carry out these studies in nonstationary regimes.[242,243,204,241]

(b) Turbulent Transport

Diffusivities calculated from Coulomb collisions, with appropriate modifications for toroidal confinement geometries (*neoclassical transport*) are not sufficient to explain the experimentally observed rate of transport. Tokamak transport is thus said to be *anomalous*. The discrepancy is generally attributed to turbulent fluctuations, but a firm proof of a correlation between turbulence and anomalous transport, let alone of a *causal* relation, is still missing. Even more uncertain is the nature of the fundamental underlying instabilities.[244]

Transport is anomalous to some extent in virtually all regimes accessed in tokamaks thus far, although neoclassical levels have been observed recently in the core of plasmas with negative magnetic shear,[210,211] a promising regime for adanced-tokamak scenarios. In particular, the application of external (NBI, radio-frequency, or microwave) heating causes a marked degradation of confinement; for this reason, this regime is known as the low mode of confinement, or L mode. Under certain conditions at sufficiently high input power, the plasma undergoes a transition to a regime of confinement closer to Ohmic levels, the H mode; even better confinement is obtained in the VH mode. A second type of enhanced-confinement state has also been achieved by creating peaked density profiles (e.g. supershots and PEP modes).[244]

A host of empirical scaling laws for the global energy confinement time (τ_E) have been proposed over the years to fit the various regimes that have been discovered and explored. One common factor is the universal increase of τ_E with machine size. In the so–called neo-Alcator scaling[245], τ_E is proportional to density up to a saturation point, beyond which it starts decreasing; this scaling provides a good description of Ohmic confinement. In L mode, τ_E is generally seen to be proportional to the plasma current and inversely proportional to the square root of the input power.[246] The H mode is simply characterized by the H factor (typically $\sim$2), which measures the increase of τ_E over its L–mode level. Similarly, H factors of the order of 4 typify the VH mode. The confinement time also exhibits a strong dependence on the plasma

shape (improving with increased elongation and triangularity[157]) and on the shape of the current profile (peaked profiles being beneficial[247]). Correlation of these scaling laws with theoretical models is still very sketchy, with the partial exception of the neo-Alcator scaling.[244]

When electrons and ions are considered separately, electron transport is found to be substantially more anomalous than ion transport. Since the classical cross-field energy diffusivity is proportional to the square root of the mass,[248] energy transport would be dominated by ions in the absence of anomalous processes. Instead, the ion and electron diffusivities are comparable in large tokamaks, and electron energy transport is in fact larger in smaller devices. The momentum diffusivity is also comparable to its energy counterpart, whereas particle diffusion proceeds at a rate 3–5 times smaller.[10,244] Diffusivities always increase towards the edge of the tokamak; indeed, the global confinement is generally very sensitive to edge conditions, in particular to the edge gradients and to the rate of recycling from the walls.

Furthermore, in many instances a simple diffusive model appears inadequate to describe tokamak transport. The existence of inward transport processes (pinch effect);[244,249] discrepancies between steady-state and perturbative, or transient, diffusion rates;[196,250,251] evidence of global profile self-organization (profile consistency[252] or profile resiliency[244]), perhaps related to marginal stability to a class of strongly growing modes[253,254]; anomalously fast global changes in diffusivity after the onset of the H mode:[255,256,61] all of these phenomena delineate an extremely complex scenario, which is still largely unexplained.

Both electrostatic and magnetic fluctuations may cause transport. In the electrostatic case the chief mechanism is the $\tilde{\mathbf{E}} \times \mathbf{B}$ drift; using a Fourier representation for the linearized perturbed electric field $\tilde{\mathbf{E}} = -i\mathbf{k}\tilde{\phi}$, the cross-field time-averaged flux of a field ξ (e.g., density, thermal energy, etc.) for a given Fourier component is equal to $\Gamma_{\xi,\rho} = (1/2cB)k_\theta \mathrm{Im}(\tilde{\phi}\tilde{\xi}^*)$. [Here, we are using a left-handed toroidal coordinate system (ρ, θ, ϕ), whose poloidal projection is shown in Fig. 4.4; we are also neglecting the poloidal field for simplicity.] Thus, transport depends on the amplitudes, cross-correlation, and relative phase of $\tilde{\phi}$ and $\tilde{\xi}$.

Transport from magnetic fluctuations is related to the formation of magnetic islands in a plasma of nonzero resistivity. Diffusion along a field line occurs at a much higher rate than across the field, since the characteristic random-walk step size is the thermal collisional mean free path (typically a few km) in the first case and the Larmor radius (a fraction of a cm) in the second case. Thus, when a radial component of the magnetic field develops, it provides a very effective diffusion path; in particular, when the size of the islands is sufficiently large, a region of stochastic field lines may form, leading to large-scale diffusion. It should be noted that since the longitudinal diffusivity is inversely proportional to the square root of the mass, this type of transport is dominated by electrons. Convective losses, being dominated by the slower species because of the requirement of ambipolarity, are considerably smaller than conductive losses.

The question of which type of turbulence is primarily responsible for anomalous

transport in tokamaks is still very much an open one, in particular in the hot plasma core, which is inaccessible to magnetic measurements. Stringer[257] advanced the argument that the nonambipolar flux along stochastic field lines in the core would act to reverse the sign of the negative electric field predicted by neoclassical theory; since measurements indicate that the electric field is generally in agreement with neoclassical predictions, he concluded that magnetic fluctuations are probably a negligible factor in transport. This conclusion is also corroborated by the observations that ion diffusivities are larger than electron diffusivities in large machines, and that convective losses constitute a sizable fraction of the total energy losses.[244] However, since a fluctuation level of only $\tilde{B}/B \sim 10^{-4}$ would be sufficient to explain the measured electron diffusivity,[10,258] and since measurements of $\tilde{B}$ in high-temperature tokamak cores are not available, the issue cannot be considered completely resolved. Also, a correlation between magnetic activity and confinement has been reported in some experiments.[197] Finally, positive electric fields measured in DIII–D[66] appear to invalidate Stringer's argument. By contrast, it is generally accepted that magnetic fluctuations in the plasma edge are too modest to influence transport there.[244,259]

The large levels of electrostatic fluctuations measured in tokamaks, especially at the edge, appear to provide a plausible explanation for anomalous transport in general.[10,260,197,261] A correlation between increases in fluctuation amplitude and in diffusivity (and a decrease in the energy confinement time) was seen in TFR[22,262,263] and more recently in TFTR,[224,226] although no clear correlation was seen in other devices.[197] BES data on TFTR have also been used to estimate the turbulent diffusivity by random-walk and strong-turbulence scaling arguments, with good success in the plasma core.[51,224] Direct measurements of the turbulent electrostatic particle flux with Langmuir probes, which are capable of resolving $\tilde{n}$, $\tilde{\phi}$ and their relative phase, have generally produced successful matches with the measured diffusivities.[227,38,264,265] In DIII–D, in–out asymmetries in the heat flux to the divertor are found to correlate with asymmetries in the fluctuation amplitude.[238]

Although diffusive processes appear to account for electrostatic turbulent transport in many cases,[10,266] the possible existence of large-scale convective cells or flows has also been investigated. Short-lived, large-scale convective filaments have been seen, for instance, in the Caltech Research Tokamak[33] and in ASDEX.[10,215] Studies in several tokamaks,[51,11] particularly in DIII–D,[267,268] have concluded that transport appears to be dominated in many cases by global effects: the measured "Bohm-like" diffusivity, $D \propto cT/(eB)$ (where T is the temperature) can be justified only with strong drift-wave turbulence arguments when the random-walk step size is of the order of the machine size.[187] [The so-called "gyro-Bohm" scaling, $D \propto \rho^* cT/(eB)$, where ρ^* is the ion gyroradius scaled to machine size, reflects a step size of the order of the gyroradius and is seen in H mode under certain conditions.[269]] These results highlight the difficulties inherent in local measurements and suggest that more comprehensive studies of the plasma as a whole may be in order.

(c) The L–H Transition

The H mode[60,168,61] is characterized by good energy confinement and is compatible with high-beta performance[270] and high rates of helium exhaust;[271] it is thus an attractive regime for a future fusion reactor. H modes have been produced in all divertor tokamaks since 1982, in many limiter tokamaks, and also in several non-tokamak devices, and with a variety of heating methods[61] (including Ohmic[272]).

The L–H transition is generally identified by an abrupt reduction in the H_α or D_α spectroscopic emission from the edge, which signals a reduction in recycling caused by decreased transport to the SOL. The measured diffusivities decrease: this is consistent with the formation of a transport barrier[273] in the edge region, whose typical width of 2–3 cm is fairly insensitive to plasma parameters.[274] Most of the reduction appears to occur in the electron and angular-momentum diffusivities, with some improvement in the particle diffusivity[275] and a modest one in the ion energy diffusivity.[276] As a result of the barrier formation, a steepening of the edge density profile and, with enough heating, of the temperature profile occurs;[59] a similar steepening is observed in the SOL also.[277]

The profiles continue to evolve typically for several tens of ms after the transition, with the high-gradient region extending further into the interior of the plasma.[278] On this time scale, a reduction in transport occurs throughout the plasma.[279,280] The global energy confinement time increases by a factor of 2–2.5 over its L–mode value and was found in DIII–D to be higher for deuterium than for hydrogen (by contrast, no isotope dependence was seen in L mode).[281]

The leading hypothesis concerning the cause of the increased confinement in H mode is turbulence stabilization by a sheared $\mathbf{E} \times \mathbf{B}$ drift.[63,278,61] This will be discussed in some detail in Chapter 6. An increase in the magnitude and shear of the radial electric field E_r at the onset of the H mode was seen first in DIII–D[282,283] and subsequently in several other tokamaks.[284,285,216] This change has now been thoroughly documented in DIII–D, thanks to a state-of-the-art charge-exchange recombination (CER) spectroscopy diagnostic with 0.5-cm spatial resolution.[286] The electric–field profile in H mode forms a negative well with a width of less than 1 cm[278] and with a minimum located just inside the LCFS: therefore, both the first and the second radial derivative of E_r are large in this region;[218] the field outside the LCFS is considerably smaller.[238] Recent DIII–D results have suggested that the change in the electric field occurs *before* the transition,[66,218] in agreement with the postulated causal relation between sheared flow and transport reduction.

It should be noted that the $\mathbf{E} \times \mathbf{B}$ velocity is quite distinct from the perpendicular plasma flow velocity, which is the sum of the $\mathbf{E} \times \mathbf{B}$ and diamagnetic velocities. It was found in DIII–D that the latter is negligible at the transition, so that the perpendicular velocity in fact undergoes a rapid change following the evolution of the electric field. However, later in H mode, the steepening of the profiles acts to increase the diamagnetic velocity, which opposes the $\mathbf{E} \times \mathbf{B}$ velocity and becomes larger than it, so that the total perpendicular ion velocity is smaller than both and is oriented in the ion diamagnetic direction.[192]

Further proof of the relation between the electric field and the H mode has been

provided by experiments in which the H mode was induced by directly applying a radial field.[62,287,288] Interestingly, the H mode was obtained also with a *positive* electric field, although the confinement improvement was smaller in that case.[289]

Given the relevance of the H mode to reactor operation, a great deal of effort has been devoted to the determination of scaling laws for the H–mode power threshold.[272] The minimum input power for the achievement of H mode is approximately proportional to the magnetic field and to the average density, with little or no dependence on the plasma current.[283,290] The critical parameter appears to be the power flow across the separatrix rather than the total heating power.[291,292] For instance, good wall conditioning and reduction of the effective charge ($Z_{\rm eff}$) of the impurities (e.g., through boronization[293]) decreases the power threshold, since a reduced impurity concentration implies lesser radiation losses; conversely, deliberate impurity injection has been used to induce a transition from H to L mode.[292] Also, the temperatures or their gradients are thought to play an important, as yet undetermined, role. In DIII–D, the ion temperature at the separatrix is always between 100 and 220 eV just before the transition, regardless of the heating method or of the total power.[291,294] Finally, the direction of the ion ∇B drift relative to the position of the X–point in a diverted plasma has a very strong effect on the power threshold: when that vector points *away* from the X–point, the threshold is up to 3.5 times larger than when the vector points *towards* the X–point.[290]

H–mode studies have provided further evidence of the relation between turbulence and anomalous transport. Broadband turbulence at the edge is quenched abruptly at the onset of the H mode.[19,295,296] Magnetic turbulence near the divertor strike point is also observed to decrease.[297] The reduction in the amplitude of the fluctuating density is typically of the order of a factor of 2,[298] occurs in a very short time[299] (< 0.1 ms), and appears to be localized to the velocity-shear layer.[283] A lesser decrease in amplitude has been reported for the SOL.[61,216,217] A clear asymmetry between the inboard and outboard edge regions has been observed, with the former undergoing considerable less change than the latter;[300] since turbulence is substantially stronger at the outer edge in L mode,[238] the L–H transition brings the inside and outside levels to comparable values. On a slower time scale, the confinement improvement in the core is also accompanied by a partial suppression of the turbulence there.[59]

Relatively little is known about the changes in the spectral characteristics and in the correlation lengths of the turbulence at the L–H transition. A decrease in the radial correlation length was measured by correlation reflectometry in DIII–D[301,46] and in JET;[232] also, studies in TEXT have shown that the decorrelation time of the turbulence is reduced in the velocity-shear layer.

The VH mode, discovered in DIII–D[64] and reproduced later in JET[65] and possibly in JT–60U,[302] has produced confinement times up to 4 times larger than in L mode. In the VH mode the transport barrier involves a larger region than in ordinary H mode, extending further inside the plasma.[303] The most plausible mechanism still appears to be turbulence stabilization by the $\mathbf{E} \times \mathbf{B}$ shear,[61] which indeed changes

in the barrier region,[304] and is accompanied by a reduction in the amplitude of the fluctuations.[214] The VH mode is usually terminated by an MHD event,[305] which reduces the confinement to normal H-mode levels.

(d) Edge Localized Modes

Edge localized modes (ELMs) are semiperiodic edge instabilities that occur in H mode and transiently destroy the transport barrier for the brief duration of the mode.[59] The average diffusion rate during an ELMing H mode is typically 15%–20% higher than during an ELM-free H mode; on the other hand, ELMs serve the useful purpose of limiting the density buildup and of cleansing the plasma from impurities that accumulate during the enhanced-confinement stage. For these reasons, ELMs are considered essential for reactor operation. ELM studies are continuing with the principal aim of providing a reliable database for ITER,[67] and special attention is being devoted to the power loads placed by ELMs on the divertor.

As the name suggests, ELMs are indeed localized to the edge: no changes in the plasma parameters are observed at $r/a < 0.8$. The duration of the ELM is typically of the order of 0.5 ms and does not vary strongly with machine size. Particle confinement appears to be affected more than energy confinement, probably because the event takes place in the source region: a single ELM can eject up to 5–10% of the plasma content.[292] ELMs were first seen in ASDEX,[306] and have since been detected in many tokamaks.[292] MHD (ideal and resistive) instabilities are believed to trigger these modes, which are characterized by levels of turbulence and confinement similar to those in L mode.

Three distinct types of ELMs have been identified. The type-I (sometimes called "giant") ELMs occur when the plasma is at or near the threshold for ideal ballooning modes,[307] owing to the steep pressure profile that exists in H mode. Both their frequency and their amplitude are increasing functions of the input power,[281] or more accurately of the power flow through the separatrix,[292] whereas the energy loss per ELM is approximately constant. The $\mathbf{E} \times \mathbf{B}$ rotation has been shown to slow down considerably during the ELM,[299] and the broadband fluctuation level increases simultaneously; in fact, precursor fluctuations in the 30–60 kHz region,[69] as well as bursty semicoherent activity,[308] have been seen by reflectometry in DIII-D up to 20–30 ms before the ELM. The type-I ELM is presently thought to be caused by the interplay of two different MHD instabilities, the ideal ballooning mode and possibly a low-n kink.[292]

Type-II ("grassy") ELMs have been observed only in DIII-D[292] at the highest input powers in strongly shaped plasmas with high triangularity,[309] when the magnetic shear is in the connecting region between the first and the second region of stability to ballooning modes.[310] These ELMs are characterized by small amplitudes and a high repetition rate and are considered the most desirable variety of ELM for reactor operation,[68] because of the relatively small energy load placed by each ELM on the wall.

Type-III ELMs occur at the lowest powers and are identified by a distinctive decrease in frequency, and increase in energy loss, for increasing input power;[168,292] experiments in TCV have shown that the critical quantity is in fact the difference between the heating power and the H–mode threshold power.[292] Resistive ballooning instabilities are thought to play a role in these ELMs,[311] which are often preceded by semicoherent (50–70 kHz) precursor oscillations in both density and magnetic field,[292] which move outward during a period of 10–20 ms[312] until they trigger the ELM proper. Type-III ELMs occur with gradients well below (30–50%) the ideal ballooning limit in DIII–D,[313] but close to it in ASDEX:[292] this discrepancy has been attributed[292] to the higher temperatures that act to stabilize the resistive ballooning modes in DIII–D, allowing ideal MHD dynamics to dominate with larger gradients. A clear instance of stabilization of type-III ELMs by a temperature increase (from a sawtooth pulse) has been documented in JET.[314]

5.2 Overview of Recent Turbulence Measurements in DIII–D

Turbulence studies have been carried out in DIII–D for many years with a steadily growing set of diagnostics.[66] The early work performed by the UCLA group with reflectometry systems[42,46] and an FIR scattering diagnostic[27] had a critical role in documenting the changes in microturbulence that accompany the L–H transition. The amplitude of the density fluctuations in the velocity-shear region was seen to decrease rapidly[296,27] at the time of the first observable change in the D_α emission signal.[69]

Improved localization of the FIR scattering measurement by means of spatially dependent rotational Doppler shifts[190] allowed an evaluation of the magnitude of the change in $\tilde{n}$ at the edge, which was estimated to be typically of the order of 50%.[298] The reduction was approximately uniform in the poloidal-wave-number range $2 < k_\theta < 5$ cm^{-1}, indicating no major change in the shape of the poloidal spectrum (which decreases monotonically[27] with k_θ) and in the poloidal correlation length; shifted and broadened frequency spectra were seen after the transition, corroborating the existence of large sheared flows.[298] Correlation reflectometry[46] was employed to investigate the change in the radial correlation length, which was found to be shorter in H mode than in L mode.[315,301]

The evolution of turbulence in the H–mode phase was also studied with the scattering system. A second, slower (tens of ms) but substantial ($> 50\%$) decrease in the fluctuation amplitude was found[188] to take place in the interior ($\rho_n < 0.9$, where ρ_n is the poloidal flux normalized to its value on the LCFS) in coincidence with the observed reduction in transport there.[280] In H mode, the relative amplitude of the turbulence ($\tilde{n}/n$) was estimated[188] to peak at $0.7 < \rho_n < 0.9$, in contrast with the L–mode case in which the peak occurs near the LCFS.

In-out asymmetries have also been documented by reflectometry measurements,[300] which suggest that L–mode turbulence has a marked ballooning character, which is substantially diminished in H mode.[238] In addition, reflectometry was employed in DIII–D in the first systematic studies of ELM turbulence; precursor oscillations were

identified for both type-I and type-III ELMs (see §5.1) and broadband turbulent activity similar to that in L mode was observed to accompany the ELM event itself.[69]

The availability of advanced fluctuation and profile diagnostics and of a charge-exchange-recombination apparatus with excellent spatial resolution in the edge region[286] has allowed the DIII–D team to address quantitatively theories and hypotheses on the mechanism responsible for the L–H transition. Thanks largely to this effort, the basic paradigm of fluctuation suppression by a sheared $\mathbf{E} \times \mathbf{B}$ drift is now universally accepted.[316,201] This same mechanism, which does not depend strongly on the physics of the underlying instability,[218] is now believed to play a fundamental role in a variety of other enhanced-confinement regimes, such as the VH mode[61], the high-internal-inductance mode obtained with peaked current profiles,[189] and the negative-central-(magnetic)-shear regime.[317]

An elegant control experiment was performed in DIII–D to corroborate this paradigm. By employing appropriate external coils, the toroidal rotation in the core of the plasma was slowed down (*magnetic braking*[318,319]); this acted to reduce the radial electric field by virtue of the radial force balance. The observed decrease in the $\mathbf{E} \times \mathbf{B}$ shear was accompanied, as expected, by an increase both in the local fluctuation level[214] and in the transport rate.[189]

A detailed study of the behavior of turbulence across the L–H transition in the shear layer and in the SOL was undertaken recently by Moyer et al.,[218] using primarily a radially scanned Langmuir probe,[71] which is capable of measuring the density and the potential, as well as the relative phase of their fluctuating components. By operating at input powers only slightly above the threshold for H mode, the time scale of the transition was extended considerably, effectively enhancing the temporal resolution of the measurement. The spatial structure of the H–mode electric-field well and of the turbulent amplitudes was thus mapped out in detail. A more complex picture emerges from these results: well into the H mode, the fluctuation amplitude near the bottom of the well (i.e. where the shear is zero) is similar to or higher than its L–mode level; however, the turbulent flux remains small owing to a dephasing between $\tilde{n}$ and $\tilde{v}_r$. This work has highlighted the need for self-consistent theories that include the phase angle, a feature missing from most current models.[218] In the SOL, the DIII–D probe generally detects a reduction in the density fluctuations of lesser magnitude than inside the LCFS; the potential fluctuations are often unchanged.[265]

More recently, probe data have been employed[241] in initial investigations of nonlinear couplings and statistical intermittency by wavelet bicoherence techniques. Data from recent experiments featuring "very slow" transitions, which show little reduction in the amplitude of the fluctuations, are also currently being analyzed.

The suppression of edge turbulence at the L–H transition has been confirmed also by a lithium-beam emission-spectroscopy system.[53] In addition, DIII–D has recently acquired a deuterium beam-emission-spectroscopy diagnostic,[52] which has been employed to study the core turbulence during negative-central-shear enhanced-confinement discharges. This system is expected to provide important new information on the spatial structure of the turbulence in the future.

5.3 PCI Fluctuation Measurements in DIII–D: Generalities

The data collection and analysis techniques employed in this work have been related at some length in §3.9. Here, we wish to stress a few important points that apply to most or all of the data that will be shown in the remainder of this chapter.

In all cases, the spectral region between 0 and 8 kHz was not accessed: digital highpass filtering was applied to remove all residual vibrational components [see §3.5(f)]. Thus, all the results obtained are subject to this constraint, and some conclusions may conceivably be altered if lower-frequency components were included, especially since the power spectra are invariably observed to increase at low frequency. In plots of the frequency spectra, the lower limit is higher than 8 kHz because averaging is performed over frequency: therefore, the lower limit is augmented by one-half the width of the averaging interval.

Antialiasing filtering was always applied at 1 MHz (3-dB point, see §3.6). When the sampling rate was reduced to 500 ksamples/s, additional filters with a 200-kHz passband were used in most cases; the experimental observation that the spectral content above 100 kHz is negligible compared with the lower-frequency signal renders these filters somewhat superfluous. In fact, the sampling rate was reduced to 200 ksamples/s in a few cases, without any additional filtering.

In all statistical estimates that are subject to a bias from noise contributions (i.e., estimates of the rms amplitude, autopower, coherence, and correlation coefficient), that bias was removed numerically on the basis of independent measurements of the white-noise level in the same run day and in fact, when feasible, in the same discharge. The signal-to-noise ratio is typically between 10 and 100; in the frequency domain, a signal-to-noise ratio of 1000 is often achieved at the lowest frequencies accessed.

Several plots in this chapter will concern the spatial variation of various quantities. The abscissa of these plots is a radial coordinate, which refers to the intersection of the PCI chords with the vessel midplane. It must always be remembered that the measurements are integrated along the chords and thus embrace a range of minor radii whose lower limit is the point shown in the plot. In the literature, various flux quantities are often used in lieu of the normalized minor radius, particularly ρ_n and ρ, which are defined, respectively, as the poloidal and the toroidal flux normalized to their respective values on the LCFS; these are not linear functions of the radius in general. In all shots, the region accessed by the PCI diagnostic is in the range $0.80 < \rho_n < 1.17$, depending on the plasma geometry; the *typical* range in most shots is $0.92 < \rho_n < 1.10$. In terms of ρ, the lower limits of these two ranges are, respectively, 0.78 and 0.90. Finally, in terms of the normalized minor radius the equivalent limits are 0.86 and 0.95.

When data are presented on turbulence, it is always with the implicit assumption that no coherent modes are observed in the frequency spectrum; these modes are usually of large amplitude and their presence completely alters the results.

A total of approximately 130 plasma discharges were studied in detail for this thesis. The results that will be related are always based on observations on several

shots, except where stated otherwise. However, as was mentioned in the prologue to this chapter, it is often difficult to identify quantitative features of the turbulence that are strictly repeatable from shot to shot, although many qualitative attributes and trends do have a universal character. For this reason, combining different discharges to increase resolution or range has generally proven to be of limited utility. Most spatially or temporally resolved data presented will thus refer to individual shots, and in fact a fairly limited number of shots will be used in the figures for the sake of consistency.

Comparisons between shots will preferentially take the form of parametric studies of individual quantities. In particular, the parametric studies that will be described here were carried out during a set of experiments designed as a parameter scan of the L–H transition power.[290] A scan was performed with single-null diverted magnetic geometries, with the following reference parameters: toroidal magnetic field $B_T = 2.1$ T, plasma current $I_p = 1.35$ MA, average density $\bar{n}_e = 4\times10^{13}$ cm^{-3}, elongation $\kappa = 2$, triangularity $\delta = 0.28$, outer and inner gaps (distances from the separatrix to the outside and inside walls, measured on the midplane) respectively 6 and 4 cm. Each parameter was then scanned over a range, while leaving all the other quantities fixed (in the case of the field scan, the current was lowered to 1 MA). A similar scan for double-null geometries was centered at $\delta = 0.83$, with all other parameters being the same as before; an additional parameter, called Dr_{sep}, was scanned for this case: this parameter is the distance between the separatrix surfaces associated with the two X-points, measured on the outer midplane, and it quantifies the balance between the X-points (0 — the reference value — for a balanced double-null, negative for lower X-point dominant, and positive for upper X-point dominant: the ion ∇B drift points towards the lower X-point). In some cases, scans of the input power were obtained as the power was gradually increased to reach the threshold.

For the purposes of our turbulence studies, these parameter scans were used not only to study the dependence of the turbulence characteristics on the global quantities listed above, but also on several other local quantities. In these cases, however, the whole database was used, without any effort to keep specific parameters constant. These local quantities include the density and its scale length [$L_{n_e} = n_e/(\partial n_e/\partial r)$], the electron temperature and its scale length, the electron pressure and its scale length, the parameter η_e (the ratio of the density scale length to the temperature scale length), and q_{95} (the value of the safety factor at $\rho = 0.95$).

In addition, we have used the following parameters of neoclassical transport theory that are relevant to some turbulence theories. The normalized ion collisionality is defined as[6] $\nu_{*i} = \nu_i Rq/(v_{ti}\epsilon^{3/2})$, where ν_i is the ion-ion Coulomb collision frequency, R is the major radius, q is the safety factor, v_{ti} is the ion thermal velocity, and $\epsilon = a/R$ is the toroidal inverse aspect ratio. The magnetic pumping rate (a form of neoclassical viscosity) μ is defined by the following approximate formulas:[320]

$$\mu = \begin{cases} 0.265q\nu_i\epsilon^{-1/2}(1-\epsilon^{1/2})^{-1} & \text{if } \nu_{*i} < 1 \text{ (banana regime)} \\ \frac{3}{2}\sqrt{\pi}\,\epsilon v_{ti}/R & \text{if } 1 < \nu_{*i} < \epsilon^{-3/2} \text{ (plateau regime)} \\ 3.07\epsilon v_{ti}^2/(qR^2\nu_i) & \text{if } \nu_{*i} > \epsilon^{-3/2} \text{ (Pfirsch-Schlüter regime).} \end{cases} \tag{5.1}$$

Owing to the difficulty of obtaining edge ion temperature values for many of these shots, the electron temperature, which was more readily available, was used instead. The effect of this substitution will be commented on for specific cases. A repetition of this study with the actual ion temperature values is planned for the future.

One final caveat concerns the definitions of the confinement regimes. It will be shown in §5.10 that the character of the turbulence changes considerably during the H–mode evolution. For the purpose of the stationary-regime measurements described in §5.4–5.7, "H mode" will refer to an early, ELM-free phase soon after the transition. In the case of correlation measurements, considerations of statistics require integration lengths of the order of 8–12 ms; therefore, short-lived events occurring just after the transition are not revealed by this type of analysis. These events will be discussed in §§5.8 and 5.9, and dynamic changes during H mode will be addressed in §5.10. L-mode data refer to a fully developed neutral-beam-heated phase, at least one beam thermalization time (typically 20–60 ms) after the beam power is applied. The neutral beams are launched in the direction of the plasma current.

5.4 Frequency- and Time-Domain Analysis

(a) Frequency Autospectrum

The broadband frequency autospectrum in the Ohmic regime is always monotonically decreasing, both inside the last closed flux surface (LCFS) and outside it [in the scrape-off layer (SOL)]. This behavior is maintained up to the highest observable frequencies: the signal-to-noise ratio drops to 1 typically between 150 and 500 kHz, depending on the discharge. In the L mode, the same behavior is observed in a majority of cases, again at all spatial locations. However, some nonmonotonic spectral functions have also been seen on chords that cross the midplane more than 3 cm inside the LCFS, in plasma geometries with the separatrix particularly close to the outer wall. Generally, these functions can be described as the sum of a monotonic function and of a feature centered at 40–60 kHz with a half-width of 20–30 kHz. This observation will be discussed in more detail in §5.8 in connection with the L–H transition. L–mode spectra in the SOL are monotonic but generally narrower.

Coherent features are often seen in the spectrum. These are generally identified as MHD instabilities and are clearly distinguished from the background by their narrow bandwidth; they are also typically of larger amplitude. With the exception of the 40–60-kHz feature mentioned above, all other semicoherent modes seen in L mode have proven, upon sufficiently long time averaging, to be in fact completely coherent. It should be noted that the 40–60-kHz feature would qualify as semicoherent according to the terminology used in some of the literature. Since in our case the feature has a width comparable to the normal width of the spectrum, it should be characterized as broadband for consistency.

The dominance of the low-frequency components of the spectrum is a direct consequence of the lack of Doppler shifts from poloidally propagating components,

which was a central result of Chapter 4 and is thus confirmed experimentally. Indeed, the rare nonmonotonic features described above correspond to inside locations where some Doppler shifts are to be expected. The spatial dependence of these features will be illustrated in §5.8.

The H–mode spectrum has a decidedly more irregular shape and varies considerably from case to case. Both irregularity and variability are more pronounced in the main plasma than in the SOL. The irregularity is caused by the appearance of multiple peaks in the region 8–100 kHz: the frequency and spectral width of the peaks do not display any obvious repeatability and also change in time during a shot. However, the spectral distribution is essentially the same at all spatial locations inside the LCFS. A broad decrease with frequency is still seen, and in some cases the peaks are absent and the spectrum is in fact monotonic; the width of the spectrum is generally somewhat greater in H mode than in L mode inside the LCFS, of the same order in the SOL.

In all the cases that were examined, the spectrum increases at low frequencies down to the cutoff value of 8 kHz. Thus, the inaccessible low-frequency region of the spectrum can be expected to be of substantial magnitude.

Typical examples of Ohmic, L–mode, and H–mode spectra are shown in Fig. 5.1. The regularity of the Ohmic and L–mode spectra suggests a fit to a simple decreasing function of frequency. When plotted on a semilogarithmic scale, the spectra are clearly convex, i.e. have a positive second derivative, which is indicative of an inverse power law (Gaussian spectra would be concave and exponential spectra would be straight lines). Inverse-power-law fits to the spectra generate exponents in the range 1–3 and averaging at 2 (the Ohmic and L–mode cases shown in Fig. 5.1 obey an $\omega^{-1.8}$ law). Values very close to 2 are particularly common. In several cases the reduced χ^2 is remarkably small, of the order of 1.

A fairly regular behavior is seen in the inverse-power-law exponent as a function of the spatial position. This behavior also clearly distinguishes the Ohmic and L–mode cases. As shown in Fig. 5.2, in the Ohmic regime the exponent peaks 1–2 cm inside the LCFS, whereas in L mode it increases for increasing radius and is maximum in the SOL. At smaller radii, not shown in the plot, a slight further decrease is generally seen in both regimes. It should be noted that the absolute value of the exponent, as well as the ratio of the Ohmic and L–mode values, changes from discharge to discharge (compare, e.g., Fig. 5.1 and Fig. 5.2); the spatial profiles, by contrast, are fairly general.

As with many other quantities that will be discussed in this chapter, the inverse-power-law exponent has been studied as a function of the several plasma parameters that were listed in §5.3. No regular behavior has been identified, with the partial exception of a two-point scan of the plasma triangularity in double-null diverted magnetic geometries. A sharp drop of the exponent, from 3.1 to 1.8, was seen when the triangularity was raised from 0.67 to 0.83; the location of the chord was 3 cm inside the LCFS on the midplane.

The nonmonotonic nature of the H–mode spectra is not conducive to a simple

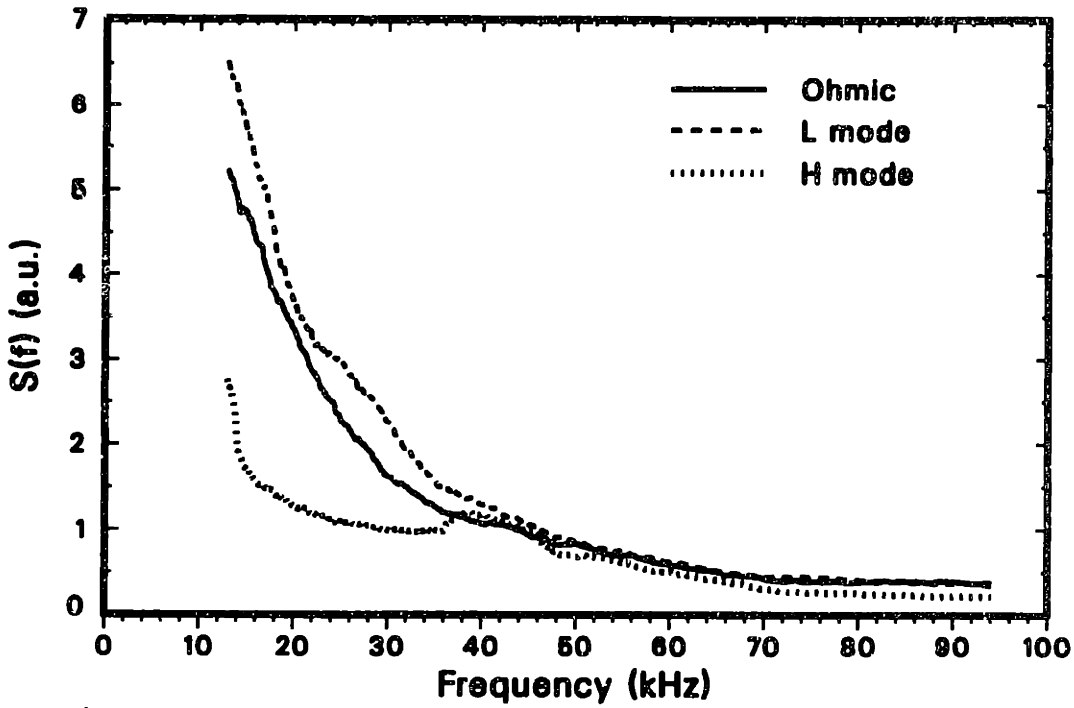

Fig. 5.1 Autopower spectra in the Ohmic, L–mode, and ELM-free H–mode phases of a discharge (B_T=2 T, I_p=1.5 MA, $\bar{n}_e$=3×10^{13} cm^{-3}). The noise level is 0.13 and the statistical error is 4%. The Ohmic power is ~1.8 MW, and the neutral-beam power is 2.3 MW in L mode and 4.6 MW in H mode. The midplane location is 0.9 cm inside the LCFS. The Ohmic and L–mode spectra obey an approximate power law $\propto f^{-1.8}$; the H–mode spectrum is nonmonotonic.

fit. In the few monotonic cases seen, inverse-power-law exponents of the order of 1 have been obtained.

Although simple inverse-power-law fits often produce satisfactory results, in many cases it is clear upon closer inspection that the L–mode spectral slope decrases subtly but abruptly at a frequency between 20 and 40 kHz. Such a case is shown in the logarithmic plot of Fig. 5.3; in this example an $f^{-1.8}$ law applies to the region below 20 kHz and an $f^{-0.7}$ dependence describes the region above it. The abruptness of the transition is evident from the figure.

(b) Time-Delayed Correlation Function

The correlation coefficient displays an oscillatory behavior whose period depends on the choice of the low-frequency cutoff value. This oscillation is removed by calculating the envelope of the coefficient, which carries more general information on the local time-delayed correlation structure.

The envelope of the autocorrelation coefficient is in most cases a monotonically decaying function, as shown in Fig. 5.4(a) (top box). In the Ohmic regime, the form of the function depends weakly on the spatial location, becoming somewhat narrower in the SOL. By contrast, in L mode the function is generally narrowest in the separatrix region and is broader both further inside and in the SOL. The H–mode function is

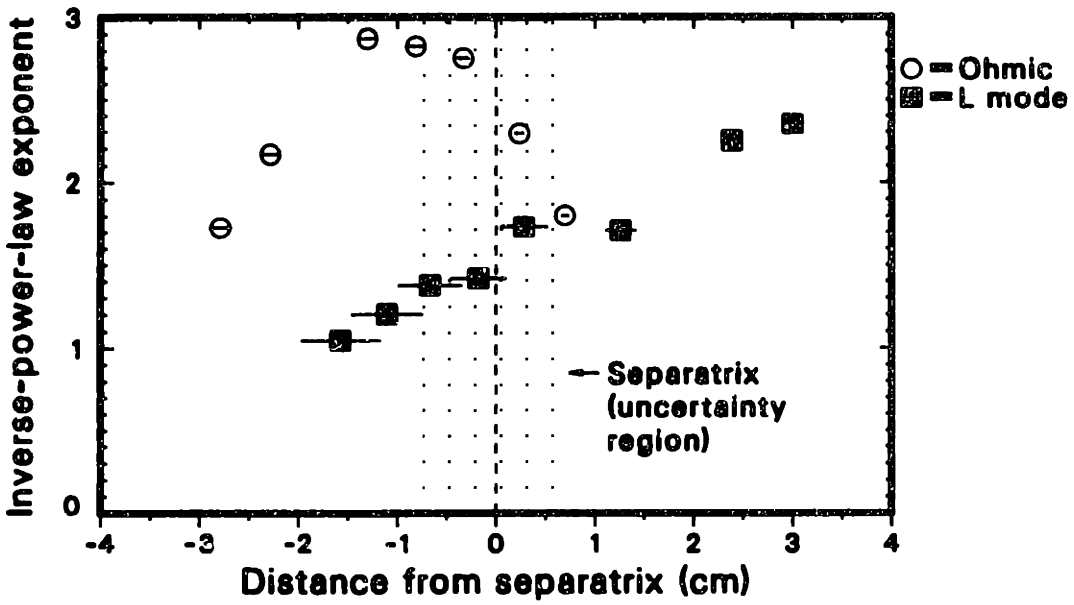

Fig. 5.2 Spatial dependence of the exponent in the inverse-power-law least-squares fit to the PCI autopower spectrum, in an Ohmic case (B_T=1.6 T, I_p=1.36 MA, $\bar{n}_e$=3×10^{13} cm^{-3}) and in an L-mode case (B_T=2.1 T, I_p=1.43 MA, $\bar{n}_e$=3×10^{13} cm^{-3}, $P_{\rm beam}$=2 MW). The abscissa is the distance from the LCFS to the PCI chord on the midplane. Error bars on the positions refer to the distance from the rightmost point; the error on the *spacing* is considerably smaller. The absolute value of the exponent is discharge-dependent, while the profile shapes are fairly general for the two regimes.

less smooth, although generally still monotonic, and changes in time, sometimes on a time scale of 10 ms or less. This behavior is consistent, as it must be, with that of the frequency autospectrum. When compared to its L-mode counterpart, the H-mode envelope is generally narrower at small delay times, reflecting the increased width of the frequency spectrum, but also exhibits a more prominent tail at large delays, a manifestation of the narrow frequency peaks that appear in H mode. The overall width of the function increases in the SOL, where it is comparable to the L-mode envelope. Interestingly, the shape of the H-mode autocorrelation coefficient fluctuates in time in the SOL also.

The envelope of the crosscorrelation coefficient between separate spatial channels displays a variety of shapes [see Fig. 5.4(a)]. As will be seen clearly in the next section, the turbulence spectrum is characterized by two counterpropagating features of comparable, but not always identical, amplitude. This is reflected in the partial left-right symmetry seen in Fig. 5.4(a) for the cases ΔR=0.49 cm and ΔR=0.95 cm (the autocorrelation function is symmetric by definition). At the longer separation of 1.93 cm, which crosses the separatrix, the inward mode prevails. The existence of two modes also explains the nonmonotonic dependence of the coefficient on ΔR (the peak of the envelope is larger at 0.95 cm than at 0.49 cm): when the two modes are in phase opposition, the value of the coefficient is depressed, although the correlation level of each mode can be high.

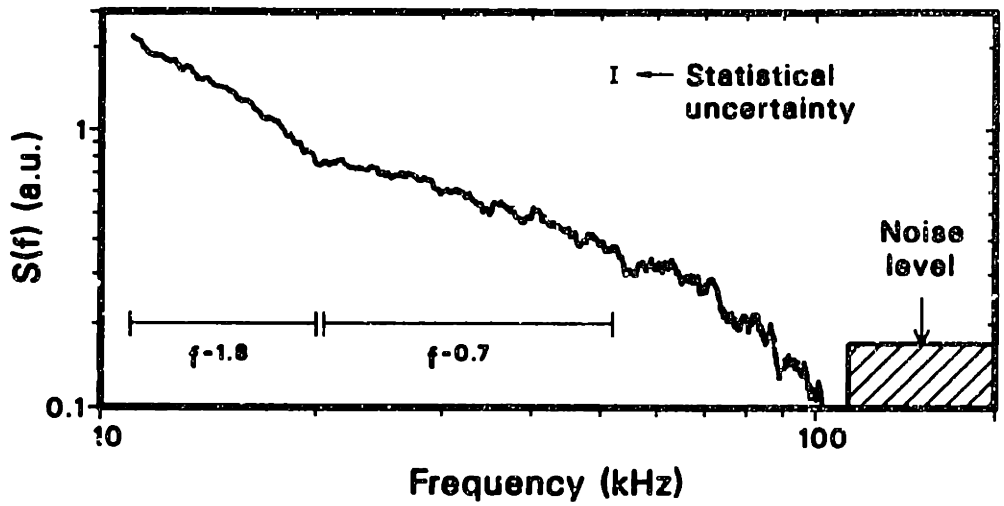

Fig. 5.3 Logarithmic plot of autopower spectrum in a neutral-beam-heated L-mode plasma (B_T=2.1 T, I_p=1.43 MA, $\bar{n}_e$=3×10^{13} cm^{-3}, $P_{\rm beam}$=2 MW), 1.5 cm inside the LCFS.

Double-peaked functions such as the 0.49-cm case in Fig. 5.4(a) are often seen, and in some cases the point of minimum near $\Delta t = 0$ is cusplike. This behavior indicates that each of the two modes has a finite group velocity, approximately equal to the value of ΔR divided by the time delay at each peak; this estimate is only approximate because each mode "pulls" the other peak closer to zero: in fact, depending on the phase relation between the modes at a given ΔR, the sum of the two single-peaked functions can result in a single-peaked function with a maximum at zero, as in the case of ΔR=0.95 cm in Fig. 5.4(a). The form of these crosscorrelation functions is thus in many ways in agreement with the approximate analytical modeling expounded in §4.4, which for the specific case of two radially counterpropagating modes yielded the form of the crosscorrelation coefficient given in Eq. (4.66). This equation constitutes a good qualitative description of the experimental function.

With guidance from theory, as will be discussed in Chapter 6, a search was conducted for variations in the time-delayed correlation structure with varying cutoffs in frequency. As shown in Fig. 5.4(b), by raising the highpass frequency to 40 kHz, the envelope of the autocorrelation coefficient changes little, but the crosscorrelation envelopes change more substantially. In particular, no double-peaked functions are found. This result is universal for L-mode plasmas, although the appropriate cutoff frequency to induce this change in behavior varies from shot to shot, ranging from 20 to 40 kHz. In cases such as that exemplified by Fig. 5.3, in which an abrupt transition in the slope of the frequency autospectrum occurs at a given frequency, applying a highpass filter at that frequency produces the results shown in Fig. 5.4(b). No such regularities have been found in H mode, where the nonstationarity of the correlations is an added problem.

The envelope of the autocorrelation coefficient is fitted routinely with an exponentially decaying function to obtain a local decorrelation coefficient [which we shall call $\tau_{R,\rm eff}$ for consistency with the terminology of Chapter 4 — see e.g. Eq. (4.53)].

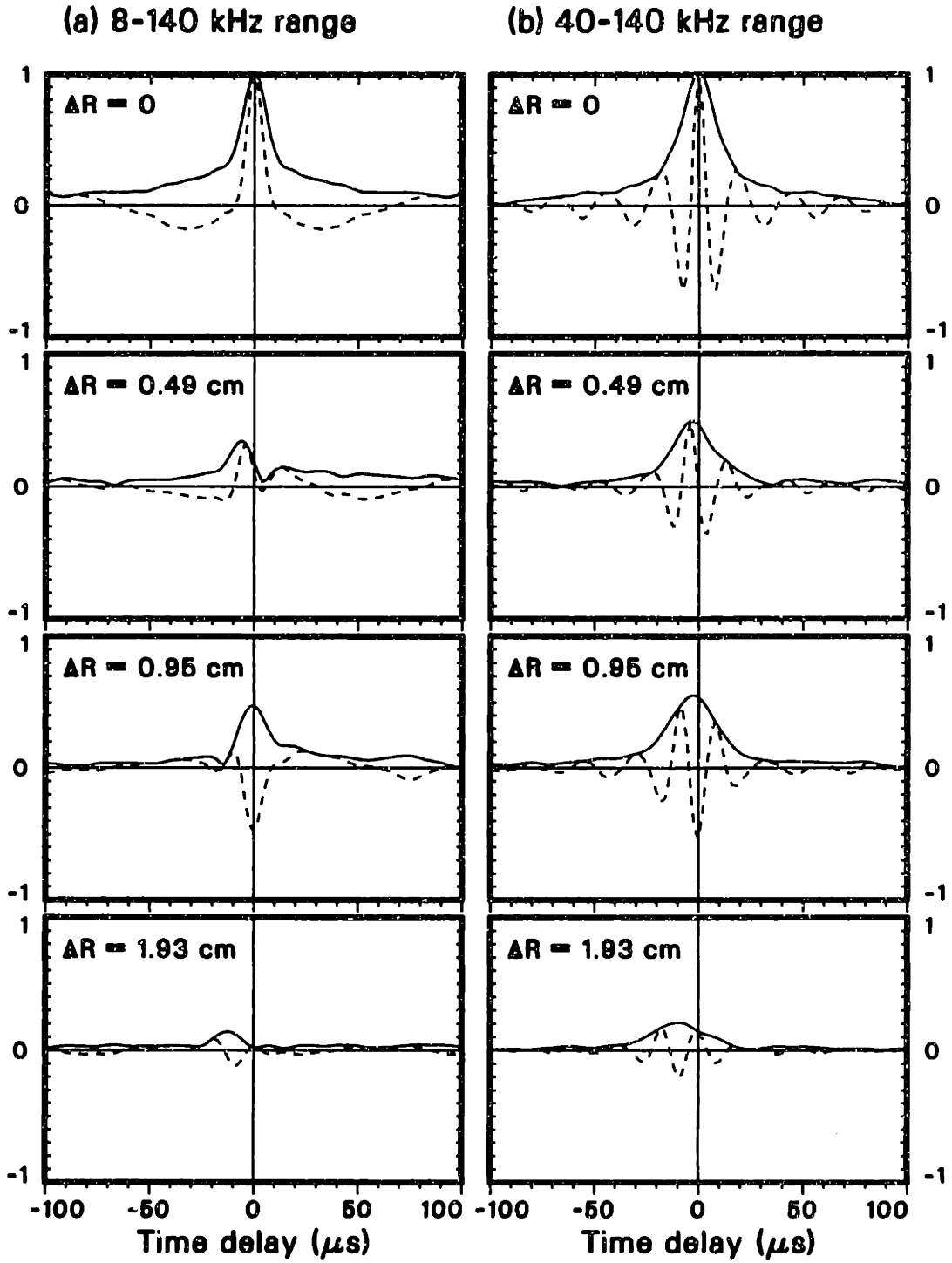

Fig. 5.4 Correlation coefficient (dashed curves) and its envelope (solid curves) for four different radial separations, with (a) full bandwidth, and (b) 40-kHz highpass filter. The minimum significant value at a 95% confidence level, which is also an approximate measure of the statistical uncertainty, is 0.02. The reference point is located 1.3 cm inside the LCFS, in a beam-heated L-mode plasma (B_T=2.1 T, I_p=1.43 MA, $\bar{n}_e$=3.5×10^{13} cm^{-3}, $P_{\rm beam}$=2 MW). The signal-to-noise ratio is $\sim$ 25.

It should be stressed that in most cases the χ^2 of the fit is rather large: thus, this

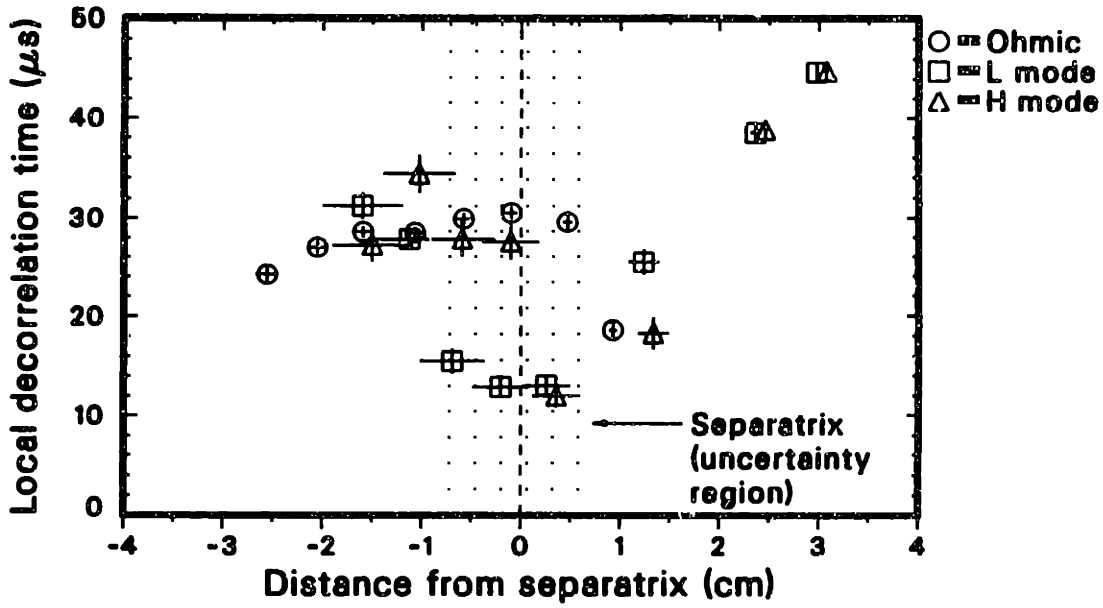

Fig. 5.5 Spatial dependence of the local decorrelation time, in the Ohmic regime (B_T=1.6 T, I_p=1.36 MA, $\bar{n}_e$=3×10^{13} cm^{-3}, $P_{\rm Ohm}$=0.65 MW), and in the L–mode and H–mode regimes (B_T=2.1 T, I_p=1.43 MA, $\bar{n}_e$=3.5×10^{13} cm^{-3}, $P_{\rm beam}$=2 MW). The abscissa is the distance from the LCFS to the PCI chord on the midplane.

functional form must be regarded only as a convenient approximation.

The spatial variation of $\tau_{R,\rm eff}$ has been studied in all three regimes (Ohmic, L mode, and H mode): a representative example is shown in Fig. 5.5. The value of $\tau_{R,\rm eff}$ varies between 10 and 50 μs. The Ohmic case is spatially uniform, except for a drop just inside the SOL. In L mode, a minimum is seen approximately at the separatrix, while $\tau_{R,\rm eff}$ is larger inside the LCFS and considerably larger in the SOL. The H–mode profile is qualitatively similar, with a sharper variation in the high-gradient region near the separatrix. It should be noted that within the spatial uncertainties the minimum in both L and H mode could be located either slightly inside or slightly outside the separatrix.

It is interesting to note that the local decorrelation time is generally larger in H mode than in L mode, although the H–mode value is somewhat variable and there are cases in which it is lower. The prevailing behavior indicates that the high-delay tail in the H–mode correlation coefficient dominates over the narrowing of the function at lower delays.

The similarity between the spatial distribution of $\tau_{R,\rm eff}$ and of the plasma pressure inside the separatrix in L and H mode would suggest a possible relation between the two quantities; such a relation, however, could not apply to the SOL turbulence nor to the Ohmic case. In fact, there is enough variation between shots to make such a parametrization impossible in general; if a relation exists, it must also contain additional variables. Similarly, the parametric scans described in §5.3 have failed to reveal any regularity of $\tau_{R,\rm eff}$, with the partial exception of an input neutral-beam power scan. This scan was performed in a diverted magnetic geometry in which the

ion ∇B drift points away from the dominant X-point: under these conditions, the threshold power is very high[290] (of the order of 15 MW), and a wide range of powers can be explored. The local decorrelation time was found to decrease slightly with increasing power.

The definition of $\tau_{R,\mathrm{eff}}$ as a *local* decorrelation time stems from the formalism of Chapter 4. There, a dispersion relation $\omega(k)$ was postulated, and an *intrinsic* decorrelation time (τ_d) was defined as twice the inverse half-width of the frequency spectrum at each given k [see Eqs. (4.23)–(4.26)]. The *local* decorrelation time is similarly related to the width of the complete frequency spectrum, including all wave numbers; thus, it will generally be a smaller quantity. In our analytical model for the line-integrated PCI measurement, $\tau_{R,\mathrm{eff}}$ was defined by Eq. (4.54), which we reproduce here for convenience:

$$\tau_{R,\mathrm{eff}} = \left(\frac{1}{\tau_d^2} + \frac{v_{T,R}^2}{\mathcal{L}_R^2} \right)^{-1/2} . \tag{5.2}$$

Here, $\mathcal{L}_R$ is the correlation length seen by PCI, and $v_{T,R}$ is the horizontal projection of the sum of the plasma velocity and of the group velocity of the fluctuations. In general, $v_{T,R}$ is essentially equal to the radial group velocity $v_{g,\rho}$.

The intrinsic decorrelation time is an important parameter for comparisons with theory, as will be explained in more detail in §6.1(d). Physically, it describes the decay of the *peak* of the envelope of the crosscorrelation coefficient for all values of the radial separation. In the language of fluid dynamics, this corresponds to switching from a Eulerian to a Lagrangian approach, putting oneself in the frame of reference of the turbulent eddy (or wave packet) as it propagates through space. The behavior of the intrinsic decorrelation time may well differ from that of its local counterpart, which is affected by the correlation length and by the group velocity.

To obtain an estimate of τ_d, we calculate the spatial Fourier transform of the complex function constructed with the correlation coefficient as the real part and its Hilbert transform as the imaginary part, for each value of the delay Δt, at a specific wave number equal to the peak value given by spatial correlation analysis (see §5.5). The modulus of the result is then normalized to a value of 1 for $\Delta t = 0$. The computation, which includes the customary exponential fit, is repeated in time, so that the time series $\tau_d(t)$ can be generated. This procedure is rather involved and requires human intervention at several intermediate steps; hence, it has only been applied to a limited number of shots. It should also be remarked that this estimation technique is somewhat arbitrary, and the results it yields can therefore only be considered as one of several possible estimates of τ_d; particular caution is suggested by the observation that the decorrelation time is a strong function of the wave number, as will be shown in §5.5(d).

A general result of this analysis is that the intrinsic decorrelation time is indeed larger than the local time inside the LCFS. Typically, τ_d is slightly larger than the *largest* of the $\tau_{R,\mathrm{eff}}$ values measured up to 2 cm inside the LCFS; in L–mode conditions,

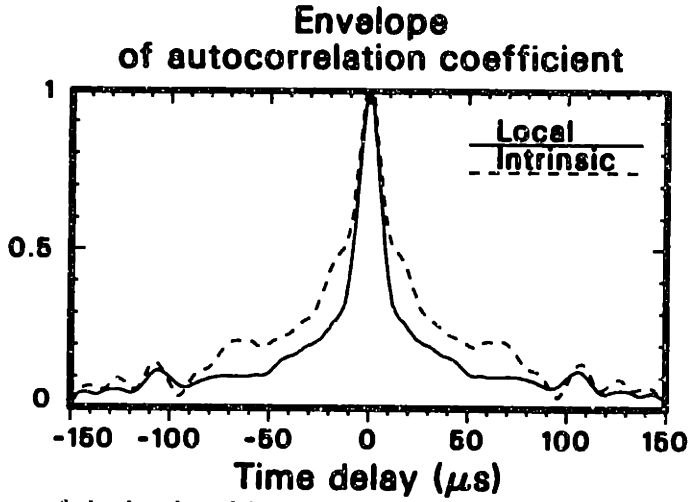

Fig. 5.6 Comparison of the local and intrinsic autocorrelation function envelopes in an L–mode case (B_T=2.1 T, I_p=1.43 MA, $\bar{n}_e$=3.5×10^{13} cm^{-3}, $P_{\rm beam}$=2 MW).The local function refers to a chord located 1.3 cm inside the LCFS. The intrinsic function is calculated at the average radial wave number, $k_{0,R}$ = 3 cm^{-1}. The 95% confidence level is 0.01. Fitted decorrelation times are 35 μs (intrinsic) and 12 μs (local).

this implies that the local value is generally up to a factor of two smaller than τ_d in the proximity of the separatrix. A comparison between the local and the intrinsic envelope is shown in Fig. 5.6 for an L–mode plasma. In the SOL, τ_d and $\tau_{R,\rm eff}$ are comparable.

We also find that τ_d is systematically larger in H mode than in the L mode, as is often, but not always, the case for the local decorrelation time. Typical values are 20–40 μs in L mode and 40–80 μs in H mode. The H–mode correlation function sometimes undergoes rapid variations in time, and the χ^2 of the fit is higher than in L mode, indicating a more irregular functional shape. It should be noted that the peak wave number generally increases at the L–H transition: thus, τ_d refers to two different values of $k_{0,R}$ in the two regimes.

The input-power scan described earlier revealed a slight but measurable decrease of the intrinsic decorrelation time with increasing power, as evidenced by Fig. 5.7.

This type of analysis may be expected to reveal the type of short-lived, long-wavelength filaments that have been seen in the edge and in the scrape-off layer (SOL) of the Caltech Research Tokamak[38] and of ASDEX,[215] were they present in DIII–D. No evidence for such structures has been found, and further corroboration is provided by a lack of high-frequency components in the frequency spectrum. However, predominantly poloidal structures would not be uncovered by this measurement; it is also possible that they have an irregular or intermittent nature and thus cannot be seen by standard Fourier analysis.

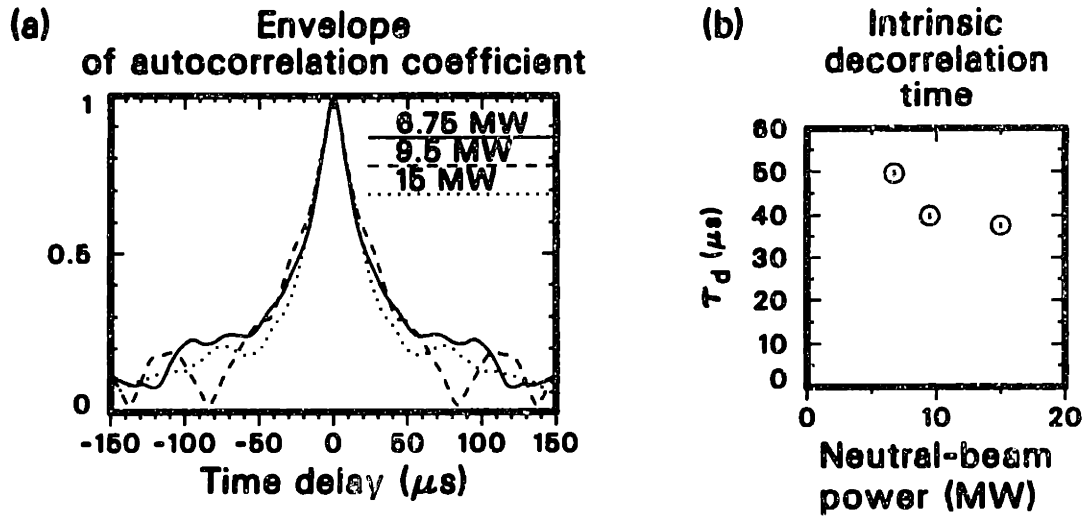

Fig. 5.7 (a) Intrinsic autocorrelation function envelopes for three different input neutral-beam powers (the 95% confidence level is 0.04); (b) intrinsic decorrelation time as a function of power. The functions are measured in L–mode plasmas (B_T=2.1 T, I_p=1.35 MA, $\bar{n}_e$=4×10^{13} cm^{-3}) in the region from the LCFS to 3 cm inside.

5.5 Spatial Correlations and Wave-Number Spectra

(a) Spatial Correlations

The spatial correlation function is a complex Hermitian function, constructed by taking the equal-time correlation coefficient as the real part and its Hilbert transform as the imaginary part. This procedure extracts information on the directionality of the modes, which would be lost by employing only the coefficient, which is an even function by definition. A large imaginary part indicates preferential propagation in one direction.

For a given time interval in a shot, eight correlation functions are obtained by using each digitized spatial channel in turn as reference. A ninth function is constructed by combining all possible pairs of channels: this generally displays some irregularities due to the spatial variation of the correlation structure. This spatial variation is investigated through a comparative study of the eight individual functions. The typical channel-to-channel spacing is 4.7 mm. Having 16 detectors available, different choices of channel-digitizer couplings have been employed, resulting in a variety of spacings and ranges. The spatial variation is, of course, smaller in the high-resolution setups (see §3.4); a minimum spacing of 0.37 mm was reached in one case.

The real part of the spatial correlation function is in most cases wavelike, with a finite spatial period, and decays spatially with a finite decay length. The period and the decay length inside the LCFS are generally longer in the L–mode regime than in the Ohmic regime. In H mode, both lengths are shorter than in L mode and generally shorter than in the Ohmic regime. Ohmic H modes display similar characteristics to auxiliary-heated H modes. In the SOL, by contrast, the correlation function does not

change significantly from L to H mode, and any change observed is usually in the opposite direction from that of the main plasma: that is, the decay length is longer in H mode. In particular, several cm into the SOL the decay length in the late H–mode phase becomes generally very long.

Examples of Ohmic, L–mode, and H–mode correlation functions inside the LCFS are shown in Fig. 5.8. The wavelike structure described is readily apparent; the spatial decay is particularly easy to visualize by inspecting the envelope of the real part of the correlation function. These cases were especially chosen because they displayed little spatial variation: thus, all possible crosscorrelations are shown together. As shown in Fig. 5.8, the imaginary part is also wavelike and has different magnitudes in the three cases. In Ohmic plasmas, the Hilbert transform is generally small and indicative of a slight outward propagation [as in Fig. 5.8(a): the direction of propagation is determined by the sign convention]; this character is preserved in the SOL, but the average magnitude is smaller (essentially no net propagation). A large variety of behaviors has been seen in L–mode plasmas: outward [as in Fig. 5.8(b)], inward, and no propagation; the imaginary part generally becomes smaller in the SOL, and vanishes several cm into the SOL. Finally, the H–mode correlation function is typically more balanced than its L–mode counterpart, and the residual propagation is in the same direction in a given discharge; the case shown in Fig. 5.8(c) is thus somewhat atypical, with a larger imaginary part than in Fig. 5.8(b).

It should be stressed that it is difficult to find regularities in these patterns, and the above considerations are by necessity qualitative. In particular, sharp differences in the direction of propagation have been observed in otherwise very similar plasmas.

The principal purpose of the high-resolution experiments was to confirm this wavelike behavior with fine radial spacing. In the Ohmic example shown in Fig. 5.9, the average channel-to-channel spacing was 0.37 mm, but only every other channel was digitized. The structure of the functions of Fig. 5.8 is clearly confirmed with striking accuracy. As was discussed in §3.2, a spatial antialiasing filter is always employed to limit the passband to the Nyquist spatial frequency, whose typical value is < 10 cm^{-1}; in the high-resolution case, the passband was raised to 40 cm^{-1}, thus allowing hypothetical fine-structure components to appear in the correlation function. In all cases, no such features were observed, as Fig. 5.9 attests. The absence of high-wave-number components was confirmed by a test that will be described later in this section.

Although the high-resolution configuration has the potential of operating partly in the Bragg regime, the considerations of §2.8 and §3.2 apply: the correlation function would be in fact the sum of a Raman-Nath and a Bragg component. The similarity of Fig. 5.9 to Fig. 5.8(a) simply indicates that the $k_z = \pm k_R^2/(2k_0)$ components (k_z is the vertical wave number and k_R the horizontal one) are either absent or behave like the $k_z = 0$ components. In addition, a spectral analysis of these data reveals that their k_R content is concentrated in the region $k_R < 10$ cm^{-1}, and thus lies in fact entirely in the Raman-Nath regime. This is universally true for all the cases analyzed for this thesis, as will be discussed in subsection 5.5(c).

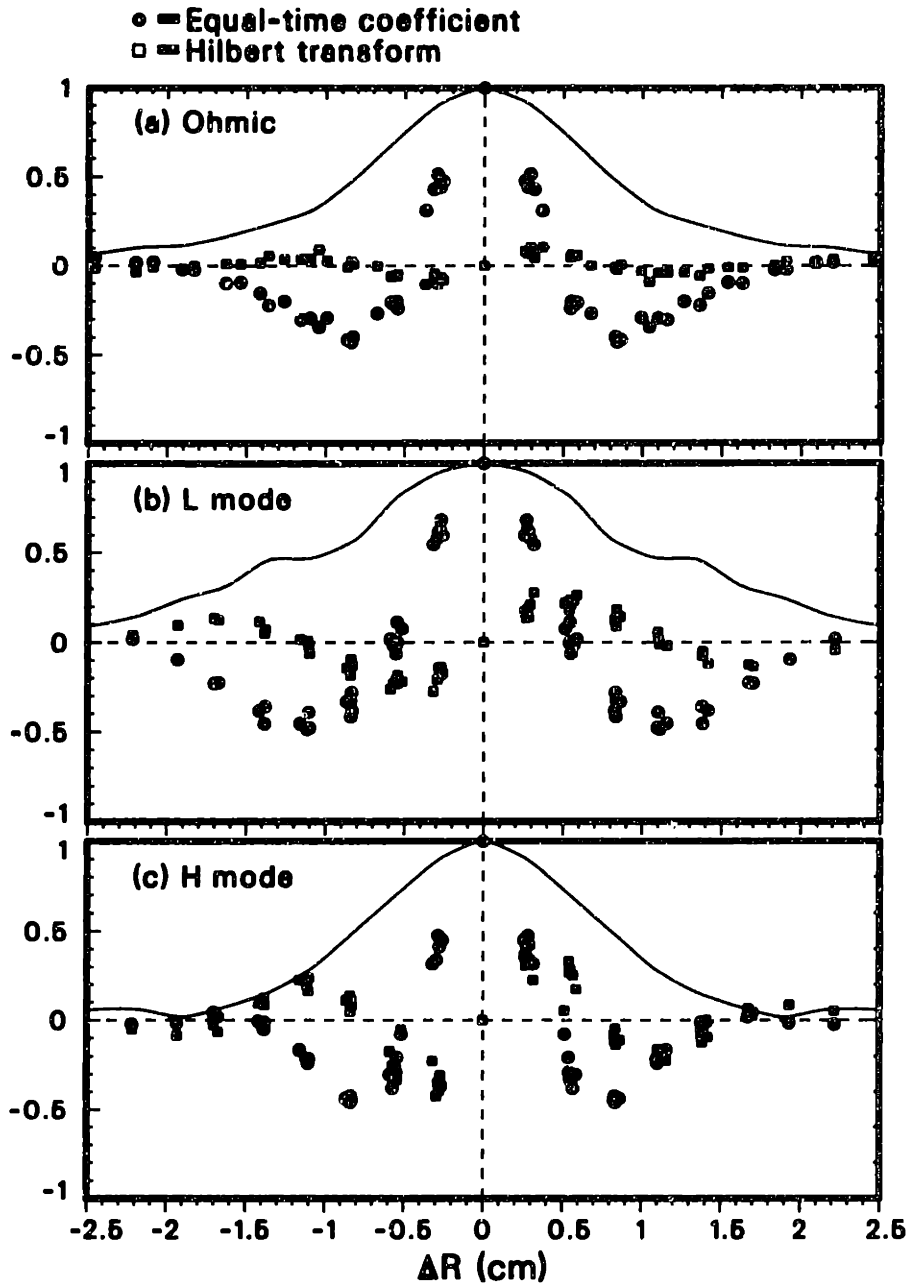

Fig. 5.8 Equal-time coefficient and its Hilbert transform for three cases: (a) Ohmic (B_T=2.1 T, I_p=1.9 MA, $\bar{n}_e$=3×10^{13} cm^{-3}, input power = 3.5 MW), (b) L mode and (c) H mode (both B_T=2.1 T, I_p=1.25 MA, $\bar{n}_e$=3.5×10^{13} cm^{-3}, input power = 6.2 MW). The solid curves represent the envelopes of the equal-time coefficient. The plots refer to the region between the LCFS and 3 cm inside. The 95% confidence level is 0.02. Fits give correlation lengths, respectively, of 1.2 cm, 1.5 cm, and 1.2 cm; and average wave numbers of 3.4 cm^{-1}, 2.8 cm^{-1}, and 3.9 cm^{-1}.

It is of interest to determine whether standing waves exist in the turbulence; these would manifest themselves in a pattern of nodes and peaks in the spatial distribution of the amplitude. Although the amplitude does vary spatially, as will be shown in the next section, no such clear pattern has generally emerged. In particular, the

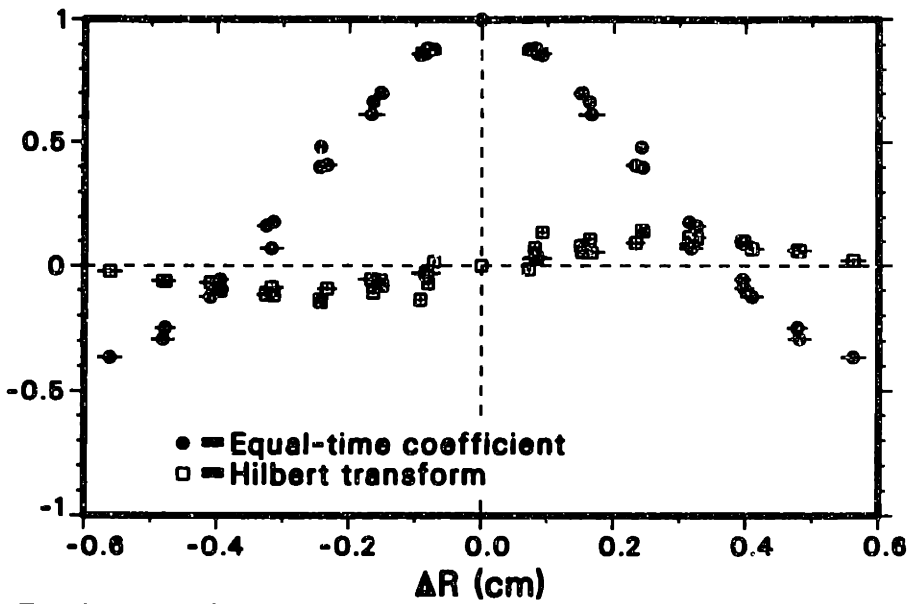

Fig. 5.9 Equal-time coefficient and its Hilbert transform from a high-resolution measurement in an Ohmic plasma (B_T=2 T, I_p=1.5 MA, $\bar{n}_e$=3.3×10^{13} cm^{-3}), in the region from the nominal position of the separatrix to 0.6 cm inside. The 95% confidence level is 0.02. The signal-to-noise ratio for all channels ranges from 4 to 10.

spatial variations are usually uniform throughout the frequency spectrum, negating the possibility of dispersive standing waves.

Two peculiar types of spatial correlation functions deserve a separate discussion; in Chapter 6 we shall attempt to interpret them. When studying the correlation structure across the separatrix in an L–mode plasma, an abnormally high correlation level is sometimes observed between the regions just inside and just outside the separatrix; however, both regions are less correlated with the points in between, which are in the proximity of the separatrix. Clearly, this type of structure departs from the usual decaying wavelike behavior. An example is shown in Fig. 5.10(a). The magnitude of the Hilbert transform is quite small, indicating no net propagation. For this phenomenon, it is useful to explore also the spatial coherency function (see §3.9) at various frequencies (this function is the frequency-domain equivalent of the complex correlation function): this is plotted for four frequencies in Fig. 5.10(b). Although the 13-kHz case could be interpreted as an ordinary wavelike pattern, the higher frequencies clearly prove that such an interpretation is not appropriate, and that the absolute correlation level has in fact a minimum somewhere between the two extreme points. In particular, the correlation between the two extremes is strikingly high at 53 and 73 kHz.

This phenomenon is observed most clearly and most frequently when the plasma current is high ($\sim$ 2 MA) and the edge safety factor q_{95} is low ($q_{95} \lesssim 4$), although a rigorous parametric scan has not been carried out. After the L–H transition, this structure is never observed across the separatrix, but in some cases it is seen in a region 3–4 cm inside the LCFS; in a later phase during the H mode, it sometimes

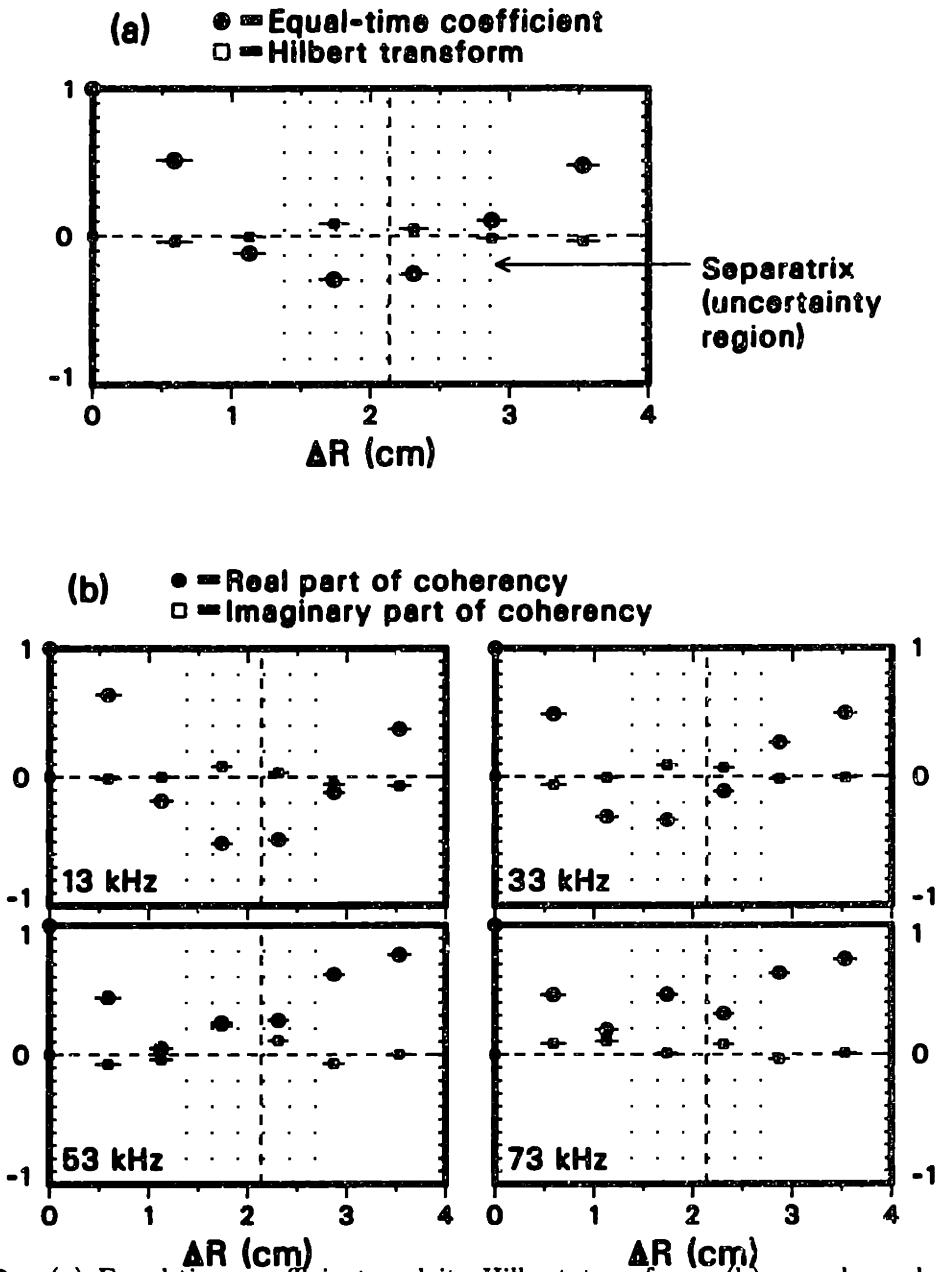

Fig. 5.10 (a) Equal-time coefficient and its Hilbert transform; (b) complex coherency function (averaged over 10 kHz) at four frequencies, in an L–mode plasma (B_T=2.16 T, I_p=2.0 MA, $\bar{n}_e$=4.4×10^{13} cm^{-3}, $P_{\rm beam}$=6 MW). The 95% confidence level is 0.02 for the coefficient and 0.07 for the coherency.

moves again to the LCFS. Weaker versions of this pattern, with lesser departures from the canonical monotonically decaying behavior, are also seen in L modes and late H modes in the region 3–5 cm outside the separatrix.

A second phenomenon with unusual characteristics is seen only in the SOL in H mode. A high level of correlation is observed throughout the SOL, beyond the width of the density gradient; moreover, as the spatial position is moved inwards, the sign of the real part of the correlation function goes sharply from positive to negative

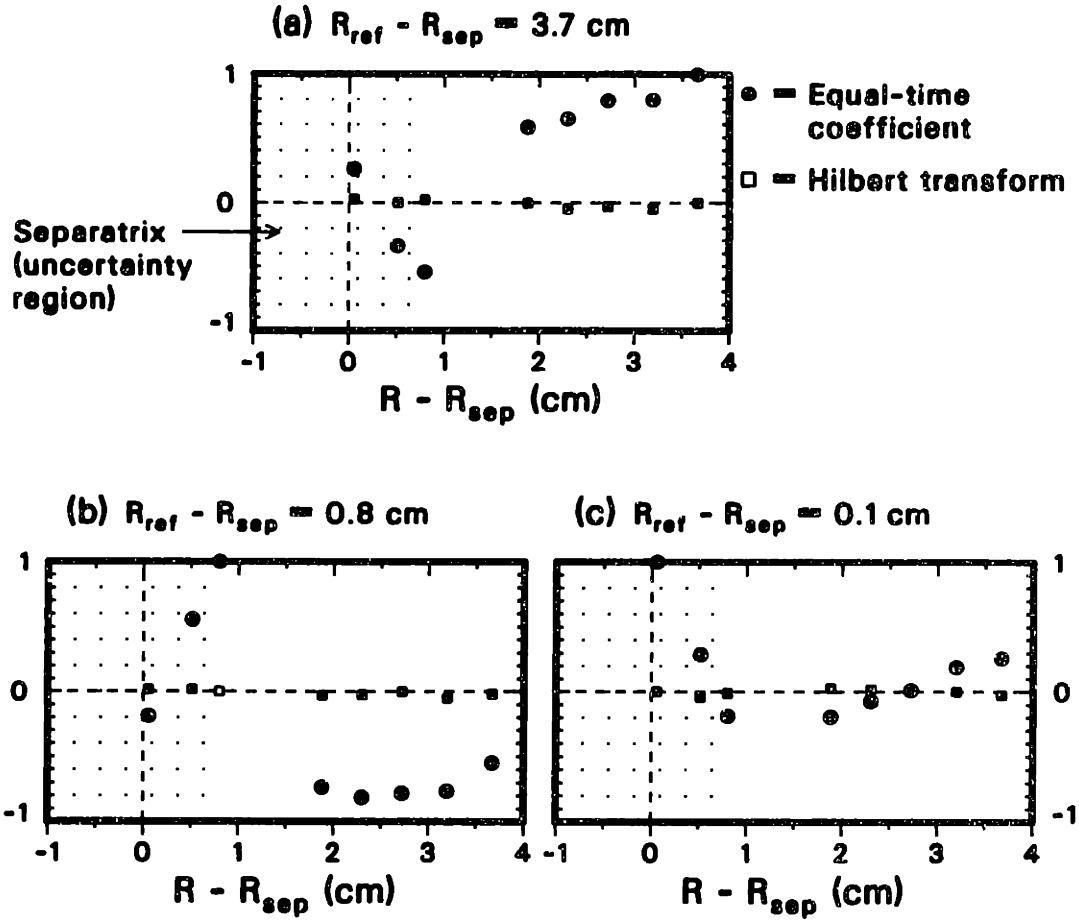

Fig. 5.11 Equal-time coefficient and its Hilbert transform, relative to three different reference points, in the SOL of an H-mode plasma (B_T=2.1 T, I_p=1.35 MA, $\bar{n}_e$=4.5×10^{13} cm^{-3}, P_{beam}=1.6 MW). The 95% confidence level is 0.03.

approximately 1–2 cm outside the LCFS, and is then reversed again when the LCFS is reached. The correlation level between the separatrix and the outer SOL is low. This behavior indicates the existence of a region between 0.5 and 1.5 cm outside the LCFS in which density fluctuations are 180° out of phase with respect to the surrounding regions. The Hilbert transform is near zero, indicating no net propagation.

An example of this structure is shown in Fig. 5.11. In plot (a), with the outermost point as reference, both the high correlation level and the sign changes are clearly seen. Plot (b), relative to the region just outside the LCFS, displays the sign reversals even more clearly. Finally, plot (c), relative to the separatrix, exhibits a more orthodox behavior, with a reduced correlation level. The time-delayed correlation function for these cases is similar to the autocorrelation function plotted at the top of Fig. 5.4(a) for points with positive equal-time correlations, and to its mirror image (peak at -1/-0.8) for points with negative correlation; in some cases the rounded peak is replaced by a cusp. These types of structures are not seen in all H modes, but we have not succeeded in identifying any dependence on the discharge conditions and parameters.

In the late H–mode phase, hybrid versions of the two phenomena just described

have been seen: these display both a sign reversal and an intermediate region of reduced correlation.

(b) Fits to the Spatial Correlation Function

In an effort to obtain convenient low-order fits to the observed correlation functions, we have found the most satisfactory model function to be of the form [Eq. (3.17)]

$$C(\Delta R; \Delta t = 0) = \exp\left[-\frac{(\Delta R)^2}{\mathcal{L}_R^2}\right]\left(\frac{1+P_R}{2}e^{ik_{0,R}\Delta R} + \frac{1-P_R}{2}e^{-ik_{0,R}\Delta R}\right); \quad (5.3)$$

this three-parameter fit provides an average wave number $k_{0,R}$, a correlation length $\mathcal{L}_R$, and a propagation coefficient P_R (1 for purely outward, -1 for purely inward propagation).

These fits provide a convenient reduced description of the correlations, but it must be remembered that they are not dictated by any theoretical model, and in fact the χ^2 is generally rather high. For a more accurate study, it is essential to investigate the experimental functions directly.

The results presented in the previous subsection can be handily restated in terms of these parameters; in particular, as shown in Fig. 5.8, the correlation length is longer in L mode than in the Ohmic regime, and slightly longer in the Ohmic regime than in H mode: values in the range 1.2–3.5 cm have been measured inside the plasma in Ohmic and L–mode conditions, and values down to 0.4 cm have been recorded in H mode; in the SOL, $\mathcal{L}_R$ is generally shorter than 1 cm. The average wave number is comparable in the Ohmic and L–mode cases (1.8–4 cm^{-1}), and larger in H mode (up to 7 cm^{-1}). The propagation coefficient is positive in all three plots of Fig. 5.8. Clearly, the structures seen in Figs. 5.10 and 5.11 do not conform to Eq. 5.3.

The spatial dependence of the correlation function is illustrated by Fig. 5.12 (L mode) and Fig. 5.13 (H mode). In L mode, little variation generally occurs within the region from the LCFS to 4 cm inside, in both confinement modes. This can be seen by comparing Figs. 5.12(a) and (b), which show the correlation functions relative to the two extreme points in the same time interval: the two functions are similar, and are fitted with similar parameters. Figs. 5.12(c) and (d) refer to a similar shot and depict the correlation function in the SOL. In the inner SOL, the correlation length is reduced and the wave number increases; deeper in the SOL, this trend is accentuated further: correlations are minimal in Fig. 5.12(d). These results are generic to L–mode conditions; similar considerations apply to Ohmic plasmas also.

In H mode, the spatial variation inside the LCFS is again modest, as seen in Figs. 5.13(a) and (b); going into the SOL, a decrease is observed in the average wave number, whereas the correlation length increases slightly: this particular variation is not systematic and changes from shot to shot. Deeper into the SOL, a clear increase in the correlation level is seen, unlike in the L–mode case. The fits are generally poorer in H mode than in L mode, indicating increased irregularity.

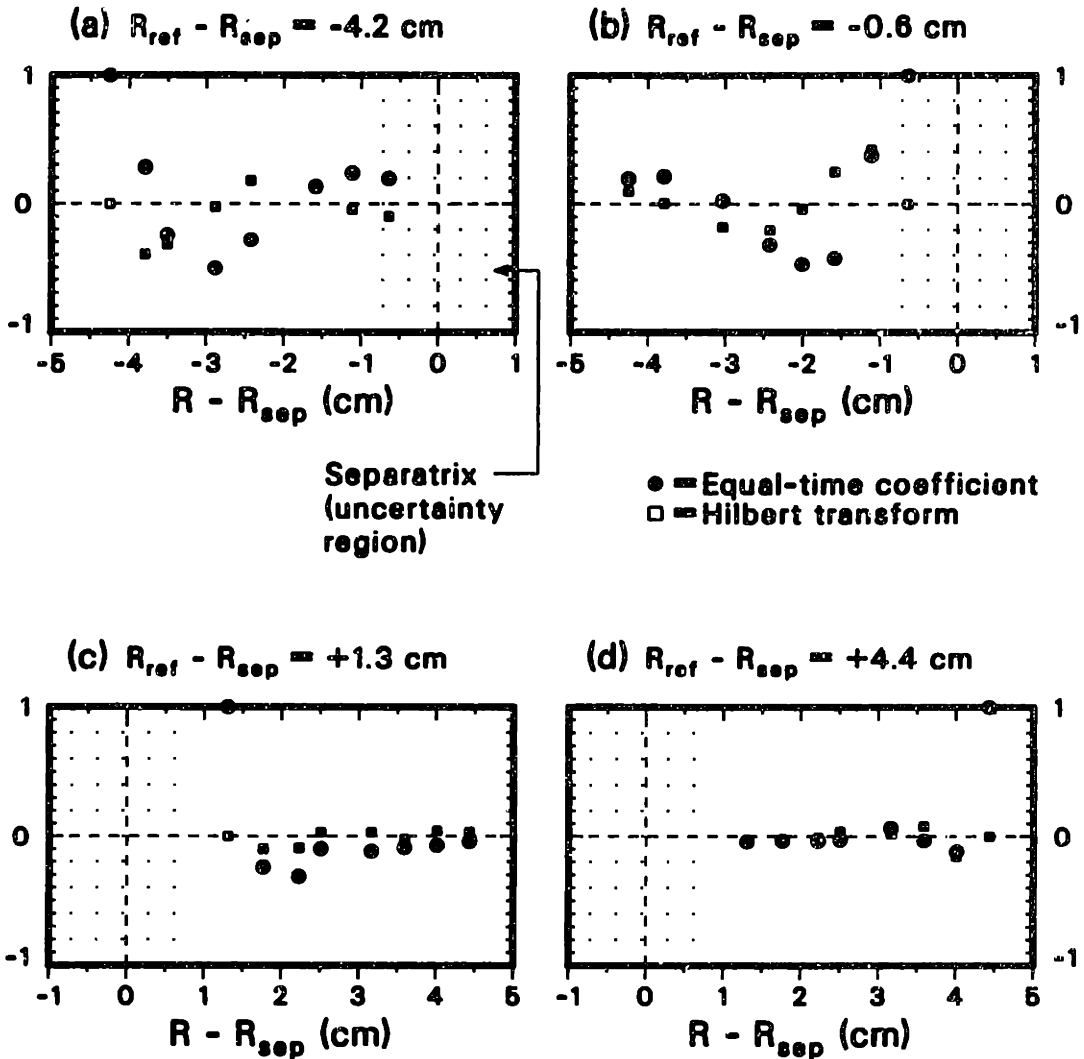

Fig. 5.12 Equal-time coefficient and its Hilbert transform, relative to two reference points inside the LCFS [(a) and (b)] and to two points in the SOL [(c) and (d)] for two similar L–mode plasmas (B_T=2.1 T, I_p=1.35 MA, $\bar{n}_e$=4×10^{13} cm^{-3}, P_{beam}=1.8 MW). The 95% confidence level is 0.03. Fits give correlation lengths, respectively, of 2.1 cm, 2.0 cm, 0.8 cm, and 0.4 cm; and average wave numbers of 2.0 cm^{-1}, 2.1 cm^{-1}, 3.2 cm^{-1}, and 4.4 cm^{-1}.

The propagation coefficient is at most a weak function of the position, with no discernible regularity.

Various frequency filters have been applied to the data in an effort to identify a dependence of the correlation length on the passband. Moving the low cutoff from 8 to 20–25 kHz generally produced little change; thus, the sharp change in the spectral slope often seen in this region (see §5.4) is not related to a change in the correlation properties. As the highpass frequency is moved to progressively higher values, the correlation length is gradually reduced.

The parametric studies listed in §5.3 were applied to the three correlation fitting parameters. Dedicated scans of global parameters, performed by varying one parameter at the time, produce only a few experimental points but have the advantage of

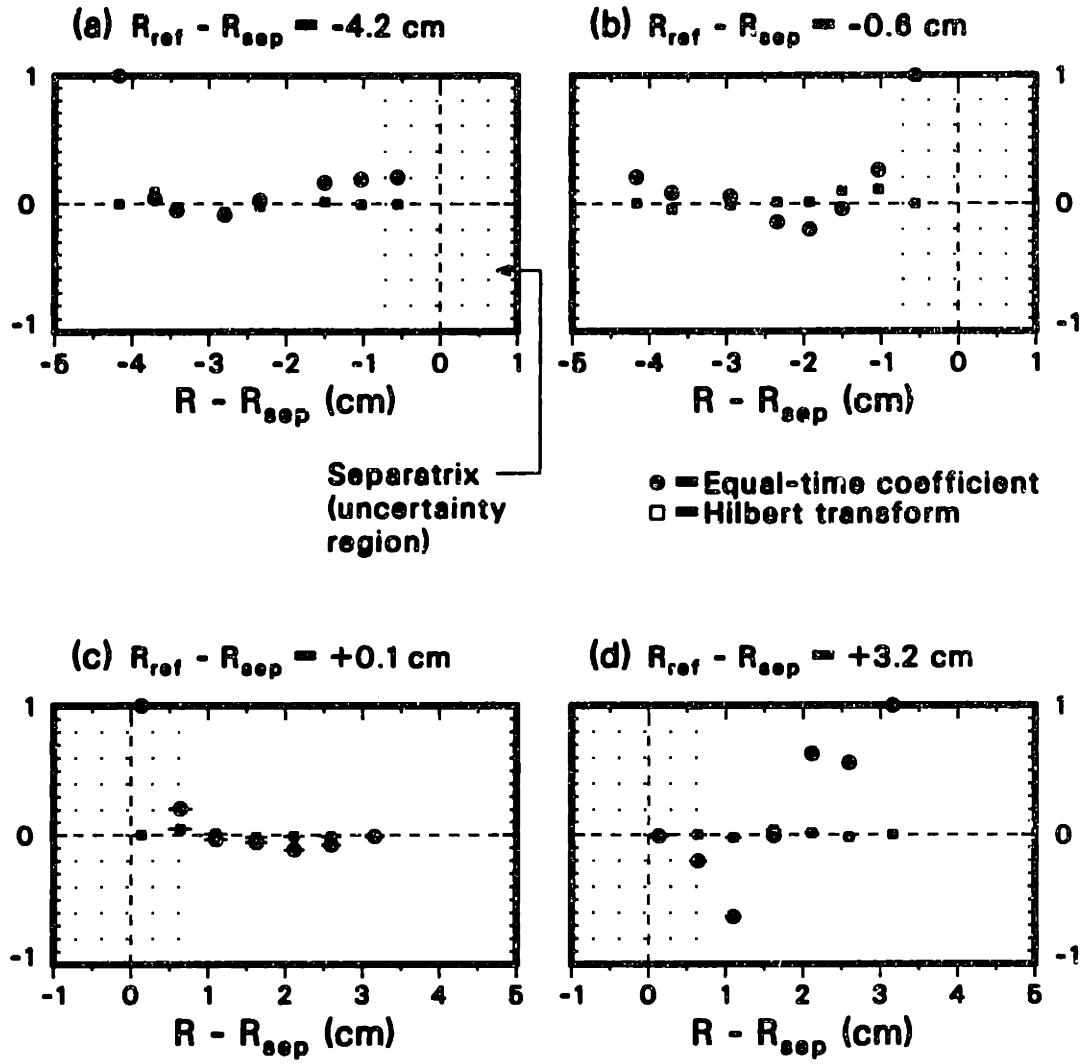

Fig. 5.13 Equal-time coefficient and its Hilbert transform, relative to two reference points inside the LCFS [(a) and (b)] and to two points in the SOL [(c) and (d)] for two similar H–mode plasmas (B_T=2.1 T, I_p=1.35 MA, $\bar{n}_e$=4×10^{13} cm^{-3}, P_{beam}=1.1–1.8 MW). The 95% confidence level is 0.03. The minimum signal-to-noise ratio at the outer edge of the SOL is 5. Fits for cases (a)–(c) give correlation lengths, respectively, of 0.9 cm, 0.7 cm, and 1.2 cm; and average wave numbers of 2.8 cm^{-1}, 2.6 cm^{-1}, and 2.3 cm^{-1}. No adequate fit could be made to case (d).

separating the independent variables. Scans of local parameters, by contrast, were made by using data from all the global scans, with no effort to keep any quantities constant. This approach was preferred in view of the difficulty of selecting the independent variables without prior knowledge; as a result, however, the local scans must be considered of a more qualitative nature. In all the scans, the correlation parameters were measured in the region between 1 and 3.5 cm inside the LCFS.

All parameter scans in H mode failed to reveal any regularities; in addition, as mentioned before, the fits are often poor in this regime. In L mode, a general result is that the dependence on global parameters appears stronger than on local parameters (but the caveat of the preceeding paragraph applies). The global scans are shown in

Fig. 5.14. Data referring to double-null diverted configurations are plotted separately from those for single-null plasmas [these geometries are shown schematically in Fig. 4.16(b)]. It should be noted that the input power is not kept constant in each scan, owing to the variation of the H–mode power threshold; therefore, the power remains as a hidden variable.

The characteristic lengths (correlation length $\mathcal{L}_R$ and average wavelength $2\pi/k_{0,R}$) are increasing functions of the input power and of the line-averaged density; their decrease with plasma current should be considered only a preliminary result, since only two points are available. No clear dependence on the toroidal magnetic field is seen. The correlation length has a definite dependence on the parameter $Dr_{\rm sep}$ also: although there is some scatter in the data at negative $Dr_{\rm sep}$, the correlation length clearly decreases for positive values of $Dr_{\rm sep}$. At the highest value $Dr_{\rm sep} = 0.6$, for which the H–mode threshold power is highest, three points are shown, corresponding to three shots with increasing input power [reflected in the scan in Fig. 5.14(a)]: in the third shot the transition to H mode was finally obtained.[290]

An additional global parameter, the thermal-energy confinement time τ_E, was also scanned without constancy constraints. The scan is shown in Fig. 5.14(f). No clear relation between τ_E and $\mathcal{L}_R$ or $k_{0,R}$ is found.

The local-parameter scans are plotted in Fig. 5.15. The parameters are measured at the intersection of the midplane with the chord on which the turbulence quantities are estimated. The average wave number did not display any regular behavior versus any parameters and was thus left out of these plots for the sake of brevity, with the exception of the ion sound gyroradius scan, which was kept for illustrative purposes and also for theoretical reasons. Studies of the correlation length as a function of the ion sound gyroradius, of the local density, of the density gradient length, of the electron temperature, and of the temperature gradient length [Figs. 5.15(a)–(e)] failed to evince any regularities. The same is true for the scan of q_{95} (the safety factor at $\rho = 0.95$). On the other hand, we observe [in Figs. 5.15(f), (g), and (i)] a scattered decrease of $\mathcal{L}_R$ with increasing $\eta_e = L_n/L_T$ and with increasing magnetic pumping rate [defined by Eq. (5.1)] and an increase of $\mathcal{L}_R$ with increasing normalized ion collisionality ν_{*i} (see §5.3). We recall that all quantities are estimated by using the electron temperature in lieu of the ion temperature. The large horizontal bars for the parameters that depend on the temperature are due to the large relative errors in the temperature measurement by Thomson scattering at the edge of the plasma. Points with relative errors larger than 100% were not used.

The propagation coefficient P_R was also studied parametrically. Figure 5.16 contains only those scans (global and local) that display some degree of regularity. All other scans were highly irregular. Points lying above the dashed median line refer to predominant outward propagation, and vice versa. P_R remains essentially constant when the magnetic field is varied [Fig. 5.16(a)], with the exception of the lowest value $B_T = 1.08$ T, which corresponds to a drop of P_R to a negative value. The propagation coefficient decreases with increasing line-averaged density but *increases* with increasing *local* density [Figs. 5.16(b) and (c)]. However, the latter is, again, an

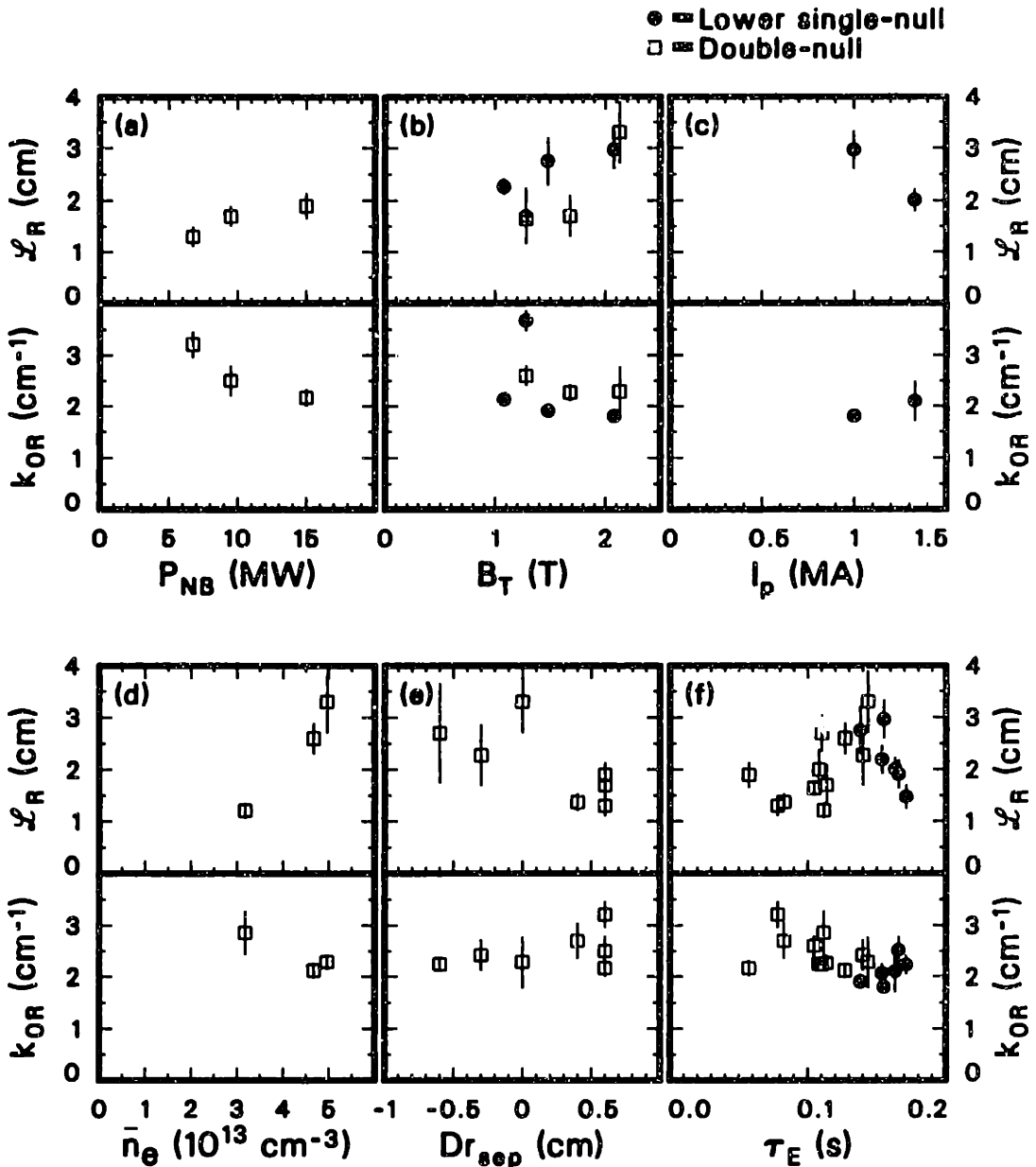

Fig. 5.14 Global parameter scans of the radial correlation length and average radial wave number for sets of lower-single-null and double-null diverted L–mode plasmas. Scans (a)–(e) were performed while keeping the other parameters constant; scan (f) combines shots from all other scans. The parameters are: (a) neutral-beam power; (b) toroidal field; (c) plasma current; (d) line-averaged density; (e) the X-point imbalance parameter Dr_{sep} (negative when the ion ∇B drift points towards the dominant X-point, and vice versa); (f) thermal-energy confinement time. The three points at $Dr_{sep} = 0.6$ in (e) correspond to the power scan in (a).

unconstrained scan. A similar increase of P_R is observed when the temperature, the density gradient length, and η_e are increased [Figs. 5.16(d)–(f)].

In general, more caution should be exercised in considering the scans of Fig. 5.16 than the scans of the characteristic lengths, as the parameter P_R exhibits considerable variability from shot to shot and from one experiment to the next. In particular,

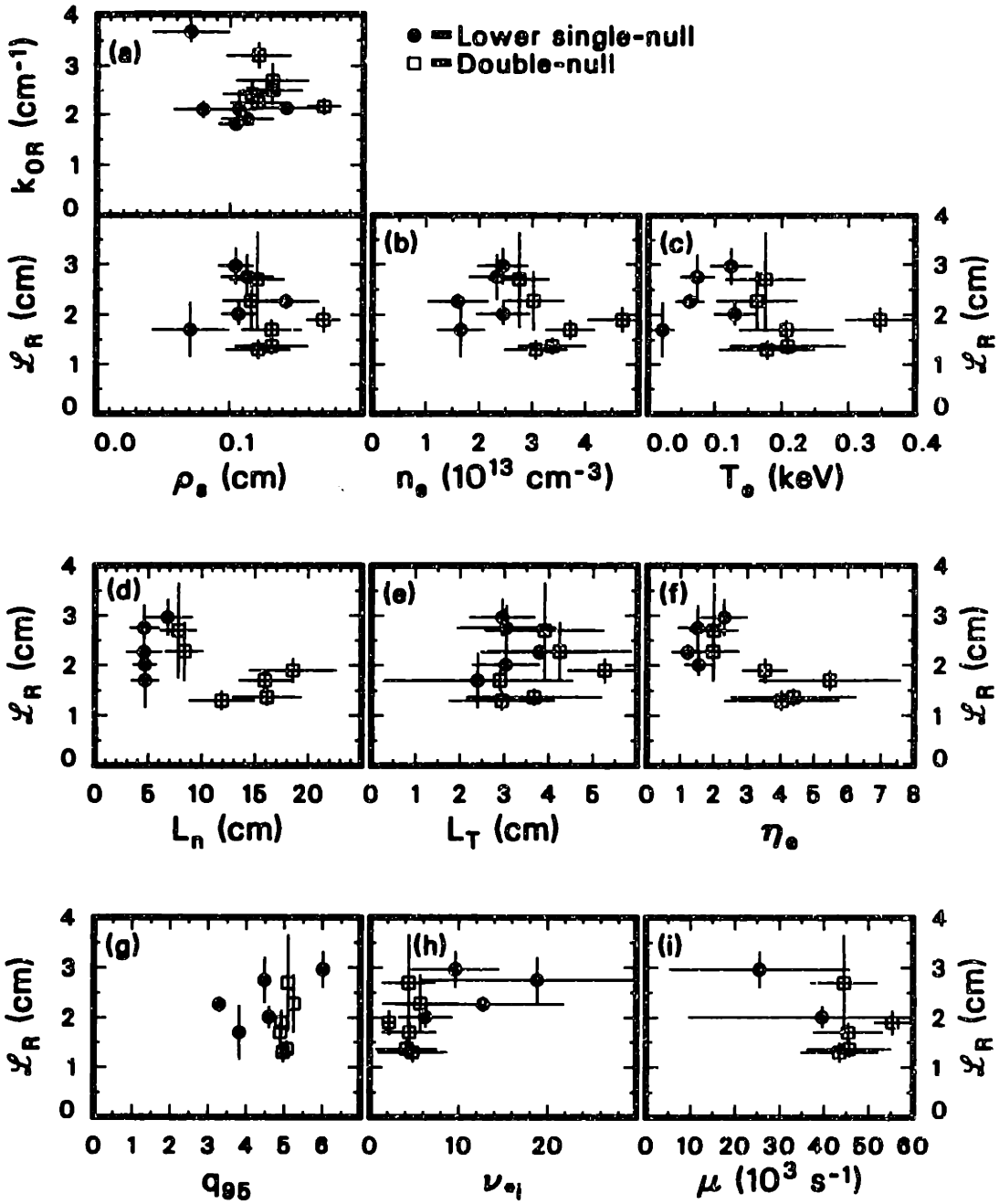

Fig. 5.15 Local parameter scans of the radial correlation length and, for case (a) only, of the average radial wave number. These scans combine lower-single-null and double-null diverted L-mode plasmas used in the global scans of Fig. 5.14. The parameters are: (a) ion sound gyroradius; (b) local electron density; (c) electron temperature; (d) density gradient length; (e) temperature gradient length; (f) $\eta_e = L_n/L_T$; (g) safety factor at $\rho = 0.95$; (h) normalized ion collisionality (see §5.3); (i) magnetic pumping rate (see §5.3).

qualitative observations indicate that shots with outward-propagating turbulence are underrepresented in this data set. A repeat of this study on a much larger database would certainly be well worth doing.

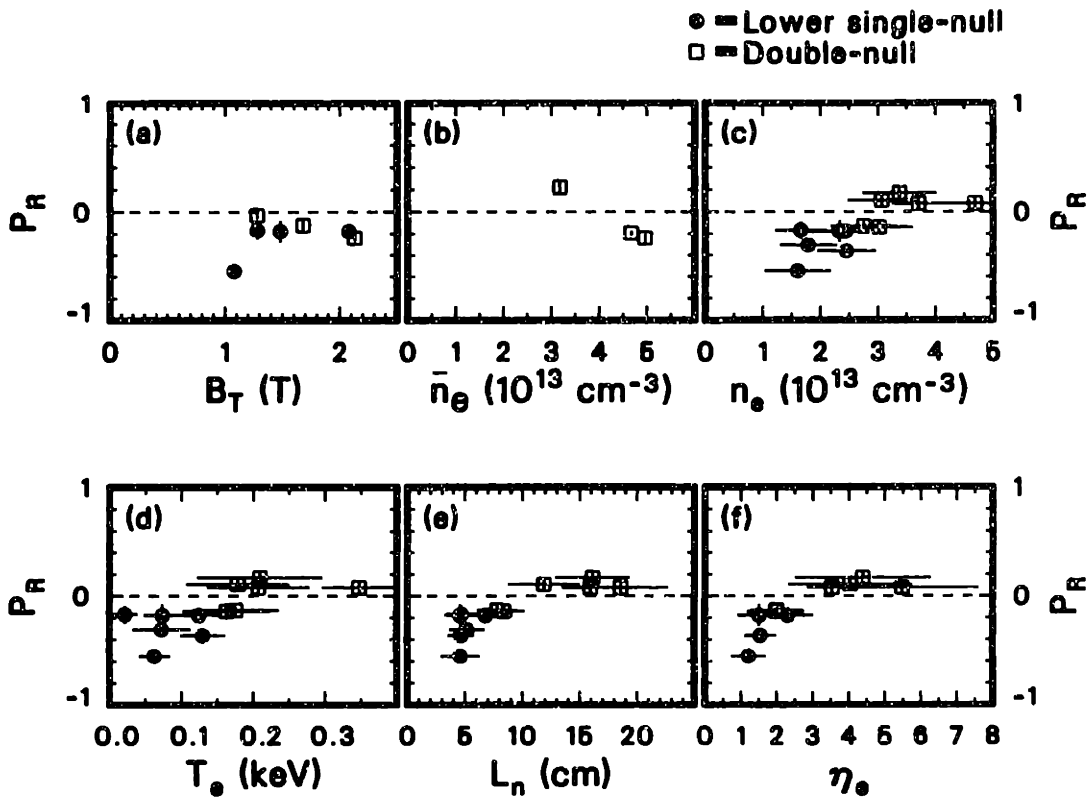

Fig. 5.16 Global and local parameter scans of the radial propagation coefficient P_R (-1 for purely inward and +1 for purely outward propagation) for sets of lower-single-null and double-null diverted L–mode plasmas. Scans (a) and (b) were performed while keeping the other parameters constant; scans (c)–(f) combine shots from all other scans. The parameters are: (a) toroidal field; (b) line-averaged density; (c) local density; (d) electron temperature; (e) density gradient length; (f) $\eta_e = L_n/L_T$ (L_T is the temperature gradient length).

(c) Wave-Number Spectra

The wave-number spectrum $s(k_R)$ is computed as the spatial Fourier transform of the complex spatial correlation function described in subsection (a). Since that function is Hermitian, the wave-number spectrum is real. As discussed in §3.9, several methods have been employed to calculate the Fourier transform; the results were generally in good agreement, and the maximum-entropy method[172–174] is preferred in general. After the Fourier transform is computed, it is divided by the PCI transfer function for the specific phase plate used in the experiment.

It should be recalled that this spectrum is, strictly speaking, a function of the horizontal wave number in the poloidal plane, with the vertical wave number equal to zero. Although the discussion of Chapter 4 allows in general an identification of this wave number with the radial wave number, we shall postpone all interpretative considerations to Chapter 6 and adopt the notation $s(k_R)$ here.

Physically, the spectrum must be positive definite; however, calculating the spectrum from experimental data with the procedure indicated is not guaranteed to generate a positive definite function. With some of the techniques employed, including

maximum entropy, it is possible to constrain the result to be positive; nevertheless, we have generally preferred not to impose that constraint and to regard the appearance of large negative values as an indication of a failure of the statistical requirements of the calculation, for instance stationarity and ergodicity. In cases of particularly irregular spacing of the digitized channels, however, the constraint of positive-definiteness has in fact been applied to improve the calculation.

All the spectra that will be shown in the remainder of this chapter are only plotted at most up to the Nyquist spatial frequency. An antialiasing filter was always used at that frequency. The width of the phase-plate groove is 560 μm, except where otherwise noted. This corresponds to $Q = 1.55$ [see §2.11(c)] and to the transfer function shown in Fig. 3.32. The minimum k_R used in the plots is $0.8 \times k_c = 0.65$ cm^{-1}. The broadening caused by diffraction, as was shown in Fig. 2.24, is of the order of 1 cm^{-1}.

As is clear from the structure of the spatial correlation function discussed in subsection (a), the spectrum $s(k_R)$ is normally double-peaked, with the two peaks at approximately symmetric positive and negative values, corresponding to the average wave number obtained from the fit. The $1/e$ width of the two curves is $\sim 4/\mathcal{L}_R$. The positive peak will be larger when P_R is positive, and vice versa.

In general, in turbulence, the assumption of random phase is used [see Eq. (4.9) and related discussion]. This implies that different spectral components are essentially uncorrelated. Any correlations, in particular between the positive- and negative-k_R components, would be revealed by standing-wave structures in the amplitudes. Since such structures are not seen in general, as discussed in subsection (a), we conclude that the two counterpropagating spectra are in fact generally uncorrelated.

Typical examples of Ohmic, L–mode, and H–mode spectra are shown in Fig. 5.17. As the range utilized for these spectra is smaller than the width of the laser beam, values below ~ 2 cm^{-1} must be regarded with caution. Confidence in the validity of the spectra at low k is gained by examining the correlation functions directly. In particular, the finite value of the peak wave number, which is a fundamental result arising from the wavelike nature of the correlation function, cannot be explained away by finite-width effects. In addition, measurements have also been made by using the complete width of the beam (sacrificing resolution and spectral bandwidth), and the structure of the low-k_R range has been seen to conform to that seen in Fig. 5.17.

Figure 5.17 displays the characteristic features of the spectra in the three confinement regimes: generally nearly balanced in the Ohmic regime; unbalanced, narrower, and with a lower $k_{0,R}$ in L mode; more balanced but more irregular, and broader, in H mode. We reiterate that the dominant direction of propagation in L mode, and the residual one in H mode, vary considerably; and that balanced cases are also seen, as Fig. 5.16 attests. By way of illustration, an inward propagating case is shown in Fig. 5.18, corresponding to the spatial functions of Figs. 5.12(a) and 5.13(a) for L and H mode. Again, the broadening and increased in-out balance of H mode are in evidence. Also, the portion of Fig. 5.18(a) with negative values of $s(k_R)$ is clearly negligible.

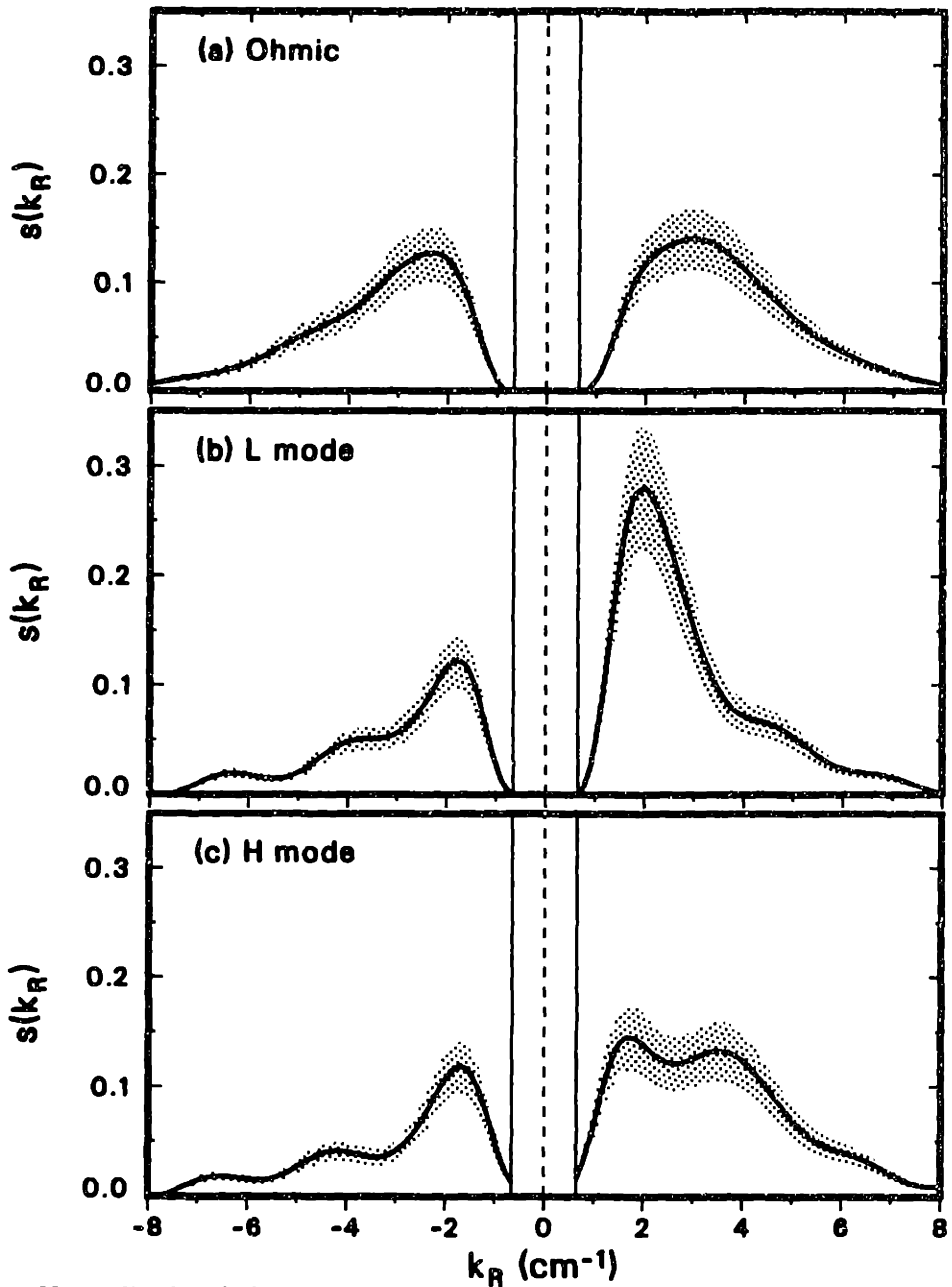

Fig. 5.17 Normalized radial wave-number spectra in the region between the LCFS and 3.5 cm inside, for three cases: (a) Ohmic (B_T=2.1 T, I_p=1.9 MA, $\bar{n}_e$=3×10^{13} cm^{-3}, input power = 3.5 MW), (b) L mode and (c) H mode (both B_T=2.1 T, I_p=1.3 MA, $\bar{n}_e$=3×10^{13} cm^{-3}, P_{beam}=15 MW). The shaded areas represent confidence intervals. The spectra are normalized to an integral of 1. The blank region near $k = 0$ is below the instrumental cutoff. Case (a) corresponds to Fig. 5.8(a).

As suggested by the spatial correlation results, the spectra in the SOL are generally broader and shifted to higher wave numbers, with the exception of the outer SOL in the late H–mode phase, which is rather well correlated and exhibits narrower spectral features.

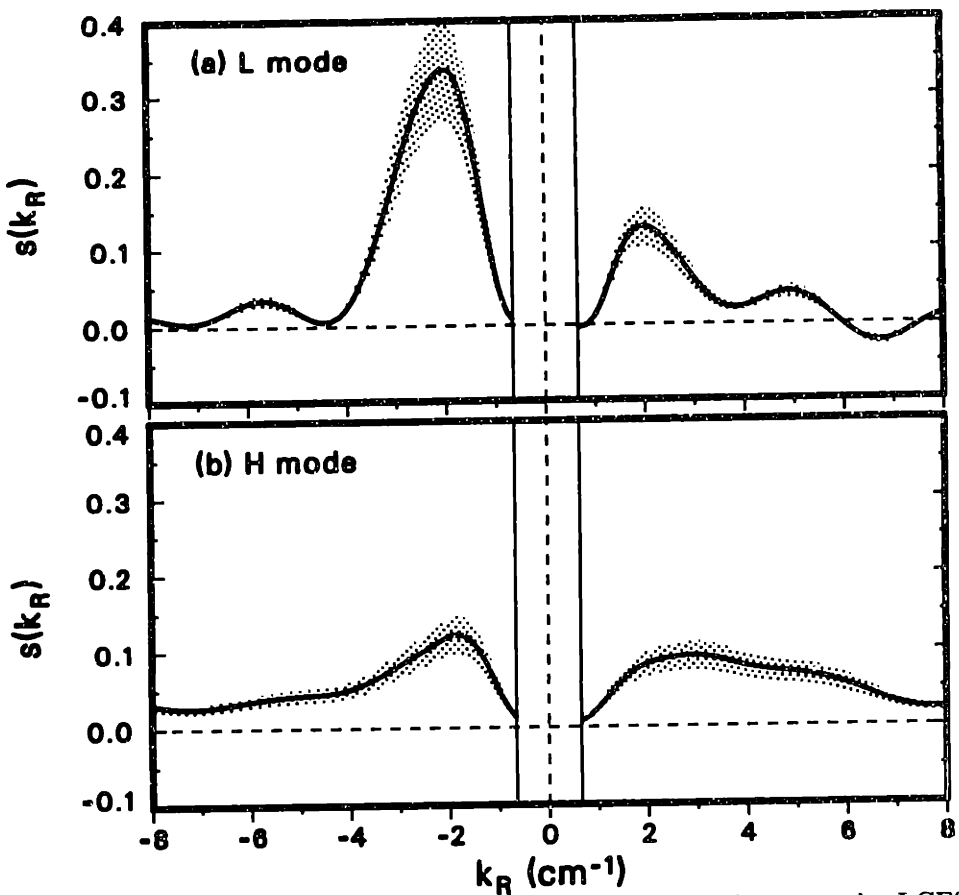

Fig. 5.18 Normalized radial wave-number spectra in the region between the LCFS and 3 cm inside, in (a) L mode (input power = 2.7 MW) and (b) H mode (3.0 MW). Plasma parameters are B_T=2.1 T, I_p=1.35 MA, $\bar{n}_e$=4×10^{13} cm^{-3}. The shaded areas represent confidence intervals. The spectra are normalized to an integral of 1. The blank region near $k = 0$ is below the instrumental cutoff. Case (a) corresponds to Fig. 5.12(a), case (b) to Fig. 5.13(a).

In one experiment, the antialiasing iris was deliberately opened to allow large-k_R component to pass through the optical system. Comparing amplitudes, frequency spectra and correlation functions for similar shots with and without the spatial filter showed that there was no observable difference. Although a spectral analysis is meaningless beyond the Nyquist frequency, aliased high-k_R components would appear below the Nyquist frequency and would affect the quantities listed above. In particular, the amplitude would be expected to increase. The lack of change is taken as a confirmation of the lack of detectable activity in the spectrum beyond ~10 cm^{-1}. Any studies of those components would require filtering out the long-wavelength part of the spectrum, in addition to employing a high-resolution configuration and a low-reflectivity phase-plate substrate (e.g. BaF_2) to enhance the signal-to-noise ratio.

In a second test, the phase plate was rotated by 90° to render the system sensitive to the toroidal, rather than the radial, component of the wave vector. The PCI cutoff value remained the same, i.e. ~0.8 cm^{-1}; and the orientation of the image was left unchanged, i.e. in the radial direction. The only aim of this test was to determine

whether toroidal spectral components with $k_\phi \gtrsim 0.65$ cm^{-1} existed at all. The signal fell below the noise level, confirming the expected lack of high-k_ϕ activity. It should be noted that this test is not particularly stringent, as measurements of the component of k along the magnetic field in other tokamaks[10,25,229] have shown it to be < 0.01 cm^{-1}, and any sizable toroidal components arising from the perpendicular wave vector would be cancelled by the line integration in PCI.

(d) Dispersion Relations

The spatial correlation properties of the turbulence have been studied also in the frequency domain. The standard procedure is to generate the complex coherency function, which takes the place of the correlation function [an example is shown in Fig. 5.10(b)]. A similar decaying wavelike behavior is observed in the frequency domain also. The greatest variability is found in H mode, which, as was discussed in §5.4, is also characterized in general by an irregular frequency spectrum. In particular, areas of increased coherence are sometimes seen at high frequency (80–120 kHz) during the H–mode phase.

By applying the usual three-parameter fits to the coherency function, the average wave number, the correlation length and the propagation coefficient can be studied as functions of frequency. The first function in particular takes the form of an approximate dispersion relation for the peak value of the wave number. Typical examples of these functions for the Ohmic, L–mode, and H–mode regimes is shown in Fig. 5.19. The trends observed in the time domain are present in these plots as well. The correlation length is longest in L mode and shortest in H mode; in the Ohmic case it is slightly longer than in H mode at low frequency, but the two are quite similar throughout the rest of the spectrum. The average wave number typically decreases in going from Ohmic to L–mode conditions and increases again in H mode, displaying also a more irregular behavior: in fact, as seen in Fig. 5.19(b), $k_{0,R}$ is often smaller in H mode than in L mode at high frequency; it should be recalled that the frequency spectrum is also broader in H mode. The propagation coefficient is generally closer to zero in the Ohmic and H–mode regimes.

The increase of $k_{0,R}$ with frequency is a general feature; in many cases, the dispersion relation is well approximated by an offset-linear function (the region below 8 kHz is, however, precluded to the measurement). The correlation length often, but not always, decreases with frequency: in L mode the three most common functional forms are (a) increasing up to a maximum in the 20–40-kHz range (where a change in the slope of the frequency spectrum occurs) and then decreasing, (b) monotonically decreasing, (c) increasing up to a maximum, then decreasing and finally becoming approximately constant above 60–70 kHz. Case (a) is shown in Fig. 5.19(a); cases (b) and (c) are shown, respectively, in Figs. 5.20(a) and (b). The average wave number remains approximately linear in all three cases. Both $k_{0,R}$ and $\mathcal{L}_R$ are generally flatter and more irregular in H mode than in L mode, and are flatter in the SOL than inside the LCFS.

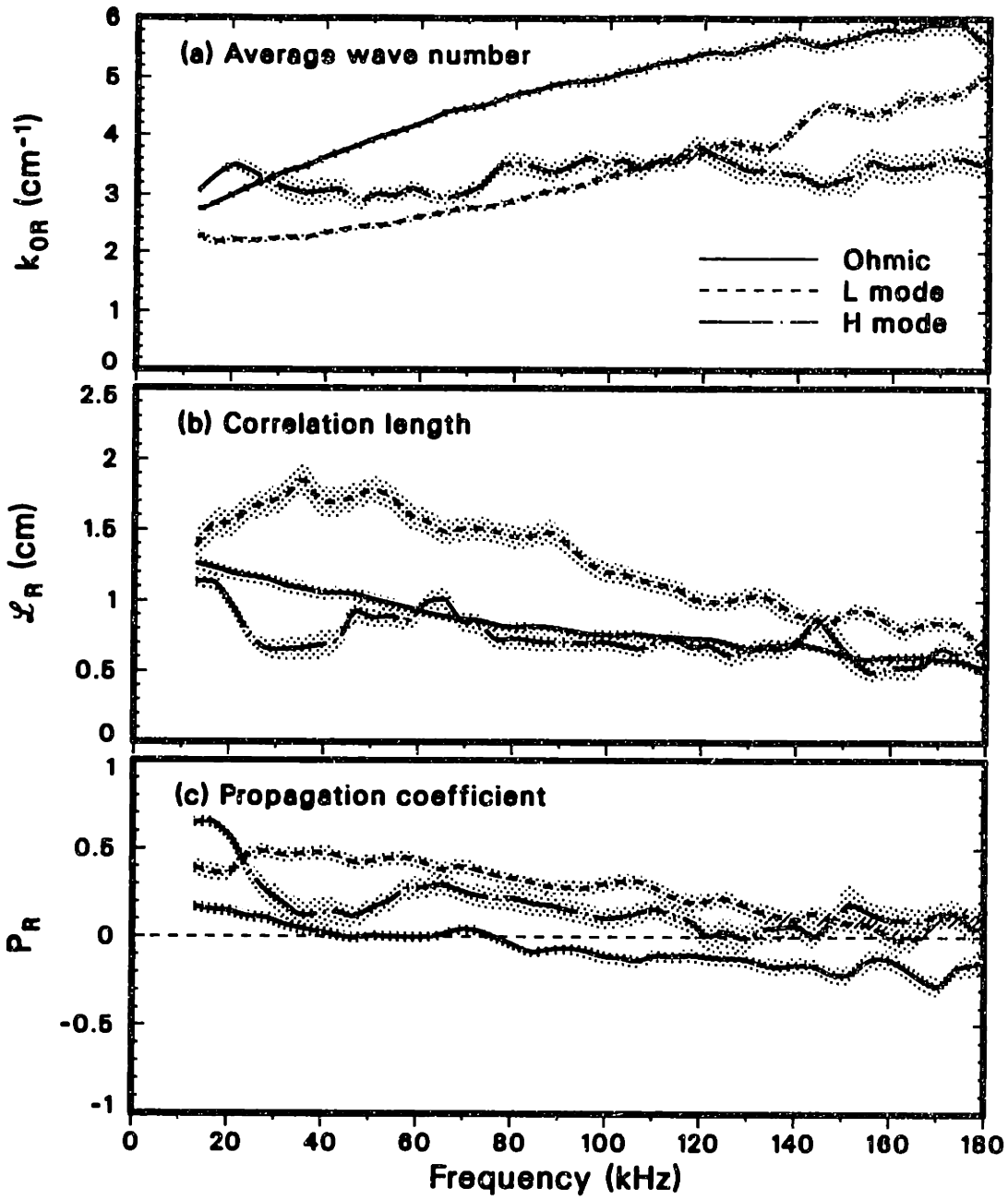

Fig. 5.19 (a) Average wave number (dispersion relation), (b) correlation length, and (c) propagation coefficient as functions of frequency, for Ohmic (B_T=2.1 T, I_p=1.9 MA, $\bar{n}_e$=3×10^{13} cm^{-3}, input power = 3.5 MW), and L-mode and H-mode plasmas (B_T=2.1 T, I_p=1.3 MA, $\bar{n}_e$=3×10^{13} cm^{-3}, $P_{\rm beam}$=15 MW), in the region between the LCFS and 3.5 cm inside. The three cases correspond to those shown in Fig. 5.17. The shaded areas indicate confidence intervals. Smoothing was performed over a 10 kHz interval.

The relatively slow variation of $\mathcal{L}_R$ agrees with the weak dependence of $\mathcal{L}_R$ in the time domain on the bandpass of the digital filter.

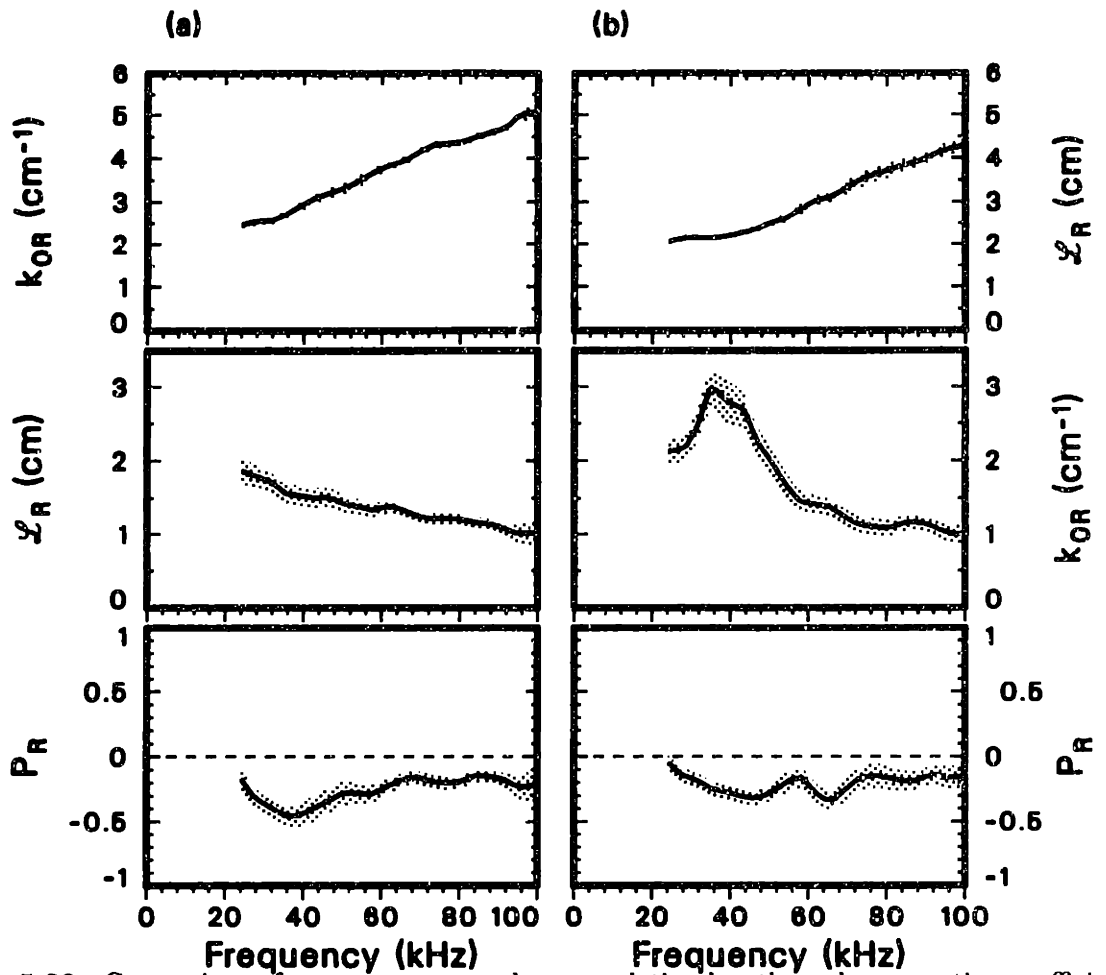

Fig. 5.20 Comparison of average wave number, correlation length, and propagation coefficient as functions of frequency for two different L-mode plasmas [(a) B_T=1.3 T, I_p=1.0 MA, $\bar{n}_e$=4×10^{13} cm^{-3}, $P_{\rm beam}$=0.6 MW, lower single-null); (b) B_T=2.16 T, I_p=1.35 MA, $\bar{n}_e$=4.5×10^{13} cm^{-3}, $P_{\rm beam}$=3.6 MW, double-null]. The measurements are made in the region between the LCFS and 3 cm inside. The shaded areas indicate confidence intervals. Smoothing was performed over a 10 kHz interval. The region below 24 kHz is not shown as it contained coherent MHD activity.

We must stress that the trends just described cannot be considered universal observations: they merely describe the prevailing behavior. For instance, some cases of flat or slightly decreasing dispersion relations have been seen, even in Ohmic plasmas. On the other hand, the general decrease of $\mathcal{L}_R$ is a nearly universal feature. This variability is, once again, greater in the case of the propagation coefficient. In L mode, in particular, P_R can be positive [Fig. 5.19(c)], negative (Fig. 5.20), or zero. Often, but not always, P_R moves towards zero at high frequencies.

It is interesting to note that, owing to the form of the dispersion relation, the character of the cross-spectral function (and coherence) is usually quite different from that of the autopower spectrum. While the latter is monotonically decreasing, the former peaks at different frequencies depending on the spatial separation: this stems from the fact that the coherence is zero at separations equal to odd multiples of

one-half the average wavelength, which is itself a function of frequency.

As a consequence of the offset-linear dispersion relations, the group velocity is normally larger and more nearly constant in frequency than the phase velocity. Typical values for the group velocity $v_{g,R}$ are in the range 1.5–4 km/s in Ohmic and L–mode plasmas, and up to 20 km/s in H mode. The phase velocity ranges from 0.3 km/s at low frequency to 2.5 km/s at high frequency in the Ohmic and L–mode cases; and from 0.3 km/s to 5 km/s in H mode. It must be remembered that these approximate velocities apply separately to both inward- and outward-propagating components, which are independent and uncorrelated to a good approximation (because of the lack of standing-wave structures).

We are now in a position to re-examine and understand the difference between the local and intrinsic decorrelation times, discussed in §5.4. Based on the model developed in §4.3, the defining relationship is Eq. 5.2. Since no macroscopic radial flows exist in the plasma, we can rewrite that expression as

$$\tau_{R,\text{eff}} = \left(\frac{1}{\tau_d^2} + \frac{v_{g,R}^2}{\mathcal{L}_R^2} \right)^{-1/2} . \tag{5.4}$$

The local decorrelation time $\tau_{R,\text{eff}}$ is thus determined primarily by the smaller of the intrinsic decorrelation time τ_d and of the correlation-length propagation time $\mathcal{L}_R/v_{g,R}$. The former was found to be the range 20–80 μs; based on the above discussion, the latter is in the range 5–25 μs in L mode, and as low as 1 μs in H mode. Thus, clearly, the local decorrelation time is in general smaller than the intrinsic one. The numerical discrepancy between $\mathcal{L}_R/v_{g,R}$ and $\tau_{R,\text{eff}}$ (which lies in the range 12–30 μs inside the LCFS) must be attributed to the crudeness of the model, which assumes that τ_d is independent of k, and posits very specific forms for the spectral functions. The discrepancy becomes very large in H mode.

The functional dependence of the intrinsic decorrelation time on the wave number has a prominent role in many theoretical models of turbulence. This function can be studied by taking the spatial Fourier transform of the complex function constructed with the correlation coefficient as the real part and its Hilbert transform as the imaginary part, for each value of the delay Δt, and normalizing the modulus of the result to a value of 1 for $\Delta t = 0$. The usual exponential fit can then be applied for each value of k_R.

The function thus obtained is plotted in Fig. 5.21 for an Ohmic, an L–mode, and an H–mode case; the function is only plotted in the region where the signal-to-noise ratio is sufficiently large to permit a reliable fit; as the spectrum becomes small, the signal-to-noise ratio decreases also (the spectra $s(k_R)$ are also plotted for reference).

In all cases examined, as shown in Fig. 5.21, the decorrelation time increases indefinitely as k_R approaches zero, down to the lowest measurable point. This infrared divergence is characterized by a power law $\tau_d \propto k_R^{-\alpha}$, with the exponent α in the range 1–1.5. In general, the form of the $\tau_d(k_R)$ function is not related in any obvious way to that of the spectrum $s(k_R)$. At large k_R, the decorrelation time either

decreases indefinitely or reaches a minimum and then begins increasing again; the latter behavior is generally seen in H mode, which is also typically more irregular, as evidenced by Fig. 5.21(c). The existence of a minimum is also often suggested by measurements in L mode, but it always occurs in a region of vanishing spectrum, rendering a definite characterization difficult in general. As was discussed in §5.4, the decorrelation time is larger in H mode than in L mode. Figure 5.21 shows that this behavior is characteristic of the entire spectrum, not just of the peak point.

(e) The Complete Wave-Number and Frequency Spectrum

The absolute $S(k_R, f)$ spectrum can be obtained by combining all the tools described in the previous subsections. The absolute spectrum is calculated as the Fourier transform in both space and time of the time-delayed correlation function. Since this spectrum is unnormalized, the calibration factors (measured with acoustic waves, see §3.8) are relevant to this calculation. Another useful spectral quantity is the conditional spectrum $s(k|f)$, which is the spatial Fourier transform of the complex coherency function and is approximately equal to $S(k, f)/S(f)$ (this relation is exact when the spectra are independent of the spatial position). Thus, at each frequency the conditional spectrum is normalized to a unity wave-number-space integral.

The information that can be gained from these spectra is summarized in the various quantities studied earlier in this chapter, with the exception of the absolute amplitude, which is the subject of the next section. Figure 5.22 contains a typical set of spectra for Ohmic, L–mode and H–mode plasmas in contour form. The spectra are compressed by taking their cubic root and then plotting the contours on a linear scale, in order to bring out the high-frequency features.

The dispersion relations discussed before are confirmed by the shapes of the spectra in Fig. 5.22 (these are in fact the same shots and time intervals used in Fig. 5.19). The monotonic decrease of the spectral amplitude with frequency is also clearly seen, as well as the more irregular features of the H–mode turbulence. Also, as will be discussed in §5.6, the amplitude of the fluctuations is strongly reduced in going from L to H mode. It is interesting to note that the frequency spectrum *at each wave number* is not always monotonic: see for example the high-k_R end of the Ohmic case in Fig. 5.22(a).

The corresponding conditional spectra are plotted in Fig. 5.23. The peak in L mode now appears at 30–40 kHz: this is a result of the correlation length having a maximum, and thus the spectral width having a minimum, at this frequency [see Fig. 5.19(a)]. As explained before, this behavior is common but not universal.

An immediate visualization of the changes occurring from L to H mode is provided by 3-dimensional plots of $S(k, f)$, as shown for two different shots in Fig. 5.24. These plots are now linear. Plot (a) is characterized by predominantly outward propagation, whereas (b) displays inward propagation. In both cases, both the monotonic dependence on frequency and the sharp reduction in amplitude from L to H mode are readily apparent.

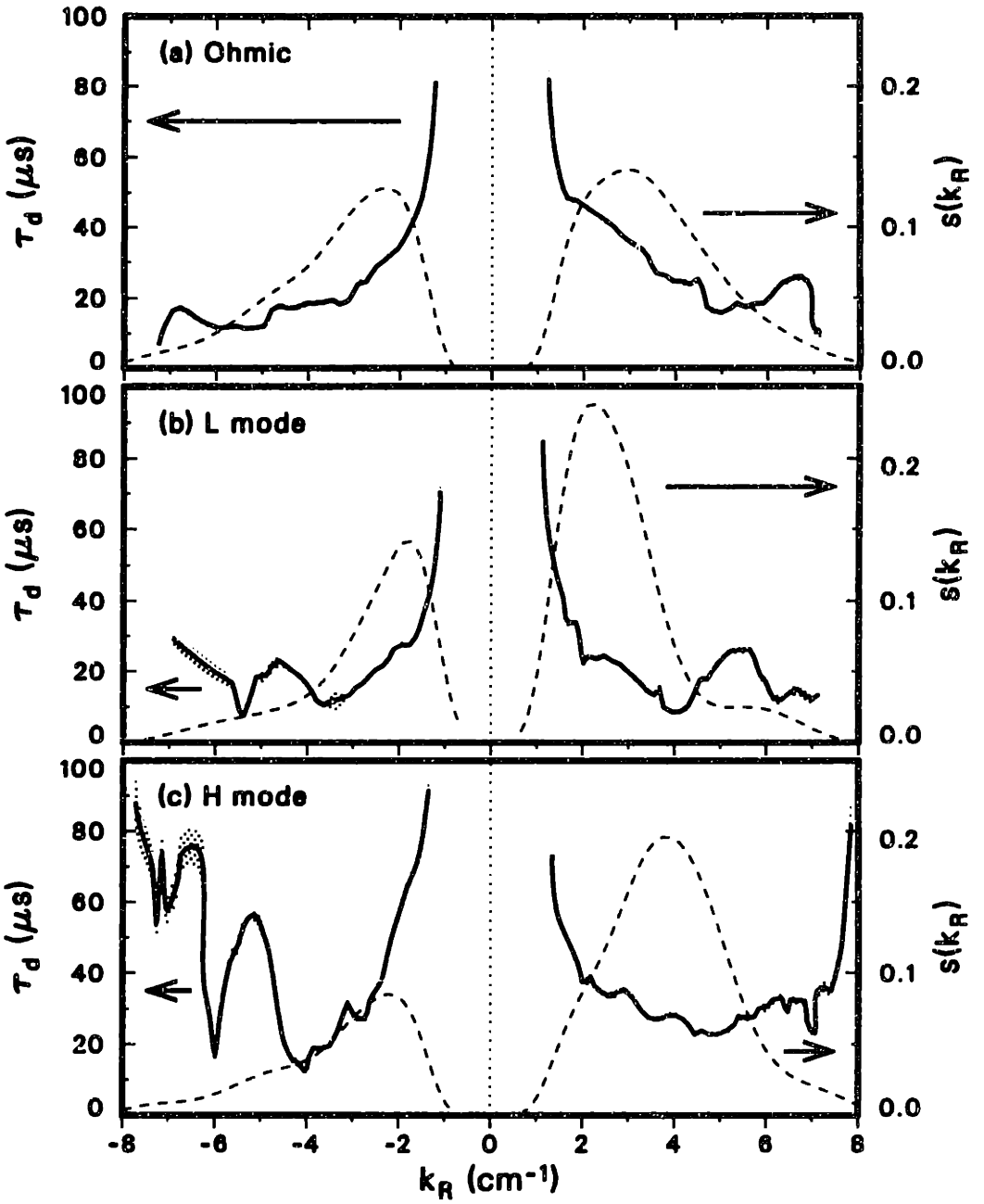

Fig. 5.21 Intrinsic decorrelation time (solid curves) and normalized spectra (dashed curves) as functions of the radial wave number in the region between the LCFS and 3.5 cm inside, for three cases: (a) Ohmic (B_T=2.1 T, I_p=1.9 MA, $\bar{n}_e$=3×10^{13} cm^{-3}, input power = 3.5 MW), (b) L mode and (c) H mode (both B_T=2.1 T, I_p=1.25 MA, $\bar{n}_e$=3.5×10^{13} cm^{-3}, input power = 6.2 MW). The shaded areas represent confidence intervals. The cases are the same as those of Fig. 5.8. The Nyquist spatial frequency is 11 cm^{-1}. Inverse-power-law fits in the region -4 < k_R < 4 cm^{-1} yield the exponents (a) 1.1, (b) 1.4, and (c) 1.2.

For completeness, in Fig. 5.25 are shown two additional examples of conditional spectra in two different L-mode plasmas; these correspond to the dispersion relations

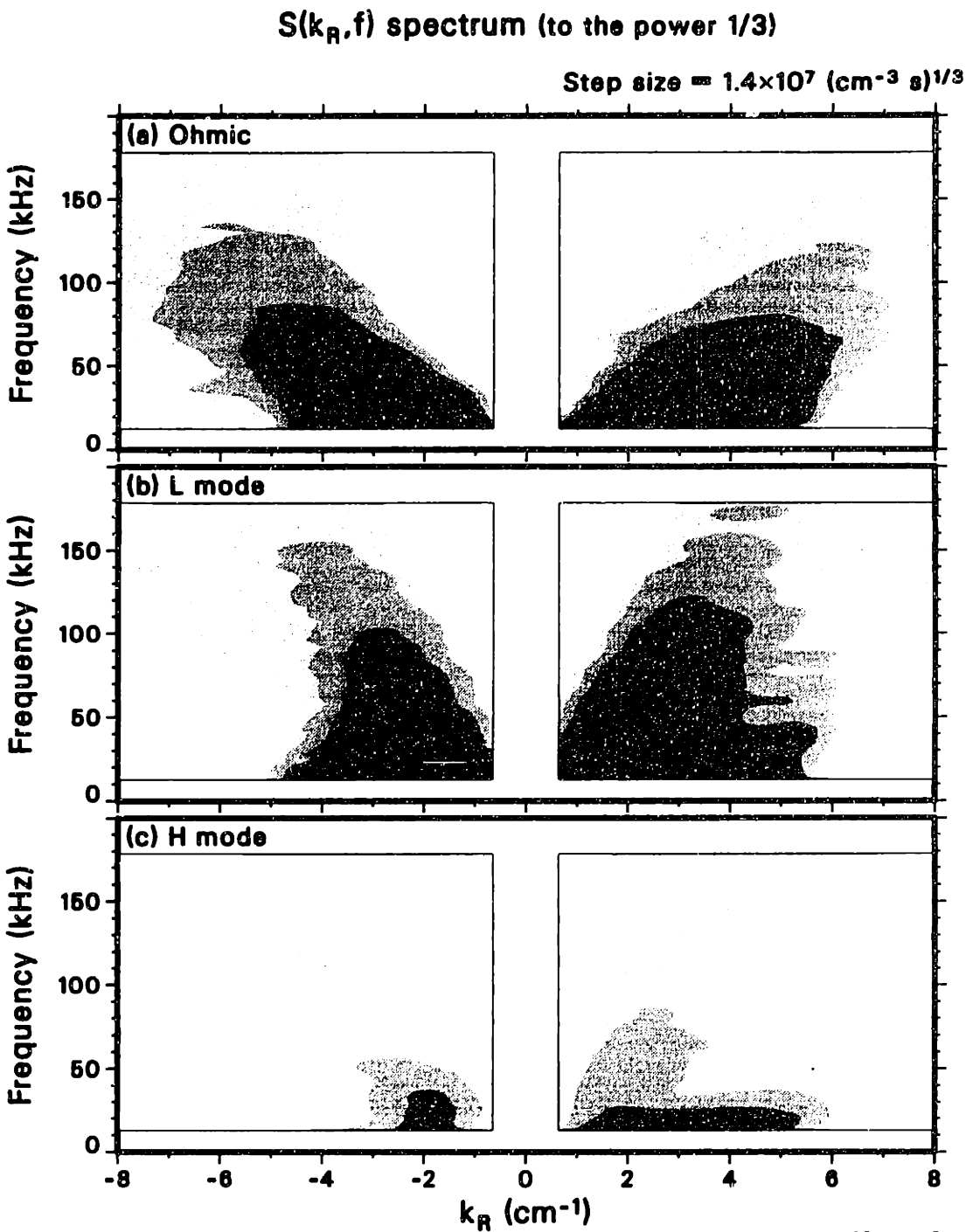

Fig. 5.22 Absolute $S(k,f)$ spectra for Ohmic (B_T=2.1 T, I_p=1.9 MA, $\bar{n}_e$=3×10^{13} cm^{-3}, input power = 3.5 MW), and L–mode and H–mode plasmas (both B_T=2.1 T, I_p=1.3 MA, $\bar{n}_e$=3×10^{13} cm^{-3}, $P_{\rm beam}$=15 MW), in the region between the LCFS and 3.5 cm inside. The cases are the same as in Fig. 5.19. Units are such that the integral of S over frequencies and wave numbers is the average square line-integrated density (in cm^{-4}). Contours are drawn using the power 1/3 for better spacing; the level is proportional to the intensity. Smoothing was performed over a 10 kHz interval.

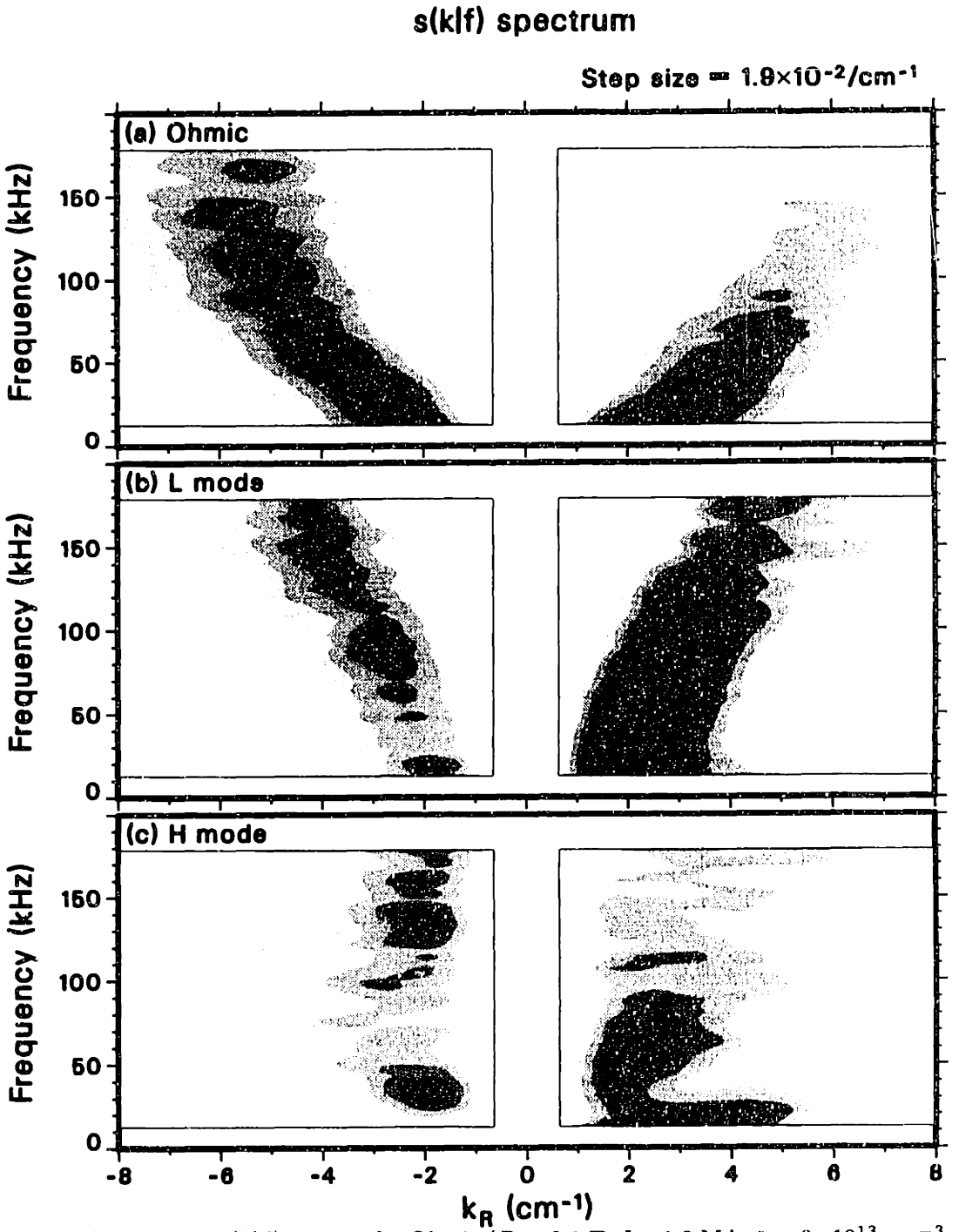

Fig. 5.23 Conditional $s(k|f)$ spectra for Ohmic (B_T=2.1 T, I_p=1.9 MA, $\bar{n}_e$=3×10^{13} cm^{-3}, input power = 3.5 MW), and L-mode and H-mode plasmas (B_T=2.1 T, I_p=1.3 MA, $\bar{n}_e$=3×10^{13} cm^{-3}, $P_{\rm beam}$=15 MW), in the region between the LCFS and 3.5 cm inside. The cases are the same as in Fig. 5.22. Units are such that the integral of S over wave numbers at each frequency is equal to one. Smoothing was performed over a 10 kHz interval.

of Fig. 5.20. As was mentioned in connection with that figure, the three cases seen in Figs. 5.25(a), 5.25(b), and 5.23(b) represent the three most common types of spectral

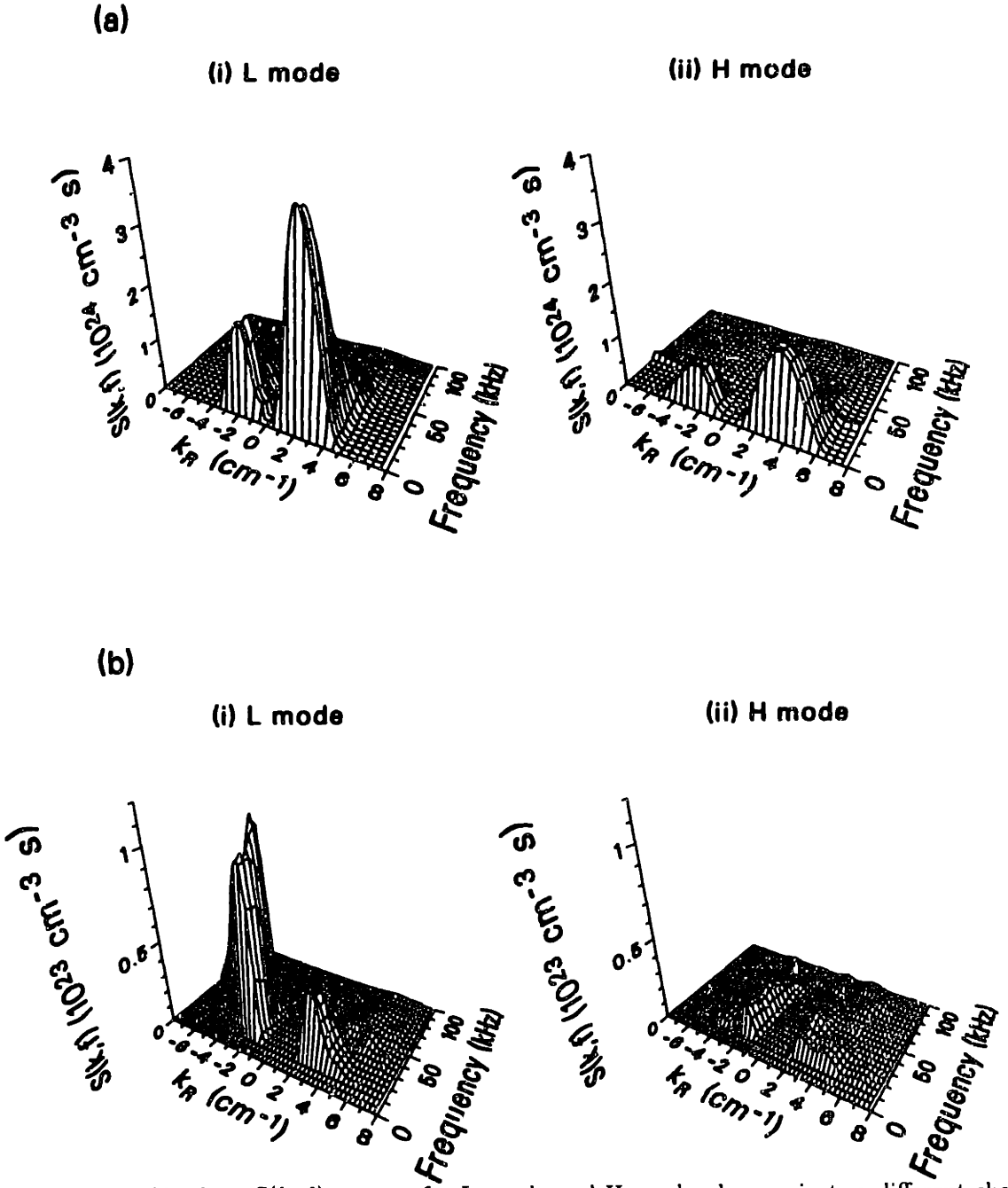

Fig. 5.24 Absolute $S(k, f)$ spectra for L-mode and H-mode plasmas in two different shots: (a) B_T=2.1 T, I_p=1.25 MA, $\bar{n}_e$=3.5×10^{13} cm^{-3}, input power = 6.2 MW [same case of Fig. 5.8 (b) and (c)]; (b) B_T=2.1 T, I_p=1.35 MA, $\bar{n}_e$=4×10^{13} cm^{-3}, input power = 2.2 MW). The spectra pertain to the region between the LCFS and 3 cm inside. Units are such that the integral of S over frequencies and wave numbers is the average square line-integrated density (in cm^{-4}). Smoothing was performed over a 10 kHz interval. The region below 24 kHz is not shown in (b) as it contained coherent MHD activity.

functions found in L mode.

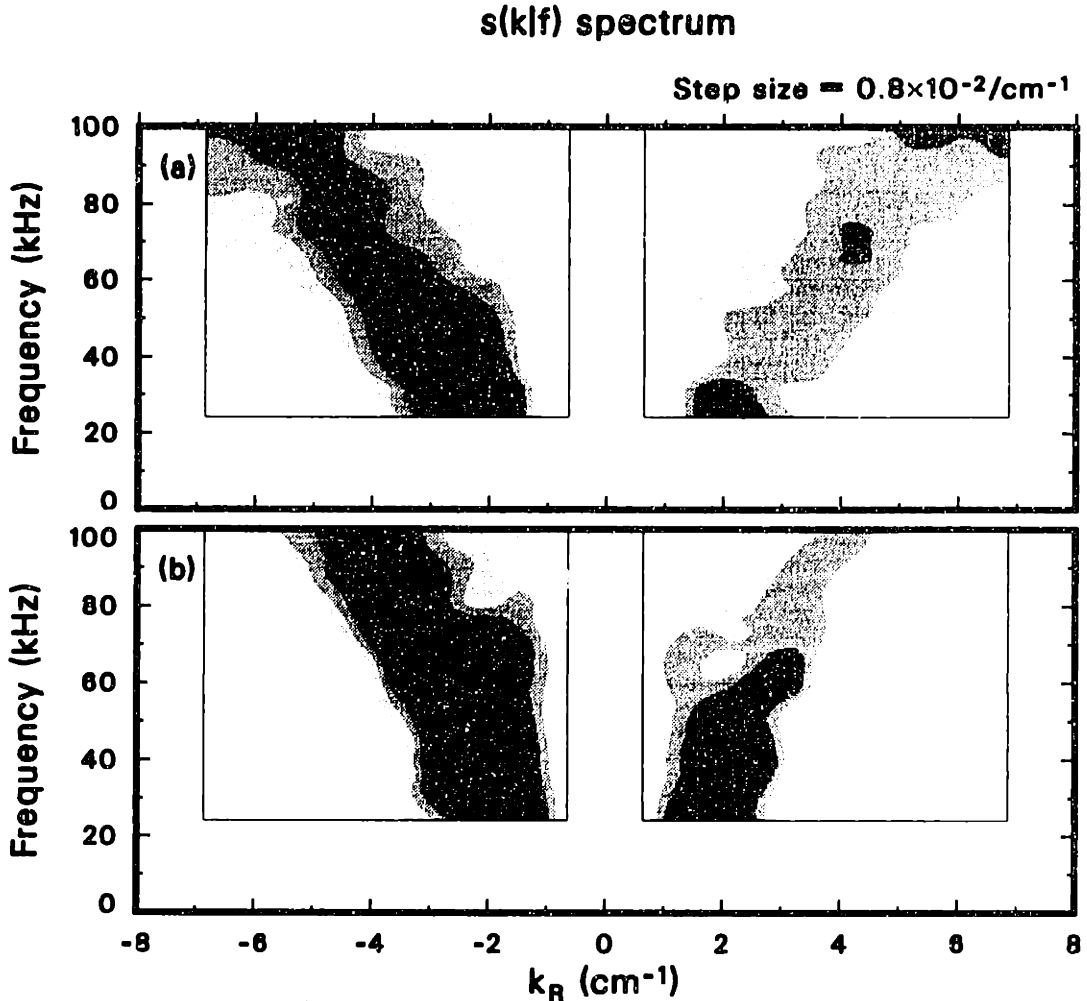

Fig. 5.25 Conditional $s(k|f)$ spectra for 2 L-mode plasmas [(a) B_T=1.3 T, I_p=1.0 MA, $\bar{n}_e$=4×10^{13} cm^{-3}, $P_{\rm beam}$=0.6 MW, lower single-null); (b) B_T=2.16 T, I_p=1.35 MA, $\bar{n}_e$=4.5×10^{13} cm^{-3}, $P_{\rm beam}$=3.6 MW, double-null], corresponding to the cases of Fig. 5.20. The measurements are made in the region between the LCFS and 3 cm inside. The integral of S over wave numbers at each frequency is equal to one. Smoothing was performed over a 10 kHz interval. The region below 24 kHz is not shown as it contained coherent MHD activity.

5.6 Fluctuation Amplitude

The rms amplitude of the line-integrated fluctuating signal is calculated in a standard fashion by averaging over time, as discussed in §3.9. The systematic error on the absolute rms value is of the order of 30–40%; thus, the absolute value is of limited significance. However, the spatial distribution of the amplitude can be studied with greater accuracy, since the uncertainties on the relative calibration factors are of the order of 10–15%. Finally, the time evolution of each rms signal is typically subject only to a small statistical error and is a very useful indicator of trends in the turbulence: this last topic will be addressed in §§5.8–5.10.

In order to obtain an average density fluctuation level, the line-integrated rms

level must be divided by the effective integration length, which is given by $(\sqrt{\pi}\mathcal{L}_z L_z)^{1/2}$ [where $\mathcal{L}_z$ is the vertical correlation length and L_z the chord length: see Eq. (4.6)]. The choice of these parameters is rather difficult. There are no direct measurements of $\mathcal{L}_z \simeq \mathcal{L}_\theta$ in DIII–D at present. On the basis of measurements of poloidal spectra in DIII–D[321,238] and of poloidal correlation measurements in other tokamaks[51], we have used $\mathcal{L}_z$ =3 cm as a reference value in our analysis; on theoretical grounds,[63] we assumed that the poloidal correlation length is the same in L and H mode.

The chord length has been taken to be the entire propagation path inside the vessel for studies of the SOL or of the distribution both inside and outside the separatrix. In some studies of the distribution only inside the main plasma, the length of the chord within the separatrix has been used, giving rise to larger average values, under the assumption that turbulence levels in the SOL are considerably smaller. Given all these assumptions, all the absolute values must be taken only as indicative ones, whereas the radial profile of the relative amplitude and comparisons between shots bear a more direct quantitative significance.

To study the radial profile, we have employed a set of similar discharges with different positions of the separatrix, amounting to an effective radial scan on the part of the PCI system. The results are shown in Fig. 5.26. The uncertainty on the relative amplitude, rather than that on the absolute amplitude, is used for the error bars, to compare the spatial points properly.

The radial profile generally exhibits a peak at a location 0.5–1.5 inside the LCFS in all confinement regimes [see Fig. 5.26(a)]. On the inboard side, the amplitude drops sharply beyond this peak; on the outboard side, the decrease is more gradual, and is followed by a plateau region in most cases in the first 2 cm of the SOL, beyond which the amplitude drops to very small values.

Typical peak values in L mode are of the order of $1\text{–}2\times10^{13}$ cm^{-2}; values both further inside and in the inner SOL are approximately 1/3–1/2 of the peak value. As shown in Fig. 5.26(b), the peak value of the average rms $\tilde{n}$, calculated using the full length of the PCI chords, is in the range $0.4\text{–}0.8\times10^{12}$ cm^{-3}; the corresponding values obtained by using only the segments inside the LCFS are $1\text{–}2\times10^{12}$ cm^{-3}, as shown in Fig. 5.26(c).

In H mode, the amplitude is smaller than in L mode everywhere inside the LCFS, and the ratio of the two is maximum in the peak region just inside the LCFS. It should be noted, however, that the magnitude of the amplitude ratio varies considerably from shot to shot, ranging typically from 1.2 to 3. In the innermost region, 4–6 cm inside the LCFS, the ratio is often close to one. In the SOL, the H–mode amplitude can be somewhat smaller than its L–mode counterpart (as in the case of Fig. 5.26), but it is also sometimes equal or larger. The shape of the profile is qualitatively similar to that in L mode, but the peaking inside the LCFS is less prominent.

In our data, the amplitude appears to be largely unaffected by auxiliary heating. Although there are no systematic scans in the Ohmic regime, the Ohmic profiles are qualitatively similar to the L–mode profiles. Moreover, no discernible change in amplitude is observed on individual chords during a period equal to the beam slowing-

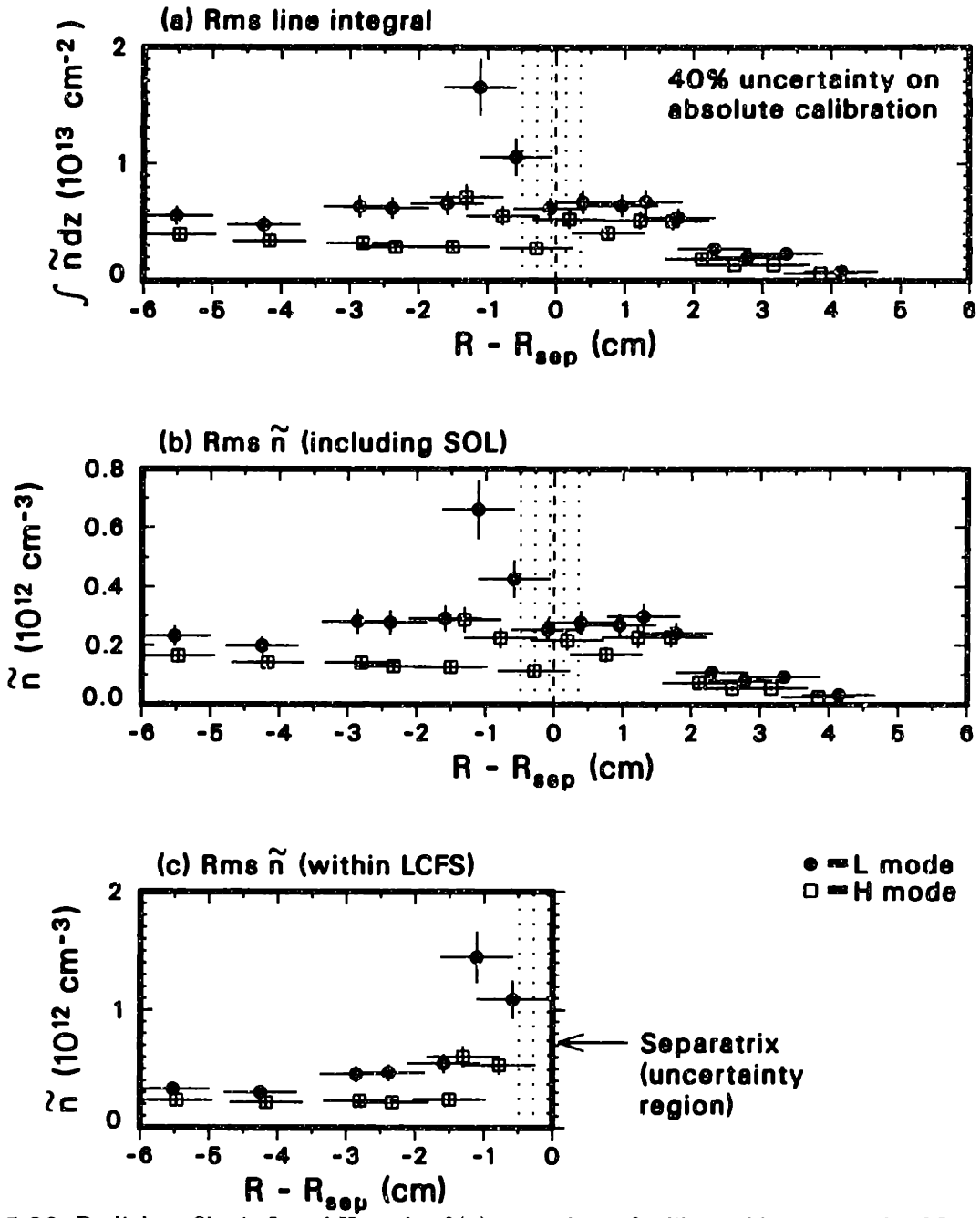

Fig. 5.26 Radial profiles in L and H mode of (a) rms values of calibrated line integrals of fluctuating density $\tilde{n}$; (b) rms values of $\tilde{n}$ averaged over entire path length, assuming a vertical correlation length $\mathcal{L}_z$ =3 cm; (c) rms values of $\tilde{n}$ averaged over region inside LCFS, with $\mathcal{L}_z$ =3 cm. Data collected from a set of similar shots with varying separatrix position (B_T=2.1 T, I_p=1.35 MA, $\bar{n}_e$=4×10^{13} cm^{-3}, P_{beam}=1.1–2.3 MW, lower single-null). Error bars are determined by channel-to-channel calibration uncertainties; the common uncertainty is 40%.

down time after the beams are turned on. The only exception to this is at the peak just inside the LCFS, where a slight increase is sometimes seen after the beam turn-on: therefore, the profile is somewhat flatter in the Ohmic regimes. It will be recalled

that after the beams are turned on the correlation length generally increases, as was shown in §5.5; also, changes both in the slope of the frequency spectrum and in the decorrelation time were documented in §5.4. Transitions from beam-heated H modes to Ohmic H modes, obtained by turning off the beams, have similarly failed to evince any change in amplitude.

The frequency autopower spectra corresponding to the rms data of Fig. 5.26(a) are shown in the 3-dimensional plots of Fig. 5.27. The peaking inside the LCFS is in evidence, as is the sharp amplitude drop from L to H mode. The spectra at locations well inside the LCFS are shifted to higher frequencies in L mode, and are fairly flat in the region 30–90 kHz; this behavior is somewhat difficult to see in Fig. 5.27(a) because of the scale. This mid-frequency range is suppressed sharply in H mode, whereas the low-frequency region, which accounts for a significant fraction of the power, is essentially unchanged. In the region closer to the LCFS, the suppression is essentially uniform across the spectrum. The lack of any kind of standing-wave structure is also evident from these plots.

As was discussed in §3.9, a progressive subtraction algorithm, which attempted to subtract from each signal the contributions from the outer layers measured on the other chords, was generally unsuccessful in producing acceptable results (i.e. the results were extremely irregular or negative powers were obtained). A simpler scheme was also tried, which consisted of subtracting only the SOL contribution from the signals inside the LCFS (weighted by their effective integration lengths). This technique was more successful, and was used in a parametric amplitude scan that employed the set of shots used in the scans described in §5.5. The scans that exhibited some regularity, as well as some irregular ones that are of theoretical interest, are shown in Fig. 5.28. Again, since shots from the same run are compared, the uncertainties on the *relative* amplitudes are used as error bars.

In general, $\tilde{n}$ failed to show any regularity; the only case shown is the power scan in Fig. 5.28(a), which suggests a slight increase in amplitude with increased power. All the other scans shown are of the relative amplitude $\tilde{n}/n$. Here, $\tilde{n}$ is the chord average as explained earlier, while n is calculated at the intersection of the chord with the midplane and is thus a peak value. Given this discrepancy, caution should be exercised in interpreting these scans: once again, the *variation* of $\tilde{n}/n$ is more significant than its absolute value. It was deemed preferable to employ this procedure than to use the line-averaged density, as the spatial distributions of $\tilde{n}$ and n are clearly different, and also in view of the large relative error on the measurement of n at the edge of the plasma. The chords used for this scan lie in the region 2–3 cm inside the LCFS, away from the layer with the largest gradient of $\tilde{n}$.

Among the scans not shown are those of the magnetic field, of the plasma current, and of the confinement time, which did not suggest any regularity. A slight decrease in $\tilde{n}/n$ with increasing power is seen; $\tilde{n}/n$ also decreases substantially as the density, the electron temperature, and the density gradient length increase. No regular behavior is seen when the temperature gradient length, the ion sound gyroradius, or the magnetic pumping rate are varied. Some correlation appears to exist between high relative

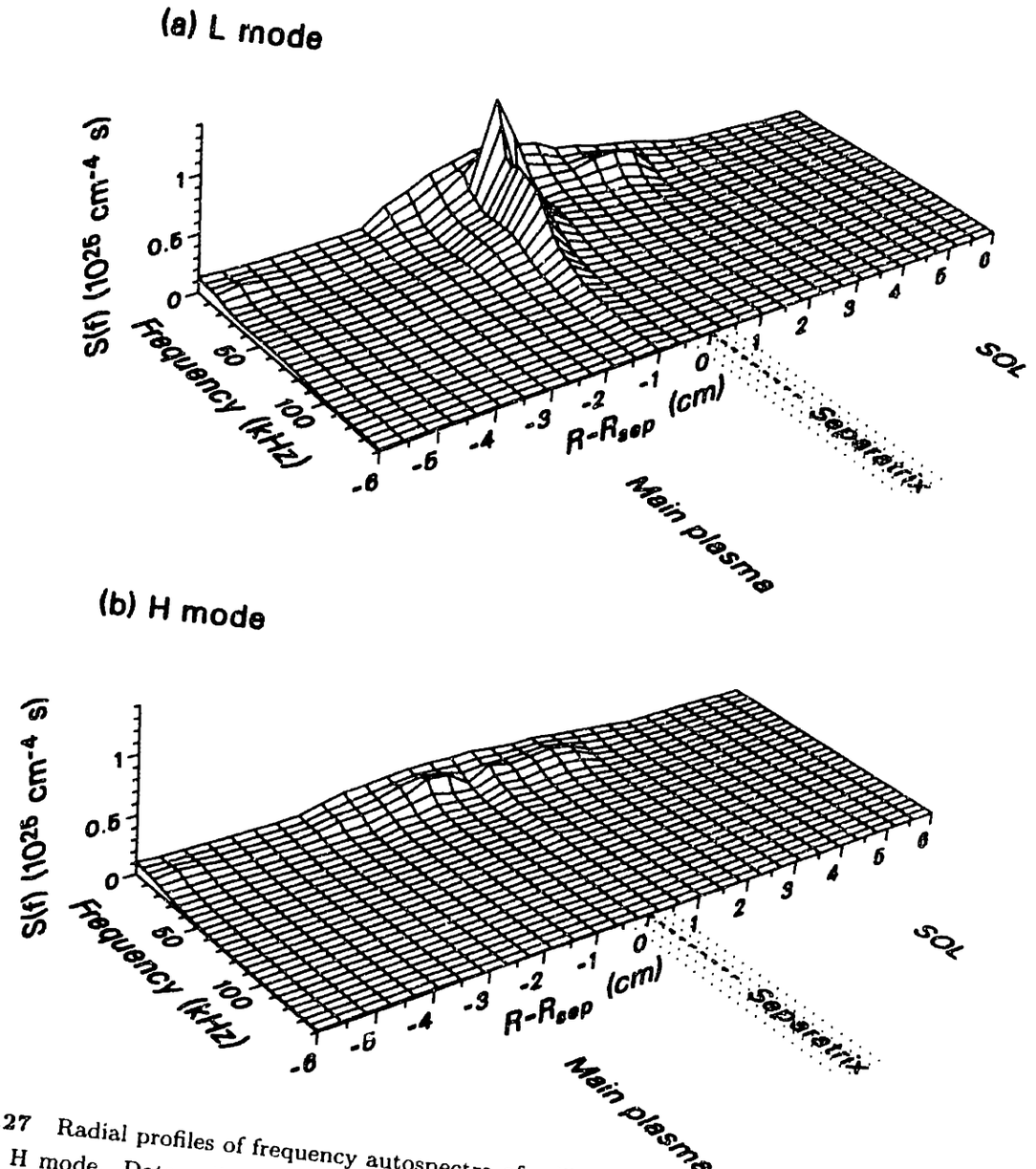

Fig. 5.27 Radial profiles of frequency autospectra of calibrated line integrals of $\tilde{n}$, in (a) L mode and (b) H mode. Data collected from a set of similar shots (same as in Fig. 5.26) with varying separatrix position (B_T=2.1 T, I_p=1.35 MA, $\bar{n}_e$=4×10^{13} cm^{-3}, P_{beam}=1.1–2.3 MW, lower single-null). Smoothing was performed over a 10 kHz interval. Relative error bars (not shown) are ~10%; the uncertainty on the absolute calibration is 40%.

fluctuation levels and inward propagation, and vice versa. No isotope scaling was available, as all measurements were carried out in deuterium plasmas. Finally, it will be noted that double-null diverted plasmas are characterized by lower relative fluctuation levels than single-null diverted plasmas.

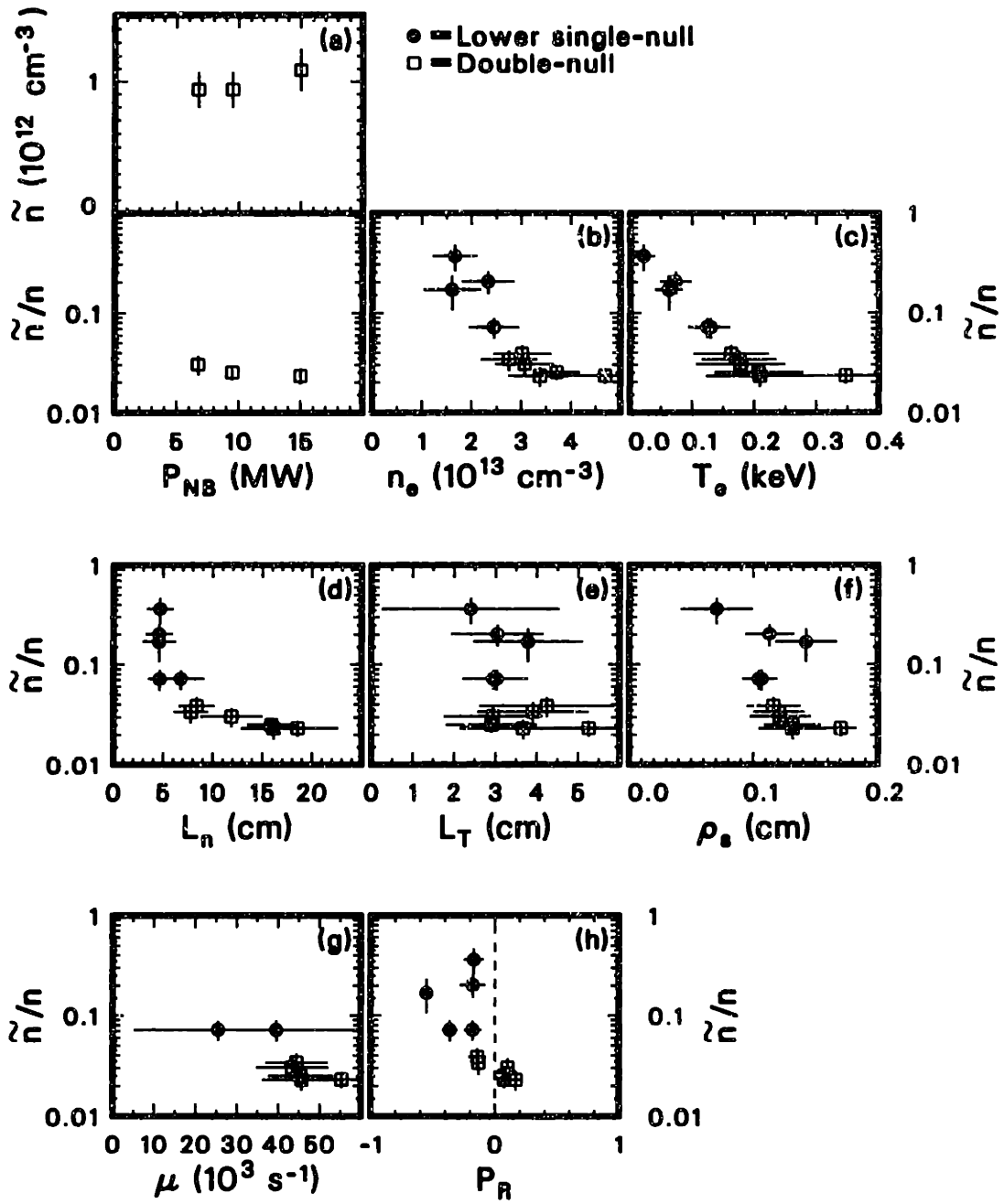

Fig. 5.28 (a) Global and (b)–(h) local parameter scans of the relative fluctuation amplitude $\tilde{n}/n$ and, for case (a) only, of the absolute fluctuation amplitude $\tilde{n}$, for sets of lower-single-null and double-null diverted L–mode plasmas. Scan (a) was performed while keeping the other parameters constant; scans (b)–(h) combine shots from all other scans. The parameters are: (a) neutral-beam power; (b) local density; (c) electron temperature; (d) density gradient length; (e) density gradient length; (f) ion sound gyroradius; (g) propagation coefficient P_R; (h) magnetic pumping rate (see §5.3). In the fraction $\tilde{n}/n$, $\tilde{n}$ is the rms value averaged over the chord length inside the LCFS, assuming a vertical correlation length of 3 cm; the density n is calculated at the intersection of the chord with the midplane. The chords are located 2–3 cm inside the LCFS. Error bars are determined by channel-to-channel calibration uncertainties; the common uncertainty is 40%.

5.7 The Probability Distribution Function

The probability distribution function (PDF) of the turbulence was studied in several plasma shots, at all the spatial locations accessed by PCI and in all confinement regimes. A normality test was performed, and the higher (third to sixth) moments of the distribution (normalized to the appropriate power of the variance) were generated in all these cases. The third moment is known as the *skewness* and the fourth moment as the *kurtosis*.[170] The fifth and sixth moments are sometimes called "superskewness" and "super kurtosis".[322] In the case of a normal (Gaussian) PDF, all moments of odd order are zero, the kurtosis K is 3, and the super kurtosis SK is 15. For this reason, it has become conventional to define a *coefficient of kurtosis* $K' = K - 3$; similarly, the coefficient of super kurtosis is $SK' = SK - 15$.

The coefficient of kurtosis is perhaps the most immediate indicator of adherence to, or departure from, normality. The kurtosis is often referred to as "flatness factor", as leptokurtic ($K > 3$) distributions are generally more peaked and platykurtic ($K < 3$) distributions less peaked than Gaussian distributions. In fact, the kurtosis has been shown to be an indifferent measure of flatness. In fluid mechanics and, more recently, in plasma physics, leptokurtic distributions have often been taken to indicate the presence of intermittent behavior.[203] However, although bursty turbulence is invariably leptokurtic, the reverse is not true: the exponential distribution, for example, is characterized by a kurtosis $K = 6$. The existence of intermittency must be determined indipendently by verifying that the dynamical system under exam lacks temporal self-similarity.[207] Similarly, platykurtic distributions suggest, but do not prove, the existence of coherent structures: a sinusoidal oscillation gives rise to a PDF with $K = 1.5$.

In this work, we have not proceeded beyond a determination of the PDF and an assessment of normality. In particular, no independent test of intermittency was performed. Care was taken to avoid time intervals with "obvious" bursty behavior, such as L–H transitions and ELMs (which, when tested, exhibited the expected leptokurtosis); similarly, regions with MHD activity were also excluded from the analysis. The usual 8-kHz highpass filter was applied in all cases. Datasets were divided into bins to determine the PDF in a hystogram fashion. Various bin widths and filters were used in an attempt to better elucidate the nature of the PDF.

When estimated over intervals shorter than 40 ms, the PDF is generally mesokurtic ($K = 3$); moreover, the higher moments are also consistent with a Gaussian distribution and the PDF can be fitted rather well by a Gaussian, with a reduced χ^2 typically of the order of 1.5–2.5 (using the statistical uncertainty introduced in §3.9). This behavior has been observed in a majority of cases in Ohmic, L-mode, and H-mode plasmas, both inside and outside the LCFS. A typical example is shown in Fig. 5.29(a), along with a superimposed Gaussian; in this example, as in most cases, the moments of third to sixth order are consistent with a Gaussian PDF within the statistical uncertainties.

The case shown in Fig. 5.29(a) is standard, with the interval from -6σ to 6σ

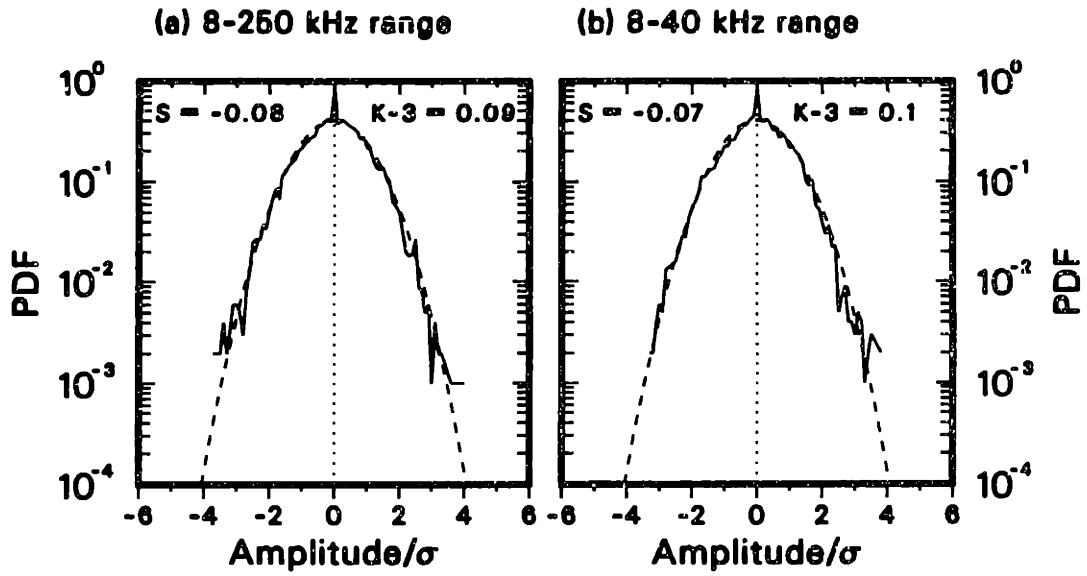

Fig. 5.29 Probability distribution function for (a) 8–250-kHz (Nyquist) bandwidth and (b) 8–40-kHz bandwidth, calculated over a 20-ms interval. The data are divided into 121 bins of width $0.1\times\sigma$. The dashed curve is a Gaussian with the same standard deviation σ. The measurement refers to an L-mode plasma (B_T=2.1 T, I_p=1.7 MA, $\bar{n}_e$=3×10^{13} cm^{-3}, input power = 2.5 MW), 2 cm inside the LCFS. The noise level is (a) $0.03\times\sigma$, (b) $0.005\times\sigma$. The 95% confidence level is (a) 4×10^{-3}, (b) 3×10^{-2}. The moments, calculated from -6σ to 6σ, are: (a) skewness $S=-0.08\pm0.04$, coefficient of kurtosis $K-3=0.09\pm0.10$, superskewness $SS=-0.6\pm0.3$, coefficient of super kurtosis $SK-15=1.0\pm1.0$; (b) $S=-0.07\pm0.10$, $K-3=0.1\pm0.3$, $SS=-0.2\pm0.9$, $SK-15=0.6\pm2.8$.

(where σ is the standard deviation) subdivided into 121 bins of width $0.1\times\sigma$, and the moments calculated over this entire interval. The sampling rate in this case was 500 ksamples/s: the number of independent samples is equal to 9680. Slight variations in the bin size, an increase of the characteristic interval to $\pm10\sigma$, and variations in the time interval from 10 to 40 ms have not evinced any significant changes beyond the statistical uncertainties. The normality of the PDF remains unaltered also when different bandwidths are selected. The PDF for the range 8–40 kHz is shown in Fig. 5.29(b); the complementary region (40–250 kHz) is also normally distributed.

Since the 95% confidence level [4×10^{-3} in Fig. 5.29(a), 3×10^{-2} in Fig. 5.29(b)] corresponds to amplitudes well below the 6σ limit, the computation of the moments was repeated within the narrower range defined by that level. Only in the second (narrow-bandwidth) case did the kurtosis change significantly, to 2.0 ± 0.1.

It should be noted that leptokurtic distributions were observed in a few cases, inside the LCFS in L and H modes. However, in no case was the kurtosis larger than 4.5.

Longer intervals were utilized in cases of exceptional regularity, especially in Ohmic and low-power L–mode plasmas. As the interval size increases beyond 50 ms, an increasing leptokurtic behavior is always observed, along with a noticeable peaking of the PDF at zero amplitude. This is not accompanied by any visible burstiness.

A comparison between a 20-ms interval and a 200-ms interval is shown in Fig.

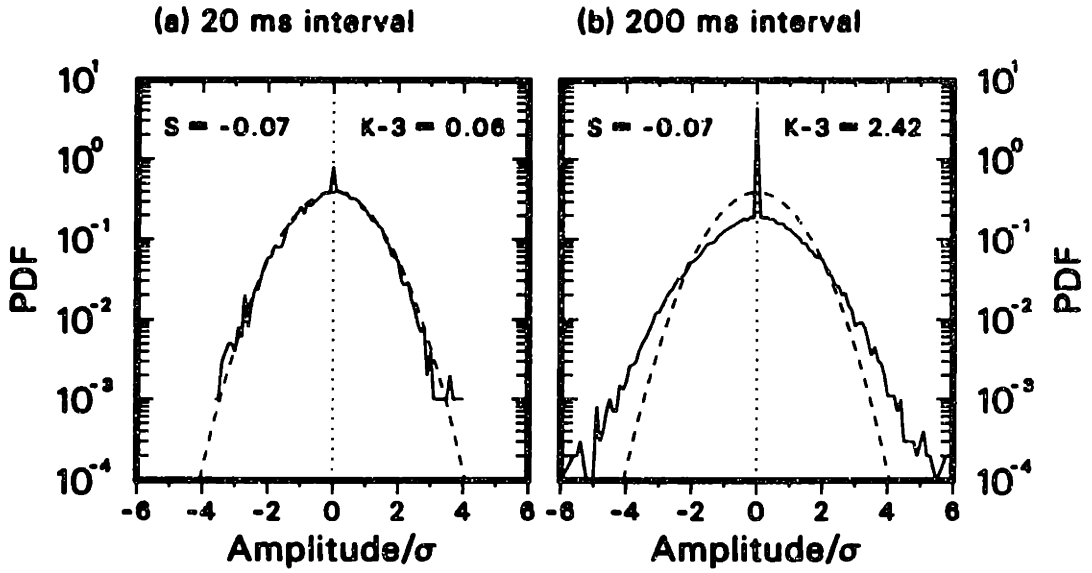

Fig. 5.21 Probability distribution function for (a) 20-ms interval and (b) 200-ms interval; the bandwidth is 8-250 (Nyquist) kHz. The data are divided into 121 bins of width $0.1\times\sigma$. The dashed curve is a Gaussian with the same standard deviation σ. The measurement refers to an L-mode plasma (B_T=2.1 T, I_p=1.7 MA, $\bar{n}_e$=3×10^{13} cm^{-3}, input power = 2.5 MW), 2 cm inside the LCFS. The noise level is (a) $0.02\times\sigma$, (b) $0.05\times\sigma$. The 95% confidence level is (a) 4×10^{-3}, (b) 4×10^{-4}. The moments, calculated from -6σ to 6σ, are: (a) skewness $S = -0.07 \pm 0.04$, coefficient of kurtosis $K-3 = 0.06\pm0.10$, superskewness $SS = -0.5\pm0.3$, coefficient of super kurtosis $SK-15 = 0.7\pm1.0$; (b) $S = -0.07 \pm 0.01$, $K - 3 = 2.42 \pm 0.03$, $SS = -0.9 \pm 0.3$, $SK - 15 = 37 \pm 1$.

5.21. In this example, the kurtosis rises to 5.42 in the longer case (which includes 96800 independent samples), while the super kurtosis reaches a value of 52. Again, variations in bin size and bandwidth do not produce any significant changes. A computation of the moments within the 95% confidence range [$\pm4.5 \times \sigma$ for the case of Fig. 5.21(b)] also generates identical values within the error bars. On the basis of the cases examined (8 spatial channels in 7 shots), values of the kurtosis between 5.3 and 5.6 appear to constitute a constant asymptotic limit. The largest interval employed in this study was 200 ms.

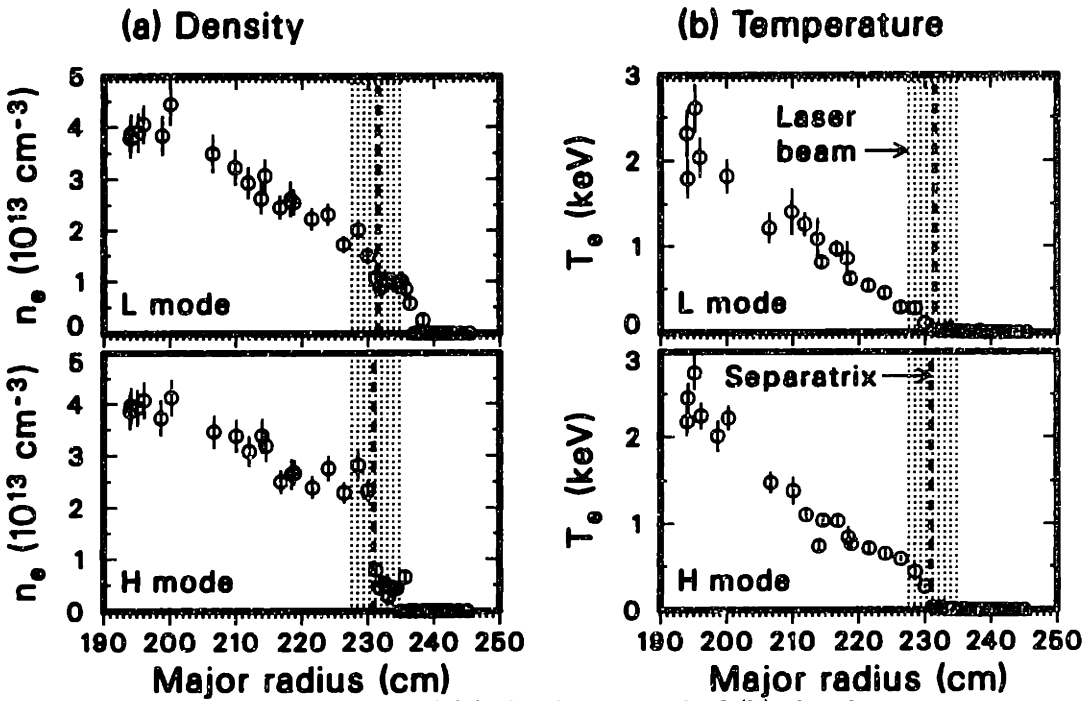

Fig. 5.31 Midplane radial profiles of (a) the density and of (b) the electron temperature in L mode (8 ms before the L–H transition, top) and in H mode (4 ms after the transition, bottom). The measurements are made by a Thomson scattering system and are mapped to the midplane via flux-surface mapping. The plasma parameters are B_T=2.1 T, I_p=1.25 MA, $\bar{n}_e$=3.5×10^{13} cm^{-3}, and input power = 6.2 MW.

5.8 The L– to H–Mode Transition

In the preceding four sections the properties of edge turbulence in various heating and confinement regimes, including the L and H modes, were presented. The differences between the L mode and the H mode have thus been elucidated systematically. In the present section we shall focus on the dynamics of the L–H transition, whereas the distinctive properties of the two regimes will not be repeated in detail.

The general phenomenology of the L–H transition was presented in §5.1(c). As was discussed there, the transition is characterized by the formation of a transport barrier at the edge of the tokamak cross section. The changes occurring in the density and electron-temperature profiles, as measured by the Thomson scattering system, are illustrated in Fig. 5.31. A clear steepening of the density gradient at the plasma boundary is observed, which leads to the formation of a pedestal inside the LCFS; a similar, although more modest, effect is also seen in the temperature profile. The data shown in Fig. 5.1 for the H mode refer to a time immediately after the transition. However, the profiles continue to evolve for several tens of ms after the L–H transition, and a confinement improvement eventually occurs throughout the discharge.

As repeatedly discussed in earlier sections, the amplitude of the turbulence at the edge, inside the LCFS, decreases abruptly at the onset of the H mode. This suppression is observed routinely by all the edge fluctuation diagnostics in DIII–D.

In all instances examined thus far, different diagnostics always detect the amplitude drop at the same time within their respective temporal resolutions: these include the reflectometer,[42] the FIR scattering system,[27] the reciprocating Langmuir probe[71] and the lithium-beam emission spectroscopy apparatus,[53] in addition to PCI. Moreover, the timing of the turbulence decrease coincides with the earliest sign of a reduction in transport through the LCFS, as indicated by the drop in the D_α spectroscopic emission signal, which is a measure of particle recycling in the edge.

An example of the simultaneity of these events is shown in Fig. 5.32: here, rms signals from two reflectometer channels, from the FIR scattering system and from PCI are compared with the D_α signal. There is good agreement on the timing of the transition, with no evidence of any delay within the temporal resolutions of the measurements. The magnitude of the change is different for different diagnostics, as they are sensitive to different spectral regions and spatial locations.

In view of the hypothesis that anomalous transport is caused primarily by turbulence, and that the transport suppression at the onset of the H mode is a result of turbulence quenching, it is of interest to explore the possibility of a delay between the latter and the former in more detail. In this regard, it is instructive to examine directly the time trace of the PCI signal rather than its rms value, which requires integration over a finite time interval. The PCI signal, appropriately filtered to eliminate the low-frequency vibration noise, is plotted in Fig. 5.33 against the D_α signal.

This particular case, in which the D_α signal varies over a period of approximately 0.8 ms, has been chosen for illustrative purposes: although the turbulence suppression is clearly much more abrupt (<0.1 ms, as seen in the detail at the bottom of the figure), it occurs approximately at the time that the D_α signal *begins* to change. A visual examination of the figure makes it impossible to state whether one event occurs before the other. This conclusion is universally true, and it applies also to cases in which the D_α signal also decreases over time periods of the order of 0.1 ms. It should be noted that similar time scales for the quenching of the turbulence have been reported by other DIII–D diagnostics.[299]

As shown in previous sections, the fluctuation amplitude is not the only characteristic turbulent quantity to be different in L and H mode. Inside the LCFS, the radial correlation length is reduced and the average radial wave number is increased at the transition: these changes occur simultaneously with the amplitude drop, although the temporal resolution of the correlation measurements is limited by the need for adequate statistics. It was also noted in §5.4(b) that both the local and the intrinsic decorrelation time are generally larger in H mode than in L mode; this change, however, has been described as a byproduct of a more pronounced modification of the *shape* of the time-delayed correlation functions, which become narrower at small time delays and broader at large time delays: the resulting net broadening is an average effect which does not exhibit the abruptness of change of the other correlation quantities discussed above.

A typical example of the time history of these quantities across an L–H transition is shown in Fig. 5.34. This example will be followed by a more detailed discussion of

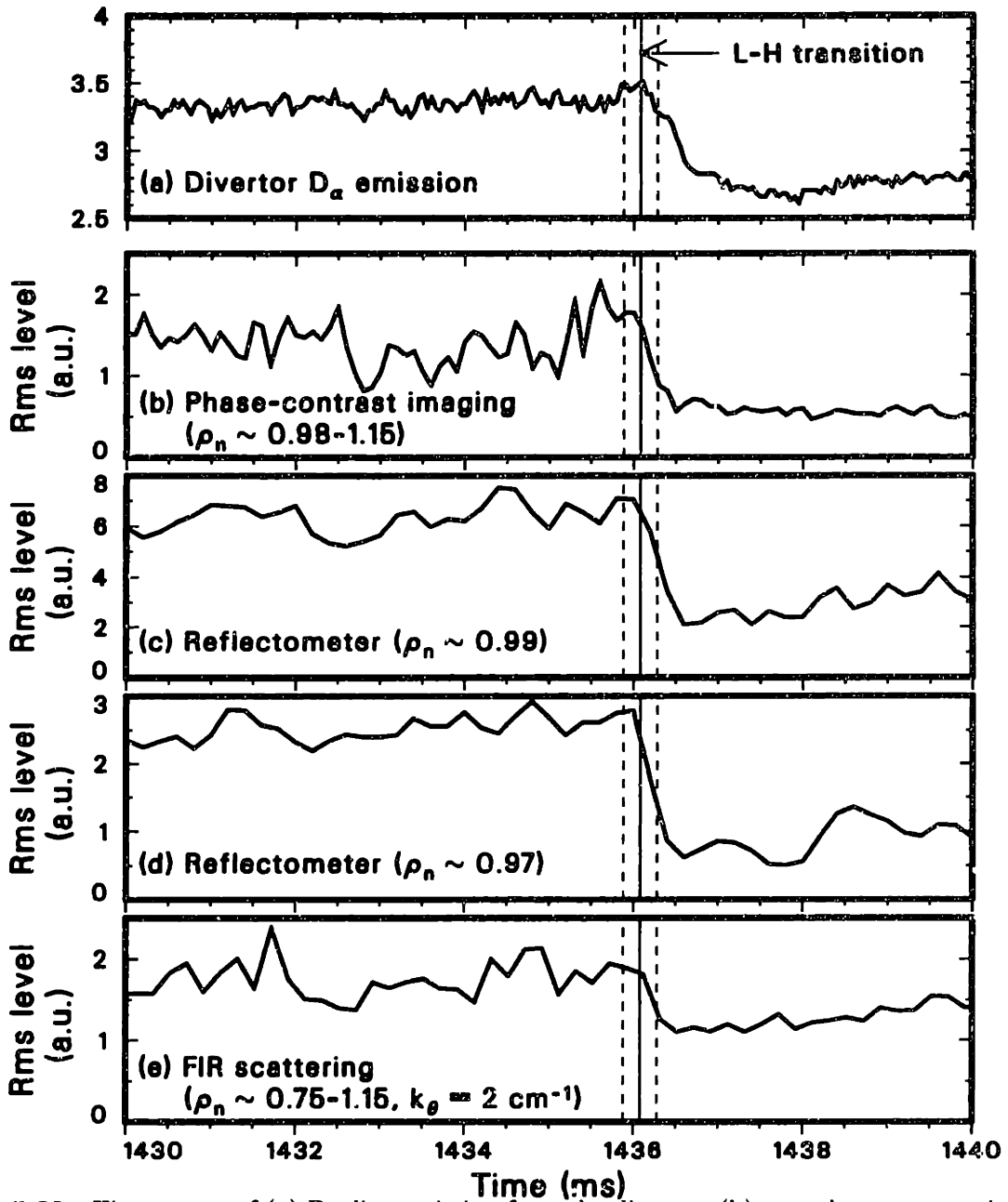

Fig. 5.32 Time traces of (a) D_α line emission from the divertor, (b) rms phase-contrast imaging (PCI) signal at a major radius located 0.5 cm inside the LCFS, (c) rms O-mode reflectometer signal from the the 1.2×10^{13}-cm^3 density layer, located ~0.5 cm inside the LCFS, (d) rms O-mode reflectometer signal from the 2.0×10^{13}-cm^3 density layer, located ~1.3 cm inside the LCFS, (e) rms FIR scattering signal corresponding to k_θ=2 cm^{-1} and to the region $0.75< \rho_n <1.15$. The PCI and the FIR scattering signals are proportional to $\tilde{n}$, whereas the reflectometer signal has a more complicated dependence on $\tilde{n}$. The time of the L-H transition is determined by the drop in the D_α signal; the dashed lines mark the temporal uncertainty of 0.2 ms given by the rms integration time. The plasma parameters are B_T=2.0 T, I_p=1.64 MA, $\bar{n}_e=3.8\times10^{13}$ cm^{-3}, and input power = 13 MW.

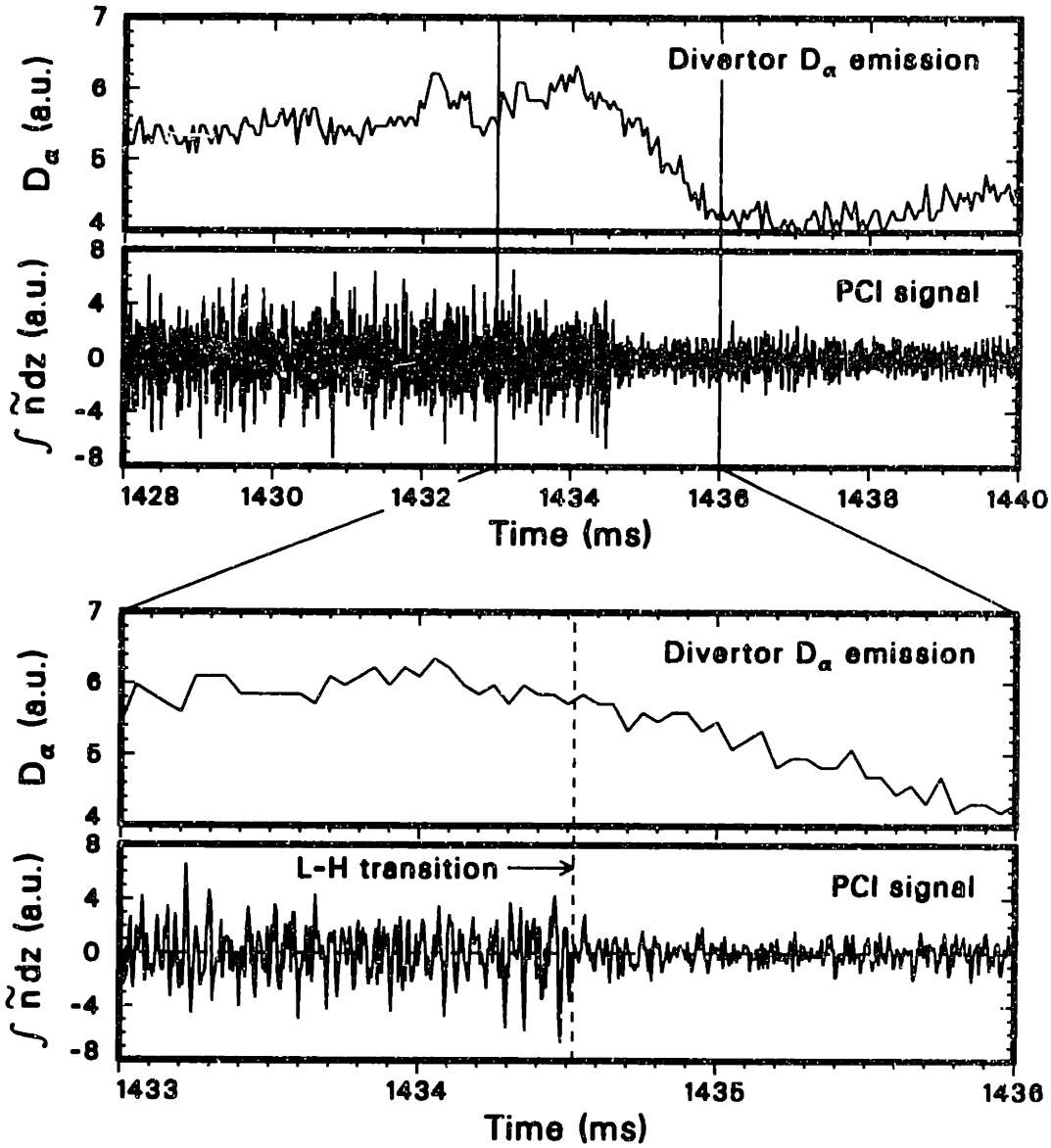

Fig. 5.33 Time traces, with a blowup of the L–H transition, of the D_α line emission from the divertor and of the phase-contrast imaging signal at a major radius located 0.4 cm inside the LCFS. The PCI signal is high-pass-filtered with a 3-dB frequency of 10 kHz. The plasma parameters are B_T=2.0 T, I_p=1.53 MA, $\bar{n}_e$=3.8×10^{13} cm^{-3}, and input power = 12.5 MW.

the behavior of the individual quantities in the remainder of this section. Figure 5.34 also serves to introduce a commonly observed phenomenon known as a *dithering* L–H transition, which is generally interpreted[292] as a series of L–H and H–L transitions occurring at a critical input power, which eventually result in the plasma settling in a steady-state H mode. The dithers in the D_α signal are accompanied by analogous dithers in the rms fluctuation amplitude. Within the resolution of the correlation estimates (±2.5 ms), the first point in Fig. 5.34 to lie entirely in H mode clearly displays both a shortened correlation length and an increased average radial wave number. The decorrelation times, although larger in average in H mode than in L

mode, are evidently much more erratic and do not change suddenly at the transition.

Although, as mentioned above, the fluctuation amplitude inside the LCFS is systematically lower in H mode than in L mode, it was shown in §5.6 that the same is not always true in the SOL; in fact, an *increase* in amplitude is observed by PCI in the majority of cases at the L–H transition. Figure 5.35 shows the time histories across a transition of the rms fluctuation amplitudes on seven radially spaced PCI chords. While the three top traces, affected by turbulence inside the plasma boundary, exhibit a clear decrease at the start of the H mode, the bottom four SOL traces show an increase in the average amplitude; in addition, the SOL signals are characterized by considerable variability in H mode.

The magnitude of the amplitude decrease inside the LCFS varies considerably from discharge to discharge, by as much as one order of magnitude: the suppression factor ranges approximately from 0.7 to 0.1, with a majority of cases lying in the vicinity of 0.5. In Chapter 6 we shall present an attempt to relate this factor to the changes in the correlation length and in the density gradient, in the context of the so-called mixing-length scaling. Here, it is interesting to observe that the suppression factors measured by other edge fluctuation diagnostics also display marked variability[298] and have a strong spatial dependence,[218] with the average factor being approximately of the order of 0.5,[298] in agreement with PCI.

The behavior of the fluctuation amplitude at the L–H transition in the SOL, as observed by PCI in DIII–D, differs from that reported by other diagnostics: a decrease in amplitude, though less pronounced than in the main plasma, has been documented for the SOL of DIII–D[61] and other devices.[215,216] This discrepancy may indicate an even stronger dependence on the spatial location or possibly on the spectral range in that region.

In the frequency domain, the amplitude suppression inside the LCFS occurs throughout most of the spectrum. However, the simultaneous spectral broadening, which was described in §5.4(a), causes the H–mode amplitude in some cases to rise above its L–mode counterpart at high frequency. A typical case, with no such crossover, is shown in logarithmic contour form in Fig. 5.36. In this case, the suppression factor is approximately 0.15 at the lowest frequency ($\sim$ 10–30 kHz) and rises to 0.5 at a frequency of 150 kHz.

The frequency broadening that accompanies the transition is evidenced by an increase in the average frequency, plotted in Fig. 5.37 alongside the D_α emission signal and the rms fluctuation amplitude. In addition, this figure shows the change in the exponent obtained from an inverse-power-law least-squares fit to the PCI autopower spectrum. As was discussed in §5.1(a), a value of 2 is typical of L mode; in H mode, the irregularity of the spectrum results in a poorer fit, but the values obtained are generally smaller than in L mode, reflecting once again the general spectral broadening: the trace in Fig. 5.37(d) confirms this behavior. A point of interest is that the variation of the shape of the spectrum occurs somewhat later than the changes both in the amplitude and in the correlation length: as shown in Fig. 5.37, both the average frequency and the inverse-power-law exponent change approximately 2 to 5

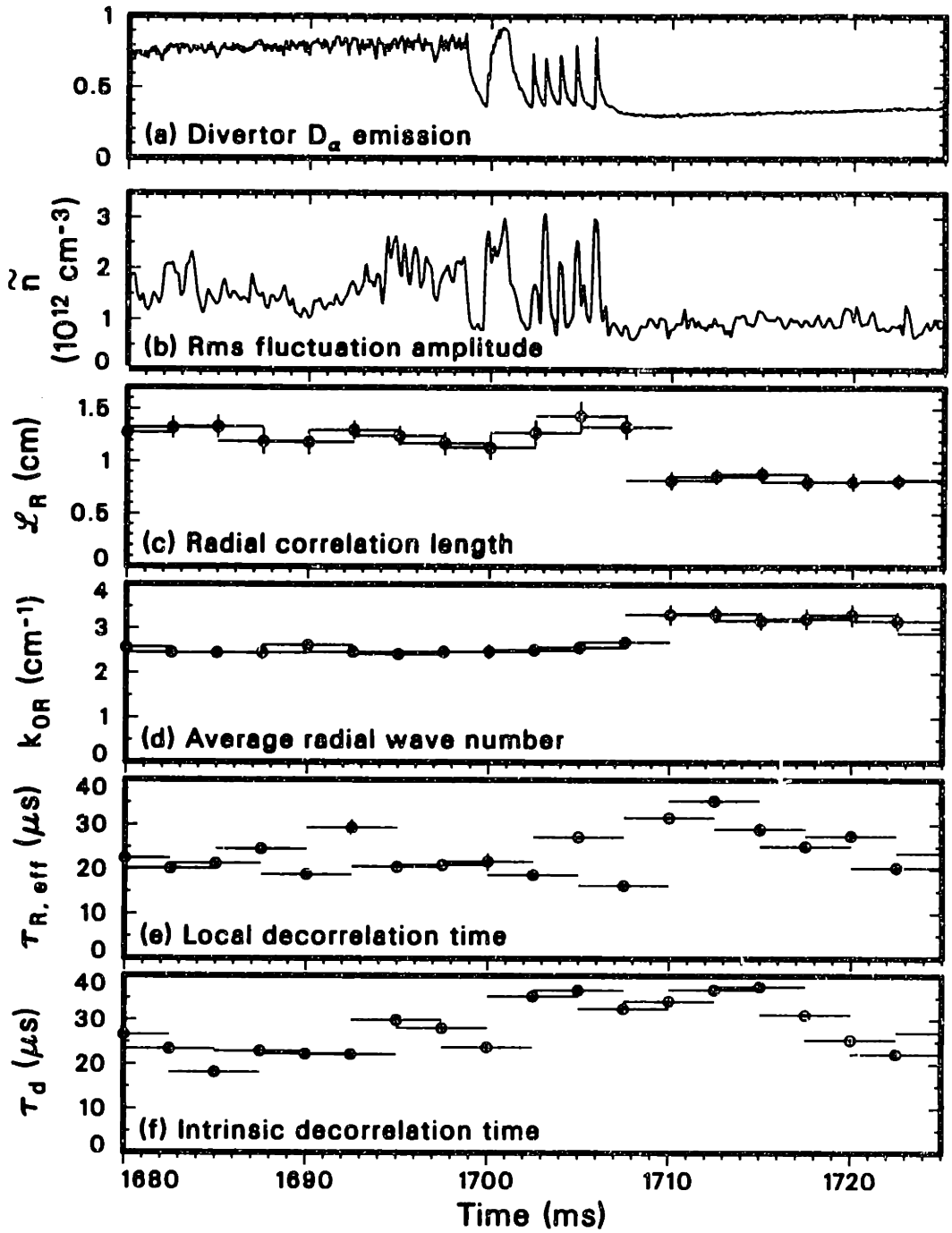

Fig. 5.34 Time traces of (a) D_α line emission from the divertor, (b) rms density fluctuation amplitude, (c) radial correlation length, (d) average radial wave number, (e) local decorrelation time, and (f) intrinsic decorrelation time. Measurements (b)–(f) are made with PCI in the region from the LCFS to 0.8 cm inside it. The dithering L–H transition is identified by the drop in the D_α signal. The absolute rms $\tilde{n}$ level is calculated over the chord segment inside the LCFS, assuming a vertical correlation length of 3 cm; the systematic error is estimated at 40% and the random error on the time trace is 6%. The plasma parameters are B_T=2.1 T, I_p=1.25 MA, $\bar{n}_e$=3.5×10^{13} cm^{-3}, input power = 6.2 MW.

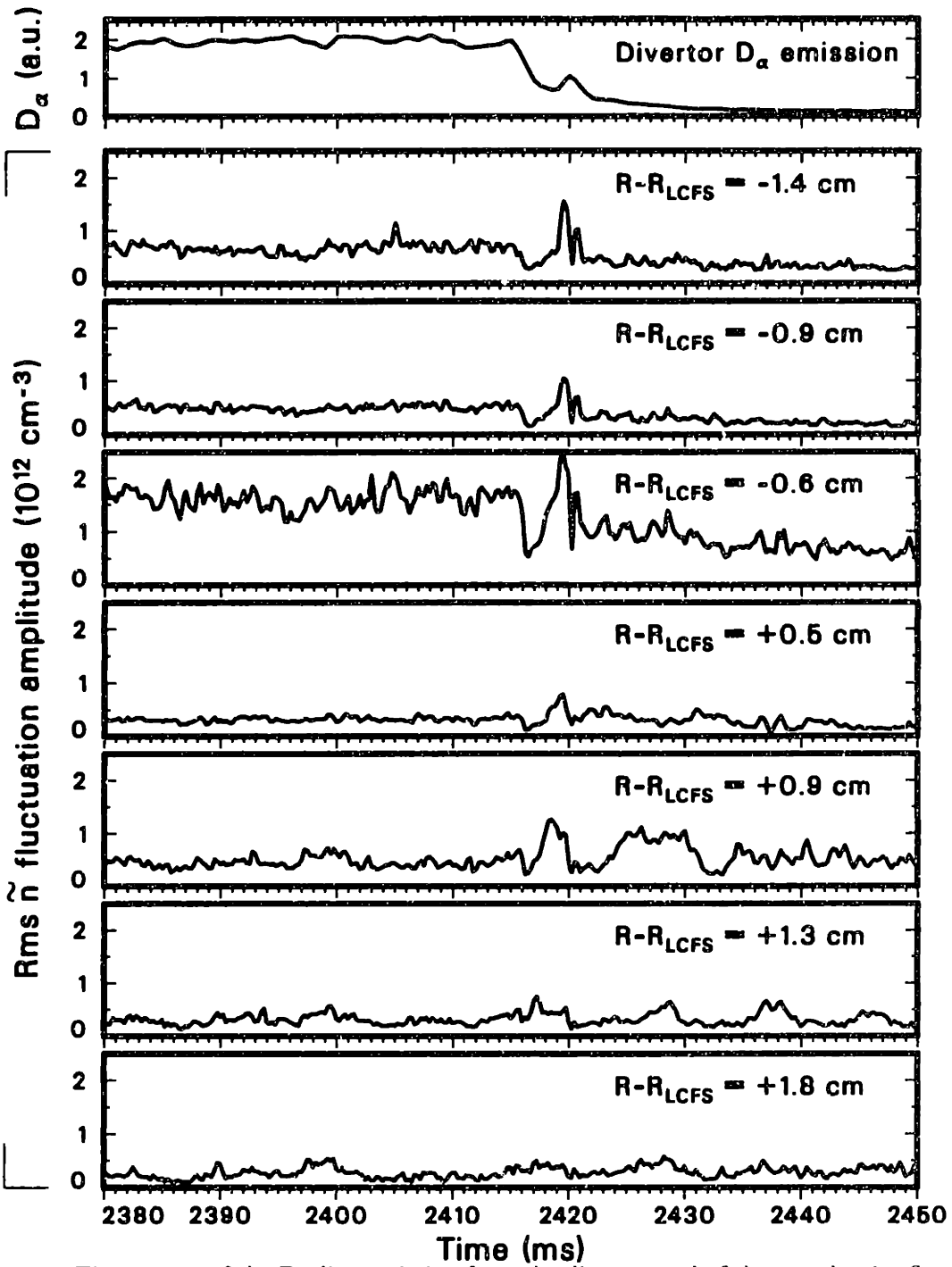

Fig. 5.35 Time traces of the D_α line emission from the divertor and of the rms density fluctuation amplitude at seven radial locations: the top three curves correspond to locations inside the LCFS, and the bottom four curves refer to the SOL. The L–H transition is identified by the drop in the D_α signal. The systematic error on the rms fluctuation level is estimated at 40% and the random error from channel to channel is 18%. The plasma parameters are B_T=2.1 T, I_p=1.37 MA, $\bar{n}_e$=4×10^{13} cm^{-3}, input power = 1.9 MW.

ms after the L–H transition.

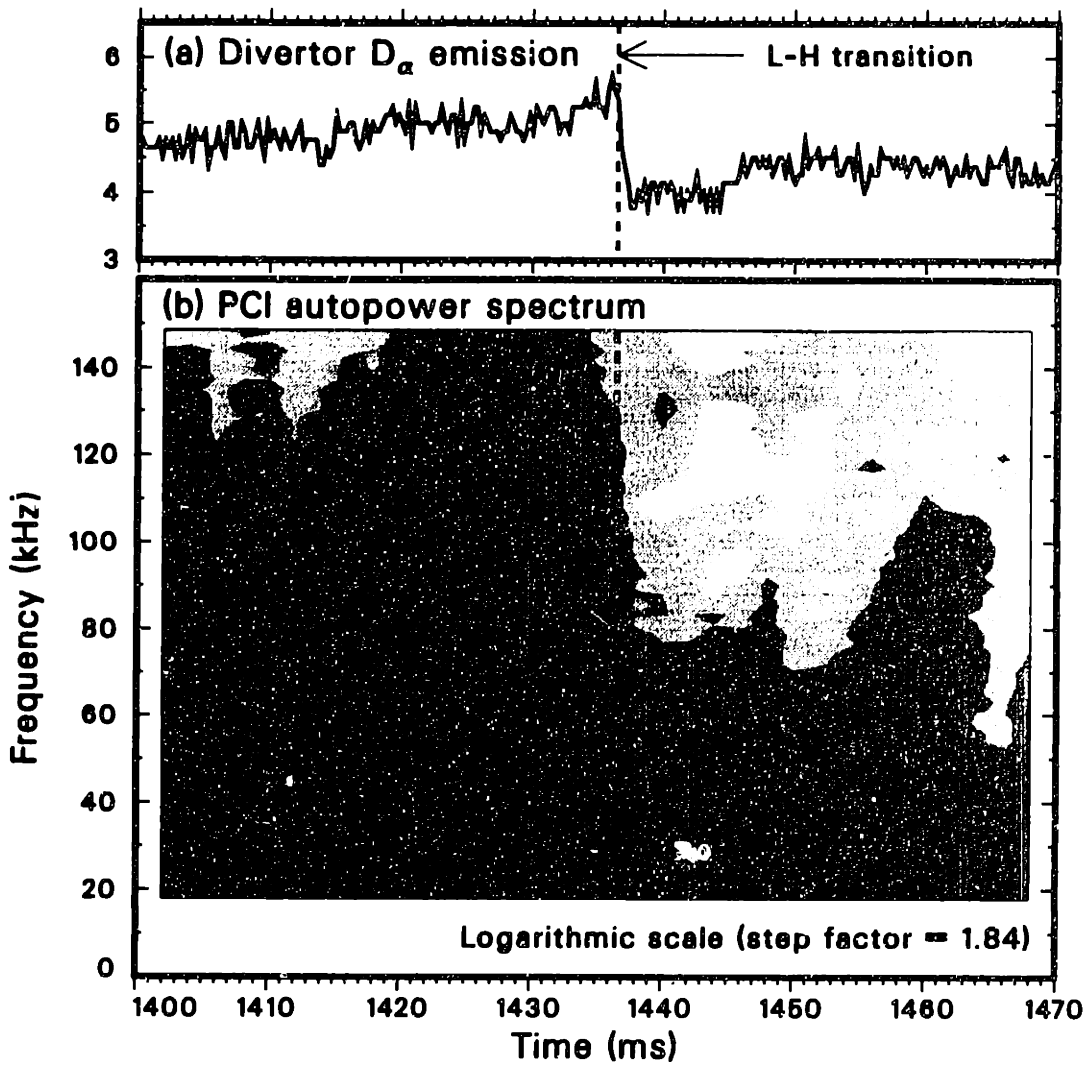

Fig. 5.36 (a) Time trace of the D_α line emission from the divertor and (b) contour plot in logarithmic scale of the time evolution of the PCI autopower spectrum 0.3 cm inside the LCFS, across the L–H transition (the level is proportional to the logarithm of the intensity). A smoothing interval of 20 kHz was used to estimate the autospectrum, with a statistical uncertainty of 11%. The plasma parameters are B_T=2.0 T, I_p=1.64 MA, $\bar{n}_e$=3.8×10^{13} cm^{-3}, and input power = 13 MW.

It was mentioned in §5.4(a) that only in rare cases are nonmonotonic features observed in the PCI autopower spectra in L mode. These cases invariably occur on chords located several cm inside the LCFS, an instance made possible only by locating the plasma boundary very close to the outer wall of the DIII-D vessel. This circumstance leads to a natural interpretation of these nonmonotonic features as the result of Doppler shifts from the increased poloidal components of the fluctuation wave vectors at the upper and lower ends of the chord, coupled with a nonzero poloidal $\mathbf{E} \times \mathbf{B}$ velocity. In some of these cases, the changes in both the $\mathbf{E} \times \mathbf{B}$ velocity and the spatial distribution of the turbulence at the L–H transition lead to a substantial modification of the shape of the spectrum, and a local spectral *increase* may occur.

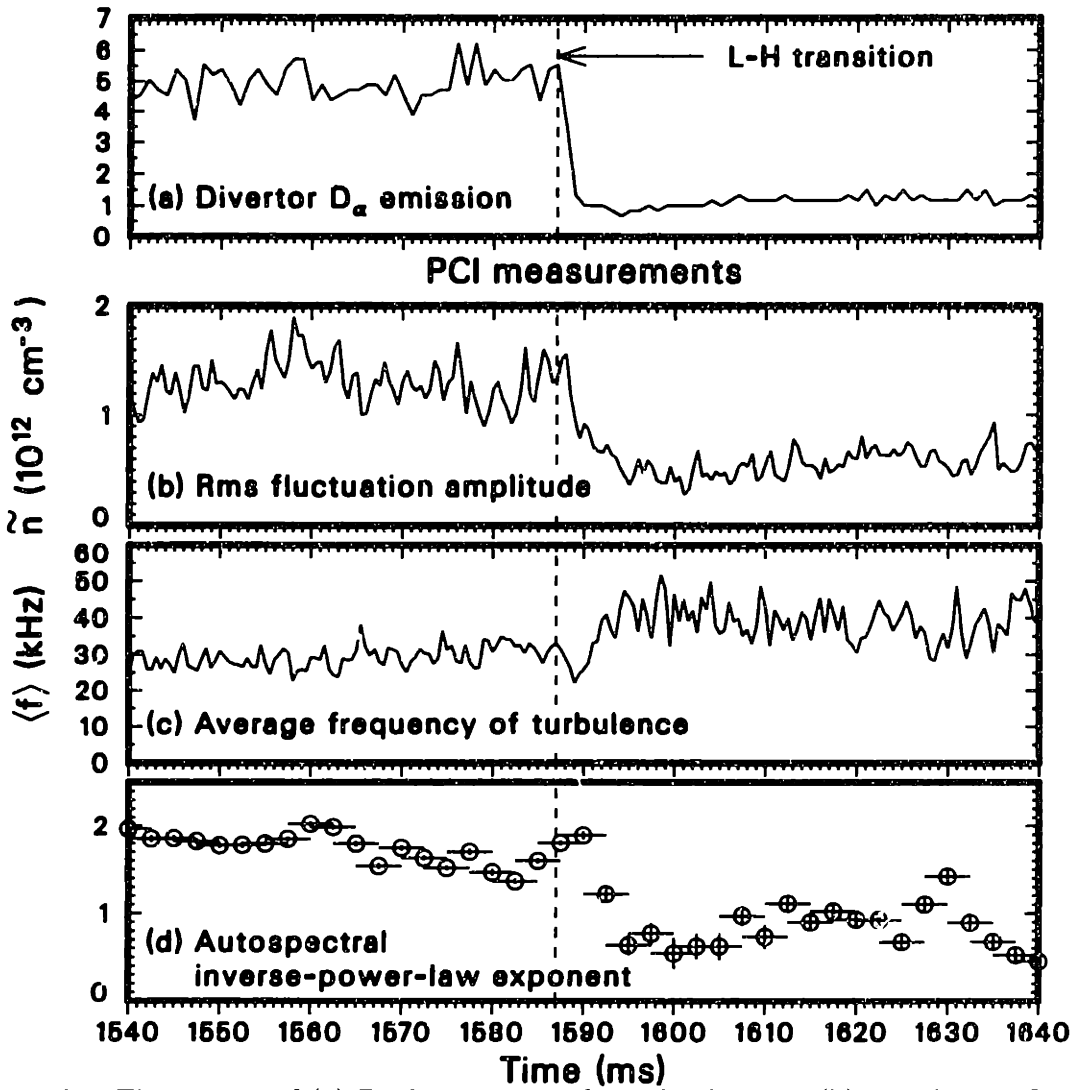

Fig. 5.37 Time traces of (a) D_α line emission from the divertor, (b) rms density fluctuation amplitude, (c) average fluctuation frequency (weighted with the autopower), (d) exponent in the inverse-power-law least-squares fit to the autopower spectrum. The PCI measurements [(b)-(d)] refer to a major radius 0.8 cm inside the LCFS. The systematic error on the rms fluctuation level is estimated at 40% and the random error is 5%. The plasma parameters are B_T=2 T, I_p=1.5 MA, $\bar{n}_e$=3×10^{13} cm^{-3}, input power = 4.1 MW.

A striking example of such a phenomenon is seen in Fig. 5.38, where a broad peak at approximately 38 kHz in L mode gives way to a considerably narrower and somewhat higher peak in H mode. However, it should be remarked that in all cases, as in the one shown in the figure, the integrated power still decreases at the L–H transition.

The different behavior of the spatial correlation characteristics at the L–H transition in the main plasma and in the SOL, which was discussed in §5.5, is exemplified by the time traces in Fig. 5.39. While the correlation length inside the LCFS decreases at the transition [Fig. 5.39(a)], in the SOL it either remains constant or increases, sometimes substantially, particularly several cm into the SOL, as shown

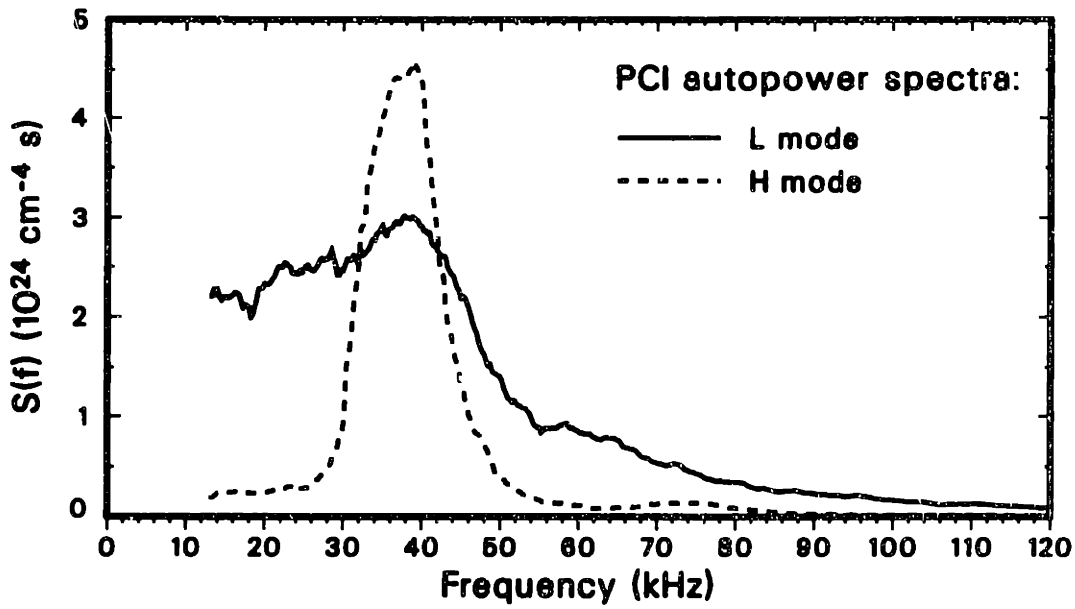

Fig. 5.38 Autopower spectra in the L-mode and H-mode phases of a discharge (B_T=2.16 T, I_p=1.35 MA, $\bar{n}_e$=4.5×10^{13} cm^{-3}, input power = 3.6 MW). The noise level is 1.4×10^{21} cm^{-4}s and the statistical error is 10%. The midplane location is 3.4 cm inside the LCFS.

in Fig. 5.39(b). The propagation coefficient can have any value between -1 (purely inward propagation) and 1 (purely outward propagation) in the main plasma in L mode, but typically becomes close to zero in H mode; in the SOL, by contrast, it is generally in the vicinity of zero both in L and H mode, as documented by Fig. 5.39.

A decrease of the correlation length inside the LCFS at the L–H transition is also usually seen in the frequency domain at all frequencies [see, e.g., Fig. 5.19(a)]. The reduction becomes weaker as the frequency increases, and the correlation length itself is typically a decreasing function of frequency in both regimes, as was discussed in §5.5(d) and as is evidenced by the time traces of the correlation length at 11 different frequencies plotted in Fig. 5.40.

As discussed earlier in this section and in §5.4(b), the time-delayed correlation functions undergo rather complex changes — qualitative as well as quantitative — at the L–H transition. In the main plasma, the shape of the envelope of the autocorrelation coefficient is substantially modified, with a narrowing at small delays and a broadening at large delays. This reflects the corresponding changes in the reciprocal frequency domain, where the autospectra become broader overall but also develop irregular, narrower peaks. As a rule, exponential fits are poorer in H mode than in L mode; nevertheless, they provide the only satisfactory method for estimating the time history of the decorrelation time, which is generally found to increase slightly at the L–H transition.

A clear example of the evolution of the autocorrelation envelope through the L–H transition is shown in contour form in Fig. 5.41(b). Both the low-delay narrowing and the high-delay broadening are in evidence. The characteristic irregularity of the

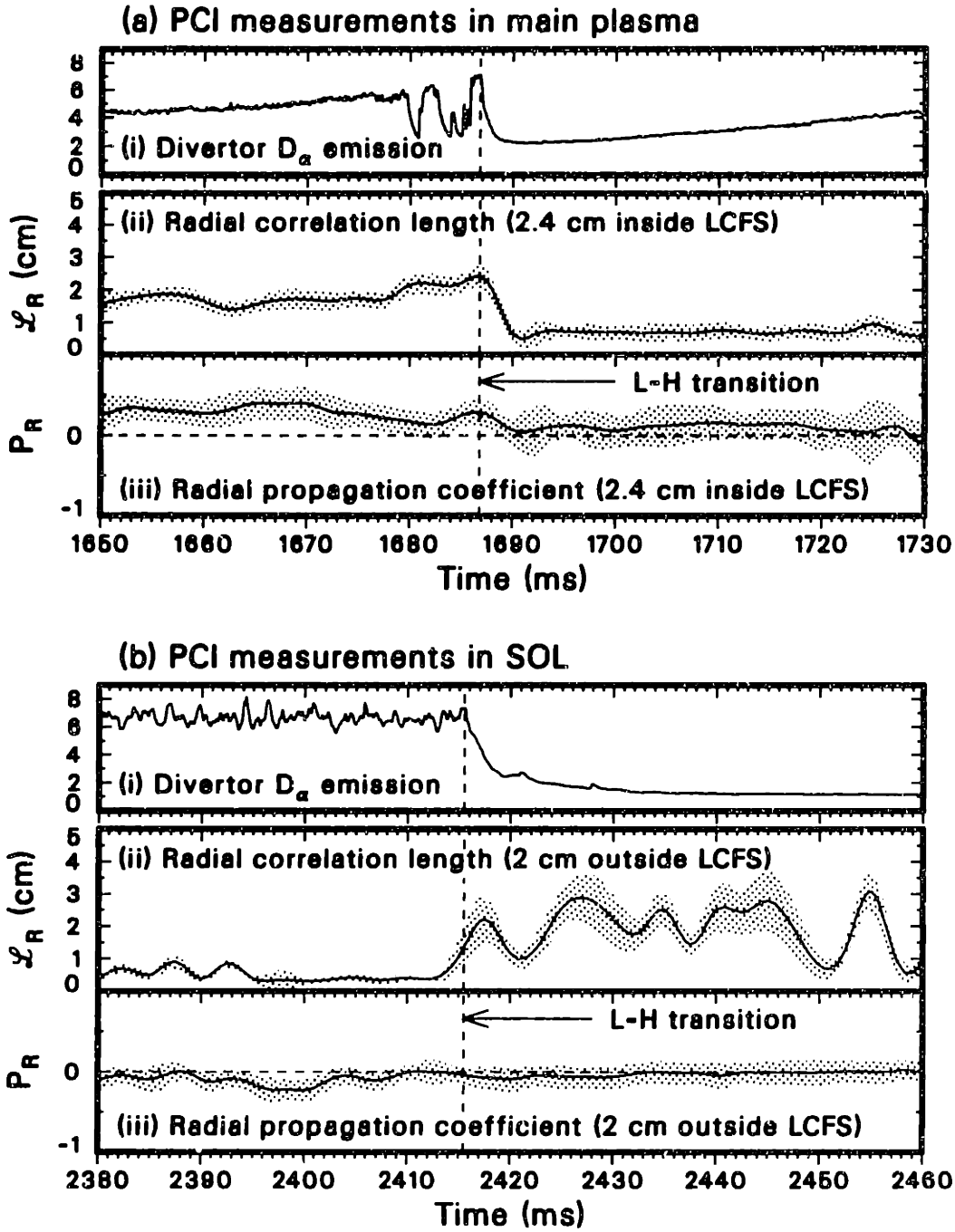

Fig. 5.39 Comparison of L-H transitions in two discharges [(a) B_T=2.1 T, I_p=1.3 MA, $\bar{n}_e$=3×10^{13} cm^{-3}, input power = 15 MW; (b) B_T=2.1 T, I_p=1.35 MA, $\bar{n}_e$=4.5×10^{13} cm^{-3}, input power = 1.6 MW)]: (i) D_α line emission from the divertor, (ii) radial correlation length, (iii) radial propagation coefficient (-1 for purely inward and +1 for purely outward propagation). The shaded areas indicate confidence intervals.

H mode, which develops only a few ms after the transition, can also be readily seen. An examination of the *intrinsic* autocorrelation envelope [calculated at the peak of the wave-number spectrum, as described in §5.4(b)] yields qualitatively similar

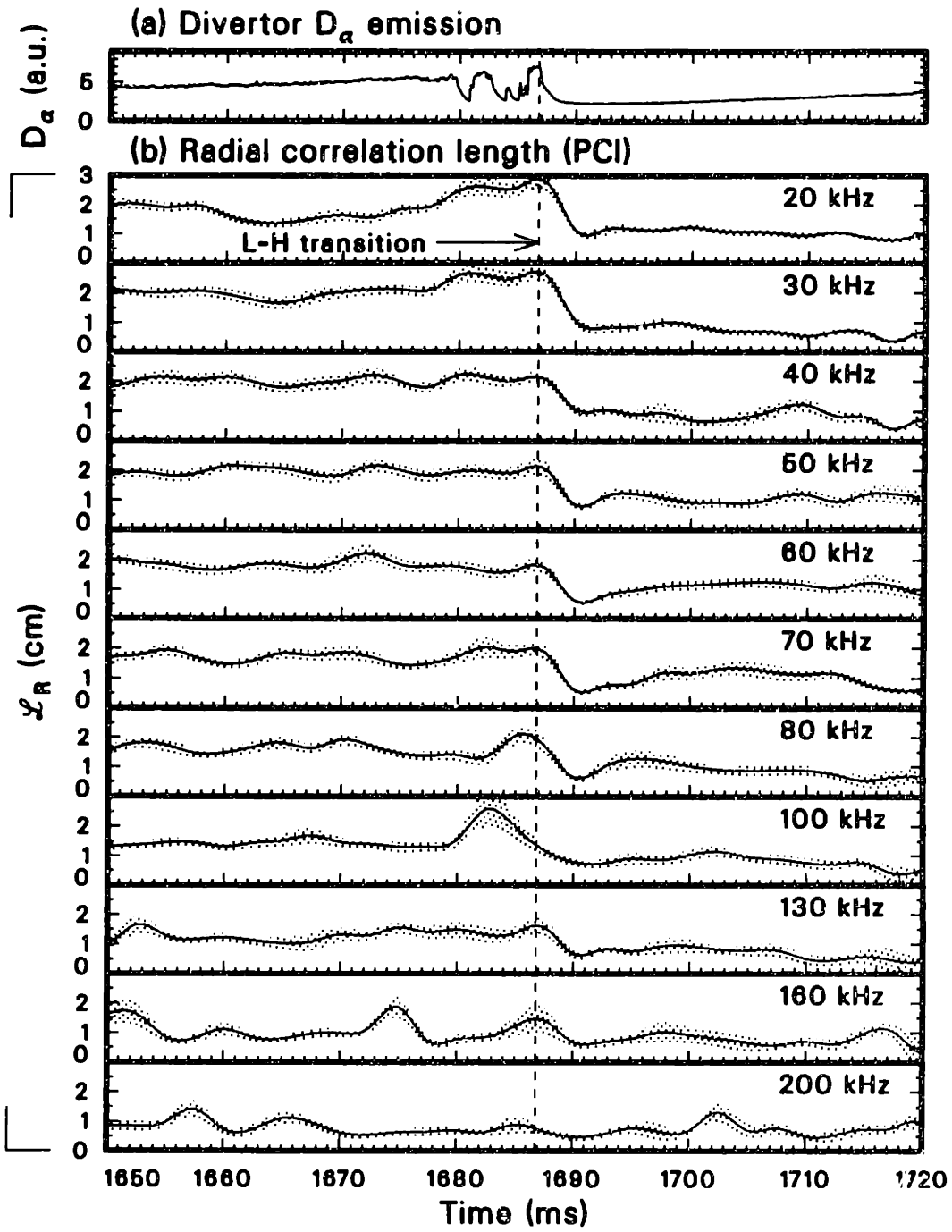

Fig. 5.40 (a) D_α line emission from the divertor, and (b) radial correlation length at an average major radius 4.3 cm inside the LCFS, calculated at 11 frequencies. Smoothing was performed over a 20-kHz interval. The temporal resolution of the correlation estimate is ±2.5 ms. The shaded areas indicat confidence intervals. The plasma parameters are B_T=2.1 T, I_p=1.3 MA, $\bar{n}_e$=3×10^{13} cm^{-3}, input power = 15 MW.

conclusions, as can be seen in Fig. 5.41(c).

In the SOL, the behavior of the correlation functions across the L–H transition is

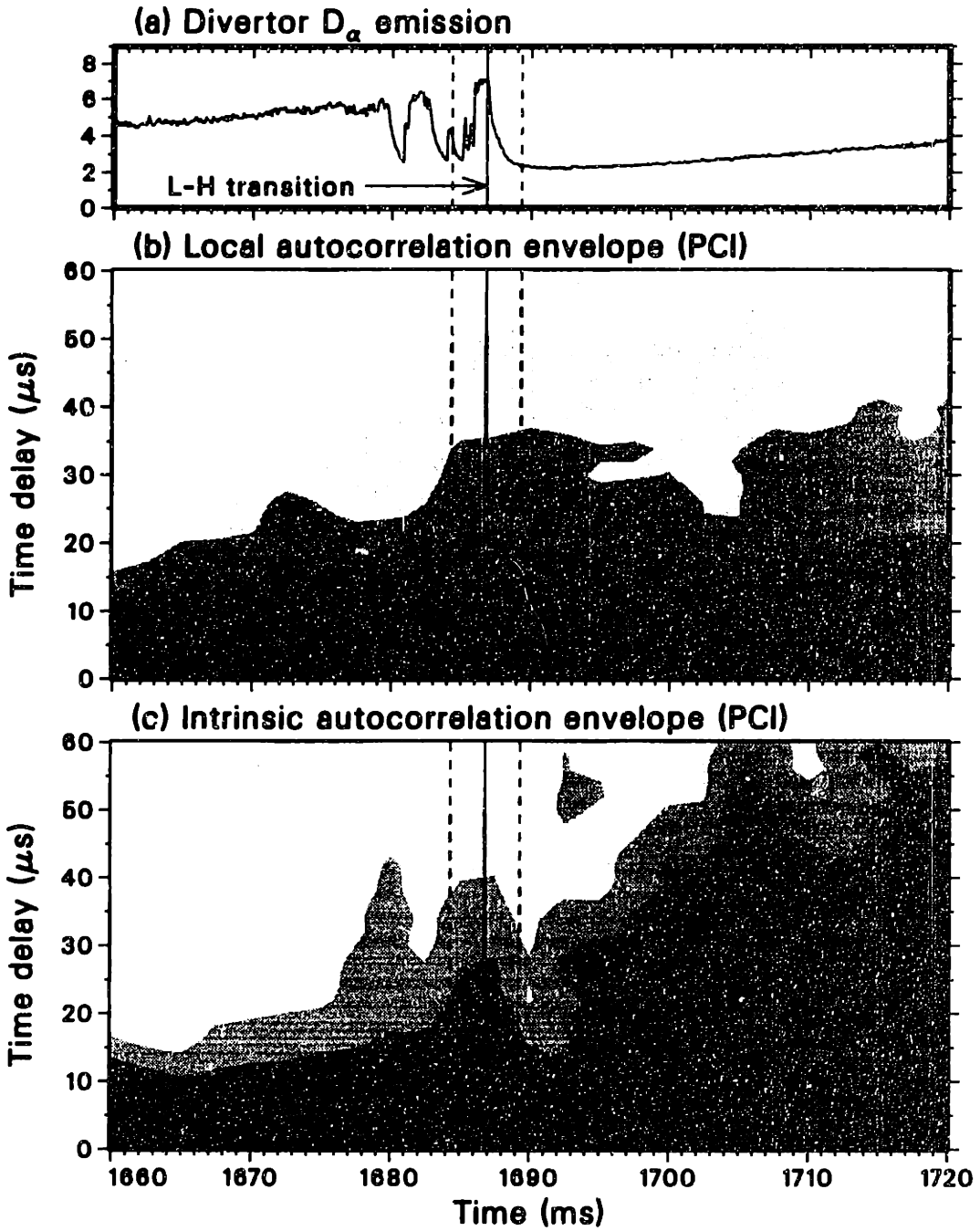

Fig. 5.41 (a) D_α line emission from the divertor, (b) contour plot of envelope of local (3.4 cm inside the LCFS) time-delayed autocorrelation function, (c) contour plot of envelope of intrinsic autocorrelation function in the region between 3.5 and 5 cm inside the LCFS. The step size in the contour plots is 0.11; the 95% confidence level is 0.05; the level is proportional to the intensity. The resolution of the correlation estimate is ±2.5 ms, as indicated by the dashed lines around the L–H transition. The plasma parameters are B_T=2.1 T, I_p=1.3 MA, $\bar{n}_e$=3×10^{13} cm^{-3}, input power = 15 MW.

more erratic. In most cases, little or no variation of the decorrelation time is observed.

However, the H–mode functions become generally even more irregular in time than their main-plasma counterparts; indeed, in some cases in which both the rms level and the correlation length in the SOL do not vary appreciably at the transition, this irregularity appears to be the only detectable effect in the SOL of the onset of H mode.

The probability distribution function (PDF) of the turbulence is almost invariably Gaussian in all regimes and in all locations, when calculated over intervals shorter than 40 ms (see §5.7). Longer intervals yield non-Gaussian, leptokurtic distributions. A study of the temporal evolution of the PDF across the L–H transition is meaningful, of course, only when short intervals are considered. An example of this kind of study is shown in Fig. 5.42, which depicts the evolution of the third to sixth moments of the PDF, estimated over half-overlapped 5-ms intervals (the even-order moments are plotted with the Gaussian value subtracted). The intrinsic intermittency of the L–H dithers yields, as expected, positive coefficients of kurtosis and of super kurtosis. However, it is strikingly clear that all moments are equal to zero, within their statistical uncertainties, both in L mode and in H mode.

To conclude this section, it is worth mentioning that a few cases of "back" H–L transitions have also been observed during this study. It is well known that a power hysteresis effect is at work in the L–H–L cycle, with the power at which the back transition occurs being lower than the L–H threshold power.[323] From the viewpoint of turbulence dynamics, however, the H–L transitions can be described as L–H transitions in reverse: both the rms level and the correlation length increase back to the original L–mode values, over a similar time scale. It should be stressed, though, that these observations were limited in number and were only of a qualitative nature.

5.9 Slow L–H Transitions

This section describes observations made during a specific experiment aimed at studying the L–H transition at input powers only slightly above the transition threshold.[218] As the input power approaches the threshold, the transition occurs on a progressively slower time scale. In particular, the reduction of transport, as measured by the spectroscopic D_α emission signal, becomes more gradual in the vicinity of the threshold. If the physical mechanisms at work during and immediately after the transition remain unchanged, this procedure permits, in effect, an experimental investigation of the transition with increased temporal resolution.

From the point of view of the turbulence measurements carried out with PCI, the results of this study were consistent with the observations detailed in the previous sections, both in L mode and in the fully developed H–mode phase; novel features emerged, however, in the transient intermediate phase identified by the gradual decrease in the D_α signal.[324] The conjecture that these features may always be present in the course of the transition is not inconsistent with measurements performed during faster transitions, as the temporal resolution would be insufficient to reveal them in those cases.

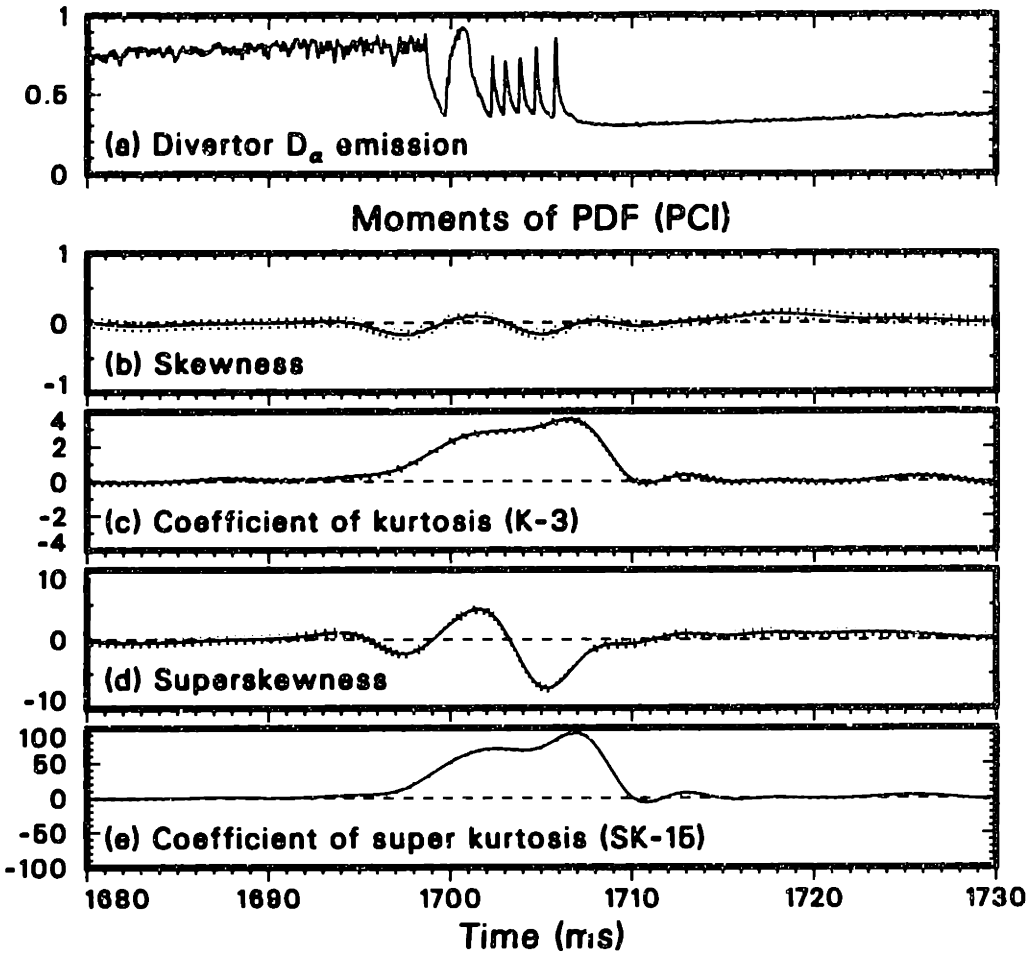

Fig. 5.42 (a) D_α line emission from the divertor, and (b–e) third, fourth, fifth, and sixth moment of the PCI probability distribution function (PDF), minus the Gaussian value (respectively 0, 3, 0, 15). The dithering L–H transition is indicated by the drop in the D_α signal. The PDF is estimated over half-overlapped 5-ms intervals (2500 samples), with a bin size equal to 0.1 standard deviations; the moments are calculated over a range of six standard deviations. The PCI major radius at the midplane is 3.4 cm inside the LCFS. The shaded areas indicate confidence intervals. The plasma parameters are B_T=2.1 T, I_p=1.25 MA, $\bar{n}_e$=3.5×10^{13} cm^{-3}, input power = 6.2 MW.

This experiment was carried out in lower-single-null diverted plasmas with a toroidal magnetic field of 2.1 T, a plasma current of 1.37 MA, and a line-averaged density of 3.2×10^{13} cm^{-3}. The neutral-beam power was 2 MW, approximately 30% higher than the threshold for obtaining H mode.[218]

The time histories of the rms fluctuation levels on three chords, two of which intersect the plasma while the other lies entirely in the SOL, are shown at the top of Fig. 5.43, along with a D_α emission signal for reference. At the start of the drop in the D_α trace, which signals the onset of the H mode, the fluctuation level on the plasma chord decreases rapidly, reaching a minimum in $\sim$ 50 μs. Only a slight drop is observed on the SOL chord. After a quiescent phase $\sim$ 0.6 ms long, the fluctuation level rises again, to a value similar to that of L mode on the plasma chords, and

to a substantially larger value on the SOL chord. This turbulent phase, which will henceforth be called the *early H–mode* phase, subsides slowly, on a 20–30 ms time scale. In the final (*late H–mode*) phase, which begins approximately when the D_α signal completes its descent, the fluctuation amplitude is lower than in L mode on the plasma chords and of the same order as in L mode on the SOL chord, in accord with past measurements (see §5.8).

The short duration of the quiescent, low-turbulence phase is evidenced by the blown-up traces shown at the bottom of Fig. 5.43. The raw PCI signals (high-pass-filtered at 8 khz as usual) are shown here because rms statistics would not be adequate on this time scale. The sudden reduction of turbulence at the L–H transition is clearly visible, as is its resurgence approximately 0.6 ms later.

Figure 5.44 shows the frequency autopower spectra of the fluctuation signals in logarithmic scale on the same three chords, calculated at three different times, respectively in L mode, in early H mode, and in late H mode. In L mode, least-squares fits to inverse power functions for all 8 chords that were digitized yielded exponents in the range 1.7–2.3 with reduced χ^2 values smaller than 1; these values are typical, as was discussed in §5.4(a).

The spectrum is shifted toward higher frequencies in early H mode and also becomes more irregular inside the LCFS. The average level is similar to that in L mode on all plasma chords and in the deep SOL, whereas it is considerably larger at the SOL location shown in Fig. 5.44(c).

Finally, the fluctuation level in late H mode is considerably lower than that in L mode on all plasma chords, whereas the two are of the same order on all SOL chords; this is, again, in agreement with past measurements. The H–mode frequency broadening is especially pronounced in these discharges, as illustrated in particularly clear fashion by Fig. 5.45, which shows the time traces of the autopower spectrum calculated at one location (inside the LCFS) for seven discrete frequencies. While the power decreases drom L to H mode at low frequency, the reverse is true at high frequency, in accordance with the spectra shown in Fig. 5.44. It must be remembered, however, that the integrated power decreases, as evidenced by the rms traces in Fig. 5.42.

The early H–mode phase contains all the new phenomenology uncovered by this experiment and thus deserves further exploration. The region within the SOL located 1 to 2 cm outside the LCFS is particularly interesting, as the amplitude of the fluctuations in largest there, and indeed it is extraordinarily large in absolute terms.

A natural line of inquiry concerning the early H–mode phase pertains to the structure of the spatial correlations. The answer is provided by Fig. 5.46, which compares the radial correlation functions in the L–mode, early-H–mode, and late-H–mode phases, relative to a reference point situated 1.5 cm outside the LCFS.

The L–mode and late-H–mode cases exhibit the usual decaying wavelike behavior [see §5.5(a)], with the correlation length in the SOL being slightly longer in H mode than in L mode [see also Fig. 5.39(b)]. By contrast, the early-H–mode case is characterized by an abnormally high correlation level between the SOL and locations

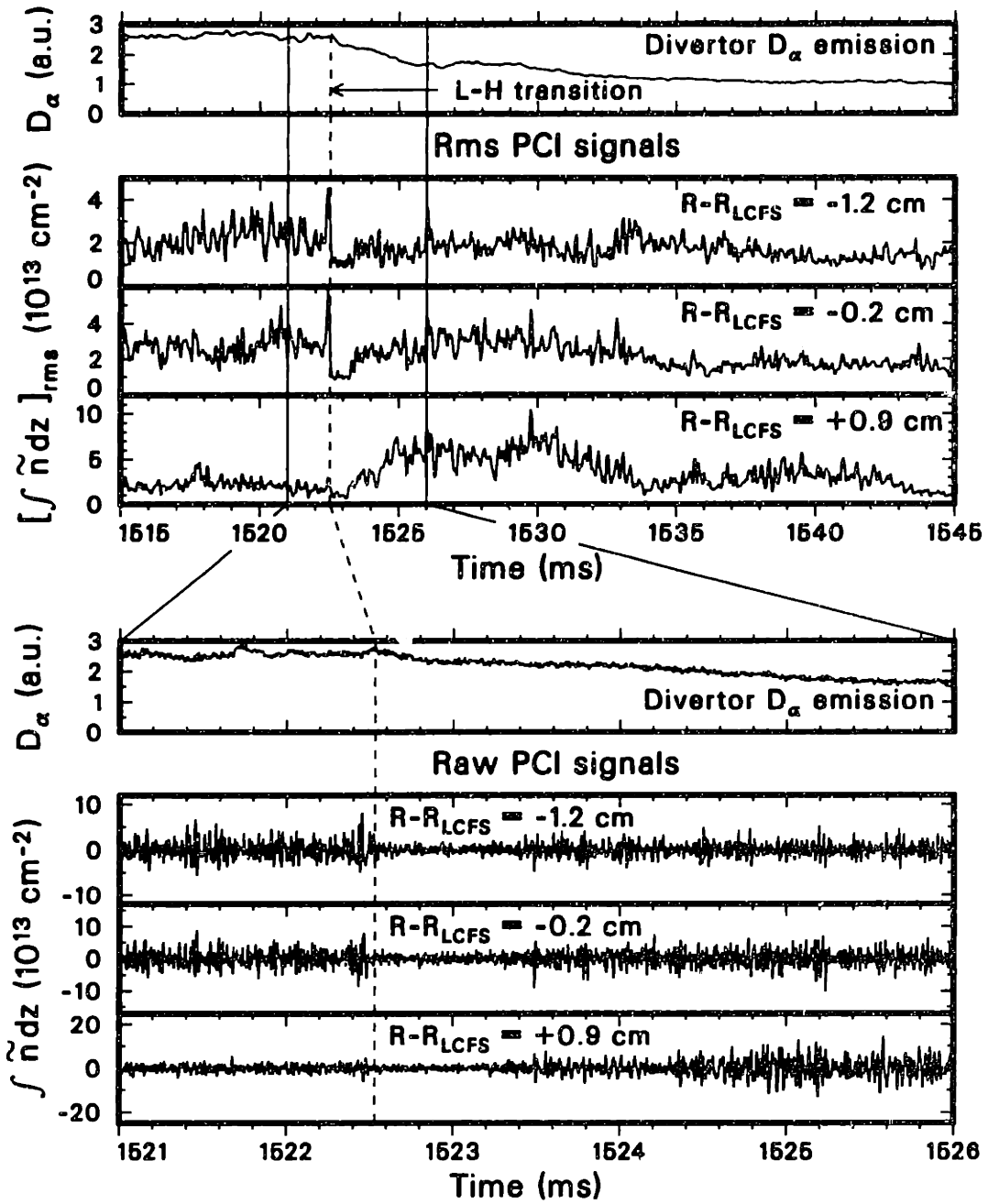

Fig. 5.43 Time traces (top) of the D_α line emission from the divertor, and of the PCI rms signals at three radial locations, the top two being inside the LCFS and the bottom one in the SOL. In the blowup of the L–H transition (bottom) the same signals are shown, but the PCI rms signals are replaced by the raw signals, high-pass-filtered at 8 kHz. Note that the vertical scales are different for different PCI channels. The absolute (systematic) PCI calibration error is estimated at 35%. The statistical uncertainty of the rms estimate is 10%. The plasma parameters are B_T=2.1 T, I_p=1.43 MA, $\bar{n}_e$=3×10^{13} cm^{-3}, input power = 2.5 MW.

inside the LCFS. Moreover, the equal-time coefficient between these points is positive everywhere, with the exception of a point at the location of maximum fluctuation am-

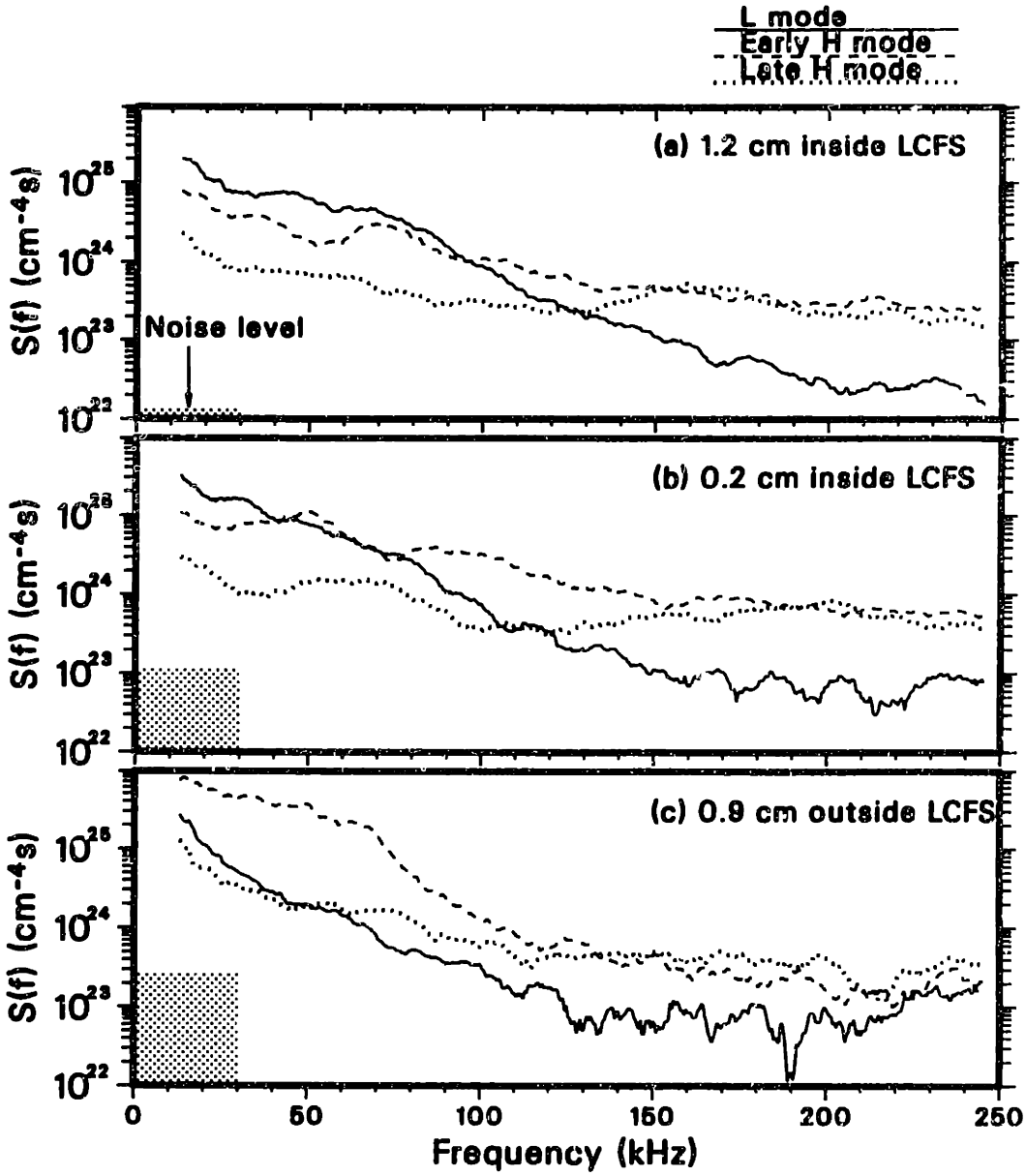

Fig. 5.44 Autopower spectra at three radial locations, in the L–mode (solid curves), early-H–mode (dashed curves), and late-H–mode (dotted curves) phases of a discharge with a slow L–H transition. The time trace of the divertor D_α emission signal for this shot is shown in Fig. 5.43. The statistical uncertainty on the spectra is 10%. The plasma parameters are B_T=2.1 T, I_p=1.43 MA, $\bar{n}_e$=3×10^{13} cm^{-3}, input power = 2.5 MW.

plitude (1 cm outside the LCFS), which is in phase opposition with all other points; such a phase-inverted layer has been observed also in a number of fully developed H modes, as was discussed in §5.5(a) in connection with Fig. 5.11, but the high, and roughly constant, correlation level between the SOL and the interior points sets this case apart from all others.

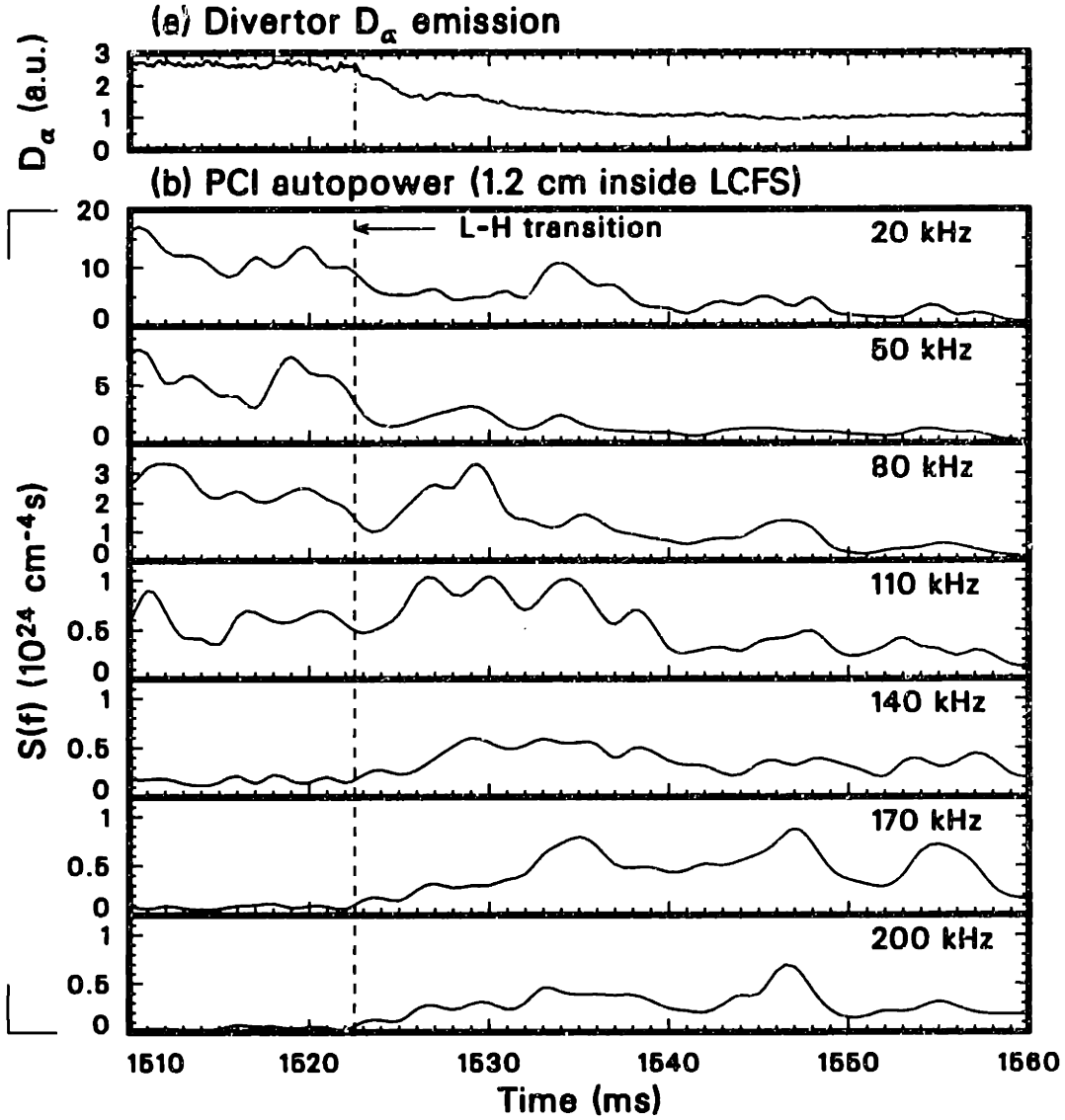

Fig. 5.45 Time traces of (a) the D_α line emission from the divertor, and of (b) the PCI autopower at a radial location 1.2 cm inside the LCFS, plotted for seven frequencies. The spectra are smoothed over a 25-kHz interval, with a resulting statistical uncertainty of 14%. The absolute (systematic) PCI calibration error is estimated at 35%. Note that the vertical scales are different for different frequencies. The plasma parameters are B_T=2.1 T, I_p=1.43 MA, $\bar{n}_e$=3×10^{13} cm^{-3}, input power = 2.5 MW.

5.10 The Evolution of Turbulence During a Plasma Discharge

In the previous two sections we have explored the dynamics of the L–H transition. The present section will address some aspects of the dynamical evolution of turbulence throughout a DIII–D discharge. The chief point that we shall attempt to demonstrate is that turbulence varies throughout a discharge in a very complex way, and can by no means be considered simply a function of the confinement regime, be it Ohmic, L–mode or H–mode. Because of the sheer diversity of behavior observed, and because

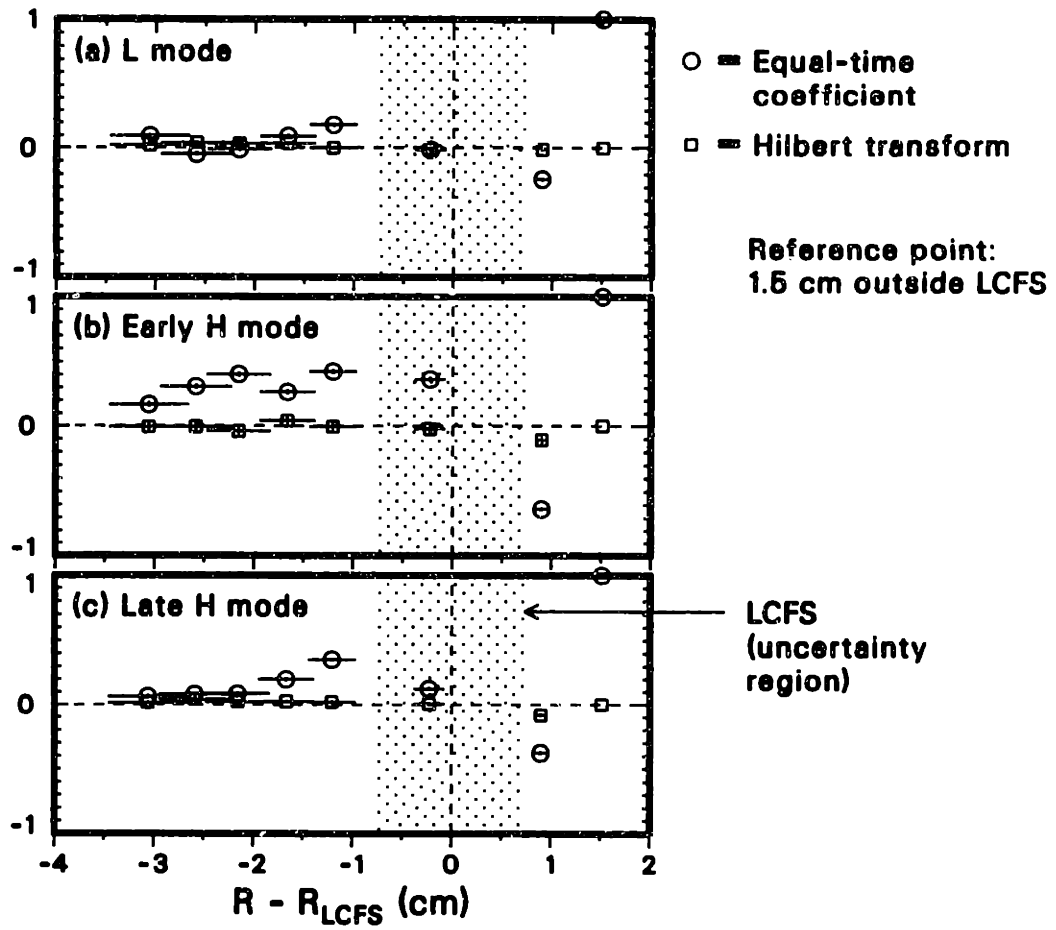

Fig. 5.46 Equal-time coefficient and its Hilbert transform, relative to a reference point located 0.9 cm outside the LCFS, in the (a) L–mode, (b) early-H–mode, and (c) late-H–mode phases of a discharge with a slow L–H transition. The 95% confidence level is 0.06. The time trace of the divertor D_α emission signal for this shot is shown in Fig. 5.43. The plasma parameters are B_T=2.1 T, I_p=1.43 MA, $\bar{n}_e$=3×10^{13} cm^{-3}, input power = 2.5 MW.

the main focus of this thesis has been on the L–H transition and on ELMs, it is impossible here to even approach a complete description. An overview of a few key observations will be offered, with the aid of one representative example for illustration.

The example is shown in Fig. 5.47, which contains the time histories throughout several confinement regimes of the divertor D_α emission signal, of the neutral-beam injected power, of the thermal-energy confinement time, of the rms PCI density fluctuation level just inside the LCFS, and of the radial correlation length.

In this discharge, an "early" neutral beam is turned on well before 1900 ms, with the purpose of inhibiting deleterious MHD instabilities ("locked modes") and of keeping the recycling low in the subsequent H–mode and VH–mode phases, thus allowing good confinement to develop. In this early-beam phase, the neutral-beam power is comparable to the Ohmic power, and the confinement time is close to its Ohmic value.

After the main beams are turned on at 1900 ms, the confinement time begins to

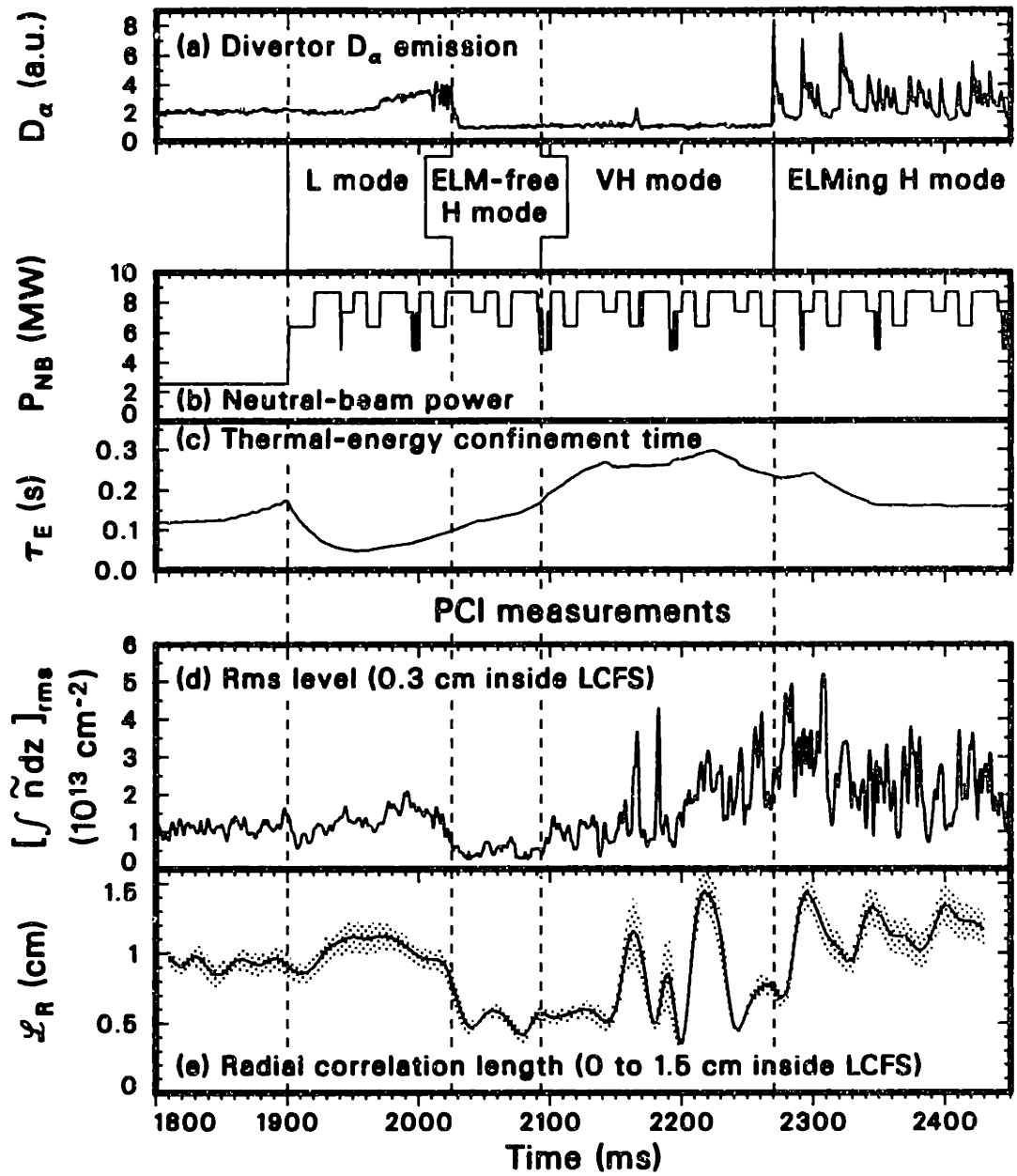

Fig. 5.47 Time traces of (a) D_α line emission from the divertor, (b) neutral-beam injected power, (c) thermal-energy confinement time, (d) PCI rms fluctuation level 0.3 inside the LCFS, and (e) radial correlation length in the region from the LCFS to 1.5 cm inside it. The absolute PCI calibration error is estimated at 35%, whereas the statistical error on the rms estimate is 3.5%. The plasma parameters are B_T=2.16 T, I_p=1.54 MA, $\bar{n}_e$=3×10^{13} cm^{-3}. The Ohmic input power is approximately 1 MW.

decrease to the L–mode level corresponding to the specific input power. After a beam slowing-down time (~60 ms), the confinement reaches its lowest level and a noticeable increase in the D_α recycling signal is observed. Throughout this phase of confinement deterioration, both the rms fluctuation level and the radial correlation length are slightly larger than in the early-beam phase. These observations are consistent with

the general results presented, respectively, in §5.6 and in §5.5(b). As was mentioned in §5.6, however, an increase in the rms level is generally seen only in this region, just inside the LCFS; elsewhere, the Ohmic and L–mode level are usually equal.

As seen in Fig. 5.47, both the rms level and the correlation length change little in time during the early-beam phase, but become more irregular after the main beam power is applied. These both appear to be general characteristics of the Ohmic and L–mode regimes. Since a longer correlation length is theoretically expected to imply larger turbulent diffusion, as will be discussed in Chapter 6, it is not surprising to observe that the correlation length in the interval 1900—2020 ms describes an arc similar and opposite to that followed by the confinement time. The relation between the two, if any, would of course be rather complex, particularly since the former is an edge quantity and the latter is a global one. However, this qualitative correlation has been observed in most of the L–mode cases examined. A similarly regular behavior in Ohmic plasmas, and a more irregular one in the L–mode regime, is seen in the time histories of the frequency spectra.

A dithering transition to H mode occurs, beginning at 2010 ms, in the case of Fig. 5.47. The D_α signal decreases sharply and the confinement time rises gradually in the early H–mode phase free of edge localized modes (ELMs). A gradual transition to VH mode follows, while the confinement time continues to increase, reaching a peak at 2225 ms. MHD activity, starting at the small peak in the D_α signal at 2165 ms and lasting until 2320 ms, begins to degrade the confinement progressively, and eventually leads to the onset of the ELMing H–mode phase at 2270 ms. The ELMs can be seen clearly as large peaks in the D_α signal; in this regime, the confinement time decreases until it reaches a steady-state value approximately equal to one-half its peak VH–mode value.

The sharp reduction of both the rms fluctuation level and the correlation length at the L–H transition, thoroughly documented in §5.8, is in evidence in Fig. 5.47 as well. The correlation length remains short until the onset of MHD activity (the delay in this event between the correlation-length trace and the D_α trace is an artifact of the different time resolutions of the two measurements). By contrast, the rms level begins increasing around 2100 ms and reaches a value approximately equal to the L–mode level. In addition, the rms trace displays a marked irregularity as a function of time in H mode.

These observations are quite general; in some cases, the correlation length also rises during the H mode, but generally remains below its L–mode value. (It must be remarked that the simultaneity of the rms increase and of the onset of VH mode is coincidental and a peculiarity of this particular discharge.) The average frequency of the fluctuations, which increases at the L–H transition (see §5.9), decreases correspondingly when the rms level rises during the H mode.

A rise of the fluctuation level during H mode has in fact been seen by a number of diagnostics; it has been shown in DIII–D[218] that the reduction of the turbulent flux just after the transition is primarily due to the suppression of the fluctuation amplitude, whereas after the amplitude recovers the flux remain low primarily because

of a dephasing of nearly 90° between the turbulent density and $\mathbf{E} \times \mathbf{B}$ velocity [see §5.1(b)]. The amplitude increase is interpreted as part of a feedback process: as the improved confinement leads to the formation of a steep pressure gradient at the plasma edge, this in turn is able to drive microinstabilities in that region.

The complex dynamics of H mode are the reason behind our choice to focus on the very early part of the H–mode phase in §§5.4–5.7, in view of our specific interest in the L–H transition. The later, more turbulent, phase of the H mode departs in significant ways from the phenomenology described in those earlier sections. A detailed study beyond the effects described here has not been carried out, and could certainly constitute a valuable future extension of this work.

Although no systematic study of the VH mode has been attempted with PCI, no evidence of distinctive VH–mode effects has been uncovered thus far. This is perhaps not surprising, as the VH mode can be described as resulting from an extension of the H–mode transport barrier to the interior of the discharge, beyond the range accessed by the PCI system.

In Fig. 5.48 the time history of the autopower spectrum for the same discharge and at the same PCI location is shown in three-dimensional form, along with the D_α signal for reference. Visible in this plot is one additional effect observed well into the H–mode phase: the formation of temporary spectral features centered at frequencies between 20 and 80 kHz. Although the H–mode spectrum is often nonmonotonic immediately after the transition, as discussed in §5.4(a), the irregularities become more prominent in the later phase. The feature centered at 35 kHz appearing at 2100 ms in Fig. 5.48 is an example of this; this feature is indeed primarily responsible for the concomitant increase in the rms level.

The MHD activity occurring from 2165 ms to 2320 ms is clearly seen in Fig. 5.48. This is a coherent mode at 30 kHz (the observed broadening is a result of the 10-kHz smoothing), which appears in the PCI signal at a larger amplitude than the background turbulence, causing a corresponding increase in the rms fluctuation level; the lengthened correlation length (see Fig. 5.47) is also a result of the high coherence of this mode. Similar large-amplitude MHD modes are often seen in the PCI signal and will be briefly commented on in §5.12.

Finally, ELMs are accompanied by a level of turbulence often higher than that of L mode, as Figs. 5.47 and 5.48 clearly attest. This turbulence only exists within each single ELM, and drops to usual H–mode levels between ELMs. The discreteness of the ELMs is not clearly seen in these figures, partly because ELMs are bunched together in this discharge and partly because the MHD mode does not vanish until 2320 ms. The ELM phenomenon is the subject of the next section.

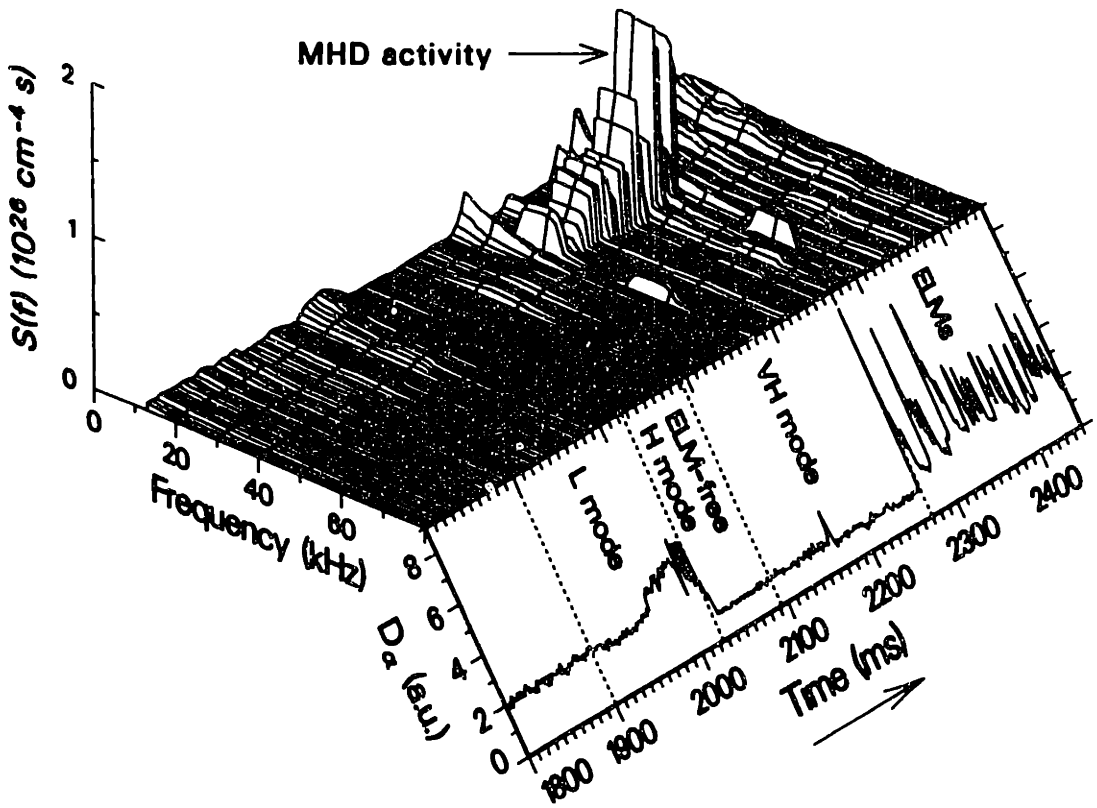

Fig. 5.48 Three-dimensional plot of the time history of the PCI autopower spectrum on a chord located 0.3 cm inside the LCFS, and time trace of the D_α line emission from the divertor. A smoothing interval of 10 kHz was used to estimate the autospectrum, with a statistical uncertainty of 10%. The absolute calibration error on the power is 70%. The plasma parameters are B_T=2.16 T, I_p=1.54 MA, $\bar{n}_e$=3×10^{13} cm^{-3}, and input power = 8 MW.

5.11 Edge Localized Modes

Edge Localized Modes (ELMs) are semiperiodic edge instabilities that occur in H mode and destroy the H–mode transport barrier temporarily; after the instability subsides (typically in a fraction of a ms), the barrier is recreated.[59] An overview of the phenomenon was provided in §5.1(d). As explained there, ELMs are considered essential for steady-state reactor operation, as they permit density control and also expel impurities and spent fusion ashes.[292]

Although ELMs are believed to be manifestations of MHD instabilities and are indeed accompanied by large fluctuation levels,[292] much remains unknown about the detailed mechanism that triggers them. The existence of several distinct types of ELMs, believed to be related to different instabilities, is an added complication.

In this section we shall present the results of a systematic study of the various types of ELMs carried out with the PCI system in the DIII–D tokamak. In addition to the type-I (or "giant") and type-III ELMs, observed in a variety of toroidal fusion devices,[292] a third variety — labeled type-II, or "grassy" — has been found only in DIII–D.[309,292] In addition, other phenomena that bear some similarity to standard

ELMs have been identified in DIII–D; in this section a brief mention will be made of the so-called "X event" that often terminates the VH–mode phase of the discharge.

From the point of view of turbulence, all ELMs are invariably accompanied by a burst of fluctuations at a level equal to or, more often, higher than that of L mode. It is clearly of considerable interest to explore whether the characteristics of this turbulence (spectral content, dispersion relation, wave-number spectra, etc.) are also similar to those of the L–mode variety, or to identify any distinguishing features.

A basic difficulty in any statistical analysis of ELM behavior is the short duration of the phenomenon, which results typically in poor statistics. In order to increase the number of statistical samples, a multiple-averaging technique has been adopted for this study; this technique, which was introduced in §3.9, entails carrying out the averages over intervals composed of several discontinuous segments, each of which lies within the lifetime of an ELM. Under the assumption that individual ELMs are characterized by similar spectral properties, this technique increases the number of samples by a factor equal to the number of segments used in the analysis. In all cases, the segments were selected carefully by eliminating all atypical ELMs and, of course, by restricting each estimate to only one class of ELMs and to a single discharge. This technique proved inapplicable to grassy ELMs, owing to their very short duration and complex dynamics, which will be briefly illustrated later in this section. It should also be mentioned that the database for type-III ELMs is considerably smaller than that for type-I ELMs, as it was limited to a single run (one experimental day).

Typical autospectra for type-I and type-III ELMs are shown in Fig. 5.49. The spectrum of type-I ELMs is compared to an L–mode spectrum for the same discharge; no L–mode data were available for comparison with the somewhat more elusive type-III ELMs. The spectral content of type-I ELMs is similar to that of L–mode turbulence, and the two spectra obey similar inverse-square laws: this similarity was confirmed in all the cases examined. The ratio of the absolute values of the spectra, on the other hand, varies considerably from shot to shot, from a factor of 1 to a factor of 20 inside the LCFS. In no case was the ELM autospectral power smaller than its L–mode counterpart; the value of $\sim$10, seen in Fig. 5.49(a), can be considered typical.

The spectrum of type-III ELMs has a broadband component, which is similar in shape and magnitude to the type-I-ELM spectrum, and a narrowband component centered at 96 kHz.[70,325] The latter part is seen in most, but not all, type-III ELMs studied; when examined within a single ELM, this component is found to be in fact completely coherent: the broadening seen in Fig. 5.49(b) is caused by slight variations in freqency from ELM to ELM, by the complete disappearance of the features in some ELMs, and by the smoothing used in the statistical analysis.

It should be noted that the smoothness of the spectra shown in Fig. 5.49 provides implicit validation to the multiple-averaging technique, as it confirms that no large variations in the spectral content occur from ELM to ELM.

The ELM spectrum is found to have little spatial dependence across the range accessed by PCI, including locations deep in the SOL. Since the L–mode fluctuation level is, by contrast, substantially lower in the deep SOL than in the main plasma,

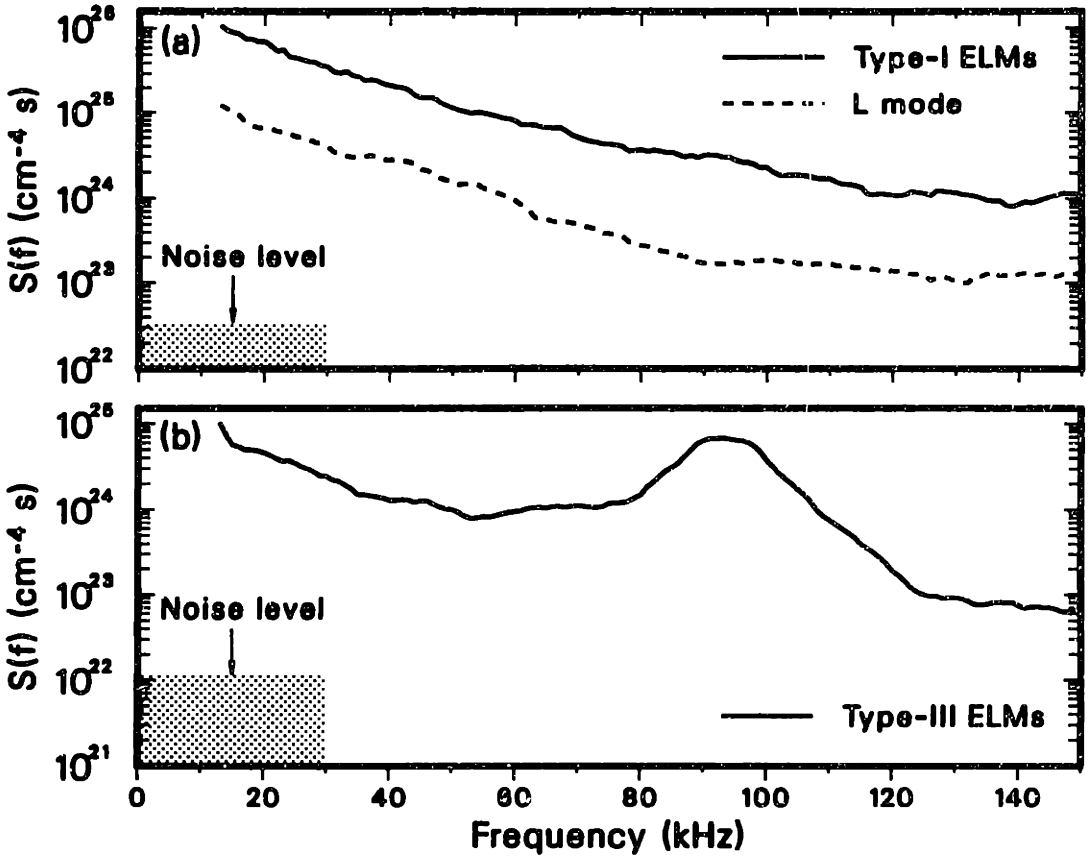

Fig. 5.49 PCI autopower spectra shown on a logarithmic scale for two discharges: (a) comparison of type-I ELMs (solid line) and L mode (dashed line); (b) type-III ELMs. L–mode data were not available for case (b). The spectra are estimated over 10-ms intervals with 10-kHz smoothing; in the case of the ELMs, the intervals are composed of (a) 10 and (b) 19 discontinuous 1-ms intervals coinciding with individual ELMs. Note that the vertical scales are different for the two plots. The location of the PCI chord is (a) 1 cm and (b) 1.7 cm inside the LCFS. The statistical uncertainty is (a) 10% and (b) 7%. The absolute calibration error on the power is (a) 60% and (b) 70%. The spectra in (a) obey approximate power laws $f^{-2.04}$ (type-I ELMs) and $f^{-2.00}$ (L mode), The plasma parameters are (a) B_T=2.16 T, I_p=2.0 MA, $\bar{n}_e$=4.4×10^{13} cm^{-3}, and input power = 6 MW; (c) B_T=2.1 T, I_p=1.0 MA, $\bar{n}_e$=5.5×10^{13} cm^{-3}, and input power = 6.9 MW.

the ratio of the ELM level to the L–mode level becomes generally quite large in the SOL.

The same segmentation technique can be employed also to generate the complete frequency and wave-number spectrum $S(k_R, f)$. Typical examples for type-I and type-III ELMs are shown in Fig. 5.50. Again, both types of spectra (with the exception of the 96-kHz coherent feature for the type-III ELMs) are qualitatively similar to the L–mode spectrum (cf., e.g., Fig. 5.22). In particular, both peak at nonzero wave numbers, both positive and negative. The main differences are a tendency of the ELM spectrum to peak at lower values of k_R (typically in the neighborhood of 1 cm^{-1}) and a slower increase of its peak wave number with frequency. Also, no instances

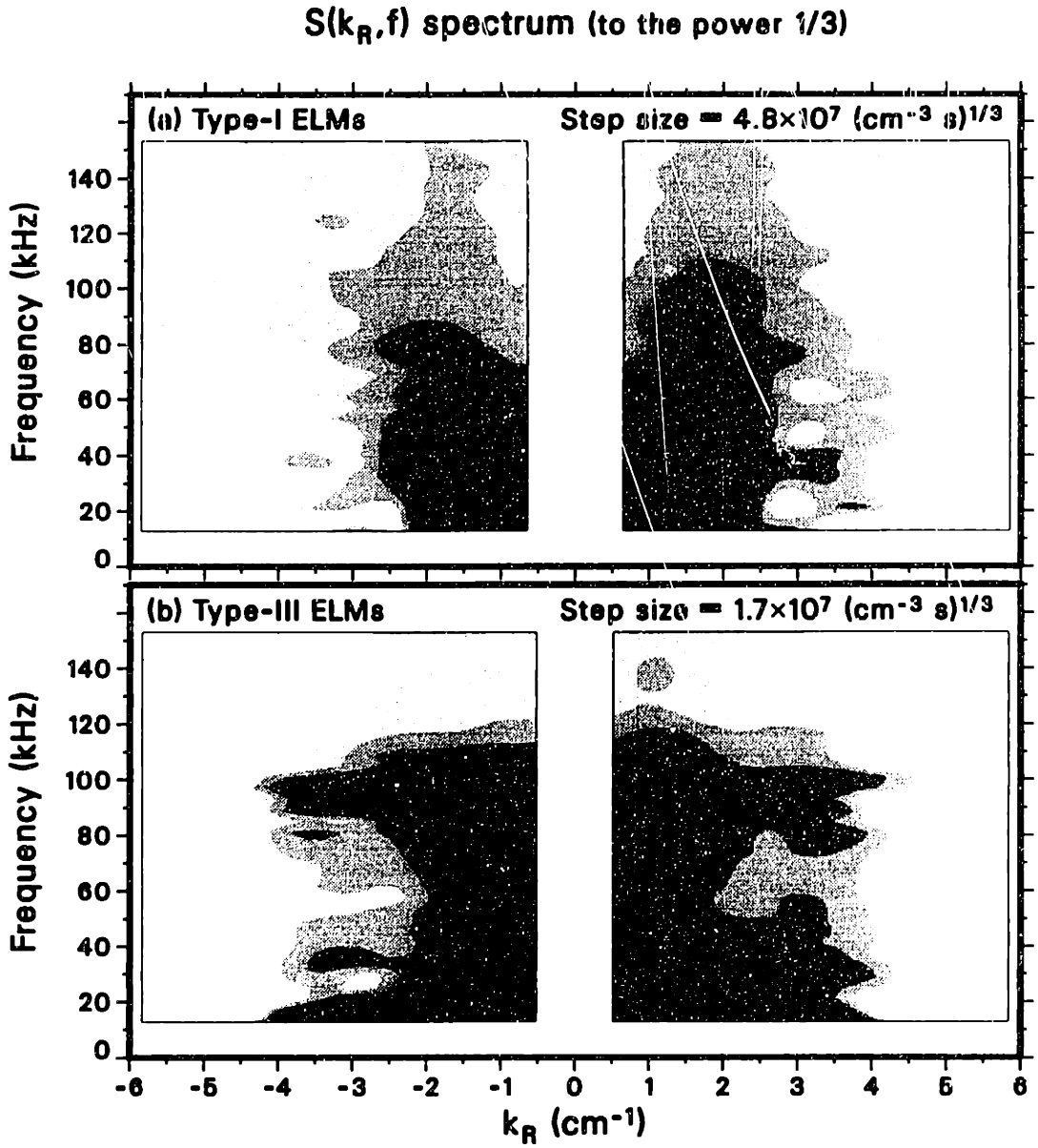

Fig. 5.50 Absolute $S(k, f)$ spectra estimated over multiple (a) type-I ELMs and (b) type-III ELMs by averaging over (a) 10 and (b) 19 separate 1-ms intervals, in the region between the LCFS and 3.5 cm inside [(a)] and 2.3 cm inside [(b)]. The data used are the same as for Fig. 5.49. Units are such that the integral of S over frequencies and wave numbers is the average square line-integrated density (in cm^{-4}). Contours are drawn using the power 1/3 for better spacing; the level is proportional to the intensity. Smoothing was performed over a 10 kHz interval. The plasma parameters are (a) B_T=2.16 T, I_p=2.0 MA, $\bar{n}_e$=4.4×10^{13} cm^{-3}, and input power = 6 MW; (b) B_T=2.1 T, I_p=1.0 MA, $\bar{n}_e$=5.5×10^{13} cm^{-3}, and input power = 6.9 MW.

of predominantly inward propagating spectra have been found during ELMs: net propagation is always outward, although it is nearly balanced in many cases (as in Fig. 5.50); by contrast, both inward and outward propagation have been observed in L mode, as was discussed in §5.5.

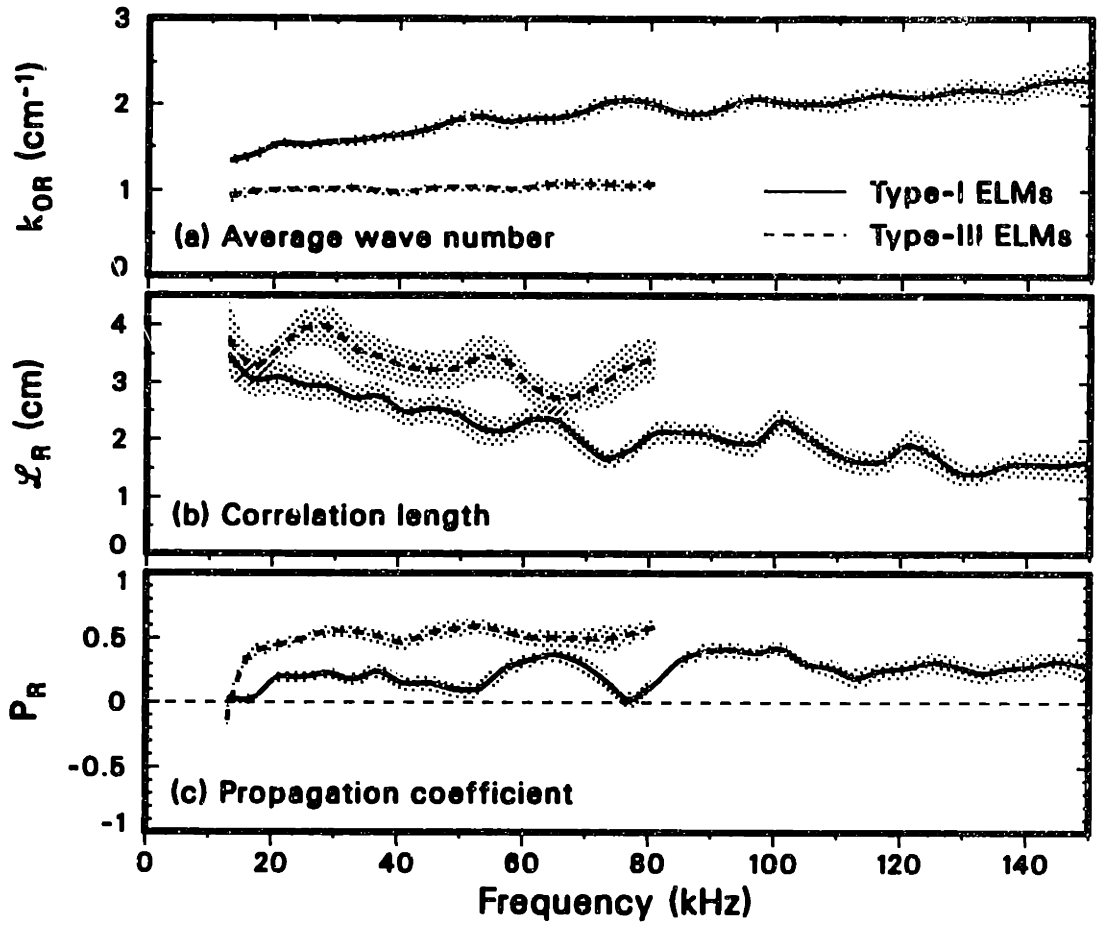

Fig. 5.51 (a) Average wave number (dispersion relation), (b) correlation length, and (c) propagation coefficient as functions of frequency, estimated over multiple ELMs by averaging over 10 separate 1-ms intervals (type-I ELMs, solid lines) and over 19 separate 1-ms intervals (type-III ELMs, dashed lines) in the region between the LCFS and 3.5 cm inside (type-I ELMs) or 2.3 cm inside (type-III ELMs). The data used are the same as for Figs. 5.49 and 5.50. The region above 80 kHz is suppressed for type-III ELMs as coherent activity invalidates the fits. The shaded areas indicate confidence intervals. Smoothing was performed over a 10 kHz interval. The values for the three parameters averaged over the bandwidths shown are k_{0R} = 1.5 cm^{-1}, $\mathcal{L}_R$ = 2.3 cm, and P_R = 0.12 for type-I ELMs, and k_{0R} = 1.0 cm^{-1}, $\mathcal{L}_R$ = 3.1 cm, and P_R = 0.23 for type-III ELMs. The plasma parameters are (a) B_T=2.16 T, I_p=2.0 MA, $\bar{n}_e$=4.4×10^{13} cm^{-3}, and input power = 6 MW; (b) B_T=2.1 T, I_p=1.0 MA, $\bar{n}_e$=5.5×10^{13} cm^{-3}, and input power = 6.9 MW.

These considerations can be visualized more readily by examining the three fitting parameters $k_{0,R}$ (average wave number), $\mathcal{L}_R$ (correlation length), and P_R (propagation coefficient, = -1 for purely inward and = +1 for purely outward propagation), as functions of the frequency. These functions are shown in Fig. 5.51 for the two types of ELMs (the type-III-ELM functions are truncated below the coherent mode, for which the fitting becomes meaningless). This figure should be compared to Figs. 5.19 and 5.20 for L mode.

The weaker dispersion of the ELM turbulence as compared with L-mode fluc-

tuations is evidenced by the slow increase of the $k_{0,R}$ function with frequency for type-I ELMs, and the nearly flat function for type-III ELMs. The behavior of the correlation length is qualitatively similar to the L–mode case, but its absolute value is generally approximately a factor of 2 to 3 larger. Finally, the propagation coefficient is always positive, confirming that net propagation is always outward.

We turn now to the topic of ELM dynamics and of the temporal correlations between the increase in the D_α emission signal, which identifies the ELM experimentally, and the fluctuation enhancement.

A comparison between the PCI rms signal and the D_α signal for a series of type-I ELMs, and for two ELMs in detail, is shown in Fig. 5.52. The detail also shows the evolution of the PCI autopower spectrum, at a location 0.5 cm inside the LCFS, in contour form. Within the resolution of the measurement, as documented in the figure, the peaks in the D_α and fluctuation signals always coincide. However, the D_α signal invariably decays more gradually than the fluctuation signal (inside the main plasma). On the other hand, the fluctuation level often begins to rise dramatically up to 2–3 ms before any change is observed in the emission signal; this "precursor" turbulence is generally observed more prominently further inside the plasma than near the boundary, but has no apparent regularity in time: as clearly demonstrated by Fig. 5.52, precursors may appear before an ELM and not before the next one. A more gradual rise in the turbulence level is seen in the blowup of Fig. 5.52, starting soon after the first ELM and leading to the second one; this activity, however, always appears to match a corrispondent slow rise in the D_α signal.

Whether these precursor fluctuations are the same phenomenon as those measured earlier with reflectometry in DIII-D[69,308] remains an open question. As was discussed in §5.1(d), the reflectometry results documented both narrowband (30–60 kHz) and semicoherent oscillations, for periods of up to 20–30 ms before a single ELM. As shown clearly by Fig. 5.52, PCI has revealed no evidence of nonmonotonic spectra, both in the precursor phase and during the ELM proper; moreover, precursors never appear more than 2–3 ms before the ELM. It is possible, however, that the different spatial locations and spectral ranges of the two measurements may account for the discrepancies, which would then simply reflect different manifestations of the same phenomenon.

PCI measurements of type-I ELMs deep in the SOL, an example of which is shown in Fig. 5.53, reveal a somewhat different phenomenology from that of the main plasma. Each ELM is followed by a series of "echoes", in the form of additional fluctuation bursts; these echoes vary in magnitude from ELM to ELM, and from chord to chord for each ELM, seemingly at random. Also, the amplitude of the bursts may exceed that of the main ELM. Since these echoes appear to be very short-lived, it may be speculated that this variability is due in part to the finite sampling rate: that is, the fluctuation peak may fall between two samples in some cases, and its amplitude would then be underestimated.

It should be noted that the measurement relative to Fig. 5.53 extends to 7.1 cm outside the LCFS; the level of turbulence associated with the ELM there is extremely

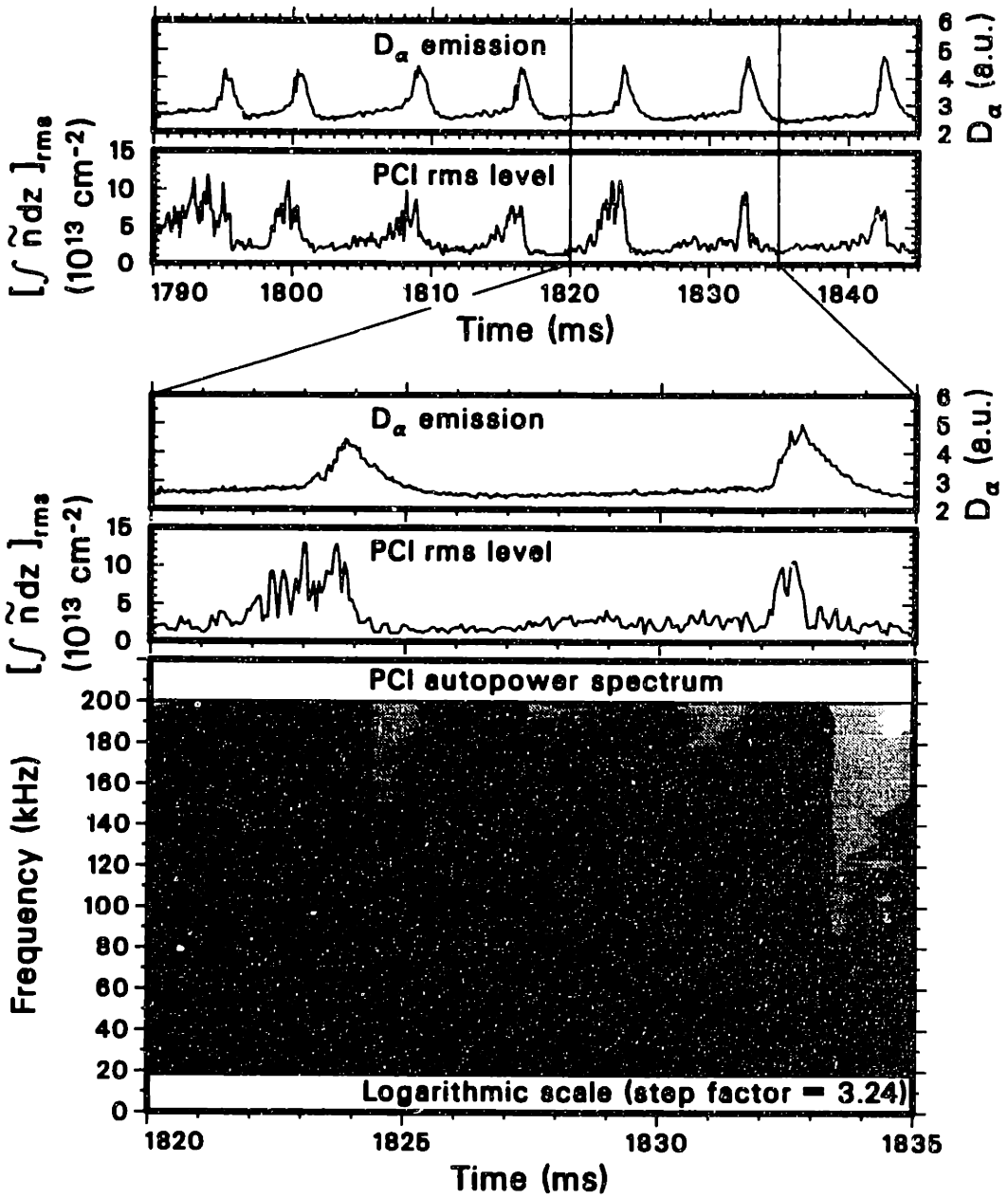

Fig. 5.52 Time traces of the D_α line emission from the divertor and of the PCI rms level (top); blowup of the same traces for two type-I ELMs, and contour plot in logarithmic scale of the time evolution of the PCI autopower spectrum (bottom; the level is proportional to the logarithm of the intensity). Precursor activity is seen before the first ELM in the blowup, but not before the second one. The PCI chord intersects the midplane 0.5 cm inside the LCFS. The statistical error on the rms level is 10%; the absolute amplitude calibration error is 40%. A smoothing interval of 20 kHz was used to estimate the autospectrum, with a statistical uncertainty of 22%. The plasma parameters are B_T=2.1 T, I_p=1.25 MA, $\bar{n}_e$=3.5×10^{13} cm^{-3}, input power = 6.2 MW.

high in comparison with any activity observed in L mode. A peculiar feature of type-I ELMs in the SOL is that the correlation level of the fluctuations is typically larger in

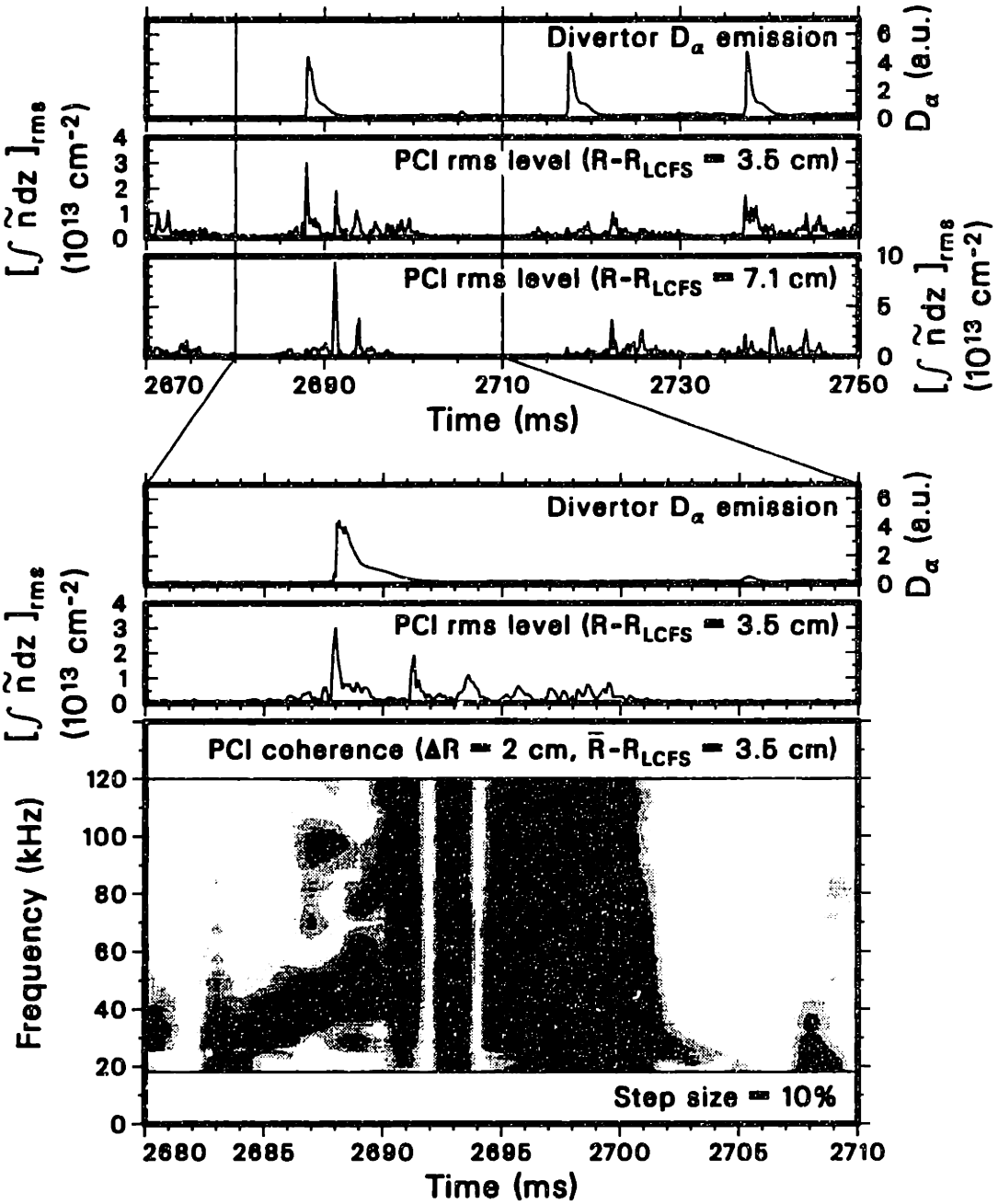

Fig. 5.53 Time traces of the D_α line emission from the divertor and of the PCI rms level at two different SOL locations, 3.5 cm and 7.1 cm outside the LCFS (top; note that the vertical scales for the two signals are different); blowup of one type-I ELM with contour plot of the time evolution of the coherence between two PCI chords 2 cm apart, with the middle point located 3.5 cm outside the LCFS (bottom; the level is proportional to the intensity). The statistical error on the rms level is 7%; the absolute amplitude calibration error is 40%. A smoothing interval of 20 kHz was used to estimate the autospectrum, with a maximum statistical uncertainty of ~12%. The plasma parameters are B_T=2.1 T, I_p=1.4 MA, $\bar{n}_e$=8×10^{13} cm^{-3}, and input power = 5 MW.

the echo phase than during the ELM itself, as shown at the bottom of Fig. 5.53 for

one specific pair of chords. Precursors are also sometimes seen in the SOL but are, as a rule, of more modest amplitude than inside the LCFS.

An examination of the dynamics of type-III ELMs leads to the establishment of a clear and seemingly universal experimental distinction of type-III from type-I ELMs. As shown in the comparison of the D_α emission signal and of the PCI rms signal in Fig. 5.54, in the case of a type-III ELM the fluctuation burst occurs well in advance of the peak in the D_α signal. This delay is always between 0.4 and 0.6 ms. The evolution of the autopower spectrum shows the characteristic monotonically decreasing spectrum with the addition of a coherent high-frequency mode at 80–100 kHz, consistent with Fig. 5.49(b).

The same discharge and time interval shown at the bottom of Fig. 5.54 are used again in Fig. 5.55 to examine the temporal evolution of the coherence between two adjacent chords (0.5 cm apart radially) across one type-III ELM. Like the autopower spectrum, the coherence is also largest 0.4 to 0.6 ms before the D_α peak: indeed, at the time the latter occurs, no significant turbulent activity remains, and usual H–mode conditions are restored.

The turbulent activity associated with type-III ELMs does not display any significant spatial variation, both inside the LCFS and in the SOL.

A different view of the evolution of the autopower spectrum in time is provided by Fig. 5.56(a), which depicts five ELM events in succession. Both the broadband turbulent activity and the high-frequency mode are clearly associated with individual ELMs, and in fact precede them as stated before. Because of the smoothing required by the autopower estimation, the coherent nature of the high-frequency mode is not revealed by this plot. However, Fig. 5.56(b) clearly shows that the radial coherence, calculated at the peak frequency of 96 kHz, is close to one across the PCI range from inside to outside the LCFS. Moreover, the cross-phase increases with radial separation, and is consistent with a coherent, outward-propagating mode with a wavelength of approximately 4.5 cm. The same result is found for all type-III ELMs that contain this mode, although the frequency varies by as much as ± 10 kHz.

However, as was mentioned earlier, not all such ELMs exhibit this mode, and no correlations were found between its onset and any other measurements. In particular, no similar coherent signal is seen in any of the signals from the soft-x-ray diode array; by contrast, normal, non-bursty MHD activity is usually detected by both PCI and the soft-x-ray diodes. Unfortunately, no fast magnetic-flux data were collected during the times of occurrence of these ELMs, rendering a comparison with magnetic measurements impossible.

As was mentioned briefly in §5.1(d), semicoherent (50–70 kHz) precursor oscillations in both density and magnetic field have been documented (with reflectometry and external magnetic coils, respectively) for periods up to 20–30 ms before individual type-III ELMs in DIII–D.[312] During the precursor phase, the mode appears to be moving outward, until it eventually triggers the ELM. It is possible that this mode may coincide with the high-frequency mode measured by PCI; because of its location at the extreme outer edge of the tokamak cross section, PCI can be expected to detect

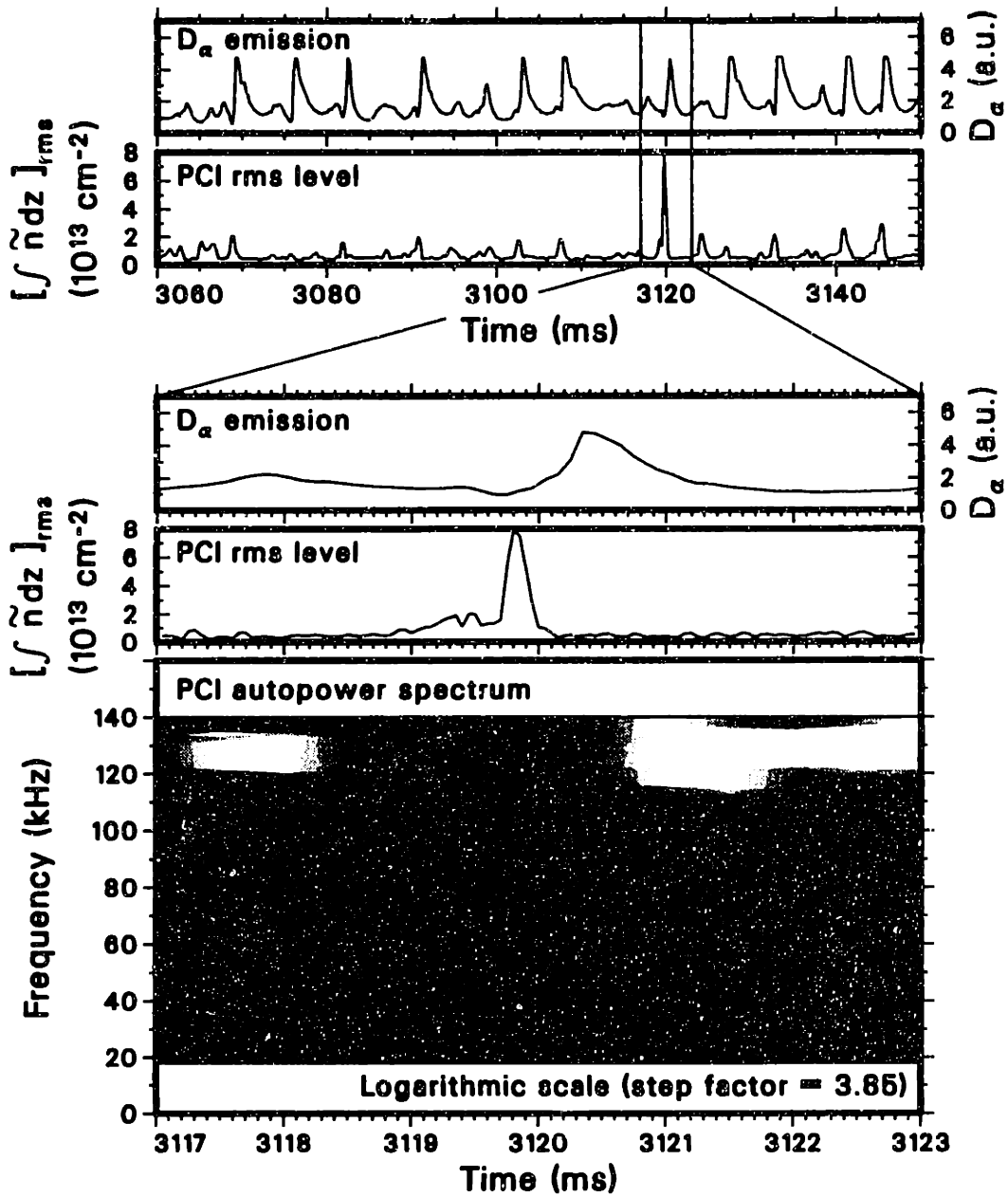

Fig. 5.54 Time traces of the D_α line emission from the divertor and of the PCI rms level (top); blowup of the same traces for one type-III ELM, and contour plot in logarithmic scale of the time evolution of the PCI autopower spectrum (bottom; the level is proportional to the logarithm of the intensity). The PCI chord intersects the midplane 1.7 cm inside the LCFS. The statistical error on the rms level is 10%; the absolute amplitude calibration error is 35%. A smoothing interval of 20 kHz was used to estimate the autospectrum, with a statistical uncertainty of 22%. The discharge is the same as for Fig. 5.49(b). The plasma parameters are B_T=2.1 T, I_p=1.0 MA, $\bar{n}_e$=5.5×10^{13} cm^{-3}, and input power = 6.9 MW.

the mode only in its latest phase, when the broadband turbulence that characterizes the ELM is already in progress (but before the D_α signal begins to rise, as we have seen). The discrepancy in frequency alone does not invalidate this hypothesis, as the

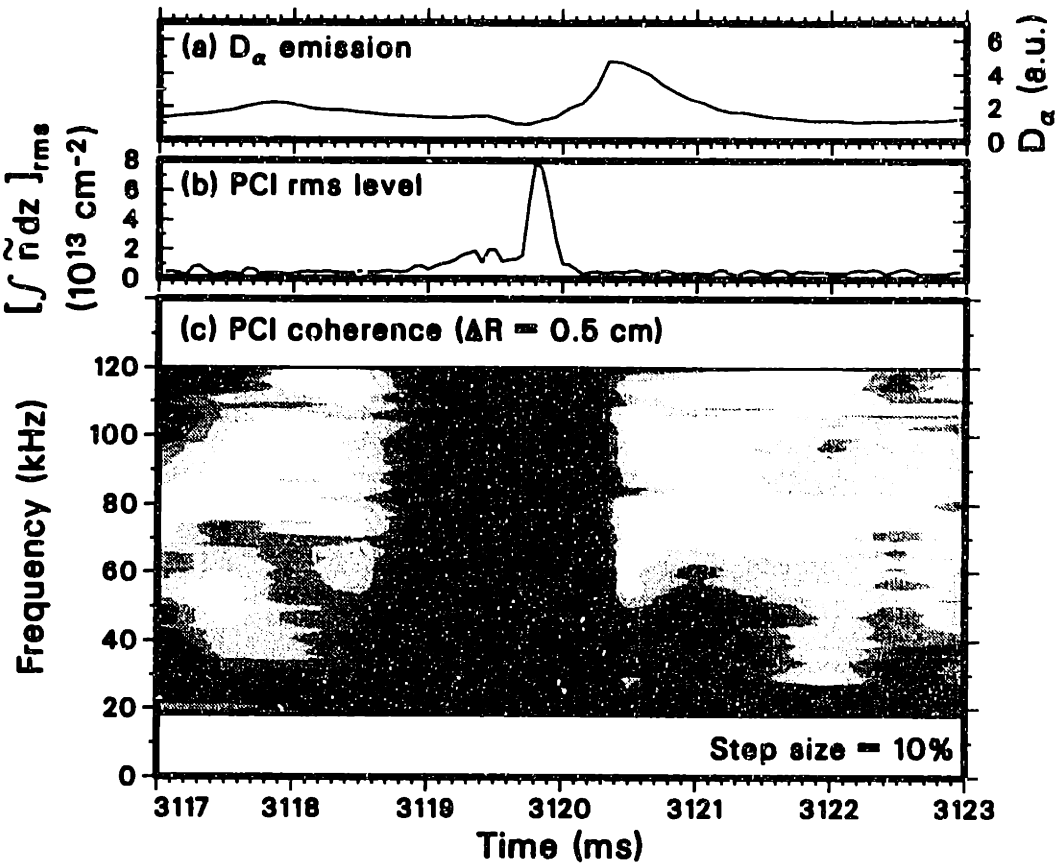

Fig. 5.55 (a) D_α line emission from the divertor, (b) PCI rms level, and (c) contour plot of the time evolution of the coherence between two PCI chords 0.5 cm apart (the level is proportional to the intensity). The PCI measurements are made 1.7 cm inside the LCFS. The statistical error on the rms level is 10%; the absolute amplitude calibration error is 35%. A smoothing interval of 20 kHz was used to estimate the coherence, with a maximum statistical uncertainty of ~12%. The interval shown is the same used at the bottom of Fig. 5.54. The plasma parameters are B_T=2.1 T, I_p=1.0 MA, $\bar{n}_e$=5.5×10^{13} cm^{-3}, and input power = 6.9 MW.

measurements described in §5.1(d) were carried out over two years prior to the PCI measurements, in considerably different plasma conditions.

Type-II, or "grassy", ELMs present qualitatively similar features to the other two types of ELMs from the point of view of edge turbulence; that is, ELM activity is accompanied by an increased and oscillating fluctuation amplitude, as shown in Fig. 5.57. However, the short duration and high repetition rate of type-II ELMs have hampered all efforts to carry out a meaningful statistical analysis with PCI thus far. As shown in the bottom part of Fig. 5.57, the period of the ELMs on the D_α and PCI signals appears similar; peaks in one signal appear to be correlated with valleys in the other, and vice versa. The continuous transition from one ELM to the next, however, makes it difficult to establish whether this is the result of a true anticorrelation or

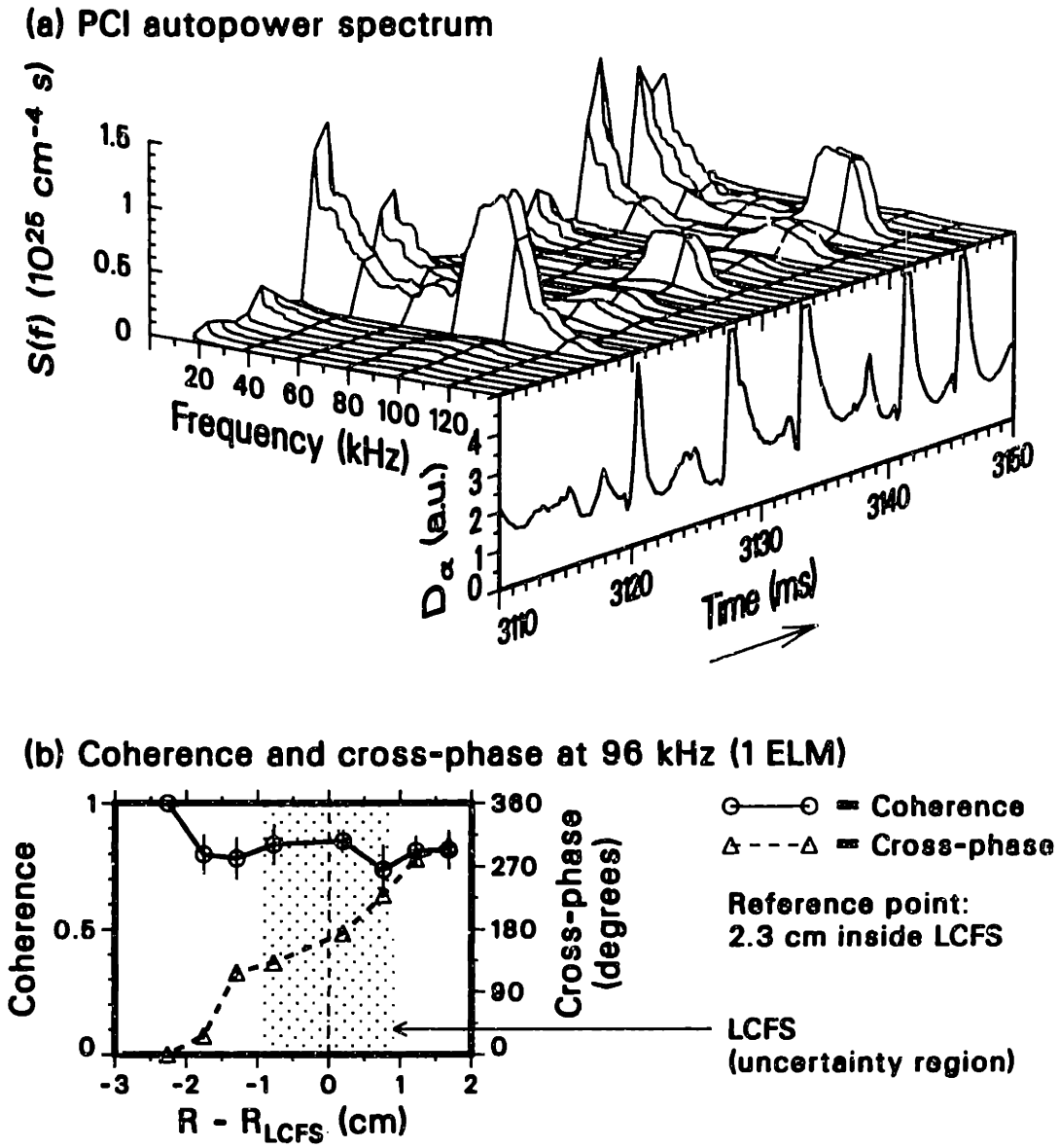

Fig. 5.56 (a) Three-dimensional plot of the evolution in time of the PCI autopower spectrum 1.7 cm inside the LCFS (estimated over a 20-kHz smoothing interval, with a statistical uncertainty of 16%), and time trace of the D_α line emission from the divertor; (b) coherence and cross-phase with respect to a chord located 2.3 cm inside the LCFS, plotted as a function of the distance from the LCFS (with maximum statistical errors of, respectively, 11% and 8°). The positive slope in the phase function indicates outward propagation; a cosine fit to the complex coherency function gives a wavelength of 4.5 cm. The discharge is the same as for Figs. 5.54 and 5.55. The plasma parameters are B_T=2.1 T, I_p=1.0 MA, $\bar{n}_e$=5.5×10^{13} cm^{-3}, and input power = 6.9 MW.

of a delay. Moreover, these observations are only qualitative and are accompanied by sufficient irregularities that a temporal correlation analysis of the two signals has produced no clear results.

To conclude this section, Fig. 5.58 shows an example of an X event signaling the termination of the VH–mode of a discharge. The X event appears as an abnormally

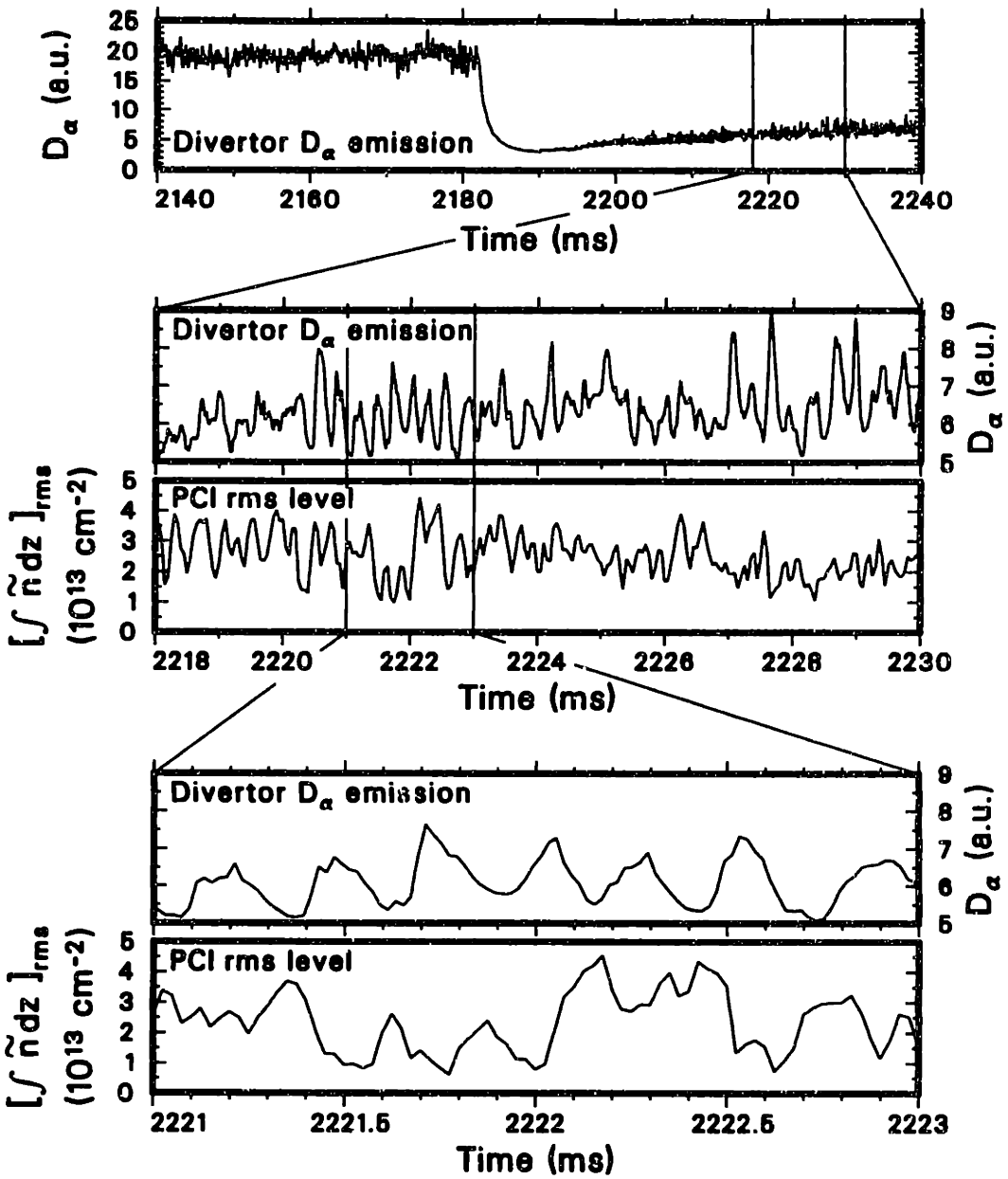

Fig. 5.57 Time trace of the D_α line emission from the divertor, showing an L–H transition and type-II ELMs (top); blowup of the same trace and PCI rms fluctuation level during type-II ELMs (middle); and further blowup of both traces (bottom). The PCI chord intersects the midplane 1.4 cm inside the LCFS. The statistical error on the rms level is 10%; the absolute amplitude calibration error is 40%. The plasma parameters are B_T=2.1 T, I_p=1.35 MA, $\bar{n}_e$=4×10^{13} cm^{-3}, and input power = 5 MW.

large type-I ELM on the D_α signal, and is generally followed by regular ELMing activity. This description also applies to the fluctuation measurements, as seen both in the PCI rms signal and in the PCI autopower spectrum, which are consistent with normal type-I-ELM activity.

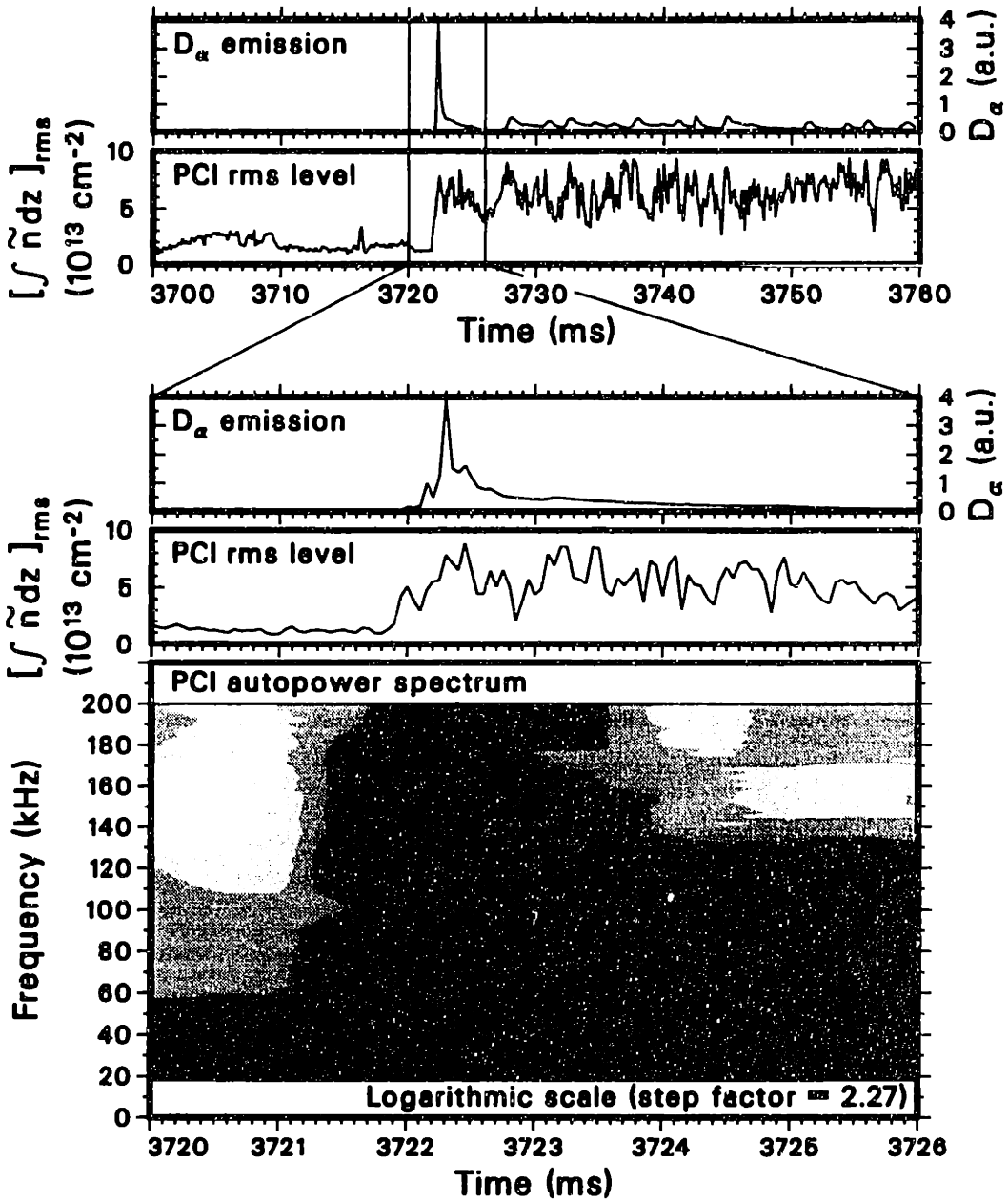

Fig. 5.58 Time traces of the D_α line emission from the divertor and of the PCI rms level (top); blowup of the same traces for an X event, and contour plot in logarithmic scale of the time evolution of the PCI autopower spectrum (bottom; the level is proportional to the logarithm of the intensity). The PCI chord intersects the midplane 1.2 cm inside the LCFS. The statistical error on the rms level is 10%; the absolute amplitude calibration error is 30%. A smoothing interval of 20 kHz was used to estimate the autospectrum, with a statistical uncertainty of 22%. The plasma parameters are B_T=2.16 T, I_p=2.0 MA, $\bar{n}_e$=9×10^{13} cm^{-3}, and input power = 5.5 MW.

5.12 Transient Phenomena

Coherent modes are often detected by PCI. These modes are generally identified as MHD phenomena, and are also detected typically by external magnetic coils and

by soft-x-ray diodes. Owing to the paucity of reports on the density content of MHD activity in the scientific literature, this constitutes a potentially rich area of investigation that is available for future studies with PCI on DIII–D. In the course of the present study, only incidental observations have been made, which will be briefly addressed in this section.

The principal distinguishing feature of MHD phenomena is their temporal coherence, which is reflected in peaked frequency spectra. The bandwidth of these coherent modes, as observed in the PCI autopower spectra, is indeed typically defined by the averaging procedure, rather than by the intrinsic width of the modes. Examples of these modes have already been shown, in Fig. 1.3 and in Fig. 5.48. Figures 5.59(a) and (b) show the coherence spectra of a PCI signal with a signal from a magnetic coil and with a signal from a soft-x-ray diode; large (> 0.8) peaks are clearly seen in both spectra at the frequency of the MHD mode, equal to 23.2 kHz.

The spatial coherence and cross-phase functions for the PCI array, with respect to a fixed reference point, are shown at that frequency in Fig. 5.59(c); it is instructive to contrast this plot with that in Fig. 5.56(b) for the coherent mode accompanying type-III ELMs: whereas the latter displays a continuously varying phase, indicative of a radially propagating wave, in the former the phase jumps abruptly from 0° to 180°, signaling the existence of a standing-wave structure. This structure is even more apparent when the real and imaginary parts of the complex coherency function are plotted [Fig. 5.59(d)]: the wave form is displayed by the real part, while the imaginary part remains close to zero (no propagation). A wavelength of approximately 6 to 8 cm can be estimated from this plot.

Since MHD modes are characterized by a poloidally varying structure, with long poloidal correlation lengths and long poloidal wavelengths (by comparison with the integration length of the PCI beam), which are routinely measured by spatial magnetic-coil arrays, it is easy to interpret the apparent standing-wave structure along the lines of the discussion of §4.4. The poloidal mode will appear to the PCI beam as a radially outward-propagating mode below the midplane and as an inward-propagating mode above the midplane (or vice versa; see, e.g., Fig. 4.10). The sum of the two counter-propagating waves, upon line integration, can be expected to produce the standing-wave pattern observed. In addition, the measured radial wavelength is equal to the poloidal wavelength of the mode divided by the average poloidal angle along the extent of the beam [see, e.g., Eq. (4.62), with the effective radial wave number $k'_{0,R}$ given by Eq. (4.48), and $\mathcal{L}_\theta \gg \mathcal{L}_\rho$]. The measurement shown in Fig. 5.59(d), with the average poloidal angle estimated at 0.15–0.3 radians, gives an estimate of 20–50 cm for the poloidal wavelength of the mode, corresponding to a poloidal quantum number $m \sim$7–20.

In a few instances in the course of this study, semicoherent phenomena have also been observed, only during the H–mode and VH–mode phases of a discharge. These events are in many ways similar to the usual coherent MHD modes, with the exception of their bandwidth, which is finite, i.e. larger than the limit set by the experimental procedure. A clear example is shown in Fig. 5.60 for an H mode evolving into a

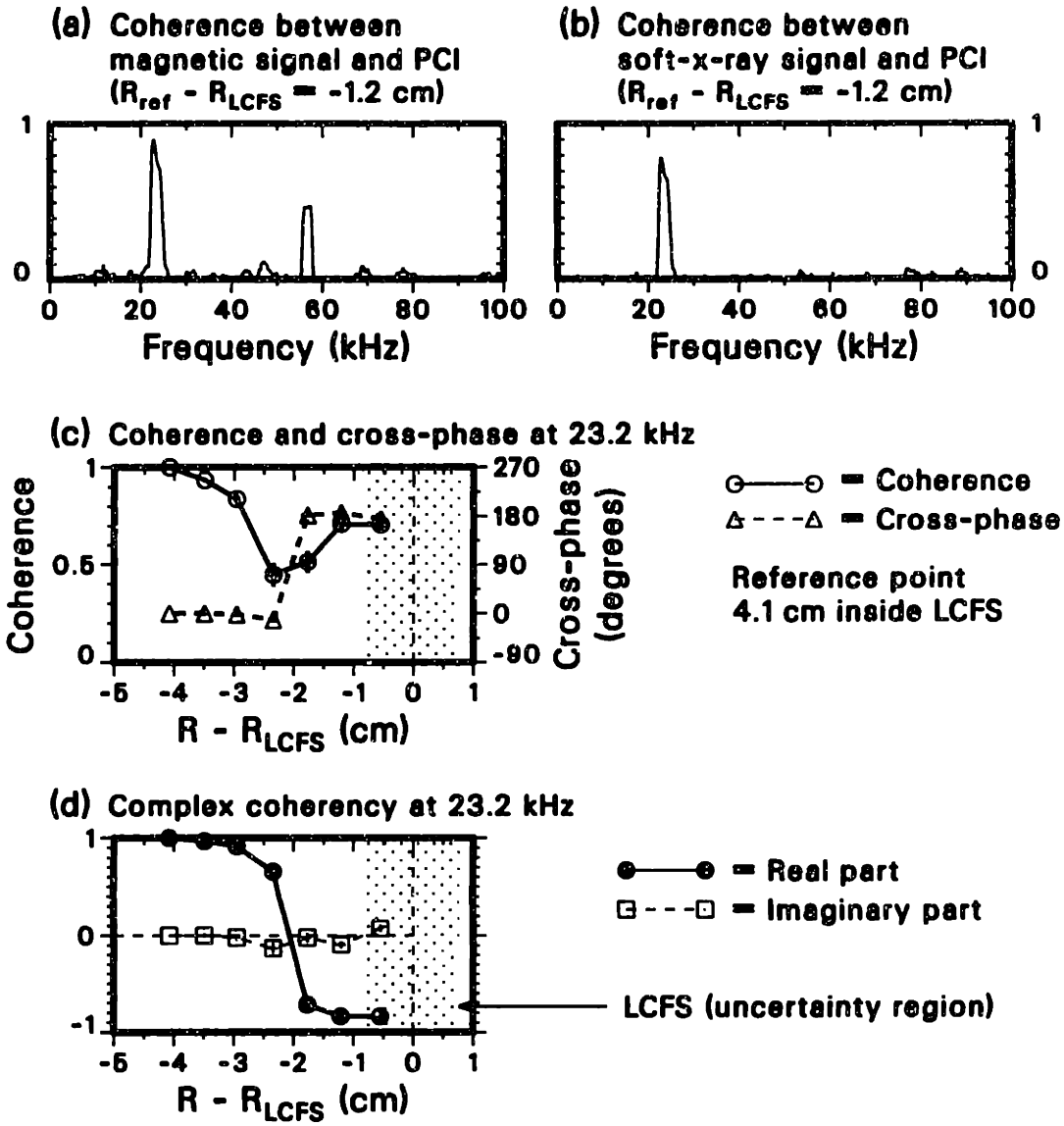

Fig. 5.59 (a) Coherence between signal from magnetic loop and PCI signal; (b) coherence between signal from soft-x-ray diode and PCI signal (the PCI location is 1.2 cm inside the LCFS); (c) coherence and cross-phase between PCI chords, with the reference point located 4.1 inside the LCFS; (d) real and imaginary parts of PCI coherency with respect to the same reference chord. The maximum statistical uncertainty is 6% for the coherence estimates, 3% for the coherency, and 6° for the cross-phase. The plasma parameters are B_T=2.16 T, I_p=2.0 MA, $\bar{n}_e$=9×10^{13} cm^{-3}, and input power = 5.5 MW.

VH mode; the large bursts of fluctuations seen in the PCI autopower spectrum are characterized by a bandwidth of approximately 10 kHz, while the smoothing interval in this estimate is 2 kHz.

These phenomena are also seen by the soft-x-ray diodes and by the magnetic loops and are thus also identified tentatively as MHD events. Their spatial structure is similar to that of the more coherent modes, and a large (>50%) level of coherence

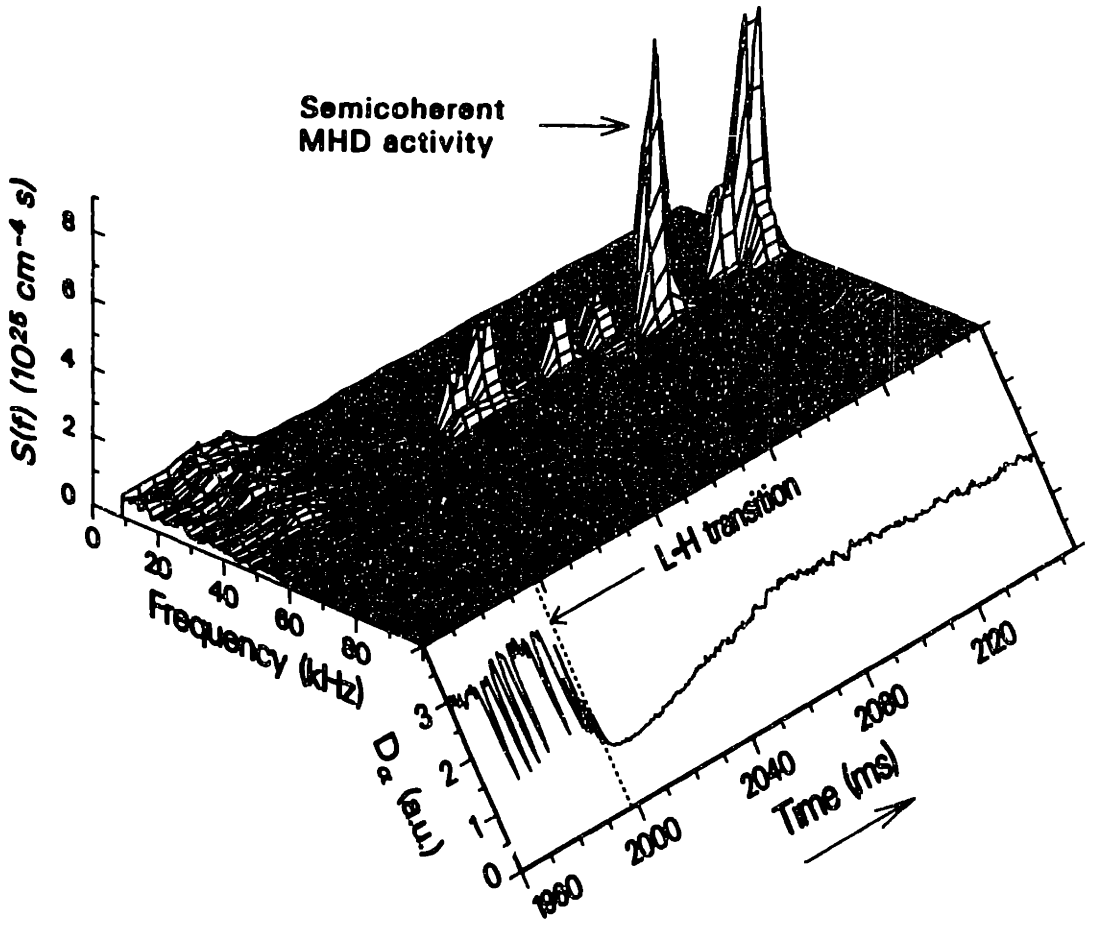

Fig. 5.60 Three-dimensional plot of the time history of the PCI autopower spectrum on a chord located 0.4 cm inside the LCFS, and time trace of the D_α line emission from the divertor. A smoothing interval of 2 kHz was used to estimate the autospectrum, with a statistical uncertainty of 22%. The absolute calibration error on the power is 45%. The plasma parameters are B_T=2.16 T, I_p=1.65 MA, $\bar{n}_e$=4.5×10^{13} cm^{-3}, and input power = 14 MW.

is observed between the PCI signals and both the magnetic and soft-x-ray signals.

As a final remark, it is worth mentioning one additional transient event that deserves further study with the PCI system: the sawtooth instability. In some cases, sawtooth crashes are accompanied by small bursts of broadband fluctuations, similar in aspect to ELMs. No systematic analysis of these events has been carried out thus far.

5.13 Concluding Remarks

A rich phenomenology of edge tokamak turbulence has been described in this chapter. The PCI system, owing to its unique properties and to its optimal location at the extreme outer edge of the DIII–D tokamak, has permitted the identification of several novel properties of the density fluctuations in that region, in a variety of plasma conditions and operating regimes. As a well-tested and mature diagnostic technique, the DIII–D PCI apparatus clearly holds great promise for future plasma physics studies, as new regimes are being explored and new theoretical advancements pose continuous challenges to experimental measurements. The results described in this chapter will be analyzed and discussed in Chapter 6.

Attempts have also been made at employing the PCI system to detect radio-frequency (rf) activity, both from externally launched waves and from secondary modes nonlinearly generated by them (parametric instabilities[80]). The present location of the PCI system is not suited to these measurements, since the waves in that region are expected to have radial wave numbers below the PCI cutoff point or poloidal structures that would cause cancellation upon vertical integration. Indeed, no detection has been possible above the noise limit, which in the case of directly launched waves was determined by direct pickup from the rf transmitter. Mechanical choppers were employed in an attempt to shift the detection frequency away from that of the source, but electronic feedthrough in the data-acquisition rf mixers still kept the noise limit well above the intrinsic detector noise.

Plans have been advanced for extending the PCI measurement to an inner location better suited to this type of study, as will be discussed in §7.4; also, in §7.1 we shall present an optically heterodyne version of PCI that can be used to circumvent the rf pickup problems mentioned above.

6 Discussion of Experimental Results

It is a good morning exercise for a research scientist to discard a pet hypothesis every day before breakfast. It keeps him young.

Konrad Lorenz, *On aggression.*

Turbulence remains one of the great unsolved problems of macroscopic classical physics, and continues to pose challenges surely as baffling as those of the post-Newtonian frontiers of physics that have been the main focus of scientific exploration in the twentieth century. The basic underlying equations, as well as some of the essential statistical tools, have been known for over a century; yet, over a hundred years after the first speculations by Lord Kelvin[326] and Reynolds[327] on the concept of eddy viscosity and over fifty years after the first attempt by Kolmogorov[205] to predict the properties of fully developed turbulence (and, one might add, five centuries after Leonardo da Vinci's pioneering observations of intermittency in fluids), the analytical approach to turbulence remains beset with prohibitive difficulties.

This is true even in the prototypical, and simplest, case of incompressible fluids, which are described by the well-known Navier-Stokes equation.[328] In spite of its outward simplicity, this equation may well contain all of turbulence,[206] including the transition to fully chaotic behavior observed at high Reynolds number. In a plasma, the addition of electromagnetic forces between charged particles to the pressure-gradient and viscous forces clearly complicates the problem even further. New degrees of freedom are introduced by the collective plasma motion: the nonlinear interaction between eddies in fluids is then augmented by the interaction between the fundamental plasma oscillation modes, and between these and the eddies.

In view of these difficulties, it is perhaps not surprising that many of the basic tenets of turbulence theory can still be legitimately criticized on a conceptual level. For example, there is no theorem yet proving the existence and uniqueness of the solution to the Navier-Stokes equation in three dimensions;[206] these fundamental properties, therefore, are strictly only conjectures. The same can be said about the nature of the averages that are involved in turbulence theory. Indeed, it may be argued that "[i]t is not meaningful to talk of the properties of a turbulent flow independently of the physical situation in which it arises. In searching for a theory of turbulence, perhaps we are looking for a chimera." (P.G. Saffman).[329] It is certainly true that any significant advances in turbulence must still rely primarily on experimental and computational efforts.

It is against this daunting backdrop that plasma physicists are attempting to shed light on some of the properties of plasma turbulence, particularly in experiments not especially designed for these studies, such as thermonuclear plasma devices, where turbulence, however, plays a fundamental role in determining the outcome of the experiment. In this chapter an attempt will be made to organize the results of

the studies that were described in the previous chapter, performed with the Phase-Contrast Imaging (PCI) system on the DIII–D tokamak, in the light of their relation with theory; it will be shown that, in spite of the difficulties, significant new understanding is emerging with direct relevance to the key problems of transport and confinement in tokamaks. It must be stressed, however, that many of the key results of this work are of a phenomenological nature.

An important property of the PCI measurements deserves mention here. As was proven and discussed at length in Chapters 4 and 5, this apparatus is sensitive to plasma density modes whose wave vectors are primarily oriented in the radial direction. Under the generally accepted assumption that edge turbulence is chiefly electrostatic, the effect of fluctuations on transport is to cause a drift of the charged particles in the $\mathbf{E} \times \mathbf{B}$ direction [see §5.1(b)]. Since the linearized perturbed electric field $\tilde{\mathbf{E}} = -i\mathbf{k}\tilde{\phi}$ is radially oriented for radial wave vectors, the $\mathbf{E} \times \mathbf{B}$ direction is essentially poloidal. It follows that radial electrostatic modes do not cause any direct loss of particles or energy through cross-field transport.

Thus, a fundamental question is: what is the relevance of radial modes to transport and to turbulence studies in general? The answer is twofold: radial modes may interact nonlinearly with modes that do cause transport and thus affect it indirectly; also, in a strong-turbulence scenario, any subclass of modes may be employed to explore the general properties of turbulence, such as spectra, correlation lengths, amplitudes, etc.. These two considerations will guide the exposition of the analysis in the remainder of Chapter 6.

This chapter is structured as follows. In §6.1 a brief introduction to the current state of the theory of turbulence in tokamaks is offered, with particular emphasis on turbulence at the edge and on its relevance to the L–H transition and to Edge Localized Modes (ELMs). Sections 6.2–6.4 address issues that are specific to the radial modes measured by PCI: §6.2 in particular explores the relation between our measurements and theoretical and numerical studies of the nonlinear generation of radial modes by poloidally propagating fluctuations of the drift-wave type; it will be shown that our observations are consistent with theoretical predictions and that the radial modes are in fact extremely important in controlling and regulating transport. Section 6.3 deals with the possible relation of radial structures observed across the plasma boundary with convective cells, while §6.4 addresses the radial correlation structure in the scrape-off layer (SOL).

The remainder of the chapter is devoted to the general properties of turbulence. Observations pertaining to the frequency and temporal domains, to the space and wave-vector domains, and to the amplitude of the fluctuations are compared with theory in §§6.5, 6.6, and 6.7, respectively. The theory of self-organized criticality and related ideas are examined in §6.8 in the light of PCI measurements. A comparison of the estimated turbulent diffusivities with the experimentally measured values is carried out in §6.9. In §6.10 a detailed discussion of theories of the L–H transition, accompanied by new tests of key predictions made possible by PCI, is presented. The topic of "slow" transitions is examined separately in §6.11. ELMs are the main

subject of §6.12, which investigates the significance of the results shown in the previous chapter in relation with recent theoretical work; some further thoughts on MHD and other transient phenomena are also offered. Brief concluding remarks are given in §6.13.

6.1 Review of Some Aspects of Tokamak Turbulence Theory

(a) Plasma Instabilities

A confined plasma is, by definition, not in thermodynamic equilibrium.[91] Thus, it attempts to evolve towards equilibrium by destroying confinement, e.g., in the most obvious way, by expanding towards the confining walls. The deviations from equilibrium are sources of free energy for instability; three fundamental such deviations can be identified:[221] the non-uniformity of density and temperature, which contains expansion free energy; the possible non-Maxwellian nature of the velocity distribution function, which is associated with velocity-space free energy; and the plasma diamagnetism, i.e. the difference between the plasma and vacuum magnetic fields, which is a source of magnetic free energy.

In a closed system such as a tokamak,[1] the velocity distribution is generally close to equilibrium, and the main sources of instability are the expansion and magnetic free energy. In particular, the conservation constraints in a closed system result in a competition between two principal destabilizing effects, the tendency of the plasma to expand to regions of lower magnetic field and the *kinking* of a plasma column to reduce the magnetic free energy, and two stabilizing effects, a strong longitudinal magnetic field (which tends to resist the kinking) and magnetic shear, that is, a variation in space of the direction of the field lines.

Rosenbluth and Rutherford[221] have provided a useful and insightful classification of instabilities in closed systems on the basis of the dynamics of electrons in the direction parallel to the magnetic field. If one writes the fluid equation of motion of the electrons along the field,

$$m_e \frac{dv_\parallel}{dt} = -eE_\parallel - m_e \nu_{ei} v_\parallel - \frac{\nabla_\parallel p_e}{n_e}, \tag{6.1}$$

where $\mathbf{E}$ is the electric field, ν_{ei} is the electron-ion collision frequency, p_e is the electron pressure, and n_e is the electron density, each term in the right-hand side of the equation can be associated with a broad class of instabilities: the electric-field term with ideal MHD, the drag term with resistive MHD, and the pressure-gradient term with microinstabilities. The left-hand inertia term may usually be neglected.

Because of their considerable virulence, ideal MHD instabilities were the subject of some of the earliest work in thermonuclear fusion. Part of the success of the tokamak configuration may be ascribed to its favorable MHD-stability properties. The theory is now well understood, and the operational limits dictated by the need for MHD stability are well known. In particular, external kink modes are stabilized by a

sufficiently large safety factor q at the edge,[330] and by a sufficiently peaked and narrow current profile;[2] internal kink modes are found to be stable at low values of β (the ratio of plasma pressure to magnetic pressure) and in general pose no significant threat to confinement in tokamaks. Pressure-gradient-driven modes, whether of the internal interchange (flutelike, with $k_{\|} \sim 0$) or ballooning[331] (localized to the exterior of the torus) type, are stabilized by a combination of magnetic shear, curvature, elongation, and low β:[191] numerical work performed in the late 70's and early 80's[332] has provided very detailed predictions for the maximum β attainable in a given configuration, which have been widely verified experimentally.

In a finite resistivity plasma, magnetic flux tubes are allowed to diffuse across the fluid, and symmetry-breaking may ensue, causing changes in the magnetic-line topology ("magnetic reconnection") and the formation of magnetic islands.[2] The so-called tearing-mode instabilities that originate from this free-energy source grow more slowly (in the ms range) than ideal MHD instabilities: thus, the plasma may adjust and recover from the onset of such an instability, as in the case of the "sawtooth" crash that occurs when the safety factor falls below 1 on the magnetic axis. In other cases, such as that of the disruptive instability, resistive MHD modes may cause the termination of the discharge.[2] In addition to tearing modes, resistive equivalents of pressure-gradient-driven MHD modes may also occur in a tokamak: resistive interchange instabilites are generally stable when the safety factor on axis is larger than 1,[221] whereas resistive ballooning modes may contribute to the observed high levels of broadband turbulence at the edge of the plasma.

Microinstabilities are fine-scale instabilities that draw their free energy from inhomogeneities in the plasma pressure. Since the geometrical details of the configuration are accordingly less important than in the case of large-scale modes, much of the early work in the linear theory of microinstabilities was carried out in simplified slab geometries, which have allowed a comprehensive analytical treatment to be developed. Over the years, both toroidal and nonlinear effects have been added to the basic theory, generating increasingly involved stability criteria, which in most cases rely crucially on complex numerical work. Electron drift waves, with or without the important added effects of particles trapped by the inhomogeneity in the magnetic field due to toroidal geometry, are believed to be a significant contributor to the observed turbulence, particularly at the edge;[10] in particular, the so-called ion-temperature-gradient (ITG), or ion-mixing, mode,[333–335] resulting from a coupling of ion drift and sound waves,[336] is currently the focus of intensive research both theoretical and experimental, and will recur throughout this chapter.

(b) Plasma Turbulence

The electromagnetic forces between charged particles and the ensuing excitation of collective modes set plasmas apart from ordinary fluids, whose turbulent dynamics are dominated by interactions between eddies with no intrinsic characteristic frequency.[186] Thus, a treatment of turbulence in plasmas must differ from that in

fluids not only because of the added complication of a larger number of degrees of freedom, but also in a purely qualitative sense. Nevertheless, some of the methodology developed in nearly a century of research in fluid turbulence has found applicability in plasma turbulence theory as well.

In some cases, the similarities are only of a mathematical nature, while the underlying physics can be very different. For instance, scaling laws for the wave-number spectra, similar to the celebrated Kolmogorov scaling for fluids,[205] have been found for specific types of waves in plasmas.[337] However, these laws are by no means general, and in fact the basic tenets of Kolmogorov's theory (scale invariance and energy cascade to small scales[207]) are not readily applicable to plasma turbulence at large: in particular, certain nonlinear couplings in plasma interactions support an inverse cascade of energy to large scales.[338]

It is worth mentioning that the limitations of Kolmogorov's theory for fluids themselves are the object of much current research also. Consider the following. A central assumption of the theory is *self-similarity* of the velocity field at inertial-range scales: that is, the statistical properties of the field are independent of the time window over which it is sampled.[206] In a self-similar flow, certain scaling laws apply to structure functions of all orders (the structure function of order p is defined as the average of the pth power of the velocity increment over a given distance). While these scaling laws are well satisfied for the low orders, increasing departures from their predictions are observed at $p \geq 4$. This indicates that the flows are increasingly non-self-similar (or *intermittent*) at the smaller scales within the inertial range, in partial violation of Kolmogorov's theory.[207]

Since the nonlinear dynamics of a plasma are dominated by wave-wave and wave-particle interactions, perturbative approaches can be adopted when those interactions can be assumed to be weak. The simplest such approximation is quasilinear theory, in which only the reaction of the oscillations on the average velocity distribution is considered.[337] Unfortunately, direct interactions between the oscillating modes begin to play a considerable role at fairly small fluctuation amplitudes, rendering such an approximation applicable only under very narrow conditions.[187]

The natural next step is to consider only the lowest-order interactions, that is, three-wave scattering and scattering of a wave by a particle (nonlinear Compton scattering):[186] this is the *weak-turbulence* approximation. In general, this expansion requires that the growth time of the perturbations be considerably large than the characteristic time of conservation of the relative phases of the different waves.[187] The weak-turbulence theory has been completely developed analytically,[339,340] in analogy with the theory of phonon-phonon interactions in solids.[341] However, its applicability has proven very limited, both in its predictive ability[221,10] and from a conceptual point of view, as the lowest-order and higher-order (four-wave, etc.) interactions are in fact in many cases of comparable strength.

Under these *strong-turbulence* conditions, perturbative approaches cannot be employed directly. It is particularly in the treatment of strong turbulence that plasma theory has benefited considerably from methods developed in fluid turbulence theory.

It must be stressed, however, that these methods have found only limited applicability, owing to the enormous analytical difficulties that they face and to the untested assumptions that they are often forced to employ.[342,343] Such assumptions are necessary, for instance, to achieve closure in renormalization schemes[344] and particularly in Kraichnan's Direct Interaction Approximation (DIA) theory.[345]

In recent years, thanks to advancements in massively parallel supercomputers, considerable progress has been made in simulating strong turbulence and related transport with numerical codes.[199] A variety of gyrokinetic[346–350] and gyrofluid[351–353] codes are now in existence, and have recently generated results in remarkably good agreement with experiment,[199] owing in no small part to the development of ingenious new solution techniques.[354–356] Results from some of these codes will be discussed in some detail in comparison with our measurements in the next section.

(c) Edge Tokamak Instabilities

The steep gradients present at the edge of a tokamak are fertile terrain for instabilities of the drift-wave type. Indeed, one branch of this mode, the collisionless or "universal" instability, was predicted early on[2] to be always unstable and to eventually provide the ultimate limit to confinement in a tokamak. Two other main branches exist, the dissipative drift wave (destabilized by finite collisionality) and the trapped-electron mode. The history of drift-wave theory is characterized by the progressive addition of increasingly realistic conditions (magnetic shear, toroidicity, etc.), resulting alternately in predictions of stability or instability.[10] When full toroidal effects are included, it is now generally expected that some of the modes will be unstable, the trapped-electron branch being probably the most relevant one at the edge.[197]

The linear theory of the ITG mode was developed analytically in the 1960's.[333–335] The mode results from a coupling of ion acoustic waves with the ion-pressure gradient, which causes a negative-compressibility instability.[336] The ITG mode was later proposed as a possible explanation of the observed inward density pinch,[357] The stability criterion for this mode is given in terms of the parameter η_i, the ratio of the ion-density-gradient length to the ion-temperature-gradient length. In the linear theory, ITG modes are predicted to be unstable for $\eta_i > 2/3$ for collisional plasmas and for $\eta_i > 2$ for collisionless plasmas (in this context, a plasma is considered collisionless when the mean free path from ion-ion collisions is long compared to the parallel wavelength).

ITG modes have long been suspected to be the chief agents in the confinement degradation that occurs in the presence of auxiliary heating (L mode), which causes large temperature gradients in general. The physics of the ITG instability is therefore used in many cases as the starting point for numerical studies of tokamak turbulence,[351,353] although trapped-electron modes have also recently been added to these codes.[356] As mentioned in the previous subsection, these studies have recently succeeded in reproducing several features of the experimental measurements, including spectral distributions, fluctuation amplitudes, and the ballooning character

of the turbulence. However, because of the strong turbulence that develops, efforts to identify any mode conclusively on the basis of experimental measurements alone have generally been unsuccessful. Thus, it will be essential to repeat these numerical studies in the future with different instability drives, with the aim of identifying distinguishing features of the different types of turbulence.

Trapped-ion modes, which may be associated with both ion and electron drift waves,[10] have been considered a good candidate for core turbulence[197] but are generally less relevant at the edge. In particular, low-frequency, nondispersive structures known as convective cells, similar to the Rayleigh-Bénard cells found in ordinary fluids heated from below in a gravitational field,[358] may be generated nonlinearly by trapped-ion modes[359,360] and can provide an efficient means of radial transport in the core. Convective cells can also appear as byproducts of a variety of other modes,[361] including ordinary drift waves and MHD instabilities, and can thus be important at the edge also,[10,358] as will be discussed in §5.3.

The large flow shear often predicted and experimentally observed at the tokamak edge, particularly in the SOL, may excite the fluid Kelvin-Helmholtz instability[63] and the parallel-ion-flow-gradient instability.[362,363] In general, the latter is more robust and goes unstable more easily;[364] in addition, the Kelvin-Helmholtz instability is stabilized by magnetic shear.[61] Recent detailed numerical studies of these instabilities with three-dimensional codes have yielded the intriguing and unconventional conjecture that their dynamics in the SOL may have a crucial role in causing the L–H transition.[365,366] We shall return briefly to these modes in connection with PCI measurements in the SOL in §6.11.

Other instability drives that are peculiar to the physics of the SOL are radiation-ionization and atomic-physics drives,[367] which may also excite drift waves and parallel-ion-flow-gradient instabilities.[368,369] Turbulence in the SOL can thus be expected to be substantially different from that in the main plasma.

Resistive MHD physics may also be at play in the edge of the plasma. Owing to its relative tractability, the resistive interchange instability[370] has been used as the basis for many nonlinear computer simulations of turbulence,[371–374] but it is not expected to be of great significance in the edge plasma region. However, resistive interchange modes may be unstable in the open field lines of the SOL;[367] the sheared flows that occur in H mode are expected to be a stabilizing force.[375]

In the plasma edge, resistive ballooning modes are often cited as the dominant instability along with ITG and trapped-electron modes.[36] In fact, recent three-dimensional computational studies of resistive-ballooning and ITG physics in a fluid plasma model have revealed considerable similarities in their excitation mechanisms.[376] Resistive-ballooning convective cells form the basis of one of the most recent among several models of the physics of the L–H transition, which is also able to reproduce the ELM instability.[377]

The rippling mode,[378] a resistive MHD instability excited by the parallel current in the presence of a temperature gradient,[10] has generally been excluded as a significant mechanism at the edge because it lacks the universality needed to explain

turbulence in all tokamaks[379] and because its typical wavelengths are too short in comparison with experimental values.[198]

Finally, as was discussed in §5.1(b), tearing modes are commonly believed to influence transport only in the core.[245,260] The short-poloidal-wavelength regio.. of the spectrum (microtearing modes) had been hypothesized to be a significant component of edge turbulence also, in view of its presumed stabilization by flow shear, such as is found in the low-turbulence H-mode regime;[380] however, a detailed analysis has shown no such stabilization to occur.[299]

(d) Turbulent Transport

The difficulties encountered in analytical treatments of strong turbulence are reflected and amplified in the task of calculating the anomalous diffusivity that it causes. In fact, the two approaches employed almost universally in estimating transport are, respectively, phenomenological and heuristic, rather than analytical.

The phenomenological approach[381] adopts the following argument. Since the linear growth rate for many modes is smaller at long wavelengths, small-scale turbulence tends to grow first; large-scale modes can then be seen as an additional inhomogeneity of the background plasma and act as an added driving force for the small-scale instabilities. Hence, energy flows to small scales, where it is damped by viscosity and Landau damping; if it is assumed that damping is of a diffusive nature and that turbulence is fully chaotic and thus isotropic, the marginality condition requires that the damping rate $Dk_\perp^2$ (where D is the diffusion coefficient) be equal to the linear growth rate γ, *at the smallest unstable* $k_\perp$. Therefore, one can conclude that[187,221,197]

$$D \sim \frac{\gamma}{k_\perp^2}. \tag{6.2}$$

The heuristic approach,[187] grounded in the concepts of strong (electrostatic) turbulence, associates a density fluctuation $\tilde{n}$ to a fluid displacement $\tilde{\xi} = L_n\tilde{n}/n$, where L_n is the density-gradient scale length. The time-averaged particle flux can then be written as $\Gamma = \gamma\tilde{n}\tilde{\xi}$. A *mixing-length* argument, similar to the time-honored ansatz used in fluid turbulence to describe eddy viscosity,[234] is then employed to relate the saturated fluid displacement to the radial correlation length, by writing $\tilde{\xi} = L_c$. By virtue of the relation $D = \Gamma L_n/n$, one then finds

$$D = \left[\gamma L_c^2\right]_{\max}. \tag{6.3}$$

Thus, in this scenario a similar relation to Eq. (6.2) is obtained, with $k_\perp$ replaced by $1/L_c$, the width of the wave-number spectrum. To the extent that any analytical approach to strong turbulence has been worked out,[382,52] similar scaling relations have been found.[221] Equation (6.3) can also be obtained on dimensional grounds in a simple random-walk model of diffusive transport.

Using simple arguments on the ordering of the coupling coefficients in three-wave interactions, Kadomtsev[187] has shown that in weak-turbulence conditions Eq.(6.3) should be replaced by

$$D = \left[\frac{\gamma_k^2}{\omega_k k_\perp^2}\right]_{\max}. \tag{6.4}$$

The growth rate γ in Eqs. (6.2)–(6.4) is usually very difficult to calculate theoretically and to measure experimentally. When experimental values are substituted in these equations, γ is normally replaced by $1/\tau_{\text{eff}}$, the reciprocal of the measured decorrelation time. Since γ should be calculated at the point of maximum diffusivity, we have chosen in this thesis to employ preferentially the value $1/\tau_d$, where τ_d is the decorrelation time calculated at the peak of the wave-number spectrum [see §5.4(b)].

It must be stressed that the arguments used here to estimate the diffusivity are by no means universal or unique. In particular, the heuristic approach relies to a great extent on the physics of drift waves and on the adiabatic-electron assumption. Under these conditions, a stable wave ($\gamma = 0$) would produce no net transport, in agreement with Eq. (6.3), because the perturbed density and velocity are 90° out of phase. In more general situations, one can envision a near-stable wave (with a large decorrelation time) that generates radial diffusion precisely because of its long lifetime.[193] In this case, a more appropriate relation, which can be constructed by dimensional arguments, is

$$D = \left[\tilde{v}^2 \tau_{\text{eff}}\right]_{\max}. \tag{6.5}$$

Throughout the history of tokamak research, many scalings of global confinement parameters have been proposed, both on purely experimental grounds and on the basis of heuristic arguments similar to the ones discussed above. The latter approaches generally refer to specific classes of instabilities. In particular, the possibility of microinstabilities evolving into global modes,[383] or other forms of "action at a distance",[384,193] which would justify the Bohm-like scaling observed in L mode, is currently a hotly debated topic. A different but related idea is that of a coupling between the SOL and the edge plasma, which allows the turbulence in the SOL to drive fluctuations in the main plasma.[385,367,366]

It is worth mentioning here one line of reasoning whose most recent incarnation is currently the object of intense research. We are referring to the idea of marginal stability:[386] if a class of strong instabilities is assumed to be active in the plasma, it may be postulated that the profiles will relax to an equilibrium state that renders the plasma marginally stable to those modes.[387] This ansatz allows one to sidestep the difficulties associated with analyzing the details of the instability, and general confinement scalings can be generated as a result. The principle of profile consistency[252] is a well-known example of such an approach.

Marginal-stability criteria recur in more recent literature,[388,389] and have more recently been expanded in the more general theory of self-organized criticality (SOC).[390] Self-organized criticality was introduced[391] with the initial aim of providing an explanation to the ubiquitous $1/f$ noise, and has then been applied to fields as diverse

as the analysis of earthquakes[392] and to plasma physics.[390] In an SOC state, transport can occur even below marginality, where it is dominated by large-scale transport "events" (or avalanches) associated with near-stable modes.[393] This scenario differs greatly from conventional random-walk diffusive models and leads to an intrinsic intermittency in the transport[394] that poses significant challenges to experimental verification of the theory. Some comments on the possibility of an experimental test will be offered in §6.8. Numerical studies of SOC models are currently in progress.[374]

(e) The L–H Transition

Several years after the experimental discovery of the H mode in ASDEX in 1982,[60] improvements in diagnostic techniques for measuring the plasma velocity profiles, the radial electric field and turbulence made finally possible a comprehensive phenomenological description of the L–H transition in DIII–D,[282,296] and subsequently in other machines.[61] These measurements in turn spurred an intensive theoretical effort that has continued for the past seven years, leading to a sound understanding of the fundamental physical mechanisms that are at play in the transition; however, while a wide consensus exists on these basic principles, many of the details remain to be worked out satisfactorily and are therefore being actively debated in the theoretical community.[201]

The central idea in the leading theories of the L–H transition is the stabilization of turbulence by a sheared $\mathbf{E} \times \mathbf{B}$ drift.[63,278,61] The decrease in the turbulence level then causes a reduction of anomalous transport. As was discussed in §5.1(c), a sharp increase in the first and second derivatives of the radial electric field is observed in the edge region at — or possibly immediately before — the transition, resulting in the formation of a negative well just inside the LCFS.[278,218] This mechanism has the universality needed to explain the broad variety of devices and experimental conditions in which the H mode has been produced.[316,201]

In general terms, one can envision several possible ways for sheared flows to act on turbulence. Following Newman et al.,[394] four distinct mechanisms can be identified: (a) linear stabilization of individual modes, whose detailed physics will be mode-dependent in general; (b) nonlinear decorrelation of turbulence in a strong-turbulence scenario; (c) dephasing between the fluctuating density (or temperature, angular momentum, etc.) and the fluctuating radial velocity[372,218]; and (d) if transport is not of a random-walk nature, but instead chiefly caused by large-scale, correlated transport events ("avalanches"), sheared flows may act to decorrelate these structures and reduce transport. Case (d) belongs to the theory of self-organized criticality,[390] which was briefly discussed at the end of the previous subsection and will not be examined further here.

Linear studies present the considerable advantage of analytical tractability, and often result in detailed criteria for the stabilization of the modes. However, the criteria are different for different instabilities, and are not always satisfied experimentally; in fact, flow shear is destabilizing in some cases, such as the Kelvin-Helmholtz[63] and

parallel-ion-velocity-gradient[362] instabilities. The effect of $\mathbf{E} \times \mathbf{B}$ shear on ITG modes has been investigated by several authors, both analytically[395,396] and numerically;[397] a reduction of transport is found in general. Hassam[398] found that $\mathbf{E} \times \mathbf{B}$ shear is always stabilizing for a variety of flutelike modes; a similar result has been obtained for drift-tearing modes.[399] A specific analysis for interchange and drift instabilities in the SOL also concluded that they are stabilized by flow shear.[375]

Excepting an early attempt to explain the L–H transition with the stabilization of microtearing modes,[380] which was later shown in fact not to occur,[299] the earliest work in this area concerned itself with the nonlinear stabilization of turbulence. An initial analysis of the effect of a radial electric field on collisional-drift-wave turbulence by Chiueh et al.[400] was expanded and generalized by Shaing et al.[401], and especially by Biglari, Diamond, and Terry,[63,402] who considered the effect of shear through the advective $\mathbf{E} \times \mathbf{B}$ nonlinearity (i.e., the change in time of the velocity of a fluid element caused by the $\mathbf{E} \times \mathbf{B}$ flow) on generic flutelike modes in cylindrical geometry. In an oft-cited paper,[63] these authors used a two-point renormalization technique for strong turbulence,[344] and concluded that the $\mathbf{E} \times \mathbf{B}$ shear caused a decorrelation of the turbulence, independent of the signs both of the electric field (E_r) and of its radial derivative (E_r').

This decorrelation can be understood in simple qualitative terms by noting that all particles in the plasma are subject to the $\mathbf{E} \times \mathbf{B}$ drift, and that a shear in that velocity will cause any radially extended (i.e., correlated) eddies to be torn apart on a sufficiently long time scale. It is interesting to note that even in the absence of true shear ($E_r' = 0$), the toroidal curvature alone would result in differential rotation of radially separated strata and thus in eddy breaking: this is the effect that was considered by Shaing et al.,[400] but was later shown to be negligible in comparison with the effect of shear ($E_r' \neq 0$) under realistic H–mode conditions.[63]

By dimensional arguments, it can be expected that a criterion for nonlinear turbulence decorrelation will involve some increasing function of the velocity shear (which has the dimensions of a frequency) being larger that the reciprocal of the intrinsic decorrelation time of the turbulence in the absence of shear, τ_d. The analysis of Ref. 63, indeed, generates the criterion

$$\omega_s > 1/\tau_d, \tag{6.6}$$

where

$$\omega_s \equiv \frac{\mathcal{L}_r}{\mathcal{L}_\theta} v'_{\mathbf{E}\times\mathbf{B}} \tag{6.7}$$

is the *shearing rate*, $v'_{\mathbf{E}\times\mathbf{B}}$ is the $\mathbf{E} \times \mathbf{B}$ velocity shear, and $\mathcal{L}_r$ and $\mathcal{L}_\theta$ are the radial and poloidal correlation lengths, respectively.

The shearing rate can be interpreted as the rate at which two points separated radially by a radial correlation length become separated poloidally by a poloidal correlation length by virtue of the sheared rotation. The adimensional critical parameter $\omega_s \tau_d$ is rather similar to the radial shear decorrelation parameter introduced in §4.2

and defined by Eq. (4.17); the main difference is that ω in the latter substitutes $1/\tau_d$ in the former. That parameter was obtained by imposing the condition that secular terms in a Doppler-shifted turbulent spectrum be negligible, so that a steady-state regime could be attained; the alternative would be an indefinite decorrelation of the turbulence as it evolves in time. That condition resulted in a prescription of the form of Eq. (6.6) [see Eq. (4.15)]. This provides an independent confirmation of the validity of this criterion. The criterion given by Eq. (6.6) has also been confirmed by a few experimental tests, in TEXT,[403] in PBX-M,[216] and in JFT2-M.[404]

Analytical scaling formulas were also found[63] for the modified radial correlation length and decorrelation time in the limit of large shear ($v'_{\mathbf{E}\times\mathbf{B}} \gg 1/\tau_d$), which are respectively

$$\mathcal{L}_{r,H} = \mathcal{L}_{r,L}(2\omega_s\tau_{d,L})^{-1/3} \tag{6.8}$$

and

$$\tau_{d,H} = \tau_{d,L}(2\omega_s\tau_{d,L})^{-2/3}. \tag{6.9}$$

Here, the subscripts L and H refer to L-mode (no-shear) and H-mode (large-shear) conditions, respectively. From these equations it becomes apparent that both a temporal and a spatial decorrelation occur.

These scaling laws can be obtained by heuristic arguments also. In the equation for the density evolution, the steady-state condition requires that the diffusive term Dn'' balance the shear-decorrelation term $v'_{\mathbf{E}\times\mathbf{B}}\tilde{n}r/\mathcal{L}_\theta$; using the relation $D = \mathcal{L}^2_{r,L}/\tau_d$, one then finds the characteristic radial length given by Eq. (6.8).[196] For the decorrelation time, Itoh and Itoh[405] consider a model in which turbulent eddies are stretched poloidally and compressed radially by the sheared $\mathbf{E}\times\mathbf{B}$ flow, while the area is preserved by the stretching. An initially circular fluid element is deformed into an ellipse, with the minor axis after a time t equal to $k_r^{-1}(1+\omega_s^2t^2)^{-1/2}$; taking this expression to be an effective radial wavelength and substituting it in the formula $1/\tau_{d,H} = Dk^2_{r,\mathrm{eff}}$ for $t = \tau_{d,H}$, one finds, for $\omega_s\tau_d \gg 1$, Eq. (6.9). It should be noted that, although the scaling derived by this argument coincides with that of Ref. 63, the two models are conceptually quite different in their treatment of the poloidal structure of the eddies: the *tearing* of the eddies envisioned by Biglari, Diamond and Terry[63] implies that the poloidal correlation length in H mode is the same as in L mode, whereas Itoh and Itoh[405] consider an eddy *stretching* mechanism that causes the poloidal correlation length to be, in fact, longer in H mode than in L mode.

Shaing et al.,[406] employing heuristic arguments, derived results similar to those of Ref. 63, but argued that the relevant velocity is the $\mathbf{E}\times\mathbf{B}$ velocity plus the electron diamagnetic drift velocity. As a result, shear decorrelation can occur even for $E_r = 0$, and a negative electric field is more effective in inducing decorrelation than a positive field, since in the former case the $\mathbf{E}\times\mathbf{B}$ drift is in the same direction as the electron diamagnetic drift. Experimentally, spontaneous H modes are generally accompanied by negative electric fields, although H modes have been induced with positive sheared fields also.[289]

It is worth mentioning that shear decorrelation is possible in ordinary fluids as well,[407] but it is generally dominated by the onset of the Kelvin-Helmholtz instability (which, in a plasma, is stabilized by magnetic shear[61]), and has therefore received scant consideration in that context.

Considerable numerical work has also been carried out in an effort to provide more detailed prescriptions for stabilization. Staebler and Dominguez found that ITG modes are stabilized by a positive second derivative of the electric field[408,409] (as is found experimentally in the E_r well structure in H mode), and, in later work, also by a nonzero first derivative.[410] Other authors have found shear stabilization to occur for short-wavelength drift-resistive ballooning modes[411] and for tearing modes,[412] but not for long-wavelength drift waves[413] or resistive-interchange modes.[11] One quasilinear numerical analysis for trapped-electron instabilities found them to be *destabilized* by $E_r'' > 0$.[409]

Zhang and Mahajan[414] have proposed a heuristic model of turbulence suppression by a sheared flow, which attempts to reconcile different results found in previous literature that are valid in different regimes. However, their central result is of limited utility, since it is given in terms of a quantity equal to the squared ratio of the fluctuation amplitude in L mode to that in H mode, multiplied by the squared ratio of the respective average wave numbers. Experimentally, the first ratio is larger than one and the second ratio is smaller than one, and their product may be smaller or larger than one; theoretically, the two ratios have been analyzed separately in the literature, so that a scaling of the product does not contain enough information for a valid comparison.

Hahm[415] has built on the work of Biglari, Diamond and Terry[63] to provide a more general formulation valid in toroidal geometry and in the presence of magnetic shear. Later, Hahm and Burrell also included the effects of a finite toroidal aspect ratio and of a noncircular cross section,[416] and of a large toroidal velocity.[417] These effects are all factored into a more general expression for the shearing rate ω_s, which, for the case of flutelike modes with moderate magnetic shear, reduces to

$$\omega_s = \frac{\mathcal{L}_r}{\mathcal{L}_\theta} \frac{|\nabla\psi|^2}{B_\phi} \left| \frac{d^2\phi}{d\psi^2} \right|, \tag{6.10}$$

where B_ϕ is the toroidal magnetic field, $\psi = RA_\phi$ is the stream function, and the electric potential ϕ is assumed to be a flux function (this assumption can be justified by neoclassical scaling arguments[6]). This modified shearing rate is generally considerably larger on the outboard side of a flux surface than on its inboard side; this is in agreement with the observation that turbulence is less affected by shear at the inboard edge than at the outboard edge.[300]

The toroidal theory just described[415–417] is not strictly an extension of the previous analysis performed in cylindrical geometry, as it uses in fact a different (ballooning) formalism. As a result, although the criterion expressed by Eq. 6.6 remains valid [with ω_s given by Eq. (6.10)], the scaling laws found for the decorrelation time and for the radial correlation length are in fact quite different. The former is found

to have only a weak logarithmic dependence on the shearing rate, and is thus essentially the same in L mode and H mode; the correlation length obeys the scaling $\mathcal{L}_{r,H}/\mathcal{L}_{r,L} = (1+\omega_s^2\tau_{d,L}^2)^{-1/2}$, which gives an asymptotic dependence $\mathcal{L}_r \propto \omega_s^{-1}$ for $\omega_s\tau_d \gg 1$, as opposed to $\mathcal{L}_r \propto \omega_s^{-1/3}$ for the cylindrical case.[63] In general, the toroidal analysis is expected to be more applicable to a moderate-shear case.

Recently, these scalings have been used to calculate the change in the random-walk diffusivity $D = \mathcal{L}_r^2/\tau_d$ from L to H mode, yielding a result in agreement with the observed transition from Bohm-like to gyro-Bohm scaling.[418] However, any such heuristic inferences must be regarded with caution, as two-point correlation theories cannot by themselves generate any transport coefficients: a complete theory of turbulent transport must include a full self-consistent treatment of the reaction of the fluctuations on the flow and of the phase relations between different fields (e.g. density and potential). For instance, the scalings given by Biglari, Diamond and Terry[63] would imply, in a random-walk diffusive scenario, that the diffusivity is the same in L and H mode, a result that is patently false experimentally. For these reasons, the third decorrelation effect that was listed at the beginning of this subsection, that is, the dephasing between turbulent fields, can be treated properly only in the context of a self-consistent theory of the L–H transition. This requires, as a first step, an analysis of the physics of flow generation, and more specifically of the effect of turbulence on the plasma flow velocity.

The predictions of neoclassical theory for the plasma flow,[6,320] particularly in their most recent update,[419] have been found to agree with experimental measurements for impurities but not for the main ion species[192] at the edge of the tokamak. Indeed, neoclassical theory may be of limited validity in this region owing to the short gradient scale lengths (which, in first approximation, cause a squeezing of the banana orbits in the presence of a sheared electric field[420]). Specific edge effects must then be considered to explain the sudden generation of large sheared flows at the onset of the H mode.

Shaing et al.[406] proposed ion orbit loss as the dominant mechanism of flow generation. High-energy ions in banana orbits situated within a banana width (poloidal ion gyroradius) from the plasma boundary are lost and produce a net negative electric field, which generates a poloidal $\mathbf{E}\times\mathbf{B}$ flow, damped in turn by viscosity. With the addition of the standard nonlinear turbulence suppression mechanism, a self-consistent system of equations can be written, which results in a bifurcation at a critical value of the collisionality.

This model, which has undergone several iterations,[421,422] has succeeded in explaining certain aspects of the L–H transition[61] but has also encountered some important difficulties: L–H transitions have been obtained at a very wide range of collisionalities and the rotation of the main ions is not always in the electron diamagnetic direction,[192] as this theory would predict; also, the width of the large-flow region is expected to increase with temperature,[423] whereas it is approximately constant experimentally; finally, it is difficult to extend any model that depends on ion orbit loss to the VH mode, in which confinement improvement extends well beyond

a banana width from the LCFS.[61]

A model advanced by Itoh and Itoh,[424] which has been progressively expanded over the years,[425,426] also bases the ion dynamics at the edge on the ion orbit loss mechanism, but completes the set of equations with an anomalous electron flux rather than with the drag from parallel viscosity as in Shaing's model.[427] It is a general feature of neoclassical transport that the flux is intrinsically ambipolar, that is, the transport equations imply automatically that the electron and ion fluxes are equal; however, when turbulence-induced fluxes are considered, this automatic ambipolarity is lost, and ambipolarity must be imposed as an additional constraint (to preserve charge neutrality).[257] This is known as non-intrinsically-ambipolar diffusion. In the Itohs' model, the ion and electron fluxes are constrained to be equal at the LCFS, and a bifurcated solution is obtained, leading to the possibility of a phase transition (the L–H transition) for certain values of the edge density and temperature.[428]

In addition to the difficulties associated with ion orbit loss, mentioned above, this model has also been faulted[61] for its prediction that the electric field should always be positive, in marked disagreement with experiment. Also, an attempt was made to expand the theory to explain the VH mode,[426] but a numerical solution of the complete set of equations has failed to find any transport barriers in the core of the plasma.[429]

A rather different flow-generation mechanism, which does not rely on ion orbit loss, has been proposed by Hassam et al.,[427,430] employing an idea advanced earlier by Stringer.[431] If a poloidal asymmetry develops in the anomalous particle diffusivity, and the diffusivity exceeds the poloidal-flow damping rate (mostly due to magnetic pumping, a form of neoclassical viscosity, and thus of the order of the ion-ion collision frequency), a flow instability ("Stringer spinup") can develop.[431] This instability may cause the onset of the H mode.[432]

This model, unlike Shaing's, does not depend strongly on the collisionality regime, and unlike both Shaing's and the Itohs', does not restrict flow generation to a layer within a poloidal ion gyroradius from the LCFS: thus, it is consistent in principle with VH–mode observations. However, ion rotation is predicted to be always in the electron diamagnetic drift direction, in conflict with experimental results.[61]

A model that must be rejected because of its lack of universality is that of Tendler and Rozhansky,[433,434] which ties the H mode with the existence of an X point and is thus inconsistent with limiter H modes.

In a series of papers, Hinton and Staebler[435–437] have presented a study of electric-field generation that included the effect of changes in the pressure gradient (through the momentum balance equation). A bifurcation is obtained in the pressure gradient rather than in the poloidal rotation as in Shaing's model.[406] This approach has the considerable merit that the model is built into a transport code, which includes transport equations for particles, energy and momentum, and is thus not zero-dimensional as in all previous cases. In addition, this model has been successful in reproducing the VH mode and, in fact, has yielded a prediction for the penetration depth of the transport barrier.[437] The main element that is missing from

this analysis is the reactive effect of fluctuations on the electric field.

Turbulence can drive a flow through the Reynolds stress, which appears formally in the advective nonlinearity in the momentum balance equation: the effect can be at play whenever $d(< \tilde{v}_r \tilde{v}_\theta >)/dr \neq 0$.[438] This requires both radial propagation ($\tilde{v}_\theta = ik_r\tilde{\phi}/B$) and radial inhomogeneity.[439] In general, when a broad range of poloidal wave numbers exists in the spectrum, cancellation occurs and the Reynolds stress is small. However, near the LCFS the radial symmetry is broken and the average effect may be nonzero; in addition, a large fraction of the residual Reynolds stress may be contributed by the low-k_θ region of the spectrum. By the same mechanism, convective cells may also generate a flow: in this case, one can visualize the phenomenon as a vortex "peeling off" into the shear flow, thus providing energy to it.[440,441]

The Reynolds stress can provide the "missing link" necessary to close the loop in a self-consistent model of the interplay of flow (and thus electric field) and turbulence, and of the L–H transition. This has been referred to as a predator-prey scenario, with the flow shear as the predator and the density fluctuations in the role of the prey.[362] In the initial work of Diamond, Carreras, et al.,[442,362] the fluctuation evolution was modeled by assuming a linear instability growth, a nonlinear diffusive flow of energy to other modes (mode-mode coupling), and damping by sheared flow; the latter was given heuristically as the simplest term in a one-point fluctuation model that satisfies the symmetry requirements, i.e., as a damping rate ω_s^2/γ_0, where γ_0 is the linear growth rate: thus, it is considerably different from the rate derived in the two-point correlation theory of Biglari, Diamond, and Terry.[63] The flow is driven by the Reynolds stress (dynamo effect)[443] and damped by magnetic pumping.

Combining the two evolution equations, one finds two equilibrium solutions, which are identified with L and H mode; the L–mode solution is stable when the product of the linear growth rate and of the Reynolds stress is smaller than the product of the nonlinear mode-coupling damping rate and of the magnetic-pumping damping rate.[442] The L–H transition can then be formally described as a second-order phase transition, with the flow as the order parameter: the H mode is the ordered state, with the turbulent energy being channeled into an ordered flow. Quantitative expressions were then given for the first time for the power threshold for H mode and for the time scale of the transition, which were in fair agreement with experimental results.

In later versions of this work,[444,68] the set of equations was expanded to describe self-consistently also the evolution of the pressure gradient and of the electric field, with the final aim of providing a complete theory of the H mode, the VH mode and ELMs. In its most recent incarnation,[68] this model has succeeded in reproducing several aspects of the complex dynamics of H mode. In particular, as the reduced turbulence level in H mode becomes unable to sustain the sheared flow through the Reynolds stress, it is substituted in this role by the increased pressure gradient, which is the chief flow-generating force in the later stages of H mode. This is in good agreement with experimental observations.[61]

This theory is fundamentally zero-dimensional. However, spatial dependence

has been added through simple diffusive terms for all the quantities, with the aim of providing a model of the VH mode.[68] The VH mode is described as the result of a flow-shear front propagating inwards,[445] but many details remain unexplained: in particular, no clear explanation has been found for the absence of ELMs in this regime.

In spite of its success, this theory is still incomplete. In particular, it does not address the fundamental question of the cross-phase between turbulent fields, e.g. density and velocity, which is found experimentally to be the dominant cause of transport reduction in late H mode.[218] Some work along these lines has been carried out, both analytically[370] and numerically,[372] for the specific case of the resistive-interchange instability: it was found that both a nonzero first derivative and a nonzero second derivative can induce a dephasing between $\tilde{n}$ and $\tilde{\phi}$, thus reducing transport independently of any changes in the fluctuation levels. Additional work on the dephasing caused by diamagnetic effects has appeared in more recent literature.[446]

A recent paper[447] provides a different self-consistent model of the L–H transition, using the physics of the resistive-ballooning instability. The set of equations was solved numerically, and two stable solutions were found and identified with L and H mode.

(f) Edge Localized Modes

The theoretical understanding of ELMs is considerably more limited than that of the L–H transition. As was discussed in §5.1(d), ELMs are generally believed to be triggered by MHD instabilities at the edge; listed in order of appearance for increasing input power, type-III ELMs are associated with resistive ballooning instabilities, type-I ELMs with ideal ballooning and low-n kink instabilities, and type-II ELMs (found only in DIII–D[292]) with ideal ballooning instabilities. The X event that usually terminates the VH mode is thought to be a kink-induced "monster" ELM.[68]

Much of this classification, however, remains conjectural. For instance, it has been hypothesized[68] that changes in the threshold for ideal ballooning modes due to the electric-field shear[448] may allow them to play a role in type-III ELMs also.[449]

It is clear that MHD physics alone cannot explain the full dynamics of ELMs, which are accompanied by broadband turbulence as well as coherent MHD modes. Also, the sheared rotational flows that are present in H mode are reduced for the duration of an ELM.[299] An ELM can thus be partially characterized as an H–L–H transition sequence.

Attempts have been made to weave ELMs into a self-consistent theory of the H mode,[68,449] by including the evolution of the pressure gradient, the MHD-fluctuation-induced viscosity, magnetic pumping, and quasilinear MHD ballooning dynamics; resistive ballooning modes were not considered here. This model[449] has reproduced several aspects of the evolution of ELMs for the full range of input powers, with the aid of heuristic assumptions. In particular, a low-power branch whose frequency decreases with power (type-III ELMs) has been seen in numerical solutions,[68] as

well as the opposite behavior at higher power (type-I ELMs), eventually evolving into high-frequency, low-amplitude bursts, which are identified as type-II, or grassy, ELMs. Since the model is zero-dimensional, it cannot predict the radial extent of the instabilities.

Itoh et al.[450] have recently found a limit cycle, which they named M–mode, between electrostatic and magnetic turbulence in the vicinity of the threshold for the ideal ballooning instability. This mode has been identified with type-I ELMs.

6.2 The Physics of Radial Modes

The radially propagating modes detected by PCI, which were described at length in Chapter 5 and particularly in §5.5, have characteristics that differ substantially from those of radial spectra that have been described in the literature. The most striking dissimilarity is the location of the peak in wave-number space: while the PCI spectra peak at finite k_r, previously observed spectra generally peak at $k_r = 0$.[51] However, this ostensible discrepancy vanishes upon closer inspection. In these previously reported cases, the $S(k_r)$ spectrum was integrated over a wide range of poloidal wave numbers, whereas the DIII–D PCI system selects the region of the spectrum with $k_\theta \sim 0$, as was discussed in Chapter 4. Therefore, the PCI measurements contain novel and unique information on a region of the spectrum that was hitherto mostly unexplored. Radial modes have been measured only in a few cases: we recall here the nonzero k_r peaks found in ATC,[16] and the inward-propagating modes seen in PDX.[228]

It is worth repeating here that an exact inversion of the measured PCI spectra to derive the local spectra is intrinsically impossible, since the line integration eliminates part of the local information. Our conclusion that the nonzero k_R peaks that we have measured reflect the existence of radial modes with nonzero k_r peaks must rely in part on prior knowledge and physical intuition. The computer simulations presented in §4.5 played a fundamental role in this selection process.

An important example in this context was provided in Fig. 4.17, which shows two very different local spectra and spatial distributions that give rise to similar line-integrated PCI spectra; this in particular is a predominantly negative-k_R spectrum, which has been seen in many experimental cases. As was discussed in connection with the figure, the local spectrum shown in Fig. 4.17(b) is in great contrast with spectra found in the experimental and theoretical literature, and disagrees specifically with measurements carried out in DIII–D; the spectrum shown in Fig. 4.17(a) is therefore accepted as the more probable one.

The same is true for all the spectra that are discussed in this chapter and in the previous one. In particular, the interpretation of the radial modes that are the subject of this section is given on similar grounds as the most probable one. The alternative interpretation of finite k_R components as the result of spatially inhomogeneous, poloidally propagating modes, although technically acceptable in specific cases, fails to explain the universality of such components: poloidally propagating modes would not produce nonzero k_R peaks at *all* radial locations.

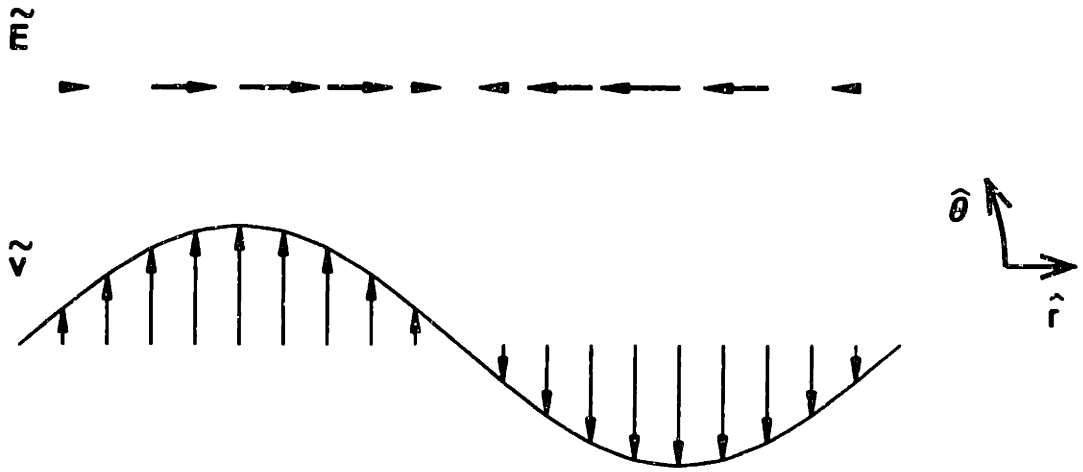

Fig. 6.1 Two-dimensional vector diagram of fluctuating electric field and corresponding $\mathbf{E} \times \mathbf{B}$ velocity for a single radial mode.

As was mentioned in the prologue to this chapter, electrostatic radial modes do not directly cause any cross-field transport, as their $\mathbf{E} \times \mathbf{B}$ velocity is oriented in the poloidal direction. This is illustrated in Fig. 6.1, which shows the instantaneous spatial distribution of the radial electric field and of the corresponding $\mathbf{E} \times \mathbf{B}$ velocity for a single radial mode. Each mode then corresponds to a sheared poloidal flow.

Radial spectra that peak at $k_r \neq 0$ have been clearly predicted, in fact, by several recent theoretical and numerical studies. The most lucid description of these modes, provided in a form that is particularly conducive to comparisons with experiment, was given in a 1994 paper by Waltz, Kerbel, and Milovich.[451] These authors carried out a study of ion-temperature-gradient (ITG) modes in a ballooning representation on a poloidal annulus of the cross section of the torus, using a three-dimensional gyro-Landau fluid computer model; this model includes the effects of Landau damping,[355] but does not account for trapped-particle effects. This and other recent models have allowed for the first time $n = 0$ radial modes to develop from the calculation.

In the past, the difficulty of separating these modes from the steady-state equilibrium flows had led researchers to eliminate them artificially from the simulation. An essential new feature in these recent codes, which has allowed the correct inclusion of radial modes, is the proper treatment of adiabatic electrons. Under the assumption that electrons, owing to their small inertia, can flow rapidly along the field lines and reach an equilibrium distribution in response to an electric field in a time much shorter than a fluctuation period, the relation $\tilde{n}/n = e\tilde{\phi}/T_e$ applies. However, if two flux surfaces are at a different potential, this assumption would imply rapid transport of electrons across the flux surfaces, which is unphysical. The modified relation $\tilde{n}/n = e(\tilde{\phi} - \langle \tilde{\phi} \rangle)/T_e$, where $\langle\rangle$ indicates a flux-surface average, is thus used in these studies.[352,356]

The radial modes are generated nonlinearly, through a wave-wave coupling pro-

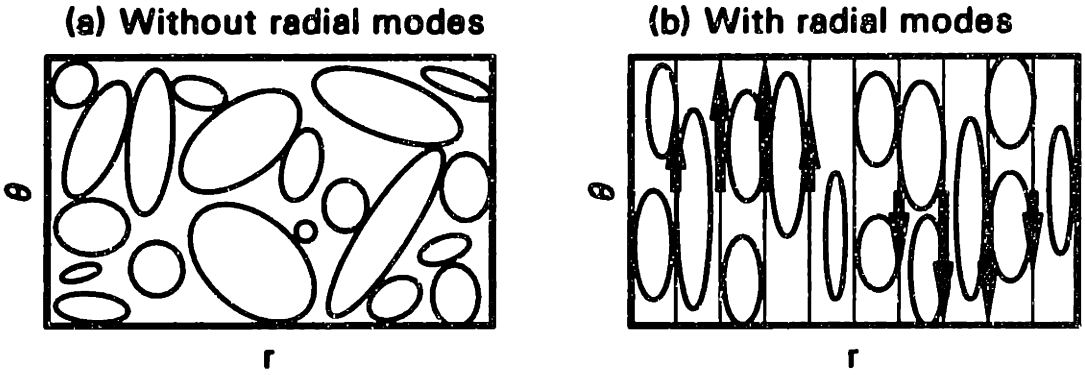

Fig. 6.2 Schematic visualization of turbulent ITG eddies (a) in the absence of radial modes and (b) in the presence of radial modes; the $\mathbf{E} \times \mathbf{B}$ velocity vectors of a single radial mode are shown.

cess, by the main ITG instabilities, which propagate in the poloidal direction. The main damping mechanism is Landau damping, with a smaller contribution from magnetic pumping.[451] The radial modes, which manifest themselves as sheared poloidal flows (see Fig. 6.1), react on the main ITG turbulence by tearing up its radial structure and reducing its radial correlation length, thus inhibiting their ability to cause radial transport. This mechanism is entirely analogous to the sheared-flow decorrelation of turbulence that is believed to be responsible for the reduction of transport in H mode (see §6.1). However, it must be noted that we are dealing here with turbulent, small-scale flows, as opposed to the steady-state, coherent, large-scale flows that are seen in H mode.

The effect of the sheared flows can be seen as a channeling of turbulent energy into ordered (in the case of H mode) or turbulent (in the case of the radial modes) flows. The effect of this redistribution on the spatial structure of the turbulent eddies is depicted schematically in Fig. 6.2.

An example of the resulting evolved spectra from the code[451] is shown in Fig. 6.3(a). The peak drive, the ITG instability, contains a large fraction of the energy and peaks at $k_r = 0$ and finite k_θ; thus, a system that measures the $S(k_r)$ spectrum integrated over all $k_\theta's$ would detect a peak at $k_r = 0$. The smaller radial modes peak at $k_\theta = 0$ and finite k_r. In Fig. 6.3(b) the computed spectrum is superimposed on the spectral region to which the PCI system is sensitive. It is immediately clear that this system would be expected to detect the radial modes and to be essentially unaffected by the main ITG turbulence. Our measurement of a finite k_r peak is thus a striking confirmation of the existence of these modes and a rare example of a theoretical prediction in plasma turbulence that has been verified experimentally.

Although they do not directly cause transport, the radial modes can be expected to have a regulating effect on it, through the shear decorrelation mechanism. A central result of the numerical work of Waltz et al.[451] was that the role of the radial modes is in fact critical. When the radial modes were artificially "turned off", it was found

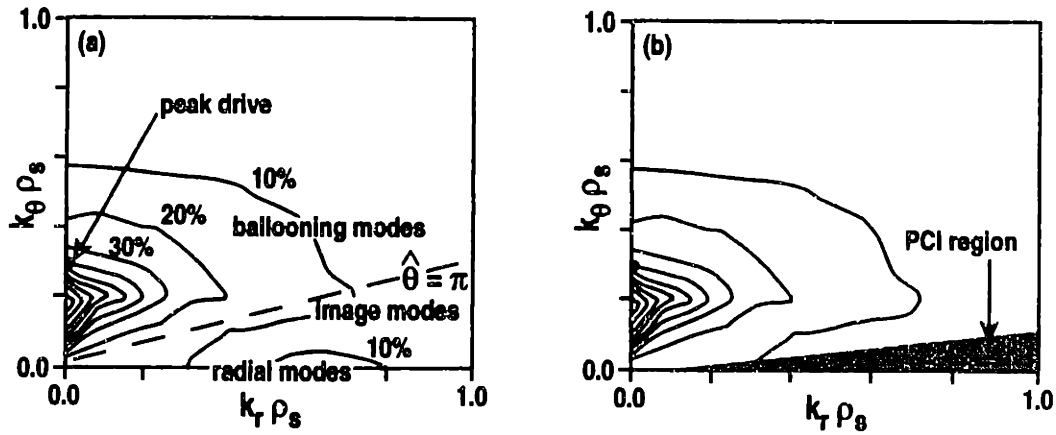

Fig. 6.3 (a) Contour plot of two-dimensional wave-number spectrum of evolved ITG turbulence, generated by a 3D gyro-Landau fluid computer simulation [reproduced with permission from Waltz, Kerbel, and Milovich, Phys. Plasmas **1**, 2229 (1994)]; (b) same plot shown with shaded area representing spectral region accessed by the DIII–D PCI system (the boundary is defined by the $1/e$ point of the responsivity function).

that the amplitude of the poloidal modes increased, and hence the diffusivity (i.e., the rate of transport), increased, the latter by approximately a factor of 10. Hence, even in L–mode conditions, anomalous transport is much smaller than it would be in the absence of the shear decorrelation effect.

We can also directly estimate the efficacy of the shear-decorrelation mechanism through the following numerical analysis. The computer simulations find that the relative potential fluctuations are larger than the relative density fluctuations:[451] that is, $e\tilde{\phi}/T_e > \tilde{n}/n$. By rearranging this expression as $\tilde{\phi} > (\tilde{n}/n)\,T_e/e$, we conclude that the quantity $(\tilde{n}/n)\,T_e/e$ can be regarded as a lower limit for the absolute potential fluctuation level $\tilde{\phi}$. Combining PCI estimates of $\tilde{n}$ with density and temperature measurements by Thomson scattering, we estimate $(\tilde{n}/n)\,T_e/e \sim$ 10–20 V; thus, $\tilde{\phi} \gtrsim$ 10 V. Since the average radial wave number k_{0r} has been shown [see §5.5(b)] to be larger than 1.8 cm^{-1}, we can set a lower limit for the radial derivative of the electric field at $d\tilde{E}/dr = k_{0r}^2\,\tilde{\phi} \gtrsim$ 32 V/cm^2. At a field of 2 T, this value corresponds to a minimum $\mathbf{E}\times\mathbf{B}$ velocity shear of $dv_{\mathbf{E}\times\mathbf{B}}/dr = 1.6\times10^6$ s^{-1}. This value is of the same order as that of the macroscopic, steady-state shear that exists in H mode and that is believed to be responsible for the dramatic turbulence suppression that accompanies the L–H transition (see §6.10).

Some caveats are in order at this juncture. This numerical analysis[452,451,202] was carried out in an annulus in the core of the plasma ($\rho \sim 0.5$). Whether it can be extrapolated to the edge is a matter of speculation. ITG modes are expected to be unstable in the edge as well, but different instabilities (particularly resistive ballooning modes) may also be at play there; in addition, the interaction with the SOL, with added complications from atomic physics and radiative effects, may also have to be taken into consideration. Finally, simulating ITG turbulence at the edge is technically more difficult. For these reasons a similar computational study has not

been attempted for the edge region thus far.

Another difficulty arises from the adiabatic-electron assumption, which is problematic at the edge. This assumption requires that the parallel component of the wave vector be nonzero, albeit very small, and that the trapped-electron population be small (in toroidal devices, a fraction of the charged particles is trapped in the magnetic mirror created by the radially decaying magnetic field on the outboard side of the torus). The latter requirement is only satisfied when collisionality is high enough to scatter electrons out of the trapped orbits in an average time shorter than the period of the orbit (*bounce time*), but not so high that parallel dynamics are affected. In the relatively collisional edge of the plasma, trapped-electron effects are expected to be important; only preliminary attempts have been made at including these effects.[356]

In addition, the scope of possible comparisons between experiment and simulations is fairly limited at present: the PCI measurements have generated a wealth of information on the radial modes that has no equivalent at present on the computational side. In particular, no information exists on the frequency spectra (although they are expected to peak at zero frequency, in agreement with observations), no studies have been made of the radial-mode spectrum in H mode, and no parametric scans have been carried out numerically to determine the scaling of the k_r peak or of the width of the radial spectrum in L mode (experimental scans are shown in Figs. 5.14 and 5.15). It is only known[451] that the k_r peak occurs at a fraction (typically $\sim 1/2$) of the reciprocal of the ion gyroradius, as shown in Fig. 6.3. This is in fair qualitative agreement with experiment, as evidenced by a comparison with Fig. 5.15(a).

Also, the numerical analysis is constrained to preserve radial parity: i.e., no distinction is made between positive and negative k_r, or outward- and inward-propagating modes. By contrast, experimental measurements show that the spectra, although balanced in many cases, can also be predominantly propagating in either direction; the dominant direction of propagation and the imbalance factor may depend on a number of plasma parameters, as illustrated by Fig. 5.16.

In spite of these limitations, the mere experimental observation of finite-wavelength radial modes constitutes an extremely promising and exciting development. A number of fluid,[358,411,376] gyrofluid[351,352,356] and gyrokinetic[347,198] computations have also predicted in recent years the existence of these modes and their fundamental role in regulating transport. Although the details may differ (there are varying opinions, for instance, on whether magnetic pumping plays a significant role in damping the radial modes), all treatments agree on the basic physical interaction between ITG and radial modes. However, as the chief focus of these studies has been transport rather than the turbulent spectra, information on the latter remains relatively scant. In view of our results, additional runs dedicated to the specific question of the dependence of the radial spectrum on the plasma parameters would certainly be desirable.

It is remarkable that similar phenomena — that is, the nonlinear generation of sheared, or zonal, flows and their reactive regulation of radial transport — had already been predicted nearly twenty years ago by Hasegawa and coworkers,[453] through

a combination of analytical[454] and numerical work for drift waves in plasmas and Rossby waves[455] in planetary atmospheres. In these works, the mechanism considered for radial-mode generation is three-wave interaction, which is known to support an inverse cascade of energy to large scales,[338] and was found numerically to generate condensation at $k_\theta = 0$ and finite k_r. The general idea of shear decorrelation was also introduced in that context,[453] and was believed to apply to the zonal flows observed in the atmosphere of Jupiter.

Although all the studies discussed thus far focus on the nonlinear dynamics of drift and ITG waves, it may also be worth revisiting the linear theory[456] to investigate whether some of the radial-mode phenomenology can be understood on the basis of linear-instability criteria alone.

It is also entirely possible, of course, that similar radial modes could arise from rather different instabilities. For instance, recent work by Cohen and Xu[366] on the physics of the Kelvin-Helmholtz and parallel-ion-velocity-gradient instabilities, using a two-dimensional computer model of the SOL, has generated spectra that exhibit nonzero k_r peaks at $k_\theta = 0$; moreover, the value of k_r at the peak increases in going from L to H mode, in qualitative agreement with PCI measurements. In this study, a finite k_r was shown to be in fact a stabilizing agent. Work is currently in progress to compare our data with additional dedicated simulations with this code.

Also, a recent numerical simulation of resistive-ballooning turbulence[457] has generated radial correlation functions with the characteristic decaying wavelike behavior observed by PCI, corresponding to radial modes with finite k_r. The value of k_r at the peak appears to decrease with decreasing plasma β in the simulation: at low β only a decaying correlation function is observed. In our parameter scans, we have found no clear dependence of $k_{0,r}$ on the temperature or on the magnetic field, and only a slight decrease of $k_{0,r}$ with increasing density (see Fig. 5.14).

The existence of radially propagating waves is also of considerable interest in relation to the Reynolds stress mechanism, which, as was discussed in §6.1, allows turbulence to drive steady-state flows and is an integral part of recent self-consistent theories of the L–H transition.[438,442,362,444,68] Turbulence can drive a flow at a rate given by $d(< \tilde{v}_r \tilde{v}_\theta >)/dr \neq 0$.[438] Thus, both a radial inhomogeneity, as is generally found at the plasma edge, and nonzero radial and poloidal wave numbers are required for this mechanism to be effective. However, in the presence of many poloidal eigenmodes, substantial cancellation generally occurs from mode summation, and the low-k_θ region of the spectrum is expected to provide the dominant contribution. This is the region accessed by PCI; thus, the nonzero k_r peak found there provides an indication that the Reynolds stress may indeed be a significant flow-generating agent.

Radial propagation is a key element in certain theories of turbulence coupling between the core and the edge[384,383,360] and between the SOL and the edge.[458,459,360] In the former case, although a nonzero k_r is not necessary for propagation in toroidal geometry,[384] a preferential group velocity in the positive radial direction is envisioned. In the case of SOL-edge coupling, the reverse is true[459] and turbulence is expected to

propagate from high to low fluctuations in general.[360] A variety of semiquantitative formulas have been given in these theories for the radial group velocity, which are generally in the range of values found by PCI [1.5–4 km/s in L mode: see §5.5(d)]. However, exact comparisons are difficult in general: for instance, linear toroidal coupling of drift waves causes a radial group velocity that is directly proportional to the sine of the poloidal angle, and is thus zero on the midplane;[459] the integration path of the PCI beam would then cover a wide range of group velocities.

In recent work by Garbet and Waltz,[360] transport is dominated by large-scale near-stable structures that propagate radially and have very long intrinsic decorrelation times. Similar predictions arise from the theory of self-organized criticality,[394,374] which will be discussed separately in §6.8. These long decorrelation times should be revealed by a spatial analysis utilizing a Lagrangian approach, i.e., following the wave packet as it propagates in space; equivalently, the intrinsic decorrelation time as a function of k_r, derived in §5.5(d) (see Fig. 5.30), should also be large around the peak of the $S(k_r)$ spectrum. Instead, our analysis has failed to reveal decorrelation times of the order of those predicted by the theory.[360] It is still possible, however, that diagnostics that span a broader spatial range [e.g., beam-emission spectroscopy (BES)[52]] may be able to detect these long-lived structures.

In addition, the existence of both inward- and outward-propagating components in the radial spectrum, with alternate and irregular dominance of one or the other, is difficult to reconcile with the predictions of any individual theory. Thus, the relationship of our results with these theoretical efforts is unclear at present.

The novelty and uniqueness of the measurements of radial spectra described in this thesis should provide motivation for studying this region of the spectrum with other diagnostics as well. A two-dimensional imaging system, e.g. with BES, would be in an ideal position not only to investigate the $k_\theta \sim 0$ portion of the spectrum, but also to determine quantitatively its relation to the remaining components; in particular, the relative amplitudes of the peak ITG drive and of the radial modes, shown in Fig. 6.3, would constitute important information and would provide a fundamental test of the computational analysis. Also, it would be of great interest to ascertain whether the radial modes are truly toroidally symmetric ($n = 0$) or whether they have a finite, albeit long, parallel wavelength; however, such a measurement would be difficult to perform: toroidally spaced probes, for instance, could not isolate the radial modes for analysis.

Measurements of correlation lengths, decorrelation times, amplitudes, etc., even when performed on the radial modes alone, as done by PCI, can generally be considered representative of the characteristics of turbulence at large, in a generic strong-turbulence scenario. However, this assumption could be refined if additional information were available on the relation between the radial modes and the main turbulence. In particular, the spectra calculated numerically[451] (see Fig. 6.3) imply that the amplitude of the radial modes, when extrapolated to the whole spectrum, would systematically underestimate the total amplitude. Also, if the poloidal spectral width of the radial modes differs from that of the main instability, the effective poloidal in-

tegration length would be different from that employed in Chapter 5 to estimate the local fluctuation amplitude. The impact of these unknown corrections, however, is rather limited, since estimates of the absolute amplitude are the least significant ones among those obtained with PCI, owing to their large intrinsic uncertainty.

6.3 Convective Cells

In §5.5(a) two peculiar types of spatial correlation structures, which did not conform to the more common decaying wavelike behavior, were presented. We shall discuss them in turn in this section and in the following one.

The first type of structure, exemplified by Fig. 5.10, is characterized by a high correlation level between points located just inside and just outside the LCFS, with a lower correlation level between each of them and the LCFS itself. We shall show now that this pattern is consistent with the existence of convective cells situated astride the separatrix.

Convective cells in plasmas are similar to the Rayleigh-Bénard cells that arise in a fluid heated from below in a gravitational field. The cells are spatially periodic, nondispersive, low-frequency ($\omega \to 0$) electrostatic instabilities, which break the symmetry of the plasma electric field by introducing a poloidal component, which in turn generates a radial $\mathbf{E} \times \mathbf{B}$ drift that can transport particles and energy radially across the field lines. These structures, which are similar to flutelike interchange modes in toroidal geometry,[460] can be generated nonlinearly by a variety of plasma modes,[361,461] including drift waves[359,462] and resistive ballooning modes.[411,377] A pictorial representation of convective cells across the plasma boundary is shown in Fig. 6.4.

In common models of convective cells, the spatial structure is assumed to be nonoscillating ($\omega = 0$), and the cells are modeled with a sinusoidal function $\cos(k_r r)\cos(k_\theta y_\theta)$, where y_θ is a coordinate along the poloidal direction.[440] In our case, the experimental data lead us to consider finite-frequency fluctuations. We can then envision that the fluctuations will not be perfectly coherent, i.e. that they will occupy a finite region of wave-number space and will have a finite correlation length. However, we must retain the characteristic standing-wave cell structure: this implies that components with positive and negative wave numbers are correlated and of equal amplitude. Thus, the random-phase postulate given in Eq. (4.9) must be modified as follows:

$$\langle \hat{n}^*(\mathbf{k}',\omega')\,\hat{n}(\mathbf{k},\omega)\rangle = \frac{\langle \tilde{n}^2\rangle}{2}\sqrt{I(\mathbf{k},\omega)I(\mathbf{k}',\omega)}\,[\delta(\mathbf{k}-\mathbf{k}')+\delta(\mathbf{k}+\mathbf{k}')]\,\delta(\omega-\omega'), \quad (6.11)$$

with the additional constraint $I(\mathbf{k},\omega) = I(-\mathbf{k},\omega)$.

We can now utilize, with opportune modifications, much of the formalism developed in Chapter 4. In particular, we adopt for simplicity a bi-Gaussian spectral function; thus we can write, by analogy with Eq. (4.23),

$$I(\mathbf{k},\omega) = \frac{\pi}{4}\mathcal{L}_r\mathcal{L}_\theta \sum_{\pm} \exp\left[-\frac{\mathcal{L}_r^2\,(\pm k_r - k_{0,r})^2}{4}\right] \exp\left[-\frac{\mathcal{L}_\theta^2\,(\pm k_\theta - k_{0,\theta})^2}{4}\right]$$

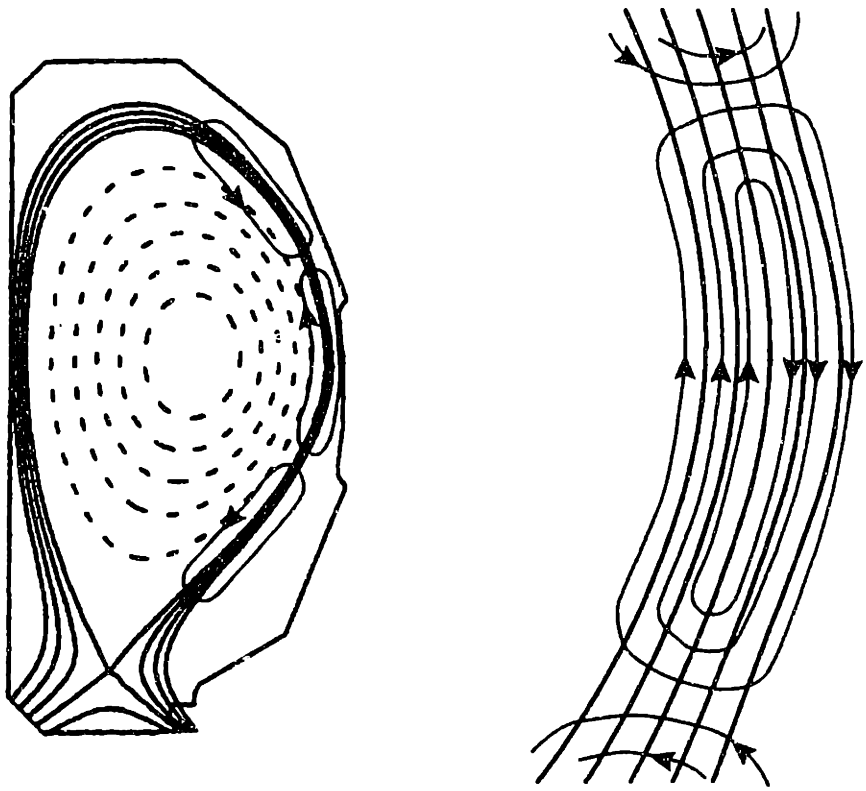

Fig. 6.4 Convective cells located across the separatrix, with detail of the outer edge of the tokamak. The contours are equipotential surfaces, and the arrows indicate the direction of the instantaneous $\mathbf{E} \times \mathbf{B}$ velocity.

$$\times \sum_{\pm} \hat{F}[\pm\omega - \omega(\mathbf{k})], \tag{6.12}$$

where $\hat{F}$ is the frequency distribution function about the dispersion relation for a given $\mathbf{k}$. The first sum over the signs is necessary to satisfy the wave-number parity requirement, while the second sum ensures that I is Hermitian.

If we now ask the question of what signal will be detected by PCI, the intuition developed in Chapter 4 allows us to conclude that it will be significant only if the poloidal wave number is small; otherwise, the line integration would cause cancellation. In general, convective cells are expected to be large-scale phenomena, with a poloidal quantum number $m \lesssim 20$; under these conditions, the poloidal wavelength $2\pi/k_{0,\theta}$ is of the order of, or longer than, the PCI integration length. Thus, we set $k_{0,\theta}$ to zero for simplicity. We also assume that the poloidal angle ϑ is negligible along the PCI path, and that the density fluctuations are homogeneous, i.e. that $\langle \tilde{n}^2 \rangle$ does not depend on r or y_θ. With guidance from §4.4, we can now write the equal-time correlation function between the signals measured on two PCI chords as

$$\Gamma_{12}(r_{\mathrm{av}}; \Delta r, 0) = \sqrt{\pi} L_\theta \mathcal{L}_\theta \langle \tilde{n}^2 \rangle \left[\exp\left(-\frac{(\Delta r)^2}{\mathcal{L}_r^2} \right) \cos(k_{0,r} \Delta r) + \exp\left(-\frac{4 r_{\mathrm{av}}^2}{\mathcal{L}_r^2} \right) \cos(2 k_{0,r} r_{\mathrm{av}}) \right], \tag{6.13}$$

where L_θ is the integration length, Δr is the radial distance between the two chords, and $r_{\rm av}$ is the radial position of the median point between them. Note, by comparison with Eq. (4.51), that the correlation function is now a function of the absolute position also, as should be expected for any standing-wave structure. Here, we take the radial origin to be on the LCFS, in accordance with the convective-cell pattern shown in Fig. 6.4.

Finally, we can derive from Eq. (6.13) the equal-time correlation *coefficient*, which can be written as

$$\gamma_{12}(r_{\rm av};\Delta r,0)=\left[\exp\left(-\frac{(\Delta r)^2}{\mathcal{L}_r^2}\right)\cos(k_{0,r}\Delta r)+\exp\left(-\frac{4r_{\rm av}^2}{\mathcal{L}_r^2}\right)\cos(2k_{0,r}r_{\rm av})\right]$$
$$\times\left[1+\exp\left(-\frac{4r_1^2}{\mathcal{L}_r^2}\right)\cos(2k_{0,r}r_1)\right]^{-1/2}$$
$$\times\left[1+\exp\left(-\frac{4r_2^2}{\mathcal{L}_r^2}\right)\cos(2k_{0,r}r_2)\right]^{-1/2}. \qquad (6.14)$$

The coherency function in frequency space takes a similar form, with a modified correlation length that takes into account the structure of the frequency-broadening function $\hat{F}$; for our present purposes it is not necessary to derive the explicit expression.

It can be easily verified from Eq. (6.14) that the correlation coefficient between two points in symmetric positions about the LCFS ($r_1=-r_2$) is always one. On the other hand, the coefficient between the LCFS and any other point ($r_1=0$, $r_2\neq 0$) is always less than one, and follows a decaying oscillatory pattern as a function of r_2. Finally, if one point is kept fixed at a given distance from the LCFS, the envelope of the coefficient (i.e. with the oscillating factor removed) reaches a minimum when the second point is on the LCFS. This behavior is qualitatively consistent with the correlation coefficient plotted in Fig. 5.10(a); the coherency functions shown in Fig. 5.10(b) also display a similar behavior.

Naturally, this model is highly idealized and cannot be expected to reproduce the measured correlation function exactly. In particular, the fact that the correlation coefficient between symmetric points about the LCFS is less than one suggests that the convective cells are accompanied by turbulence of a different nature, probably of the broadband type observed in general.

An examination of Eq. 6.12 allows one to conclude that the autocorrelation function ($\Delta r=0$) has a maximum for $r=0$ and falls to one-half the maximum value at a distance from the LCFS of one eighth of a wavelength. This should result in a partial node-peak structure in the spatial distribution of the amplitude of the PCI signal. Since the amplitude is the square root of the autocorrelation function, the excursion from peak to valley should be of 29%. The amplitude of the PCI signal is generally largest in the vicinity of the separatrix (see, e.g., Figs. 5.25 and 5.26), in agreement with expectations: however, this is true in general, not only when the peculiar correlation patterns discussed in this section are seen. Therefore, it is not

clear whether a specific change in the amplitude distribution occurs in this case. In addition, the probable presence of "normal" broadband turbulence alongside the convective-cell pattern would act to reduce the distance between peak and valley to less than 29%. Since channel-to-channel errors in the amplitude estimate are typically of the order of 10–15%, detecting the peak-node structure may be difficult in practice.

As was discussed in §5.5(a), these correlation structures are most often seen at the highest values of the plasma current, with $q_{95} \lesssim 4$; it may thus be argued that convective cells at the edge could be related to low-q resistive-MHD resonances.[439] The frequency spectrum of these fluctuations is similar to the usual one, i.e. it is monotonically decreasing. Since convective cells are expected to be chiefly low-frequency phenomena, it would certainly be of considerable interest to extend the measurement to the very-low-frequency region, below our instrumental cutoff of $\sim$8 kHz.

Both the wavelength and the correlation length of the convective cells appear to be in the order of 2–4 cm (see Fig. 5.10): it is difficult to provide a more accurate estimate within the instrumental limitations. The poloidal wavelength must be considerably longer (>10 cm) to avoid cancellation from line integration. It is possible, however, that a broader range of poloidal wave numbers may be involved: the high-k_θ region of the spectrum is simply inaccessible to PCI. In fact, it is expected theoretically[463,359] that enstrophy (mean square vorticity) should condense in this spectral region, principally because of its k^4 dependence[464] (the vorticity $\nabla \times \mathbf{v}$ is proportional to a second spatial derivative of the electric potential for $\mathbf{E} \times \mathbf{B}$ flows). In view of this, simultaneous measurements of a broader range of poloidal wave numbers (e.g. with BES or FIR scattering) would certainly be a valuable future addition to this study.

In H mode, these high-correlation structures disappear or migrate inwards into the plasma or outwards into the SOL. The correlation level between points inside and outside the LCFS becomes invariably quite small. This is consistent with the general shear-decorrelation mechanism described in §6.1, which is expected to be effective on all radially correlated fluctuation structures. In particular, convective cells may actually feed the sheared flows by virtue of the Reynolds stress, in a manner similar to that of a vortex "peeling off" into two counterstreaming flows.[440] It is interesting to note that a recent paper[377] has presented a complete theory of the L–H transition and of ELMs on the basis of resistive-ballooning convective-cell physics alone. Away from the shear layer near the LCFS, the shear decorrelation mechanism would be less effective and convective cells may survive, as indicated by our measurements.

The identification of the measured structures with convective cells can be taken as a reasonable working hypothesis in view of the several corroborating points listed above. More dedicated measurements in low-edge-q plasmas would be desirable to expand the database and attempt more comparisons with theory.

6.4 Density-Fluctuation Well in the SOL in H Mode

In this section we shall comment briefly on the H–mode phenomenology that was described at the end of §5.5(a). In some cases, the radial correlation function in the SOL takes the form exemplified by Fig. 5.11: a high correlation level exists throughout the SOL, with a narrow layer situated between 0.5 and 1.5 cm outside the LCFS oscillating 180° out of phase with respect to the regions on both sides of it. The correlation level between the SOL and the region on or just inside the LCFS is low.

Because the correlation level in the SOL is high everywhere, this structure corresponds to a distribution of $\tilde{n}$ that is approximately flat, with the exception of a negative well in correspondence with the counteroscillating layer. Indeed, in the absence of this well the $\tilde{n}$ distribution would reflect a long wavelength that would fall beyond the spectral cutoff point of the PCI system; however, the well, approximately like a delta function, acts to broaden the k_r spectrum and permits detection by PCI.

On the basis of measurements carried out with the reciprocating probe in DIII–D, the cross-phase between the fluctuating density ($\tilde{n}$) and electric potential ($\tilde{\phi}$) is known to be approximately constant in space in the SOL.[218] The phase is close to 90° (causing maximum transport) both inside and outside the LCFS in L mode, and increases to ~120° in H mode outside the LCFS, while it reaches ~180° just inside the LCFS, in correspondence with the well in the $\mathbf{E} \times \mathbf{B}$ flow velocity. If we thus assume a constant phase in the region we are exploring, we can conclude that the spatial distribution of $\tilde{\phi}$ is similar to that of $\tilde{n}$, i.e. flat except for a negative peak 1 cm outside the LCFS. The fluctuating radial electric field, equal to the negative radial derivative of $\tilde{\phi}$ is thus near zero everywhere and should have a positive and a negative peak in rapid succession in the same region, 1 cm outside the LCFS. The same is true of the fluctuating $\mathbf{E} \times \mathbf{B}$ velocity.

If these deductions are true, and we make the working assumption that turbulence is isotropic in the SOL, we can conclude that throughout most of the SOL radial transport is inhibited in H mode, even though the absolute $\tilde{n}$ level can be significant and the sine of the cross-phase between $\tilde{n}$ and $\tilde{\phi}$ is only down by a factor of two with respect to L mode.

It must be stressed that this type of structure has not been confirmed with other diagnostics, particularly the reciprocating probe. Indeed, we do not have simultaneous measurements with PCI and the probe in discharges in which this mechanism is at work. Furthermore, we have not succeeded in identifying any clear distinction between these discharges and those that exhibit a more regular wavelike correlation structure. These conclusions should thus be regarded as preliminary.

6.5 Frequency Spectra and Time-Delayed Correlation Function

In the remainder of this chapter we shall explore systematically the phenomenology of turbulence that was presented in Chapter 5, using the characteristics of the measured radial modes as a representation of the general features of edge turbulence in DIII–D. As mentioned previously, the validity of this representation is predicated upon a strong-turbulence ansatz. Similar extrapolations recur, of course, throughout the history of plasma turbulence measurements, as no single diagnostic system is capable of accessing the entire fluctuation spectrum. In our specific case, the considerations of §6.2 suggest that the greatest uncertainty in this extrapolation concerns the absolute amplitude of the radial modes in relation to the rest of the spectrum.

This section addresses the frequency- and time-domain analysis that was presented mainly in §5.4. Studies of the frequency spectra benefit especially from the radial-mode selection rule ($k_\theta \sim 0$): since the $\mathbf{E} \times \mathbf{B}$ and diamagnetic flows in the plasma lie on the flux surfaces and are thus orthogonal to radial wave vectors, radial modes are immune to Doppler shifts, and measurements carried out in the laboratory frame are essentially equal to those in the plasma frame. It must be remembered, however, that finite, albeit small, k_θ components can be detected by PCI, particularly on chords located several cm inside the LCFS; thus, small Doppler shifts may occur. However, the numerical simulations discussed in §4.5 and shown in Fig. 4.14 proved that these frequency shifts are negligible in most cases. This property of PCI allows it to make a unique and novel contribution to turbulence studies.

Experimentally, the form of the spectra shown in §5.4 is a direct confirmation of the lack of Doppler shifts: most of the energy is concentrated below 100 kHz, in marked contrast with measurements carried out with other diagnostics in DIII–D, which detect considerable activity at several hundred kHz. An extreme example was shown in Fig. 5.38 for a chord located several cm inside the LCFS; even in that case, the peak was shifted only to 38 kHz. For these reasons, spectral comparisons between PCI and other DIII–D diagnostics have proved fruitless in general, with the partial exception of the reflectometer, which is the only other system sensitive mainly to radial wave vectors. However, reflectometer spectra are usually broader than those of PCI, and indeed the poloidal-wave-number range of the reflectometer is expected to be wider than that of PCI, although a quantitative estimate is difficult for the former.

In Ohmic and L–mode plasmas, the PCI autospectra are almost invariably monotonically decreasing with frequency (see Fig. 5.1), and are generally well fitted by inverse-power laws with exponents in the range 1–3 and averaging at 2. Values very close to 2 are in fact particularly common; this inverse square law is consistent with a Lorentzian spectrum, which corresponds to an exponentially decaying time-delayed correlation function, i.e. to an imaginary part of the frequency (damping rate). Thus, steady-state or saturated turbulence may be characterized by a simple damping rate, which, however, is difficult to measure experimentally: the spectrum must saturate at sufficiently low frequencies, as required by integrability and indeed as in the case of

the Lorentzian function; since no such saturation is observed above the instrumental cutoff point of 8 kHz, it must occur at an unknown lower frequency, which would also provide a measure of the damping rate.

The spatial dependence of the inverse-power-law exponent, shown in Fig. 5.2, is difficult to interpret simply, especially since it is considerably different in Ohmic and L mode. It may be argued that the larger exponent measured deep in the SOL could be indicative of a more coherent spectrum there; also, the increased decorrelation time in that region, shown in Fig. 5.5, corroborates that inference, which may be construed as a sign of weaker turbulence in the SOL than in the main plasma.

The decorrelation time was also found to decrease for increasing neutral-beam power (see Fig. 5.7). This, again, appears to indicate that the increased drive causes a stronger turbulent state.

Few theoretical predictions exist for the frequency spectrum of the turbulence. One such prediction, for drift-resistive waves,[465] is indeed an inverse square law, in agreement with our measurements. Experimentally, in most cases — and especially in tokamaks — laboratory-frame frequencies are dominated by Doppler shifts; when this is so, indeed, the frequency spectrum is often assumed simply to be equal in form to the wave-number spectrum[51] (this is known as Taylor's hypothesis and is widely used in fluid mechanics[206]). In plasmas with small flow velocities (stellarators, reverse field pinches), and in tokamaks when Doppler-shift subtraction was possible, similar inverse-square laws have again been found.[197] Thus, there is good agreement among the measurements reported.

There is also general agreement on the basic observation that tokamak plasma fluctuations have a turbulent nature, revealed by the finite width of the frequency spectrum measured at each wave number, and, moreover, that turbulence is strong, since that width is comparable to the value of the frequency at the peak.[10,23,219]

One of the testable predictions of the theory of self-organized criticality (SOC)[393,394,374] is the form of the autopower spectrum. This is found, from numerical simulations, to obey a f^{-4} power law at high frequency (the region of single-avalanche transport events), and to undergo a sharp transition to a f^{-1} law at lower frequency (associated with interacting avalanches); at even lower frequency a flat (uncorrelated) region is found, followed finally by an anticorrelated region with positive exponent (typically 1/2), due to large-scale discharge events.[393] All these regions pertain to the spectrum of transport events, while the local turbulence spectrum is generally characterized by larger frequencies. The discharge-event region is thought to be irrelevant in the case of tokamak plasmas,[394] because it involves time scales longer than the confinement time. The f^{-1} and f^{-4} spectra, on the other hand, have been confirmed by specific tokamak simulations.[394,374]

Experimentally, we have often seen a sharp transition from one inverse-power law to a different one at frequencies of the order of 20 kHz (see Fig. 5.3); however, the exponents are in disagreement with SOC predictions, and in fact the exponent is always *smaller* in absolute value at the higher frequencies. It is quite possible that these spectra are those of the local turbulence rather than those of the transport-

event envelope. Indeed, there is no quantitative prediction yet for the characteristic frequencies of the SOC spectrum for relevant modes such as ITG or resistive ballooning instabilities. The model used thus far has involved resistive interchange modes because of their greater tractability;[374] the range given for the f^{-1} region of the spectrum in this model, calculated for the edge plasma of DIII–D, is approximately 1–25 kHz. However, it is likely that electrostatic turbulence (e.g., ITG modes) would give rise to substantially lower frequencies, which may fall below the 8-kHz PCI cutoff. This consideration provides additional motivation for taking measures to lower that cutoff value.

The nonmonotonic features often observed in the H–mode autopower spectra could be interpreted as semicoherent spectral regions, indicative of a weaker turbulent state than in L mode; this is also reflected in the larger decorrelation times measured (see, e.g., Fig. 5.5, especially for the points on and just inside the separatrix). However, the overall H–mode spectrum occupies a broader bandwidth: thus, a decorrelation effect also occurs at the transition from L to H mode.

The narrowband features in H mode do not appear to have similar characteristics to the semicoherent mode often seen in DIII–D, especially by the reciprocating probe.[218] That mode, which occurs late in H mode, is in fact more coherent and is estimated to have too short a poloidal wavelength to be detected by PCI in general. However, it bears some resemblance to a semicoherent MHD mode observed in some H–mode cases with PCI and shown in Fig. 5.60, which will be touched upon again in §6.12.

The time-delayed correlation function can exhibit a variety of shapes, as was discussed in §5.4. Simulations based on the SOC paradigm display double-peaked correlation functions, which reflect the dual nature of the avalanche process: avalanches are caused both by "bumps" propagating down the pressure profile and by voids propagating upwards; this, in fact, is one of the distinguishing features of the SOC in comparison with a marginal-stability state, which supports only downward displacements.[394] Double-peaked correlation envelopes are often measured by PCI [see, e.g., the second box from the top in Fig. 5.4(a)]; in some cases, they result in a cusp near the point $\Delta t = 0$. Moreover, by applying an appropriate high-pass filter the double peak is usually replaced by a single peak [see Fig. 5.4(b)], as would be predicted by the SOC theory, since the double-peaked structure is due to the low-frequency transport-event spectrum rather than to the higher-frequency turbulence spectrum.

However, this agreement is likely to be incidental: the form of the frequency spectra does not conform to SOC predictions, as was discussed above, and the double-peaked correlation functions can be easily interpreted as the result of two counterpropagating wave packets, which our spatial correlation analysis has shown always to exist (see §6.2). This was shown explicitly by the analytical modeling carried out in §4.4, particularly in Eq. (4.66); as noted there, the two counterpropagating radial modes give rise to either a single-peaked or a double-peaked correlation envelope, depending on the relative values of the radial separation, the decorrelation time, and the radial group velocity.

As in the case of the frequency spectra, few concrete predictions of the turbulence decorrelation time have appeared in the theoretical literature; an exception to this is a recent study of global, or "general", drift-wave eigenmodes, which attempted to explain the Bohm-like confinement scaling in L mode on the basis of toroidal coupling of drift waves.[383] The global decorrelation time is estimated there as $\tau_d = qR/v_{ti}$, where q is the safety factor, R is the major radius, and v_{ti} is the ion thermal velocity. This quantity is in the range 0.03–0.8 ms for DIII–D, and can be in agreement with our experimental values (see §5.4) at the low end of that range (for ion temperatures $\gtrsim$ 1 keV).

The dependence of the instrinsic decorrelation time on the wave number is of considerable interest in the context of theories of turbulent transport. The functional dependences shown in Fig. 5.30 are characterized by an infrared divergence of the type $\tau_d \propto k^{-\alpha}$, with $1 \lesssim \alpha \lesssim 1.5$. The Nyquist limit and the signal-to-noise ratio at high k make it difficult to assess whether an ultraviolet divergence also exists, although H–mode data [Fig. 5.30(c)] appear to support this hypothesis.

Infrared divergence was predicted[338] by the solution of the Hasegawa-Mima equation[464] for the nonlinear evolution of collisionless drift waves in a fluid approximation; however, an exponent $\alpha = 3$ was found. In spite of the slower divergence observed experimentally, the results are compatible with the possibility of an infrared "catastrophe",[390] since a diffusivity $D = \sum_k < \tilde{v}^2 >_k \tau_d(k)$ would then imply that transport is dominated by large-scale events. This has been proposed as an explanation for the "global" Bohm scaling in L mode, particularly in connection with the ideas of self-organized criticality.[390] However, the observed transition to gyro-Bohm scaling in H mode requires the disappearance of the infrared divergence,[390] which is found instead to remain unchanged in H mode [see Fig. 5.30(c)]. This suggests that more theoretical work is needed to fully understand the implications of this divergence.

6.6 Spatial Correlations and Wave-Number Spectra

In this section the phenomenology of the spatial turbulence structure, described in §5.5, will be reviewed and discussed.

The structure of the wave-number spectrum measured by PCI is dominated by the peculiarities of the radial-mode spectrum, in particular by the peak at finite k_r. The peak occurs at a value equal to a fraction of the reciprocal of the ion gyroradius, similar to the peak value predicted for the *poloidal* spectrum of collisional drift waves[466,467] at low β.

At large k_r, the spectrum decays rapidly, as was shown in §5.5. This is in qualitative agreement with theoretical expectations. Quantitatively, a number of asymptotic scalings for the $S(k)$ spectrum have appeared in the literature: representative examples are the asymptotic $k^{-17/6}$ dependence[465] and the similar k^{-3} scaling[468] found for collisional drift waves, the $k^{-3/2}$ law[315] and the $k^{-2.4}$ scaling[338] predicted for collisionless drift waves, and the $k^{-3.25}$ dependence of ITG modes.[469] These inverse power laws all have exponents in the range 1.5–3.25. Unfortunately, the experimental resolution and the smoothness of the data at high k are not sufficient to verify these scalings in any quantitatively meaningful way.

The measured radial correlation length is typically of the order of 10–40 ion sound gyroradii. It is often problematic to compare this value with theoretical predictions,[336] as the latter typically involve parameters that are unknown or difficult to measure: this applies, e.g., to predictions for ITG modes,[469] for global drift waves[383] and for trapped-ion modes.[470] Early semiquantitative predictions for ITG modes[334] ($\mathcal{L}_r \sim \rho_i L_s/L_T$, where ρ_i is the ion gyroradius, and L_s and L_T are the magnetic-shear and temperature-gradient scale lengths, respectively) generate values that are somewhat smaller than the experimentally observed range. Also, a three-dimensional slab fluid simulation of drift-resistive ballooning modes carried out specifically for the edge of DIII–D[411] yielded a prediction $\mathcal{L}_r \sim$0.8 cm, which also falls short of the experimental values. On the other hand, a simple scaling for the radial width of toroidal drift modes,[10,383] $\mathcal{L}_r \sim \sqrt{\rho_i L_n}$ (where L_n is the density-gradient scale length), generates values in fair agreement with experiment, if L_n is taken to be of the order of the plasma minor radius.

The results reported in §5.5(b) on the spatial variation of the correlation length (see Figs. 5.12 and 5.13) find no correspondence in theory. It is perhaps not surprising that the correlation length is shorter in the SOL than in the main plasma in L mode, in view of the narrowness (i.e., large gradients) of the SOL. However, the correlation length in the SOL, unlike in the main plasma, is considerably larger in H mode, in spite of the increased narrowness of the SOL; this counterintuitive observation indicates that a qualitatively different type of turbulence exists in H mode, replacing the L–mode activity that is suppressed by the sheared flows: it could be argued, for instance, that Kelvin-Helmholtz or parallel-ion-velocity-gradient instabilities, which can be excited by the sheared flow, may be at work in the H–mode regime in the SOL.

Simulations of self-organized criticality[374] find long correlation lengths in the low-frequency region of the spectrum, indicative of large-scale transport events, or avalanches (see discussion in §6.5). These long correlation lengths reflect the long decorrelation times of the events, which remain correlated as they propagate down the slope of the pressure profile; thus, they should be revealed by a Lagrangian analysis, for instance by studying the correlation length as a function of frequency. These measurements, discussed in §5.5(d), have shown that the correlation length is generally a decreasing function of frequency, but no significant quantitative departures from the Eulerian correlation lengths have been detected (see Figs. 5.19 and 5.20). This corroborates the speculation, advanced in the previous section, that even if an SOC state indeed exists in the plasma, the transport-event region of the frequency spectrum lies below the 8-kHz instrumental cutoff of the PCI system.

The dominance of long-wavelength modes in the turbulence spectrum is a common feature of many measurements is a number of different plasma experiments. In general, most of the fluctuation energy has been found to be concentrated at $k \lesssim 0.2/\rho_i$, especially at the edge and particularly in larger tokamaks;[10,185,230,213,188] in smaller tokamaks the spectrum is often found to peak in the region $k \sim 1/\rho_i$.[47]

Correlation lengths may be expected to differ in different machines, and indeed a fairly wide range of values, from 0.2 to 4 cm, has been reported in the literature.[10,471,231,230,51,47,232] It is somewhat surprising, however, that the radial correlation lengths measured by correlation reflectometry in the edge of DIII–D[233,46] are generally 3 to 5 times shorter than those measured by PCI, albeit in different discharges. This discrepancy is unresolved at present: possible causes may involve the slightly different spatial locations and spectral regions of the two measurements. Results from a new heterodyne reflectometer system are being processed at present and should soon be available for more detailed comparisons.

The dependence of the average radial wave number and of the radial correlation length on local and global plasma parameters in L mode was examined in §5.5(b). As was discussed there, only a few regular trends were found; even in those cases, it is not meaningful to attempt any functional fits, because of the small number of points (in the case of global-parameter scans) or because the data are too scattered (for local-parameter scans). In general, we have found a stronger dependence of the turbulence quantities on the global plasma parameters than on the local ones: this appears to be in qualitative agreement with the measured Bohm-like scaling of the confinement time in L mode, which is theoretically associated with large-scale (or "global") transport events (i.e. involving spatial scales larger than the ion gyroradius).[187,383]

The ability of turbulence to cause radial transport is generally related to the width of the radial correlation region: i.e., a long correlation length would be expected to coincide with higher anomalous diffusivity. Thus, the increase of the characteristic lengths (correlation length, $\mathcal{L}_r$, and average wavelength, $2\pi/k_{0,r}$) with increasing input power and their decrease with increasing current [see Fig. 5.14(a) and (c)] appear consistent with the L–mode scaling of the diffusivity, which is proportional to the square root of the power and inversely proportional to the current.[246] By contrast,

this line of reasoning does not lead to a simple interpretation of the increase of the characteristic lengths with increasing average density; part of this increase may be attributed to a slight increase in input power, but this does not appear sufficient to justify it: an intrinsic dependence on the density thus seems probable.

The sharp decrease of the correlation length when the parameter Dr_{sep} goes from negative to positive [see Fig. 5.14(e)] provides an intriguing link between predictions of neoclassical theory and strong-turbulence shear-decorrelation concepts. We recall that a negative value of Dr_{sep} indicates that the ion ∇B drift points towards the dominant X–point, and vice versa. The H–mode power threshold increases sharply when Dr_{sep} goes from negative to positive.[290] An explanation that has been proposed[472,473] for this observation, within the realm of neoclassical theory, is based on poloidal temperature gradients in the SOL, which point away from the X–point: when the ion ∇B drift also points away from the X–point, the gradients cause an outward energy flux on the outboard side of the tokamak and an inward flux on the inboard side; upon poloidal averaging, the outward flux dominates: thus, confinement is degraded and the power threshold for transition to the high-confinement regime is correspondingly increased. The reverse is true for the case of the ion ∇B drift pointing towards the X–point.

In L mode, the diffusivity, or equivalently the confinement time, appears to depend on the power flow across the separatrix rather than on the total heating power.[291,292] It may thus be argued that the turbulent correlation length should also be a function of the power flow across the LCFS. Therefore, the shorter correlation length found when the ion ∇B drift points away from the X–point may be a result of the lower energy confinement and lower power flow in that case. A shorter radial correlation length, in turn, renders the shear-decorrelation mechanism less effective, since the shearing rate — the key decorrelation parameter — is proportional to the correlation length [cf. Eq. (6.7)]. Thus, under these conditions the H–mode power threshold can be expected to be higher, as is seen experimentally.

Although theoretical models generally suggest that the characteristic spatial scale of the turbulence should scale as some function of the ion sound gyroradius,[221] we have not identified any such dependence. A similar result was obtained with FIR scattering measurements in the TEXT tokamak.[197]

The radial correlation length $\mathcal{L}_r$ decreases as the parameter η_e is increased [see Fig. 5.15(f)]. In general, η_e is of the same order as η_i, which is a measure of the ITG instability drive.[334] The variation of $\mathcal{L}_r$ can then be tentatively attributed to the excitation of a larger number of modes when η_i is large, resulting in a broader k_r spectrum and thus in a shorter correlation length. The scattered decrease of $\mathcal{L}_r$ with increasing magnetic pumping rate [see Fig. 5.15(i)] could also be ascribed to a similar phenomenon: magnetic pumping damps the poloidal plasma flow, which has an inhibiting effect on the turbulence; increasing pumping could then result in increased excitation of ITG moes. The dependence of $\mathcal{L}_r$ on the normalized ion collisionality ν_{*i} probably also reflects the hidden dependence on the magnetic pumping rate: since most of the data fall in the plateau and Pfirsch-Schlüter regimes, the magnetic

pumping rate is a monotonically decreasing function of ν_{*i} (see Eq. 5.1).

The propagation coefficient P_R, a measure of the predominant radial direction of propagation of the turbulence, has also been studied as a function of several plasma parameters. Some trends have emerged, as was discussed in §5.5(b); however, to our knowledge there is no theoretical prediction to which these results can be compared: although radial propagation has been explored in several theoretical papers,[384,383,458,360] each analysis tends to favor one direction of propagation or the other, and no parametric dependence of the directionality is given. For this reason, the parameter scans shown in Fig. 5.16 are offered as a mere phenomenological result for future theoretical consideration.

To conclude this section, we briefly examine the frequency dependence of the spatial correlation parameters, presented in §5.5(d). The correlation length and the average wavelength normally decrease with frequency. This is in general agreement with the fact that most dispersion relations in plasma physics are monotonically increasing.[91] The approximate offset-linear dispersion relation measured in most cases by PCI (see Figs. 5.19 and 5.20) suggests that the group velocity may be the fundamental parameter that defines the spectral distribution of the turbulence. However, it is possible that these dispersion relations are specific to the radial modes rather than determined by general properties of turbulence.

The group velocity is of the order of 1.5–4 km/s in Ohmic and L–mode plasmas, and up to 20 km/s in H mode. These velocities are substantially subsonic, although the H–mode values may approach the ion sound velocity in the SOL (with temperatures of the order of 10 eV). It is likely that these group velocities are determined by some form of linear (toroidal) or nonlinear coupling of drift-wave modes that gives rise to radial propagation. Theoretical studies of these types of coupling[384,360,458,316] have indeed generated group velocities comparable to the experimental values.

6.7 Fluctuation Amplitude and Test of the Mixing-Length Scaling

As we turn to the issue of the absolute amplitude of the fluctuations, it is worth summarizing a few cautionary notes that have appeared several times in this chapter and in the previous ones. At present, estimates of the absolute amplitude of the line-integrated fluctuations are subject to considerable experimental uncertainties, primarily associated with the difficulty of modeling the spatial pattern of the acoustic waves used to calibrate the system; additional uncertainties are contributed by signal-to-noise limitations. As discussed in §3.8, the typical accuracy on the absolute amplitude is 30–40%, while the random channel-to-channel error (with the systematic component removed) is of the order of 10–15%; this can also be taken as a measure of the shot-to-shot error, at least for discharges belonging to the same experimental run.

Estimates of the average density-fluctuation level are even more problematic, since they require a division of the PCI signal by an effective integration length, equal to $(\sqrt{\pi}\mathcal{L}_z L_z)^{1/2}$, where $\mathcal{L}_z$ is the vertical (essentially poloidal) correlation length and L_z is the geometric integration length. These two quantities are known only in an approximate way. In particular, since we lack systematic and direct measurements of the poloidal correlation length in DIII–D, in all cases in this thesis we have used a value of 3 cm, with an estimated uncertainty of ± 1 cm, on the basis of poloidal-wave-number spectra measured by FIR scattering.[321,238]

Of course, even when an rms amplitude is calculated, it cannot be legitimately interpreted as a local measurement, but only as an average along the corresponding PCI chord. As was shown in §4.1, a formal inversion to obtain local values is impossible unless certain symmetry assumptions are made: no such assumptions have been deemed valid in the edge plasmas of DIII–D.

Beyond the intrinsic instrumental uncertainties discussed above, there are also uncertainties associated with components of the turbulence that are not accessed by the measurement. In wave-number space, PCI selects wave vectors with $k_\theta \simeq 0$; dividing the measured amplitude by the effective integration length mentioned earlier gives a correct value for the average fluctuation level only if the turbulence spectrum peaks at $k_\theta = 0$ and if its poloidal width is constant for all values of k_r (see discussion in §4.4). We know in fact that there is a substantial spectral feature that peaks at finite k_θ; however, the considerations of §6.2 lead us to believe that the portion of the spectrum seen by PCI does indeed peak at k_θ: the main uncertainty in estimating the total amplitude is then due to the unknown relative magnitude of the two components.

In frequency space, PCI data below 8 kHz are filtered out. Since the spectra always increase indefinitely as the frequency decreases towards 8 kHz, it can be expected that the unmeasured low-frequency components contain a sizable fraction of the turbulent energy.

The two effects just described are difficult to estimate quantitatively. Hence, we have not attempted to correct for these effects and we must simply accept that our estimates of the average fluctuation amplitude will underestimate the true value in

general.

Parametric studies of the relative fluctuation amplitude, $\tilde{n}/n$, shown in Fig. 5.27, have evinced certain clear trends in some cases. The amplitude of the turbulence increases slightly with applied power, in qualitative accord with the confinement degradation that occurs when auxiliary heating is applied; the *relative* amplitude, however, decreases, because of a concomitant increase in density in the cases shown in Fig. 5.27(a). No clear dependence was found on the plasma current, which has a strong correlation with the diffusivity, and on the magnetic field and the ion sound gyroradius, which are critical quantities in turbulence theory. Past measurements in TEXT, by contrast, did report some dependence (although weak) on the current and on the magnetic field.[185]

The relative fluctuation amplitude is a decreasing function of both the density and the electron temperature [see Fig. 5.27(b) and (c)]. The former result is in agreement with several previously reported scalings.[10] Less information exists on temperature scalings. In some cases, for instance in TEXT[185] and Alcator C,[23] a mode traveling in the ion diamagnetic direction was observed to appear at high density, with a corresponding increase in the fluctuation level. The lack of such a mode in our data may then be attributed to the peculiarities of the radial-mode spectrum.

Also, a decreasing dependence of the relative amplitude on the density-gradient scale length L_n is found [Fig. 5.27(d)], whereas no clear correlation with changes in the temperature-gradient scale length is seen [Fig. 5.27(e)]. In general drift-wave models, the instability drive is inversely dependent on L_n: thus, the large value of $\tilde{n}/n$ at low L_n appears consistent with this scenario. Also, this inverse scaling is in qualitative agreement with the mixing-length relation,[235] $\tilde{n}/n \sim \mathcal{L}_r/L_n$, especially since the radial correlation length $\mathcal{L}_r$ is not strongly dependent on L_n [see Fig. 5.15(d) and §6.6]. More will be said about the mixing-length scaling later in this section.

On the other hand, the drive for the ITG mode is strongly depedent on the ion-temperature gradient: however, it must be remembered that the gradient length shown in Fig. 5.27(e) is for the *electron temperature*; thus, the lack of correlation shown here cannot be deemed conclusive.

It must also be remembered that these local-parameter scans are all unconstrained: in comparing, e.g., Figs. 5.27(b), (c) and (d), the "true" dependence may be on n_e, on T_e, on L_n, or on a combination of the three.

A variety of measurements in tokamaks have reported that the relative fluctuation amplitude $\tilde{n}/n$ increases sharply towards the plasma boundary.[10,23,228,185,213,188] At least part of this increase is due to the negative density gradient, and direct information on the spatial distribution of the absolute level $\tilde{n}$ is generally unavailable.

In our measurements (see §5.6), the line-integrated fluctuation amplitude was found to be relatively flat in the region from 6 cm inside to 1 cm outside the LCFS, with the exception of a sharp peak located approximately 1 cm inside the LCFS (see Figs. 5.25 and 5.26). Since the contribution from the inner layer of the SOL is not negligible, it is difficult to provide an accurate estimate of the integration length in

the vicinity of the LCFS; thus, the information on the distribution of $\tilde{n}$ that can be extracted from these measurements is rather limited. The peak inside the LCFS, however, confirms clearly that this region (the shear layer in H mode) has larger turbulence levels and is thus likely to have an important role in the dynamics of anomalous transport.

As the PCI system is capable of measuring both the absolute amplitude of the density fluctuations and their radial correlation length, PCI data can be used to test the mixing-length scaling.

The mixing-length concept is rooted in fluid-turbulence theory[234] and has been often adopted as an *ansatz* in strong-turbulence models in plasmas.[187] The ansatz, which can be expressed as

$$\frac{\tilde{n}}{n} \sim \frac{\mathcal{L}_r}{L_n}, \tag{6.15}$$

bears a simple intuitive interpretation. As fluctuations, driven by a density gradient, grow towards a turbulent state, their amplitude is assumed to saturate at a level such that the gradient is flattened over the extent of a radial correlation length. The mixing-length scaling has been found to be approximately consistent with several experimental measurements,[10,208,196] although significant discrepancies have also been reported.[10,196,224,235] Also, some theoretical models that do not rely on a mixing-length postulate and can thus put it to the test have found fluctuation amplitudes, e.g. for trapped-ion modes,[470] lower than the ones predicted by the scaling.

A proper test of the mixing-length scaling with line-integrated measurements requires some manipulation of Eq. (6.15). By rearranging the terms, squaring the result, and integrating it along the PCI line of sight, we can write

$$\int \tilde{n}^2 \mathcal{L}_z dz \sim \int \left(\frac{dn}{dr}\right)^2 \mathcal{L}_r^2 \mathcal{L}_z dz. \tag{6.16}$$

The left-hand side of this equation is the mean square value of the PCI signal. The right-hand side can be estimated from the density profile measured by Thomson scattering and mapped to the PCI chord, and by using the radial correlation length measured with PCI; the vertical correlation length $\mathcal{L}_z$, as before, is estimated at 3 ± 1 cm. The calculation is performed by a computer code, which computes the line integral of a cubic spline fit to the integrand on the right-hand side of Eq. (6.16). The result is expressed as the square root of the ratio of the left-hand side to the right-hand side of Eq. (6.16), written as $\tilde{n}/n_{\mathrm{ml}}$, where

$$n_{\mathrm{ml}} \equiv \left[\frac{1}{L_z}\int \left(\frac{dn}{dr}\right)^2 \mathcal{L}_r^2 dz\right]^{1/2}; \tag{6.17}$$

here L_z is the integration length.

The mixing-length test has been applied to several plasma discharges. Results vary considerably, but some notable trends have emerged. In L mode, the fluctuation

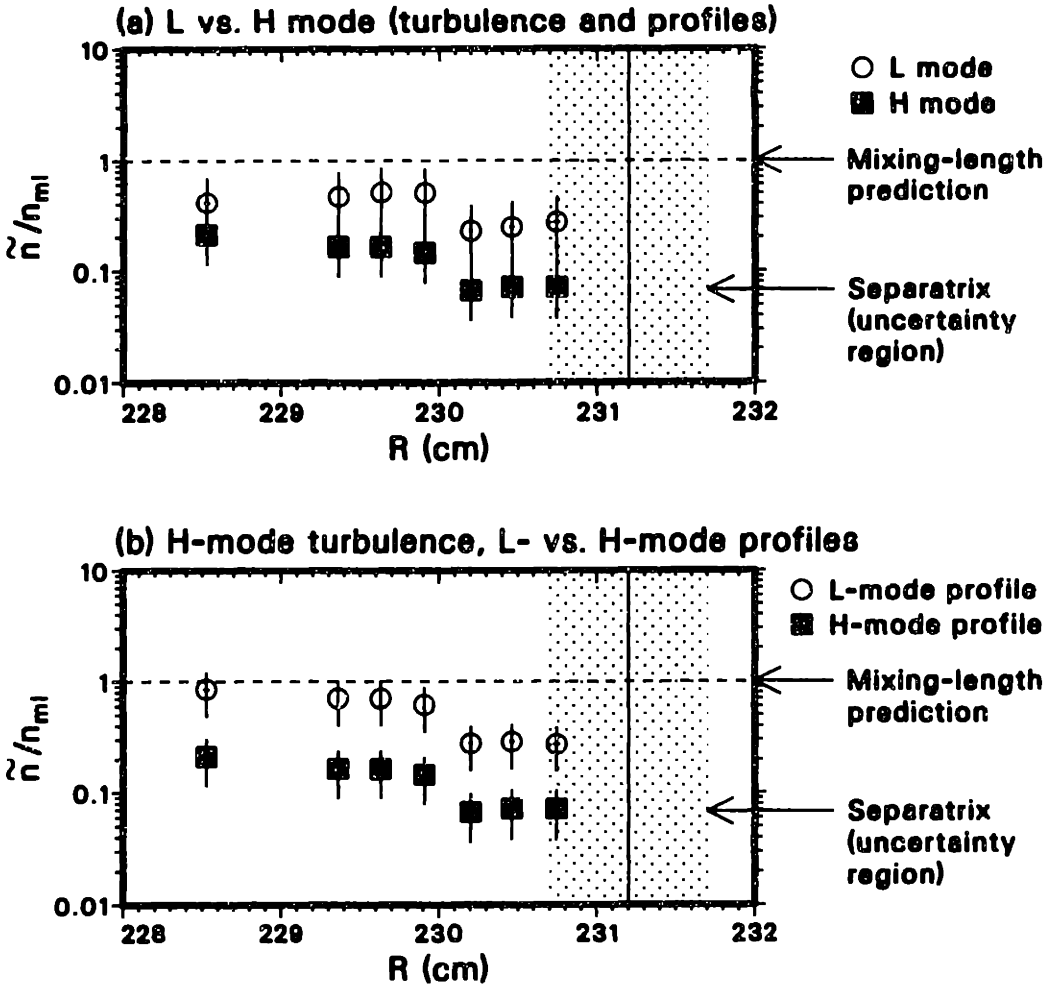

Fig. 6.5 Rms fluctuation density normalized to the value predicted by the mixing-length scaling, (a) for L and H mode, using the respective density gradients, and (b) for H mode, comparing the values obtained by using, respectively, the L-mode and the H-mode density gradient. The vertical correlation length was estimated to be 3 cm; the measured radial correlation lengths are 1.19 cm in L mode and 0.82 cm in H mode. The abscissa is the major radius of the PCI chord on the midplane. The plasma parameters are B_T=2.1 T, I_p=1.25 MA, $\bar{n}_e$=3.5×10^{13} cm^{-3}, input power = 6.2 MW.

amplitude is generally within one order of magnitude of the mixing-length value, and is lower than it in most cases. In H mode, $\tilde{n}/n_{ml}$ is normally approximately one order of magnitude lower than in L mode, although in a few cases the two were found to be comparable. A typical case for L and H mode, for seven different PCI chords, is shown in Fig. 6.5(a). The spatial variations seen in the figure are not particularly significant, as their character changes considerably from shot to shot.

As was discussed at the beginning of this section, PCI estimates of the absolute amplitude $\tilde{n}$ are believed to underestimate the true value. Thus, L-mode results are roughly consistent with a mixing-length scaling, indicating the presence of strongly

turbulent activity. The sub-mixing-length scaling of H–mode plasmas then may possibly suggest a transition to a weaker-turbulence regime; thus, the mechanisms that suppress the fluctuations in H mode could cause a qualitative, as well as quantitative, change in the nature of the turbulence. This is in general agreement with theories that have attempted to explain the transition from a Bohm-like to a gyro-Bohm diffusivity scaling from L to H mode as a transition from strong to weak turbulence.[390,394,389]

However, a caveat is in order. The drop of $\tilde{n}$ below the mixing-length value in H mode is due both to a relatively modest decrease in $\tilde{n}$ and to an often sharp increase in the density gradient. In other words, the fluctuation amplitude drops *even though* the instability drive becomes in fact larger; in fact, as the H mode evolves, the enhanced drive does indeed cause the amplitude to increase again, as was shown in §5.10 (see, e.g., Fig. 5.47). The early H mode, used for the mixing-length test, is thus a transient phase, during which the turbulence suppressed by the flow shear has not had enough time to recover under the effect of the increased gradient drive. It is of some interest, then, to test the mixing-length scaling in H mode also by calculating n_{ml} from the *L–mode* density profile (but using the H–mode correlation lengths).

The result is shown in Fig. 6.5(b) alongside the one calculated previously by employing the H–mode profile. Clearly, by using the L–mode profile the fluctuation amplitude in H mode becomes considerably closer to the mixing-length value, and the scaling is in fact quite similar to the L–mode scaling shown in Fig. 6.5(a). This reflects the fact that the decrease in the amplitude $\tilde{n}$ at the L–H transition is of the same order as the decrease in the radial correlation length. Thus, if this line of reasoning is correct, it must be concluded that a strong-turbulence mixing-length scaling applies equally to L–mode and H–mode plasmas.

6.8 Self-Organized Criticality

Self-organized criticality (SOC) is one of the most promising among recent developments in plasma turbulence theory.[390,394,374] As it is still in a very early phase, this theory — which was introduced briefly in §6.1 — has offered thus far only a few preliminary predictions that could be tested experimentally. At various points in the course of this chapter, several possible tests have been explored. The aim of this section is to provide a brief summary of these ideas, with some additional considerations.

The frequency spectrum in an SOC is found from numerical analysis to be characterized by a number of distinct regions, characterized by different power laws and by sharp transitions from one region to the next.[393,394] While similarly sharp changes in slope have been documented with PCI, there is substantial disagreement on the power laws. It was argued in §6.5 that the spectrum measured by PCI is the local turbulence spectrum, whereas the characteristic spectra of the large-scale transport events that are the hallmark of an SOC are likely to be located at very low frequency, below the 8-kHz PCI cutoff point.

Some qualitative agreement was found in the form of the PCI time-delayed correlation functions, which are often double-peaked as found in numerical SOC analyses. In view of the above considerations on the frequency spectrum, this agreement was deemed incidental, particularly since the form of the correlation functions bears a simple explanation in terms of the well-documented coexistence of inward- and outward-propagating radial modes.

The infrared divergence in wave-number space of the intrinsic decorrelation time, also discussed in §6.5, could be related to a dominance of the diffusivity on the part of large-scale (i.e., low-k) events.[390] However, the infrared divergence survives in H mode, in disagreement with predictions.

Finally, our measurements failed to reveal Lagrangian correlation lengths (that is, calculated in the frame of reference of the traveling wave packet) substantially longer than their Eulerian (i.e., local) counterparts, as discussed in §6.6.

An important additional feature of SOC models is intermittency in transport.[394,474] The intermittency is a result of the statistics and probability dynamics of large-scale transport events, and is not related to any intermittency in the turbulence itself;[394] indeed, a flux associated with fluctuations that obey Gaussian statistics is characterized by non-Gaussian statistics,[373] which is a necessary (though not sufficient) condition for intermittency. It should also be noted that intermittency itself is not a sufficient condition for an SOC state to exist: intermittency is also seen in supercritical transport.[374]

Assessing whether a given dynamical system is intermittent is very difficult experimentally, as it involves studying the spatial and temporal structures of the fluctuations over large scale ranges, to test whether scale invariance is broken. Generally, only normality tests on the probability distribution function (PDF) are performed: a Gaussian or platykurtic[170] PDF (i.e., with $K \leq 3$, where K is the kurtosis) would

rule out intermittency, whereas a leptokurtic PDF ($K > 3$) would be compatible with, but not prove, intermittency.

As was discussed in §5.7, the PDF of PCI data, when estimated over intervals shorter than ~40 ms, was generally found to be Gaussian in all heating and confinement regimes. Moreover, the separate PDFs of the low-frequency and high-frequency regions of the spectrum (separated at 40 kHz) are also Gaussian. No intermittency can therefore exist over time scales of the order of 40 ms or less.

Over longer intervals, particularly approaching 200 ms, the PDF invariably becomes more peaked and leptokurtic, with an asymptotic kurtosis of 5.3–5.6. This behavior may thus be indicative of intermittency over long time scales, in agreement with the SOC paradigm that attributes transport to "rare", large-scale events.[390,374] Intermittency is meaningful only if it involves spatial scales in the "inertial range", i.e. larger than the dissipation range for Landau damping ($k_\parallel v_{ti}/\omega \gtrsim 1$) and viscous gyrodamping ($k_\perp \rho_i \gtrsim 1$);[203,204] in the dissipation range intermittency is expected to arise from the dynamics of mode damping. In general, knowledge of the wave-number spectra allows us to conclude that the PDFs measured belong indeed to the inertial range.

Also, the time scales involved support the conclusion that the frequency spectrum of these events lies well below 8 kHz. Direct observation and characterization of these events is likely to be very difficult with any experimental technique.

6.9 Estimates of Turbulent Diffusivity

The transport of particles and energy caused by electrostatic turbulence is an important consideration for thermonuclear plasmas. By contrast, the power flux due to the electrostatic fields themselves is generally negligible: the kinetic-energy content of electrostatic modes is always far larger than its electrostatic potential energy. This can be seen easily by writing the kinetic energy as $\mathcal{E}_{\text{kin}} = nm_i\tilde{v}^2/4$ and the potential energy as $\mathcal{E}_{\text{pot}} = \tilde{E}^2/(16\pi)$; with $\tilde{v}$ equal to the $\mathbf{E}\times\mathbf{B}$ velocity, we find that the ratio of the potential to the kinetic energy is approximately $\mathcal{E}_{\text{pot}}/\mathcal{E}_{\text{kin}} = v_A^2/(4c^2)$, where v_A is the Alfvén velocity: this ratio is typically in the range $1\text{–}3\times10^{-4}$.

Thus, the direction and magnitude of the group velocity are of far lesser significance to confinement than those of the $\mathbf{E}\times\mathbf{B}$ velocity. In a turbulent state, these quantities, as well as the cross-phase between the fluctuating scalars (e.g. density and radial velocity), are difficult to calculate and predict in general. Experimentally, in the case of a scalar measurement such as that performed by PCI, we can only attempt to estimate the fluxes and the diffusivities on the basis of generic strong-turbulence assumptions.

Here, we use a random-walk approximation, and estimate the diffusivity as $D_{\text{rw}} = \mathcal{L}_r^2/\tau_d$, where $\mathcal{L}_r$ is the radial correlation length and τ_d is the intrinsic decorrelation time, both of which are measured by PCI. We find that D_{rw} is typically in the range 1–20 m^2/s. These values are roughly of the same order as the ion diffusivity at the edge, where the estimate is made; however, it should be noted that transport analysis, hence a determination of the diffusivity, is particularly problematic in this region.

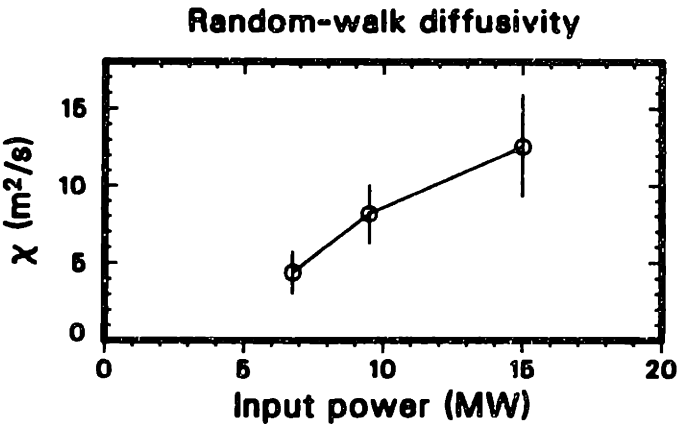

Fig. 6.6 Random-walk diffusivity, calculated as the ratio of the square of the radial correlation length to the intrinsic decorrelation time, as a function of input neutral-beam power in an L–mode plasma. The plasma parameters are B_T=2.1 T, I_p=1.35 MA, $\bar{n}_e$=4×10^{13} cm^{-3}.

By way of illustration, Fig. 6.6 shows D_{rw} as a function of the neutral-beam power in L mode, combining data from Figs. 5.7(b) and 5.14(a). The random-walk diffusivity increases with power, in qualitative agreement with the diffusivity scaling in L mode (proportional to the square root of the power[246]).

In a random-walk model, the confinement degradation that occurs when auxiliary heating is applied appears to be caused mostly by a decrease in the decorrelation time in the edge region (see, e.g., Fig. 5.5 for τ_d in the Ohmic and L–mode regimes), and to a lesser extent by an increase in the correlation length [as was discussed in §5.5(a)].

6.10 Tests of Theories of the L–H Transition

The review of the theoretical work on the L–H transition in §6.1(e) touched on several ideas concerning the cause of the suppression of turbulence and transport that accompanies the transition. It is now generally accepted that the shear in the plasma flow velocity, particularly the $\mathbf{E} \times \mathbf{B}$ velocity, plays a crucial role in the transition. However, as discussed in §6.1(e), several different mechanisms whereby shear can affect turbulence have been proposed. In particular, a number of papers[375,395,396,398] have found various criteria for *linear* stabilization of the relevant instabilities. These criteria are generally different for different modes and involve the linear drives (i.e. gradients) rather than the properties of the turbulence. Thus, although some of these criteria can be and have been verified by experimental measurements, these tests do not generally involve fluctuation diagnostics specifically. In this section, therefore, we shall concentrate on the *nonlinear* shear stabilization of turbulence.

The prototypical nonlinear shear-decorrelation criterion, set forth by Biglari, Diamond, and Terry,[63] is found in Eq. (6.6), which is repeated here for convenience: $\omega_s > \omega_T$, where $\omega_s \equiv v'_{\mathbf{E}\times\mathbf{B}}\mathcal{L}_r/\mathcal{L}_\theta$ is the shearing rate and $v'_{\mathbf{E}\times\mathbf{B}}$ is the velocity shear, and $\omega_T \equiv 1/\tau_d$ is the reciprocal of the decorrelation time in the absence of

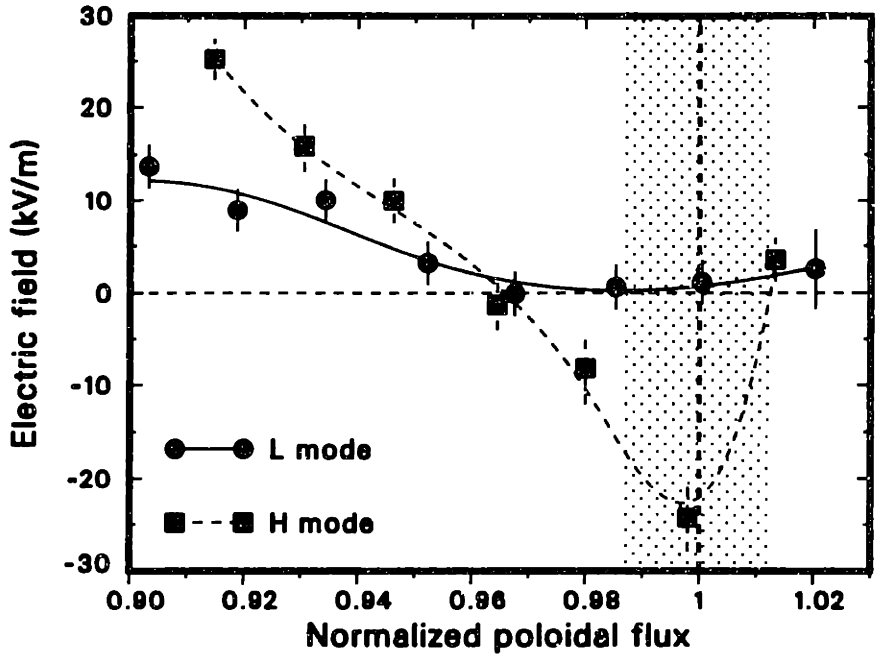

Fig. 6.7 Profiles of the radial electric field in the outer 10% of the plasma cross section, determined by charge-exchange recombination spectroscopy and fitted by a cubic spline, in L and H mode. The plasma parameters are B_T=2.16 T, I_p=1.54 MA, $\bar{n}_e$=3×10^{13} cm^{-3}, input power = 8.5 MW.

shear (L mode). While other details differ, sometimes substantially, this criterion has been widely accepted and has appeared as a key ingredient in a number of other theories.[415,405,414] In one study,[406] the $\mathbf{E} \times \mathbf{B}$ drift was replaced by the total electron flow ($\mathbf{E} \times \mathbf{B}$ plus diamagnetic drift). In the following discussion we shall address only the more common criterion, involving only the $\mathbf{E} \times \mathbf{B}$ velocity.

The PCI system is capable of determining simultaneously two of the parameters involved in the shear-decorrelation criterion, that is the radial correlation length $\mathcal{L}_r$ and the intrinsic decorrelation time τ_d. Moreover, these parameters can be studied as they vary in time, with a resolution of a few ms. A quantitative test of the criterion then becomes possible. As before, the poloidal correlation length is estimated from wave-number spectra measured in the past by FIR scattering:[321,238] the estimated value is 3±1 cm. This is also consistent with published data from BES measurements in TFTR.[51] The electric-field profile is measured by charge-exchange recombination spectroscopy, and the profile is then fitted with a cubic spline, as shown in Fig. 6.7 for an L–mode and an H–mode case in the outermost 10% of the plasma cross section.

Using all the above ingredients, the quantities ω_s and ω_T are compared in the spatial plots of Fig. 6.8. The quantities derived from PCI measurements are determined by statistical averages in the region $0.95\rho_n < 1.0$ (where ρ_n is the normalized poloidal flux). This range is visualized by the segment drawn for ω_T. The largest contribution to the error bar for ω_s is given by the estimate of the poloidal correlation length. As can be seen clearly in the figure, the shear decorrelation criterion is found to be well satisfied in H mode, whereas the quantities ω_s and ω_T are approximately

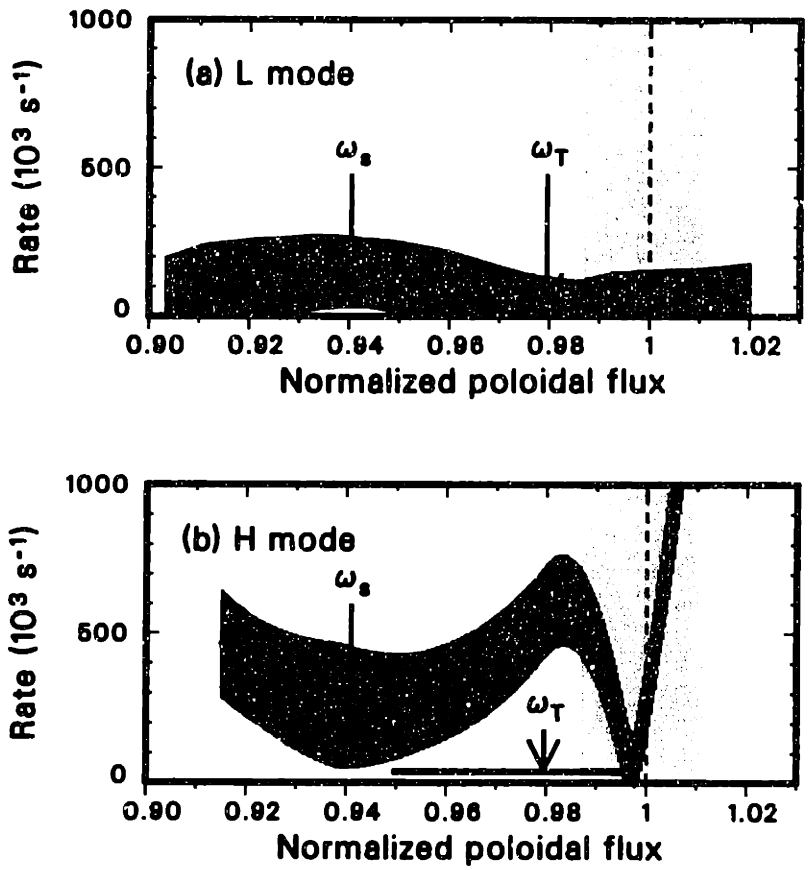

Fig. 6.8 Shearing rate ω_s vs. intrinsic turbulence decorrelation rate ω_T in L and H mode. The shearing rate, $\omega_s = (\mathcal{L}_r/\mathcal{L}_\theta)(dv_{\mathbf{E}\times\mathbf{B}}/dr)$, is determined from the electric-field profiles shown in Fig. 6.7, from the radial correlation length measured by PCI, and from an estimate of 3±1 cm for the poloidal correlation length based on FIR scattering measurements; the shaded area indicates a confidence interval. The decorrelation rate, equal to the reciprocal of the intrinsic decorrelation time, is shown as a segment over the spatial range used by PCI to estimate its value. The plasma parameters are B_T=2.16 T, I_p=1.54 MA, $\bar{n}_e$=3×10^{13} cm^{-3}, input power = 8.5 MW.

of the same order in L mode, in agreement with theory.[63]

Two theories of the L–H transition provide explicit, and different, scalings for the radial correlation lengths and decorrelation times in L and H mode. The Biglari-Diamond-Terry (BDT) analysis,[63] carried out in cylindrical geometry, is expected to be valid in the limit of large $\mathbf{E} \times \mathbf{B}$ shear; the Hahm-Burrell (HB) theory,[416] developed in toroidal geometry, should be more applicable to the moderate-shear case. PCI measurements have allowed for the first time a quantitative test of these models.

The experimentally measured ratio of the H–mode and L–mode radial correlation lengths, for a set of DIII–D discharges, is plotted alongside the two scalings in Fig. 6.9, as a function of the shear decorrelation parameter $\omega_s\tau_d$. The BDT scaling is[63]

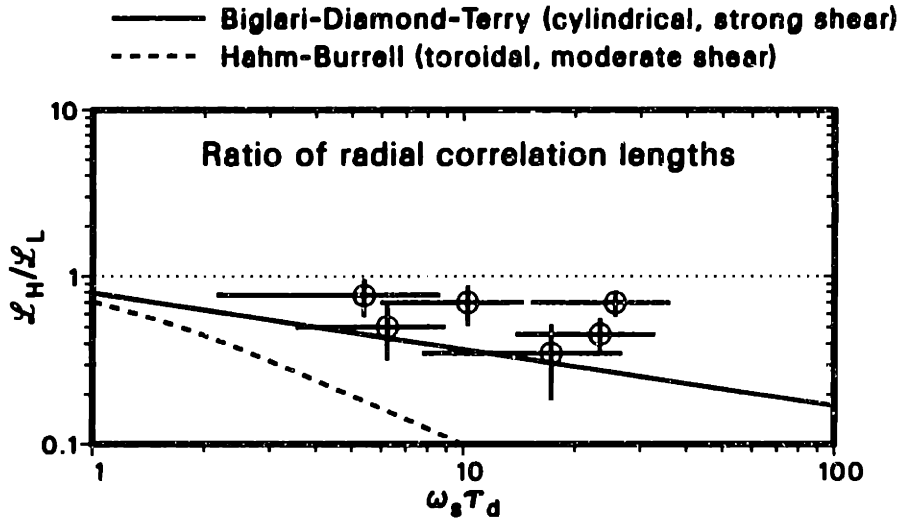

Fig. 6.9 Ratio of the radial correlation lengths in H and L mode, as a function of the shearing rate multiplied by the intrinsic turbulence decorrelation time: values measured by PCI (circles), prediction of Biglari-Diamond-Terry theory[63] for strong shear in cylindrical geometry (solid line), and prediction of Hahm-Burrell theory[416] for moderate shear in toroidal geometry (dashed line). The experimental values refer to the region $0.95 < \rho_n < 1.0$, where ρ_n is the normalized poloidal flux.

$\mathcal{L}_H/\mathcal{L}_L \simeq (2\omega_s\tau_d)^{-1/3}$, where the subscripts L and H denote L–mode and H–mode quantities, respectively; the HB scaling is[416] $\mathcal{L}_H/\mathcal{L}_L \simeq (1+\omega_s^2\tau_d^2)^{-1/2}$. Within the error bars, the BDT scaling appears to provide a reasonable fit, as would be expected from the large value of the $\mathbf{E}\times\mathbf{B}$ shear (measured by the abscissa $\omega_s\tau_d$). The HB scaling is considerably less satisfactory.

The ratios of the intrinsic decorrelation times for the same set of shots are plotted in Fig. 6.10, again with the BDT and HB fits. The BDT scaling is $\tau_H/\tau_L \simeq (2\omega_s\tau_d)^{-2/3}$. The HB scaling includes only a logarithmic dependence on a complicated combination of parameters; for practical purposes, a constant value of 1 (i.e. decorrelation time essentially unchanged from L to H mode) can be used. In this case, the roles of the two fits are reversed and the HB scaling fits the data better than the BDT scaling. This discrepancy may be attributed to the incomplete nature of the theories that generate these scalings, which only consider the effect of flow shear on the turbulence, through a two-point correlation analysis, but are not self-consistent. Indeed, as was observed in §6.1(e), the BDT scalings would imply equal diffusivities in L and H mode in a random-walk scenario, an obviously false result; thus, it is perhaps reasonable that the BDT scalings for $\mathcal{L}_r$ and τ_d are not both valid.

In self-consistent theories, however, the decorrelation time has been modeled only in an ad hoc manner. The dependence of τ_d on shear is a power law[442,362] $\tau_d \propto \omega_s^{-2}$;

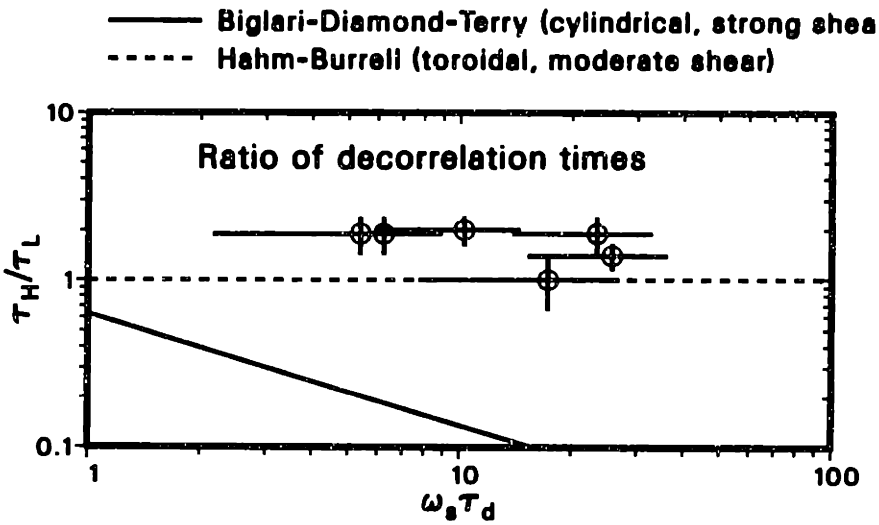

Fig. 6.10 Ratio of the intrinsic decorrelation times in H and L mode, as a function of the shearing rate multiplied by the intrinsic turbulence decorrelation time: values measured by PCI (circles), prediction of Biglari-Diamond-Terry theory[63] for strong shear in cylindrical geometry (solid line), and prediction of Hahm-Burrell theory[416] for moderate shear in toroidal geometry (dashed line). The experimental values refer to the region $0.95 < \rho_n < 1.0$, where ρ_n is the normalized poloidal flux.

by inspecting Fig. 6.10, it is easy to see that this scaling law is even less satisfactory than the BDT scaling. Indeed, the decorrelation time is experimentally found to *increase* slightly at the L–H transition in most cases, as the figure shows. This may simply indicate an increased stability of the modes, which leads to a smaller growth rate and thus to a larger decorrelation time; or it could be argued that the chief L–mode instabilities (e.g., ITG modes) are drastically suppressed in H mode and are replaced by new and less virulent instabilities (perhaps Kelvin-Helmholtz or parallel-ion-flow-gradient modes), which would then have altogether different characteristics. In this case, a proper test of the nonlinear scalings discussed above would require an isolated analysis of the modes that are suppressed, a very difficult task in practice.

A complete self-consistent theory of the L–H transition would require also an explicit calculation of the anomalous diffusivity. As was discussed in §6.1(d), only heuristic or phenomenological estimates can be used at present. The most widely used estimate is based on a random-walk model, with the diffusivity given by $D_{\rm rw} = \mathcal{L}_r^2/\tau_d$. The ratio of the experimental random-walk diffusivities in H and L mode, calculated for the same set of discharges of Figs. 6.9 and 6.10, is plotted in Fig. 6.11. This ratio is in the range 0.1–0.4. Thus, the diffusivity drops by more than the factor of two that would be expected by the doubling of the confinement time typically seen from L to H mode. However, it must be remembered that the PCI measurements are carried

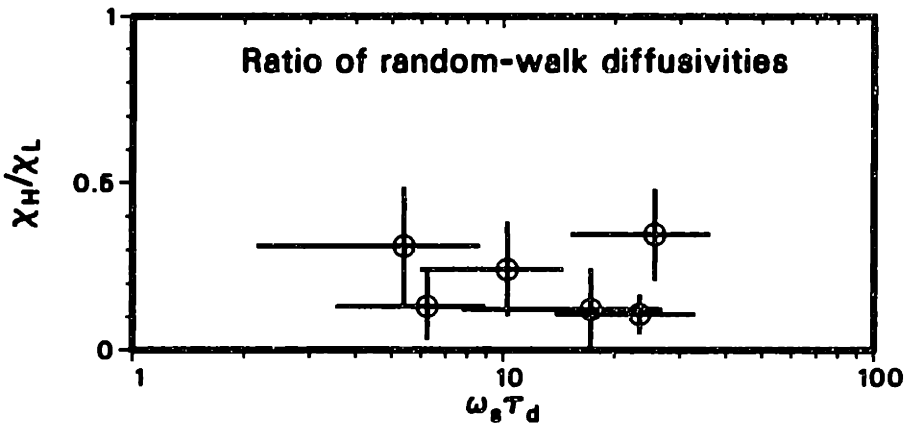

Fig. 6.11 Ratio of experimental random-walk diffusivities in H and L mode, as a function of the shearing rate multiplied by the intrinsic turbulence decorrelation time. The diffusivity is calculated as the square of the radial correlation length divided by the intrinsic decorrelation time: both quantities are determined from PCI measurements. The experimental values refer to the region $0.95 < \rho_n < 1.0$, where ρ_n is the normalized poloidal flux.

out at the edge, where the transport barrier forms first, while the confinement time is a global quantity. It can thus be argued that the local diffusivity (a quantity that is difficult to measure accurately at the edge) may decrease by more than a factor of two, in agreement with the random-walk estimate.

Among the PCI observations that are unexplained at present, one deserves special mention. As was shown in §5.10 (see Fig. 5.37), both the average frequency of the turbulence and the exponent in the inverse-power-law fit to the frequency spectrum change (the former increases, the latter decreases) 2 to 5 ms *after* the L–H transition; by contrast, the amplitude of the turbulence and the radial correlation length are always seen to change at the time of the transition within the temporal resolution of the measurement. Future theoretical investigations of the L–H transition should address this discrepancy in behavior.

6.11 Slow L–H Transitions

"Slow" L–H transitions, obtained by operating at input powers only slightly above the H–mode threshold, are characterized by a peculiar phenomenology, which was described in §5.9. The peculiarity is an intense turbulent activity that begins approximately 0.6 ms after the L–H transition and raises the fluctuation level to a value comparable to that of L mode, and in some locations larger than it. As measured by PCI, this activity peaks on a chord that intersects the midplane about 1 cm outside the LCFS. During this turbulent phase, which lasts up to 20–30 ms, the D_α emission signal continues to decrease slowly: thus, the turbulence does not affect confinement significantly; when the D_α signal reaches its H–mode steady-state value, the turbulent activity subsides and normal H–mode fluctuation levels are established.

The location of the peak in amplitude, combined with its exceptionally large magnitude in absolute terms, suggests that this activity is localized to the SOL, particularly to a region 1 to 2 cm outside the LCFS. The inner chords would also be affected by this activity as they cross the SOL, but to a lesser extent, since the integration length is longest on the chord intersecting this region at an approximately tangential angle. This is consistent with observations. Also, the irregularities in the frequency spectrum inside the LCFS could be explained as the sum of two distinct spectra: that of the SOL and that of the main plasma. Only the latter would appear on the outside chords.

In this early-H–mode phase, the large correlation level between the SOL and locations inside the LCFS, shown in Fig. 5.46, is also consistent with a large-amplitude turbulence localized to a region within the SOL, if the additional assumption of a long poloidal correlation length is made. The inner chords intersect this region at some poloidal distance from the location of the SOL chords, so that a long poloidal correlation length would allow their line-integrated signals to be well correlated.

The physical mechanisms at play in this early-H–mode activity are unclear at present. This SOL turbulence may be related to a parallel-ion-velocity-gradient (PIFG) instability[362] (or possibly a Kelvin-Helmholtz instability[63]). Unfortunately, measurements of the parallel velocity in these shots, while suggesting the existence of large gradients, do not have a sufficiently large signal-to-noise ratio to provide a clear answer. Even if better measurements were available, it would be difficult to verify the conditions for the PIFG instability, as they depend crucially on the signs of the poloidal and toroidal wave numbers;[366] the latter is particularly difficult to measure. To pursue this line of inquiry further, specific simulations are needed with existing codes.[366]

6.12 Edge Localized Modes and Other Transient Events

As was discussed in §6.1(f), much remains unknown about the physics of Edge Localized Modes (ELMs). In particular, there has been no theoretical work predicting the characteristics of the broadband turbulence that accompanies the ELMs. The phenomenological studies of ELMs performed with PCI in DIII–D, that were presented in §5.11, are thus mainly offered as material for future theoretical interpretation. In this section we shall merely explore some points of interest that have emerged from those studies.

The broadband turbulence within a type-I or type-III ELM is, within the resolution of the measurements, similar to L–mode turbulence. In particular, the frequency spectra are entirely analogous; the characteristic spectral lengths (correlation length and average wavelength) are slightly longer for ELMs, and their monotonically decreasing dependence on frequency is somewhat weaker. The main differences between ELM and L–mode turbulence are its amplitude (typically a factor of 3–4 higher for ELMs), its spatial location (predominantly in the vicinity of the LCFS in L mode, whereas it encompasses most of the SOL during an ELM), and its predominant radial direction of propagation (indifferent in L mode, always outward during an ELM).

In view of the similarity of the turbulence signatures in L mode and during an ELM, the ELM could be described as an H–L "back" transition followed by an L–H transition. The remaining differences in the turbulence, as well as the greater speed of the ELM termination in comparison with an L–H transition, may be ascribed to the different pressure profiles in the two cases.[69]

The chief difference between type-I and type-III ELMs, in terms of their broadband-turbulence content, is the timing of their appearance in relation to the peak in the D_α signal: the peak in the fluctuation amplitude precedes the D_α peak by 0.4–0.6 ms in the case of a type-III ELM, whereas the two are simultaneous for a type-I ELM. This key new result should be a focus of both theoretical analysis and further measurements with other diagnostics. The magnitude of the delay for type-III ELMs is qualitatively consistent with typical growth times involved in resistive MHD instabilities;[221] it may then be argued that the onset of a resistive ballooning instability, believed to trigger the type-III ELM,[311] would cause transport and expulsion of particles on such a time scale, after which a peak in the recycling signal can be expected to occur. By contrast, ideal-MHD time scales are in the μs range; this is consistent with the lack of measurable delay seen in the case of type-I ELMs.

The peculiar phenomenology of type-I ELMs in the SOL, where seemingly random "echoes" to the primary ELM event are often seen in the PCI signal (see Fig. 5.53), is also rather intriguing. It may be speculated that as the rate of transport returns to H–mode levels after the occurrence of an ELM, the readjustment of the profiles may lead to local violations of the ideal balooning stability condition in the SOL.

An important question in any study of ELMs is the relation of the broadband turbulence to the various MHD instabilities that are believed to trigger the ELMs.

It is generally believed that the onset of the MHD mode causes a self-consistent adjustment of the plasma equilibrium,[68] which leads in turn to an increased level of turbulence, probably through a temporary slowing down of the sheared flows[299] that regulate turbulence in H mode. The ELM is terminated when conditions for H mode are reestablished.

This general picture is consistent with the lack of coherent activity observed by PCI during or before a type-I ELM, again because of the rapid growth of ideal MHD instabilities (in the μs range); however, it should be noted that semicoherent precursor activity to type-I ELMs has been documented by reflectometry in DIII–D,[69,308] in possible disagreement with this interpretation. On the other hand, the considerably slower growth rates of resistive MHD events can explain the observation of a coherent mode during the duration of a type-III ELM (see Fig. 5.56). The outward propagating character of this mode also suggests that it may be a manifestation of a semicoherent mode seen earlier by reflectometry:[312] in that case, the precursor oscillations were observed to move radially outwards during a period of 10–20 ms until they triggered the ELM; at this point, they should indeed be expected to be visible on the PCI signal, which is only affected by the outermost region of the plasma.

To conclude this section, it is worth recalling that coherent modes are observed not only during type-III ELMs but in a variety of plasmas, primarily during H mode (see §5.12). No systematic study of these phenomena has yet been carried out with PCI data. We merely note here that these modes do not appear to influence the broadband turbulence significantly; however, it would certainly be worth carrying out a more accurate characterization of the interaction of coherent and broadband fluctuations through bicoherence analysis.

The semicoherent bursts occasionally seen in H mode (see Fig. 5.60) could be related to a semicoherent mode seen often by the reciprocating probe in DIII–D well into H mode.[218] This possible correspondence, as well as the nature of the mode, should be explored further in the future.

6.13 Conclusions

As was announced in the prologue to this chapter, many of the key results described in this thesis are of a phenomenological nature and thus await further theoretical analysis. However, it has also been shown that PCI measurements have already allowed direct verification of theoretical predictions in several areas, and qualitative interpretations of the results have been offered in several other cases.

In some ways, theory and experiment in the field of plasma turbulence have now reached a symbiotic and specular relationship. Verification of existing theories requires measurements that are currently beyond our present capabilities (e.g. the turbulent Reynolds stress); at the same time, however, experiments are providing information that theory has thus far been unable to address (e.g., in the case of PCI, the parametric dependence of radially propagating turbulence). Further progress, thus, can likely only come from fundamental innovation, both in analytical and numerical methods and in experimental techniques.

In view of the inherent difficulties that characterize the study of turbulence, both theoretically and experimentally, the progress reported in this thesis is rather encouraging, and provides special validation to the specific diagnostic approach of laser imaging. Further work both with the existing PCI instrument on DIII–D and with new instruments yet to be developed would be certain to further advance our knowledge of plasma turbulence and anomalous transport in tokamaks.

7 Other Applications of Phase-Contrast Imaging

The mergence of two of the most vital areas of contemporary optics, image processing and laser technology, has provided experimenters in fluid dynamics and plasma physics with a powerful new diagnostic tool. Novel imaging techniques are constantly being devised, and the field will undoubtedly continue to find new applications in the future.

This chapter is devoted to a few selected applications of the phase-contrast imaging (PCI) technique, which spring naturally from the main work described in this thesis. These methods are directly applicable to the specific environment of tokamak plasmas, and could in fact be explored experimentally by modifying the DIII–D PCI apparatus. The basic ideas are not new and have been proposed previously by other authors. However, a thorough analysis was lacking, and the following discussion attempts to fill the gap between the conceptual and the practical.

This chapter is configured as follows. A heterodyne version of PCI is considered in §7.1; possible advantages over the homodyne case are discussed, and the main properties of the technique, including responsivity and sensitivity, are analyzed briefly and compared with those of homodyne PCI. Section 7.2 shows how the symmetry properties of the phenomenon under study may be exploited to improve the spatial resolution of the measurements; the chief limitation of transmission techniques, namely, the lack of resolution along the direction of propagation of the beam, may be circumvented by an appropriate choice of beam geometry. An alternative method that can be employed to achieve a similar result is presented in §7.3: in this scheme, the line-integrated signals from two crossed beams are correlated to localize the measurement to the intersection region; third- and fourth-order correlations may also be used to study the nonlinear coupling between plasma modes. The discussion in §§7.2 and 7.3 is not limited to the phase-contrast method, rather it applies to any line-integrated imaging technique. Finally, some suggestions for future work and possible upgrades of the DIII–D PCI system are offered in §7.4.

7.1 Heterodyne Phase-Contrast Imaging

When a phase-contrast imaging apparatus is employed to investigate externally launched rf waves, measures must be taken against the possibility of electromagnetic pickup of the source signal in the detection electronics. Owing to the instrinsically high sensitivity of the diagnostic technique and to the narrow bandwidth of the source, it may be difficult in practice to shield the electronics to such a degree that direct pickup becomes undetectable. As Weisen pointed out,[142] such problems can be prevented altogether by employing an optically heterodyne configuration, so that the measured signal appears at a different frequency than that of the reference signal.

For an internal-reference system such as PCI, the simplest heterodyne configuration is obtained through intensity modulation of the laser power. The resulting power flux can be written in the general form

$$\mathcal{E}_{\text{het}}(\mathbf{x}_\perp, t) = \alpha\mathcal{E}\big[1 + \beta\cos(\omega_m t)\big], \tag{7.1}$$

where ω_m is the modulation frequency and $\mathcal{E}$ is the total flux available from the laser source; here, $0 < \alpha \leq 1$, as the time-averaged flux cannot be larger than $\mathcal{E}$, and $0 < \beta \leq 1$, as the instantaneous flux cannot be negative.

Since the modulational factor is independent of $\mathbf{x}_\perp$, the analysis of the response properties of PCI that was carried out in §§2.10 and 2.11 is also applicable to the heterodyne case. Both the dc signal $\mathcal{E}_{\text{dc}}$ and the fluctuating signal $\tilde{\mathcal{E}}$ calculated previously are now simply multiplied by the factor $\alpha\big[1 + \beta\cos(\omega_m t)\big]$. Therefore, the nonfluctuating signal will now have an actual dc component and a component at the modulation frequency ω_m; similarly, the fluctuating component will appear both at its natural frequency ω and at the shifted frequencies $\omega_m \pm \omega$, in two symmetric sidebands about ω_m. Whether detection is effected on a single sideband or on both sidebands, the spatial response properties of this heterodyne system are identical to those of homodyne PCI.

Differences arise, however, in the signal-to-noise ratios of the two configurations. A preliminary observation is that in the case of double-sideband processing (accomplished, e.g., by straight mixing of the detector signal with the modulation reference signal, followed by quadrature detection), the noise power is twice that of the corresponding homodyne case, owing to the contributions of the two sidebands. There is, therefore, an unavoidable loss of a factor of two in the signal-to-noise ratio. In single-sideband processing, the loss is greater, since although the noise is not doubled, the signal power is reduced by a factor of four, as is the signal-to-noise ratio. However, single-sideband processing must generally be used when the objective of the measurement is the detection of an rf signal, since the two sidebands are too far apart to be processed by the same electronics.

With reference to the discussion in §2.12, we can now calculate the power levels of the different types of noise in the heterodyne case, normalized to the homodyne noise power. Single-sideband detection will be assumed. Shot noise is determined

entirely by the dc component of the local-oscillator flux; hence, we can write

$$\frac{v^2_{n,\mathrm{LO,het}}}{v^2_{n,\mathrm{LO,hom}}} = \alpha. \tag{7.2}$$

In the case of intrinsic detector-preamplifier noise, we obtain instead

$$\frac{v^2_{n,D,\mathrm{het}}}{v^2_{n,D,\mathrm{hom}}} = 1. \tag{7.3}$$

The signal ratio can be written

$$\frac{v^2_{s,\mathrm{het}}}{v^2_{s,\mathrm{hom}}} = \alpha^2\beta^2/4. \tag{7.4}$$

Therefore, we obtain the following expressions for the signal-to-noise ratio:

$$\left(\frac{S}{N}\right)_{\mathrm{het}} \Big/ \left(\frac{S}{N}\right)_{\mathrm{hom}} = \begin{cases} \alpha\beta^2/4 & \text{if shot noise dominates} \\ \alpha^2\beta^2/4 & \text{if intrinsic noise dominates.} \end{cases} \tag{7.5}$$

Clearly, in both cases the optimum heterodyne performance is achieved with $\alpha = \beta = 1$, with a degradation of a factor of four from the homodyne configuration.

In a saturation-limited regime, when power in both the homodyne and the heterodyne case must be attenuated, one must impose the constraint $\alpha(1+\beta) = 1$. Thus, in this case Eq. (7.5) must be modified as follows:

$$\left(\frac{S}{N}\right)_{\mathrm{het}} \Big/ \left(\frac{S}{N}\right)_{\mathrm{hom}} = \begin{cases} \beta^2/[4(1+\beta)] & \text{if shot noise dominates} \\ \beta^2/[4(1+\beta)^2] & \text{if intrinsic noise dominates.} \end{cases} \tag{7.6}$$

These ratios are maximized when $\beta = 1$ (and $\alpha = 0.5$), and they are equal to 1/8 and 1/16 in, respectively, the shot-noise and intrinsic-noise regimes.

In the case of rf detection, the degradation in the performance of a heterodyne PCI system may well be compensated by the elimination of direct pickup.

An intensity-modulation scheme can be implemented experimentally in several ways. An electro-optic modulator employs a birefringent crystal, whose index of refraction changes in response to an applied electric field. In combination with appropriate polarizers, these crystals can produce linear intensity modulation of up to approximately 40%, around a mean power equal to one-half the input power, at frequencies up to 500 MHz. Thus, since $\alpha = 0.5$ and $\beta \lesssim 0.4$, optimal performance is not attained. In the unsaturated regime [Eq. (7.5)] one finds a signal-to-noise reduction factor of 0.02 in the shot-noise-dominated case, and of 0.01 in the intrinsic-noise-dominated case.

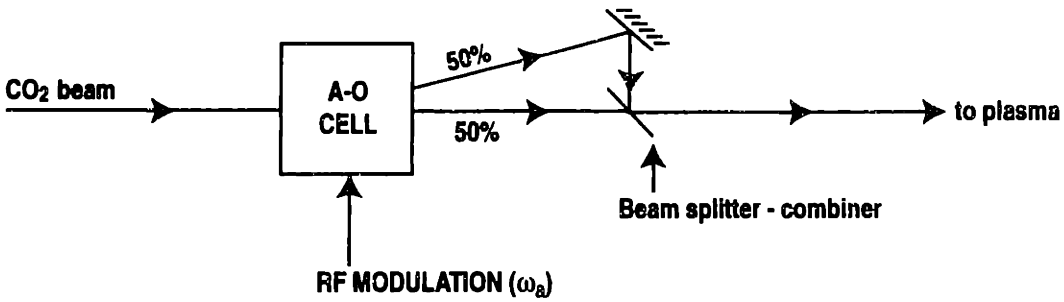

Fig. 7.1 Intensity modulation scheme employing an acousto-optic modulator.

Acousto-optic modulators may also be used. When a radio-frequency signal (of frequency ω_a) is applied to an acousto-optic cell, the power of the input laser beam is apportioned between two output beams: the direct beam travels in the same direction and has the same frequency as the input beam, whereas the diffracted beam is deflected and is shifted in frequency by ω_a. The fraction of diffracted power depends on the applied rf power. The power in both beams can be modulated by modulating the intensity of the rf source [generally, $\omega_m \lesssim \omega_a/4$; note that the maximum value of $\omega_a/(2\pi)$ is typically of the order of 80 MHz]. The power fluxes in the deflected and undeflected beams can be written, respectively,

$$\mathcal{E}_d = A\mathcal{E}\left(\frac{1 + B\cos(\omega_m t)}{1 + B}\right) \tag{7.7}$$

and

$$\mathcal{E}_u = \mathcal{E} - \mathcal{E}_d, \tag{7.8}$$

where A is approximately proportional to the peak rf power applied to the cell, and can range typically from 0 to 0.8. The modulation coefficient B can range from 0 to 1.

If the deflected beam is employed, one finds $\alpha = A/(1 + B)$ and $\beta = B$; if the direct beam is used instead, one can write $\alpha = 1 - A/(1+B)$ and $\beta = AB/(1+B-A)$. In both cases, it can be easily shown by using Eq. (7.5) that the highest signal-to-noise ratio is obtained by maximiming A and B, subject to their respective constraints, i.e., by setting $A \simeq 0.8$ and $B = 1$. For the deflected beam, this gives a signal-to-noise factor of 0.1 in the shot-noise regime, and of 0.04 in the intrinsic-noise regime. For the direct beam, those factors are, respectively, 0.07 and 0.04. This method is therefore preferable to that based on the electro-optic modulator, and use of the deflected beam is preferable to use of the direct beam.

An even better performance can be achieved by using an acousto-optic modulator with an unmodulated rf drive and a 50% deflection factor ($A = 0.5$ and $B = 0$), and by then recombining the two beams (see Fig. 7.1). Now the modulation frequency is $\omega_m = \omega_a$. The parameters are $\beta = 1$ and, because of the 50% power loss at the beam combiner, $\alpha = 0.5$; hence, the signal-to-noise factors are 1/8 (shot-noise regime) and 1/16 (intrinsic-noise regime).

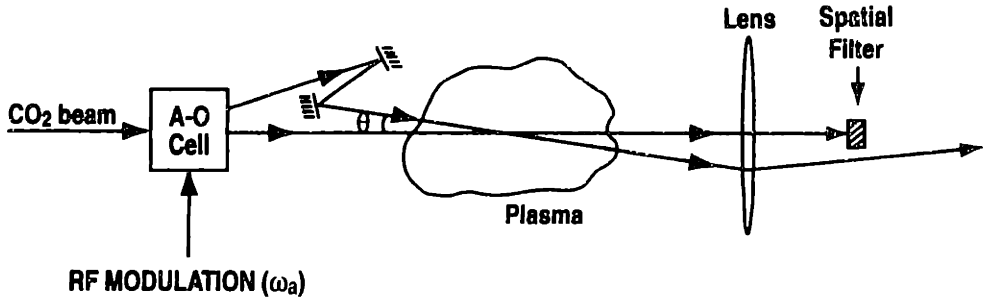

Fig. 7.2 Intensity modulation by misalignment of two frequency-shifted beams.

Higher efficiencies, that is, higher values of α may be attained by allowing two laser modes to beat at slightly different wavelengths. However, if enough power is available to reach the saturation level of the detector (the optimal operational point in all cases), the fundamental limits on the signal-to-noise ratio remain 1/8 and 1/16 of the homodyne value for, respectively, the shot-noise and intrinsic-noise regimes.

It should be noted that in all these intensity-modulation schemes, the nonfluctuating component of the power flux appears both at zero frequency and at the modulation frequency ω_m. If the preamplifiers are ac-coupled, the dc component is eliminated as in the homodyne case; however, the shifted signal will be transmitted by the electronics up to the mixing stage, and could potentially limit the dynamic range of the system, depending on the saturation level of the electronics.

Weisen[142] also proposed a different configuration, in which the direct and diffracted beams from an acousto-optic cell are made to cross in the plasma at a small angle θ (see Fig. 7.2), which must be larger than the largest scattering angle to be resolved. The spatial filter in the focal plane is the same as in the central-dark-ground method, with a conjugate area of zero transmissivity and a perfectly transmitting complementary area. The optical axis of the system coincides with the direction of propagation of one of the beams.

The phase-contrast signal is now the interference signal between the zeroth-order field in the oblique beam and the scattered field in the straight beam. This signal is modulated in both space (in the direction of deflection) and time, being proportional to $\cos(\omega_m t - \theta k_0 x)$, with $\omega_m = \omega_a$. This system is in effect an interferometer and not strictly an internal-reference system; however, it retains the most desirable property of an internal-reference system, that is, the insensitivity to vibrations, since the two beams utilize the same optical components.

This technique permits to improve the contrast by increasing the fraction of the power that is carried by the straight beam, just as in the homodyne case one can reduce the transmissivity of the conjugate area. If enough power is available, the signal-to-noise degradation can reach the theoretical limit of 1/2. An additional advantage is that the nonfluctuating power flux that reaches the detector is now strictly a dc signal, and an ac-coupled preamplifier will prevent it from saturating the electronics.

7.2 Localization of the Measurement by Symmetry Considerations

A line-integrated measurement is intrinsically unable to provide information on the spatial distribution of the quantity under exam along the direction of integration. However, when the phenomenon under study is known *a priori* to possess certain spatial symmetry properties, the geometry of beam propagation can generally be chosen in a way that minimizes the uncertainties introduced by the integration. As was discussed in §4.1, when symmetry properties allow to reduce the dimensionality of the problem, it may be possible in some cases to remove those uncertainties altogether.

(a) Localization by Toroidal Launching

As a very simple example, suppose that turbulence is known to be distributed homogeneously in a certain direction, not only in its statistical correlation properties but also in its instantaneous form: that is, the spatial spectrum in that direction, at any given time, is a delta function centered at a wave number of zero. Clearly, then, that spatial variable can be eliminated from the problem. If the beam is launched in that particular direction, the line integration does not reduce the amount of information, and in fact it serves the useful purpose of increasing the signal. Ideally, an imaging system can then provide a two-dimensional mapping in the perpendicular plane with arbitrary spatial resolution.

Turbulence in tokamak plasmas does possess a similar symmetry property, albeit not such a simple one. Turbulence is known to be symmetrically distributed along the magnetic field lines.[181,182] This allows to reduce the dimensionality of the problem from three to two; however, the variable of integration clearly cannot coincide with the symmetry variable, since the magnetic-field lines are curved around the torus. Thus, the line integration in general will take the form of a convolution integral in the two remaining independent variables.

To take maximum advantage of the symmetry, the direction of propagation should be approximately toroidal, i.e., it should be tangent to the toroidal magnetic-field lines[83] (see Fig. 7.3). We shall make the temporary assumption that the helicity of the lines can be ignored, that is, that the poloidal field can be ignored in comparison with the toroidal field. In cylindrical coordinates, the fluctuating density will then take the functional form $\tilde{n} = \tilde{n}(R, z)$. If we now take a chord whose major radius and elevation at the tangency point are respectively R_b and z_b, the line integral along the chord can be written

$$\Upsilon(R_b, z_b) \equiv \int \tilde{n}\, dl = \int_{R_b^2}^{\infty} \tilde{n}(R, z_b) \frac{d(R^2)}{\sqrt{R^2 - R_b^2}}, \tag{7.9}$$

which can be recast as an Abel integral equation by an appropriate change of variables. Hence, Abel's inversion[178] can be employed to derive the dependence of $\tilde{n}$ on R from a series of measurements on different chords with different values of R_b. The dependence on z is measured by simply varying the elevation of the chord.

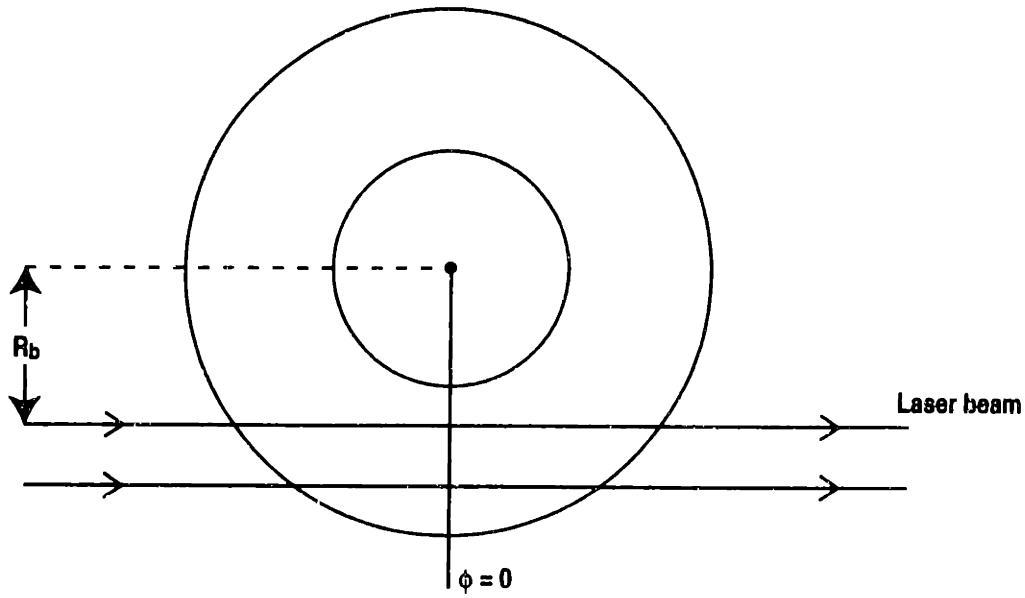

Fig. 7.3 Top view of a tokamak with a tangentially launched laser beam.

If the helicity of the field lines is taken into account, the problem becomes more complex. To examine the problem, we must first qualify the concept of symmetry along the field lines. That symmetry, in its previously stated form, would imply that the wavelength and the correlation length along each line are infinite; on an ergodic flux surface, this implies total symmetry over the entire surface. Since this is contrary to observation, the parallel wavelength and correlation length must in fact be finite. Indeed, measurements of these quantities have been limited to distances shorter than the circumference of the torus.[181,182] We shall therefore assume that the parallel correlation length is shorter than the toroidal circumference.

For the purposes of our problem, we can now identify each field line by the major radius and elevation of its intersection with the reference azimuthal half-plane $\phi = 0$, which is taken to be the plane of closest approach of the probing beam to the axis of the torus (see Fig. 7.3). We can thus write $\tilde{n}(R, \phi, z) = \tilde{n}(R_0, 0, z_0)$, where

$$\begin{cases} R_0 = F(R, \phi, z) \\ z_0 = G(R, \phi, z). \end{cases} \tag{7.10}$$

These functions are single-valued because of the finiteness of the parallel correlation length.

A given chord within the laser beam is identified by the coordinates R_b and z_b of its intersection with the half-plane $\phi = 0$. The cylindrical coordinates of a point along a chord can be parametrized as follows:

$$\begin{cases} R = (R_b^2 + \zeta^2)^{1/2} \\ \phi = \arctan(\zeta / R_b) \\ z = z_b, \end{cases} \tag{7.11}$$

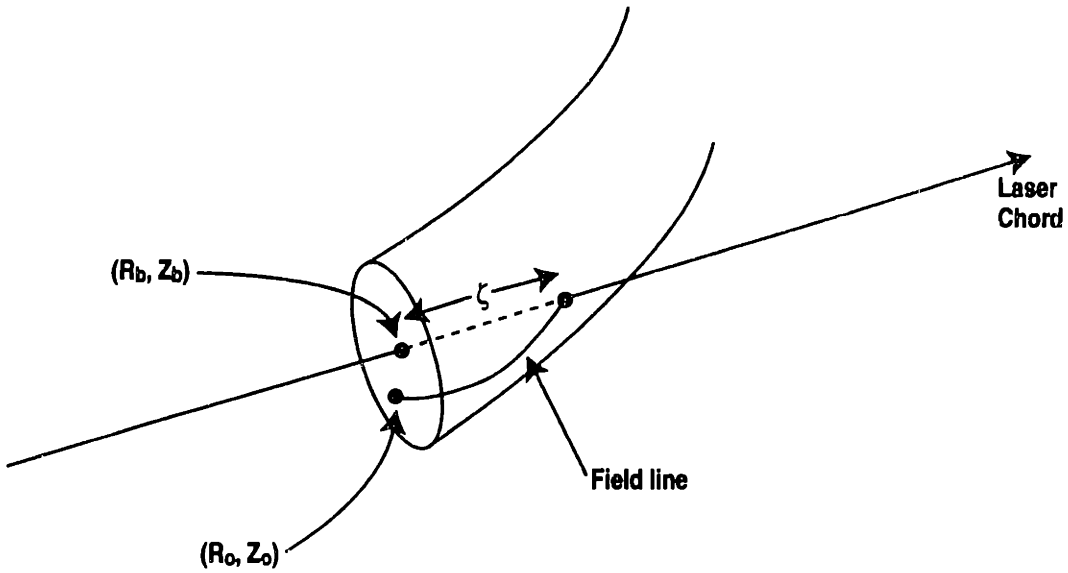

Fig. 7.4 Illustration of projection of points along the laser chord onto reference plane through field-line mapping.

where ζ is a linear coordinate along the chord, with its origin at $\phi = 0$. Thus, a point ζ along a chord is connected by a field line to a point with coordinates $R_0 = F'(\zeta; R_b, z_b)$, $\phi = 0$, and $z_0 = G'(\zeta; R_b, z_b)$ (see Fig. 7.4), where

$$\begin{cases} F'(\zeta; R_b, z_b) = F\Big((R_b^2 + \zeta^2)^{1/2}, \arctan(\zeta/R_b), z_b\Big) \\ G'(\zeta; R_b, z_b) = G\Big((R_b^2 + \zeta^2)^{1/2}, \arctan(\zeta/R_b), z_b\Big). \end{cases} \tag{7.12}$$

In these equations, R_b and z_b are parameters that identify the chord. We now want to define the inverse function of F' with respect to the variable ζ; this function will be multivalued in general. Therefore, we formally define the discrete set of functions $\zeta = F_i'^{-1}(R_0; R_b, z_b)$, for $i = 1, \ldots, m$, where each function is defined over a subdomain $\Omega_i(R_b, z_b)$ of the R_0 axis. Finally, we can define the functions

$$z_0 = \mathcal{Z}_i(R_0; R_b, z_b) \equiv G'\Big(F_i'^{-1}(R_0; R_b, z_b); R_b, z_b\Big). \tag{7.13}$$

These m equations jointly describe a curve in the half-plane $\Phi = 0$; this curve is the projection of the laser-beam chord on that half-plane through field-line mapping (see Fig. 7.5).

We can now formally write

$$\begin{aligned} \Upsilon(R_b, z_b) &= \int \tilde{n}\Big((R_b^2 + \zeta^2)^{1/2}, \arctan(\zeta/R_b), z_b\Big) d\zeta \\ &= \sum_{i=1}^{m} \int_{\Omega_i(R_b, z_b)} \tilde{n}\Big(R_0, 0, \mathcal{Z}_i(R_0; R_b, z_b)\Big) \left(\frac{\partial F_i'^{-1}}{\partial R_0}\right) dR_0, \end{aligned} \tag{7.14}$$

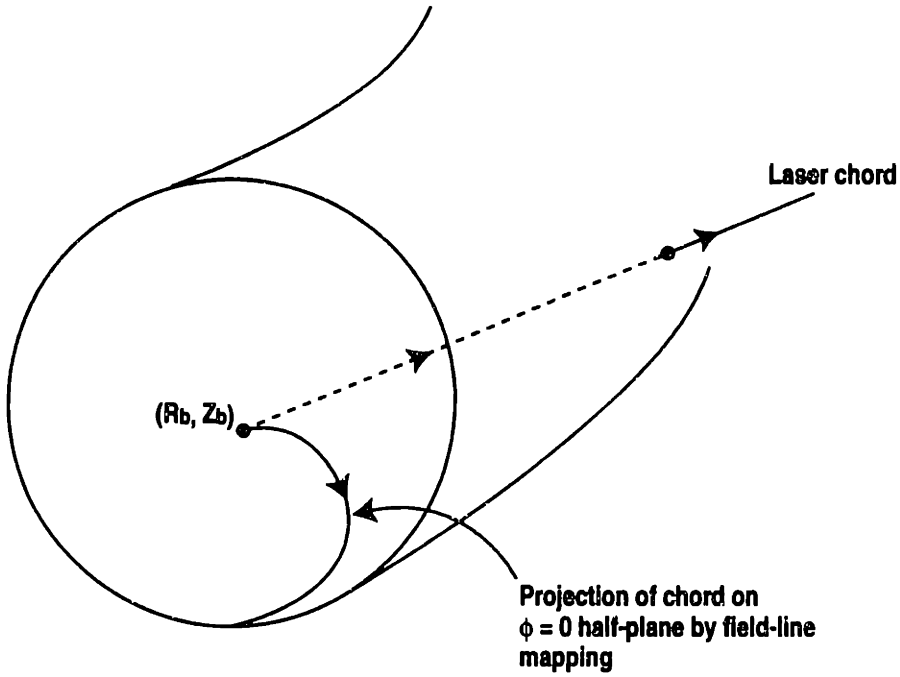

Fig. 7.5 Projected trajectory of a laser beam by field-line mapping.

where

$$\left(\frac{\partial F_i'^{-1}}{\partial R_0}\right) = \left(\frac{\zeta}{\sqrt{R_b^2+\zeta^2}}\frac{\partial F}{\partial R} + \frac{R_b}{R_b^2+\zeta^2}\frac{\partial F}{\partial \phi}\right)^{-1}. \tag{7.15}$$

This expression is to be evaluated at $\zeta = F_i'^{-1}(R_0; R_b, z_b)$, with R, ϕ, and z given by Eq. (7.11).

Equation (7.14) can be cast in the form of a two-dimensional Volterra equation of the first kind[148]:

$$\Upsilon(R_b, z_b) = \sum_{i=1}^{m} \int_{-\infty}^{+\infty} dz_0 \int_{\Omega_i(R_b,z_b)} \mathcal{K}_i(R_b, z_b; R_0, z_0)\, \tilde{n}(R_0, 0, z_0)\, dR_0, \tag{7.16}$$

where the kernel components are

$$\mathcal{K}_i(R_b, z_b; R_0, z_0) = \left(\frac{\partial F_i'^{-1}}{\partial R_0}\right) \delta\Big(z_0 - \mathcal{Z}_i(R_0; R_b, z_b)\Big). \tag{7.17}$$

In the simple case of Eq. (7.9), we find $m = 2$, $F_1'^{-1}(R_0; R_b, z_b) = +(R_0^2 - R_b^2)^{1/2}$, $F_2'^{-1}(R_0; R_b, z_b) = -(R_0^2 - R_b^2)^{1/2}$, and $\mathcal{Z}_i(R_0; R_b, z_b) = z_b$.

In the more general case, Eq. (7.16) must be solved by a method of successive approximations.[475] In practice, the small value of the pitch angle will aid in the solution. In particular, if the magnetic shear is small in the region of interest, the direction of launching can be oriented to be tangent to the field lines, with a nonzero vertical component; Eq. (7.16) is then well approximated by Eq. (7.9).

A CO_2-laser fluctuation imaging experiment that employs toroidal launching is currently in progress on the CDX-U tokamak at Princeton University.[147]

(b) Localization by Spatial Filtering

The symmetry of fluctuations along the field lines can also be exploited in conjunction with spatial filtering to achieve spatial localization along the direction of propagation. This technique, which has been applied to scattering and imaging experiments employing vertical launching,[476,477] is based on the existence of two separate selection rules for the detectable wave vectors: the symmetry along the magnetic-field lines implies that the wave vector must be perpendicular to the field, and the scattering selection rule (see §2.3) forces the vector to be perpendicular to the direction of propagation of the beam. Therefore, the measured wave vector at each point along the beam must be perpendicular to the plane defined by the beam axis and by the local magnetic field. The combined effects of toroidal geometry and magnetic shear cause the direction of the wave vector to be different at different points along the beam. Spatial filtering can then be used to select a direction, thus localizing the measurement to the region in which that particular direction satisfies the selection rules.

In the case of vertical propagation, the wave vectors must be horizontal. The angle formed by the wave vector and the major radius is equal to $\theta_k = \arctan(B_R/B_\phi)$, where B_R and B_ϕ are respectively the radial and azimuthal components of the magnetic field in cylindrical coordinates (see Fig. 7.6). The angle θ_k is usually small, but it varies along the direction of the beam, typically changing sign across the midplane. The azimuthal (toroidal) component of the wave vector can be selected by spatial filtering within the intrinsic resolution of the measurement, i.e., for a Gaussian beam with half-width w_0, $\Delta k_\phi \simeq \pm 2/w_0$. Hence, the spatial resolution that can be achieved, for a given radial wave number k_R, is approximately given by

$$\Delta z \simeq \pm 2 w_0 \left| \frac{B_\phi}{k_R} \right| \left| \frac{\partial B_R}{\partial z} \right|^{-1} . \tag{7.18}$$

Unfortunately, in many cases B_R varies little over large portions of the cross section. In the geometry of the DIII–D PCI apparatus, which has access only to the outer edge of the tokamak, some degree of resolution could be achieved by this method only for wavelengths of the order of a few mm, far shorter than the range of interest for our studies.

For a possible alternative launching geometry in DIII–D (see §7.4) with a major radius $R = 2$ m, a test case for a lower-single-null diverted plasma with plasma current $I_p = 1.37$ MA and central toroidal field $B_T = 2.1$ Tesla yielded the following result: the quantity B_R/B_ϕ is essentially constant in the region $0.5 \leq r/a \leq 0.9$ (where r/a is the normalized minor radius), taking the value -0.1 above the midplane and $+0.1$ below it. The variation from -0.1 to $+0.1$ occurs in a small region around the midplane ($r/a \simeq 0.4$). The only goal that can be achieved by the filtering technique

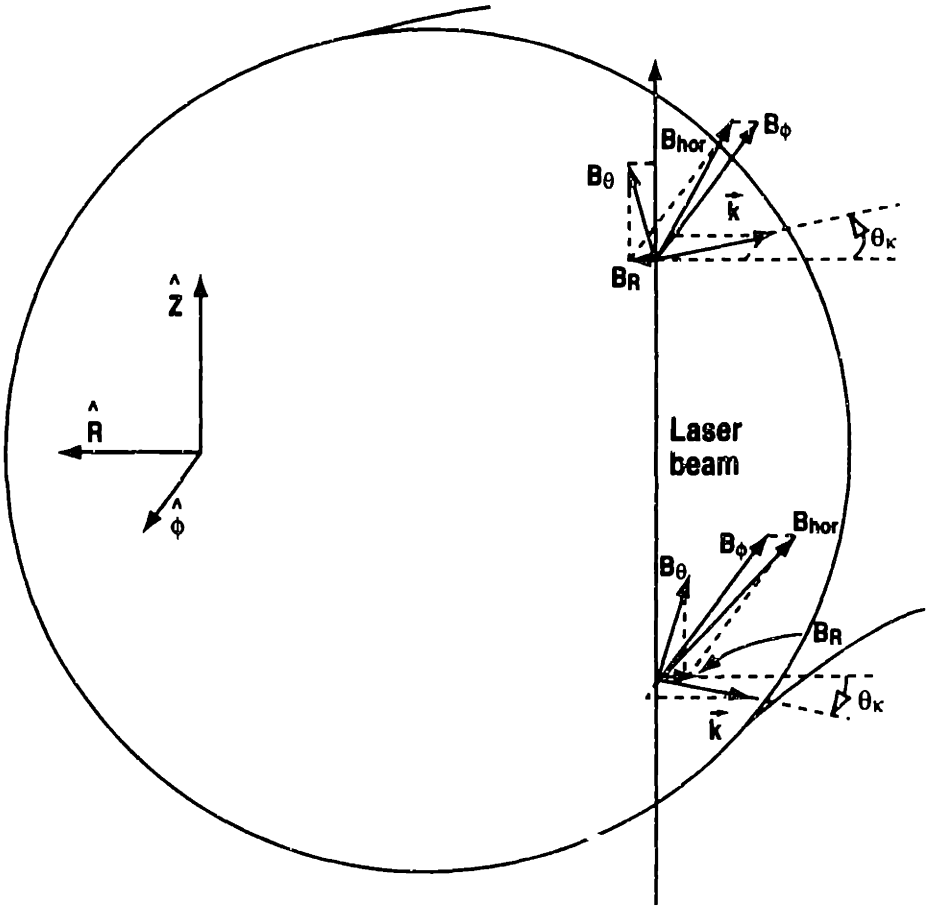

Fig. 7.6 Selection rules for the wave vector, which must be perpendicular to the magnetic field and to the direction of propagation of the laser beam.

in this case is to distinguish between the upper and lower regions and detect any up-down asymmetries. For this to be possible, the wave number must satisfy the condition $2/(w_0|k_R|) \lesssim 0.2$.

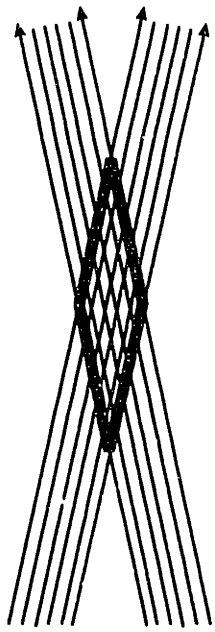

Fig. 7.7 Crossed-beam imaging geometry.

7.3 Crossed-Beam Correlation Technique

The crossed-beam correlation technique was developed in the context of scattering from plasma density fluctuations by Surko and Slusher,[177] and was subsequently applied to the Alcator A and Alcator C[23] tokamaks. The technique employs two intersecting laser beams, which provide measurements of the density fluctuations integrated along the respective directions of propagation. The correlation function of the two signals is predominantly affected by fluctuations occurring near the intersection point. In the case of plasma turbulence, the correlation volume is sufficiently small to allow this technique to provide a substantial improvement in the spatial resolution of the measurement.

A crossed-beam scheme may be employed also in conjunction with an imaging technique,[83] although to our knowledge such an experiment has not been carried out yet. In exploring this scenario, we shall ignore all diffraction effects arising from the finite widths of the beams, and assume simply that the measured signals are proportional to the line integrals of the fluctuations along the respective chords.

(a) Second-Order Correlations

In general, a number of discrete measurements will be carried out along parallel chords within each of the two beams (see Fig. 7.7). Correlation functions may be calculated between each chord of the first beam and each chord of the second beam; each pair will cross at a point located within the intersection region, which is in the shape of a parallelogram (a rhombus when the beam diameters are equal), as seen in Fig. 7.7.

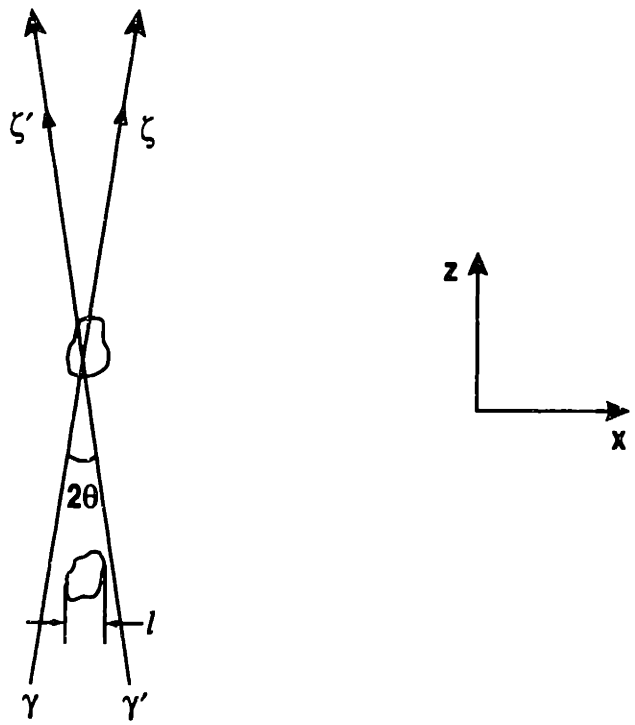

Fig. 7.8 Two-chord crossed-beam correlation geometry. The two localized areas of turbulence shown have a characteristic correlation length l. The area at the intersection contributes to the signal, whereas the other one does not.

In the following analysis, we shall use much of the formalism that was developed in Chapter 4. We consider a two-dimensional system, with two beams propagating in the (x, z) plane at angles $\pm\theta$ to the z-axis; in particular, we choose the origin of the system to be the intersection point of the two chords under consideration. We want to calculate the following correlation function:

$$\Gamma_{12}(t,t') \equiv \left\langle \int_{\gamma} \tilde{n}(\mathbf{x},t)d\zeta \int_{\gamma'} \tilde{n}(\mathbf{x}',t')d\zeta' \right\rangle, \tag{7.19}$$

where ζ and ζ' are the coordinates along chords γ and γ', respectively (see Fig. 7.8), and the angular brackets <> denote the operation of ensemble averaging.

The postulate of random phase [Eq. (4.9)] allows us to write the pointwise correlation function in the quasi-homogeneous approximation as [Eq. 4.20)]

$$\begin{aligned}\left\langle \tilde{n}(\mathbf{x},t)\,\tilde{n}(\mathbf{x}',t')\right\rangle = \frac{1}{(2\pi)^3}\left\langle \tilde{n}^2\left(\mathbf{x}_{\mathrm{av}},t_{\mathrm{av}}\right)\right\rangle \int dk_R \int dk_z \int d\omega\; I(\mathbf{k},\omega) \\ \times \exp\left[i\mathbf{k}\cdot(\mathbf{x}-\mathbf{x}') - i\omega(t-t')\right],\end{aligned} \tag{7.20}$$

where $\mathbf{x}_{\mathrm{av}} = (\mathbf{x}+\mathbf{x}')/2$ and $t_{\mathrm{av}} = (t+t')/2$. The validity of this approximation rests on the assumptions

$$\begin{cases} \left|\nabla \ln\left(\left\langle \tilde{n}^2\right\rangle\right)\right|^{-1} \gg \mathcal{L} \\ \left|\partial \ln\left(\left\langle \tilde{n}^2\right\rangle\right)/\partial t\right|^{-1} \gg \tau_d, \end{cases} \tag{7.21}$$

where $\mathcal{L}$ is a characteristic correlation length, and τ_d is the decorrelation time of the fluctuations.

As in §4.3, we adopt here the following model for the spectral function $I(\mathbf{k}, \omega)$:

$$I(\mathbf{k},\omega) = \frac{\pi}{2}\mathcal{L}_x\mathcal{L}_z \sum_{\pm} \exp\left[-\frac{\mathcal{L}_x^2\,(\pm k_x - k_{0,x})^2}{4}\right] \exp\left[-\frac{\mathcal{L}_z^2\,(\pm k_z - k_{0,z})^2}{4}\right] \times \hat{F}_1[\pm\omega - \omega(\mathbf{k})], \tag{7.22}$$

where $\mathcal{L}_x$ and $\mathcal{L}_z$ are the correlation lengths in the x and z directions, respectively; also,

$$\hat{F}_1(\omega') = \sqrt{\pi}\,\tau_d \exp\left[-\frac{\omega'^2\tau_d^2}{4}\right], \tag{7.23}$$

where $\omega' = \pm\omega - \omega(\mathbf{k})$, and

$$\omega(\mathbf{k}) = \omega_0 + \mathbf{v}_g \cdot (\mathbf{k} - \mathbf{k}_0). \tag{7.24}$$

Here, $\omega_0 = \omega(\mathbf{k}_0)$ and $\mathbf{v}_g$ is the group velocity.

The pointwise correlation function in this model is similar to the expression given in Eq. (4.28), with some necessary modifications. Here, it takes the form

$$\left\langle \tilde{n}(\mathbf{x},t)\,\tilde{n}(\mathbf{x}',t')\right\rangle = \left\langle \tilde{n}^2(\mathbf{x}_{\mathrm{av}},t_{\mathrm{av}})\right\rangle F_1(t-t') \exp\left[-\left(\frac{u_x^2}{\mathcal{L}_x^2} + \frac{u_z^2}{\mathcal{L}_z^2}\right)\right] \times \cos\Big[\mathbf{k}_0\cdot(\mathbf{x}-\mathbf{x}') - \omega_0(t-t')\Big], \tag{7.25}$$

where

$$\mathbf{u} = \mathbf{x} - \mathbf{x}' - (t-t')\mathbf{v}_g, \tag{7.26}$$

and $F_1(t-t')$ is the inverse Fourier transform of $\hat{F}_1(\omega')$, that is,

$$F_1(\tau) = \exp\left(-\frac{\tau^2}{\tau_d^2}\right). \tag{7.27}$$

To pursue the issue of locality, we choose a Gaussian spatial distribution, constant in time, of the form

$$\left\langle \tilde{n}^2(\mathbf{x}_{\mathrm{av}},t_{\mathrm{av}})\right\rangle = \tilde{n}_0^2 \exp\left(-\frac{(x_{\mathrm{av}}-x_0)^2}{\eta_x^2} - \frac{(z_{\mathrm{av}}-z_0)^2}{\eta_z^2}\right). \tag{7.28}$$

The condition imposed by Eq. (7.21), averaged over the Gaussian curves, now implies $\eta_x \gg \mathcal{L}_x$ and $\eta_z \gg \mathcal{L}_z$. All the coordinates can be expressed as functions of ζ and ζ' (see Fig. 7.8) as follows:

$$\begin{cases} x - x' = (\zeta + \zeta')\sin\theta \\ z - z' = (\zeta - \zeta')\cos\theta \end{cases} \tag{7.29}$$

and

$$\begin{cases} x_{\mathrm{av}} = (\zeta - \zeta')(\sin\theta)/2 \\ z_{\mathrm{av}} = (\zeta + \zeta')(\cos\theta)/2. \end{cases} \tag{7.30}$$

Equation (7.19) can now be calculated, using Eqs. (7.25), (7.28), (7.29), and (7.30), and with a change of variables to $(\zeta - \zeta')$ and $(\zeta + \zeta')/2$. The calculation is tedious but straightforward, and yields the result

$$\begin{aligned} \Gamma_{12}(\tau) = \tilde{n}_0^2 \frac{\pi \mathcal{L}_z' \eta_z'}{\cos^2\theta} \exp\left(-\frac{\tau^2}{\tau_d^2}\right) \exp\left(-\frac{\mathcal{L}_z'^2 k_{0,z}^2}{4} - \eta_z'^2 k_{0,x}^2 \tan^2\theta\right) \\ \times \exp\left(-\frac{[z_0 - \tau v_{g,x}/(2\tan\theta)]^2}{\eta_z^2 + \mathcal{L}_x^2/(4\tan^2\theta)}\right) \exp\left(-\frac{(x_0 - \tau v_{g,z}\tan\theta/2)^2}{\eta_x^2 + \mathcal{L}_z^2\tan^2\theta/4}\right) \\ \times \cos\left(2z_0 k_{0,x}\frac{\eta_z'^2}{\eta_z^2}\tan\theta + 2x_0 k_{0,z}\frac{\mathcal{L}_z'^2}{4\eta_x^2}\tan\theta - \Omega_0'\tau\right), \end{aligned} \tag{7.31}$$

where $\tau = t - t'$; also,

$$\mathcal{L}_z' = \left(\frac{1}{\mathcal{L}_z^2} + \frac{\tan^2\theta}{4\eta_x^2}\right)^{-1/2}, \tag{7.32}$$

$$\eta_z' = \left(\frac{1}{\eta_z^2} + \frac{4\tan^2\theta}{\mathcal{L}_x^2}\right)^{-1/2}, \tag{7.33}$$

and

$$\Omega_0' = \omega_0 - k_{0,z}v_{g,z}\frac{\mathcal{L}_z'^2}{\mathcal{L}_z^2} - k_{0,x}v_{g,x}\frac{4\eta_z'^2\tan^2\theta}{\mathcal{L}_x^2}. \tag{7.34}$$

Let us first examine Eq. (7.31) in the case $\tau = 0$ (equal-time correlation function). The localization of the measurement is defined by the two exponential functions in the second line of Eq. (7.31). The first exponential indicates that the measurement is localized to a vertical region of half-width $\mathcal{L}_x/(2\tan\theta)$ around the intersection point. This can be understood physically as follows: if turbulent activity exists in a region in which the beams are separated by a distance larger than a correlation length, the signal is exponentially small (see Fig. 7.8). Of course, this argument requires that turbulence be sufficiently localized, that is, $\eta_z \ll \mathcal{L}_x/(2\tan\theta)$. Under normal conditions, when the correlation lengths $\mathcal{L}_z$ and $\mathcal{L}_x$ are of the same order, for $\tau = 0$ the exponential involving x_0 reduces to $\exp(-x_0^2/\eta_x^2)$; this term simply carries the obvious requirement that the intersection point lie within the turbulent region in the x direction.

The exponential functions involving $\mathbf{k}_0$ in Eq. (7.31) provide selection rules for the measurable wave vectors. Normally, with $\mathcal{L}_z \ll \eta_x$, we find from Eq. (7.32) that $\mathcal{L}_z' \simeq \mathcal{L}_z$. Therefore, the selection rule for $k_{0,z}$ is simply $|k_{0,z}| \lesssim 2/\mathcal{L}_z$; that is, since the beams propagate in a nearly vertical direction, the component of the wave vector along the z direction must be equal to zero — within a tolerance of the order of the reciprocal of the correlation length — to avoid cancellation from line averaging.

The condition on $k_{0,x}$ arises because the two beams propagate in slightly different directions. If the condition $\eta_z \ll \mathcal{L}_x/(2\tan\theta)$ is satisfied, we find from Eq. (7.33) $\eta_z' \simeq \eta_z$. The horizontal distance traveled by each beam within the turbulent region is equal to $2\eta_z \tan\theta$; correspondingly, the selection rule for $k_{0,x}$ is $|k_{0,x}| \lesssim 1/(\eta_z \tan\theta)$.

The first phase term [in the third line of Eq. (7.31)] $\sim 2k_{0,x} z_0 \tan\theta$ is also simple to interpret: this is the average phase shift caused by the k_x spectrum at a horizontal distance $2z_0 \tan\theta$. The second phase term is due to the vertical separation of the beams in the turbulent region; since that separation varies considerably over the horizontal extent of the turbulence ($2\eta_x$), the rms phase shift is much smaller — by a factor $\mathcal{L}_z^2/(2\eta_x/\tan\theta)^2$ — than its mean value $2k_{0,z}x_0/\tan\theta$.

It is important to explore the role of the angle θ in the correlation function. The vertical localization of the measurement improves with increasing θ, as the beams become separated beyond a correlation length at shorter distances from the intersection point. However, the overall signal decreases with increasing θ, owing to two distinct effects: the integration volume becomes smaller, and the joint selection rules for the two beams become increasingly restrictive.

The first effect can be quantified by examining a simple case in which $\mathcal{L}_x = \mathcal{L}_z \equiv \mathcal{L}$, $\eta_x = \eta_z \equiv \eta$, $\mathbf{k}_0 = 0$, and $\mathbf{x}_0 = 0$. Then, the equal-time correlation function, from Eq. (7.31), can be written

$$\Gamma_{12}(0) = \tilde{n}_0^2 \frac{\pi \mathcal{L}_z' \eta_z'}{\cos^2\theta}. \tag{7.35}$$

This is a monotonically decreasing function of θ in the range 0–45° (and then increasing again from 45° to 90°, as required by the symmetry of the problem). Its value at $\theta = 0$ is given by the familiar expression for the autocorrelation function $\tilde{n}_0^2 \pi \mathcal{L}\eta$; its value at $\theta = 45°$ is $\sim \tilde{n}_0^2 \pi \mathcal{L}^2$, a factor $\mathcal{L}/\eta$ smaller.

The shrinking of the accessible wave-vector space, caused by the selection rules for the misaligned beams, is reflected mathematically in the exponential functions of $k_{0,z}$ and $k_{0,x}$ in Eq. (7.31). The strongest dependence on θ is in the term $\exp(-\eta^2 k_{0,x}^2 \tan^2\theta)$.

It is clear, therefore, that the choice of the angle θ must strike a compromise between the conflicting requirements of spatial localization and of a large signal amplitude.

To conclude our analysis of Eq. (7.31), we briefly examine the time-delayed case ($\tau \neq 0$). Under the conditions $\mathcal{L}_z' \simeq \mathcal{L}_z$ and $2\eta_z \tan\theta \ll \mathcal{L}_x$, the shifted frequency [cf. Eq. (7.34)] is $\Omega_0' \simeq \omega_0 - k_{0,z} v_{g,z}$. By comparison with Eq. (7.24), we can also write $\Omega_0' \simeq \omega(k_{0,x}, 0)$; that is, this is the frequency corresponding to the $k_z = 0$ component of the turbulence, as mandated by the selection rules that we have discussed above. The shift caused by the selection rule on $k_{0,x}$ is smaller, since that selection rule is less stringent, as was shown earlier.

The localization conditions are modified for $\tau \neq 0$ in the presence of a finite group velocity. The correlation function at a given τ carries information on a localized region that is not centered in the intersection point, rather in the point with coordinates $x_0 = \tau v_{g,z} \tan\theta/2$, $z_0 = \tau v_{g,x}/(2\tan\theta)$. At this location, the vertical and horizontal

separations of the beams are equal to the respective distances covered by the turbulent wave packet in the time τ. Taking the case of a uniform horizontal distribution ($\eta_x \to \infty$) for simplicity, and retaining the condition $2\eta_z \tan\theta \ll \mathcal{L}_x$, we find that the dependence of the peak signal on z_0 is $\propto \exp[-4z_0^2 \tan^2\theta/(\mathcal{L}_x^2 + \tau_d^2 v_{g,x}^2)]$.

It should be noted that an imaging configuration allows one to study the spatial distribution of the fluctuations. If the vertical dimension of the rhombus shown in Fig. 7.7 is larger than the characteristic localization length, i.e. if $2w_0/\sin\theta > \mathcal{L}_x/(2\tan\theta)$, performing correlation measurements on different pairs of chords permits to map the spatial distribution of turbulence within the rhombus.

(b) Signal-to-Noise Ratio

The considerations made thus far are valid, strictly speaking, only if the ensemble averages can be calculated exactly. In reality, these are estimated by sample averages based on a finite number m of realizations. The previous analysis assumed the limit $m \to \infty$. When m is instead finite, turbulence originating outside the intersection region contributes statistically to the correlation function, taking the appearance of statistical "noise". We proceed now to calculate that contribution. We shall assume that $x_0 = 0$ and $z_0 = 0$.

The variance of the estimate of the correlation function Γ_{12} is estimated by the quantity[165]

$$\sigma_\Gamma^2 = \frac{\sigma^2}{m-1}, \tag{7.36}$$

where σ^2 is the sample variance of the estimate of Γ_{12}. The signal-to-noise ratio for Γ_{12} can then be written

$$\left(\frac{S}{N}\right)_\Gamma = \frac{|\Gamma_{12}|}{\sigma_\Gamma}. \tag{7.37}$$

The sample variance takes the form

$$\sigma^2 = \left\langle \int_\gamma \tilde{n}(\mathbf{x}_1,t)d\zeta_1 \int_\gamma \tilde{n}(\mathbf{x}_2,t)d\zeta_2 \int_{\gamma'} \tilde{n}(\mathbf{x}_1',t')d\zeta_1' \int_{\gamma'} \tilde{n}(\mathbf{x}_2',t')d\zeta_2' \right\rangle - \Gamma_{12}^2(t-t'). \tag{7.38}$$

To calculate this expression, we assume joint Gaussian statistics (with zero mean value) for the density fluctuations at any four points in the plasma; we can then write the fourth-order moment of the fluctuations as follows:[165]

$$\langle \tilde{n}_1\tilde{n}_2\tilde{n}_3\tilde{n}_4 \rangle = \langle \tilde{n}_1\tilde{n}_2 \rangle \langle \tilde{n}_3\tilde{n}_4 \rangle + \langle \tilde{n}_1\tilde{n}_3 \rangle \langle \tilde{n}_2\tilde{n}_4 \rangle + \langle \tilde{n}_1\tilde{n}_4 \rangle \langle \tilde{n}_2\tilde{n}_3 \rangle . \tag{7.39}$$

Equation (7.38) can then be written

$$\sigma^2 = \Gamma_{11}^2(0)\Gamma_{22}^2(0) + \Gamma_{12}^2(t-t'), \tag{7.40}$$

where Γ_{11} and Γ_{22} are the equal-time autocorrelation functions of the line integrals of $\tilde{n}$ along chords γ and γ', respectively (see Fig. 7.8). [We have implicitly assumed that

$\langle \tilde{n}^2 \rangle$ is constant in time, as indicated by Eq. (7.28).] Each of these two functions can be calculated formally in the same way as Γ_{12} from Eq. (7.19), the only difference being the coordinate transformations: Eqs. (7.29) and (7.30) must be replaced by

$$\begin{cases} x - x' = \pm(\zeta - \zeta')\sin\theta \\ z - z' = (\zeta - \zeta')\cos\theta \end{cases} \tag{7.41}$$

and

$$\begin{cases} x_{\mathrm{av}} = \pm(\zeta + \zeta')(\sin\theta)/2 \\ z_{\mathrm{av}} = (\zeta + \zeta')(\cos\theta)/2, \end{cases} \tag{7.42}$$

where the plus sign applies to chord γ and the minus sign applies to chord γ'. Carrying out the integration, we find

$$\Gamma_{11}(0) = \tilde{n}_0^2 \pi \mathcal{L}_\gamma \eta_\gamma \exp\left(-\frac{\mathcal{L}_\gamma^2 k_{0,\gamma}^2}{4}\right), \tag{7.43}$$

where $k_{0,\gamma}$ is the projection of $\mathbf{k}_0$ on the chord γ. Also,

$$\mathcal{L}_\gamma = \left(\frac{\cos^2\theta}{\mathcal{L}_z^2} + \frac{\sin^2\theta}{\mathcal{L}_x^2}\right)^{-1/2}, \tag{7.44}$$

and

$$\eta_\gamma = \left(\frac{\cos^2\theta}{\eta_z^2} + \frac{\sin^2\theta}{\eta_x^2}\right)^{-1/2}. \tag{7.45}$$

The expression for $\Gamma_{22}(0)$ is obtained by that for $\Gamma_{11}(0)$ by replacing $k_{0,\gamma}$ with $k_{0,\gamma'}$.

We simplify further by assuming $\mathbf{k}_0 = 0$; we also take $\tau = 0$, to obtain the *peak* signal-to-noise ratio. We can finally substitute Eq. (7.36) in Eq. (7.37), making use of Eqs. (7.31), (7.40), and (7.43), and write

$$\left(\frac{S}{N}\right)_\Gamma = (m-1)^{1/2}\left(1 + \frac{\mathcal{L}_\gamma^2 \eta_\gamma^2}{\mathcal{L}_z'^2 \eta_z'^2}\cos^4\theta\right)^{-1/2}. \tag{7.46}$$

When $\mathcal{L}_x = \mathcal{L}_z \equiv \mathcal{L}$ and $\eta_x = \eta_z \equiv \eta$, substituting Eqs. (7.32), (7.33), (7.44), and (7.45) in Eq. (7.46), we obtain

$$\left(\frac{S}{N}\right)_\Gamma = (m-1)^{1/2}\left(1 + \frac{(\tan^2\theta + 4\eta^2/\mathcal{L}^2)(\tan^2\theta + \mathcal{L}^2/4\eta^2)}{(1+\tan^2\theta)^2}\right)^{-1/2}. \tag{7.47}$$

This function decreases monotonically from $\sim (m/2)^{1/2}$ at $\theta = 0$, to $\sim m^{1/2}\mathcal{L}/\eta$ at $\theta = 45°$ (assuming $m \gg 1$ and $\eta \gg \mathcal{L}$). For $\theta \ll 1$ and $2\eta\theta/\mathcal{L} \gg 1$, one can write approximately

$$\left(\frac{S}{N}\right)_\Gamma \simeq m^{1/2}\frac{\mathcal{L}}{2\theta\eta}. \tag{7.48}$$

Thus, as expected, the signal-to-noise ratio is proportional to the square root of the number of realizations and to the length of the region to which the measurement is localized.

In many cases, one is concerned with extracting a signal from the intersection region in the presence of noise from a turbulent region located elsewhere along the beams. If the rms amplitude of the latter turbulence is $\tilde{n}_{\text{out}}$, and its spatial extent is η_{out}, the signal-to-noise ratio can be written approximately

$$\left(\frac{S}{N}\right)_{\Gamma} \simeq m^{1/2} \frac{\tilde{n}_0^2}{\tilde{n}_{\text{out}}^2} \frac{\mathcal{L}}{2\theta\eta_{\text{out}}}. \tag{7.49}$$

Thus, for this technique to be meaningful, the condition

$$m > \frac{\tilde{n}_{\text{out}}^4}{\tilde{n}_0^4} \frac{4\theta^2\eta_{\text{out}}^2}{\mathcal{L}^2} \tag{7.50}$$

must be satisfied.

In practice, data averaging is usually performed over time, under the assumptions of stationarity and ergodicity. In the case of digital sampling, the number of realizations is then equal to the product of the averaging time T and of the sampling rate; in the case of analog averaging, or when the digital sampling rate is larger than $2\Delta f$ (where Δf is the bandwidth of the fluctuations), one can write $m = 2T\Delta f$.

Similar considerations can be applied to the frequency cross-spectral function. The signal-to-noise ratio expressed by Eq. (7.47) applies to the spectral function also, with $m = T/\Delta t$, where in the case of averaging over time, Δt is the interval over which the Fourier integrals are calculated, and in the case of averaging over frequencies, Δt is one-half the reciprocal of the averaging interval.

Carrying out the correlation calculations by software provides the experimenter with the crucial ability to repeat the procedure on different intervals, using different smoothing functions, and so on. An obvious consistency check can be performed, for instance, by increasing the number of statistical samples and studying the trend of the results: the measured amplitude should decrease as the number of samples increases, and the phase should vary randomly, until the signal-to-noise ratio becomes substantially larger than one; from that point on, i.e., when the signal originates predominantly in the correlation region, no significant changes should be observed.

Coherent edge modes with long poloidal correlation lengths would, of course, invalidate this argument. However, these modes are easily identified experimentally by their narrow bandwidth, and they can be filtered out in the analysis of the turbulent part of the spectrum. Moreover, it should be possible to determine the radial location of such modes by comparing the phase difference between the signals from two crossed chords with the difference between the signals from two parallel chords within either beam: this will give the separation between the beams and thus the radial location. This is another example of the considerable advantages of a multichordal (imaging) technique with respect to a simple forward-scattering measurement.

(c) Higher-Order Correlations

When line-integrated signals are measured on parallel chords within an imaging configuration, their second-order correlation functions provide information on the spatial structure and on the wave-number spectrum of the turbulence in the perpendicular direction. This technique, which was discussed at length in Chapter 4 and was employed routinely in our measurements, conveys information that is averaged along the direction of integration and is thus poorly localized.

In the preceding discussion within this section, it was shown that the same correlation techniques, when applied to two crossed beams, provide spatially resolved data, localized in the intersection region. However, the phase information is lost in the correlation procedure, and the *local* wave-number spectrum cannot be reconstructed.

By resorting to higher-order correlation functions in a crossed-beam configuration, it is possible to extract phase information from the measurement, while at the same time localizing this information to the intersection region. The ultimate result of this procedure, however, is not the wave-number spectrum; rather, it is a function that is related to the nonlinear interaction between modes in the plasma. In addition, the signal-to-noise ratio is generally smaller than in the case of second-order correlation analysis. Nevertheless, this technique deserves consideration, in view of the exciting results of recent studies of nonlinear interactions in plasmas,[219,478,242] and by virtue of its very attractive promise of combined spatial and wave-number resolution. We shall analyze the third-order case in some detail and then offer some comments on higher-order correlations.

We want to calculate the third-order correlation function for the chords γ_1, γ_2, and γ_3, shown in Fig. 7.9. This function is defined as

$$\Gamma_{123}(t_1,t_2,t_3) \equiv \left\langle \int_{\gamma_1} \tilde{n}(\mathbf{x}_1,t_1)d\zeta_1 \int_{\gamma_2} \tilde{n}(\mathbf{x}_2,t_2)d\zeta_2 \int_{\gamma_3} \tilde{n}(\mathbf{x}_3,t_3)d\zeta_3 \right\rangle. \tag{7.51}$$

The origin of the coordinate system is set at the intersection of γ_1 and γ_3; the origins of the linear coordinates ζ_1, ζ_2, and ζ_3 are chosen to coincide with the points, respectively, $z_1 = 0$, $z_2 = 0$, and $z_3 = 0$.

By analogy with our previous analysis, we adopt a quasi-homogeneous approximation, expressing the pointwise third-order correlation function in the form

$$\langle \tilde{n}(\mathbf{x}_1,t_1)\tilde{n}(\mathbf{x}_2,t_2)\tilde{n}(\mathbf{x}_3,t_3)\rangle = \left\langle \tilde{n}^2(\mathbf{x}_{\mathrm{av}},t_{\mathrm{av}})\right\rangle^{3/2} \mathcal{F}_3(\mathbf{u}_1,\mathbf{u}_2;\tau_1,\tau_2), \tag{7.52}$$

where $\mathbf{x}_{\mathrm{av}} = (\mathbf{x}_1 + \mathbf{x}_2 + \mathbf{x}_3)/3$, $t_{\mathrm{av}} = (t_1 + t_2 + t_3)/3$, $\mathbf{u}_1 = \mathbf{x}_1 - \mathbf{x}_3$, $\mathbf{u}_2 = \mathbf{x}_2 - \mathbf{x}_3$, $\tau_1 = t_1 - t_3$, and $\tau_2 = t_2 - t_3$.

The choice of the variables on which the correlation form factor $\mathcal{F}_3$ depends is dictated by the requirements of spatial and temporal invariance. It should be noted that if the probability distribution functions of $\tilde{n}$ (at any three locations and times) are jointly Gaussian, the function $\mathcal{F}_3$ is zero.[165,479] In particular, the equal-time, normalized triple autocorrelation form factor $\mathcal{F}_3(0,0;0,0)$ is the *skewness* of the distribution of $\tilde{n}$, which is zero for any even distribution function.

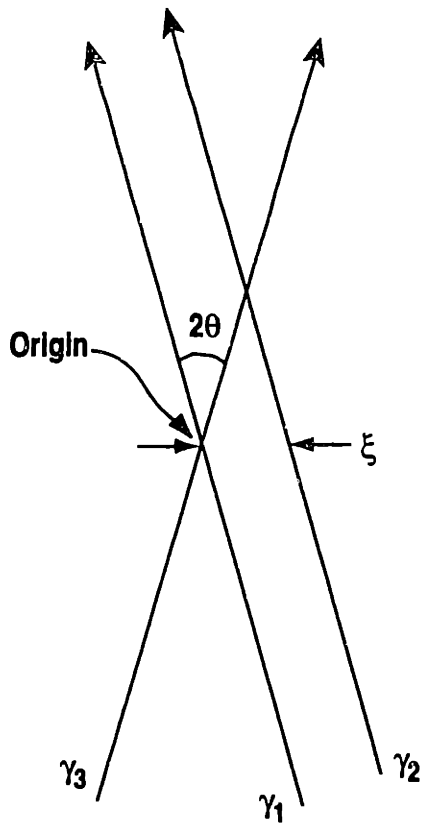

Fig. 7.9 Three-chord correlation geometry.

In general, the distribution will be nearly Gaussian in a strongly turbulent regime, characterized by rapid growth and decay of transient structures,[478] whose nonlinear interaction results in complete randomization of the phases and in the absence of a well-defined dispersion relation. At the other extreme lies a regime characterized by a set of uncorrelated, noninteracting modes; in this case the distribution is strongly non-Gaussian, but the triple correlation again vanishes because of the statistical independence of the modes.

The third-order correlation function becomes relevant in intermediate situations, including the weak-turbulence scenario, the strong-turbulence scenario when total randomization has not occurred, and the case of nonlinear interaction between a semicoherent mode and background plasma turbulence.[219] In these cases, which have frequently been observed in thermonuclear plasmas, the triple correlation carries information on the degree of nonlinear coupling between the modes.

To elucidate this connection, we write the form factor $\mathcal{F}_3$ in the form of a Fourier integral:

$$\mathcal{F}_3(\mathbf{u}_1, \mathbf{u}_2; \tau_1, \tau_2) = \frac{1}{(2\pi)^6} \int d^2k_1 \int d^2k_2 \int d\omega_1 \int d\omega_2 \; I_3(\mathbf{k}_1, \mathbf{k}_2; \omega_1, \omega_2) \times \exp\bigl[i(\mathbf{k}_1 \cdot \mathbf{u}_1 + \mathbf{k}_2 \cdot \mathbf{u}_2 - \omega_1\tau_1 - \omega_2\tau_2)\bigr], \tag{7.53}$$

where the Hermitian function I_3 is the third-order cumulant spectrum, or *bispec-*

trum,[480] which measures the statistical dependence between the three waves $(\mathbf{k}_1, \omega_1)$, $(\mathbf{k}_2, \omega_2)$, and $(\mathbf{k}_1 + \mathbf{k}_2, \omega_1 + \omega_2)$. By virtue of Eqs. (7.52) and (7.53) we can write

$$\langle \hat{n}(\mathbf{k}_1, \omega_1) \hat{n}(\mathbf{k}_2, \omega_2) \hat{n}(\mathbf{k}_3, \omega_3) \rangle = \langle \tilde{n}^2(\mathbf{x}_{\mathrm{av}}, t_{\mathrm{av}}) \rangle^{3/2} I_3(\mathbf{k}_1, \mathbf{k}_2; \omega_1, \omega_2)\, \delta(\mathbf{k}_1 + \mathbf{k}_2 + \mathbf{k}_3)\, \delta(\omega_1 + \omega_2 + \omega_3). \quad (7.54)$$

We can express the three-wave interaction in the form of the quadratic nonlinearity[187]

$$\hat{n}(\mathbf{k}, \omega) = \hat{n}_l(\mathbf{k}, \omega) + \int d^2k' \int d\omega'\; A(\mathbf{k}', \mathbf{k} - \mathbf{k}'; \omega', \omega - \omega') \times \hat{n}(\mathbf{k}', \omega')\, \hat{n}(\mathbf{k} - \mathbf{k}'; \omega - \omega'), \quad (7.55)$$

where $\hat{n}_l$ is the component of the density fluctuation spectrum $\hat{n}$ that is independent of the quadratic interaction term. Multiplying Eq. (7.55) by $\hat{n}^*(\mathbf{k}_1, \omega_1)$ and $\hat{n}^*(\mathbf{k}_2, \omega_2)$, calculating the ensemble average, and making use of Eq. (7.54), the following relation is obtained between the coupling coefficient A and the triple correlation function I_3:

$$I_3^*(\mathbf{k}_1, \mathbf{k}_2; \omega_1, \omega_2) = \langle \tilde{n}^2 \rangle^{1/2} I(\mathbf{k}_1, \omega_1) \Big[2I(\mathbf{k}_2, \omega_2) A(\mathbf{k}_1, \mathbf{k}_2; \omega_1, \omega_2) + \delta(\mathbf{k}_1 + \mathbf{k}_2) \times \delta(\omega_1 + \omega_2) \iint A(\mathbf{k}', -\mathbf{k}'; \omega', -\omega')\, I(\mathbf{k}', \omega')\, d^2k' d\omega' \Big], \quad (7.56)$$

where we have neglected four-wave interaction terms; here, $I(\mathbf{k}, \omega)$ is the second-order spectral function, or power spectrum, defined by Eq. (4.9).

To investigate the issue of locality, we adopt again a Gaussian form for $\langle \tilde{n}^2 \rangle$, but we assume homogeneity in the x direction for simplicity: thus we write

$$\langle \tilde{n}^2(\mathbf{x}_{\mathrm{av}}, t_{\mathrm{av}}) \rangle = \tilde{n}_0^2 \exp\left(-\frac{(z_{\mathrm{av}} - z_0)^2}{\eta_z^2} \right). \quad (7.57)$$

The function I_3 is left unspecified.

We can now calculate the triple-chord correlation function expressed by Eq. (7.51). Given its dependence on τ_1 and τ_2, it is simpler to calculate directly its double Fourier transform; using Eqs. (7.52), (7.53), and (7.57), we can write

$$\hat{\Gamma}_{123}(\omega_1, \omega_2) = \frac{\tilde{n}_0^3}{(2\pi)^4} \int d^2k_1 \int d^2k_2\; I_3(\mathbf{k}_1, \mathbf{k}_2; \omega_1, \omega_2) \int d\zeta_1 \int d\zeta_2 \int d\zeta_3 \times \exp\left(-\frac{3}{2} \frac{(z_{\mathrm{av}} - z_0)^2}{\eta_z^2} \right) \exp\big[i(\mathbf{k}_1 \cdot \mathbf{u}_1 + \mathbf{k}_2 \cdot \mathbf{u}_2) \big]. \quad (7.58)$$

To carry out the triple chord integration, we must first express all coordinates as functions of ζ_1, ζ_2, and ζ_3, as follows:

$$\begin{cases} u_{1,x} = -(\zeta_1 + \zeta_3) \sin\theta \\ u_{1,z} = (\zeta_1 - \zeta_3) \cos\theta, \end{cases} \quad (7.59)$$

$$\begin{cases} u_{2,x} = -(\zeta_2 + \zeta_3)\sin\theta + \xi/2 \\ u_{2,z} = (\zeta_2 - \zeta_3)\cos\theta, \end{cases} \tag{7.60}$$

and

$$z_{\text{av}} = (\zeta_1 + \zeta_2 + \zeta_3)(\cos\theta)/3, \tag{7.61}$$

where ξ is the horizontal projection of the distance between γ_1 and γ_2 (see Fig. 7.9).

The triple integration in Eq. (7.58) is performed readily by means of a linear change of variables to the set $(\zeta_1+\zeta_2+\zeta_3;\ \zeta_1-\zeta_2+\zeta_3;\ \zeta_3)$; since two delta functions appear in the result, the integrations over $k_{1,z}$ and $k_{2,z}$ can be carried out also. The result is

$$\begin{aligned} \hat{\Gamma}_{123}(\omega_1,\omega_2) = {} & \frac{(6\pi)^{1/2}}{3\cos^3\theta}\eta_z\tilde{n}_0^3\frac{1}{(2\pi)^2}\int dk_{2,x}\exp\left(ik_{2,x}\frac{\xi}{2}\right)\int dk_{1,x} \\ & \times\exp\left[-\frac{2}{3}\eta_z^2(k_{1,x}+k_{2,x})^2\tan^2\theta\right]\exp\left[-2iz_0(k_{1,x}+k_{2,x})\sin\theta\right] \\ & \times I_3\left(k_{1,x},\frac{k_{1,x}-2k_{2,x}}{3}\tan\theta,\ k_{2,x},\frac{k_{2,x}-2k_{1,x}}{3}\tan\theta\,;\omega_1,\omega_2\right). \end{aligned} \tag{7.62}$$

It should be noted that the selection rules that are implicit in the functional form of I_3 in Eq. (7.62) imply that the components of $\mathbf{k}_1$ and $\mathbf{k}_2$ in the direction of γ_1 (and γ_2) are equal. In general, the vertical wave numbers will be small, because they are expressed by linear combinations of the horizontal wave numbers, multiplied by the small factor $\tan\theta$.

To determine the localization properties of this measurement in a qualitative fashion, we can assign a characteristic width $\bar{\kappa}_x$ to the bispectrum I_3 as a function of $(k_{1,x}+k_{2,x})$. We then define a third-order horizontal correlation length $\mathcal{L}_{3,x} = 2\sqrt{2}/\bar{\kappa}_x$. The double integral in Eq. (7.62) can be recast as an integral over the sum and difference of $k_{1,x}$ and $k_{2,x}$; at $\xi = 0$, the integral over $(k_{1,x}+k_{2,x})$ will vanish for $|z_0| \gtrsim \mathcal{L}_{3,x}/(2\sin\theta)$ [assuming, as before, $\eta_z < \mathcal{L}_{3,x}/(2\tan\theta)$]. Therefore, the localization properties of the triple correlation function are similar to those of the second-order crossed-beam correlation function, with $\mathcal{L}_{3,x}$ replacing $\mathcal{L}_x$. In general, these two correlation lengths will be of comparable magnitude.

As anticipated, the function $\hat{\Gamma}_{123}$ retains also phase information, through the term $\exp(i\xi k_{2,x}/2)$. Thus, by varying the position of the chord γ_2 within the beam, thereby repeating the measurement for different values of ξ, the spatial distribution of $\hat{\Gamma}_{123}$ can be reconstructed. Under the assumptions $z_0 = 0$ and $\theta \ll 1$, the Fourier transform of $\hat{\Gamma}_{123}$ with respect to $\xi/2$ yields, to zeroth order in θ,

$$\hat{\Gamma}_{123}(k_{2,x};\omega_1,\omega_2) \simeq \left(\frac{2}{3}\pi\right)^{1/2}\eta_z\tilde{n}_0^3\int I_3(k_{1,x},0,k_{2,x},0;\omega_1,\omega_2)\,dk_{1,x}. \tag{7.63}$$

This quantity represents the third-order correlation between a purely horizontal mode of wave number $k_{2,x}$ and all other horizontally propagating modes, and is localized to the intersection region of the beams.

The signal-to-noise ratio can be estimated by repeating the steps of part (b) of this section. Adopting again a quasinormal approximation, and ignoring all crosscorrelation terms in comparison with the autocorrelation terms, the sample variance for Γ_{123} may be written, by analogy with Eq. (7.40),

$$\sigma^2 \simeq \Gamma_{11}(0)\Gamma_{22}(0)\Gamma_{33}(0), \tag{7.64}$$

and the signal-to-noise ratio takes the form

$$\left(\frac{S}{N}\right)_{\Gamma_{123}} = (m-1)^{1/2}\frac{|\Gamma_{123}|}{\sigma}. \tag{7.65}$$

Guided by the second-order case, we estimate Γ_{123} at $\tau_1 = 0$, $\tau_2 = 0$, and $\xi = 0$. If the bispectrum is approximately isotropic, assuming again $\theta \ll 1$, but $\eta_z\theta \gg \mathcal{L}_3$, and using Eq. (7.62), we can write approximately

$$\begin{aligned}\Gamma_{123}(0,0) &\simeq \left(\frac{2}{3}\pi\right)^{1/2}\frac{\eta_z\tilde{n}_0^3}{(2\pi)^4}\int dk_{1,x}\int dk_{2,x}\int d\omega_1\int d\omega_2\; I_3(k_{1,x},0,k_{2,x},0;\omega_1,\omega_2)\\ &\quad\times\exp\left[-\frac{2}{3}\eta_z^2\,(k_{1,x}+k_{2,x})^2\theta^2\right]\\ &\sim O\left(\tilde{n}_0^3\,|\mu_3|\frac{\mathcal{L}_3^3}{\theta}\right),\end{aligned} \tag{7.66}$$

where μ_3 is the skewness of the distribution of $\tilde{n}$.

Substituting Eqs. (7.64) and (7.66) in Eq. (7.65), and using Eq. (7.43) with $\mathbf{k}_0 = 0$, we finally obtain the order-of-magnitude relation

$$\left(\frac{S}{N}\right)_{\Gamma_{123}} \sim O\left(m^{1/2}|\mu_3|\frac{\mathcal{L}_3^{3/2}}{\theta\,\eta^{3/2}}\right). \tag{7.67}$$

In the case of noise from turbulence localized outside the intersection region, with rms amplitude $\tilde{n}_{\text{out}}$ and effective vertical extent η_{out}, we can write, by analogy with Eq. (7.49),

$$\left(\frac{S}{N}\right)_{\Gamma_{123}} \sim O\left(m^{1/2}|\mu_3|\,\frac{\tilde{n}_0^3}{\tilde{n}_{\text{out}}^3}\,\frac{\mathcal{L}_3^{3/2}}{\theta\,\eta_{\text{out}}^{3/2}}\right). \tag{7.68}$$

Imposing $S/N \geq 1$ results in the approximate condition

$$m \gtrsim \frac{\tilde{n}_{\text{out}}^6}{\tilde{n}_0^6}\,\frac{1}{\mu_3^2}\,\frac{\theta^2\eta_{\text{out}}^3}{\mathcal{L}_3^3}. \tag{7.69}$$

Clearly, this condition is considerably more demanding than that expressed by Eq. (7.50) for the two-chord case, owing to the dependence on the sixth power of the

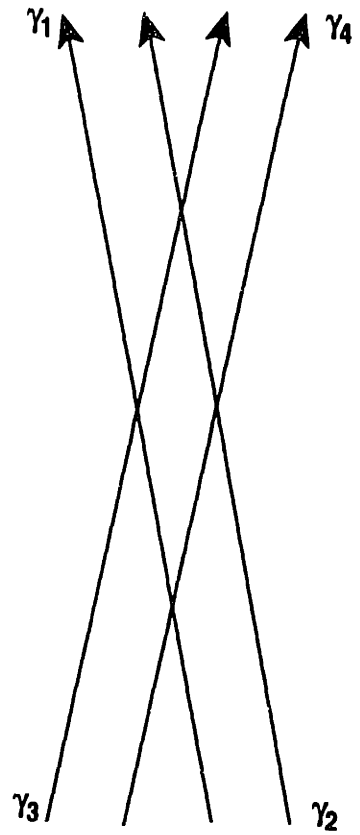

Fig. 7.10 Four-chord correlation geometry.

density ratio, on the third power of $\eta_{\text{out}}/\mathcal{L}_3$, and on the second power of the reciprocal of $|\mu_3|$. Still, in quasi-steady-state conditions, when long averaging times are available, it may be possible to obtain a signal-to-noise greater than one.

Similar considerations apply to higher-order correlation functions. In the fourth-order case, one would employ the geometry shown in Fig. 7.10, and calculate the function

$$\Gamma_{1234} \equiv \left\langle \int_{\gamma_1} \tilde{n}_1 d\zeta_1 \int_{\gamma_2} \tilde{n}_2 d\zeta_2 \int_{\gamma_3} \tilde{n}_3 d\zeta_3 \int_{\gamma_4} \tilde{n}_4 d\zeta_4 \right\rangle - \Gamma_{12}\Gamma_{34} - \Gamma_{13}\Gamma_{24} - \Gamma_{14}\Gamma_{23}. \quad (7.70)$$

This function is the quadruple line integral of the fourth-order cumulant,[480] whose spectrum is related to four-wave interactions among plasma modes. The function Γ_{1234} is again localized to the intersection region and contains horizontal wave-number information. Its signal-to-noise ratio is approximately

$$\left(\frac{S}{N}\right)_{\Gamma_{1234}} \sim O\left(m^{1/2}\mu_4 \frac{\tilde{n}_0^4}{\tilde{n}_{\text{out}}^4} \frac{\mathcal{L}_4^2}{\theta\eta_{\text{out}}^2}\right), \quad (7.71)$$

where $\mu_4 = \langle\tilde{n}^4\rangle / \langle\tilde{n}^2\rangle^2 - 3$ is the *coefficient of kurtosis* of the probability distribution function of $\tilde{n}$, which vanishes in the case of Gaussian probability distributions.

An impractically large number of realizations would likely be necessary for this signal-to-noise ratio to rise above one. The ratio diminishes further when higher orders are considered.

7.4 Suggestions for Future Upgrades on DIII–D

In this section a few suggestions are offered on possible additions to the DIII–D PCI system. The first ones to be discussed involve only software development for data analysis, while the remainder of the section examines possible material upgrades and hardware development.

In recent years the limits of traditional statistical analysis, in its application to plasma fluctuation studies, have been recognized with ever greater clarity. The concomitant development of advanced statistical techniques, which proved to be particularly suited to this field of investigation, has led several researchers to include those new methods in their data-analysis procedures, often with interesting and novel results. The phase-contrast imaging technique, in particular, could reap significant benefits from third-order correlation analysis and wavelet analysis.

The higher-order correlation techniques examined in the previous section may be applied also to parallel chords within a single beam. In particular, the normalized third-order correlation spectral function in frequency space, or *bicoherence*, is an important quantity that carries information on the nonlinear (quadratic) interaction between triplets of modes. In the experimental conditions found in tokamaks, there is a rich variety of modes that are known to interact nonlinearly, giving rise to generalized turbulent states. Bicoherence methods have been employed to advantage in the study of these interactions.[219,478] Digital bispectral analysis is now a well-established technique,[480] and its application to the DIII–D PCI system would significantly expand the capabilities of the system.

Wavelet analysis is a recent method[240] that has found extensive applications in the fields of turbulence and chaos. This technique addresses the problem of nonstationarity, which hampers traditional methods based on Fourier decomposition and time averaging. In wavelet analysis, a signal is decomposed in pseudo-Fourier components that depend on both frequency (fast events) and time (slow evolution). This method presents similarities with the quasi-homogeneous approximation[109] that was used in our models of plasma turbulence in Chapter 4 and in the present chapter. The wavelet technique has been shown to be better suited than traditional Fourier analysis to the investigation of transient or short-lived events, such as are often observed in tokamak plasmas (particularly in the vicinity of a phase transition, such as the L– to H–mode transition). Recently, the wavelet and bicoherence methods have been combined to explore nonlinear coupling between short-lived turbulent structures.[242]

Various forms of conditional analysis could also be beneficial. In particular, statistical analysis with a condition imposed on the amplitude[481,231] can be useful in isolating large-amplitude fluctuations that may behave differently from the small-scale turbulence and that may dominate transport in tokamaks, according to some theories.[390,462,360]

Two possible material upgrades of the DIII–D PCI apparatus have been proposed, of considerably different scale. The more modest upgrade, which was briefly mentioned in §3.7, consists of installing a dual-axis feedback vibration-compensation system for the image plane, in addition to the existing one for the focal plane. This upgrade would permit to greatly improve the *absolute* spatial resolution of the measurement. This system would be a simplified replica of the existing one, with more relaxed performance specifications: a damping factor of 1/5 at 20 Hz would be sufficient to ensure an absolute spatial resolution of $\sim$ 1 mm.

In the second material upgrade under consideration, a second line of sight would be made available further inside the tokamak. The major radius at this location is approximately 2 meters, corresponding to a normalized minor radius as small as 0.2 in certain plasma geometries (see Fig. 7.11). The larger size of the interior ports would permit a beam diameter of 12.5 cm, which would also constitute the upper limit on the measurable horizontal wavelengths.

One important application of this configuration would be the detection and characterization of the externally launched rf waves that are used for fast-wave current drive[75] (see §1.1). This interior location corresponds to the region of greatest interest, where the physics of wave absorption is important; at the same time, the wavelength of the waves in this region lies in the range that is accessible to PCI. In general, in the case of a coherent wave, line averaging does not subtract information from the measurement; in addition, the wave front of the fast wave can be modeled by means of existing computer codes. A direct spatial mapping of the phase and amplitude of the fast wave would be an unprecedented achievement, and would greatly contribute to our understanding of the physics of wave propagation and absorption.

In the study of turbulence, the lack of localization due to line averaging would constitute a more serious problem in this future geometry than in the present one. However, as shown in Fig. 7.11, a crossed-beam configuration could also be employed. As was shown in the previous section, correlation techniques applied to two crossed beams allow to localize the measurement to the intersection region. With an angle of $\sim 17°$ between the chords, a localized spatial mapping of the fluctuation amplitude distribution could be obtained within a parallelogram that spans a vertical range of 68 cm and a horizontal range of 10.2 cm. This would permit a detailed, spatially resolved study of core turbulence, on which far less is known than on turbulence at the edge.

It should be noted that the large $\mathbf{E} \times \mathbf{B}$ poloidal drifts observed in many cases in the edge of DIII–D may provide additional means to discriminate the correlated core turbulence from the random contributions from the edge through frequency analysis, as has been done for FIR scattering measurements.[190] Thus, under these circumstances, it may be possible to relax the requirement on the number of realizations [given formally by Eq. (7.50)].

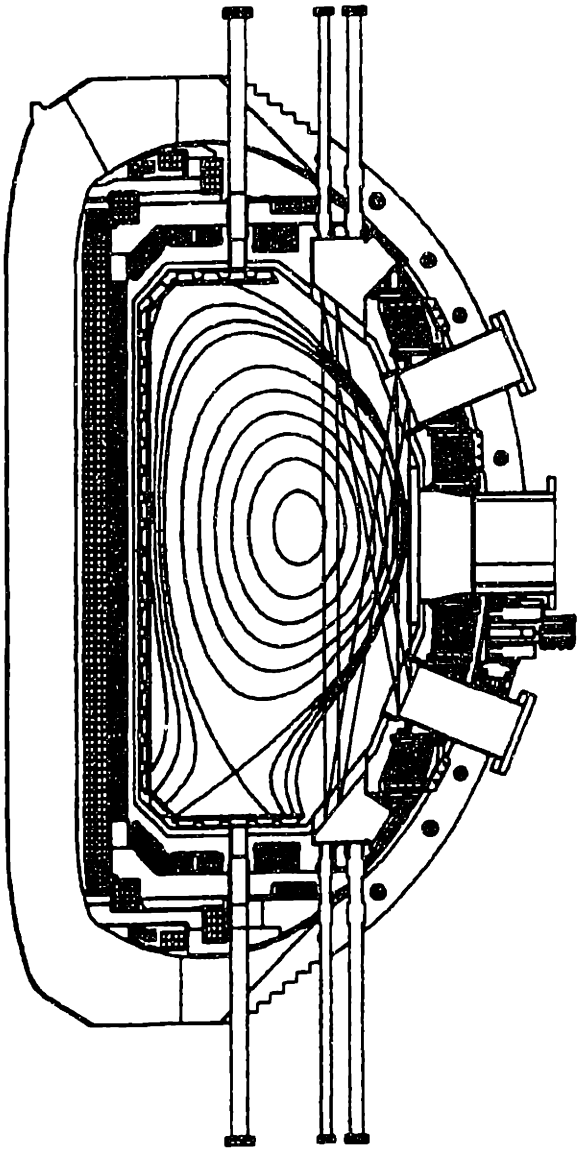

Fig. 7.11 Interior-beam upgrade and crossed-beam geometry in DIII–D.

8 Summary and Conclusions

A novel technique for measuring plasma density fluctuations, phase-contrast imaging (PCI), has been perfected and applied to the edge of the DIII–D tokamak. This thesis has described a variety of results obtained with this diagnostic system, and has provided a complete theoretical treatment and a numerical analysis of the technique. Future applications and suggestions for future work have also been explored.

8.1 Summary

The principles of the measurement are grounded in the physics of light-plasma interaction, and have been derived by following the two complementary and equivalent approaches of scattering and propagation in a dielectric. The Born and Rytov approximations were then introduced, and the latter was shown to be preferable in the specific case of this technique. This approximation was then employed to investigate in detail the general properties of scattering and imaging measurements in the various possible detection schemes (near-, intermediate-, and far-field). This analysis included for the first time the effects of a finite, although small, fluctuation frequency. An extension of geometrical optics to the finite-frequency case was also given and was shown to be equivalent to the scattering framework in the Raman-Nath limit.

The response properties of the phase-contrast technique were then derived analytically for the first time for a truncated Gaussian beam, and were compared with the response functions of several other techniques under the same conditions. A comparison of the signal-to-noise ratio of these techniques was also provided.

The layout and the properties of the PCI apparatus on DIII–D were described in detail. Particular emphasis was placed on the successful design and implementation of a novel feedback vibration-stabilization system, which is an essential component of the proof of principle of this technique on large tokamaks.

As the PCI technique provides line-integrated measurements, it is intrinsically nonlocal. This limitation and its implications were discussed in considerable detail. In the specific case of the DIII–D apparatus, geometrical constraints reduce the uncertainties associated with the line integration. The effect of these constraints was explained qualitatively in an intuitive fashion, and was then explored rigorously with the aid of an analytical model of plasma turbulence. This analytical work was supplemented by a more accurate numerical analysis, which confirmed the main results of the initial qualitative considerations. In particular, it was found that the DIII–D PCI measurement is mostly sensitive to wave vectors oriented in the radial direction, and, for this reason, is essentially unaffected by Doppler shifts from plasma rotation. This important result implies that the frequency spectra can be measured directly in the plasma frame of reference.

All diagnostics used in the study of plasma fluctuations are sensitive to a subset of the total spectrum, both in frequency and wave-number space. In addition, each diagnostic system can only access a finite region of space. For this reason, each

technique is specific to the peculiar components of the fluctuations that it is able to measure; however, under general strong-turbulence assumptions, each measurement can also be considered representative of the properties of turbulence at large. Thus, in the case of PCI in DIII–D, we have explored the detailed properties of radial modes (that is, modes with purely radial wave vectors) and the more general properties of turbulence.

The phenomenology was presented systematically in terms of time- and frequency-domain correlations, spatial correlations and wave-number spectra, amplitude, and probability distribution function; further details were provided on the temporal dynamics of the turbulence, particularly across the L–H transition and during Edge Localized Modes (ELMs).

Radial modes have been shown to be characterized by nonzero peaks in the wave-number spectrum. These modes, observed and documented for the first time in this thesis, were predicted earlier by theoretical and numerical work, which concluded that they play a fundamental role in regulating transport. This study thus constitutes a rare example of a theoretical prediction in plasma turbulence that has been clearly verified experimentally.

The existence of convective cells, possibly related to resistive-ballooning resonances, is consistent with measurements performed with PCI in L–mode plasmas with low safety factor at the edge. These structures, which can cause substantial cross-field transport, are found to disappear in H mode, in agreement with theory.

Several phenomenological results have been obtained on the general properties of turbulence, extending previous measurements to areas that are often of interest for comparison with theory. These include, as mentioned earlier, the frequency spectra in the plasma frame (which typically follow an inverse power law), the dependence on frequency of the correlation length and of the average wave number (dispersion relation, typically increasing in an offset-linear fashion), and the probability distribution function (Gaussian over short time scales, non-Gaussian over time scales longer than 40 ms, indicating possible long-time-scale intermittency).

Also, the variations of the key turbulence quantities with the plasma parameters have been systematically analyzed. Of the more regular cases, some were found to be consistent with theoretical or independent experimental results, whereas others were simply offered for future theoretical consideration. The random-walk diffusivity was found to increase with input power in L mode, and to decrease sharply at the L–H transition, in accord with the behavior of the anomalous plasma diffusivity; in addition, the numerical value of the random-walk diffusivity is close to that of the ion diffusivity at the edge.

Measurements of the fluctuation amplitude and of the correlation length were employed to test the mixing-length criterion. This was found to be satisfied by Ohmic and L–mode plasmas, whereas H–mode plasmas had fluctuation amplitudes well below the mixing-length level. This result may indicate that the L–H transition can be described as a transition from strong to weak turbulence; however, this conclusion may be invalidated by considerations of H–mode dynamics, which await a more

extensive analysis.

Important new results were obtained in the area of the L–H transition. A number of theories of the transition have been in existence for several years, several of them awaiting experimental confirmation. A quantitative criterion for the occurrence of the L–H transition, based on the concept of shear decorrelation of turbulence, has emerged from the most widely accepted theoretical analysis. The ability of the PCI system to provide time-resolved measurements of correlation lengths and decorrelation times has been instrumental in performing a test of this criterion with unprecedented accuracy; the criterion has thus been clearly verified. Furthermore, two independent and rather different quantitative predictions for the changes in the correlation length and in the decorrelation time at the transition have also been tested for the first time, with mixed results: each of the two theories was successful in predicting only one of the two quantities.

A systematic study of Edge Localized Modes (ELMs) was also carried out. A multiple-interval averaging technique was employed to obtain statistically relevant results on intrinsically transient events. Many similarities were found in the spectra and dispersion relations of turbulence during ELMs and in L mode, although the absolute fluctuation amplitude is generally substantially larger in the case of ELMs. Thus, from the point of view of turbulence, ELMs are similar to H–L–H transition sequences; the difference in amplitude and in the speed of the transition may be ascribed to the different pressure profiles in the two cases. Systematic differences between type-I and type-III ELMs were discovered: the fluctuation burst in a type-I ELM is simultaneous with the peak in outward transport, and the spectrum contains only broadband turbulence; by contrast, the fluctuation peak precedes the point of maximum transport by 0.4–0.6 ms and the spectrum contains also an outward-propagating, coherent mode at approximately 100 kHz. These differences may be related to the very different characteristic time scales of ideal and resistive MHD, respectively.

A few possible additional applications of PCI have been presented. Heterodyne PCI can be employed to improve the signal-to-noise ratio in the case of synchronous detection; its properties have been shown to be very similar to those of homodyne PCI. Improvements in the localization of the measurements can be achieved by symmetry constraints or by crossed-beam correlation techniques; the latter in particular has been proposed for a future upgrade on DIII–D. PCI can also be employed to measure radio-frequency waves; one of the purposes of the proposed upgrade is, indeed, to characterize for the first time the spatial structure of the fast waves used in current-drive experiments.

8.2 Suggestions for Future Work

Laser-imaging techniques are still in their infancy in the realm of plasma fluctuation studies. It is certainly desirable to develop new and increasingly sophisticated techniques, particularly to improve the spatial localization of the measurements. New ideas will undoubtedly surface in the future and will lead to advances as spectacular as those already experienced by fluid dynamics.

The PCI technique itself can be expanded and adapted to different configurations, laser wavelengths, and detection techniques. The applications that were discussed and analyzed in Chapter 7 in particular are feasible with present-day technology and have the potential of generating new knowledge in the field of plasma fluctuations. The upgrade that has been proposed for DIII–D (see §7.4) would explore both the heterodyne PCI technique and the crossed-beam correlation technique, and would lead to two prized and novel results: a spatially localized mapping of the turbulence distribution in the plasma core and a first-time study of the spatial structure of fast waves.

Additions to both the software and the hardware of the present DIII–D system can also be implemented with great potential benefits. On the hardware side, photoconductive infrared detectors have now achieved performances considerably superior to those of the detector currently in use: an improvement of the sensitivity by at least one order of magnitude would be easy to obtain. Also, a second feedback stabilization system for the image plane, in addition to the present one for the focal plane, would considerably reduce the absolute spatial uncertainty of the measurement (see §3.5) and possibly decrease the lowest accessible frequency below 8 kHz.

On the software and data-analysis side, higher-order correlation techniques, such as bicoherence analysis, would be very beneficial for examining the spectra of nonlinear wave-wave interactions in the turbulence. Also, wavelet analysis could be employed to provide a more accurate characterization of transient events, such as the L–H transition and ELMs (see §7.4).

The present PCI system is currently operational on DIII–D and is available for further physics studies. In this thesis we have focused by necessity on a number of specific topics, such as radial modes, the L–H transition, mixing-length scalings, and ELMs. Investigation of these topics is by no means complete, and further studies, particularly utilizing dedicated plasma shots, would be extremely desirable: this is especially true of ELMs and of the mixing-length scalings. A larger database of ELMs is certainly needed for a more complete characterization, and a more detailed analysis of type-II, or grassy, ELMs is in order; the mixing-length scaling has been tested in H mode only just after the transition, and the dynamic changes during the complex H–mode phase remain to be explored.

More generally, the evolution of turbulence throughout a discharge, particularly in the late-H–mode phase, should be studied systematically. Other topics that have only received preliminary attention in this thesis, but are nevertheless of great interest, are the following: parametric scans of the turbulence quantities, convective cells,

the VH mode, SOL dynamics in the early-H–mode phase, the effect of sawteeth on turbulence, MHD and other coherent and semicoherent events.

8.3 Conclusions

The study of turbulence, whether in fluids or in plasmas, remains one of the most challenging areas of classical physics. Although it is often motivated by practical concerns — in the case of fusion plasmas, confinement — this area of research is also fascinating in itself and continues to provide momentum to an incessant expansion of the boundaries of mathematical, computational, and experimental techniques.

In some ways, because of its resilience to "classical", or conventional, approaches and of its ability to supply new surprises at every step, turbulence has had a fundamental role in challenging some of our most cherished notions and in changing the very way we think of a physical system. Turbulence may well prove to be the stuff of twenty-first century physics.

Appendix A

Derivation of the Scattering Equation

In this appendix the scattering equation (2.22) is derived from the wave equation expressed in integral form [Eq. (2.21)]. The scattering equation is usually obtained in the literature[86,29] from the expressions for the radiation fields produced by accelerated charges. It is shown here that the problem of scattering can be treated entirely within the framework of a plasma dielectric model. This, of course, is to be expected; the present alternative derivation, however, serves to better elucidate the nature of the necessary approximations.

Our starting point is the integral wave equation (2.21):

$$\mathbf{E}(\mathbf{x},t) = \mathbf{E}_0(\mathbf{x})e^{-i\omega_0 t} + \int \frac{1}{R}\left[-r_e n_e' \mathbf{E}' + \frac{1}{4\pi}\nabla'(\mathbf{E}'\cdot\nabla' \ln \epsilon')\right]_{\text{ret}} d^3x', \qquad (A.1)$$

where the prime indicates quantities to be calculated at $(\mathbf{x}_\perp', t')$, t' is the retarded time ($t' = t - R/c$), and $R = |\mathbf{x}_\perp - \mathbf{x}_\perp'|$. We assume that for all points in the plasma the relation $R \gg L$ holds, where L is a characteristic dimension of the interaction region (see Fig. 2.1), and that $k_0 R \gg 1$, where $k_0 = \omega_0/c$. This allows us to ignore all integrals in which terms $\propto 1/(k_0 R)^2$ multiply quantities that are localized to the plasma region, such as $(1-\epsilon)$ or $\nabla\epsilon$. We also make the assumption, justified by Eqs. (2.1) and (2.11), that $|1-\epsilon| \ll 1$. Furthermore, ϵ is taken to vary on a much slower time scale than $1/\omega_0$. A key ingredient in the following analysis is Coulomb's law, which can be written as

$$\nabla\cdot\mathbf{E} = -\frac{1}{\epsilon}\mathbf{E}\cdot\nabla\epsilon. \qquad (A.2)$$

We concentrate now on the second term within the square brackets in Eq. (A.1). The spatial derivatives are *intrinsic* derivatives with respect to the spatial variable $\mathbf{x}'$. On the other hand, the expression in square brackets as a whole depends on $\mathbf{x}'$ also through the retarded time $t' = t - |\mathbf{x} - \mathbf{x}'|/c$. If we denote the *total* differential operator with respect to $\mathbf{x}'$ as ∇_T', we can write

$$\nabla' = \nabla_T' - (\nabla' t')\frac{\partial}{\partial t'} = \nabla_T' - \frac{\hat{\mathbf{n}}}{c}\frac{\partial}{\partial t'}, \qquad (A.3)$$

where $\hat{\mathbf{n}}$ is a unit vector in the direction of $\mathbf{x} - \mathbf{x}'$. Hence, we can write

$$\frac{1}{4\pi}\int \frac{1}{R}\left[\nabla'\left(\frac{\mathbf{E}'\cdot\nabla'\epsilon'}{\epsilon'}\right)\right]_{\text{ret}} d^3x' = \mathcal{I}_1 + \mathcal{I}_2, \qquad (A.4)$$

where

$$\mathcal{I}_1 = \frac{1}{4\pi}\int \frac{1}{R}\left[\nabla_T'\left(\frac{\mathbf{E}'\cdot\nabla'\epsilon'}{\epsilon'}\right)\right]_{\text{ret}} d^3x' \qquad (A.5)$$

and

$$\mathcal{I}_2 = \frac{i\omega_0}{4\pi c}\int \frac{\hat{\mathbf{n}}}{R}\left[\frac{\mathbf{E}'\cdot\nabla'\epsilon'}{\epsilon'}\right]_{\text{ret}} d^3x', \tag{A.6}$$

where the substitution $\partial/\partial t' \to -i\omega_0$ has been effected. Calculating the integral in Eq. (A.5) by parts, we obtain

$$\mathcal{I}_1 = -\frac{1}{4\pi}\int \frac{\hat{\mathbf{n}}}{R^2}\left[\frac{\mathbf{E}'\cdot\nabla'\epsilon'}{\epsilon'}\right]_{\text{ret}} d^3x' \simeq 0, \tag{A.7}$$

where the last equality is justified by the $1/R^2$ dependence of the integrand. Using Eq. (A.3), Eq. (A.6) can be recast as

$$\mathcal{I}_2 = \mathcal{I}_3 + \mathcal{I}_4, \tag{A.8}$$

where

$$\mathcal{I}_3 = \frac{i\omega_0}{4\pi c}\int \frac{\hat{\mathbf{n}}}{R}\left[\frac{\mathbf{E}'\cdot\nabla'_T(\epsilon'-1)}{\epsilon'}\right]_{\text{ret}} d^3x', \tag{A.9}$$

and

$$\mathcal{I}_4 = -\frac{i\omega_0}{4\pi c}\int \frac{\hat{\mathbf{n}}}{R}\left[\frac{\hat{\mathbf{n}}\cdot\mathbf{E}'}{c\epsilon'}\frac{\partial(\epsilon'-1)}{\partial t'}\right]_{\text{ret}} d^3x'. \tag{A.10}$$

The function $\mathcal{I}_3$ can now be calculated with an integration by parts:

$$\begin{aligned}\mathcal{I}_3 = {} & \frac{i\omega_0}{4\pi c}\int \frac{1}{R^2}\left[(\epsilon'-1)\frac{\mathbf{E}'-2\hat{\mathbf{n}}(\hat{\mathbf{n}}\cdot\mathbf{E}')}{\epsilon'}\right]_{\text{ret}} d^3x' \\ & - \frac{i\omega_0}{4\pi c}\int \frac{\hat{\mathbf{n}}}{R}\left[(\epsilon'-1)\nabla'_T\cdot\left(\frac{\mathbf{E}'}{\epsilon'}\right)\right]_{\text{ret}} d^3x'.\end{aligned} \tag{A.11}$$

Again, the first integral can be neglected thanks to the $1/R^2$ dependence of the integrand. In the second integral we replace ∇'_T with $\nabla' + (\hat{\mathbf{n}}/c)\,\partial/\partial t'$ [Eq. (A.3)], obtaining

$$\begin{aligned}\mathcal{I}_3 = {} & -\frac{i\omega_0}{4\pi c}\int \frac{\hat{\mathbf{n}}}{R}\left[\frac{\epsilon'-1}{\epsilon'}\left(\nabla'\cdot\mathbf{E}' - \frac{\mathbf{E}'\cdot\nabla'\epsilon'}{\epsilon'}\right)\right]_{\text{ret}} d^3x' \\ & + \frac{i\omega_0}{4\pi c^2}\int \frac{\hat{\mathbf{n}}}{R}\left[\frac{\epsilon'-1}{\epsilon'}\left(i\omega_0 - \frac{1}{\epsilon'}\frac{\partial(\epsilon'-1)}{\partial t'}\right)(\hat{\mathbf{n}}\cdot\mathbf{E}')\right]_{\text{ret}} d^3x'.\end{aligned} \tag{A.12}$$

Substituting Eqs. (A.6), (A.12), and (A.10) in Eq. (A.8), we find

$$\begin{aligned}\frac{i\omega_0}{4\pi c}\int \frac{\hat{\mathbf{n}}}{R}\left[\left(1-2\,\frac{\epsilon'-1}{\epsilon'}\right)\frac{\mathbf{E}'\cdot\nabla'\epsilon'}{\epsilon'}\right]_{\text{ret}} d^3x' \\ = \frac{i\omega_0}{4\pi c^2}\int \frac{\hat{\mathbf{n}}}{R}\left[\frac{\epsilon'-1}{\epsilon'}\left(i\omega_0 - 2\,\frac{\partial\ln(\epsilon'-1)}{\partial t'}\right)(\hat{\mathbf{n}}\cdot\mathbf{E}')\right]_{\text{ret}} d^3x',\end{aligned} \tag{A.13}$$

where use has been made of Eq. (A.2). The time derivative of $\ln(\epsilon' - 1)$ in the right-hand side of Eq. (A.13) can be ignored in comparison with ω_0; also, we can replace ϵ' with 1 in the denominator. Similarly, the quantity $(\epsilon' - 1)/\epsilon$ can be neglected in the left-hand side, which then becomes identical with the right-hand side of Eq. (A.6). Thus, we can combine Eqs. (A.6) and (A.13) and write

$$\mathcal{I}_2 = -\frac{\omega_0^2}{4\pi c^2} \int \frac{\hat{\mathbf{n}}}{R} [(\epsilon' - 1)(\hat{\mathbf{n}} \cdot \mathbf{E}')]_{\text{ret}} \, d^3x'. \tag{A.14}$$

Using Eqs. (A.7) and (A.14), with ϵ given by Eq. (2.11), Eq. (A.4) can now be written

$$\frac{1}{4\pi} \int \frac{1}{R} \left[\nabla' \left(\frac{\mathbf{E}' \cdot \nabla' \epsilon'}{\epsilon'} \right) \right]_{\text{ret}} d^3x' = \int \frac{\hat{\mathbf{n}}}{R} [r_e n_e' (\hat{\mathbf{n}} \cdot \mathbf{E}')]_{\text{ret}} \, d^3x'. \tag{A.15}$$

Finally, making use of the vector identity $\mathbf{E}' - \hat{\mathbf{n}}\,(\hat{\mathbf{n}} \cdot \mathbf{E}') = -\hat{\mathbf{n}} \times (\hat{\mathbf{n}} \times \mathbf{E}')$, we can rewrite Eq. (A.1) as

$$\mathbf{E}(\mathbf{x}, t) = \mathbf{E}_0(\mathbf{x}) e^{-i\omega_0 t} + r_e \int \left[n_e' \frac{\hat{\mathbf{n}} \times (\hat{\mathbf{n}} \times \mathbf{E}')}{R} \right]_{\text{ret}} d^3x'. \tag{A.16}$$

This concludes the derivation.

Appendix B

Evaluation of Diffraction Effects

We want to derive the diffraction ratio [Eq. (2.66)]

$$\mathcal{D}(x_\perp, z; a, z_\Sigma) \equiv \frac{|E_0(\mathbf{x}_\perp, z; a, z_\Sigma)|}{|E_0(\mathbf{x}_\perp, z; \infty)|} \tag{B.1}$$

at an arbitrary point beyond a screen S in which is a circular aperture Σ of radius a (see Fig. 2.5). We recall that when the condition $2z/(k_0^3 w_0^4) \ll 1$ is satisfied, Eqs. (2.63) and (2.65) are applicable.

The numerator in the right-hand side of Eq. (B.1) can be calculated from Eq. (2.65). Substituting for $\mathbf{E}_0$ from Eq. (2.63) with z replaced by z_Σ and adopting a scalar notation (justified by the scalar nature of the equations), we obtain

$$\begin{aligned} E_0(\mathbf{x}_\perp, z; a, z_\Sigma) = &\left(\frac{8\pi}{c}P\right)^{1/2}\left(\frac{2}{\pi}\right)^{1/2}\frac{\exp[ik_0(z+z_\Sigma)]}{i\pi\zeta w_0(1+\zeta_\Sigma^2)^{1/2}}\exp(-i\arctan\zeta_\Sigma) \\ &\times \exp\left(\frac{i}{\zeta}u^2\right)\int_0^{a/w_0} du'\,u'\exp\left(\frac{i}{\zeta}u'^2\right)\exp\left(-\frac{u'^2}{1+i\zeta_\Sigma}\right) \\ &\times \int_0^{2\pi}\exp\left(\frac{-2i}{\zeta}uu'\cos\phi\right)d\phi. \end{aligned} \tag{B.2}$$

Here, the longitudinal coordinates have been normalized to the Rayleigh length $z_R = k_0 w_0^2/2$, i.e., $\zeta \equiv z/z_R$ and $\zeta_\Sigma \equiv z_\Sigma/z_R$; the perpendicular coordinates have been normalized to the Gaussian half-width w_0, i.e., $\mathbf{u} \equiv \mathbf{x}_\perp/w_0$ and $\mathbf{u}' \equiv \mathbf{x}'_\perp/w_0$. The integral over the aperture was expressed in polar coordinates. The integration over ϕ gives the result $2\pi J_0(2uu'\zeta^{-1}\cos\phi)$.

The undiffracted field is given simply by Eq. (2.63) calculated at $z + z_\Sigma$:

$$\begin{aligned} E_0(\mathbf{x}_\perp, z; \infty) = &\left(\frac{8\pi}{c}P\right)^{1/2}\left(\frac{2}{\pi}\right)^{1/2}\frac{\exp[ik_0(z+z_\Sigma)]}{w_0\left[1+(\zeta+\zeta_\Sigma)^2\right]^{1/2}} \\ &\times \exp\left[-i\arctan(\zeta+\zeta_\Sigma)\right]\exp\left[-\frac{u^2}{1+i(\zeta+\zeta_\Sigma)}\right]. \end{aligned} \tag{B.3}$$

Using Eqs. (B.2) and (B.3) in Eq. (B.1) we obtain after some rearrangement

$$\mathcal{D}(x_\perp, z; a, z_\Sigma) = \left| \frac{1}{1+\zeta_\Sigma^2} \left(1 - i\,\frac{1+\zeta_\Sigma(\zeta+\zeta_\Sigma)}{\zeta}\right) \right.$$
$$\times \exp\left[\frac{u^2}{1+(\zeta+\zeta_\Sigma)^2}\left(1 + i\frac{1+\zeta_\Sigma(\zeta+\zeta_\Sigma)}{\zeta}\right)\right]$$
$$\times \int_0^{a^2/w_0^2} \exp\left[\frac{Y}{1+\zeta_\Sigma^2}\left(1 - i\frac{1+\zeta_\Sigma(\zeta+\zeta_\Sigma)}{\zeta}\right)\right]$$
$$\left. \times J_0\left(\frac{2u}{\zeta}\sqrt{Y}\right) dY \right|, \qquad (B.4)$$

where the integration variable is $Y \equiv u_\perp'^2$.

The quantity $\mathcal{D}$ is a measure of the perturbation introduced in the incident gaussian beam by diffraction from the aperture. If the integral over Y is extended to infinity, $\mathcal{D}$ becomes 1 for all values of $x_\perp$, z, and z_Σ, and the Gaussian function (B.3) is unaltered.

For finite values of a, the integral in Eq. (B.4) must be evaluated numerically. This evaluation was carried out in the following fashion: the parameters were assigned the values $\zeta = 0.003$, $\zeta_\Sigma = 0.05$, and $\alpha = a/w_\Sigma = 1$ (where $w_\Sigma = w_0(1+\zeta_\Sigma^2)^{1/2}$ is the half-width in the aperture plane), which are typical for our setup (described in Chapter 3); each of these three parameters was then varied independently over a range around the initial value, while the other two parameters were kept fixed, and for each case $\mathcal{D}$ was plotted as a function of $x_\perp/a$.

Figure B.1 shows a representative set of three curves in the α scan; Fig. B.1(b) in particular is the reference point for all three scans. The function is close to 1 for $x_\perp < a$ and drops to low values for $x_\perp > a$. This matches the intuitive expectation that the diffracted field profile should approximate the profile at the screen, which is Gaussian for $x_\perp < a$ and is zero for $x_\perp > a$. Also, $\mathcal{D}$ oscillates around 1 up to a certain radius and then falls off suddenly; the oscillation amplitude is larger in the center and at the edge of this region and smaller in between. It appears natural to characterize the "goodness" of the approximation by means of three quantities: the maximum deviation from 1 in the central region (the most important region for diagnostic purposes, since the power density is higher there), the maximum deviation at the edge, and the ratio of the cutoff radius to the aperture radius a. The first quantity is 20% at $a/w_\Sigma = 0.8$, drops to $\sim$ 10% at $a/w_\Sigma = 1$, and decreases more slowly at larger aperture radii. The edge deviation, by contrast, depends little on a and is $< 10\%$ over a wide range ($0.8 \leq a/w_\Sigma \leq 2$). The cutoff radius is also weakly dependent on a: it increases with a and is larger than $0.95 \times a$ for $a/w_\Sigma \geq 0.7$.

The z scan, three examples of which are shown in Fig. B.2, indicates that the edge deviation is affected little by changes in z, whereas the central deviation increases and the cutoff radius decreases as z is increased. To keep the central deviation below

10% and the cutoff radius above 95% of the aperture radius (for $a/w_\Sigma = 1$), z/z_R must be kept below 0.007. Experimentally, this is a parameter that is defined by the geometry of the plasma chamber. In our case, as will be seen in Chapter 3, z/z_R ranges from $\sim$ 0.003 to 0.007 over the length of the plasma column.

Finally, there is no noticeable change when the position of the waist is changed relative to the aperture plane, with z_Σ/z_R varying from 0 to 0.5 (Fig. B.3). In the conditions of our experiment, this variation corresponds to a displacement of $\sim$ 172 meters, far more than the optical path of our whole apparatus. This parameter is therefore irrelevant under these conditions.

In closing, it is worth mentioning that in real experimental situations every measurement is made over a finite region of space. In particular, with an imaging configuration such as that used in the present work, information is collected over a finite radial range, owing to the finite area of the detector elements. If that extent is comparable to or larger than the spatial period of the diffraction oscillations, averaging occurs and the effect of diffraction is consequently reduced. This is indeed the case in the setup described in Chapter 3: the typical averaging distance is $\sim 0.08 \times a$, whereas the oscillation period in the reference case of Fig. B.1(b) is $\sim 0.025 \times a$. We can thus consider the effects of diffraction negligible for our setup.

Appendix C

Derivation of the Scattering Signal in the Rytov Approximation

We wish to recast Eq. (2.48),

$$\psi_1(\mathbf{x},t) = -e^{-\psi_0(\mathbf{x},t)} r_e \int \frac{1}{R} \left[n_e' e^{\psi_0'} \right]_{\text{ret}} d^3x', \tag{C.1}$$

in a form that explicitly displays the density spectrum

$$\hat{n}_e(\mathbf{k}_\perp, \omega; z) = \iint e^{-i\mathbf{k}_\perp \cdot \mathbf{x}_\perp + i\omega t} n_e(\mathbf{x}_\perp, z, t) d^2x_\perp dt. \tag{C.2}$$

The unperturbed field e^{ψ_0} is assumed to be monochromatic, i.e., $e^{\psi_0(\mathbf{x},t)} = e^{-i\omega_0 t} E_0(\mathbf{x})$. Substituting for n_e from the inverse Fourier transform of Eq. (C.2) we can write

$$\begin{aligned} \psi_1(\mathbf{x},t) = -\frac{e^{i\omega_0 t}}{E_0(\mathbf{x},t)} \frac{r_e}{(2\pi)^3} \int d^2x_\perp' \int \frac{dz'}{R} \int d^2k_\perp e^{i\mathbf{k}_\perp \cdot \mathbf{x}_\perp'} \\ \times \int d\omega\, \hat{n}_e(\mathbf{k}_\perp, \omega; z') e^{-i\omega(t-R/c)} E_0(\mathbf{x}_\perp', z') e^{-i\omega_0(t-R/c)}, \end{aligned} \tag{C.3}$$

which can be rearranged to give

$$\begin{aligned} \psi_1(\mathbf{x},t) = -\frac{1}{E_0(\mathbf{x},t)} \frac{r_e}{(2\pi)^3} \int d\omega e^{-i\omega t} \int dz' \int d^2k_\perp\, \hat{n}_e(\mathbf{k}_\perp, \omega; z') \\ \times \int \frac{e^{i(\omega_0+\omega)R/c}}{R} e^{i\mathbf{k}_\perp \cdot \mathbf{x}_\perp'} E_0(\mathbf{x}_\perp', z') d^2x_\perp'. \end{aligned} \tag{C.4}$$

In the analysis that follows we shall always implicitly assume that the frequency spectrum of the density fluctuations satisfies the condition $\omega \ll \omega_0$. Accordingly, *multiplicative* terms of order ω/ω_0 will be neglected. However, *phase terms or exponents* proportional to ω may still be significant and cannot in general be ignored, as will become clear at the end of our discussion. The integral over $\mathbf{x}_\perp'$ in Eq. (C.4) can be simplified by adopting a parabolic, or Fresnel, approximation. To properly assess the necessary requirements, a somewhat circuitous route must be followed. The integral over $\mathbf{x}_\perp'$, which we shall call $\mathcal{I}$, has the form of a convolution integral. Since the two-dimensional Fourier transform of $\exp(ik_s R)/R$ is $2\pi i (k_s^2 - k_\perp^2)^{-1/2} \exp[iz(k_s^2 - k_\perp^2)^{1/2}]$, we can write the Fourier transform of $\mathcal{I}$ as

$$\hat{\mathcal{I}}(\mathbf{K}) = \frac{2\pi i}{(k_s^2 - K^2)^{1/2}} \exp\left[i(z-z')(k_s^2 - K^2)^{1/2} \right] A_0(\mathbf{K} - \mathbf{k}_\perp; z'), \tag{C.5}$$

where $k_s = (\omega_0 + \omega)/c$ and A_0 is the 2D spatial Fourier transform of E_0. The condition for the applicability of the Fresnel expansion, which was stated in the discussion following Eq. (2.57), is

$$\frac{|z - z'|K^4}{8k_0^3} \ll 1. \tag{C.6}$$

Here, $\mathbf{K}$ indicates the sum of the spectral components of the *unperturbed* field E_0 and of the density perturbation $\hat{n}_e$. If Eq. (C.6) holds, we can apply the approximation given by Eq. (2.57) to Eq. (C.5); in addition, since $k/k_0 \ll 1$ and $k_0 w_0 \gg 1$ [Eq. (2.64)], we can replace the denominator $(k_s^2 - K^2)^{1/2}$ with k_s. The result is

$$\hat{\mathcal{I}}(\mathbf{K}) = \frac{2\pi i}{k_s} \exp\left[i(z - z')\left(k_s + \frac{K^2}{2k_s}\right)\right] A_0(\mathbf{K} - \mathbf{k}_\perp; z'). \tag{C.7}$$

The inverse Fourier transform of Eq. (C.7) has again the form of a convolution product:

$$\begin{aligned}\mathcal{I} &= \frac{e^{i(\omega_0+\omega)(z-z')/c}}{z - z'} \int \exp\left[i\frac{\omega_0 + \omega}{c}\frac{|\mathbf{x}_\perp - \mathbf{x}'_\perp|^2}{2(z - z')} + i\mathbf{k}_\perp \cdot \mathbf{x}'_\perp\right] E_0(\mathbf{x}'_\perp, z')d^2x'_\perp \\ &= \frac{2\pi i c}{\omega_0 + \omega} \exp\left[i\mathbf{k}_\perp \cdot \mathbf{x}_\perp - i\frac{ck_\perp^2}{\omega_0 + \omega}\frac{z - z'}{2} + i\frac{\omega}{c}\frac{2\omega_0 + \omega}{\omega_0 + \omega}(z - z')\right] \\ &\times \left[\frac{k_0}{2\pi i}\frac{e^{ik_0(z_u - z')}}{(z_u - z')} \int \exp\left(i\frac{k_0}{2(z_u - z')}|\mathbf{x}_{u\perp} - \mathbf{x}'_\perp|^2\right) E_0(\mathbf{x}'_\perp, z')d^2x'_\perp\right],\end{aligned} \tag{C.8}$$

where we have introduced the *unperturbed coordinates*

$$z_u \equiv \frac{\omega_0 z + \omega z'}{\omega_0 + \omega} \tag{C.9}$$

and

$$\mathbf{x}_{u\perp} \equiv \mathbf{x}_\perp - (z_u - z')\frac{\mathbf{k}_\perp}{k_0}. \tag{C.10}$$

Recalling Eq. (2.59), which describes the evolution of the unperturbed field $\mathbf{E}_0$ in the paraxial approximation, we see that the expression collected in the square brackets at the end of Eq. (C.8) is simply equal to $E_0(\mathbf{x}_{u\perp}, z_u)$. We can now use Eq. (C.8) in Eq. (C.4) and obtain

$$\begin{aligned}\psi_1(\mathbf{x}, t) = -\frac{i}{(2\pi)^2}\frac{r_e}{k_0} \int d\omega e^{-i\omega t} \int dz' \exp\left[i\frac{\omega}{c}\frac{2\omega_0 + \omega}{\omega_0 + \omega}(z - z')\right] \\ \times \int d^2k_\perp \exp\left(i\mathbf{k}_\perp \cdot \mathbf{x}_\perp - i\frac{ck_\perp^2}{\omega_0 + \omega}\frac{z - z'}{2}\right) \\ \times \hat{n}_e(\mathbf{k}_\perp, \omega; z')\frac{E_0(\mathbf{x}_{u\perp}, z_u)}{E_0(\mathbf{x})},\end{aligned} \tag{C.11}$$

where the multiplier $c/(\omega_0+\omega)$ has been replaced with $1/k_0$.

We now specialize our considerations to the case of a Gaussian beam. We note the useful relations, which can be derived from Eq. (C.9),

$$\frac{z-z'}{\omega_0+\omega}=\frac{z-z_u}{\omega}=\frac{z_u-z'}{\omega_0}. \tag{C.12}$$

The ratio between the projected and incident fields in Eq. (C.11) can be written, by virtue of Eq. (2.63), as

$$\frac{E_0(\mathbf{x}_{u\perp},z_u)}{E_0(\mathbf{x})}=\frac{\gamma}{\gamma_u}\exp[ik_0(z_u-z)]\exp\left[-\left(\frac{1}{\gamma_u}-\frac{1}{\gamma}\right)\frac{x_\perp^2}{w_0^2}\right] \times\exp\left(\frac{\zeta_u-\zeta'}{\gamma_u}\mathbf{k}_\perp\cdot\mathbf{x}_\perp\right)\exp\left(-\frac{(\zeta_u-\zeta')^2}{\gamma_u}\frac{k_\perp^2w_0^2}{4}\right), \tag{C.13}$$

where the longitudinal coordinates have been normalized to the Rayleigh length $z_R=k_0w_0^2/2$: thus, $\zeta\equiv z/z_R$, $\zeta'\equiv z'/z_R$, and $\zeta_u\equiv z_u/z_R$. We have also introduced the collimation parameters[105] $\gamma\equiv 1+i\zeta$, $\gamma'\equiv 1+i\zeta'$, and $\gamma_u\equiv 1+i\zeta_u$. The origin of the z axis is taken to be at the beam waist.

Substituting for the field ratio from Eq. (C.13), Eq. (C.11) becomes

$$\psi_1(\mathbf{x},t)=-\frac{i}{(2\pi)^2}\frac{r_e}{k_0}\int e^{-i\omega t}d\omega\int dz'\frac{\gamma}{\gamma_u}\exp\left[i\frac{\omega}{c}(z-z')\right] \times\exp\left[-\left(\frac{1}{\gamma_u}-\frac{1}{\gamma}\right)\frac{x_\perp^2}{w_0^2}\right]\int d^2k_\perp\exp\left(i\frac{\gamma'}{\gamma_u}\mathbf{k}_\perp\cdot\mathbf{x}_\perp\right) \times\exp\left[-i\frac{\gamma'}{\gamma_u}\frac{k_\perp^2}{2k_0}(z_u-z')\right]\hat{n}_e(\mathbf{k}_\perp,\omega;z'). \tag{C.14}$$

For completeness we can also write the Rytov phase for the case in which the unperturbed field is a plane wave. This can easily be obtained from Eq. (C.14) in the limit $w_0\to\infty$, $\gamma=\gamma'=\gamma_u=1$, $\zeta w_0^2=2z/k_0$, $\zeta' w_0^2=2z'/k_0$, and $\zeta_u w_0^2=2z_u/k_0$. The result is

$$\psi_1(\mathbf{x},t)=-\frac{i}{(2\pi)^2}\frac{r_e}{k_0}\int d\omega e^{-i\omega t}\int dz' e^{i\frac{\omega}{c}(z-z')}\int d^2k_\perp e^{i\mathbf{k}_\perp\cdot\mathbf{x}_\perp} \times\exp\left[-i\frac{k_\perp^2}{2k_0}(z_u-z')\right]\hat{n}_e(\mathbf{k}_\perp,\omega;z'). \tag{C.15}$$

(a) Far-Field Detection

Let us know explore Eq. (C.14) in the specific case of extreme-far-field detection. This is accomplished experimentally by measuring the field in the front focal plane of

a focusing optic (see Fig. 2.7). The effect of a thin lens of focal length F and infinite aperture in the paraxial approximation is to introduce a spatially dependent phase shift[103]

$$\Delta\Phi_l(\mathbf{x}_\perp) = -\frac{k_0}{2F}x_\perp^2. \qquad (C.16)$$

To simplify calculations, we now revert to the Born scheme by assuming $|\psi_1| \ll 1$ and we study the Born field $e^{\psi_0}\psi_1$. We are now considering the region of free space beyond the end of the plasma column and we can exploit the fact that the Born field follows the laws of free-space propagation. This would not be true of the full Rytov field $\exp(\psi_0+\psi_1)$. We cannot simply use the propagation equation (2.59) because the scattered field is no longer monochromatic. However, in the presence of a spectrum of frequencies, $\omega_s = \omega_0 + \omega$, the linearity of the Helmholtz equation (2.52) permits us to obtain the correct time-dependent solution simply as a superposition of the individual frequency components given by Eq. (2.59), with k_0 replaced by ω_s/c. In view of the scalar nature of the problem, all equations will be written in scalar form.

We can now apply the free-space propagation integral [Eq. (2.59)] or its reciprocal wave-number equivalent [Eq. (2.58)] to each ω_s component and derive the field in the lens plane z_l as a function of the field in an arbitrary plane z_1 beyond the plasma. To calculate the field at the lens focus, we can then make use of the Fourier transforming properties of lenses. If we denote the frequency spectrum of the field directly in front of the lens as $E_l(\mathbf{x}_\perp;\omega_s)$, the field in the focal plane will be given by[103]

$$E_f(\mathbf{x}_\perp;\omega_s) = \frac{-i\omega_s}{2\pi Fc}\exp\left[i\frac{\omega_s}{c}\left(F+\frac{x_\perp^2}{2F}\right)\right] A_l\left(\frac{\omega_s}{c}\frac{\mathbf{x}_\perp}{F},\omega_s\right), \qquad (C.17)$$

where A_l is the two-dimensional (2D) spatial Fourier transform of E_l. Hence, the field distribution in the focal plane is proportional to the Fourier transform of the field in front of the lens. The proportionality factor contains a phase, which is a function of $\mathbf{x}_\perp$ (focal-plane coordinates) or, equivalently, of $\mathbf{k}_\perp$, through the relation

$$\mathbf{k}_\perp = \frac{\omega_s}{c}\frac{\mathbf{x}_\perp}{F}. \qquad (C.18)$$

This well-known result can be obtained in a simple fashion by applying the phase shift given by Eq. (C.16) to the field and then calculating the diffraction integral [Eq. (2.59)] for $z = F$.

Before we proceed to calculate the Born field, it is useful to derive an expression for the unperturbed field E_{0f} (the subscript f denotes that the field is calculated at the lens focus). The Gaussian field spectrum at the beam waist is given by Eq. (2.61); this can be used in Eq. (2.58) to find the field spectrum in the lens plane, A_l. Finally, Eq. (C.17), with $\omega_s = \omega_0$, yields the focal-plane field distribution. This rather simple calculation gives the result

$$E_{0f}(\mathbf{x}_\perp, z_l+F) = -i\left(\frac{8\pi}{c}P\right)^{1/2}\left(\frac{2}{\pi}\right)^{1/2}\frac{k_0 w_0}{2F}\exp\left(-\frac{k_0^2 w_0^2}{4F^2}x_\perp^2\right)$$

$$\times \exp\left[ik_0\left(z_l + F + \frac{x_\perp^2}{2F} - \frac{z_l x_\perp^2}{2F^2}\right)\right]. \qquad (C.19)$$

Each frequency component of the Born field in the plane of the lens is equal to the product of the corresponding component of the Rytov phase given by Eq. (C.14) and of the unperturbed field given by Eq. (2.63), both calculated at $z = z_l$. The 2D spatial Fourier transform of the Born field is then

$$\begin{aligned} A_{1l}(\mathbf{k}_\perp, \omega_s) = &-\frac{i}{(2\pi)^2}\frac{r_e}{k_0}\left(\frac{8\pi}{c}P\right)^{1/2}\left(\frac{2}{\pi}\right)^{1/2}\frac{e^{ik_0 z_l}}{w_0\gamma}\int dz'\frac{\gamma}{\gamma_u}\exp\left[i\frac{\omega}{c}(z_l - z')\right] \\ &\times \int d^2k'_\perp \exp\left[-i\frac{\gamma'}{\gamma_u}\frac{k'^2_\perp}{2k_0}(z_u - z')\right]\hat{n}_e(\mathbf{k}'_\perp, \omega; z') \\ &\times \int \exp\left(-\frac{x_\perp^2}{\gamma_u w_0^2}\right)\exp\left[i\left(\frac{\gamma'}{\gamma_u}\mathbf{k}'_\perp - \mathbf{k}_\perp\right)\cdot\mathbf{x}_\perp\right]d^2x_\perp. \qquad (C.20) \end{aligned}$$

The integral over $\mathbf{x}_\perp$ in the last line of Eq. (C.20) can be readily calculated: the result is $\pi w_0^2\gamma_u \exp\left[-\left|\mathbf{k}_\perp - (\gamma'/\gamma_u)\mathbf{k}'_\perp\right|^2 w_0^2\gamma_u/4\right]$. We can now use Eq. (C.20) in Eq. (C.17) to obtain the Born field E_{1f} in the focal plane; dividing E_{1f} by the unperturbed field [Eq. (C.19)] and Fourier transforming the result with respect to ω finally yields the Rytov phase ψ_{1f}. After some tedious but straightforward algebraic manipulations, we obtain the following result:

$$\begin{aligned} \psi_{1f}(\mathbf{x}_\perp, t) = &-\frac{ir_e}{(2\pi)^2 k_0}\int d\omega \exp\left\{-i\omega\left[t - \frac{z_l + F}{c} + \frac{x_\perp^2}{2cF^2}(z_l - F)\right]\right\} \\ &\times \exp\left[-\frac{x_\perp^2}{F^2}\frac{z_R\omega}{c}\left(1 + \frac{\omega}{2\omega_0}\right)\right]\int d^2k_\perp \exp\left(-\frac{k_\perp^2 w_0^2}{4}\right) \\ &\times \exp\left(\frac{\omega_s}{\omega_0}\frac{z_R}{F}\mathbf{k}_\perp\cdot\mathbf{x}_\perp\right)\int dz' \exp\left[-i\left(1 + \frac{\omega_s}{\omega_0}\frac{x_\perp^2}{2F^2}\right)\frac{\omega}{c}z'\right] \\ &\times \exp\left(i\frac{\omega_s}{\omega_0}\frac{z'}{F}\mathbf{k}_\perp\cdot\mathbf{x}_\perp\right)\exp\left(-i\frac{k_\perp^2}{2k_0}z'\right)\hat{n}_e(\mathbf{k}_\perp, \omega; z'), \qquad (C.21) \end{aligned}$$

where $\omega_s = \omega_0 + \omega$.

We note in passing that if one wants to expand the Rytov exponential to second order or beyond, one cannot simply use the various powers of the ψ_{1f} phase derived here. The field $E_0\psi_1^l$, for $l > 1$, does *not* satisfy the Helmholtz equation, and therefore it is not legitimate to use Eq. (C.20). Instead, one must first calculate the 2D Fourier transform of the field $E_0\psi_1^l$ in the near field, then insert it into the propagation equation (2.58), and finally evaluate the focal-plane distribution by means of Eq. (C.17). So the present derivation is only valid in the Born approximation.

Before we proceed to calculate $u_f(\mathbf{x}_\perp, t) = |E_{0f}|^2\psi_{1f}$, we recognize at this point that some terms in Eq. (C.21) can be neglected, upon multiplication by E_{0f}, under

one rather weak assumption. It is convenient to introduce here a fictitious ordering parameter $\tau \ll 1$; for the purposes of the following considerations, τ can be identified with $(\omega/\omega_0)^{1/2}$, and we shall ignore all exponents of order τ^l, with $l > 0$. Our assumption is that $k_\perp^2 w_0^2 \sim O(\tau^l)$, with $l \geq -1$, for the entire spectrum under exam: this is clearly a generous upper limit on $k_\perp$, but one that will allow us to ignore terms of order $k_\perp^2 w_0^2(\omega/\omega_0)$. We can now quantify also the Fresnel conditions given by Eq. (2.62) for the Gaussian beam and by Eq. (C.6) for the Rytov phase, by writing the three relations $2|z_l|/(k_0^3 w_0^4) \sim O(\tau^l)$, $2|z'|/(k_0^3 w_0^4) \sim O(\tau^l)$, and $|z_l - z'|k_\perp^4/8k_0^3 \sim O(\tau^l)$, with $l \geq 1$.

We observe now that in the complete Born field $E_{0f}\psi_{1f}$ the sum of the leading terms in the real exponents is $-(k_0^2 w_0^2/4F^2)|\mathbf{x}_\perp - F\mathbf{k}_\perp/k_0|^2$. We can therefore assume that at the observation point the inequality

$$|\mathbf{x}_\perp| \lesssim \frac{Fk_\perp}{k_0}\left(1 + \frac{2}{k_\perp w_0}\right) \tag{C.22}$$

holds. Thus, in our ordering hierarchy, $x_\perp^2 k_0^2 w_0^2/F^2 \sim O(\tau^m)$ with $m \geq -1$. On the basis of these arguments, the exponent $x_\perp^2 \omega z_R(1 + \omega/2\omega_0)/(cF^2) \simeq (\omega/\omega_0)x_\perp^2 \times k_0^2 w_0^2/2F^2 \sim O(\tau^m)$, with $m \geq 1$, can be neglected. Similarly, we can ignore the exponent $(\omega/\omega_0)(z_R/F)(\mathbf{k}_\perp \cdot \mathbf{x}_\perp) \lesssim (\omega/2\omega_0)(k_\perp^2 w_0^2)^{1/2}(x_\perp^2 k_0^2 w_0^2/F^2)^{1/2} \sim O(\tau^m)$, with $m \geq 1$.

Under these assumptions, Eqs. (C.19) and (C.21) can be combined to yield

$$\begin{aligned} u_f(\mathbf{x}_\perp, t) = -i\frac{E_{f,00}^2}{(2\pi)^2}\frac{r_e}{k_0}\exp\left(-\frac{k_0^2 w_0^2}{2F^2}x_\perp^2\right)\int d\omega e^{-i\omega t'}\int d^2k_\perp \exp\left(-\frac{k_\perp^2 w_0^2}{4}\right) \\ \times \exp\left(\frac{z_R}{F}\mathbf{k}_\perp \cdot \mathbf{x}_\perp\right)\int dz' \exp\left[-i\left(1 + \frac{\omega_s}{\omega_0}\frac{x_\perp^2}{2F^2}\right)\frac{\omega}{c}z'\right] \\ \times \exp\left(i\frac{\omega_s}{\omega_0}\frac{z'}{F}\mathbf{k}_\perp \cdot \mathbf{x}_\perp\right)\exp\left(-i\frac{k_\perp^2}{2k_0}z'\right)\hat{n}_e(\mathbf{k}_\perp, \omega; z'), \end{aligned} \tag{C.23}$$

where $E_{f,00} = 2(P/c)^{1/2}k_0 w_0/F$ is the Gaussian field amplitude at $\mathbf{x}_\perp = 0$, and we have introduced the retarded time $t' = t - (z_l + F)/c + (z_l - F)x_\perp^2/(2cF^2)$.

Since $\tilde{n}_e$ is a real quantity, the spectral function $\hat{n}_e(\mathbf{k}_\perp, \omega; z)$ must be Hermitian, i.e., $\hat{n}_e(\mathbf{k}_\perp, \omega; z) = \hat{n}_e^*(-\mathbf{k}_\perp, -\omega; z)$. Therefore, Eq. (C.23) can be rewritten

$$u_f(\mathbf{x}_\perp,t) = -i\frac{E_{f,00}^2}{(2\pi)^2}\frac{r_e}{k_0}\int_0^\infty d\omega \int d^2k_\perp \exp\left(-\frac{k_0^2 w_0^2}{2F^2}x_\perp^2 - \frac{k_\perp^2 w_0^2}{4}\right)$$
$$\times \int dz' |\hat{n}_e(\mathbf{k}_\perp,\omega;z')| \exp\left(-i\frac{\omega^2}{c\,\omega_0}\frac{x_\perp^2}{2F^2}z'\right)$$
$$\times \exp\left(i\frac{\omega}{\omega_0}\frac{z'}{F}\mathbf{k}_\perp\cdot\mathbf{x}_\perp\right)\exp\left(-i\frac{k_\perp^2}{2k_0}z'\right)$$
$$\times \sum_{\pm}\exp\left(\pm\frac{z_R}{F}\mathbf{k}_\perp\cdot\mathbf{x}_\perp\right)\exp\left\{\mp i\omega\left[t' + (1+x_\perp^2/2F^2)\frac{z'}{c}\right]\right.$$
$$\left.\pm i\beta(\mathbf{k}_\perp,\omega;z) \pm i\frac{z'}{F}\mathbf{k}_\perp\cdot\mathbf{x}_\perp\right\}, \qquad (C.24)$$

where $\beta(\mathbf{k}_\perp,\omega;z) = -(i/2)\ln(\hat{n}_e/\hat{n}_e^*)$ is the phase of the spectrum. This equation can be rearranged to display the sinusoidal time dependence explicitly:

$$u_f(\mathbf{x}_\perp,t) = \frac{E_{f,00}^2}{(2\pi)^2}\frac{r_e}{k_0}\int_0^\infty d\omega \int d^2k_\perp \exp\left(-\frac{k_0^2 w_0^2}{2F^2}x_\perp^2 - \frac{k_\perp^2 w_0^2}{4}\right)\int dz'$$
$$\times |\hat{n}_e(\mathbf{k}_\perp,\omega;z')|\left[\mathcal{I}_r\cos(\omega t' + \phi_r) + i\mathcal{I}_i\cos(\omega t' + \phi_i)\right], \qquad (C.25)$$

where $\mathcal{I}_r(\mathbf{k}_\perp,\omega;\mathbf{x}_\perp,z')$ and $\mathcal{I}_i(\mathbf{k}_\perp,\omega;\mathbf{x}_\perp,z')$ are real quantities defined by

$$\mathcal{I}_{\substack{r\\i}}(\mathbf{k}_\perp,\omega;\mathbf{x}_\perp,z') = \left[2\cosh\left(2\frac{z_R}{F}\mathbf{k}_\perp\cdot\mathbf{x}_\perp\right) \mp 2\cos\left(2\frac{\omega}{\omega_0}\frac{z'}{F}\mathbf{k}_\perp\cdot\mathbf{x}_\perp\right.\right.$$
$$\left.\left. - \frac{K^2}{k_0}z' - \frac{\omega^2}{c\omega_0}\frac{x_\perp^2}{F^2}z'\right)\right]^{1/2}, \qquad (C.26)$$

and the phases obey the relations

$$\phi_{\substack{r\\i}}(\mathbf{k}_\perp,\omega;\mathbf{x}_\perp,z') = \Phi \pm \arctan\left[\tanh\left(\frac{z_R}{F}\mathbf{k}_\perp\cdot\mathbf{x}_\perp\right)\right.$$
$$\left.\times \begin{matrix}\cot\\ \tan\end{matrix}\left(\frac{\omega}{\omega_0}\frac{z'}{F}\mathbf{k}_\perp\cdot\mathbf{x}_\perp - \frac{K^2}{2k_0}z' - \frac{\omega^2}{c\omega_0}\frac{x_\perp^2}{2F^2}z'\right)\right], \qquad (C.27)$$

where

$$\Phi = z'\left[\frac{\omega}{c}\left(1+\frac{x_\perp^2}{2F^2}\right) - \frac{\mathbf{k}_\perp\cdot\mathbf{x}_\perp}{F}\right] - \beta(\mathbf{k}_\perp,\omega;z'). \qquad (C.28)$$

Equation (C.24) can be simplified considerably by adding a further approximation. We assume that the Gaussian beam is at least weakly collimated throughout

the length of the plasma column; this is quantified by the following requirements: $(z'/z_R)w_0^2k_\perp^2 \sim O(\tau^{-1})$ and $z'/z_R \sim O(\tau^{-1})$ (it is understood here that the specified order indicates only a lower limit). Owing to the possibility of a τ^{-1} dependence, these conditions, along with the previously stated ones, impose rather weak constraints. Note now that the inequality in Eq. (C.22) implies also that $(z'/z_R)x_\perp^2k_0^2w_0^2/F^2 \sim O(\tau^{-1})$. We can now neglect the following phase terms: $\omega(1 \pm \omega/\omega_0)z'x_\perp^2/(cF^2) \simeq (\omega/2\omega_0)(z'/z_R)(x_\perp^2k_0^2w_0^2/F^2)$ $\sim O(\tau)$, and $(\omega/\omega_0)(z'/F)(\mathbf{k}_\perp \cdot \mathbf{x}_\perp) \lesssim (\omega/2\omega_0)(z'/z_R)(x_\perp^2k_0^2w_0^2/F^2)^{1/2} \times (k_\perp^2w_0^2)^{1/2} \sim O(\tau)$.

Equation (C.24) now becomes

$$
\begin{aligned}
u_{f\frac{r}{i}}(\mathbf{x}_\perp,t) = -\frac{E_{f,00}^2}{(2\pi)^2}\frac{r_e}{k_0}\int_0^\infty d\omega \int d^2k_\perp \exp\left(-\frac{k_\perp^2w_0^2}{8}\right) \\
\times \int dz' |\hat{n}_e(\mathbf{k}_\perp,\omega;z')| \Bigg\{ \exp\left[-\frac{k_0^2w_0^2}{2F^2}\left(\mathbf{x}_\perp - \frac{F}{2k_0}\mathbf{k}_\perp\right)^2\right] \\
\times \begin{matrix}\sin\\ \cos\end{matrix}\left[\omega t' - z'\left(\frac{\mathbf{k}_\perp\cdot\mathbf{x}_\perp}{F} - \frac{k_\perp^2}{2k_0} - \frac{\omega}{c}\right) - \beta\right] \\
\mp \exp\left[-\frac{k_0^2w_0^2}{2F^2}\left(\mathbf{x}_\perp + \frac{F}{2k_0}\mathbf{k}_\perp\right)^2\right] \\
\times \begin{matrix}\sin\\ \cos\end{matrix}\left[\omega t' - z'\left(\frac{\mathbf{k}_\perp\cdot\mathbf{x}_\perp}{F} + \frac{k_\perp^2}{2k_0} - \frac{\omega}{c}\right) - \beta\right]\Bigg\},
\end{aligned}
\tag{C.29}
$$

where u_{fr} and u_{fi} denote respectively the real and imaginary parts of u_f.

Under the same conditions, in the region defined by Eq. (C.22) we can derive the Rytov phase by simply dividing Eq. (C.29) by the square modulus of Eq. (C.19). The result is

$$
\begin{aligned}
\psi_{1f}(\mathbf{x}_\perp,t) = -\frac{ir_e}{(2\pi)^2k_0}\int_0^\infty d\omega \int d^2k_\perp \exp\left(-\frac{k_\perp^2w_0^2}{4}\right) \\
\times \sum_{\pm} |\hat{n}_e(\mathbf{k}_\perp,k_{z\pm},\omega)| \exp\left(\pm\frac{k_0w_0^2}{2F}\mathbf{k}_\perp\cdot\mathbf{x}_\perp\right)\exp\Bigg[\mp i\omega t'' \\
\pm iz_p\mathbf{k}_\perp\cdot\left(\frac{\mathbf{x}_\perp}{F} \mp \frac{\mathbf{k}_\perp}{2k_0}\right) \pm i\Gamma(\mathbf{k}_\perp,k_{z\pm},\omega)\Bigg],
\end{aligned}
\tag{C.30}
$$

where z_p is an average plasma coordinate, and we have introduced a new retarded time $t'' = t - (z_l + F - z_p)/c + (z_l - F)x_\perp^2/(2cF^2)$; also, we have introduced the full four-dimensional spectrum $\hat{n}(\mathbf{k}_\perp,\omega)$, with phase $\Gamma(\mathbf{k},\omega) = -(i/2)\ln(\hat{n}_e/\hat{n}_e^*)$, and $k_{z\pm} = \omega/c - \mathbf{k}_\perp\cdot(\mathbf{x}_\perp/F \mp \mathbf{k}_\perp/2k_0)$.

We now proceed to calculate the signal in the case of the modified heterodyne configuration obtained by orienting the LO beam along the vector $\mathbf{k}_0 + \mathbf{K}_{\mathrm{LO}}$. The

signal is given by [Eq. (2.76)]

$$U_{p,\mathrm{het}}(\mathbf{x}_\perp) = 2\rho\,\mathrm{Re}\Big[\big(\mathbf{E}_{0f}(\mathbf{x}_\perp)\cdot\mathbf{E}^*_{0f}(\mathbf{x}_\perp - F\mathbf{K}_{\mathrm{LO}}/k_0)\big) \times \psi_1(\mathbf{x}_\perp)e^{i(\langle\varphi_1(\mathbf{x}_\perp)\rangle+\Omega_{\mathrm{LO}}t-\varphi_{\mathrm{LO}})}\Big]. \tag{C.31}$$

Substituting from Eqs. (C.19) and (C.30) in Eq. (C.31), we find

$$\begin{aligned} U_{p,\mathrm{het}}(\mathbf{x}_\perp,t) = {} & \frac{2}{(2\pi)^2}\rho E^2_{f,00}\frac{r_e}{k_0}\int_0^\infty d\omega\int d^2k_\perp \\ & \times\Bigg\{|\hat{n}_e(\mathbf{k}_\perp,k_{z+},\omega)|\exp\left[-\frac{k_0^2w_0^2}{2F^2}\left(\mathbf{x}_\perp-\frac{F}{k_0}\frac{\mathbf{K}_{\mathrm{LO}}+\mathbf{k}_\perp}{2}\right)^2\right] \\ & \times\exp\left[-\frac{w_0^2}{8}(\mathbf{K}_{\mathrm{LO}}-\mathbf{k}_\perp)^2\right]\sin\big[(\Omega_{\mathrm{LO}}-\omega)t+\theta_{H+}\big] \\ & -|\hat{n}_e(\mathbf{k}_\perp,k_{z-},\omega)|\exp\left[-\frac{k_0^2w_0^2}{2F^2}\left(\mathbf{x}_\perp-\frac{F}{k_0}\frac{\mathbf{K}_{\mathrm{LO}}-\mathbf{k}_\perp}{2}\right)^2\right] \\ & \times\exp\left[-\frac{w_0^2}{8}(\mathbf{K}_{\mathrm{LO}}+\mathbf{k}_\perp)^2\right]\sin\big[(\Omega_{\mathrm{LO}}+\omega)t+\theta_{H-}\big]\Bigg\}, \end{aligned} \tag{C.32}$$

where

$$\begin{aligned} \theta_\pm(\mathbf{x}_\perp) = {} & \pm z_p\mathbf{k}_\perp\cdot\left(\frac{\mathbf{x}_\perp}{F}\mp\frac{\mathbf{k}_\perp}{2k_0}\right)\pm\Gamma(\mathbf{k}_\perp,k_{z\pm},\omega)\pm\frac{\omega}{c}(z-z_p) \\ & +\left(1-\frac{z_l}{F}\right)\mathbf{K}_{\mathrm{LO}}\cdot\left(\mathbf{x}_\perp-\frac{F}{2k_0}\mathbf{K}_{\mathrm{LO}}\right)+\langle\varphi_1\rangle-\varphi_{\mathrm{LO}}. \end{aligned} \tag{C.33}$$

(b) Near- and Intermediate-Field Detection

We now proceed to study the Rytov phase ψ_1 for near- and intermediate-field detection (Fig. 2.11). In the case of intermediate-field detection, the Born approximation will be implicitly assumed.

The starting point is again Eq. (C.14), which we rearrange as follows:

$$\begin{aligned} \psi_1(\mathbf{x},t) = {} & -\frac{i}{(2\pi)^2}\frac{r_e}{k_0}\int d\omega e^{-i\omega t}\int d^2k_\perp\int dz'\hat{n}_e(\mathbf{k}_\perp,\omega;z')\frac{\gamma}{\gamma_u}e^{i\frac{\omega}{c}(z-z')} \\ & \times\exp\left[-\left(\frac{1}{\gamma_u}-\frac{1}{\gamma}\right)\frac{x_\perp^2}{w_0^2}\right]\exp\left(i\frac{\gamma'}{\gamma_u}\mathbf{k}_\perp\cdot\mathbf{x}_\perp\right) \\ & \times\exp\left[-i\frac{k_\perp^2w_0^2}{4}\frac{\gamma'}{\gamma_u}(\zeta_u-\zeta')\right]. \end{aligned} \tag{C.34}$$

We can now make some relatively weak assumptions that will simplify this expression. We assume that the beam remains collimated between the interaction and the detection region, and retain only terms up to first order in $|\zeta - \zeta'|$ in the exponents. As in the far-field case, we introduce an ordering parameter $\tau \ll 1$ which we take now to be of the same order as $|\zeta - \zeta'|$. We also take ω/ω_0 to be of first order or smaller, so that terms of order $|\zeta - \zeta'|\omega/\omega_0$ can also be discarded. We then impose a weak upper limit on the value of $k_\perp$ by requiring that $k_\perp w_0(1+\zeta^2)^{1/2} \sim O(\tau^{-1})$. We also note that in the Born field $\mathbf{E}_0 e^{\psi_1}$ the sum of the real parts of the exponents is, to leading order, $-[1/w_0^2(1+\zeta^2)]\left|\mathbf{x}_\perp - \mathbf{k}_\perp w_0^2(\zeta-\zeta')/2\right|^2$; this results in the inequality

$$|\mathbf{x}_\perp| \lesssim w_0(1+\zeta^2)^{1/2} + \frac{k_\perp w_0^2|\zeta-\zeta'|}{2}. \qquad (C.35)$$

We can therefore state that $x_\perp^2/w_0^2(1+\zeta^2) \sim O(\tau^0)$. Finally, the Fresnel conditions [Eqs. (2.62) and (C.6)] can be expressed as $|\zeta|/(k_0 w_0)^2 \sim O(\tau^2)$, $|\zeta'|/(k_0 w_0)^2 \sim O(\tau^2)$, and $|z-z'|k_\perp^4/(8k_0^3) \sim O(\tau^2)$. It is important to note that the first two relations are the only conditions imposed on the distance from the waist to the interaction and detection region, i.e. on ζ and ζ'. Since $k_0 w_0$ is generally a very large number, those conditions may be compatible with rather large values of ζ and ζ', while their *difference* must be small.

Using Eq. (C.12) we now find that, to first order, $\gamma/\gamma_u \simeq 1 + i(\zeta-\zeta_u)/(1+\zeta^2)$ $\simeq 1 + i(\omega/\omega_0)(\zeta-\zeta')/(1+\zeta^2) \simeq 1$. Also, the term $(x_\perp^2/w_0^2)(1/\gamma_u - 1/\gamma) \simeq i(x_\perp^2/w_0^2)$ $(\zeta-\zeta_u)/(1+\zeta^2) \simeq i[x_\perp^2/w_0^2(1+\zeta^2)](\omega/\omega_0)(\zeta-\zeta')$ is of second order and can be neglected. With these approximations, and exploiting the Hermitian character of $\hat{n}_e$, Eq. (C.34) becomes, to first order in τ,

$$\begin{aligned}\psi_1(\mathbf{x},t) = -\frac{i}{(2\pi)^2}\frac{r_e}{k_0}\int_0^\infty d\omega \int d^2k_\perp \int dz' |\hat{n}_e(\mathbf{k}_\perp,\omega;z')| \sum_\pm e^{\mp i\omega t} e^{\pm i\frac{\omega}{c}(z-z')} \\ \times \exp\left\{\pm i\left[1 - \frac{\zeta}{1+\zeta^2}(\zeta-\zeta')\left(1 \mp \frac{\omega}{\omega_0}\right)\right]\mathbf{k}_\perp\cdot\mathbf{x}_\perp\right\}\exp\left[\pm i\beta(\mathbf{k}_\perp,\omega;z')\right] \\ \times \exp\left[\pm\frac{\zeta-\zeta'}{1+\zeta^2}\left(1\mp\frac{\omega}{\omega_0}\right)\mathbf{k}_\perp\cdot\mathbf{x}_\perp - \frac{(\zeta-\zeta')^2}{1+\zeta^2}\left(1\mp\frac{2\omega}{\omega_0}\right)\frac{w_0^2k_\perp^2}{4}\right] \\ \times \exp\left\{-i(\zeta-\zeta')\left[1 - \left(\frac{\zeta(\zeta-\zeta')}{1+\zeta^2} \pm \frac{\omega}{\omega_0}\right)\left(1\mp\frac{\omega}{\omega_0}\right)\right]\frac{w_0^2k_\perp^2}{4}\right\}. \qquad (C.36)\end{aligned}$$

We can rearrange Eq. (C.36) to display the sinusoidal time dependence explicitly, obtaining

$$\begin{aligned}\psi_1(\mathbf{x},t) = \frac{1}{(2\pi)^2}\frac{r_e}{k_0}\int_0^\infty d\omega\int d^2k_\perp\int dz' \exp\left[-\frac{(\zeta-\zeta')^2}{1+\zeta^2}\frac{w_0^2k_\perp^2}{4}\right]|\hat{n}_e(\mathbf{k}_\perp,\omega;z')| \\ \times\left[\mathcal{J}_r\cos(\omega t' + \theta_r) + i\mathcal{J}_i\cos(\omega t' + \theta_i)\right], \qquad (C.37)\end{aligned}$$

where the retarded time is redefined as $t' = t - z/c$, and $\mathcal{J}_r(\mathbf{k}_\perp, \omega; \mathbf{x}_\perp, z')$ and $\mathcal{J}_i(\mathbf{k}_\perp, \omega; \mathbf{x}_\perp, z')$ are real quantities defined by

$$\mathcal{J}_{\substack{r\\i}}(\mathbf{k}_\perp, \omega; \mathbf{x}_\perp, z') = \exp\left[-\frac{\omega}{\omega_0}\frac{\zeta - \zeta'}{1+\zeta^2}\mathbf{k}_\perp \cdot \mathbf{x}_\perp\right]\left\{2\cosh(2\Upsilon)\right.$$
$$\left. \mp 2\cos\left[(\zeta - \zeta')\left(1 + \frac{\omega^2}{\omega_0^2} - \frac{\zeta(\zeta - \zeta')}{1+\zeta^2}\right)\frac{w_0^2 k_\perp^2}{2}\right]\right\}^{1/2}, \quad (C.38)$$

where

$$\Upsilon = \frac{\zeta - \zeta'}{1+\zeta^2}\mathbf{k}_\perp \cdot \mathbf{x}_\perp + \frac{\omega}{\omega_0}\frac{(\zeta - \zeta')^2}{1+\zeta^2}\frac{w_0^2 k_\perp^2}{2}. \quad (C.39)$$

The phases satisfy the relations

$$\theta_{\substack{r\\i}}(\mathbf{k}_\perp, \omega; \mathbf{x}_\perp, z') = \Theta \mp \arctan\left\{\begin{matrix}\cot\\ \tan\end{matrix}\left[(\zeta - \zeta')\left(1 + \frac{\omega^2}{\omega_0^2} - \frac{\zeta(\zeta - \zeta')}{1+\zeta^2}\right)\frac{w_0^2 k_\perp^2}{4}\right.\right.$$
$$\left.\left. + \frac{\omega}{\omega_0}\left(1 - \frac{\zeta(\zeta - \zeta')}{1+\zeta^2}\right)\mathbf{k}_\perp \cdot \mathbf{x}_\perp\right] \times \tanh\Upsilon\right\}, \quad (C.40)$$

where

$$\Theta = \frac{\omega}{c}z' - \left[1 - \frac{\zeta(\zeta - \zeta')}{1+\zeta^2}\right]\mathbf{k}_\perp \cdot \mathbf{x}_\perp$$
$$+ \frac{\omega}{\omega_0}\left(\frac{\zeta(\zeta - \zeta')}{1+\zeta^2} - 1\right)(\zeta - \zeta')\frac{w_0^2 k_\perp^2}{4} - \beta(\mathbf{k}_\perp, \omega; z'). \quad (C.41)$$

These expressions cannot be simplified further unless some stronger conditions are imposed on the length of the interaction region and/or on the distance between the plasma and the detector plane. The weakest requirement we can choose is the *low-divergence condition*

$$L_z \ll \frac{k_0}{k_\perp}w_0. \quad (C.42)$$

This inequality, which must be satisfied by all spectral components in the plasma (or by those that will not be stopped by post-detection filtering), means that the scattered wave components, after propagating throughout the length of the plasma column, must not stray outside the width of the gaussian beam, measured at the waist (see Fig. 2.10). We can bring Eq. (C.42) within the ordering hierarchy by requiring that $L_z k_\perp/(k_0 w_0) \sim O(\tau)$. This can also be restated by saying that the quantity $|\zeta_1' - \zeta_2'|k_\perp w_0$ is of first order in τ for any two points ζ_1' and ζ_2' in the plasma. To simplify things further, we also eliminate all first-order terms and keep only terms of zeroth order or larger.

Under these conditions, z' can be replaced by a constant z_p in all the exponentials in Eq. (C.36) except $\exp(\mp i\omega z'/c)$ and $\exp(\pm i w_0^2 k_\perp^2 \zeta'/4)$. The integral over z' can

formally be eliminated by introducing the longitudinal wave number spectrum, and Eq. (C.36) becomes

$$\psi_1(\mathbf{x},t) = -\frac{i}{(2\pi)^2}\frac{r_e}{k_0}\int_0^\infty d\omega \int d^2k_\perp \sum_{\pm} |\hat{n}_e(\mathbf{k}_\perp, k_{z\pm}, \omega)| e^{\mp i\omega t''}$$
$$\times \exp\left[\pm i\left(1 - \frac{\zeta(\zeta-\zeta_p)}{1+\zeta^2}\right)\mathbf{k}_\perp\cdot\mathbf{x}_\perp\right] \exp\left[\pm\frac{\zeta-\zeta_p}{1+\zeta^2}\mathbf{k}_\perp\cdot\mathbf{x}_\perp\right]$$
$$\times \exp\left[\pm i\Gamma(\mathbf{k}_\perp, k_{z\pm}, \omega)\right] \exp\left[-\frac{(\zeta-\zeta_p)^2}{1+\zeta^2}\frac{w_0^2k_\perp^2}{4}\right]$$
$$\times \exp\left[-i(\zeta-\zeta_p)\left(1 - \frac{\zeta(\zeta-\zeta_p)}{1+\zeta^2} \mp \frac{\omega}{\omega_0}\right)\frac{w_0^2k_\perp^2}{4}\right], \qquad (C.43)$$

where $\zeta_p = z_p/z_R$. Here we have introduced a new retarded time relative to the propagation from the plasma to the detector, $t'' = t - (z - z_p)/c$, and $k_{z\pm} = \omega/c \mp k_\perp^2/(2k_0)$; also, $\Gamma(\mathbf{k},\omega) = -(i/2)\ln(\hat{n}_e/\hat{n}_e^*)$ is the phase of the $(\mathbf{k},\omega)$ spectrum. If, in particular, we impose $L_z k_\perp^2/k_0 \ll 1$ (Raman-Nath limit) and $\omega L_z/c \ll 1$, the Rytov phase will simply be proportional to the $k_z = 0$ component of the density, viz., its line integral.

The relatively simple dependence of the Rytov phase on the detector-plane coordinates $\mathbf{x}_\perp$ suggests that a spatial Fourier analysis of the signal could yield useful information on the $(\mathbf{k}_\perp,\omega)$ spectrum. This could be accomplished by using a two-dimensional detector array, for instance. We calculate now the temporal and spatial Fourier transform of the signal:

$$\hat{u}(\mathbf{K},\Omega;z) = \iint (\mathbf{E}_0\cdot\mathbf{E}_0^*)\,\psi_1(\mathbf{x}_\perp,z,t)e^{-i(\mathbf{K}\cdot\mathbf{x}_\perp - \Omega t)}d^2x_\perp dt. \qquad (C.44)$$

The Gaussian field intensity can be taken from Eq. (2.63), which gives simply

$$\mathbf{E}_0\cdot\mathbf{E}_0^* = \frac{E_{00}^2}{1+\zeta^2}\exp\left(-\frac{2x_\perp^2}{w_0^2(1+\zeta^2)}\right), \qquad (C.45)$$

where $E_{00} = 4(P/cw_0^2)^{1/2}$. Using Eqs. (C.45) and (C.43) in Eq. (C.44), expressing $\hat{n}_e(\mathbf{k},\omega)$ again as $\int \hat{n}_e(\mathbf{k}_\perp,\omega;z')\exp[-ik_z(z'-z_p)]dz'$, and carrying out the integrations over time, space, and frequency, we obtain

$$\hat{u}_{\substack{H\\a}}(\mathbf{K},\Omega;z) = \frac{E_{00}^2w_0^2}{4}\frac{r_e}{k_0}e^{-i\pi/4}\int d^2k_\perp \exp\left[-\frac{(\zeta-\zeta_p)^2}{1+\zeta^2}\frac{w_0^2k_\perp^2}{8}\right]$$
$$\times \exp\left[-\frac{w_0^2(1+\zeta^2)}{8}\left|\mathbf{K} - \mathbf{k}_\perp\left(1 - \frac{\zeta(\zeta-\zeta_p)}{1+\zeta^2}\right)\right|^2\right]$$
$$\times \exp\left[i\frac{\Omega}{\omega_0}(\zeta-\zeta_p)\frac{w_0^2k_\perp^2}{4}\right]\int dz'\,\hat{n}_e(\mathbf{k}_\perp,\Omega;z')e^{i\Omega(z-z')/c \pm i\pi/4}$$
$$\times \begin{matrix}\sin\\\cos\end{matrix}\left[(\zeta'-\zeta_p)\frac{w_0^2k_\perp^2}{4} - (\zeta-\zeta_p)\frac{w_0^2}{4}(\mathbf{k}_\perp\cdot\mathbf{K})\right], \qquad (C.46)$$

where $\hat{u}_H$ and $\hat{u}_a$ denote respectively the Hermitian and anti-Hermitian components of $\hat{u}$.

We now calculate the frequency spectrum of the Rytov phase, $\hat{\psi}_1(\mathbf{x};\Omega) = \int \psi_1(\mathbf{x},t)\exp(i\Omega t)\,dt$, in the limit in which both the plasma and the detector lie within the Gaussian near field,[105] defined by the condition $|\zeta - \zeta'|w_0 k_\perp \ll 1$ (see Fig. 2.10). More precisely, we assume $|\zeta - \zeta'|w_0 k_\perp \sim O(\tau)$. From Eq. (C.43), expressing $\hat{n}_e(\mathbf{k},\omega)$ again as $\int \hat{n}_e(\mathbf{k}_\perp,\omega;z')\exp[-ik_z(z'-z_p)]dz'$, we derive

$$\psi_1(\mathbf{x},t) = -\frac{i}{(2\pi)^2}\frac{r_e}{k_0}\int_{-\infty}^{\infty} d\omega e^{-i\omega t}\int d^2k_\perp e^{i\mathbf{k}_\perp\cdot\mathbf{x}_\perp} \times \int \hat{n}_e(\mathbf{k}_\perp,\omega;z')\exp\left[i\left(\frac{\omega}{c}-\frac{k_\perp^2}{2k_0}\right)(z-z')\right]dz'. \qquad (C.47)$$

A comparison with Eq. (C.15) shows that the Rytov phase in the Gaussian-near-field approximation is the same as in the plane-wave approximation. The frequency spectrum is

$$\hat{\psi}_{\substack{H\\a}}(\mathbf{x};\Omega) = -\frac{1}{2\pi}\frac{r_e}{k_0}\int d^2k_\perp e^{i\mathbf{k}_\perp\cdot\mathbf{x}_\perp}\int dz' e^{i\Omega(z-z')/c} \times \hat{n}_e(\mathbf{k}_\perp,\omega;z') \times \begin{matrix}\sin\\ i\cos\end{matrix}\left[\frac{k_\perp^2}{2k_0}(z-z')\right], \qquad (C.48)$$

where, again, the subscripts H and a denote the Hermitian and anti-Hermitian components, respectively.

To conclude, we calculate the crosscorrelation functions of the real and imaginary parts of the Rytov phase. By virtue of Eq. (C.47) we can write

$$\left\langle \begin{matrix}\xi_1\\ \tilde{\varphi}_1\end{matrix}(\mathbf{x}_\perp,z,t)\begin{matrix}\xi_1\\ \tilde{\varphi}_1\end{matrix}(\mathbf{x}'_\perp,z,t')\right\rangle = \frac{1}{(2\pi)^4}\frac{r_e^2}{k_0^2}\int d^2k_{\perp1}\int d^2k_{\perp2}\, e^{i(\mathbf{k}_{\perp1}\cdot\mathbf{x}_\perp - \mathbf{k}_{\perp2}\cdot\mathbf{x}'_\perp)} \times \int d\omega_1\int d\omega_2\int dz'_1\int dz'_2\, e^{i[(\omega_1-\omega_2)z/c]} \times \exp\left[i\omega_2\left(t'+\frac{z'_2}{c}\right) - i\omega_1\left(t+\frac{z'_1}{c}\right)\right] \times \begin{matrix}\sin\\ \cos\end{matrix}\left[\frac{k_{\perp1}^2}{2k_0}(z-z'_1)\right] \times \begin{matrix}\sin\\ \cos\end{matrix}\left[\frac{k_{\perp2}^2}{2k_0}(z-z'_2)\right] \times \langle \hat{n}_e(\mathbf{k}_{\perp1},\omega_1;z'_1)\,\hat{n}_e^*(\mathbf{k}_{\perp2},\omega_2;z'_2)\rangle\,. \qquad (C.49)$$

We can now substitute for the correlation function from Eq. (2.89) in Eq. (C.49); changing the longitudinal variables to $z' = (z'_1+z'_2)/2$ and $\Delta = z'_1 - z'_2$, and carrying out the integrations over $\mathbf{k}_{\perp2}$, ω_2, and Δ, we obtain

$$\left\langle \begin{matrix} \xi_1 \\ \tilde{\varphi}_1 \end{matrix}(\mathbf{x}_\perp, z, t) \begin{matrix} \xi_1 \\ \tilde{\varphi}_1 \end{matrix}(\mathbf{x}'_\perp, z, t') \right\rangle = \frac{r_e^2}{2(2\pi)^4 k_0^2} \int d\omega e^{-i\omega(t-t')} \int d^2k_\perp \, |G(\mathbf{k}_\perp, \omega)|^2$$
$$\times e^{i\mathbf{k}_\perp \cdot (\mathbf{x}_\perp - \mathbf{x}'_\perp)} \int dz' \sqrt{\pi} \mathcal{L}_z \left\langle \tilde{n}_e^2(z') \right\rangle e^{-D_c^2/4}$$
$$\times \left\{ e^{-Q_c^2/4} \cosh\left(\frac{Q_c D_c}{2}\right) \mp \cos\left[\frac{k_\perp^2}{k_0}(z - z')\right] \right\}, \tag{C.50}$$

where we have removed the subscript 1 from $\mathbf{k}_\perp$ and ω, and we have defined $Q_c = k_\perp^2 \mathcal{L}_z/(2k_0)$ and $D_c = \omega \mathcal{L}_z/c$.

Appendix D

Time-Dependent Geometrical Optics

In this appendix the equations of geometrical optics are derived from the wave equation (2.12). Our treatment is similar to the standard derivation (see e.g. Born and Wolf[92]), but it is expanded to include the time dependence of the eikonal and amplitude functions. The magnetic permeability μ is assumed to be unity.

(a) Geometrical Optics

The wave fields are written in the form

$$\mathbf{E}(\mathbf{x},t) = \mathbf{e}(\mathbf{x},t)e^{-i\omega_0 t}e^{ik_0\mathcal{S}(\mathbf{x},t)} \tag{D.1}$$

and

$$\mathbf{H}(\mathbf{x},t) = \mathbf{h}(\mathbf{x},t)e^{-i\omega_0 t}e^{ik_0\mathcal{S}(\mathbf{x},t)}, \tag{D.2}$$

where $\mathcal{S}(\mathbf{x},t)$ is a real function, called the *eikonal* or optical-path function. Substituting for $\mathbf{E}$ from Eq. (D.1) in the wave equation

$$(\nabla^2 - \frac{\epsilon}{c^2}\frac{\partial^2}{\partial t^2})\mathbf{E} + \nabla(\mathbf{E}\cdot\nabla\ln\epsilon) = 0 \tag{D.3}$$

and arranging terms by powers of k_0, we find

$$\begin{aligned} &k_0^2\left[\epsilon\left(1-\frac{\dot{\mathcal{S}}}{c}\right)^2 - (\nabla\mathcal{S})^2\right]\mathbf{e} \\ &+ ik_0\left[2(\nabla\mathcal{S}\cdot\nabla)\mathbf{e} + 2\frac{\epsilon}{c}\left(1-\frac{\dot{\mathcal{S}}}{c}\right)\dot{\mathbf{e}} + \mathbf{e}\nabla^2\mathcal{S} - \epsilon\ddot{\mathcal{S}}\mathbf{e}/c^2 + \nabla\mathcal{S}(\mathbf{e}\cdot\nabla\ln\epsilon)\right] \\ &+ \nabla^2\mathbf{e} - \epsilon\ddot{\mathbf{e}}/c^2 + \nabla(\mathbf{e}\cdot\nabla\ln\epsilon) = 0. \end{aligned} \tag{D.4}$$

The geometrical-optics approximation is the limit $\lambda \to 0$. At this stage the magnitude of ϵ is arbitrary. We now retain only the lowest-order terms in λ, that is, the k_0^2 terms. The result is the *eikonal equation*,

$$(\nabla\mathcal{S})^2 - \epsilon\,(1-\dot{\mathcal{S}}/c)^2 = 0. \tag{D.5}$$

The surfaces $\mathcal{S}$ = constant are called the *geometrical wave fronts.* To clarify the significance of the eikonal equation, we make use of Eq. (D.5) to define the unit vector

$$\mathbf{s} = \frac{\nabla\mathcal{S}}{\sqrt{\epsilon}(1-\dot{\mathcal{S}}/c)}. \tag{D.6}$$

The light rays of geometrical optics are everywhere tangent to $\mathbf{s}$, that is, the ray equation can be written as

$$\frac{d\mathbf{x}}{dl} = \mathbf{s}, \tag{D.7}$$

where l is the length of arc of the ray.

A connection between the intuitive concept of light rays and physical optics can be established by calculating the Poynting vector, averaged over a time period large with respect to $1/\omega_0$. By making use of Faraday's law to leading order in $1/k_0$,

$$\mathbf{h} = \frac{\nabla\mathcal{S} \times \mathbf{e}}{1 - \dot{\mathcal{S}}/c}, \tag{D.8}$$

one can write the time-averaged Poynting vector as

$$\langle \mathbf{S} \rangle = \frac{c}{8\pi}\mathrm{Re}(\mathbf{E} \times \mathbf{H}^*) = \frac{c}{8\pi}\mathrm{Re}(\mathbf{e} \times \mathbf{h}^*) = \frac{c}{8\pi}\frac{1}{1 - \dot{\mathcal{S}}/c}[(\mathbf{e}\cdot\mathbf{e}^*)\nabla\mathcal{S} - (\nabla\mathcal{S}\cdot\mathbf{e})\mathbf{e}^*]. \tag{D.9}$$

By virtue of Coulomb's law to leading order,

$$\nabla\mathcal{S} \cdot \mathbf{e} = 0, \tag{D.10}$$

Eq. (D.9) simplifies to

$$\langle \mathbf{S} \rangle = \frac{c}{8\pi}\frac{(\mathbf{e}\cdot\mathbf{e}^*)}{1 - \dot{\mathcal{S}}/c}\nabla\mathcal{S} = 2\frac{c}{\epsilon\,(1 - \dot{\mathcal{S}}/c)}w_e\nabla\mathcal{S}, \tag{D.11}$$

where $w_e = \epsilon\,(\mathbf{e}\cdot\mathbf{e}^*)/(16\pi)$ is the time-averaged electric energy density. Finally, Ampère's law, $\mathbf{e} = -(1/\epsilon)(1 - \dot{\mathcal{S}}/c)^{-1}(\nabla\mathcal{S} \times \mathbf{h})$, combined with Eq. (D.8), permits us to write

$$\begin{aligned} w_e &= \frac{\epsilon}{16\pi}(\mathbf{e}\cdot\mathbf{e}^*) = -\frac{1}{16\pi}\frac{1}{1 - \dot{\mathcal{S}}/c}(\nabla\mathcal{S} \times \mathbf{h})\cdot\mathbf{e}^* \\ &= \frac{1}{16\pi}\frac{1}{1 - \dot{\mathcal{S}}/c}\mathbf{h}\cdot(\nabla\mathcal{S} \times \mathbf{e}^*) = \frac{1}{16\pi}(\mathbf{h}\cdot\mathbf{h}^*) = w_m, \end{aligned} \tag{D.12}$$

where w_m is the average magnetic energy density. Thus, we can rewrite Eq. (D.11) as

$$\langle \mathbf{S} \rangle = \frac{c}{\epsilon(1 - \dot{\mathcal{S}}/c)}w\nabla\mathcal{S} = \frac{c}{\sqrt{\epsilon}}w\mathbf{s}, \tag{D.13}$$

where $w = w_e + w_m$ is the total energy density. Hence, the unit vector $\mathbf{s}$ defines the direction of energy flow, and Eq. (D.13) gives the velocity of energy propagation as $c/\sqrt{\epsilon}$.

The evolution of the amplitude $\mathbf{e}$ is described by the next order of approximation. By setting the ik_0 terms in Eq. (D.4) equal to zero, we obtain

$$\sqrt{\epsilon}\left(1-\frac{\dot{\mathcal{S}}}{c}\right)\left(\frac{\partial \mathbf{e}}{\partial l}+\frac{\sqrt{\epsilon}}{c}\frac{\partial \mathbf{e}}{\partial t}\right)+\frac{1}{2}\left(\nabla^2\mathcal{S}-\epsilon\frac{\ddot{\mathcal{S}}}{c^2}\right)\mathbf{e}+\frac{1}{2}(\mathbf{e}\cdot\nabla\ln\epsilon)\nabla\mathcal{S}=0, \quad (D.14)$$

where $\partial/\partial l=\epsilon^{-1/2}(1-\dot{\mathcal{S}}/c)^{-1}(\nabla\mathcal{S}\cdot\nabla)$ denotes the component of the gradient tangent to the ray. From this equation we can derive two separate equations for the wave intensity $e^2=\mathbf{e}\cdot\mathbf{e}^*$ and for the unit polarization vector $\mathbf{e}/e$. Taking the scalar product of Eq. (D.14) with $\mathbf{e}^*$, adding the complex conjugate, and making use of Eq. (D.10), we obtain the intensity equation

$$\sqrt{\epsilon}\left(1-\frac{\dot{\mathcal{S}}}{c}\right)\left(\frac{\partial e^2}{\partial l}+\frac{\sqrt{\epsilon}}{c}\frac{\partial e^2}{\partial t}\right)+\left(\nabla^2\mathcal{S}-\epsilon\frac{\ddot{\mathcal{S}}}{c^2}\right)e^2=0. \quad (D.15)$$

Dividing Eq. (D.14) by e, we find

$$\sqrt{\epsilon}\left(1-\frac{\dot{\mathcal{S}}}{c}\right)\left(\frac{\partial(\mathbf{e}/e)}{\partial l}+\frac{1}{2e^3}\frac{\partial e^2}{\partial l}\mathbf{e}+\frac{\sqrt{\epsilon}}{c}\frac{\partial(\mathbf{e}/e)}{\partial t}+\frac{\sqrt{\epsilon}}{c}\frac{1}{2e^3}\frac{\partial e^2}{\partial t}\mathbf{e}\right)$$
$$+\frac{1}{2}\frac{\mathbf{e}}{e}\left(\nabla^2\mathcal{S}-\epsilon\frac{\ddot{\mathcal{S}}}{c^2}\right)+\frac{1}{2e}(\mathbf{e}\cdot\nabla\ln\epsilon)\nabla\mathcal{S}=0, \quad (D.16)$$

which, upon subtraction of Eq. (D.15) multiplied by $\mathbf{e}/(2e^3)$, can be rewritten

$$\sqrt{\epsilon}(1-\frac{\dot{\mathcal{S}}}{c})\left(\frac{\partial(\mathbf{e}/e)}{\partial l}+\frac{\sqrt{\epsilon}}{c}\frac{\partial(\mathbf{e}/e)}{\partial t}\right)+\frac{1}{2}\left(\frac{\mathbf{e}}{e}\cdot\nabla\ln\epsilon\right)\nabla\mathcal{S}=0. \quad (D.17)$$

This equation shows explicitly that depolarization along a light ray is only due to the polarization charge density $\rho=-(1/4\pi)\mathbf{E}\cdot\nabla\ln\epsilon$ [cf. Eq. (2.14)].

Note that the intensity equation (D.15) can be integrated along a light ray, yielding

$$\ln e(l_2,t)=[\ln e(l_1,t')]_{\text{ret}}-\frac{1}{2}\int_{l_1}^{l_2}\left[(\nabla^2\mathcal{S}-\epsilon\ddot{\mathcal{S}}/c^2)(1-\dot{\mathcal{S}}/c)^{-1}\epsilon^{-1/2}\right]_{\text{ret}}dl, \quad (D.18)$$

where the subscript *ret* indicates that the quantity in brackets is to be evaluated at the retarded time $t'=t-(\sqrt{\epsilon}/c)\int_l^{l_2}dl'$.

(b) Geometrical Optics in the Rytov Approximation

To bring the geometrical-optics approximation into the framework of the Rytov scheme (see §2.4), we need to introduce now the Rytov ordering parameter, that is,

$|1-\epsilon| \ll 1$. We write the eikonal as $\mathcal{S}(\mathbf{x},t) = \mathcal{S}_0(\mathbf{x}) + \mathcal{S}_1(\mathbf{x},t)$ and the amplitude as $e(\mathbf{x},t) = e_0(\mathbf{x})\eta(\mathbf{x},t)$, and we assume that $\mathcal{S}_1/\mathcal{S}_0$ and $\ln\eta$ are of order $|1-\epsilon|$. The connection with the Rytov phases is established by writing

$$\psi_0 = \ln e_0 + ik_0(\mathcal{S}_0 - ct) \tag{D.19}$$

and

$$\psi_1 = \ln\eta + ik_0\mathcal{S}_1. \tag{D.20}$$

It is important to note that there are now two independent ordering parameters, $1/k_0$ and $|1-\epsilon|$, and that both expansion orders must be defined at each step of the analysis.

To zeroth order in $|1-\epsilon|$, we can write $\epsilon \to 1$, and since $\mathcal{S}_0$ does not depend on time, the eikonal equation (D.5) reduces to

$$|\nabla\mathcal{S}_0| = 1. \tag{D.21}$$

If we are considering an incident wave traveling along the z direction (see Fig. 2.1), we can simply take

$$\mathcal{S}_0(\mathbf{x}) = z. \tag{D.22}$$

Thus, the light rays are straight lines parallel to the z axis. Similarly, Eq. (D.15) reduces simply to

$$\frac{\partial e_0}{\partial z} = 0, \tag{D.23}$$

while Eq. (D.17) states that there are no depolarization effects.

These results show that the zeroth-order field distribution in the $(x$–$y)$ plane does not vary with z. If, in particular, the field distribution is Gaussian, we conclude that no apodization effects are observed at this level of approximation (i.e., zeroth-order Rytov and first-order geometrical optics). This can easily be understood by re-examining Eq. (2.63), which describes the evolution of the Gaussian field, and noticing that all apodization effects are of order $1/k_0^2$. In particular, we can now use Eq. (2.63) to quantify the defining conditions for this level of approximation as $1/(k_0 z_R) \ll 1$ and $z/z_R \ll 1$, i.e.

$$\frac{k_0^2 w_0^2}{2} \gg 1 \tag{D.24}$$

and

$$2z/(k_0 w_0^2) \ll 1. \tag{D.25}$$

These conditions can also be derived within the geometrical-optics formalism. The term that we have ignored at this level of approximation is the second-order term $\nabla^2 e_0$ in Eq. (D.4). For a Gaussian the peak value of this term is $-4e_0/w_0^2$. The requirement that this term be negligible with respect to the zeroth-order term $k_0^2 e_0$

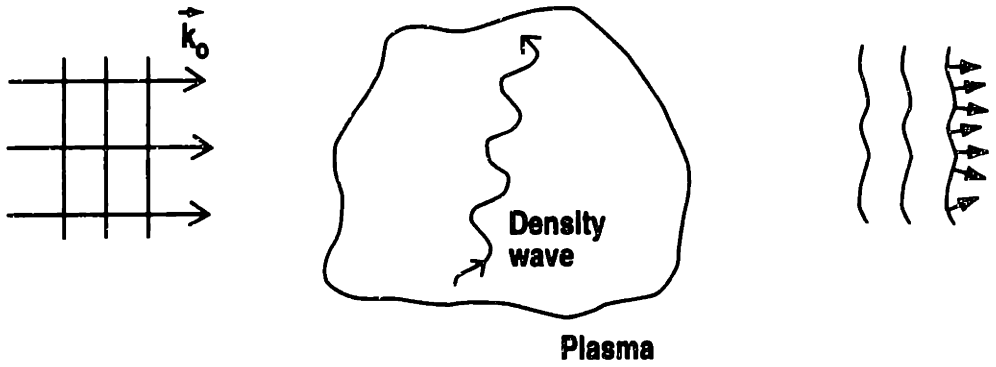

Fig. D.1 Modified wave fronts and light rays from density perturbation in the plasma.

yields Eq. (D.24), within a factor of two. The other condition is subtler, as we cannot simply require that $\nabla^2 e_0$ be smaller than the first-order term, since the latter is zero. One must solve instead the new equation

$$\nabla^2 e_0 + 2ik_0 \frac{\partial e_0}{\partial z} = 0. \qquad (D.26)$$

If the approximation $\nabla^2 e_0 \simeq -4e_0/w_0^2$ is used, the solution is $e_0(z) \simeq e_0(0) \times \exp(-iz/z_R)$. Imposing this exponent to be small implies Eq. (D.25).

We now examine the geometrical-optics equations to first order in $|1-\epsilon|$. Since we expect $\mathcal{S}_1/\mathcal{S}_0$ to be of order $|1-\epsilon|$, we ignore the quadratic terms $(\nabla \mathcal{S}_1)^2$ and $\dot{\mathcal{S}}_1^2$. Thus, the eikonal equation (D.5) can be written

$$2\nabla \mathcal{S}_0 \cdot \nabla \mathcal{S}_1 + 2\frac{\dot{\mathcal{S}}_1}{c} + (1-\epsilon) = 0, \qquad (D.27)$$

which, by virtue of Eq. (D.22), becomes

$$2\frac{\partial \mathcal{S}_1}{\partial z} + 2\frac{\dot{\mathcal{S}}_1}{c} + (1-\epsilon) = 0. \qquad (D.28)$$

The solution to this equation can be expressed in the form

$$\mathcal{S}_1(\mathbf{x}_\perp, z, t) = \frac{1}{2}\int_{z_0}^{z} \left[\epsilon\left(\mathbf{x}_\perp, z', t - \frac{z-z'}{c}\right) - 1\right] dz', \qquad (D.29)$$

where z_0 is an arbitrary point outside the plasma, where S_1 is zero. In the derivation of Eq. (D.5) it was seen that at this level of approximation in the geometrical-optics hierarchy the amplitude of the field is unaffected; thus, $\eta = 1$. By analogy with the arguments in §2.4, for the simple case of a uniform and constant ϵ, the condition for ignoring the quadratic terms $(\nabla \mathcal{S}_1)^2$ and $\dot{\mathcal{S}}_1^2$ in Eq. (D.27) is gleaned easily from Eq. (D.29): the requirement is $|1-\epsilon| \ll 4$, as we found in §2.4 [Eq. (2.51)].

The ray trajectory is given by Eqs. (D.7) and (D.6), which at this approximation level yield, by virtue of Eqs. (D.22) and (D.29),

$$\frac{d\mathbf{x}}{dl} \simeq \hat{\mathbf{z}} + \frac{1}{2}\int (\nabla_\perp \epsilon) dz', \qquad (D.30)$$

where $\hat{\mathbf{z}}$ is a unit vector in the z direction. The ray trajectories and wave fronts are depicted in Fig. D.1.

For the specific case of a plasma, operating the substitution [Eq. (2.11)]

$$\epsilon - 1 = -4\pi r_e \tilde{n}_e / k_0^2 \tag{D.31}$$

and using Eq. (D.20), Eq. (D.29) becomes

$$\psi_1(\mathbf{x}_\perp, z, t) = -i\lambda_0 r_e \int \tilde{n}_e[\mathbf{x}_\perp, z', t - (z - z')/c]\, dz', \tag{D.32}$$

which is identical with Eq. (2.84). This equation was derived within the Rytov formalism as the zeroth-order limit for $Q \to 0$ and $Q_d \to 0$, where $Q = L_z k_\perp^2 / 2k_0$, $Q_d = (z - z_p)k_\perp^2 / 2k_0$, and L_z is a characteristic length of the plasma column. It is therefore reasonable to expect those limits to be equivalent to the geometrical-optics limit.

To prove this equivalence, we must use the geometrical-optics equations to first order in $1/k_0$. Keeping only first-order terms in $|1 - \epsilon|$, the integral solution for the intensity, Eq. (D.18), becomes

$$\ln \eta(l_2, t) = [\ln \eta(l_1, t')]_{\text{ret}} - \frac{1}{2} \int_{l_1}^{l_2} [\nabla^2 \mathcal{S}_1 - \ddot{\mathcal{S}}_1 / c^2]_{\text{ret}}\, dl, \tag{D.33}$$

Since the term in square brackets is of first order, the zeroth-order trajectory can be used for the integration, i.e., $dl = dz$. We can now write

$$\ln \eta(z, t) = -\frac{1}{2} \int_{z_0}^{z} [\nabla^2 \mathcal{S}_1 - \ddot{\mathcal{S}}_1 / c^2]_{\text{ret}}\, dz', \tag{D.34}$$

where the integrand must be evaluated at the retarded time $t' = t - (z - z')/c$, and z_0 is a point encountered by the wave before entering the plasma. Using Eqs. (D.29) and (D.31), we can calculate

$$\nabla^2 \mathcal{S}_1 = -\frac{1}{(2\pi)^3} \frac{2\pi r_e}{k_0^2} \int d\omega e^{-i\omega t} \int d^2 k_\perp e^{i\mathbf{k}_\perp \cdot \mathbf{x}_\perp} \left[\frac{\partial \hat{n}_e}{\partial z} + i \frac{\omega}{c} \hat{n}_e - \left(\frac{\omega^2}{c^2} + k_\perp^2 \right) \int_{z_0}^{z} \hat{n}_e(\mathbf{k}_\perp, \omega; z') e^{i(z - z')\omega / c} dz' \right] \tag{D.35}$$

and

$$\ddot{\mathcal{S}}_1 / c^2 = \frac{1}{(2\pi)^3} \frac{2\pi r_e}{k_0^2} \int d\omega e^{-i\omega t} \frac{\omega^2}{c^2} \int d^2 k_\perp e^{i\mathbf{k}_\perp \cdot \mathbf{x}_\perp} \times \int_{z_0}^{z} \hat{n}_e(\mathbf{k}_\perp, \omega; z') e^{i(z - z')\omega / c} dz', \tag{D.36}$$

where $\hat{n}_e$ is the spectrum defined in Eq. (C.2). Substituting Eqs. (D.35) and (D.36) in Eq. (D.34) and integrating to a point z located outside the plasma, we find

$$\ln \eta(z,t) = -\frac{1}{(2\pi)^3}\frac{\pi r_e}{k_0^2}\int d\omega e^{-i\omega t}\int d^2k_\perp e^{i\mathbf{k}_\perp\cdot\mathbf{x}_\perp}\int_{z_0}^{z} dz'' e^{i\omega(z-z'')/c} \times\left[-i\frac{\omega}{c}\hat{n}_e(\mathbf{k}_\perp,\omega;z'')+k_\perp^2\int_{z_0}^{z''}\hat{n}_e(\mathbf{k}_\perp,\omega;z')e^{i(z''-z')\omega/c}dz'\right]. \tag{D.37}$$

Inverting the order of integration between z' and z'' in the last term, and carrying out the integration over z'', we find

$$\ln \eta(z,t) = -\frac{1}{(2\pi)^3}\lambda_0 r_e\int d\omega e^{-i\omega t}\int d^2k_\perp e^{i\mathbf{k}_\perp\cdot\mathbf{x}_\perp} \times\int_{z_0}^{z}\hat{n}_e(\mathbf{k}_\perp,\omega;z')e^{i\omega(z-z')/c}\left[-i\frac{\omega}{2\omega_0}+\frac{k_\perp^2}{2k_0}(z-z')\right]dz'. \tag{D.38}$$

In our treatment of the Rytov expansion we made the assumption that all multiplicative terms of order ω/ω_0 could be ignored. If we accordingly ignore the first term in the square brackets, we can then take the temporal Fourier transform of Eq. (D.38), and, by using Eq. (D.20), we finally obtain

$$\hat{\psi}_{1H}(\mathbf{x}_\perp;\Omega) = -\frac{1}{2\pi}\frac{r_e}{k_0}\int d^2k_\perp e^{i\mathbf{k}_\perp\cdot\mathbf{x}_\perp} \times\int_{z_0}^{z}\hat{n}_e(\mathbf{k}_\perp,\Omega;z')\,e^{i\Omega(z-z')/c}\,\frac{k_\perp^2}{2k_0}(z-z')dz', \tag{D.39}$$

where $\hat{\psi}_{1H}$ denotes the Hermitian component of ψ_1; this expression coincides with Eq. (2.81) to first order in Q and Q_d. The correspondence between the geometrical-optics approximation and the limit $Q \to 0$ and $Q_d \to 0$ is thus confirmed. It should be noted that the first-order geometrical-optics equations do not affect the eikonal; since the imaginary part of ψ_1 is proportional to $\mathcal{S}_1$ [Eq. (D.20)], the anti-Hermitian component of $\hat{\psi}_1$ is also unaffected. Correspondingly, the first correction to the anti-Hermitian component of Eq. (2.81) is of second order in Q and Q_d.

To first order in $|1-\epsilon|$, using Eq. (D.21), the depolarization equation (D.17) is reduced to

$$\left(\frac{\partial(e_z/e_0)}{\partial z}+\frac{1}{c}\frac{\partial(e_z/e_0)}{\partial t}\right) = -\frac{1}{2}\left(\frac{\mathbf{e}_0}{e_0}\cdot\nabla\ln\epsilon\right). \tag{D.40}$$

Taking a harmonic component $\propto e^{i\mathbf{k}_\perp\cdot\mathbf{x}_\perp}$ of the perturbed dielectric constant $(\epsilon-1)$ in the direction of $\mathbf{e}_0$, we can write approximately

$$\left|\frac{e_z}{e_0}\right| \sim k_\perp L_z|1-\epsilon|/2. \tag{D.41}$$

For this term to be negligible with respect to the Rytov phase ik_0S_1, given to zeroth order (in the geometrical-optics sense) by Eq. (D.29), we must require

$$k_\perp \ll k_0. \tag{D.42}$$

This result is identical with Eq. (2.27), which expressed the condition for neglecting depolarization effects in the wave equation.

To complete our proof of the validity of the geometrical-optics expansion, we must now examine the terms in the wave equation (D.4) that are of first order in $1/k_0$, and determine the conditions under which they can be neglected in comparison with the zeroth-order terms. (In the Rytov expansion, of course, all these terms must be calculated to first order in $|1-\epsilon|$.) These conditions, combined with the requirements that $Q \ll 1$ and $Q_d \ll 1$, which are necessary to ensure that $|\eta - 1| \ll 1$, will define the geometrical-optics limit in which Eq. (D.32) is valid.
The terms we need to examine are:

$$|ik_0e_0\nabla^2\mathcal{S}_1| \sim k_0k_\perp^2|1-\epsilon|L_ze_0/2;$$

$$|ik_0e_0\ddot{\mathcal{S}}_1/c^2| \sim k_0\omega^2|1-\epsilon|L_ze_0/2c^2;$$

and

$$|ik_0\nabla\mathcal{S}_0(\mathbf{e}_0\cdot\nabla\epsilon)| \sim k_0k_\perp|1-\epsilon|e_0.$$

The term involving $\dot{\mathbf{e}}$ is negligible if $\ln\eta \ll 1$, which has already been proven. The remaining term involving $\mathbf{e}_1$ is automatically negligible if all the others are. Each of these terms must be small in comparison with $|k_0^2(1-\epsilon)e_0|$. The resulting inequalities are, respectively,

$$k_\perp^2L_z/(2k_0) \ll 1, \tag{D.43}$$

$$k_\perp \ll k_0, \tag{D.44}$$

and

$$\omega \ll 2\omega_0. \tag{D.45}$$

Equation (D.43) reiterates the Raman-Nath condition $Q \ll 1$, Eq. (D.44) is the condition for small-angle scattering, and Eq. (D.45) is a relation that was assumed throughout the derivation of the Rytov equations. To these three relations we only need add $Q_d \ll 1$, i.e.,

$$k_\perp^2(z-z_p)/(2k_0) \ll 1, \tag{D.46}$$

where z_p is an average plasma coordinate. Equations (D.43)–(D.46) define the geometrical-optics approximation in the context of the Rytov expansion.

Appendix E

Calculation of an Integral

We want to calculate the integral

$$\mathcal{I} = \int_0^{2\pi} \frac{J_1\left[\sqrt{y^2+z^2-2yz\cos\phi}\right]}{\sqrt{y^2+z^2-2yz\cos\phi}} d\phi, \tag{E.1}$$

where ϕ denotes the angle between the two-dimensional vectors $\mathbf{y}$ and $\mathbf{z}$. We use the known relation[155]

$$\frac{J_1(|\mathbf{x}|)}{|\mathbf{x}|} = \frac{1}{2\pi} \int P_1(|\mathbf{K}|) e^{i\mathbf{K}\cdot\mathbf{x}} d^2K, \tag{E.2}$$

where

$$P_1(K) = \begin{cases} 1 & \text{if } |K| \leq 1 \\ 0 & \text{otherwise.} \end{cases} \tag{E.3}$$

Substituting Eq. (E.2) in (E.1) we find

$$\mathcal{I} = \frac{1}{2\pi} \int_0^{2\pi} d\phi \int P_1(|\mathbf{K}|) e^{i\mathbf{K}\cdot(\mathbf{y}-\mathbf{z})} d^2K. \tag{E.4}$$

We can now introduce polar coordinates in the $\mathbf{K}$ plane, using the $\mathbf{y}$ vector as reference, and write

$$\mathcal{I} = \frac{1}{2\pi} \int_0^{2\pi} d\phi \int_0^1 K dK \int_0^{2\pi} e^{iKy\cos\theta} e^{-iKz\cos(\phi-\theta)} d\theta, \tag{E.5}$$

where θ is the angle between $\mathbf{y}$ and $\mathbf{K}$. This equation can be rearranged with a change of variables $\phi' = \phi - \theta$ to give

$$\mathcal{I} = \frac{1}{2\pi} \int_0^1 K dK \int_0^{2\pi} e^{iKy\cos\theta} d\theta \int_0^{2\pi} e^{-iKz\cos\phi'} d\phi'. \tag{E.6}$$

The integrals over the angles are readily calculated, with the result

$$\mathcal{I} = 2\pi \int_0^1 J_0(Ky) J_0(Kz) K dK. \tag{E.7}$$

This integral is also known,[155] and the final result is

$$\mathcal{I} = \frac{2\pi}{y^2 - z^2} \left[y J_1(y) J_0(z) - z J_1(z) J_0(y) \right]. \tag{E.8}$$

Appendix F

Transfer Function of a Generalized Spatial Filter

Our starting point is Eq. (2.118) for the first-order power flux $\tilde{\mathcal{E}}$, rewritten here in the limit $a \to \infty$ and for a one-dimensional configuration at $y = 0$:

$$\tilde{\mathcal{E}}(Mx, 0, t) = \frac{c}{4\pi M^2} \operatorname{Im}\{[T \circ E][T \circ (E\tilde{\varphi})]^*\}, \tag{F.1}$$

where it is understood that the right-hand side must be calculated at the object and at the retarded time $t - t_d$, t_d being the propagation time from the plasma to the detector. We shall calculate the convolution products via inverse Fourier transforms of the products in wave-number space. The ingredients we need are Eq. (2.170),

$$\hat{T}(k) = \sqrt{\rho_-}\, e^{i\alpha} H(-k - k_c) + \sqrt{\rho_+}\, e^{i\beta} H(k - k_c) + \sqrt{\rho} P_{k_c}(k), \tag{F.2}$$

and the one-dimensional Fourier transform of Eq. (2.132),

$$\hat{E}_{p0}(k) = 4 \left(\frac{\pi P}{c}\right)^{1/2} \exp\left(-\frac{w_0^2 k^2}{4}\right), \tag{F.3}$$

where we have removed the subscript x from k for simplicity. Also, with a sinusoidal input $\tilde{\varphi} = \hat{\varphi}_K \cos(Kx + \vartheta_0)$, we can write

$$\hat{I}(k) \equiv \int E_{p0}(x)\tilde{\varphi}(x) e^{-ikx} dx = 2\left(\pi \frac{P}{c}\right)^{1/2} \tilde{\varphi}_K \left[\exp\left(-\frac{w_0^2 (k-K)^2}{4} + i\vartheta_0\right) + \exp\left(-\frac{w_0^2 (k+K)^2}{4} - i\vartheta_0\right)\right], \tag{F.4}$$

where we have made use of Eq. (2.132).

Now Eq. (F.1) can be rewritten

$$\tilde{\mathcal{E}}(Mx) = \frac{c}{4\pi M^2} \frac{1}{(2\pi)^2} \operatorname{Im}\left[\left(\int \hat{T}\hat{E}_{p0} e^{ikx} dk\right)\left(\int \hat{T}^* \hat{I}^* e^{-ikx} dk\right)\right]. \tag{F.5}$$

A straightforward, albeit tedious, calculation yields the result

$$\tilde{\mathcal{E}}(Mx, t) = \mathcal{T}_x(K)\hat{\varphi}_K(t - t_d) \cos\big(Kx + \vartheta_0 + \theta_x(K)\big), \tag{F.6}$$

where

$$\mathcal{T}_x(K) = u_0(x)\sqrt{A^2 + B^2}, \tag{F.7}$$

and

$$\theta_x(K) = -\arctan(B/A). \tag{F.8}$$

The functions A and B are defined by

$$A(K;x) = -(\sqrt{\rho\rho_-}\sin\alpha + \sqrt{\rho\rho_+}\sin\beta)\mathrm{Re}(\mathcal{W}_0 - \mathcal{W}_+) + \frac{\rho_- - \rho_+}{2}\mathrm{Im}(\mathcal{W}_0 - \mathcal{W}_+)$$
$$+ \left(\sqrt{\rho\rho_-}\cos\alpha - \sqrt{\rho\rho_+}\cos\beta - \frac{\rho_- - \rho_+}{2}\right)\mathrm{Im}(\mathcal{W}_0\mathcal{W}_+^*), \tag{F.9}$$

and

$$B(K;x) = (\sqrt{\rho\rho_-}\sin\alpha + \sqrt{\rho\rho_+}\sin\beta)\mathrm{Im}(\mathcal{W}_-) + \frac{\rho_- - \rho_+}{2}\mathrm{Re}(\mathcal{W}_-)$$
$$+ \left(\sqrt{\rho\rho_-}\cos\alpha - \sqrt{\rho\rho_+}\cos\beta - \frac{\rho_- - \rho_+}{2}\right)\mathrm{Re}(\mathcal{W}_0\mathcal{W}_-^*), \tag{F.10}$$

where

$$\mathcal{W}_0(x) = \mathrm{erf}\left(\frac{k_c w_0}{2} - i\frac{x}{w_0}\right), \tag{F.11}$$

$$\mathcal{W}_\pm(K;x) = \frac{W_1(K;x) \pm W_2(K;x)}{2}, \tag{F.12}$$

and

$$\mathcal{W}_{\frac{1}{2}}(K;x) = \mathrm{erf}\left[\frac{(k_c \pm K)w_0}{2} - i\frac{x}{w_0}\right]. \tag{F.13}$$

Also,

$$u_0(x) = \frac{2P}{\pi M^2 w_0^2} e^{-2x^2/w_0^2} \tag{F.14}$$

is the dc power flux in the absence of a spatial filter.

For signal-to-noise ratio considerations we shall need the dc power flux also. This can be obtained from Eq. (2.117), written in the form

$$\mathcal{E}_{\mathrm{dc}}(Mx) = \frac{c}{8\pi M^2}\frac{1}{(2\pi)^2}\left(\int \hat{T}\hat{E}_{p0}e^{ikx}dk\right)\left(\int \hat{T}^*\hat{E}_{p0}e^{-ikx}dk\right). \tag{F.15}$$

Substituting Eqs. (F.3) and (F.2) in Eq. (F.15), and using Eq. (F.14), we find

$$\mathcal{E}_{\mathrm{dc}}(Mx) = u_0(x)\left|\sqrt{\rho_-}\,e^{i\alpha}\frac{1-\mathcal{W}_0^*}{2} + \sqrt{\rho_+}\,e^{i\beta}\frac{1-\mathcal{W}_0}{2} + \sqrt{\rho}\,\mathrm{Re}(\mathcal{W}_0)\right|^2. \tag{F.16}$$

(a) Imaging Conditions

Let us now study Eq. (F.6) in the limit $K \gg k_c$ and $K \gg 1/w_0$. In this limit, $\mathcal{W}_1 \to 1$, $\mathcal{W}_2 \to -1$, $\mathcal{W}_+ \to 0$, and $\mathcal{W}_- \to 1$. Thus Eqs. (F.9) and (F.10) become, respectively,

$$A(\infty; x) = -(\sqrt{\rho\rho_-}\sin\alpha + \sqrt{\rho\rho_+}\sin\beta)\mathrm{Re}(\mathcal{W}_0) + \frac{\rho_- - \rho_+}{2}\mathrm{Im}(\mathcal{W}_0), \qquad (F.17)$$

and

$$B(\infty; x) = \frac{\rho_- - \rho_+}{2} + \left(\sqrt{\rho\rho_-}\cos\alpha - \sqrt{\rho\rho_+}\cos\beta - \frac{\rho_- - \rho_+}{2}\right)\mathrm{Re}(\mathcal{W}_0). \qquad (F.18)$$

It is clear from these expressions and Eq. (F.8) that the phase shift $\theta_x(K)$ is in general a function of x even in the limit $K \to \infty$. The dependence on x is folded into the function $\mathcal{W}_0$. For configurations that render $\theta_x(\infty)$ independent of x, it is shown in §2.13 that Eq. (F.6) can be replaced by the *approximate* expression [Eq. (2.179)]

$$\tilde{\mathcal{E}}(Mx, t) \simeq \mathcal{T}(K)W(x)\hat{\varphi}_K(t - t_d)\cos\big(Kx + \vartheta_0 + \theta(K)\big), \qquad (F.19)$$

which will be valid for large K. Here,

$$W(x) = \mathcal{T}_x(\infty)/\mathcal{T}_{x=0}(\infty), \qquad (F.20)$$

$$\mathcal{T}(K) = \mathcal{T}_{x=0}(K), \qquad (F.21)$$

and

$$\theta(K) = \theta_{x=0}(K). \qquad (F.22)$$

In order to obtain true phase imaging, one must not only require that θ_x be independent of x, but also that $\theta = 0$ or $\theta = \pi$; this condition, by virtue of Eq. (F.8), translates into $B(\infty; x) = 0$ for all values of x. Using Eq. (F.18), we can then write

$$\rho_- = \rho_+ \qquad (F.23)$$

and

$$\cos\alpha = \cos\beta, \qquad (F.24)$$

which further implies $\alpha = \beta$, since the solution $\alpha = -\beta$ leads to a null signal. These conditions define a generalized form of phase contrast, with arbitrary phase shift instead of $\pm\pi/2$. Using Eqs. (F.7) and (F.17), we find the transfer function at high K

$$\mathcal{T}_x(\infty) = -2u_0(x)\sqrt{\rho\rho_-}\,\mathrm{Re}\big(\mathcal{W}_0(x)\big)\sin\beta. \qquad (F.25)$$

The maximum signal, for a given ρ, is achieved for $\rho_- = \rho_+ = 1$ and $\alpha = \beta = \pm\pi/2$. Thus, we arrive at the following important results: the only filter in this class to produce a phase image is a generalized phase-contrast filter, and the phase-contrast

filter proper is the one the maximizes the signal. It is important to note that this conclusion holds for arbitrary values of $k_c w_0/2$. However, the arguments presented in §§2.11 and 2.12 show that an optimal reponse function is obtained for $k_c w_0/2 \simeq 1.5$.

For the phase-contrast case (choosing the solution $\alpha = \beta = -\pi/2$ for consistency with the configuration described in §2.11), we substitute Eq. (F.25) in Eq. (F.20) and find

$$W(x) = e^{-x^2/w_0^2} \frac{\mathrm{Re}(\mathcal{W}_0(x))}{\mathrm{erf}\, Q}, \tag{F.26}$$

where $Q = k_c w_0/2$. This expression coincides with Eq. (2.134) in the limit $a \to \infty$, as expected. Also, substitution of Eq. (F.7) in Eq. (F.21) yields

$$\mathcal{T}(K) = 2\sqrt{\rho}\, u_0(0)\left[\mathrm{erf}\, Q - \mathcal{W}_+(K;0)\right], \tag{F.27}$$

which is identical with Eq. (2.141). Finally, substituting Eq. (F.8) in Eq. (F.22) we obtain

$$\theta(K) = 0. \tag{F.28}$$

Thus the phase shift (at $x = 0$) is 0 for *arbitrary* K.

If we now return to the general case, but assume that $k_c w_0/2 \simeq 1.5$, we find that the function $\mathcal{W}_0$ differs from 1 by less than 6% throughout the region $|x/w_0| < 1$. In this case, $\theta_x(\infty)$ becomes approximately independent of x. Using Eqs. (F.7), (F.8), (F.17), and (F.18), and assuming $\mathcal{W}_0 = 1$, we can write

$$\mathcal{T}_x(\infty) = u_0(x)\sqrt{\rho}\left[\rho_- + \rho_+ - 2\sqrt{\rho_-\rho_+}\cos(\alpha+\beta)\right]^{1/2}, \tag{F.29}$$

and

$$\theta_x(\infty) = \arctan\left(\frac{\sqrt{\rho_-}\cos\alpha - \sqrt{\rho_+}\cos\beta}{\sqrt{\rho_-}\sin\alpha + \sqrt{\rho_+}\sin\beta}\right). \tag{F.30}$$

Also, Eq. (F.16) yields the simple result

$$\mathcal{E}_{\mathrm{dc}}(x) = \rho u_0(x), \tag{F.31}$$

signifying that approximately all the power flux, attenuated by the transmissivity ρ, is used in the LO component. The signal-to-noise ratio considerations of §2.12 thus apply. For a given ρ, both the signal [Eq. (F.29)] and the signal-to-noise ratio are maximized when $\rho_- = \rho_+ = 1$ and $\alpha = \pm\pi - \beta$. Whenever these conditions are satisfied, one obtains the same signal-to-noise ratio as in the phase-contrast case. From Eq. (F.30), the condition for phase imaging [$\theta(\infty) = 0$ or π] is now $\sqrt{\rho_-}\cos\alpha = \sqrt{\rho_+}\cos\beta$. Again, the phase-contrast configuration ($\rho_- = \rho_+ = 1$ and $\alpha = \beta = \pm\pi/2$) is the only one to achieve phase imaging while maximizing the signal-to-noise ratio.

For the subclass of filters defined by the relations $\rho_- = \rho$ and $\alpha = 0$ (which has the practical advantage of requiring only a two-zone filter, as discussed in §2.13), in

the $Q \simeq 1.5$ case, the phase-imaging condition $\theta_x(\infty) = 0$ becomes, thanks to Eq. (F.30),

$$\cos\beta = \sqrt{\rho/\rho_+}\,. \tag{F.32}$$

This condition can be satisfied only when $\rho \leq \rho_+$. From Eq. (F.29) we find $\mathcal{T}_x(\infty) = u_0(x)\sqrt{\rho}\sqrt{\rho_+ - \rho}$, which, for a given ρ, is maximized by $\rho_+ = 1$. The signal-to-noise ratio is a factor of $(1-\rho)/4$ lower than in the phase-contrast case. Under these conditions, using Eqs. (F.7), (F.9), and (F.10) in Eq. (F.21), with $\mathcal{W}_0 = 1$, we find

$$\mathcal{T}(K) = u_0(0)\sqrt{\rho}\sqrt{1-\rho}\,[1 - \mathcal{W}_+(K;0)]. \tag{F.33}$$

This function is plotted in Fig. 2.29(b).

This scheme requires an additional caveat when a small value of ρ is chosen to improve contrast. If $\sqrt{\rho}$ is of the same order as $|1-\operatorname{erf} Q|$, the approximations used to find the conditions for phase imaging are no longer applicable. One must use instead the full expression for the phase shift [Eq. (F.8)], which, combined with Eq. (F.22), yields

$$\theta(K) = \pm\arctan\left(\frac{\mathcal{W}_-(K;0)}{\operatorname{erf} Q - \mathcal{W}_+(K;0)}\sqrt{1-\rho}\,\frac{1-\operatorname{erf} Q}{2\sqrt{\rho}}\right), \tag{F.34}$$

which in the limit $K \to \infty$ becomes

$$\theta(\infty) = \pm\arctan\left(\frac{\sqrt{1-\rho}}{\operatorname{erf} Q}\,\frac{1-\operatorname{erf} Q}{2\sqrt{\rho}}\right). \tag{F.35}$$

Hence, the condition for phase imaging is $|1-\operatorname{erf} Q| \ll 2\sqrt{\rho}$. This condition is a subtle effect of the finite width of the beam and does not appear in a simplified plane-wave analysis. Its meaning can be elucidated by observing that the dc flux at the center of the beam is, by virtue of Eq. (F.16),

$$\mathcal{E}_{\mathrm{dc}}(0) = u_0(0)\left[\rho + \frac{1-\rho}{4}(1-\operatorname{erf} Q)^2\right]. \tag{F.36}$$

The small factor $(1-\operatorname{erf} Q)^2/4$ represents the fraction of dc power that falls on the positive k region of the spatial filter, which has a transmissivity of 1. The useful part of the dc power is the fraction that is transmitted by the central region of the filter. Although a majority of the dc power is concentrated in the central region, it is then reduced by the transmissivity ρ. The condition for phase imaging thus states that the LO power must be larger than the dc power lost in the wings of the spatial filter.

In practice, since $\operatorname{erf} Q$ decreases rapidly with increasing k_c, a careful choice of the k_c parameter will ensure that the phase-imaging condition is satisfied; conversely, however, the margin for error is rather limited. For example, if $\rho = 0.027$ (reflectivity of BaF_2), a value of $Q = 1.5$ results in $\theta = 32°$, whereas at $Q = 2$ the shift is reduced to $\theta = 5°$.

The function $\theta(K) = \theta_{x=0}(K)$ is plotted in Fig. 2.29(b) for the case $\rho = 0.17$. In this case the imaging condition is well satisfied even for $Q = 1.5$.

(b) Schlieren Techniques

We shall now proceed to explore some special cases in this class of spatial filters, which correspond to techniques found in the literature. The knife-edge schlieren configuration is obtained by setting $\rho_- = 0$, $\rho_+ = 1$, $\beta = 0$, and $k_c = 0$. Using the symmetry properties[97] $\mathrm{erf}(-z) = -\mathrm{erf}z$ and $\mathrm{erf}(z^*) = (\mathrm{erf}\, z)^*$, we find the relation $\mathcal{W}_1(K;x) = -\mathcal{W}_2^*(K;x)$, and we conclude that $\mathcal{W}_+$ is imaginary and $\mathcal{W}_-$ is real. Also, $\mathcal{W}_0(x) = \mathrm{erf}(-ix/w_0)$ is imaginary. Using Eqs. (F.7), (F.8), (F.17), and (F.18), we can write

$$\mathcal{T}_x(\infty) = -\frac{1}{2}u_0(x)\left[1 - \mathcal{W}_0^2(x)\right]^{1/2} \tag{F.37}$$

and

$$\theta_x(\infty) = \arctan\left(\frac{1}{i\mathcal{W}_0(x)}\right). \tag{F.38}$$

The function $\mathcal{W}_0$ is tabulated in mathematical table books[97] and can also be easily calculated by series expansion. The value of θ decreases monotonically from 90° at $x = 0$ to 31° at $x = w_0$. This large variation will inevitably cause substantial distortion of any sinusoidal input signal.

From Eq. (F.16) we calculate

$$\mathcal{E}_{\mathrm{dc}}(Mx) = \frac{1}{4}u_0(x)\left[1 - \mathcal{W}_0^2(x)\right]. \tag{F.39}$$

Limiting our analysis to the point $x = 0$, we see that the dc signal is multiplied by $1/(4\rho)$ with respect to the phase contrast case, whereas the ac signal is multiplied by $1/(4\sqrt{\rho})$. Repeating the steps of §2.12, in the regime in which shot noise dominates, we find $S/N \propto \tilde{\mathcal{E}}^2/\mathcal{E}_{\mathrm{dc}}$: thus the signal-to-noise ratio is reduced by a factor of 1/4; when intrinsic detector-preamplifier noise is dominant, or in a saturation-limited regime, the signal-to-noise ratio has the dependence $S/N \propto \tilde{\mathcal{E}}^2$, and the reduction factor becomes 1/16.

The approximate weighting and transfer functions can be calculated from Eqs. (F.20) and (F.21):

$$W(x) = e^{-2x^2/w_0^2}\left[1 - \mathcal{W}_0^2(x)\right]^{1/2}, \tag{F.40}$$

and

$$\mathcal{T}(K) = -\frac{u_0(0)}{2}\,\mathrm{erf}\left(\frac{Kw_0}{2}\right). \tag{F.41}$$

The phase shift θ is not a useful parameter in this case, owing to the spatial variation described above.

A modified schlieren configuration can be obtained by eliminating the negative orders while keeping the zeroth order. This is obtained by setting $\rho = 1$, $\rho_- = 0$, $\rho_+ = 1$, and $\beta = 0$. As before, we substitute Eqs. (F.17) and (F.18) in Eqs. (F.7) and (F.8), with the results

$$\mathcal{T}_x(\infty) = \frac{1}{2}u_0(x)\left|1 + \mathcal{W}_0(x)\right|, \tag{F.42}$$

and

$$\theta_x(\infty) = -\arctan\left(\frac{1 + \mathrm{Re}(\mathcal{W}_0)}{\mathrm{Im}(\mathcal{W}_0)}\right). \tag{F.43}$$

If we again assume $k_c w_0/2 \simeq 1.5$, we find $\mathcal{T}_x(\infty) \simeq u_0(x)$ and $\theta_x(\infty) \simeq \pi/2$. Thus, the responsivity of this technique is one-half that of phase contrast (at $\rho = 1$) and the phase shift is 90°. The dc component is obtained from Eq. (F.16):

$$\mathcal{E}_{\mathrm{dc}} = \frac{1}{4}u_0(x)\left|1 + \mathcal{W}_0\right|^2 \simeq u_0(x), \tag{F.44}$$

where the last equality holds for the standard condition $k_c w_0/2 \simeq 1.5$. Thus, once again, the dc power includes approximately all the power available. Since the signal is one-half as large as in the case of phase contrast, the signal-to-noise ratio is degraded by a factor of 1/4 in both the shot-noise and intrinsic-noise (or saturated) regimes.

From Eqs. (F.20), (F.21), and (F.22) we obtain (for arbitrary Q)

$$W(x) = e^{-2x^2/w_0^2}\,\frac{|1 + \mathcal{W}_0(x)|}{1 + \mathrm{erf}\,Q}, \tag{F.45}$$

$$\mathcal{T}(K) = \frac{u_0(0)}{2}(1 + \mathrm{erf}\,Q)\,\mathcal{W}_-(K;0), \tag{F.46}$$

and

$$\theta(K) = \frac{\pi}{2}. \tag{F.47}$$

Thus, the phase shift is independent of K for all values of Q. The functions $\mathcal{T}$ and θ are plotted in Fig. 2.29(c).

(c) Compensation of Plasma Transfer Function

Finally, we consider a situation in which the plasma geometry itself imposes upon the phase a transfer function characterized by a $-\pi/4$ phase shift for negative k, and by a $\pi/4$ phase shift for positive k.[147] The spatial filter is a modified version of a schlieren filter, with the negative and zeroth orders unshifted in phase, and the positive orders shifted by γ. We can treat the problem by combining the transfer functions of the plasma and of the filter in a function of the type described by Eq. (F.2), with parameters $\alpha = -\pi/4$ and $\beta = \gamma + \pi/4$. For simplicity, we assume from the start the condition $k_c w_0/2 \simeq 1.5$ which implies $\mathcal{W}_0 \simeq 1$. Also, as in the phase-contrast case, the dc power flux is simply $\rho u_0(x)$. Substituting Eqs. (F.17) and (F.18) in Eqs. (F.7) and (F.8), we find

$$\mathcal{T}_x(\infty) = u_0(x)\sqrt{\rho}\left(\rho_+ + \rho_- - 2\sqrt{\rho_+\rho_-}\cos\gamma\right)^{1/2} \tag{F.48}$$

and

$$\theta_x(\infty) = -\arctan\left(\frac{\sqrt{\rho_-} - \sqrt{2\rho_+}\cos(\gamma + \pi/4)}{\sqrt{\rho_-} - \sqrt{2\rho_+}\sin(\gamma + \pi/4)}\right). \tag{F.49}$$

It follows that the condition for phase imaging ($\theta = 0$ or π) is[147]

$$\gamma = \arccos\left(\frac{\rho_-}{2\rho_+}\right)^{1/2} - \frac{\pi}{4}. \tag{F.50}$$

With this constraint, Eq. (F.48) becomes

$$\mathcal{T}_x(\infty) = u_0(x)\sqrt{\frac{\rho}{2}}\left(\sqrt{\rho_-} \pm \sqrt{2\rho_+ - \rho_-}\right), \tag{F.51}$$

where the $\pm$ signs correspond to the two γ values that satisfy Eq. (F.50). To maximize the signal-to-noise ratio, one must maximize the absolute value of the quantity in parentheses in Eq. (F.51), subject to the constraints $\rho_- \leq 1$, $\rho_+ \leq 1$, and $2\rho_+ \geq \rho_-$. It is easily found that the maximum value is attained by the upper branch at $\rho_+ = \rho_- = 1$, corresponding to $\gamma = -\pi/2$. The responsivity is $\mathcal{T}_x(\infty) = \sqrt{2\rho}\,u_0(x)$; thus the signal-to-noise ratio is a factor of two lower than in the phase-contrast case. The reason for this is simply that the combined plasma-filter system under these conditions is equivalent to a generalized phase-contrast system with a phase shift of 45° instead of 90°.

The authors of Ref. 146 apparently failed to consider the upper-branch solution that leads to this optimal set of parameters. The filter that they considered for their numerical simulations is characterized by $\rho_- = \rho \ll \rho_+ = 1$ and $\gamma = \pi/4$ (lower branch). The transfer function is $\mathcal{T}_x(\infty) = -\sqrt{\rho}\,u_0(x)$; hence, the signal-to-noise ratio is reduced by a factor of four with respect to phase contrast. However, this type of filter has the considerable advantage, shared by all filters of the schlieren type, of

being divided in only two zones instead of three. This simplifies in general the task of aligning the optical system and reduces its sensitivity to mechanical vibrations.

This scheme requires an additional caveat, as in the case of the two-zone phase-imaging filter described by Eq. (F.32): if the quantity $\sqrt{\rho}$ is of the same order as $|1 - \operatorname{erf} Q|$, the approximations used to find the conditions for phase imaging are no longer applicable. One must use the full expressions [Eqs. (F.7) and (F.8)], which, upon substitution in Eqs. (F.21) and (F.22), yield

$$\mathcal{T}(K) = \sqrt{\rho}\, u_0(0) \Bigg\{ \rho \left(\operatorname{erf} Q - \mathcal{W}_+\right)^2 \left(1 - \sqrt{\rho/2}\right)^2 + \frac{\mathcal{W}_-^2}{\rho} \left[\frac{1-\rho}{2} - \frac{1 + \rho(\sqrt{2}-1)}{2} \operatorname{erf} Q \right]^2 \Bigg\}_{x=0}^{1/2}, \tag{F.52}$$

and

$$\theta(K) = -\arctan \left[\mathcal{W}_- \left(\frac{1 - \operatorname{erf} Q}{2\sqrt{\rho}} \frac{1-\rho}{(1 - \sqrt{\rho/2})(\operatorname{erf} Q - \mathcal{W}_+)} + \frac{1}{1 - \sqrt{2/\rho}} \frac{\operatorname{erf} Q}{\operatorname{erf} Q - \mathcal{W}_+} \right) \right]_{x=0}. \tag{F.53}$$

In the limit $K \to \infty$, the phase-imaging condition requires that $|1 - \operatorname{erf} Q| \ll 2\sqrt{\rho}$. The implications of this condition were discussed in the paragraph following Eq. (F.34). The functions $\mathcal{T}$ and θ are shown in Fig. 2.29(d).

Appendix G

Density Correlation Function in a Gaussian-Spectrum Model

We want to calculate the correlation function expressed by Eq. (4.22), making use of Eq. (4.23) for the spectral function, of Eq. (4.24) for the dispersion relation, of either Eq. (4.25) or Eq. (4.26) for the frequency form factor, and of Eq. (4.19) to express the wave vectors in flux coordinates. The integral over ω is calculated easily by noting that the inverse Fourier transform of $\hat{F}_1(\omega')$ is

$$F_1(\tau) = \exp\left(-\frac{\tau^2}{\tau_d^2}\right), \tag{G.1}$$

and that of $\hat{F}_2(\omega')$ is

$$F_2(\tau) = \exp\left(-\frac{|\tau|}{\tau_d}\right). \tag{G.2}$$

The remaining integral over k_R and k_z is proportional to a two-dimensional inverse Fourier transform of a generalized two-dimensional Gaussian function, which takes the following general form:

$$\mathcal{I} = \frac{1}{(2\pi)^2}\int dk_R \int dk_z \exp\left(-A^2k_R^2 - B^2k_z^2 - C^2 + Dk_R + Ek_z + Fk_Rk_z\right) \times \exp(i\xi_R k_R + i\xi_z k_z)dk_R dk_z. \tag{G.3}$$

One finds by direct integration that this integral converges if and only if

$$\mathcal{D} = 4A^2B^2 - F^2 > 0, \tag{G.4}$$

yielding the result

$$\mathcal{I} = \frac{1}{2\pi\sqrt{\mathcal{D}}}\exp\left(\frac{-4A^2B^2C^2 + C^2F^2 + EDF + B^2D^2 + A^2E^2}{\mathcal{D}}\right) \times \exp\left(\frac{-A^2\xi_z^2 - B^2\xi_R^2 - F\xi_z\xi_R}{\mathcal{D}}\right) \times \exp\left(i\,\frac{2DB^2\xi_R + 2EA^2\xi_z + EF\xi_R + DF\xi_z}{\mathcal{D}}\right). \tag{G.5}$$

In our case, the discriminant is equal to

$$\mathcal{D} = \frac{\mathcal{L}_\rho^2\mathcal{L}_\theta^2}{32}\left[1 + \cos^2(\vartheta - \vartheta')\right] + \frac{\mathcal{L}_\rho^4 + \mathcal{L}_\theta^4}{64}\sin^2(\vartheta - \vartheta'), \tag{G.6}$$

which always satisfies the convergence condition expressed by Eq. (G.4). Here, ϑ and ϑ' are the poloidal angles at the positions $\mathbf{x}$ and $\mathbf{x}'$, respectively (see Fig. 4.4).

We can now write the general result as follows:

$$\begin{aligned} C_{12}(\mathbf{x},t;\mathbf{x}',t') &\equiv \langle \tilde{n}(\mathbf{x},t)\,\tilde{n}(\mathbf{x}',t')\rangle \\ &= \langle \tilde{n}^2(\mathbf{x}_{\mathrm{av}},t_{\mathrm{av}})\rangle \,\frac{\mathcal{L}_\rho \mathcal{L}_\theta}{8\sqrt{\mathcal{D}}}\,F(t-t') \\ &\quad \times \exp\!\left[-i(\omega_0 - \mathbf{k}_0\cdot\mathbf{v}_g)(t-t')\right]\mathcal{E}_1\mathcal{E}_2\mathcal{E}_3 + \text{c.c.}, \end{aligned} \tag{G.7}$$

where $\mathbf{x}_{\mathrm{av}} = (\mathbf{x}+\mathbf{x}')/2$, $t_{\mathrm{av}} = (t+t')/2$, $\mathcal{D}$ is given by Eq. (G.6), and F takes one of the two forms given by Eqs. (G.1) and (G.2). Also,

$$\begin{aligned} \mathcal{E}_1 = \exp\Bigg(-\frac{\mathcal{L}_\rho^2\mathcal{L}_\theta^2}{32\,\mathcal{D}} \Big\{ &(k_{0,\rho}^2\mathcal{L}_\rho^2 + k_{0,\theta}^2\mathcal{L}_\theta^2)\left[1-\cos(\vartheta-\vartheta')\right]^2 \\ &+ (k_{0,\rho}^2\mathcal{L}_\theta^2 + k_{0,\theta}^2\mathcal{L}_\rho^2)\sin^2(\vartheta-\vartheta') \Big\} \Bigg), \end{aligned} \tag{G.8}$$

$$\begin{aligned} \mathcal{E}_2 = \exp\Bigg(-\frac{1}{32\,\mathcal{D}} \Big\{ &u_R^2\left[\mathcal{L}_\rho^2(\sin^2\vartheta + \sin^2\vartheta') + \mathcal{L}_\theta^2(\cos^2\vartheta + \cos^2\vartheta')\right] \\ &+ u_z^2\left[\mathcal{L}_\rho^2(\cos^2\vartheta + \cos^2\vartheta') + \mathcal{L}_\theta^2(\sin^2\vartheta + \sin^2\vartheta')\right] \\ &+ 2u_z u_R(\mathcal{L}_\theta^2 - \mathcal{L}_\rho^2)\sin(\vartheta+\vartheta') \Big\} \Bigg), \end{aligned} \tag{G.9}$$

and

$$\mathcal{E}_3 = \exp(i\mathbf{q}\cdot\mathbf{u}), \tag{G.10}$$

where

$$\mathbf{u} = \mathbf{x} - \mathbf{x}' - (t-t')\mathbf{v}_T, \tag{G.11}$$

$$\begin{aligned} q_R = \frac{1}{64\,\mathcal{D}} \Big\{ &\left[k_{0,\rho}\mathcal{L}_\rho^4(\sin\vartheta - \sin\vartheta') + k_{0,\theta}\mathcal{L}_\theta^4(\cos\vartheta - \cos\vartheta')\right]\sin(\vartheta - \vartheta') \\ &+ \mathcal{L}_\rho^2\mathcal{L}_\theta^2\left[k_{0,\rho}(\cos\vartheta + \cos\vartheta') - k_{0,\theta}(\sin\vartheta + \sin\vartheta')\right]\left[1+\cos(\vartheta-\vartheta')\right] \Big\}, \end{aligned} \tag{G.12}$$

$$\begin{aligned} q_z = \frac{1}{64\,\mathcal{D}} \Big\{ &\left[-k_{0,\rho}\mathcal{L}_\rho^4(\cos\vartheta - \cos\vartheta')\right]\sin(\vartheta - \vartheta') + k_{0,\theta}\mathcal{L}_\theta^4(\sin\vartheta - \sin\vartheta') \\ &+ \mathcal{L}_\rho^2\mathcal{L}_\theta^2\left[k_{0,\rho}(\sin\vartheta + \sin\vartheta') + k_{0,\theta}(\cos\vartheta + \cos\vartheta')\right]\left[1+\cos(\vartheta-\vartheta')\right] \Big\}, \end{aligned} \tag{G.13}$$

$$\mathbf{v}_T = \mathbf{v}_g + \mathbf{v}_{E,\mathrm{av}}, \tag{G.14}$$

and

$$\mathbf{v}_{E,\mathrm{av}} = \frac{\mathbf{v}_E(\mathbf{x}) + \mathbf{v}_E(\mathbf{x}')}{2}. \tag{G.15}$$

In the special case $\vartheta = \vartheta'$, we find $\mathcal{D} = \mathcal{L}_\rho^2\mathcal{L}_\theta^2/16$, $\mathcal{E}_1 = 1$, $\mathcal{E}_2 = \exp\bigl[-(u_\rho^2/\mathcal{L}_\rho^2 + u_\theta^2/\mathcal{L}_\theta^2)\bigr]$, and $\mathcal{E}_3 = \exp(i\mathbf{k}_0 \cdot \mathbf{u})$ [where we have made use of the coordinate transformation given by Eq. (4.19)]. Hence, Eq. (G.7) reduces to

$$C_{12}(\mathbf{x}, t; \mathbf{x}', t') = \bigl\langle \tilde{n}^2(\mathbf{x}_{\mathrm{av}}, t_{\mathrm{av}}) \bigr\rangle \, F(t - t') \exp\left[-\left(\frac{u_\rho^2}{\mathcal{L}_\rho^2} + \frac{u_\theta^2}{\mathcal{L}_\theta^2} \right) \right]$$
$$\times \cos\Bigl[\mathbf{k}_0 \cdot (\mathbf{x} - \mathbf{x}') - (\omega_0 + \mathbf{k}_0 \cdot \mathbf{v}_{E,\mathrm{av}})\,(t - t') \Bigr]. \tag{G.16}$$

We shall now calculate the function [Eq. (4.3)]

$$\Gamma_{12}(R_{\mathrm{av}}, t_{\mathrm{av}}; r, \tau) = \iint C_{12}(R_{\mathrm{av}}, z_{\mathrm{av}}, t_{\mathrm{av}}; r, \zeta, \tau)\, dz_{\mathrm{av}}\, d\zeta, \tag{G.17}$$

where $R_{\mathrm{av}} = (R + R')/2$, $z_{\mathrm{av}} = (z + z')/2$, $t_{\mathrm{av}} = (t + t')/2$, $r = R - R'$, $\zeta = z - z'$, and $\tau = t - t'$. We make the assumption, justified in §4.4, that the angles ϑ and ϑ' do not depend on the variable ζ. Their functional forms are, therefore, $\vartheta = \vartheta(R_{\mathrm{av}}, z_{\mathrm{av}}; r)$ and $\vartheta' = \vartheta(R_{\mathrm{av}}, z_{\mathrm{av}}; -r)$. The only remaining dependence of the integrand C_{12} on ζ is through the variable u_z in the coefficients $\mathcal{E}_2$ and $\mathcal{E}_3$. Thus, the integral over ζ in Eq. (G.17) has the form of the inverse Fourier transform of a Gaussian. The result can be expressed as follows:

$$\Gamma_{12}(R_{\mathrm{av}}, t_{\mathrm{av}}; r, \tau) = \int dz_{\mathrm{av}} \bigl\langle \tilde{n}^2(R_{\mathrm{av}}, z_{\mathrm{av}}, t_{\mathrm{av}}) \bigr\rangle \frac{\sqrt{\pi}\mathcal{L}_\rho\mathcal{L}_\theta}{\sqrt{2\mathcal{D}'}} F(\tau)$$
$$\times \exp\bigl[-i(\omega_0 - \mathbf{k}_0 \cdot \mathbf{v}_g)\tau\bigr] \mathcal{E}_1\mathcal{E}_4\mathcal{E}_5\mathcal{E}_6 + \text{c.c.}, \tag{G.18}$$

where

$$\mathcal{D}' = \mathcal{L}_\rho^2 (\cos^2\vartheta + \cos^2\vartheta') + \mathcal{L}_\theta^2 (\sin^2\vartheta + \sin^2\vartheta'), \tag{G.19}$$

$$\mathcal{E}_4 = \exp\left(-\frac{8\mathcal{D}}{\mathcal{D}'} q_z^2 \right), \tag{G.20}$$

$$\mathcal{E}_5 = \exp\left(-\frac{1}{128} \frac{u_R^2}{\mathcal{D}\mathcal{D}'} \Bigl\{ (\mathcal{L}_\rho^2 - \mathcal{L}_\theta^2)^2 \bigl[\sin(2\vartheta) - \sin(2\vartheta')\bigr]^2 + 16\, \mathcal{L}_\rho^2\mathcal{L}_\theta^2 \Bigr\} \right), \tag{G.21}$$

and

$$\mathcal{E}_6 = \exp\left[iu_R \left(q_R + q_z \frac{(\mathcal{L}_\rho^2 - \mathcal{L}_\theta^2)\sin(\vartheta + \vartheta')}{\mathcal{D}'} \right) \right]. \tag{G.22}$$

When $\vartheta = \vartheta'$, one finds $\mathcal{D} = \mathcal{L}_\rho^2 \mathcal{L}_\theta^2/16$ and $\mathcal{D}' = 2\mathcal{L}_R^2$, where

$$\mathcal{L}_R = \left(\mathcal{L}_\rho^2 \cos^2\vartheta + \mathcal{L}_\theta^2 \sin^2\vartheta\right)^{1/2}. \tag{G.23}$$

Also, $\mathbf{q} = \mathbf{k}_0$, $\mathcal{E}_1 = 1$, $\mathcal{E}_4 = \exp(-\mathcal{L}_z^2 k_{0,z}^2/4)$, $\mathcal{E}_5 = \exp(-u_R^2/\mathcal{L}_R^2)$, and $\mathcal{E}_6 = \exp(ik'_{0,R}u_R)$, where

$$\mathcal{L}_z = \left(\frac{\sin^2\vartheta}{\mathcal{L}_\rho^2} + \frac{\cos^2\vartheta}{\mathcal{L}_\theta^2}\right)^{-1/2}, \tag{G.24}$$

and

$$\begin{aligned} k'_{0,R} &= k_{0,R} + k_{0,z}\frac{(\mathcal{L}_\rho^2 - \mathcal{L}_\theta^2)\sin(2\vartheta)}{2\mathcal{L}_R^2} \\ &= \frac{k_{0,\rho}\,\mathcal{L}_\rho^2 \cos\vartheta - k_{0,\theta}\,\mathcal{L}_\theta^2 \sin\vartheta}{\mathcal{L}_R^2}. \end{aligned} \tag{G.25}$$

(Note that when $\mathcal{L}_\rho = \mathcal{L}_\theta$, one finds $k'_{0,R} = k_{0,R}$.) Hence, for $\vartheta = \vartheta'$, Eq. (G.18) simplifies to

$$\begin{aligned} \Gamma_{12}(R_{\rm av}, t_{\rm av}; r, \tau) = \int dz_{\rm av}\sqrt{\pi}\mathcal{L}_z \left\langle \tilde{n}^2(R_{\rm av}, z_{\rm av}, t_{\rm av})\right\rangle F(\tau) \exp\left(-\frac{\mathcal{L}_z^2 k_{0,z}^2}{4}\right) \\ \times \exp\left(-\frac{(r - \tau v_{T,R})^2}{\mathcal{L}_R^2}\right)\cos\left(rk'_{0,R} - \tau\Omega_{\rm eff}\right), \end{aligned} \tag{G.26}$$

where

$$\Omega_{\rm eff} = \omega_0 - \mathbf{k}_0 \cdot \mathbf{v}_g + k'_{0,R}\, v_{T,R}. \tag{G.27}$$

Bibliography

[1] K. Miyamoto, *Plasma Physics for Nuclear Fusion* (MIT Press, Cambridge, MA, 1976).

[2] J. Wesson, *Tokamaks* (Clarendon Press, Oxford, U.K., 1987).

[3] N. Fisch, Rev. Mod. Physics **59,** 175 (1987).

[4] J.L. Luxon and L.G. Davis, Fusion Technol. **8,** 441 (1985).

[5] R.D. Stambaugh for the DIII–D Team, General Atomics Report GA-A21840, Proceedings of the 15th International Conference on Plasma Physics and Controlled Nuclear Fusion Research, Sevilla, 1994 (to be published).

[6] F.L. Hinton and R.D. Hazeltine, Rev. Mod. Phys. **48,** 239 (1976).

[7] L.A. Artsimovich, Nucl. Fusion **12,** 215 (1972).

[8] J. Hugill, Nucl. Fusion **23,** 331 (1983).

[9] B.B. Kadomtsev and O.P. Pogutse, Nucl. Fusion **11,** 67 (1971).

[10] P.C. Liewer, Nucl. Fusion **25,** 543 (1985).

[11] B.A. Carreras, Plasma Phys. Control. Fusion **34,** 1825 (1992).

[12] S.V. Mirnov and I.B. Semenov, Sov. J. At. En. **30,** 1 (1971).

[13] S. von Goeler, W. Stodiek, and N. Sauthoff, Phys. Rev. Lett. **33,** 1201 (1974).

[14] R.W. Motley and W.P. Ernst, Phys. Fluids **18,** 922 (1975).

[15] E. Mazzucato, Phys. Rev. Lett. **36,** 792 (1976).

[16] C.M. Surko and R.E. Slusher, Phys. Rev. Lett. **37,** 1747 (1976).

[17] Equipe TFR, Proc. of 8th European Conf. on Controlled Fusion and Plasma Physics, Prague, 1977 (European Physical Society, Petit-Lancy, Switzerland), Vol. I, p. 2.

[18] E. Mazzucato, Phys. Rev. Lett. **48,** 1828 (1982).

[19] R.E. Slusher, C.M. Surko, J.F. Valley, T. Crowley, E. Mazzucato, and K. McGuire, Phys. Rev. Lett. **53,** 667 (1984).

[20] N. Bretz, P. Efthimion, J. Doane, and A. Kritz, Rev. Sci. Instrum. **59,** 1538 (1988).

[21] R.E. Slusher and C.M. Surko, Phys. Rev. Lett. **40,** 400 (1978).

[22] TFR Group and A. Truc, Plasma Phys. Contr. Fusion **26,** 1045 (1984).

[23] R.L. Watterson, R.E. Slusher, and C.M. Surko, Phys. Fluids **28,** 2857 (1985).

[24] A. Semet, A. Mase, W.A. Peebles, N.C. Luhmann, Jr., and S. Zweben, Phys. Rev. Lett. **45,** 445 (1980).

[25] T. Saito, Y. Hamada, T. Yamashita, M. Ikeda, M. Nakamura, and S. Tanaka, Nucl. Fusion **21,** 1005 (1981).

[26] H. Park, D.L. Brower, W.A. Peebles, N.C. Luhmann, R.L. Savage, and C.X. Yu, Rev. Sci. Instrum. **56,** 1055 (1985).

[27] R. Philipona, E.J. Doyle, N.C. Luhmann, Jr., W.A. Peebles, C.L. Rettig, R.J. Groebner, K.H. Burrell, P. Gohil, H. Matsumoto, and R.D. Stambaugh, Rev. Sci. Instrum. **61,** 3007 (1990).

[28] E. Holzhauer, G. Dodel, and ASDEX Team, Rev. Sci. Instrum. **61,** 2817 (1990).

[29] R.E. Slusher and C.M. Surko, Phys. Fluids **23,** 472 (1980).
[30] R. Nazikian and L.E. Sharp, Rev. Sci. Instrum. **58,** 2086 (1987).
[31] H. Weisen, Rev. Sci. Instrum. **59,** 1544 (1988).
[32] I.H. Hutchinson, *Principles of plasma diagnostics* (Cambridge University Press, Cambridge, 1987).
[33] S.J. Zweben, J. McChesney, and R.W. Gould, Nucl. Fusion **23,** 825 (1983).
[34] N.V. Ivanov, I.A. Kovan, and I.B. Semenov, Fiz. Plazmy **3,** 960 (1977) [Sov. J. Plasma Phys. **3,** 526 (1977)].
[35] C.W. Barnes and J.D. Strachan, Phys. Fluids **26,** 2668 (1983).
[36] B.A. Carreras, P.H. Diamond, M. Murakami, J.L. Dunlap, J.D. Bell, H.R. Hicks, J.A. Holmes, E.A. Lazarus, V.K. Pare, P. Similon, C.E. Thomas, and R.M. Wieland, Phys. Rev. Lett. **50,** 503 (1983).
[37] S.J. Zweben and R.J. Taylor, Nucl. Fusion **21,** 193 (1981).
[38] S.J. Zweben and R.W. Gould, Nucl. Fusion **25,** 171 (1985).
[39] Ch. P. Ritz, R.D. Bengtson, S.J. Levinson, and E.J. Powers, Phys. Fluids **27,** 2956 (1984).
[40] E. Mazzucato and R. Nazikian, Plasma Phys. Contr. Fusion **33,** 261 (1991).
[41] TFR Group, Plasma Phys. Control. Fusion **27,** 1299 (1985).
[42] E.J. Doyle, T. Lehecka, N.C. Luhmann, Jr., W.A. Peebles, R. Philipona, K.H. Burrell, R.J. Groebner, H. Matsumoto, T.H. Osborne, and the DIII–D Group, Rev. Sci. Instrum. **61,** 3017 (1990).
[43] E. Mazzucato and R. Nazikian, Proc. of 19th European Conf. on Controlled Fusion and Plasma Physics, Innsbruck, 1992 (European Physical Society, Petit-Lancy, Switzerland), Vol. II, p. 1055.
[44] A. Costley et al., Rev. Sci. Instrum. **61,** 3487 (1990).
[45] P. Cripwell, A.E. Costley, and A.E. Hubbard, Proc. of 16th European Conf. on Controlled Fusion and Plasma Physics, Venice, 1989 (European Physical Society, Petit-Lancy, Switzerland), Vol. I, p. 75.
[46] T.L. Rhodes, W.A. Peebles, and E.J. Doyle, Rev. Sci. Instrum. **63,** 4661 (1992).
[47] E. Mazzucato and R. Nazikian, Phys. Rev. Lett. **71,** 1840 (1993).
[48] J.H. Irby, S. Horne, I.H. Hutchinson, and P.C. Stek, Plasma Phys. Control. Fusion **35,** 601 (1993).
[49] R. Nazikian and E. Mazzucato, Rev. Sci. Instrum. **66,** 392 (1995).
[50] R.J. Fonck, P.A. Duperrex, and S.F. Paul, Rev. Sci. Instrum. **61,** 3487 (1990).
[51] R.J. Fonck, G. Cosby, R.D. Durst, S.F. Paul, N. Bretz, S. Scott, E. Synakowski, and G. Taylor, Phys. Rev. Lett. **70,** 3736 (1993).
[52] R.D. Durst, R.J. Fonck, T.A. Thorson, K. Tritz, C.M. Greenfield, and S.F. Paul, Bull. Am. Phys. Soc. **39,** 1647 (1994).
[53] D.M. Thomas, Rev. Sci. Instrum. **66,** 806 (1995).
[54] H. Evensen, D. Brouchous, D. Diebold, M. Doczy, R.J. Fonck, and D. Nolan, Rev. Sci. Instrum. **63,** 4928 (1992).
[55] R.D. Durst, E. A. Denhartog, R.J. Fonck, J.S. Kim, and Y. Karzhavin, Rev. Sci. Instrum. **66,** 842 (1995).

[56] T.A. Thorson, R.D. Durst, and R.J. Fonck, Rev. Sci. Instrum. **66,** 639 (1995).
[57] T.P. Crowley, P.M. Schoch, J.W. Heard, R.L. Hickock, and X. Yang, Nucl. Fusion **32,** 1295 (1992).
[58] G. Cima, C. Watts, and R.F. Gandy, Rev. Sci. Instrum. **66,** 798 (1995).
[59] R.J. Groebner, Phys. Fluids B **5,** 2343 (1993).
[60] F. Wagner, G. Becker, K. Behringer, D. Campbell, A. Eberhagen, W. Engelhardt, G. Fussmann, O. Gehre, J. Gernhardt, G. von Gierke, G. Haas, M. Huang, F. Karger, M. Keilhacker, O. Klüber, M. Kornherr, K. Lackner, G. Lisitano, G.G. Lister, H.M. Mayer, D. Meisel, E.R. Müller, H. Murrmann, H. Niedermeyer, W. Poschenrieder, H. Rapp, H. Röhr, F. Schneider, G. Siller, E. Speth, A. Stäbler, K.H. Steuer, G. Venus, O. Vollmer, and Z. Yü, Phys. Rev. Lett. **49,** 1408 (1982).
[61] K.H. Burrell, Plasma Phys. Control. Fusion **36,** A291 (1994).
[62] R.J. Taylor, M.L. Brown, B.D. Fried, H. Grote, J.R. Liberati, G.J. Morales, P. Pribyl, D. Darrow, and M. Ono, Phys. Rev. Lett. **63,** 2365 (1989).
[63] H. Biglari, P.H. Diamond, and P.W. Terry, Phys. Fluids B **2,** 1 (1990).
[64] G.L. Jackson, J. Winter, T.S. Taylor, K.H. Burrell, C.M. Greenfield, R.J. Groebner, T. Hodapp, K. Holtrop, E.A. Lazarus, L.L. Lao, S.I. Lippmann, T.H. Osborne, T.W. Petrie, J. Phillips, R. James, D.P. Schissel, E.J. Strait, A.D. Turnbull, W.P. West, and DIII–D Team, Phys. Rev. Lett. **67,** 3098 (1991).
[65] JET Team, Plasma Phys. and Control. Fusion **36,** A23 (1994).
[66] K.H. Burrell, M.E. Austin, T.N. Carlstrom, S. Coda, E.J. Doyle, P. Gohil, R.J. Groebner, J. Kim, R.J. La Haye, L.L. Lao, J. Lohr, R.A. Moyer, T.H. Osborne, W.A. Peebles, C.L. Rettig, T.L. Rhodes, and D.M. Thomas, Proceedings of the 15th International Conference on Plasma Physics and Controlled Nuclear Fusion Research, Sevilla, 1994 (International Atomic Energy Agency, Vienna, 1995), Vol. I, p. 221.
[67] P-H. Rebut et al., Fusion Engineering and Design **22,** 7 (1993).
[68] P.H. Diamond, V.B. Lebedev, Y.M. Liang, A.V. Gruzinov, I. Gruzinova, M. Medvedev, B.A. Carreras, D.E. Newman, L. Charlton, K.L. Sidikman, D.B. Batchelor, E.F. Jaeger, C.Y. Wang, G.G. Craddock, N. Mattor, T.S. Hahm, M. Ono, B. Leblanc, H. Biglari, F.Y. Gang, and D.J. Sigmar, Proceedings of the 15th International Conference on Plasma Physics and Controlled Nuclear Fusion Research, Sevilla, 1994 (to be published).
[69] E.J. Doyle, R.J. Groebner, K.H. Burrell, P. Gohil, T. Lehecka, N.C. Luhmann, Jr., H. Matsumoto, T.H. Osborne, W.A. Peebles, and R. Philipona, Phys. Fluids B **3,** 2300 (1991).
[70] S. Coda, M. Porkolab, and T.N. Carlstrom, Rev. Sci. Instrum. **63,** 4974 (1992).
[71] J.G. Watkins, J. Salmonson, R. Moyer, R. Doerner, R. Lehmer, L. Schmitz, and D.N. Hill, Rev. Sci. Instrum. **63,** 4728 (1992).
[72] G.A. Collins et al., Phys. Fluids **29,** 2260 (1986).
[73] T.H. Stix, Nucl. Fusion **15,** 737 (1975).
[74] A.S. Kaye, Plasma Phys. Control. Fusion **35,** A71 (1993).

[75] R.I. Pinsker, F.W. Baity, S.C. Chiu, J.S. deGrassie, C.B. Forest, R.H. Goulding, D.J. Hoffman, H. Ikezi, Y.R. Lin-Liu, T.C. Luce, C.C. Petty, M. Porkolab, R. Prater, J.P. Squire, D.W. Swain, and the DIII-D Group, Proc. of 21th European Conf. on Controlled Fusion and Plasma Physics, Montpellier, 1994 (European Physical Society, Petit-Lancy, Switzerland), Vol. III, p. 1118.
[76] M. Ono, Phys. Fluids B **5,** 241 (1993).
[77] Y. Takase, J.D. Moody, C.L. Fiore, F.S. McDermott, M. Porkolab, and J. Squire, Phys. Rev. Lett. **59,** 1201 (1987).
[78] H. Weisen, G. Borg, B. Joye, A.J. Knight, and J.B. Lister, Phys. Rev. Lett. **62,** 434 (1989).
[79] J.H. Lee, E.J. Doyle, N.C. Luhmann, Jr., W.A. Peebles, C.C. Petty, R.I. Pinsker, C.L. Rettig, and T.L. Rhodes, Rev. Sci. Instrum. **66,** 1225 (1995).
[80] M. Porkolab, Fusion Engineering and Design **12,** 93 (1990).
[81] R. Pinsker, M.J. Mayberry, M. Porkolab, and R. Prater, Proc. 8th Topical Conf. on RF Power in Plasmas, Irvine, CA (1989), p. 314.
[82] S. Coda and M. Porkolab, Rev. Sci. Instrum. **66,** 454 (1995).
[83] R. Nazikian and B. Grek, Rev. Sci. Instrum. **61,** 2899 (1990).
[84] S. Coda and M. Porkolab, Proc. of 21th European Conf. on Controlled Fusion and Plasma Physics, Montpellier, 1994 (European Physical Society, Petit-Lancy, Switzerland), Vol. I, p. 854.
[85] N.J. Peacock, D.C. Robinson, M.J. Forrest, and P.D. Wilcock, Nature **224,** 488 (1969).
[86] J. Sheffield, *Plasma scattering of electromagnetic radiation* (Academic Press, New York, 1975).
[87] D.E. Evans and J. Katzenstein, Rep. Prog. Phys. **32,** 207 (1969).
[88] D. Veron, in *Infrared and millimiter waves, Vol. 2* (ed. K.J. Button, Academic Press, New York, 1979).
[89] M.A. Heald and C.B. Wharton, *Plasma diagnostics with microwaves* (John Wiley & Sons, New York, 1965).
[90] M.E. Manso, Plasma Phys. Contr. Fusion **35,** B141 (1993).
[91] N.A. Krall and A.W. Trivelpiece, *Principles of Plasma Physics* (San Francisco Press, Inc., San Francisco, 1986).
[92] M. Born and E. Wolf, *Principles of optics* (Pergamon Press, Oxford, 1980).
[93] J.D. Jackson, *Classical Electrodynamics* (John Wiley & Sons, New York, 1975).
[94] L. Brillouin, Ann. de Physique **17,** 103 (1921).
[95] C.V. Raman and N.S.N. Nath, Proc. Ind. Acad. Sci. A **2,** 406, 413 (1935).
[96] W.R. Klein and W.D. Cook, IEEE Trans. Sonics Ultrasonics **SU-14,** 123 (1967).
[97] *Handbook of mathematical functions*, ed. M. Abramowitz and I.A. Stegun (National Bureau of Standards, Applied Math Series No. 55, Washington, DC, 1964).
[98] S.M. Rytov, Izv. Akad. Nauk SSSR, Ser. Fiz. **2,** 223 (1937).
[99] A.M. Gondhalekar, Ph.D. Thesis, Univ. of Manchester, 1968.
[100] J.W. Strohbehn, Proc. IEEE **56,** 1301 (1968).

[101] A. Ishimaru, *Wave propagation and scattering in random media* (Academic Press, New York, 1978).
[102] M. Slaney, A.C. Kak, and L.E. Larsen, IEEE Trans. Microwave Theory Tech. **MTT-32,** 860 (1984).
[103] J.W. Goodman, *Introduction to Fourier optics* (McGraw-Hill, San Francisco, 1968).
[104] A.E. Siegman, *Lasers* (University Science Books, Mill Valley, California, 1986).
[105] J. Howard and L.E. Sharp, Plasma Phys. Contr. Fusion **34,** 1133 (1992).
[106] D.E. Evans, M. von Hellermann, and E. Holzhauer, Plasma Phys. **24,** 819 (1982).
[107] J. Howard, Rev. Sci. Instrum. **61,** 1086 (1990).
[108] D.C. Robinson and R.E. King, Proc. of 3rd Int. Conf. on Plasma Physics and Controlled Fusion Research, Novosibirsk, 1990 (IAEA, Vienna, 1991), Vol. I, p. 263.
[109] W.H. Carter and E. Wolf, Opt. Commun. **67,** 85 (1988).
[110] R. Nazikian, Rev. Sci. Instrum. **61,** 3004 (1990).
[111] K.L. Bowles, Phys. Rev. Lett. **1,** 454 (1958).
[112] E.E. Salpeter, Phys. Rev. **120,** 1528 (1960).
[113] A.W. DeSilva, D.E. Evans, and M.J. Forrest, Nature **203,** 1321 (1964).
[114] P.F. Little and S.M. Hamberger, Nature **209,** 972 (1966).
[115] J.P. Baconnet, G. Cesari, A. Coudeville, and J.P. Watteau, Phys. Lett. A **29,** 19 (1969).
[116] S.A. Ramsden, R. Benesch, W.E.R. Davies, and P.K. John, I.E.E.E. J. Quantum Electronics (USA) **QE-2,** 267 (1966).
[117] C.M. Surko, R.E. Slusher, D.R. Moler, and M. Porkolab, Phys. Rev. Lett. **29,** 81 (1972).
[118] H. Rohr, Phys. Lett. A **25,** 167 (1967).
[119] H. Bohmer and M. Raether, Phys. Rev. Lett. **16,** 1145 (1966).
[120] D.E. Evans, E.J. Doyle, D. Frigione, M. von Hellermann, and A. Murdoch, Plasma Phys. **25,** 617 (1983).
[121] D. Veron, Opt. Commun. **10,** 95 (1974).
[122] C.A.J. Hugenholtz and B.J.H. Meddens, Rev. Sci. Instrum. **53,** 171 (1982).
[123] P.E. Young, D.P. Neikirk, P.P. Tong, D.B. Rutledge, and N.C. Luhmann, Rev. Sci. Instrum. **56,** 81 (1985).
[124] J. Howard, Rev. Sci. Instrum. **61,** 1086 (1990).
[125] L.E. Sharp, Plasma Phys. **25,** 781 (1983).
[126] W.A. Peebles, R.L. Savage, Jr., D.L. Brower, S.K. Kim, T. Lehecka, J. Howard, E.J. Doyle, and N.C. Luhmann, Jr., Int. J. Infrared Millimeter Waves **8,** 1355 (1987).
[127] F.C. Jahoda and G.A. Sawyer, in *Methods of experimental physics*, Vol. 9B (ed. R.H. Lovberg and H.R. Griem, Academic Press, New York, 1971).
[128] H.M. Presby and D. Finkelstein, Rev. Sci. Instrum. **38,** 1563 (1967).
[129] S.K. Kim, D.L. Brower, W.A. Peebles, and N.C. Luhmann, Jr., Phys. Rev. Lett. **60,** 577 (1988).

[130] J. Howard, W.A. Peebles, D.L. Brower, S.K. Kim, and N.C. Luhmann, Jr., Rev. Sci. Instrum. **61,** 2829 (1990).
[131] H. Weisen, Plasma Phys. Contr. Fusion **28,** 1147 (1986).
[132] E. Hecht, *Optics* (Addison-Wesley, Reading, 1987).
[133] A.H. Bennett, H. Jupnik, H. Osterberg, and O.W. Richards, *Phase microscopy* (John Wiley & Sons, New York, 1951).
[134] K. Bratuscheck, Z. Wiss. Mikroskopie **9,** 145 (1892).
[135] A.E. Conrady, J. Roy. Micr. Soc. **1905,** 150 (1905).
[136] J. Rheinberg, J. Roy. Micr. Soc. **1905,** 152 (1905).
[137] F. Zernike, Physica **1,** 689 (1934).
[138] F. Zernike, Mon. Not. Roy. Astr. Soc. **94,** 377 (1934).
[139] C.R. Burch, Mon. Not. Roy. Astr. Soc. **94,** 384 (1934).
[140] A. Köhler and W. Loos, Naturwiss. **29,** 49 (1941) [Textile Res. J. **17,** 82 (1947)].
[141] F. Zernike, Physica **9,** 686, 974 (1942).
[142] H. Weisen, *La méthode du contraste de phase appliquée à l'étude des fluctuations de densité dans le tokamak TCA,* Thesis No. 659, Ecole Polytechnique Fédérale de Lausanne (1986).
[143] H. Weisen, Ch. Hollenstein, and R. Behn, Plasma Phys. Contr. Fusion **30,** 293 (1988).
[144] K. Matsuo, K. Tanaka, K. Muraoka, and M. Akazaki, Jpn. J. Appl. Phys. **30,** 1102 (1991).
[145] K. Tanaka, K. Matsuo, S. Koda, M. Bowden, K. Muraoka, K. Kondo, T. Furukawa, F. Sano, H. Zushi, T. Mizuuchi, S. Besshou, H. Okada, K. Nagasaki, M. Wakatani, T. Obiki, and S. Sudo, J. Phys. Soc. Jpn. **62,** 3092 (1993).
[146] R. Chatterjee, G.A. Hallock, and M.L. Gartman, Rev. Sci. Instrum. **66,** 457 (1995).
[147] E. Lo, J. Wright, and R. Nazikian, Rev. Sci. Instrum. **66,** 1180 (1995).
[148] P.P. Zabreyko, A.I. Koshelev, M.A. Krasnosel'skii, S.G. Mikhlin, L.S. Rakovshchik, and V. Ya. Stet'senko, *Integral equations – a reference text* (Noordhoff International Publishing, Leyden, The Netherlands, 1975).
[149] *The infrared handbook*, ed. W.L. Wolfe and G.J. Zissis (prepared by the Environmental Research Institute of Michigan for the Office of Naval Research, Dept. of the Navy, Washington, DC, 1985).
[150] C.T. Elliott, *Infrared detectors,* in *Handbook on semiconductors, Vol. 4,* pp. 727-798 (ed. C. Hilsum, North-Holland, Amsterdam, 1981).
[151] R.L. Petritz, Proc. IRE **47,** 1459 (1959).
[152] H. Levinstein, Appl. Optics **4,** 639 (1965).
[153] K.M. van Vliet, Appl. Optics **6,** 1145 (1967).
[154] J.C. Slater and N.H. Frank, *Electromagnetism* (McGraw-Hill, New York, NY, 1969).
[155] I.S. Gradshteyn and I.M. Ryzhik, *Table of integrals, series, and products* (Academic Press, Orlando, 1980).

[156] J.L. Luxon for the DIII–D team, General Atomics Report GA-A21814, Proceedings of the 18th Symposium on Fusion Technology, Karlsruhe, Germany, 1994 (to be published).
[157] T.S. Taylor, H. St. John, A.D. Turnbull, Y.R. Lin-Liu, K.H. Burrell, V. Chan, M.S. Chu, J.R. Ferron, L.L. Lao, R.J. La Haye, E.A. Lazarus, R.L. Miller, P.A. Politzer, D.P. Schissel, and E.J. Strait, Plasma Phys. Control. Fusion **36,** B229 (1994).
[158] R. Prater, R.A. James, C.C. Petty, R.I. Pinsker, M. Porkolab, F.W. Baity, S.C. Chiu, J.S. deGrassie, R.H. Goulding, R.W. Harvey, D.J. Hoffman, H. Ikezi, H. Kawashima, Y.R. Lin-Liu, T.C. Luce, and V. Trukhin, Plasma Phys. Control. Fusion **35,** A53 (1993).
[159] J.R. Ferron and E.J. Strait, Rev. Sci. Instrum. **63,** 4789 (1992).
[160] R.D. Phelps and S. Coda, *Engineering and design of a CO_2 phase contrast interferometer system for DIII–D*, General Atomics Report GA-A21839, 1994.
[161] R.D. Phelps, *DIII–D in-vessel port cover and shutter assembly for the phase contrast interferometer*, General Atomics Report GA-A21532, 1994.
[162] W.J. Smith, *Modern Optical Engineering* (McGraw-Hill, New York, 1990).
[163] R.D. Dorf, *Modern Control Systems* (Addison-Wesley, Reading, 1989).
[164] H.M. James, N.B. Nichols, and R.S. Phillips, *Theory of Servomechanisms* (McGraw-Hill, New York, 1947).
[165] J.S. Bendat and A.G. Piersol, *Random Data* (John Wiley & Sons, New York, 1986).
[166] M.B. Priestley, *Non-linear and Non-stationary Time Series Analysis* (Academic Press, London, 1988).
[167] D.R. Brillinger, *Time Series: Data Analysis and Theory* (Holt, Rinehart and Winston, New York, 1975).
[168] K.H. Burrell, et al., Plasma Phys. Control. Fusion **31,** 1649 (1989).
[169] P.R. Bevington, *Data Reduction and Error Analysis for the Physical Sciences* (McGraw-Hill, New York, 1969).
[170] W.T. Eadie, D. Dryard, F.E. James, M. Roos, and B. Sadoulet, *Statistical Methods in Experimental Physics* (North-Holland, Amsterdam, 1971).
[171] P.E. Gill and G.F. Miller, J. Comput. **15,** 80 (1972).
[172] Y. Censor, SIAM Review **23,** 444 (1981).
[173] G.T. Herman and A. Lent, Math. Programming Stud. **9,** 15 (1978).
[174] G.T. Herman, A. Lent, and S.W. Rowland, J. Theoret. Biol. **42,** 1 (1973).
[175] J.M. Beall, Y.C. Kim, and E.J. Powers, J. Appl. Phys. **53,** 3933 (1982).
[176] L.L. Lao, J.R. Ferron, R.J. Groebner, W. Howl, H. St. John, E.J. Strait, and T.S. Taylor, Nucl. Fusion **30,** 1035 (1990).
[177] C.M. Surko and R.E. Slusher, Phys. Fluids **23,** 2425 (1980).
[178] D.N. Ghosh Roy, *Methods of Inverse Problems in Physics* (CRC Press, Boca Raton, 1991).
[179] R.S. Granetz and J.F. Camacho, Nucl. Fusion **25,** 727 (1985).
[180] D.E. Baldwin and A.N. Kaufman, Phys. Fluids **12,** 1526 (1969).

[181] Ch. P. Ritz, E.J. Powers, T.L. Rhodes, R.D. Bengtson, K.W. Gentle, Hong Lin, P.E. Phillips, A.J. Wootton, D.L. Brower, N.C. Luhmann, Jr., W.A. Peebles, P.M. Schoch, and R.L. Hickok, Rev. Sci. Instrum. **59,** 1739 (1988).
[182] S.J. Zweben and S.S. Medley, Phys. Fluids B **1,** 2058 (1989).
[183] D.O. Gough, Philos. Trans. R. Soc. London, Ser. A **313,** 27 (1984).
[184] A. Lazarian, Plasma Phys. Control. Fusion **36,** 1013 (1994).
[185] D.L. Brower, W.A. Peebles, and N.C. Luhmann, Jr., Nucl. Fusion **27,** 2055 (1987).
[186] V.N. Tsytovich, *An Introduction to the Theory of Plasma Turbulence* (Pergamon Press, Oxford, 1972).
[187] B.B. Kadomtsev, *Plasma Turbulence* (Academic Press, London, 1965).
[188] R. Philipona, E.J. Doyle, N.C. Luhmann, Jr., W.A. Peebles, C.L. Rettig, R.J. Groebner, K.H. Burrell, P. Gohil, H. Matsumoto, and R.D. Stambaugh, Phys. Fluids B **5,** 87 (1993).
[189] K.H. Burrell, E.J. Doyle, P. Gohil, R.J. Groebner, J. Kim, R.J. La Haye, L.L. Lao, R.A. Moyer, T.H. Osborne, W.A. Peebles, C.L. Rettig, T.H. Rhodes, and D.M. Thomas, Phys. Plasmas **1,** 1536 (1994).
[190] C.L. Rettig, E.J. Doyle, W.A. Peebles, K.H. Burrell, R.J. Groebner, T.H. Osborne, and N.C. Luhmann, Jr., Rev. Sci. Instrum. **66,** 848 (1995).
[191] J.P. Freidberg, *Ideal Magnetohydrodynamics* (Plenum Press, New York, 1987).
[192] J. Kim, K.H. Burrell, P. Gohil, R.J. Groebner, Y.-B. Kim, H.E. St. John, R.P. Seraydarian, and M.R. Wade, Phys. Rev. Lett. **72,** 2199 (1994).
[193] P. Gohil, K.H. Burrell, R.J. Groebner, J. Kim, and R.P. Seraydarian, Proc. of 21th European Conf. on Controlled Fusion and Plasma Physics, Montpellier, 1994 (European Physical Society, Petit-Lancy, Switzerland), Vol. II, p. 858.
[194] T.N.L. Patterson, Math. Comp. **22,** 847 (1968).
[195] R. Piessens, E. de Doncker-Kapenga, C. Überhuber, and D. Kahaner, *QUADPACK, A Subroutine Package for Automatic Integration* (Springer-Verlag, Berlin, 1983).
[196] J.D. Callen, Phys. Fluids B **4,** 2142 (1992).
[197] A.J. Wootton, et al., Phys. Fluids B **2,** 2879 (1990).
[198] S.E. Parker, et al., Phys. Plasmas **1,** 1461 (1994).
[199] *Flow visualization and image analysis* (ed. F.T.M. Nieuwstadt, Kluwer Academic Publishers, Dordrecht, The Netherlands, 1993).
[200] R.J. Adrian, in *New approaches and concepts in turbulence*, pp. 341–348 (ed. Th. Dracos and A. Tsinober, Birkhäuser Verlag, Basel, 1993).
[201] K.H. Burrell, T.N. Carlstrom, S. Coda, E.J. Doyle, P. Gohil, R.J. Groebner, J. Kim, R.A. Moyer, W.A. Peebles, C.L. Rettig, T. Rhodes, and D.M. Thomas, Plasma Phys. Control. Fusion **38,** 1313 (1996).
[202] R.E. Waltz, et al., Phys. Plasmas **2,** 2408 (1995).
[203] R. Jha, et al., Phys. Rev. Lett. **69,** 1375 (1992).
[204] R. Jha and Y.C. Saxena, Phys. Plasmas **3,** 2979 (1996).

[205] A.N. Kolmogorov, Dokl. Akad. Nauk SSSR **30,** 299 (1941) [Proc. R. Soc. Lond., Ser. A **434,** 9 (1991)].
[206] U. Frisch, *Turbulence* (Cambridge University Press, Cambridge, 1995).
[207] U. Frisch and S.A. Orszag, Phys. Today **43**(1), 24 (1990).
[208] C.M. Surko and R.E. Slusher, Science **221,** 817 (1983).
[209] J. Sheffield, Rev. Mod. Phys. **66,** 1015 (1994).
[210] L.L. Lao, et al., Phys. Plasmas **3,** 1951 (1996).
[211] M.C. Zarnstorff, et al., Bull. Am. Phys. Soc. **40,** 1747 (1995).
[212] N. Bretz, R. Nazikian, W. Bergin, M. Diesso, J. Felt, and M. McCarthy, Rev. Sci. Instrum. **61,** 3031 (1990).
[213] S.F. Paul, N. Bretz, R.D. Durst, R.J. Fonck, Y.J. Kim, E. Mazzucato, and R. Nazikian, Phys. Fluids B **4,** 2922 (1992).
[214] C.L. Rettig, et al., Phys. Fluids B **5,** 2428 (1993).
[215] M. Endler, Nucl. Fusion **35,** 1307 (1995).
[216] G. Tynan, et al., Plasma Phys. Control. Fusion **36,** A285 (1994).
[217] E. Holzhauer, et al., Plasma Phys. Control. Fusion **36,** A3 (1994).
[218] R. Moyer, et al., Phys. Plasmas **2,** 2397 (1995).
[219] H.Y.W. Tsui, K. Rypdal, Ch.P. Ritz, and A.J. Wootton, Phys. Rev. Lett. **70,** 2565 (1993).
[220] H.Y.W. Tsui, et al., Phys. Fluids B **5,** 1274 (1993).
[221] M.N. Rosenbluth and P.H. Rutherford, in *Fusion,* Vol. 1 (ed. E. Teller, Academic Press, New York, 1981).
[222] D.L. Brower, et al., Proc. of 10th Int. Conf. on Plasma Physics and Controlled Fusion Research, London, 1984 (IAEA, Vienna, 1985), Vol. I, p. 273.
[223] W.L. Rowan, et al., Nucl. Fusion **27,** 1105 (1987).
[224] R. Fonck, et al., Bull. Am. Phys. Soc. **38,** 1960 (1993).
[225] D.W. Ross, et al., Nucl. Fusion **31,** 1355 (1991).
[226] R.D. Durst, et al., Phys. Rev. Lett. **71,** 3135 (1993).
[227] S.J. Levinson, J.M. Beall, E.J. Powers, and R.D. Bengston, Nucl. Fusion **24,** 527 (1984).
[228] R.E. Slusher and C.M. Surko, Bull. Am. Phys. Soc. **28,** 1173 (1983).
[229] A.E. Costley, P. Cripwell, and T. Fukuda, Proc. of 19th European Conf. on Controlled Fusion and Plasma Physics, Innsbruck, 1992 (European Physical Society, Petit-Lancy, Switzerland), Vol. I, p. 199.
[230] R.J. Fonck, et al., Plasma Phys. Control. Fusion **34,** 1993 (1992).
[231] A.V. Filippas, et al., Bull. Am. Phys. Soc. **38,** 1952 (1993).
[232] P. Cripwell and A.E. Costley, Proc. of 18th European Conf. on Controlled Fusion and Plasma Physics, Berlin, 1991 (European Physical Society, Petit-Lancy, Switzerland), Vol. 14B, Part I, p. 17.
[233] T.L. Rhodes, et al., Bull. Am. Phys. Soc. **35,** 1975 (1990).
[234] L. Prandtl, Zs. angew. Math. Mech. **5,** 136 (1925).
[235] R.V. Bravenec, et al., Phys. Fluids B **4,** 2127 (1992).
[236] H.Y.W. Tsui, et al., Phys. Fluids B **5,** 2491 (1993).

[237] B. LaBombard and B. Lipschultz, Nucl. Fusion **27,** 81 (1987)
[238] E.J. Doyle, T. Rhodes, et al., Proceedings of the 14th International Conference on Plasma Physics and Controlled Nuclear Fusion Research, Würzburg, 1992 (IAEA, Vienna, 1993), vol. I, p. 235.
[239] D.E. Graessle, S.C. Prager, and R.N. Dexter, Phys. Rev. Lett. **62,** 535 (1989).
[240] C.K. Chui, *An introduction to wavelets* (Academic Press, Boston, 1992).
[241] R.A. Moyer, R. Lehmer, T.E. Evans, R.W. Conn, and L. Schmitz, Plasma Phys. Control. Fusion **38,** 1273 (1996).
[242] B.Ph. van Milligen, C. Hidalgo, and E. Sánchez, Phys. Rev. Lett. **74,** 395 (1995).
[243] B.Ph. van Milligen, et al., Phys. Plasmas **2,** 3017 (1995).
[244] F. Wagner and U. Stroth, Plasma Phys. Control. Fusion **35,** 1321 (1993).
[245] M. Greenwald and the ALCATOR C Group, Phys. Rev. Lett. **53,** 352 (1984).
[246] D.W. Swain, Nucl. Fusion **21,** 1409 (1981).
[247] L.L. Lao, et al., Phys. Rev. Lett. **70,** 3435 (1993).
[248] S.I. Braginskii, in *Review of Plasma Physics* (Consultants Bureau, New York, 1965), Vol. 1, p. 205.
[249] T.C. Luce, C.C. Petty, and J.C.M. de Haas, Phys. Rev. Lett. **68,** 52 (1992).
[250] N.J. Lopes Cardozo and J.C.M. deHaas, Nucl. Fusion **30,** 521 (1990).
[251] P.C. Efthimion, C.W. Barnes, M.G. Bell, H. Biglari, N. Bretz, P.H. Diamond, G. Hammett, W. Heidbrink, R. Hulse, D. Johnson, Y. Kusama, D. Mansfield, S.S. Medley, R. Nazikian, H. Park, A. Ramsey, G. Rewoldt, S.D. Scott, B.C. Stratton, E. Synakowski, W.M. Tang, G. Taylor, M.C. Zarnstorff, and S.J. Zweben, Phys. Fluids B **3,** 2315 (1991).
[252] B. Coppi, Comments Plasma Phys. Controlled Fusion **5,** 261 (1980).
[253] W.M. Manheimer and T.M. Antonsen, Jr., Phys. Fluids **22,** 957 (1979).
[254] H.P. Furth, Plasma Phys. Control. Fusion **28,** 1305 (1986).
[255] T.K. Kurki-Suonio, R.J. Groebner, and K.H. Burrell, Nucl. Fusion **32,** 133 (1992).
[256] J.G. Cordey, et al., Plasma Phys. Control. Fusion **36,** A267 (1994).
[257] T.E. Stringer, Nucl. Fusion **32,** 1421 (1992).
[258] J.D. Callen, Phys. Rev. Lett. **39,** 1540 (1977).
[259] G. Giruzzi, R.F. Steimle, and D.R. Roberts, Proc. of 22th European Conf. on Controlled Fusion and Plasma Physics, Bournemouth, 1995 (European Physical Society, Petit-Lancy, Switzerland), Vol. 19C, part 1, p. 850.
[260] J.D. Callen, B.A. Carreras, and R.D. Stambaugh, Phys. Today **45**(1), 34 (1992).
[261] C. Watts, et al., Phys. Plasmas **3,** 2013 (1996).
[262] Equipe TFR, Plasma Phys. **25,** 641 (1983).
[263] TFR Group and A. Truc, Nucl. Fusion **26,** 1303 (1986).
[264] Ch. P. Ritz, R.V. Bravenec, P.M. Schoch, R.D. Bengtston, J.A. Boedo, J.C. Forster, K.W. Gentle, Y. He, R.L. Hickock, Y.J. Kim, H. Lin, P.E. Phillips, T.L. Rhodes, W.L. Rowan, P.M. Valanju, and A.J. Wootton, Phys. Rev. Lett. **62,** 1844 (1989).
[265] R.A. Moyer, et al., Bull. Am. Phys. Soc. **40,** 1836 (1995).

[266] J.D. Bell, et al., Nucl. Fusion **24,** 997 (1984).
[267] C.C. Petty, T.C. Luce, et al., Phys. Rev. Lett. **74,** 1763 (1995).
[268] C.C. Petty, et al., Phys. Plasmas **2,** 2342 (1995).
[269] T.C. Luce, et al., Bull. Am. Phys. Soc. **40,** 1791 (1995).
[270] E.A. Lazarus, et al., Phys. Fluids B **4,** 3644 (1992).
[271] D.L. Hillis, et al., Proceedings of the 14th International Conference on Plasma Physics and Controlled Nuclear Fusion Research, Würzburg, 1992 (IAEA, Vienna, 1993), vol. I, p. 577.
[272] T.N. Carlstrom, Plasma Phys. Control. Fusion **38,** 1149 (1996).
[273] F. Wagner, et al., Phys. Rev. Lett. **53,** 1453 (1984).
[274] P. Gohil, K.H. Burrell, E.J. Doyle, R.J. Groebner, J.Kim, and R.P. Seraydarian, Nucl. Fusion **34,** 1057 (1994).
[275] ASDEX team, Nucl. Fusion **29,** 1959 (1989).
[276] K.H. Burrell, et al., Proceedings of the 13th International Conference on Plasma Physics and Controlled Nuclear Fusion Research, Washington, DC, 1990 (International Atomic Energy Agency, Vienna, 1991), Vol. I, p. 123.
[277] J.G. Watkins, et al., J. Nucl. Mater. **196–198,** 829 (1992).
[278] K.H. Burrell, T.N. Carlstrom, E.J. Doyle, D. Finkenthal, P. Gohil, R.J. Groebner, D.L. Hillis, J. Kim, H. Matsumoto, R.A. Moyer, T.H. Osborne, C.L. Rettig, W.A. Peebles, T.L. Rhodes, H. St. John, R.D. Stambaugh, M.R. Wade, and J.G. Watkins, Plasma Phys. Controlled Fusion **34,** 1859 (1992).
[279] G. Becker, et al., Nucl. Fusion **23,** 1293 (1983).
[280] T.K. Kurki-Suonio, et al., Nucl. Fusion **33,** 301 (1993).
[281] D.P. Schissel, K.H. Burrell, J.C. DeBoo, R.J. Groebner, A.G. Kellman, N. Ohyabu, T.H. Osborne, M. Shimada, R.T. Snider, R.D. Stambaugh, T.S. Taylor, and the DIII-D Research Team, Nucl. Fusion **29,** 185 (1989).
[282] R.J. Groebner, P. Gohil, K.H. Burrell, T.H. Osborne, R.P. Seraydarian, and H. St. John, Proc. of 16th European Conf. on Controlled Fusion and Plasma Physics, Venice, 1989 (European Physical Society, Petit-Lancy, Switzerland), Vol. I, p. 245.
[283] R.J. Groebner, K.H. Burrell, and R.P. Seraydarian, Phys. Rev. Lett. **64,** 3015 (1990).
[284] R.C. Isler, et al., Phys. Fluids B **4,** 2104 (1992).
[285] K. Ida, S. Hidekuma, M. Kojima, Y. Miura, S. Tsuji, K. Hoshino, M.Mori, N. Suzuki, T. Yamauchi, and the JFT-2M Group, Phys. Fluids B **4,** 2552 (1992).
[286] P. Gohil, et al., in Fusion Engineering (Proc. 14th IEEE/NPSS Symp. California, 1991), IEEE, New Jersey, Vol. 2, p. 1199 (1992).
[287] R. Weynants, R.J. Taylor, P.E. Vandenplas, F. Durodie, B. Schweer, D. Bora, T. Delvigne, J. Devos, K.H. Dippel, M. Gaigneaux, G. Giesen, Y.T. Lie, A.M. Messiaen, R. Moyer, U. Samm, R.P. Schorn, C. Strickelmann, R. Van Nieuwenhove, G. Van Oost, G.H. Wolf, and J.W. Yang, Proc. of 17th European Conf. on Controlled Fusion and Plasma Physics, Amsterdam, 1990 (European Physical Society, Petit-Lancy, Switzerland), Contributed papers, Vol. 14B, Part I, p. 287.

[288] O. Sakai, Y. Yasaka, and R. Itatani, Phys. Rev. Lett. **70,** 4071 (1993).
[289] R.R. Weynants, et al., Nucl. Fusion **32,** 837 (1992).
[290] T.N. Carlstrom, et al., Plasma Phys. Control. Fusion **36,** A147 (1994).
[291] T.N. Carlstrom and R.J. Groebner, Phys. Plasmas **3,** 1867 (1996).
[292] H. Zohm, Plasma Phys. Control. Fusion **38,** 105 (1996).
[293] G.L. Jackson and the DIII–D Team, J. Vac. Sci. Technol. A **10,** 1244 (1992).
[294] R.J. Groebner, T.N. Carlstrom, K.H. Burrell, P. Gohil, J. Kim, and G. Staebler, Plasma Phys. Control. Fusion **38,** 1249 (1996).
[295] T. Crowley and E. Mazzucato, Nucl. Fusion **25,** 507 (1985).
[296] T. Lehecka, E.J. Doyle, R. Philipona, N.C. Luhmann, Jr., and W.A. Peebles, Proc. of 16th European Conf. on Controlled Fusion and Plasma Physics, Venice, 1989 (European Physical Society, Petit-Lancy, Switzerland), Vol. I, p. 123.
[297] K.H. Burrell, et al., Phys. Rev. Lett. **59,** 1432 (1987).
[298] C.L. Rettig, et al., Nucl. Fusion **33,** 643 (1993).
[299] K.H. Burrell, T.N. Carlstrom, E.J. Doyle, P. Gohil, R.J. Groebner, T. Lehecka, N.C. Luhmann, Jr., H. Matsumoto, T.H. Osborne, W.A. Peebles, and R. Philipona, Phys. Fluids B **2,** 1405 (1990).
[300] T.L. Rhodes, et al., Nucl. Fusion **33,** 1787 (1993).
[301] T.L. Rhodes, et al., Bull. Am. Phys. Soc. **36,** 2474 (1991).
[302] Y. Koide, et al., Plasma Phys. Control. Fusion **36,** A195 (1994).
[303] G.L. Jackson, J. Winter, T.S. Taylor, C.M. Greenfield, K.H. Burrell, T.N. Carlstrom, J.C. DeBoo, E.J. Doyle, R.J. Groebner, L.L. Lao, C. Rettig, D.P. Schissel, E.J. Strait, and the DIII–D Research Team, Phys. Fluids B **4,** 2181 (1992).
[304] K.H. Burrell, T.H. Osborne, R.J. Groebner, C.L. Rettig, Proc. of 20th European Conf. on Controlled Fusion and Plasma Physics, Lisbon, 1993 (European Physical Society, Petit-Lancy, Switzerland), Vol. 17C, p. 27.
[305] T.H. Osborne, et al., Nucl. Fusion **35,** 23 (1995).
[306] M. Keilhacker, G. Becker, K. Bernhardi, A. Eberhagen, M. El Shaer, G. Fussmann, O. Gehre, J. Gernhardt, G. von Gierke, E. Glock, G. Haas, F. Karger, O. Klüber, M. Kornherr, K. Lackner, G. Lisitano, G.G. Lister, J. Massig, H.-M. Mayer, K. McCormick, D. Meisel, E. Meservey, E.R. Müller, H. Murmann, H. Niedermeyer, W. Poschenrieder, H. Rapp, H. Röhr, F. Schneider, G. Siller, P. Smeulders, F. Soldner, E. Speth, A. Stäbler, K. Steinmetz, K.-H. Steuer, Z. Szymanski, G. Venus, O. Vollmer, and F. Wagner, Plasma Phys. Controlled Fusion **26,** 49 (1984).
[307] P. Gohil, M. Ali Mahdavi, L. Lao, K.H. Burrell, M.S. Chu, J.C. DeBoo, C.L. Hsieh, N. Ohyabu, R.T. Snider, R.D. Stambaugh, and R.E. Stockdale, Phys. Rev. Lett. **61,** 1603 (1988).
[308] E.J. Doyle, T. Lehecka, N.C. Luhmann, Jr., W.A. Peebles, and R. Philipona, Proc. of 17th European Conf. on Controlled Fusion and Plasma Physics, Amsterdam, 1990 (European Physical Society, Petit-Lancy, Switzerland), Contributed papers, Vol. 14B, Part II, p. 203.
[309] T. Ozeki, et al., Nucl. Fusion **30,** 1425 (1990).

[310] J.M. Greene and M.S. Chance, Nucl. Fusion **21,** 453 (1981).
[311] H. Zohm, et al., Nucl. Fusion **32,** 489 (1992).
[312] E.J. Doyle, et al., Proc. of 18th European Conf. on Controlled Fusion and Plasma Physics, Berlin, 1991 (European Physical Society, Petit-Lancy, Switzerland), Vol. 15C, p. 285.
[313] H. Zohm, et al., Proc. of 19th European Conf. on Controlled Fusion and Plasma Physics, Innsbruck, 1992 (European Physical Society, Petit-Lancy, Switzerland), Vol. 16C, p. 243.
[314] G.T.A. Huysmans, et al., Proc. of 19th European Conf. on Controlled Fusion and Plasma Physics, Innsbruck, 1992 (European Physical Society, Petit-Lancy, Switzerland), Vol. 16C, p. 247.
[315] P.W. Terry and P.H. Diamond, in *Statistical physics and chaos in fusion plasmas* (eds. C.W. Horton, Jr., and L.E. Reichl, Wiley, New York, 1984).
[316] R.J. Groebner, M.E. Austin, K.H. Burrell, T.N. Carlstrom, S. Coda, E.J. Doyle, P. Gohil, J. Kim, R.J. La Haye, C.L. Hsieh, L.L. Lao, J. Lohr, R.A. Moyer, C.L. Rettig, T. Rhodes, G.M. Staebler, R.E. Stockdale, D.M. Thomas, and J.G. Watkins, Proceedings of the International Conference on Plasma Physics, Foz do Iguacu, Brazil, 1994 (American Institute of Physics, Woodbury, NY, 1995), AIP Conf. Proc. **345**, 74 (1995).
[317] P.H. Diamond, et al., submitted to Phys. Rev. Lett. (1996).
[318] R.J. La Haye, et al., Phys. Fluids B **4,** 2098 (1992).
[319] R.J. La Haye, R.J. Groebner, A.W. Hyatt, J.T. Scoville, Nucl. Fusion **33,** 349 (1993).
[320] S.P. Hirshman and D.J. Sigmar, Nucl. Fusion **21,** 1079 (1981).
[321] C.L. Rettig, Ph.D. Thesis, University of California, Los Angeles, 1993.
[322] J.L. Lumley, *Stochastic tools in turbulence* (Academic Press, New York, 1970).
[323] F. Ryter, et al., Plasma Phys. Control. Fusion **36,** A99 (1994).
[324] S. Coda, M. Porkolab, and K.H. Burrell, Proc. of 22th European Conf. on Controlled Fusion and Plasma Physics, Bournemouth, 1995 (European Physical Society, Petit-Lancy, Switzerland), Vol. 19C, part 1, p. I-297.
[325] S. Coda, M. Porkolab, K.H. Burrell, and T.N. Carlstrom, Proc. of 20th European Conf. on Controlled Fusion and Plasma Physics, Lisboa, Portugal, 1993 (European Physical Society, Petit-Lancy, Switzerland), Vol. 17C, p. III-1179.
[326] Kelvin, Lord (Sir W. Thomson), Phil. Mag. **24,** 342 (1887).
[327] O. Reynolds, Phil. Trans. R. Soc. London A **186,** 123 (1894).
[328] C.L.M.H. Navier, Mém. Acad. Roy. Sci. **6,** 389 (1823).
[329] T. Dracos, in *New approaches and concepts in turbulence*, p. 1 (ed. Th. Dracos and A. Tsinober, Birkhäuser Verlag, Basel, 1993).
[330] M.D. Kruskal and M. Schwartzschild, Proc. R. Soc. London Ser. A **223,** 348 (1954).
[331] B. Coppi, Phys. Rev. Lett. **39,** 939 (1977).
[332] F. Troyon, R. Gruber, H. Saurenmann, S. Semenzato, and S. Succi, Plasma Phys. **26,** 209 (1984).

[333] M. Porkolab, Phys. Lett. **22,** 427 (1966); **23,** 336(E) (1966).
[334] B. Coppi, M.N. Rosenbluth, and R.Z. Sagdeev, Phys. Fluids **10,** 582 (1967).
[335] M. Porkoláb, Nucl. Fusion **8,** 29 (1968).
[336] H. Biglari, et al., Proceedings of the 12th International Conference on Plasma Physics and Controlled Nuclear Fusion Research, Nice, 1988 (International Atomic Energy Agency, Vienna, 1989), Vol. 2, p. 261.
[337] R.Z. Sagdeev and A.A. Galeev, *Nonlinear Plasma Theory* (Benjamin, New York, NY, 1969).
[338] A. Hasegawa and K. Mima, Phys. Rev. Lett. **39,** 205 (1977).
[339] M. Camac, A.R. Kantrowitz, M.M. Litvak, R.M. Patrick, and H.E. Petschek, Nucl. Fusion, Suppl. Pt. 2, 423 (1962).
[340] W.E. Drummond and D. Pines, Nucl. Fusion, Suppl. Pt. 3, 1049 (1962).
[341] O. Madelung, *Introduction to Solid-State Theory* (Springer-Verlag, Heidelberg, 1978).
[342] J.A. Krommes, in *Basic plasma physics,* Vol. II (eds. A.A. Galeev and R.N. Sudan, North Holland, Amsterdam, 1984).
[343] R.H. Kraichnan and D. Montgomery, Rep. Prog. Phys. **43,** 547 (1980).
[344] T.H. Dupree, Phys. Fluids **15,** 334 (1972).
[345] R.H. Kraichnan, Phys. Rev. **109,** 1407 (1958).
[346] W.W. Lee, J. Comput. Phys. **72,** 243 (1987).
[347] B.I. Cohen, T.J. Williams, A.M. Dimits, and J.A. Byers, Phys. Fluids B **5,** 2967 (1995).
[348] S.E. Parker, et al., Phys. Plasmas **3,** 1959 (1996).
[349] H.E. Mynick and S.E. Parker, Phys. Plasmas **2,** 1217 (1995).
[350] H.E. Mynick and S.E. Parker, Phys. Plasmas **2,** 2231 (1995).
[351] M. Kotschenreuther, W. Dorland, M.A. Beer, and G.W. Hammett, Phys. Plasmas **2,** 2381 (1995).
[352] M.A. Beer, S.C. Cowley, and G.W. Hammett, Phys. Plasmas **2,** 2687 (1995).
[353] K. Thomsen, et al., Plasma Phys. Control. Fusion **36,** A243 (1994).
[354] A.M. Dimits and W.W. Lee, J. Comput. Phys. **107,** 309 (1993).
[355] G.W. Hammett and F.W. Perkins, Phys. Rev. Lett. **64,** 3019 (1990).
[356] M.A. Beer, Ph.D. Thesis, Princeton Unversity, 1994.
[357] B. Coppi and C. Spight, Phys. Rev. Lett. **41,** 551 (1978).
[358] J.F. Drake, P.N. Guzdar, and A.M. Dimits, Phys. Fluids B **3,** 1937 (1991).
[359] P.H. Diamond and H. Biglari, Phys. Rev. Lett. **65,** 2865 (1990).
[360] X. Garbet and R.E. Waltz, Phys. Plasmas **3,** 1898 (1996).
[361] H. Okuda and J.M. Dawson, Phys. Fluids **16,** 408 (1973).
[362] P.H. Diamond, Y.-M. Liang, B.A. Carreras, and P.W. Terry, Phys. Rev. Lett. **72,** 2565 (1994).
[363] W. Daughton and S. Migliuolo, Phys. Plasmas **3,** 3185 (1996).
[364] J. Drake, et al., Nucl. Fusion **32,** 1657 (1992).
[365] X.Q. Xu, R.H. Cohen, J.A. Crotinger, and A.I. Shestakov, Phys. Plasmas **2,** 686 (1995).

[366] R.H. Cohen and X. Xu, Phys. Plasmas **2,** 3374 (1995).
[367] X. Garbet, L. Laurent, J.-P. Roubin, and A. Samain, Nucl. Fusion **31,** 967 (1991).
[368] J.-N. Leboeuf, D.K. Lee, B.A. Carreras, et al., Phys. Fluids B **3,** 2291 (1991).
[369] A.S. Ware, P.H. Diamond, H. Biglari, B.A. Carreras, J.N. Leboeuf, and L.A. Charlton, Phys. Fluids B **4,** 877 (1992).
[370] A.S. Ware, P.W. Terry, P.H. Diamond, and B.A. Carreras, Plasma Phys. Control. Fusion **38,** 1343 (1996).
[371] B.A. Carreras, et al., Phys. Fluids B **5,** 1491 (1993).
[372] B.A. Carreras, V.E. Lynch, L. Garcia, and P.H. Diamond, Phys. Plasmas **2,** 2744 (1995).
[373] B.A. Carreras, C. Hidalgo, E. Sánchez, et al., Phys. Plasmas **3,** 2664 (1996).
[374] B.A. Carreras, D. Newman, V.E. Lynch, and P.H. Diamond, Phys. Plasmas **3,** 2903 (1996).
[375] J.G. Cordey, et al., Plasma Phys. Control. Fusion **37,** 773 (1995).
[376] A. Zeiler, D. Biskamp, J.F. Drake, and P.N. Guzdar, Phys. Plasmas **3,** 2951 (1996).
[377] W. Horton, G. Hu, and G. Laval, Phys. Plasmas **3,** 2912 (1996).
[378] H.P. Furth, J. Killeen, and M.N. Rosenbluth, Phys. Fluids **6,** 459 (1963).
[379] B.A. Carreras, P.W. Gaffney, and H.R. Hicks, Phys. Fluids **25,** 1231 (1982).
[380] N. Ohyabu, G.L. Jahns, R.D. Stambaugh, and E.J. Strait, Phys. Rev. Lett. **58,** 120 (1987).
[381] B.B. Kadomtsev and O.P. Pogutse, Rev. Plasma Phys. **5,** 249 (1970).
[382] T.H. Dupree, Phys. Fluids **9,** 1773 (1966).
[383] J.B. Taylor, H.R. Wilson, and J.W. Connor, Plasma Phys. Control. Fusion **38,** 243 (1996).
[384] N. Mattor and P.H. Diamond, Phys. Rev. Lett. **72,** 486 (1994).
[385] H.L. Berk, et al., Nucl. Fusion **33,** 263 (1993).
[386] W.M. Manheimer, J. Phys. (Paris) **40,** C7-269 (1979).
[387] H. Biglari, P.H. Diamond, and M.N. Rosenbluth, Phys. Fluids B **1,** 109 (1989).
[388] R.R. Dominguez and M.N. Rosenbluth, Nucl. Fusion **29,** 844 (1989).
[389] Y. Kishimoto, et al., Phys. Plasmas **3,** 1289 (1996).
[390] P.H. Diamond and T.S. Hahm, Phys. Plasmas **2,** 3640 (1995).
[391] P. Bak, C. Tang, and K. Wiesenfeld, Phys. Rev. Lett. **59,** 381 (1987).
[392] J.M. Carlson and J.S. Langer, Phys. Rev. Lett. **62,** 2632 (1989).
[393] T. Hwa and M. Kardar, Phys. Rev. A **45,** 7002 (1992).
[394] D.E. Newman, B.A. Carreras, P.H. Diamond, and T.S. Hahm, Phys. Plasmas **3,** 1858 (1996).
[395] S. Migliuolo and A.K. Sen, Phys. Fluids B **2,** 3047 (1990).
[396] B. Basu and B. Coppi, Phys. Fluids B **4,** 2817 (1992).
[397] J.Y. Kim, Y. Kishimoto, M. Wakatani, and T. Tajima, Phys. Plasmas **3,** 3689 (1996).
[398] A.B. Hassam, Comments Plasma Phys. Controlled Fusion **14,** 275 (1991).
[399] H.R. Strauss, Phys. Fluids B **4,** 3 (1992).

[400] T. Chiueh, P.W. Terry, P.H. Diamond, and J.E. Sedlak, Phys. Fluids **29,** 231 (1986).
[401] K.C. Shaing, G.S. Lee, B.A. Carreras, W.A. Houlberg, and E.J. Crume, Proceedings of the 12th International Conference on Plasma Physics and Controlled Nuclear Fusion Research, Nice, 1988 (International Atomic Energy Agency, Vienna, 1989), Vol. II, p. 13.
[402] H. Biglari, et al., Proceedings of the 13th International Conference on Plasma Physics and Controlled Nuclear Fusion Research, Washington, DC, 1990 (International Atomic Energy Agency, Vienna, 1991), Vol. II, p. 191.
[403] Ch. P. Ritz, H. Lin, T.L. Rhodes, and A.J. Wootton, Phys. Rev. Lett. **65,** 2543 (1990).
[404] S. Ohdachi, et al., Plasma Phys. Control. Fusion **36,** A201 (1994).
[405] K. Itoh and S.-I. Itoh, Plasma Phys. Control. Fusion **38,** 1 (1996).
[406] K.C. Shaing, E.C. Crume, Jr., and W.A. Houlberg, Phys. Fluids B **2,** 1492 (1990).
[407] J. Thompson, J. Atmospheric Sciences **27,** 1107 (1970).
[408] G.M. Staebler and R.R. Dominguez, Nucl. Fusion **31,** 1891 (1991).
[409] R.R. Dominguez and G.M. Staebler, Phys. Fluids B **5,** 3876 (1993).
[410] G.M. Staebler and R.R. Dominguez, Nucl. Fusion **33,** 77 (1993).
[411] P.N. Guzdar, J.F. Drake, et al., Phys. Fluids B **5,** 3712 (1993).
[412] M. Persson, Nucl. Fusion **31,** 382 (1991).
[413] B.A. Carreras, et al., Phys. Fluids B **4,** 3115 (1992).
[414] Y.Z. Zhang and S.M. Mahajan, Phys. Fluids B **4,** 1385 (1992).
[415] T.S. Hahm, Phys. Plasmas **1,** 2940 (1994).
[416] T.S. Hahm and K.H. Burrell, Phys. Plasmas **2,** 1648 (1995).
[417] T.S. Hahm and K.H. Burrell, Plasma Phys. Control. Fusion **38,** 1427 (1996).
[418] T.S. Hahm and K.H. Burrell, Phys. Plasmas **3,** 427 (1996).
[419] Y.B. Kim, P.H. Diamond, and R.J. Groebner, Phys. Fluids B **3,** 2050 (1991).
[420] R.D. Hazeltine, Phys. Fluids B **1,** 2031 (1989).
[421] K.C. Shaing, Phys. Fluids B **4,** 171 (1992).
[422] K.C. Shaing, et al., Plasma Phys. Control. Fusion **36,** A75 (1994).
[423] T.E. Stringer, Nucl. Fusion **33,** 1249 (1993).
[424] S.-I. Itoh and K. Itoh, Phys. Rev. Lett. **60,** 2276 (1988).
[425] S.-I. Itoh and K. Itoh, Nucl. Fusion **29,** 1031 (1989).
[426] S.-I. Itoh, et al., Plasma Phys. Control. Fusion **36,** A261 (1994).
[427] A.B. Hassam, T.M. Antonsen, J.F. Drake, and C.S. Liu, Phys. Rev. Lett. **66,** 309 (1991).
[428] S.-I. Itoh and K. Itoh, J. Phys. Soc. Jpn. **59,** 3815 (1990).
[429] A. Fukuyama, et al., Plasma Phys. Control. Fusion **36,** A159 (1994).
[430] D.R. McCarthy, J.F. Drake, P.N. Guzdar, and A.B. Hassam, Phys. Fluids B **5,** 1188 (1993).
[431] T.E. Stringer, Phys. Rev. Lett. **22,** 1770 (1969).
[432] A.B. Hassam, et al., Phys. Fluids B **5,** 2519 (1993).

[433] M. Tendler and V. Rozhansky, Comments Plasma Phys. Controlled Fusion **13,** 191 (1990).
[434] V. Rozhansky and M. Tendler, Phys. Fluids B **4,** 1626 (1992).
[435] F.L. Hinton, Phys. Fluids B **3,** 696 (1991).
[436] F.L. Hinton and G.M. Staebler, Phys. Fluids B **5,** 1281 (1993).
[437] G.M. Staebler, et al., Phys. Plasmas **1,** 909 (1994).
[438] B.A. Carreras, L. Garcia, and V.E. Lynch, Phys. Fluids B **3,** 1438 (1991).
[439] P.H. Diamond and Y.B. Kim, Phys. Fluids B **3,** 1626 (1991).
[440] J.F. Drake, J.M. Finn, P.N. Guzdar, V. Shapiro, V. Shevchenko, F. Waelbroeck, A.B. Hassam, C.S. Liu, and R. Sagdeev, Phys. Fluids B **4,** 488 (1992).
[441] J.F. Drake, A. Zeiler, and D. Biskamp, Phys. Rev. Lett. **75,** 4222 (1995).
[442] P.H. Diamond, V. Shapiro, V. Shevchenko, Y.-B. Kim, M.N. Rosenbluth, B.A. Carreras, K. Sidikman, V.E. Lynch, L. Garcia, P.W. Terry, and R.Z. Sagdeev, Proceedings of the 14th International Conference on Plasma Physics and Controlled Nuclear Fusion Research, Würzburg, 1992 (IAEA, Vienna, 1993), vol. II, p. 97.
[443] A.V. Gruzinov, P.H. Diamond, V.B. Lebedev, Phys. Plasmas **1,** 3148 (1994).
[444] B.A. Carreras, D. Newman, P.H. Diamond, and Y.-M. Liang, Phys. Plasmas **1,** 4014 (1994).
[445] P.H. Diamond, V.B. Lebedev, et al., Phys. Plasmas **2,** 3685 (1995).
[446] M. Isichenko and P.H. Diamond, Phys. Plasmas **2,** 2007 (1995).
[447] P.N. Guzdar and A.B. Hassam, Phys. Plasmas **3,** 3701 (1996).
[448] M. Medvedev and P.H. Diamond, Phys. Plasmas **2,** 727 (1995).
[449] V.B. Lebedev, et al., Phys. Plasmas **2,** 3345 (1995).
[450] K. Itoh, et al., Plasma Phys. Control. Fusion **37,** 707 (1995).
[451] R.E. Waltz, et al., Phys. Plasmas **1,** 2229 (1994).
[452] R.E. Waltz, et al., Proceedings of the U.S./Japan Workshop on Ion Temperature Gradient Driven Turbulent Transport (eds. W. Horton, M. Wakatani, and A. Wootton, American Institute of Physics, New York, 1994), p. 251.
[453] A. Hasegawa, C.G. Maclennan, and Y. Kodama, Phys. Fluids **22,** 2122 (1979).
[454] A. Hasegawa and M. Wakatani, Phys. Rev. Lett. **59,** 1581 (1987).
[455] G.P. Williams, J. Atmos. Sci. **35,** 1399 (1978).
[456] B. Coppi and F. Pegoraro, Nucl. Fusion **17,** 969 (1977).
[457] L. Garcia, et al., Bull. Am. Phys. Soc. **41,** 1398 (1996).
[458] X. Garbet, et al., Proc. of 19th European Conf. on Controlled Fusion and Plasma Physics, Innsbruck, 1992 (European Physical Society, Petit-Lancy, Switzerland), Vol. II, p. 1437.
[459] X. Garbet, L. Laurent, J.P. Roubin, and A. Samain, Proceedings of the 14th International Conference on Plasma Physics and Controlled Nuclear Fusion Research, Würzburg, 1992 (IAEA, Vienna, 1993), Vol. 2, p. 213.
[460] A.B. Hassam and R.M. Kurlsrud, Phys. Fluids **22,** 2097 (1979).
[461] C.Z. Cheng and H. Okuda, Nucl. Fusion **18,** 587 (1978).

[462] V.B. Lebedev, P.H. Diamond, V.D. Shapiro, and G.I. Soloviev, Phys. Plasmas **2,** 4420 (1995).
[463] F.Y. Gang, B.D. Scott, and P.H. Diamond, Phys. Fluids B **1,** 1331 (1989).
[464] A. Hasegawa and K. Mima, Phys. Fluids **21,** 87 (1978).
[465] P.W. Terry and P.H. Diamond, Phys. Fluids **28,** 1419 (1985).
[466] R.E. Waltz, Phys. Fluids **28,** 577 (1985).
[467] R.E. Waltz and R.R. Dominguez, Phys. Fluids **26,** 3338 (1983).
[468] M. Wakatani and A. Hasegawa, Phys. Fluids **27,** 611 (1984).
[469] P.W. Terry, P.H. Diamond, K.C. Shaing, L. Garcia, and B.A. Carreras, Phys. Fluids **29,** 2501 (1986).
[470] T.S. Hahm and W.M. Tang, Phys. Plasmas **3,** 242 (1996).
[471] M. Krämer and A. Carlson, Proc. of 16th European Conf. on Controlled Fusion and Plasma Physics, Venice, 1989 (European Physical Society, Petit-Lancy, Switzerland), Vol. III, p. 923.
[472] F.L. Hinton, Nucl. Fusion **25,** 1457 (1985).
[473] F.L. Hinton and G.M. Staebler, Nucl. Fusion **29,** 405 (1989).
[474] T. Sato and the Complexity Simulation Group, Phys. Plasmas **3,** 2135 (1996).
[475] S.G. Mikhlin, *Integral equations* (Pergamon Press, Oxford, 1957).
[476] A. Truc, A. Quéméneur, P. Hennequin, D. Grésillon, F. Gervais, C. Laviron, J. Olivain, S.K. Saha, and P. Devynck, Rev. Sci. Instrum. **63,** 3716 (1992).
[477] S. Kado et al., submitted to Jpn. J. Appl. Phys. (1995).
[478] K. Rypdal and F. Øynes, Phys. Lett. A **184,** 114 (1994).
[479] A.W. Lohmann and B. Wirnitzer, Proc. IEEE **72,** 889 (1984).
[480] Y.C. Kim and E.J. Powers, IEEE Trans. Plasma Sci. **7,** 120 (1979).
[481] T. Huld, et al., Phys. Fluids B **3,** 1609 (1991).